Integration of Ferroelectric and Piezoelectric Thin Films

Integration of Ferroelectric and Piezoelectric Thin Films

Concepts and Applications for Microsystems

Edited by
Emmanuel Defaÿ

iSTE WILEY

First published 2011 in Great Britain and the United States by ISTE Ltd and John Wiley & Sons, Inc.

Apart from any fair dealing for the purposes of research or private study, or criticism or review, as permitted under the Copyright, Designs and Patents Act 1988, this publication may only be reproduced, stored or transmitted, in any form or by any means, with the prior permission in writing of the publishers, or in the case of reprographic reproduction in accordance with the terms and licenses issued by the CLA. Enquiries concerning reproduction outside these terms should be sent to the publishers at the undermentioned address:

ISTE Ltd
27-37 St George's Road
London SW19 4EU
UK

www.iste.co.uk

John Wiley & Sons, Inc.
111 River Street
Hoboken, NJ 07030
USA

www.wiley.com

© ISTE Ltd 2011

The rights of Emmanuel Defaÿ to be identified as the author of this work have been asserted by him in accordance with the Copyright, Designs and Patents Act 1988.

Library of Congress Cataloging-in-Publication Data

Integration of ferroelectric and piezoelectric thin films: concepts and applications for microsystems / edited by Emmanuel Defaÿ.
p. cm.
Includes bibliographical references and index.
ISBN 978-1-84821-239-8
1. Piezoelectric devices--Materials. 2. Ferroelectric thin films. 3. Miniature electronic equipment--Materials. I. Defaÿ, Emmanuel.
TK7872.P54I58 2011
621.3815'2--dc22

2010048939

British Library Cataloguing-in-Publication Data
A CIP record for this book is available from the British Library
ISBN 978-1-84821-239-8

Printed and bound in Great Britain by CPI Antony Rowe, Chippenham and Eastbourne.

MIX
Paper from responsible sources
FSC
www.fsc.org
FSC® C013604

Table of Contents

Preface xiii
Emmanuel DEFAŸ

General Introduction xvii

Chapter 1. Dielectricity, Piezoelectricity, Pyroelectricity and Ferroelectricity 1
Emmanuel DEFAŸ

1.1. Crystal structure 1
1.1.1. Crystal = lattice + pattern 1
1.1.2. Seven primitive lattices – 14 Bravais lattices 4
1.1.3. Two-hundred and thirty space groups 5
1.1.4. Thirty-two point groups (or crystal classes) 5
1.1.5. Reticular planes 7
1.1.6. X-rays "see" crystals 8
1.2. Piezoelectricity, pyroelectricity and ferroelectricity definitions 9
1.3. Simplified examples. 10
1.3.1. Dielectric effect 10
1.3.2. Piezoelectric effect 12
1.3.3. Pyroelectric effect 13
1.3.4. Ferroelectric effect 14
1.3.5. Electrostrictive effect 15
1.4. Three typical structures: wurtzite, ilmenite and perovskite 16
1.4.1. Wurtzite structure. 16
1.4.2. Ilmenite structure 17
1.4.3. Perovskite structure. 18
1.5. Bibliography 23

Chapter 2. Thermodynamic Study: a Structural Approach 25
Emmanuel DEFAŸ

2.1. History. 25
2.2. Revisiting statistical thermodynamics 26
2.2.1. Introduction 26
2.2.2. Notion of equilibrium, statistical postulate 27
2.2.3. Numbers of accessible states of a system. 28
2.2.4. Energy variation – work and heat 31
2.2.5. Heat transfer: entropy and absolute temperature. 33
2.2.6. Thermal energy: heat transfer. 35
2.2.7. Quasistatic transformation with work and heat transfer 37
2.2.8. Example of a constant pressure and temperature experiment 39
2.3. State functions 41
2.4. Linear equations – piezoelectricity 44
2.5. Non linear equations – electrostriction. 47
2.6. Bibliography 48

Chapter 3. Ferroelectric-paraelectric Phase Transition Thermodynamic Modeling 49
Emmanuel DEFAŸ

3.1. Hypothesis on Gibbs' elastic energy 49
3.2. Second-order transition. 52
3.3. Effects of stresses 58
3.4. First-order transition 60
3.5. Conclusion 65
3.6. Bibliography 65

Chapter 4. Mechanical Formalism. 67
Emmanuel DEFAŸ

4.1. Introduction. 67
4.2. Hooke's law 67
4.3. Definitions of local strains 69
4.3.1. Local strains in small strains hypothesis 69
4.3.2. Meaning of matrix $\overline{\overline{S}}$. 75
4.4. Definition of local strains 77
4.4.1. The strain tensor 77
4.4.2. Physical meaning of T_{ij} 81
4.4.3. Equations of motion in a deformable solid 82
4.5. Stress-strain relation. 83
4.5.1. Hooke's generalized law. 83
4.5.2. Dynamic relation 84
4.6. Elastic energy density. 86

4.6.1. Expression of elastic energy density 86
4.6.2. Symmetry of the elasticity tensor 88
4.7. Expression of the elasticity tensor as a function of elements of symmetry 89
4.8. Bibliography 93

Chapter 5. Dielectric Formalism 95
Emmanuel DEFAŸ

5.1. Introduction 95
5.2. The dielectric effect seen by Faraday 95
5.3. Electric polarization and displacement 99
5.4. The dielectric constant 104
5.5. The local field in dielectrics: polarization catastrophe 105
5.6. Dielectric relaxation 109
5.6.1. The various relaxations 109
5.6.2. Kramers-Kronig relations 112
5.7. Electric energy density 115
5.8. Bibliography 117

Chapter 6. Piezoelectric Formalism 119
Emmanuel DEFAŸ and Mathieu PIJOLAT

6.1. Thermodynamic equations 119
6.2. Reducing coefficients using crystal symmetry 121
6.2.1. Example of a calculation: point group *3m* 122
6.3. One-dimensional microscopic model 126
6.4. Electromechanical coupling coefficient 130
6.5. Piezoelectric coefficients of key materials 134
6.6. Calculating coupling as a function of crystal orientation 136
6.7. Piezoelectric coefficients in the case of ferroelectric materials 138
6.8. Relation between piezoelectric formalism and matter 139
6.9. Bibliography 141

Chapter 7. Acoustic Formalism 143
Alexandre REINHARDT

7.1. Propagation of bulk waves 143
7.1.1. Propagation of bulk waves in an elastic medium 143
7.1.2. Elastic wave propagation in a piezoelectric medium 153
7.2. Bulk wave resonator 163
7.2.1. Piezoelectric plate vibrations 163
7.2.2. Plate delimited by arbitrary acoustic impedance media 171
7.2.3. Bimorph plate 173

7.2.4. Piezoelectric plate between two electrodes 176
7.2.5. Equivalent electric circuit 181
7.3. Bulk acoustic waves filter 185
7.4. Bibliography 190

Chapter 8. Electrostrictive Formalism 191
Emmanuel DEFAŸ

8.1. Foundations of electrostriction 191
8.2. Thermodynamic model of electrostriction – case of the resonator . . . 192
8.3. The electrostriction tensor 195
8.4. Microscopic model of electrostriction 197
8.4.1. One-dimensional model 197
8.4.2. Origin of spontaneous polarization in perovskite crystals 199
8.5. Electrostrictive resonator 202
8.6. Bibliography 206

Chapter 9. Electric Characterization 207
Emmanuel DEFAŸ, Gwenaël LE RHUN and Emilien BOUYSSOU

9.1. Static piezoelectric characterization of thin films 207
9.1.1. Notion of effective coefficients. 207
9.1.2. Piezoelectric characterization of coefficient e_{31eff} 208
9.1.3. Model 210
9.1.4. Example of characterization: PZT films 213
9.2. Piezoelectric and atomic force microscopy 215
9.2.1. Atomic force microscope 215
9.2.2. Piezoresponse force microscope 218
9.3. Ferroelectric measurement 225
9.3.1. Sawyer-Tower circuit 227
9.3.2. Virtual ground circuit 229
9.4. Dielectric measurement. 232
9.5. Leakage current in metal/insulator/metal structures 236
9.5.1. Metal/insulator contact: definitions 236
9.5.2. Conduction mechanisms limited by the interfaces 240
9.5.3. Bulk-limited conduction mechanisms 243
9.6. Bibliography 245

Chapter 10. Piezoelectric Resonators and Filters 249
Alexandre REINHARDT and Christophe BILLARD

10.1. Acoustic resonators: principle and history 249
10.1.1. Quartz resonators 249
10.1.2. High-frequency operation of resonators 251

10.1.3. Perfecting FBAR and SMR resonators 256
10.2. BAW technology 269
10.2.1. Introduction 269
10.2.2. BAW filter topology 270
10.2.3. Parameters of the BAW resonator and their impact on filter response 272
10.2.4. Examples of realizations 280
10.3. CRF technology 283
10.3.1. Introduction 283
10.3.2. Operating principles of CRF filters 283
10.3.3. Example of implementations 287
10.4. Bibliography 291

Chapter 11. High Overtone Bulk Acoustic Resonator (HBAR) 297
Mathieu PIJOLAT, Chrystel DEGUET and Sylvain BALLANDRAS

11.1. About HBAR 297
11.1.1. Generalities 298
11.1.2. Principle 298
11.1.3. Description of the spectrum 299
11.2. Technology 302
11.2.1. Technological constraints 302
11.2.2. Choice of materials 303
11.2.3. Geometry of resonators 304
11.3. Examples of implementations 305
11.3.1. LNO on LNO 305
11.3.2. Validation of parameter extractions: LNO on HBAR/FBAR Si 309
11.4. Conclusions about HBAR 312
11.5. Bibliography 313

Chapter 12. Electrostrictive Resonators 315
Alexandre VOLATIER, Brice IVIRA, Christophe ZINCK, Nizar BEN HASSINE and Emmanuel DEFAŸ

12.1. Introduction 315
12.2. State of the art 316
12.2.1. Introduction 316
12.2.2. Formalism of the electrostrictive resonator 317
12.3. Experimental implementations 326
12.3.1. 70/30 BST resonator without acoustic insulation 326
12.3.2. STO resonator on Bragg mirror 333
12.3.3. BST resonator on an acoustic Bragg mirror 338
12.3.4. BST resonator on a membrane 340

12.4. Simulation of a filter with electrostrictive resonators 341
12.5. Status of perovskite electrostrictive resonators 342
12.6. PZT-based tunable frequency ferroelectric acoustic resonator 344
12.6.1. Introduction 344
12.6.2. Technology 345
12.6.3. RF characterization and discussion 346
12.7. Nonlinear effect in piezoelectric AlN 348
12.7.1. Introduction 348
12.7.2. Piezoelectric-electrostrictive phenomenological model 349
12.7.3. Application: AlN resonator on a Bragg mirror 351
12.7.4. Conclusion with nonlinear AlN 354
12.8. Conclusion with electrostriction 354
12.9. Bibliography 355

Chapter 13. Thin Film Piezoelectric Transducers 357
Matthieu CUEFF, Patrice REY, Fabien FILHOL and Emmanuel DEFAŸ

13.1. Introduction 357
13.2. State of the art 358
13.3. Resonant membranes 361
13.3.1. Technology of PZT resonant membranes 361
13.3.2. Frequency characterization of membranes 363
13.3.3. A resonant pressure sensor 364
13.3.4. Conclusion on the study of Si/PZT resonant membranes 366
13.4. Resonant micromirror 366
13.4.1. Introduction 366
13.4.2. Technology and design of the resonant micromirror 366
13.4.3. Characterization of the devices 369
13.4.4. Conclusion about micromirrors 371
13.5. Piezoelectric micro-switch 371
13.5.1. Interest in piezoelectric films for micro-switches 371
13.5.2. General description of the component 373
13.5.3. Analytical development of the bimorph beam as actuator of the micro-switch 374
13.5.4. Stack chosen for the piezoelectric actuator 383
13.5.5. Multilayer analytical model 384
13.5.6. Effect of temperature compensation 386
13.5.7. The piezoelectric film 387
13.5.8. Releasing the membrane 387
13.5.9. Electrical characterizations 388

13.6. Sign of piezoelectric coefficients 391
13.7. Bibliography 394

List of Authors 397

Index 399

Preface

The idea of this book came about in 2008 following a discussion with Michel Bruel about the works on materials of the perovskite family carried out at the CEA-LETI, the Electronics and Information Technology Laboratory of the French Atomic Energy Commission, at the Minatec campus in Grenoble, France. It quickly occurred to us that we should gather the studies concerning this field we have been involved in since the beginning of the 2000s in one document. Upon reflection, it seemed interesting to extend the theme of the book to piezoelectric materials in order to include the thematics of acoustic resonators, about which we also had some excellent realizations. Several people also came to assist in writing this book, taking care of a section or a chapter corresponding to their field of speciality.

In this book about piezoelectric thin films, I wanted to cover the rather exhaustive theoretical bases, associating them with state-of-the-art applications in 2010. Of course, there are reference books on piezoelectric materials, such as the piezoelectricity standards (*IEEE Standard on Piezoelectricity, ANSI/IEEE Std 176-1987*) or Royer and Dieulessaint's famous book (*Ondes Élastiques dans les Solides* [*Elastic Waves in Solids*], Masson, Paris, 1974). There are also very good books on the ferroelectric phenomenon, such as Lines and Glass (M.E Lines, A.M. Glass, *Principles and Applications of Ferroelectrics and Related Materials*, Clarendon Press, Oxford, 1977) or more recently Dragan Damjanovic's article (D. Damjanovic, "Ferroelectric, dielectric and piezoelectric properties of ferroelectric thin films and ceramics", *Rep. Prog. Phys.*, Vol. 61, pp. 1267-1324, 1998).

To me it seemed worth gathering together the two pillars necessary for a deep understanding of piezoelectric films, while at the same time adding other essential notions:

– the stress-strain mechanical formalism;

– the dielectric formalism; and also

– an important issue of acoustic wave propagation.

The notion of thermodynamic equilibrium is also largely detailed in order to properly stress the foundations of piezoelectricity that originate from the energy exchange between the electrical and mechanical field. The nonlinear phenomenon of electrostriction, essential for describing perovskite materials like PZT, is also described.

The typical reader of this book is a student, researcher or engineer wishing to approach the field of piezoelectricity from the basics. He or she can clearly start reading from any chapter, as they are largely independent. Nevertheless, we took special care to see to it that the notations chosen are compatible between chapters, to ensure a coherent overall reading. Indeed, the different fields necessary for describing piezoelectricity generally present identical notations that can cause confusion. I hope that this book will bring some pertinent information to the interested reader through piezoelectric microsystems, and that he or she will share part of the pleasure we had in writing it.

To conclude, I would like to thank the people who participated in developing this book, either through direct contribution or indirect assistance. I will start with Michel Bruel, one of the figureheads of LETI, and Marc Aïd, the person in charge of the radiofrequency components laboratory, and Claude Massit then Buno Mourey, successively in charge of the microsystems department of LETI, who were a constant support throughout these few months of work. Next I would like to thank Alexandre Reinhardt (acoustics) and Gwenaël LeRhun (electrical characterization), two of my closest colleagues, who were the first to agree to participate in this book. Emilien Bouyssou of STMicroelectronics in Tours (electrical measurements, accuracy) also quickly agreed, benefiting us with information on the industrial approach for integrating PZT in silicon technology. Christophe Billard (RF filters), Mathieu Pijolat, Chrystel Deguet and Sylvain Ballandras (HBAR), Matthieu Cueff, Fabien Filhol and Patrice Rey (actuators), Brice Ivira, Nizar Ben Hassine and Alexandre Volatier (electrostriction) and Christophe Zinck (ferroelectric resonators) were of great assistance for contributions in their fields. I must also thank Sylvain Ballandras (Franche-Comté Electronics, Mechanics, Thermal transfers, Optics, Science and Technology – Femto-ST), Paul Muralt (Swiss Federal Institute of Technology Lausanne – EPFL), Brahim Dkhil (Centrale Paris) and Jens Kreisel (Grenoble Institute of Technology – INPG) for their constant support and the positive energy they were able to and still can communicate to me. I would also like to thank José Olivarès for the many discussions we had, especially on the subject of statistical thermodynamics.

This book is also the result of two excellent projects that we produced with Pascal Ancey (STMicroelectronics in Crolles) and Lianjiu Liu (Freescale): thanks go to them.

I would also like to thank all the people who contributed to producing the mechanisms displayed. Although it is impossible to name them all, I am thinking of François Perruchot, Aurélien Suhm, Guy Parat, Aude Lefèvre, Patrice Gergaud, Denis Pellissier, Amy N'Hary, Laurent Figuière, François Chapuis, Xiaohong Zhu, Sylvia Sanchez, Julie Abergel, David Pinceau, David Wolozan, Fabien Dumont, Grégory Caruyer, Patrick Emery, Julie Guillan, Benoit Guigues, Frédéric Domingue, Patrick Lassagne, Pierre-Antoine Deléan and Marie Thérèse Delaye, as well as LETI's silicon platform.

Finally, my thoughts go to my wife and my two daughters for their perpetual patience and their support.

Emmanuel DEFAŸ

January 2011

General Introduction

The piezoelectric effect was discovered by the Curie brothers in 1880. Since then, many applications have come into being: time base, precision actuators, sonar, echographic probe and, more recently, radio-frequency filters for mobile phones. This field is set to be further developed because of the growing need for actuators and sensors of all sorts, especially for communication and healthcare. Piezoelectricity is very well adapted to these fields as it links the electrical or electronic world to the mechanical world in a linear manner. This is why mastering good piezoelectric materials is fundamental for developing these applications. In the microsystems framework, great advances in thin-film piezoelectric materials have been achieved since the middle of the 1990s. Lead zirconate titanate ($Pb(Zr,Ti)O_3$ called PZT) and aluminum nitride (AlN) are, today, the spearheads of these thin-film materials, as we will see in detail in this book.

This book begins with a chapter that endeavors to specify the microscopic properties of dielectrics: ferroelectricity, piezoelectricity, pyroelectricity and electrostriction. Certain notions of crystallography are taken up, since the crystalline nature of matter produces a good part of these properties.

Chapter 2 is devoted to thermodynamic notions indispensable for the precise description of the state of equilibrium and energy exchanges. It is this approach that enables us to define electromechanical coupling.

Next, we take on the description of paraelectric-ferroelectric phase transition, which is very useful for describing the piezoelectrics of ferroelectric nature, such as those of the perovskite family (PZT, for example).

Chapter 4 is dedicated to the study of stress-strain relations, indispensable for putting the piezoelectric effect in the form of an equation.

Chapter 5 describes dielectric materials by adding stresses to the main fields, such as electric displacement. The notion of dielectric relaxation is also taken up. Once these bases have been expanded on, we go into detail about the piezoelectric formalism in a macroscopic but also microscopic way, even if the latter is less useful for applications in Chapter 6.

Chapter 7 is a rather detailed exposition on the acoustic formalism adapted to piezoelectric films. Acoustic filters and the main applications of acoustic resonators are also approached from an analytical angle.

Chapter 8 is dedicated to electrostrictive nonlinear effect, less well-known, but very important for describing the piezoelectric linear effect of perovskites and increasingly used in applications.

The next chapter endeavors to describe the principle means of electric characterizations of these piezoelectric films: macroscopic then local piezoelectric measurements, ferroelectric, dielectric measurement and finally, leakage current measurement.

Next we move on to the application chapters. Chapter 10 is reserved for resonators and filters that use piezoelectric thin films. This application is currently the most beautiful industrial piezoelectric film success. Chapter 11, most of all, is devoted to electrostrictive thin films used for variable frequency resonators. Although this solution is not yet industrially exploited, it constitutes a real alternative for the future. Chapter 12 discusses electrostrictive resonators. The last chapter describes some thin-film piezoelectric transducers, after having given a few figures of merit essential for choosing materials depending on the function of the target applications.

Chapter 1

Dielectricity, Piezoelectricity, Pyroelectricity and Ferroelectricity

1.1. Crystal structure

1.1.1. *Crystal = lattice + pattern*

The notions of piezoelectricity, pyroelectricity and ferroelectricity are closely linked to the crystalline nature of materials. Indeed, the study of the crystal structure of materials enables us to see what arrangements of atoms are susceptible to showing one or other property. We will discuss some core notions of crystallography in order to bring out the main conclusions that can be drawn from this approach [ESN 94].

A crystal is defined as follows: the atoms that make up a crystal form a pattern that periodically repeats itself in the three spatial dimensions. A crystal is an object whose dimensions are large compared to the atoms that constitute it. The periodicity of its structure results in the properties of the crystal being identical, depending on the dimensions and planes given, no matter the initial reference point. This is what we call *translational symmetry*. This notion is important as it will enable us to implement symmetry operations that will be used to classify the crystals.

As a simple example of a periodicity-based property, let us cite silicon cleavage, which is always split in the same directions, or the hexagonal structure of quartz crystals that is visible to the naked eye.

Chapter written by Emmanuel DEFAŸ.

The notions that constitute the foundations of the study of crystallography are the lattice and pattern of a crystal. The lattice is made up of points called nodes that periodically repeat themselves in space, but the lattice does not contain any atoms. The atoms of the crystal belong to the pattern that is attached to the lattice node.

Figure 1.1 is a diagram representing a crystal with its lattice and its pattern.

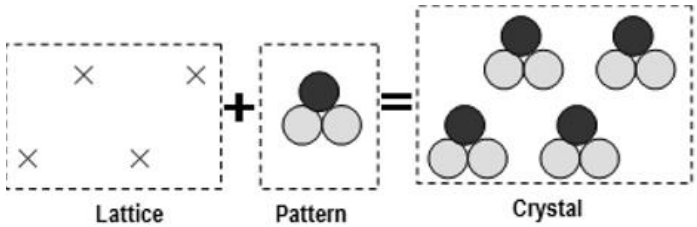

Figure 1.1. *Lattice + pattern = crystal*

To help with comprehension, it is useful to start with a classic example: sodium chloride (*NaCl*). Crystal packing is made up of a regular succession Na^+ and Cl^- ions in the three spatial dimensions, as represented in Figure 1.2.

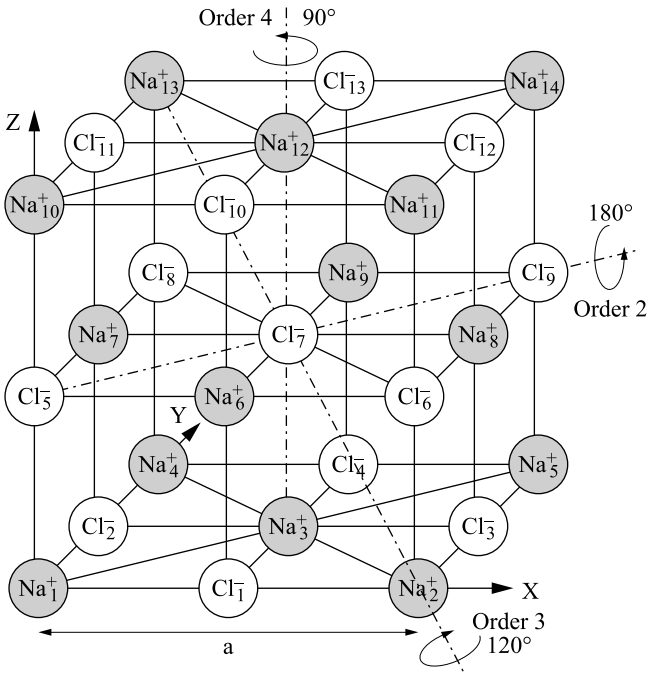

Figure 1.2. *Crystal packing of NaCl*

More specifically, we can say that the *NaCl* consists of the spatial packing of cubes, such as *C* (Na^+_1, Na^+_2, Na^+_5, Na^+_4, Na^+_{10}, Na^+_{11}, Na^+_{14}, Na^+_{13}). On the other hand, it is not possible from cube (Na^+_1, Cl^-_1, Na^+_3, Cl^-_2, Cl^-_5, Na^+_6, Cl^-_7, Na^+_7). Packing can be initiated from several equal points of the lattice. In this case, they are points on the corners of the cube *C* (Na^+_1, Na^+_2, Na^+_5…) or those that are in the center of the faces of *C* (Na^+_3, Na^+_6, Na^+_7…).

It is these nodes that constitute the *lattice* called the *translational lattice*. A pattern is attached to each node. Here, the latter is made up of a pair of ions Na^+ and Cl^-. For example, Na^+_1-Cl^-_1 or Na^+_1-Cl^-_2 or even Na^+_1-Cl^-_5. The structure of *NaCl* can be described as two interpenetrating face-centered cubic lattices with a gap between them of a distance *a/2* in one of the three spatial dimensions, depending on the pattern chosen (*x* axis if Na^+_1-Cl^-_1).

This description is not the most compact possible, although it is the simplest. The face-centered cubic lattice constitutes a *multiple lattice*.

This means that several patterns are contained in one lattice. There are four of them here (each corner node counts for *1/8* and each node on a face counts for *1/2*). Nevertheless, it is possible to define, for each packing, an *elementary lattice* that contains only one pattern.

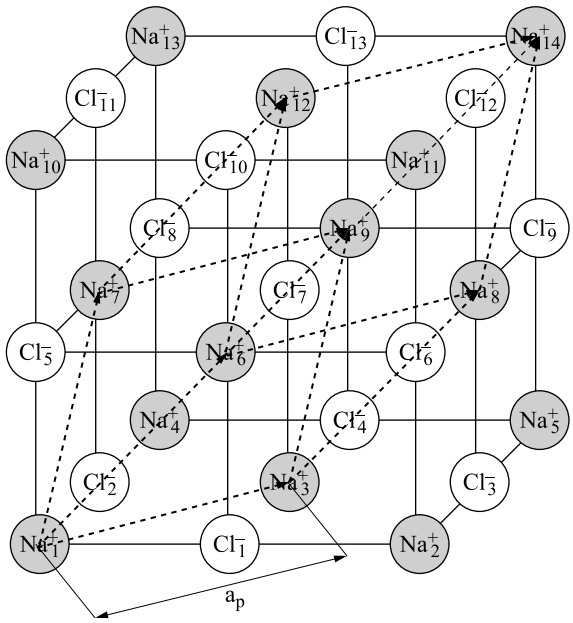

Figure 1.3. *Trigonal elementary lattice of the face-centered cubic packing of NaCl*

In the case of *NaCl* (and face-centered cubic in general), this lattice is illustrated in Figure 1.3.

It is a *rhombohedral* lattice that stretches out on a large diagonal of face-centered cubes, in which the angles between the directions of the polyhedron are 60° and the lengths of the base vectors of the elementary lattice are equal.

1.1.2. *Seven primitive lattices – 14 Bravais lattices*

If we now concentrate on the lattice, we can see that there are symmetries from which lattice nodes can be deduced from each other. These are the *translational symmetries of the lattice*. Going back to the example in Figure 1.3, there are several axes of rotation that leave the lattice unchanged. For example, the "order 3" axis along a large diagonal of cube *C* allows a 120° rotation without the lattice being modified.

It is the same thing for "order 4" and "order 2" axes for the respective rotations of 90° and 180°. There are planes of symmetry such as (Na^+_1, Na^+_5, Na^+_{14}, Na^+_{10}). There are also centers of symmetry (here, each lattice point is one). These lattice symmetries must be compatible with spatial periodicity, which limits their number. Therefore, we can show that they are limited to rotations of order 2, 3, 4 and 6 (i.e. angle rotation $2\pi/n$ for order n simply expressed n), mirror planes (expressed m) and centers of symmetry (expressed $\bar{1}$).

Seven possible *lattice types* result from this:

– cubic (a=b=c, α=β=γ=90°);

– hexagonal (a=b≠c, α=β=90°, γ=120°);

– tetragonal (a=b≠c, α=β=γ=90°);

– rhombohedral ($a=b=c$, $\alpha=\beta=\gamma\neq 90°$);

– orthorhombic ($a\neq b\neq c$, $\alpha=\beta=\gamma=90°$);

– monoclinic ($a\neq b\neq c$, α= γ=90°≠ β);

– triclinic ($a\neq b\neq c$, $\alpha\neq \beta\neq \gamma$).

Here, a, b, c, α, β and γ are the parameters of each lattice (Latin letters = distance and Greek letters = angle) with α being the angle between axes y and z, β, between x and z and γ between x and y.

As we were able to see for *NaCl*, it is sometimes simpler to define a multiple lattice to describe the structure. Therefore, face-centered cubic lattices are simpler to

use than the rhombohedral primitive lattice (see Figure 1.3). This causes us to take into consideration new lattices called *Bravais lattices*. This results in a total of 14 possible lattices, with or without a multiple lattice. The seven multiple lattices that are added to the primitive lattices above are the centered cubic, face-centered cubics, centered tetragonal, base-centered orthorhombic, centered orthorhombic, face-centered orthorhombic and base-centered monoclinic lattices.

1.1.3. *Two-hundred and thirty space groups*

Beyond lattice symmetries, it is possible to take microscopic symmetries into consideration if we now consider the pattern attached to the lattice. The final crystal symmetry will therefore be the combination of lattice and pattern symmetries. Crystal symmetry, however, can never exceed that of the lattice, as can be seen in Figure 1.1. The pattern must therefore have a symmetry that is less than or equal to the lattice, otherwise these symmetry elements would be directly in the lattice. We can show that to be compatible with spatial periodicity, the symmetry elements belonging to the pattern must have a glide: they are *helicoid rotations* and *glide reflections* (not presented here). Taking into consideration lattice and pattern symmetries enables us to determine all the mathematically possible combinations for transforming a crystal in itself (group theory). We end up with 230 crystal structure possibilities, which are called “space groups”.

1.1.4. *Thirty-two point groups (or crystal classes)*

Now, to analyze the macroscopic properties of crystals, the hypothesis of crystal homogeneity must be considered. This means that the properties observed cannot depend on the initial point considered in the crystal. From the structural point of view, all symmetry elements describing macroscopic properties should refer to one single point. This description no longer depends on the starting point considered. This way of classifying crystals therefore results in *32 crystal classes* or *point groups* (a name given because of the need to reduce the reference to one single point for elements of symmetry). We should remember that here we are considering the crystal and not the lattice alone. The crystal has a degree of symmetry at best equal to that of its lattice.

On the other hand, Curie’s principle tells us that the symmetry of the effect (piezoelectric, for example) is always greater than or equal to the symmetry of the cause (the crystal). Therefore, the point group symmetries of a given crystal correspond to the intersection of the symmetries of the macroscopic properties with those of that crystal. Macroscopic properties can be morphology, etch figures, optical properties (especially rotatory power), piezoelectricity and pyroelectricity.

Crystal system	Crystal class	Symmetry elements	Degree of symmetry	Laue classes (center of symmetry)	Piezo - pyro
Triclinic	$\bar{1}$	$\bar{1}$	2	Yes	No
	1	1	1	No	Pyro
Monoclinic	2/m	2/m	4	Yes	No
	2	2	2	No	Pyro
	m	m	2	No	Pyro
Ortho-rhombic	mmm	2/m2/m 2/m	8	Yes	No
	222	222	4	No	Piezo
	mm2	mm2	4	No	Pyro
Tetragonal	4/mmm	4/m2/m 2/m	16	Yes	No
	422	422	8	No	Piezo
	4mm	4mm	8	No	Pyro
	$\bar{4}$ 2m	$\bar{4}$ 2m	8	No	Piezo
	4/m	4/m	8	Yes	No
	4	4	4	No	Pyro
	$\bar{4}$	$\bar{4}$	4	No	Piezo
Trigonal	$\bar{3}$ m	$\bar{3}$ 2m	12	Yes	No
	32	32	6	No	Piezo
	3m	3m	6	No	Pyro
	$\bar{3}$	$\bar{3}$	6	Yes	No
	3	3	3	No	Pyro
Hexagonal	6/mmm	6/m2/m 2/m	24	Yes	No
	622	622	12	No	Piezo
	6mm	6mm	12	No	Pyro
	$\bar{6}$ 2m	$\bar{6}$ 2m	12	No	Piezo
	6/m	6/m	12	Yes	No
	6	6	6	No	Pyro
	$\bar{6}$	$\bar{6}$	6	No	Piezo
Cubic	m $\bar{3}$ m	4/m $\bar{3}$ 2/m	48	Yes	No
	432	432	24	No	No
	$\bar{4}3m$	$\bar{4}3m$	24	No	Piezo
	m $\bar{3}$	2/m $\bar{3}$	24	Yes	No
	23	23	12	No	Piezo

Table 1.1. *Crystal classes with their crystal system, symmetry elements, degree of symmetry, those that show a center of symmetry (Laue classes), those that are piezoelectric and pyroelectric*

These 32 crystal classes are particularly interesting as they enable us to anticipate the piezoelectric, pyroelectric and ferroelectric properties of crystal structures. These crystal classes are classified according to their crystal system. The

latter is identical to the lattice for all crystals except for rhombohedral crystals, which can have a hexagonal lattice (hence of higher symmetry). We therefore talk about the trigonal rather than rhombohedral crystal system.

From the crystal classes listed in Table 1.1 with their symmetry elements, we can see those that are interesting due to their piezoelectric and pyroelectric properties (which will be more clearly defined in the next section). The symmetry elements are the centers of symmetry, the axes and the rotations. The degree of symmetry is the number of replica points from any single point by using the symmetry elements of the crystal class.

We will note that crystal classes with the highest degree of symmetry for each crystal system are called holohedral classes. They are the only ones that keep the same degree of symmetry as their lattice. The other classes are called merohedral. This notion was used by the Curie brothers to define the crystal classes susceptible to showing a piezoelectric effect (hemihedral classes, which indicate a degree of symmetry twice as weak as that of the holohedral class) [CUR 80, CUR 81]. Laue classes correspond to all the crystal classes that have a center of symmetry.

1.1.5. *Reticular planes*

In a given three-dimensional lattice, we choose a point, O, that will be the origin reference point (O, a_1, a_2, a_3). Every plane whose intersection with these axes occurs at points (a_1/h,0,0), (0, a_2/k,0) and (0,0, a_3/l) with integers h, k and l is a *reticular plane*. A reticular plane does not necessarily pass through the lattice nodes. h, k and l are the *Miller indices* of the plane considered, called (h,k,l). For a family of planes, we write $\{h, k, l\}$. We can also define the direction [u,v,w] with u,v,w integers that correspond to the vector $u\ a_1+v\ a_2+w\ a_3$. If we are interested in a type of direction, we write $<u,v,w>$. Figure 1.4 represents the plane (111) and direction [111].

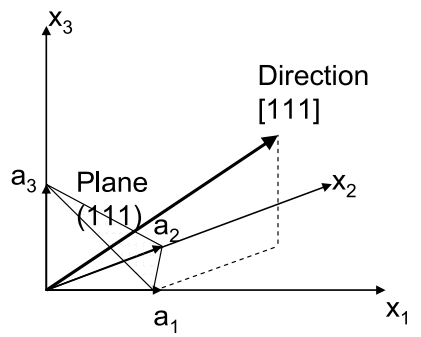

Figure 1.4. *Definition of reticular directions and planes in a lattice*

A very practical notion can also be defined to observe the symmetries: stereographic projection. We must imagine a sphere with a plane (*hkl*) at its center (see Figure 1.5). This plane is reduced to a point on the equatorial plane of the sphere by first imagining the intersection, I, of the normal of this plane with the sphere. We then link this point with the pole of the opposite half-sphere. The straight line between this pole and point I cuts the equatorial plane at a point called *hkl*. This is stereographic projection.

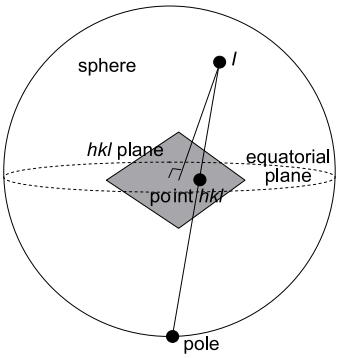

Figure 1.5. *Illustration of the construction of a stereographic projection of a* hkl *plane*

1.1.6. *X-rays "see" crystals*

X-rays play a deciding role in characterizing crystallized material. Indeed, X-rays diffract through the material, since their wavelength exhibits the same order of magnitude of inter-atomic distances. Diffraction conditions depend on reticular distances between the characteristic planes of the material, the angle of incidence of the X-ray beam and the wavelength of the X-rays. What we can retain, in substance, is that diffraction of the X-rays comes from a diffusion induced by interaction between the electrons of the material and the incident X-ray beam. The phase conditions between all the waves diffused are translated by constructive or destructive waves that induce characteristic diffraction patterns not only of the lattice, but also of the space group.

Indeed, each lattice has a diagram of diffraction modulated by microscopic and lattice symmetries. These modulations are translated through the extinction of certain rays according to the symmetries of the substance analyzed and the variations in intensity of the different diffraction peaks. From this single technique, it is therefore possible to determine the space group of an unknown substance as a function of the position of the diffraction peaks, eventual extinctions and intensity of the peaks.

1.2. Piezoelectricity, pyroelectricity and ferroelectricity definitions

We just saw that crystallized material can be classified according to 32 crystal classes. Given that a crystal environment is composed of electrically charged particles, the appearance of polarization charges through mechanical strain is therefore predictable. Thus, the symmetry conditions of crystal structure enable us to determine the atom arrangements susceptible to giving a piezoelectric effect. To do this, the crystal must not have a center of symmetry, which is the case in 21 out of the 32 existing crystal classes: those that have a center of symmetry are the *Laue* classes. Out of these 21 classes, one displays no piezoelectric effect because the movement of the charges during mechanical solicitation does not induce the appearance of a dipole (class *432*). Therefore, 20 classes are piezoelectric: during the application of a mechanical constraint, the crystal loses shape and the centers of gravity of positive charges separate from those of negative charges at the level of each crystal lattice, the effect of which is the production of a dipole moment. Quartz α is a piezoelectric material.

Out of these 20 classes, 10 are pyroelectric, i.e. they have an electric polarization in the absence of an applied electric field. The preferred direction of polarization is called the *polar axis*. These classes are called pyroelectric because of the variation in amplitude of the dipole moment when the temperature changes. This can be measured by charge flow in a closed external circuit. Aluminum nitride (AlN) and zinc oxide (ZnO) are pyroelectric.

Among pyroelectric crystals, we can distinguish ferroelectric ones for which the polar axis – the support of a permanent dipole – is mobile in the crystal lattice under the influence of an external electrical field. It is possible to reverse the direction of remanent polarization if the applied field is sufficiently strong. The *perovskite* family, including $BaTiO_3$ and $Pb(Zr,Ti)O_3$, and the *ilmenite* family, including lithium niobate and tantalate ($LiNbO_3$, $LiTaO_3$), are ferroelectric materials.

The classification of the 32 crystal classes according to these different denominations is summed up in Figure 1.6 [EYR 67].

It is understood that for these properties to appear, the materials must be insulant. In other words, an electric field must be able to form inside the material. This electric field will have an opposing influence depending on the sign of the material charges. The effects discussed focus on the fixed charges in the material that cannot escape, unlike the conduction electrons of a metal for example. The electric field will slightly displace the charges (amplitude less than the Angstrom) in order to make dipole moments or moments of greater order appear.

In the case of the 11 centrosymmetric classes, certain electromechanical effects can also appear. It is the electrostrictive phenomenon that forms in all insulating materials, whether they are crystal or not.

Later we will describe the three structures that are the most used in integrated piezoelectric and ferroelectric applications: *perovskite* structure (PZT, BST), *ilmenite* structure (LNO, LTO) and *wurtzite* structure (AlN, ZnO). In the next section, we will first describe each of the effects stated through simplified examples.

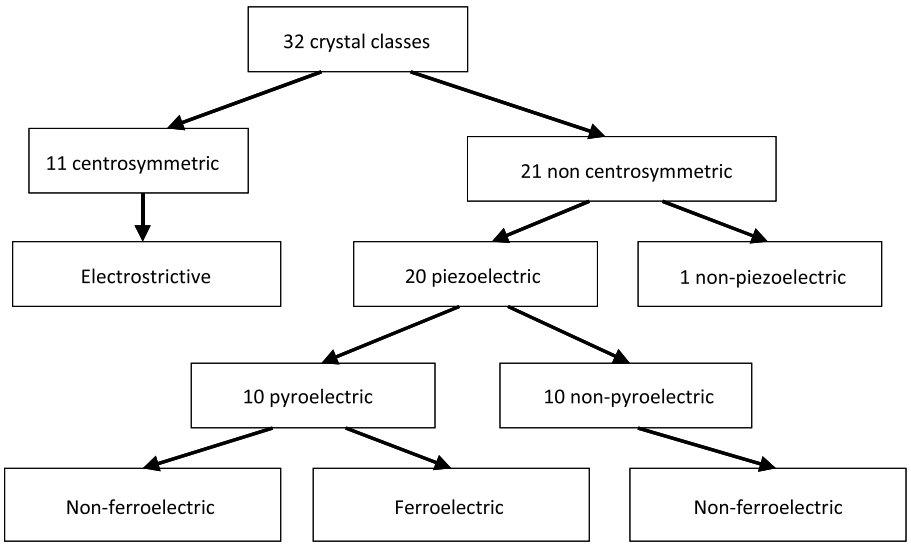

Figure 1.6. *Grouping of crystal classes according to their piezoelectric, pyroelectric, ferroelectric and electrostrictive properties*

1.3. Simplified examples

1.3.1. *Dielectric effect*

As we stated before, an ideal dielectric material does not allow charges to pass through. Electrostatic effects can occur inside the dielectric, which leads to the creation or modification of dipole moments. In the case of real dielectrics, it is possible for some charges to pass through the dielectric and contribute to the leakage current. This effect is modeled either through adding a resistance in parallel with the ideal capacitor or through the use of a complex dielectric permittivity whose imaginary part translates these resistive losses.

Generally speaking, the behavior of a dielectric is shown in the form of a diagram in Figure 1.7 in the configuration of a planar capacitor. When applying an electric field between the electrodes, dipole moments are created in the dielectric. It is from their properties that the behavior of capacitors can be explained, as we will see in the chapter dedicated to dielectrics.

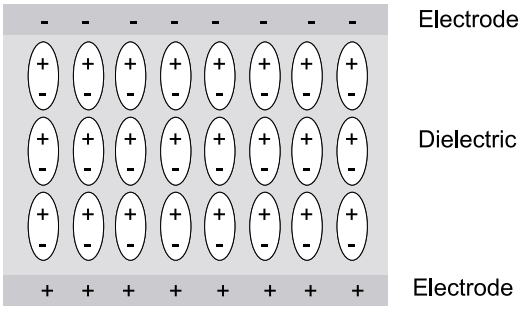

Figure 1.7. *Sketch of a dielectric during the application of an external electric field: dipoles are created in the dielectric material*

Conversely, if a force is applied to the terminals of a planar capacitor involving a dielectric with a symmetry center, no charge appears at the extremes of the dielectric as the symmetry of the material is always conserved. There is therefore no appearance of the dipole moment. This effect is presented in the form of a two-dimensional diagram in Figure 1.8 where a cubic lattice is represented. The dielectric can be qualified as *paraelectric*, as opposed to ferroelectric: there is no center of symmetry therefore there is no dipole moment. We do, however, observe a change of the dielectric constant. This change can lead to important changes in the case of very high permittivity dielectrics, such as perovskite materials.

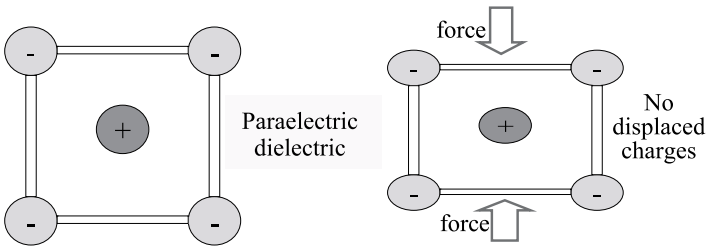

Figure 1.8. *Diagrammatic representation of a cubic lattice during application of a force to the extremities of the lattice. The center of symmetry is conserved therefore there is no dipole moment in the dielectric*

1.3.2. *Piezoelectric effect*

The piezoelectric effect linearly links a mechanical variable to an electric variable. The direct effect was discovered by the Curie brothers in 1880: the effect translates the creation of electrical charges during the application of a mechanical constraint on the piezoelectric material [CUR 80]. Lippmann suggested the existence of the reverse effect one year later thanks to energy considerations (like the formalism of which we will go into detail later) [LIP 81]. The same Curie brothers experimentally proved its existence a few months later by deflecting a clever collection of two very thin quartz beams when a voltage was applied. This induced the appearance of a mechanical strain in the material during the application of an electrical field.

Figure 1.9 is a diagrammatical representation of these two piezoelectric effects.

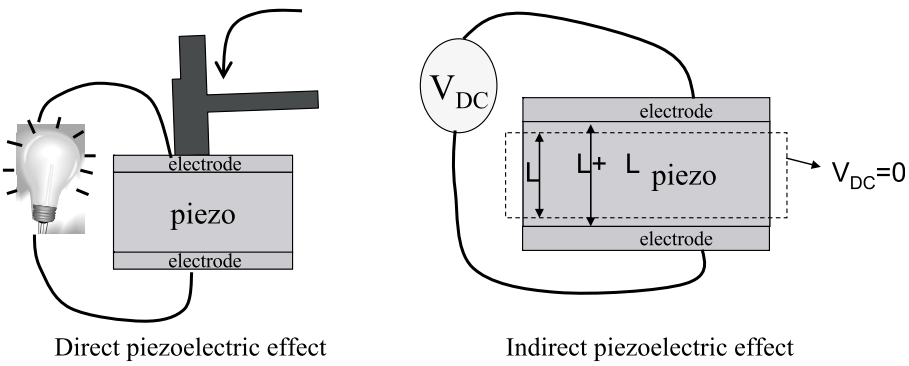

Figure 1.9. *Diagram of direct and indirect piezoelectric effects*

Using Figure 1.10a, we can illustrate this property using a simplified crystal structure that looks like low-temperature quartz (quartz α, from point group *32*). The axis of order 3 is perpendicular to the page.

In Figure 1.10b, the arrangement of positive and negative ions does not result in any permanent equivalent dipole moment in the material in the absence of external force. The equivalent dipole moments were represented projected on a plane perpendicular to axis 3. When a force is applied (Figure 1.10c), the amplitude of the dipole moments varies in a different way: there is the appearance of a non-null equivalent dipole moment in this plane of the material. This is the direct piezoelectric effect.

The effect is linear: reversing the force leads to a reversal of the sign of the dipole created and this dipole is proportional to the amplitude of the force. It is said that quartz is a *non pyroelectric piezoelectric* because of the absence of a microscopic permanent polarization (no dipole moment in the absence of external solicitation). As we have seen, this is the case in 10 crystal classes.

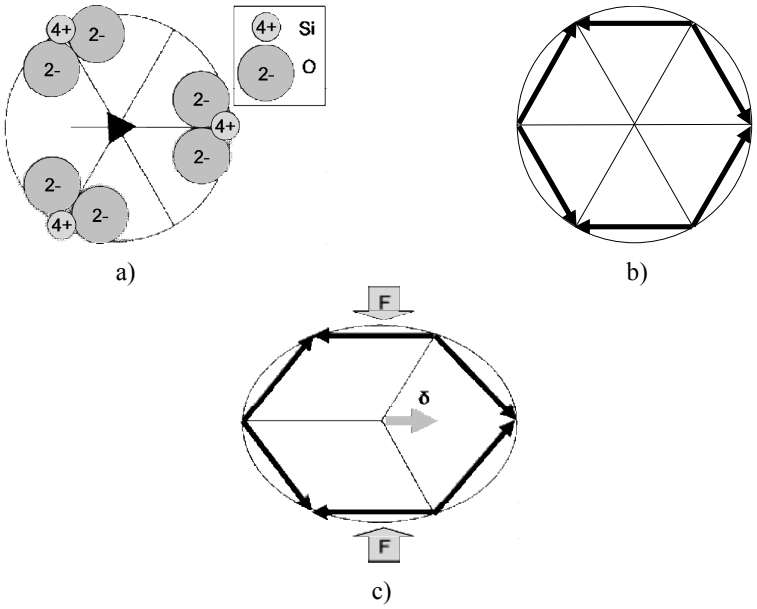

Figure 1.10. *a) Diagram of quartz (point group 32) in a plane perpendicular to axis 3 represented by the black triangle (groups SiO_2 are not in the same helicoidal axis-plane); b) projection of dipole moments in a plane perpendicular to axis 3. There is no spontaneous dipole moment (sum of null dipole moments); and c) state of dipole moments when an external force, F, is applied in the vertical direction. There is the appearance of a dipole moment in the horizontal direction (δ = dipole moment)*

1.3.3. *Pyroelectric effect*

The pyroelectric effect was discovered before the piezoelectric effect in tourmaline crystals. This effect translates the appearance or disappearance of charges on the extremities of the pyroelectric crystal when temperature changes. The explanation is due to the change in volume induced by dilation of the crystal with temperature. Just as a pyroelectric crystal has spontaneous polarization in a given crystallographic direction, the change in volume results in a change in dipole length and therefore dipole moment.

Figure 1.11 translates the representation of a two-dimensional crystal lattice showing a permanent dipole. The lattice does not have a center of symmetry as the positive charge does not coincide with the barycenter of the negative charges (the barycenter is represented in Figure 1.11 by a dotted circle carrying the minus sign).

Applying a force, an electric field or a temperature change leads to a change in the thickness of the lattice and therefore the dipole moment, hence the appearance of charges on the extremities of the dielectric. The dielectric is, in this case, called *pyroelectric piezoelectric* and often simply *pyroelectric*.

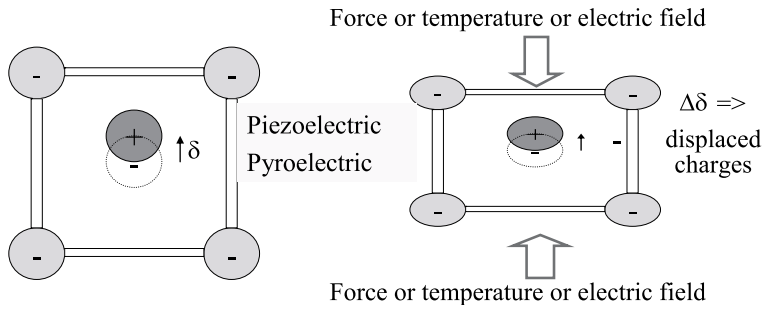

Figure 1.11. *Diagrammatic representation of a pyroelectric crystal lattice. There is a permanent spontaneous polarization because of the permanent dipole moment, δ, in each lattice. The dipole changes according to an applied force, an applied temperature or electric field change. The dotted circle represents the barycenter of negative charges*

1.3.4. *Ferroelectric effect*

Among crystals that are pyroelectric, therefore having a permanent dipole moment in each lattice, there are some whose spontaneous polarization can be modulated by an electric field. It is even possible to reverse the sign of spontaneous polarization when a sufficiently strong electric field (called a coercive field) is applied. The archetype of these ferroelectric materials is the perovskite phase, which we will speak about again later.

Figure 1.12 represents an example of a ferroelectric perovskite phase in which the reversible permanent dipole movement according to the electric field is represented by movements of the Ti^{4+} ion in the center of the oxygen octahedron.

This view is quite far from the real movement of each ion of the lattice but it enables the existence of the two stable states of polarization, called remanent in this phase. These two stable states of polarization (up and down) are represented in

Figure 1.12. The dielectric is called *ferroelectric*. It is in fact pyroelectric and piezoelectric.

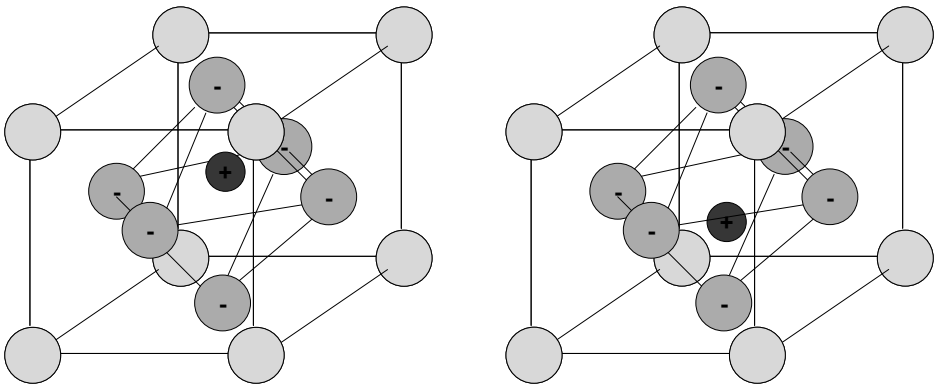

Figure 1.12. *Diagrammatic representation of a ferroelectric perovskite lattice according to the sign of the tension applied to its terminals*

1.3.5. *Electrostrictive effect*

We could ask ourselves the question about the mechanical behaviors of a paraelectric dielectric during the application of a voltage. A mechanical but nonlinear strain appears. This quadratic change, which does not depend on the sign of the voltage applied, translates the property of *electrostriction*. One way of simply understanding this effect is represented in a diagram in Figure 1.13. We return to the symmetrical lattice of the paraelectric dielectric. The effect can be split in two (in theory), which enables us to see what happens in reality. First, there is the appearance of a dipole moment because the charges are attracted by their opposites. The structure therefore loses its center of symmetry.

In this configuration, nothing prevents an induced piezoelectric effect because the two necessary conditions are gathered – no center of symmetry and applied voltage. The material therefore becomes thicker and at the same time shorter in the direction perpendicular to the applied electric field. Thus we find the quadratic effect through the combination of two linear effects (when excitation is weak): the linear effect of the dipole creation and induced piezoelectric linear effect.

It is possible to re-make the argument by reversing the sign of applied voltage. The direction of the dipole moment created is therefore reversed, which leads to a strain identical to the case above. In reality, the electrostrictive effect undoubtedly is not broken down across these two takes, but this enables us to make a correct argument: an electrostrictive material always becomes thicker and the effect is

quadratic. This effect is in competition with the electrostatic attraction of electrodes, which is also quadratic. Experimentally, we can observe that some polymers can exhibit a stronger electrostatic effect than electrostrictive effect. In the case of an alternative excitation, V, to the frequency, $f(V=V_0 cos2\pi ft)$, an electrostrictive material gives an answer in the form of a mechanical vibration to the frequency $2f$.

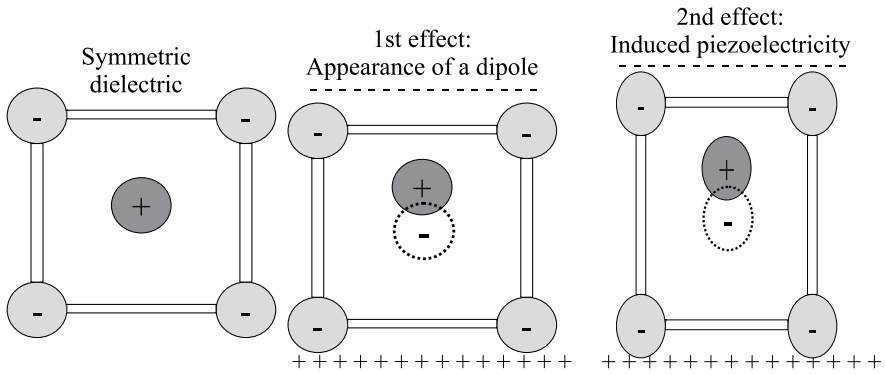

Figure 1.13. *Diagrammatic representation of the electrostrictive effect*

1.4. Three typical structures: wurtzite, ilmenite and perovskite

1.4.1. *Wurtzite structure*

Wurtzite structure corresponds to that of AlN and ZnO. These two materials were studied in thin films in the 1980s then put to one side during the advent of perovskites. Interest in wurtzites was renewed at the beginning of the 2000s, however. This was first because of the volume acoustic wave acoustic filters that almost exclusively use AIN as a piezoelectric material, mainly for its very high acoustic quality factor (low acoustic losses), as well as electro-luminescent diodes. Second, interest increased because of the propensity of ZnO to grow in the form of nanowires under certain conditions.

This structure has a hexagonal lattice and is part of the *6mm* point group. It can be seen as a juxtaposition of two compact hexagonal structures for the two sorts of ions composing the structure (see Figure 1.14a for AIN). The two structures are shifted following the c axis by a distance of $3/8c$. This is what explains the spontaneous polarization for this structure, even in the absence of the electric field. It is therefore a pyroelectric structure. Lattice parameters, by choosing a hexagonal lattice, are the following for AIN: a = 3.112 Å and c = 4.982 Å. The stereographic projection of the *6mm* point group is given in Figure 1.14b. We recognize the c axis

represented by the hexagon in the center of the circle that carries the axis of order 6 (perpendicular to the page) and six mirrors at 60° that contain the *c* axis. There is no mirror cutting axis 6, hence the absence of a center of symmetry. The "*x*"s represent the equivalent points obtained through symmetry of the point group (here 12, which represent a hemihedry of the hexagonal crystal system, see Table 1.1).

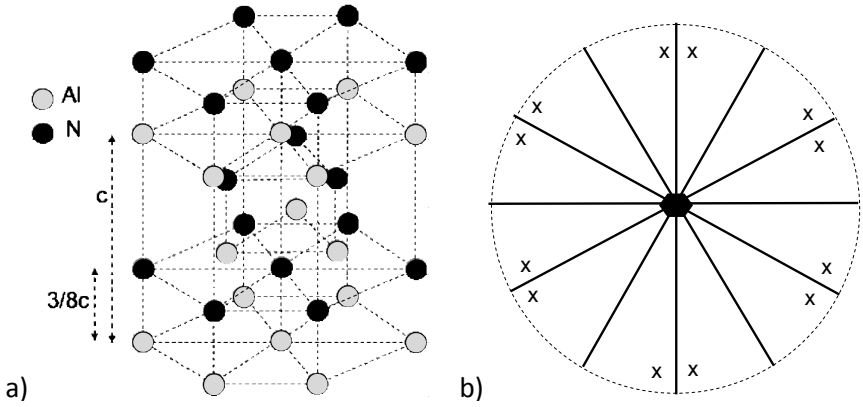

Figure 1.14. *a) AlN wurtzite structure: representation of the hexagonal lattice; and b) stereographic projection of the 6mm point group with the degree of symmetry*

1.4.2. *Ilmenite structure*

Ilmenite structure corresponds to that of lithium niobate and tantalate, which are very useful for surface acoustic wave (SAW) resonators and filters. Below Curie temperature, the point group of this structure is *3m* (trigonal crystal system, rhombohedral lattice). The ternary axis corresponds to that of polarization. A $LiNbO_3$ perspective view is given in Figure 1.15a. The lattice parameters of LNO in the rhombohedral lattice for which the pattern is constituted of two $LiNbO_3$ groups are a = 5,492Å and α = 55°53'. This structure can be seen as a compact A-B packing of oxygen planes, i.e. like the regular packing of balls of the same diameter by repeating two successive planes A and B (in a structure called *compact hexagonal*). This packing induces oxygen octahedrons (inclined in relation to the ternary axis) in which Li or Nb or no cations can be found. $LiNbO_3$ has a well-defined succession of ions filling these octahedral cavities (Nb, Li, empty, Nb, Li…) as can be seen in Figure 1.15a. Cations are not centered in the middle of the octahedra because of the difference between the dimensions of the cations. The Curie temperature of $LiNbO_3$ is around 1,200°C. Beyond this temperature, it is paraelectric in the $\bar{3}m$ point group.

Figure 1.15b represents the stereographic projection of the *3m* point group. The ternary axis, represented by a triangle, is perpendicular to the page. Three 120° mirrors contain the ternary axis. The "*x*"s represent the equivalent points obtained by symmetry. The sum of these points gives the degree of symmetry of the point group (here six, which represents a hemihedry of the trigonal crystal system, see Table 1.1).

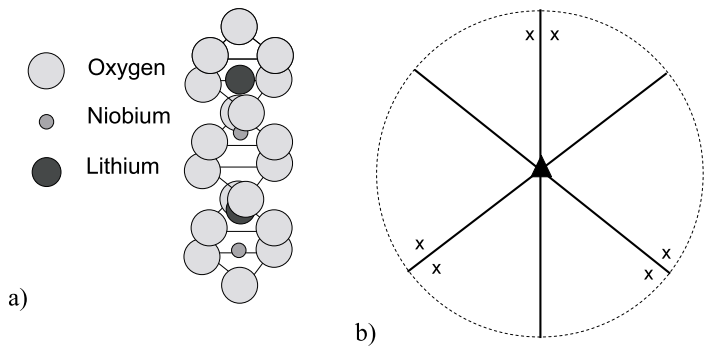

Figure 1.15. *a) Ferroelectric structure of $LiNbO_3$ of point group 3m; and b) stereographic projection of symmetry elements of point group 3m*

Due to their intense use in acoustic filters, LNO and LTO exist in monocrystal substrates of significant size (up to 150 mm). This gives us the unique opportunity to produce large-surface single-crystal thin piezoelectric films transferred to silicon substrate through the Smart Cut^{TM} technique or molecular sticking/thinning (we will discuss these techniques in detail in Chapter 11).

It is also possible to choose many different orientations enabling us to vary the properties according to the desired functions (volume, compression, shear wave, etc.).

1.4.3. *Perovskite structure*

1.4.3.1. *Introduction*

Perovskite structure (from the name of natural perovskite, $CaTiO_3$) is the most well-known and studied ferroelectric structure. It is described from its simple cubic phase (point group *m3m*), which appears above its Curie temperature. This phase, which presents a center of symmetry, is therefore not ferroelectric but it allows for a simpler description. Perovskite structure has the form ABO_3. In what follows, we will take $Pb(Zr,Ti)O_3$ (PZT) as an example. Figure 1.16 is a representation of a cubic perovskite lattice originating from site A (Pb). A is a cation with a large ionic radius

(Pb for PZT), which is bivalent and has a coordinance of 12. B is a cation with a smaller radius (Zr or Ti, depending on the PZT sites), which is tetravalent and has a coordinance of 6. In a cubic arrangement, A occupies the vertices, B the center and oxygen occupies the center of the six faces. The B ion is found in the center of the oxygen octahedron.

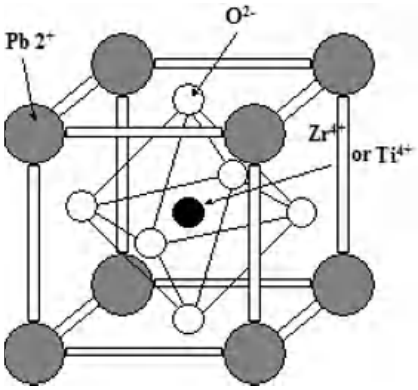

Figure 1.16. *Cubic perovskite lattice of PZT*

The chemical formula of PZT is $Pb(Zr_xTi_{1-x})O_3$. The number x is equal to [Zr]/[Zr]+[Ti].

Basically, the perovskite lattice of PZT can be of three different forms depending on the temperature and the Zr/Ti relation:

– cubic (point group *m3m*) when the temperature is above the Curie temperature (T_c), which corresponds to the paraelectric phase that does not show a dipole moment;

– tetragonal (point group *4mm*), when the temperature is below T_c and x <0.45 (titanium dominance). This phase shows a permanent dipole moment throughout the cubic lattice strain;

– rhombohedral (point group *3m*) when the temperature is below T_c and x >0.5 (zirconium dominance). This phase also shows a permanent dipole moment.

It is noteworthy that when x is included between approximately 0.45 and 0.5, the phase obtained is termed *morphotropic*. It has long been believed that this phase is simply a mixture of the tetragonal and rhombohedral phases. In 2000, however, Noheda *et al.* showed the presence of a monoclinic phase in this area of the phase diagram [NOH 99]. It is the presence of this monoclinic phase that best explains the ferroelectric and piezoelectric properties of PZT in this morphotropic zone because

of a greater polarization facility [MIT 69]. Figure 1.17 represents a PZT phase diagram according to [JAF 71].

Zone A in Figure 1.17 is an antiferroelectric phase characteristic of lead zirconate ($PbZrO_3$). This property means that locally perovskite lattices each present a dipole moment but their directions are systematically opposed between neighbors. This induces a null macroscopic polarization.

The two ferroelectric phases are obtained by paraelectric cubic lattice strain and therefore present a permanent dipole moment. For the tetragonal phase, one side of the cube is stretched out to give the c [001] axis, whereas the two other sides are compressed to give the tetragonal axes [100] and [010]. The point group is therefore *4mm*. For the rhombohedral phase, the cube is stretched out along a diagonal that crosses the lattice entirely, for example in direction [111]. The point group is therefore *3m*. A diagrammatic representation of how these phases are obtained is given in Figure 1.18.

Depending on the different phases of the perovskite lattice, the direction of polarization is not the same. Therefore, when symmetry is tretragonal, the pole axis follows direction [100] of the original cubic lattice, i.e. following the c axis of the tetragonal phase.

When symmetry is rhombohedral, the pole axis follows direction [111] of the original cubic lattice. An example of spontaneous polarization directions for the two ferroelectric phases is represented in Figure 1.18 [JON 62].

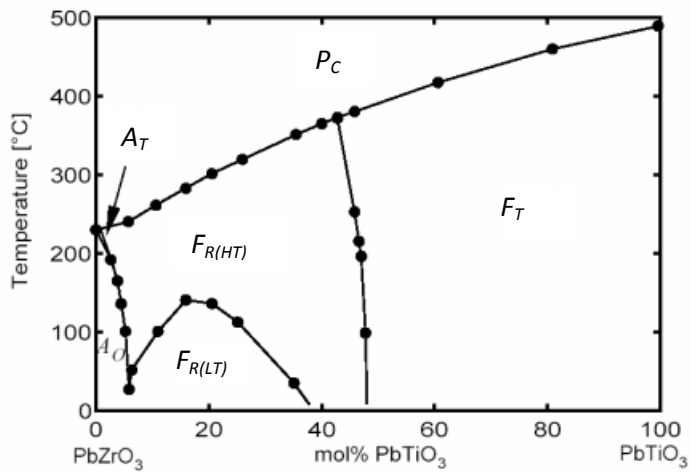

Figure 1.17. *PZT phase diagram [JAF 71]*

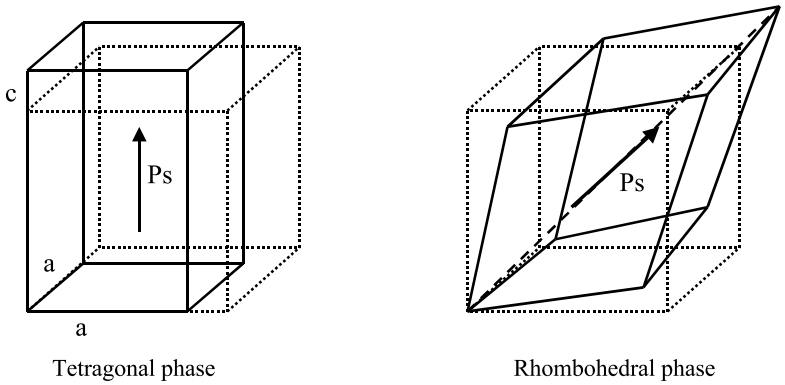

Figure 1.18. *PZT cubic perovskite lattice strain giving the tetragonal and rhombohedral phases based on the Zr/Zr+Ti relation. The dotted lines delimit the core cubic phase*

1.4.3.2. *Ferroelectricity in the perovskite phase*

As we have seen, the notion of ferroelectricity is based on the fact that spontaneous polarization of the material can vary according to the application of an external electric field. The direction of the pole axis can even be reversed if this field is sufficiently intense. The state of macroscopic polarization of a ferroelectric material based on the electric field of excitation therefore represents a hysteresis loop (see Figure 1.19) in a way similar to ferromagnetic materials, to which the ferroelectrics owe their name by analogy.

Ferroelectric material is subdivided into domains. All the elementary dipoles are oriented in the same direction in each domain. The size of these domains varies depending on the electric field. In the case of PZT, the form, number and size of the domains depend on the growth conditions and external mechanical and electrical constraints. When an electric field is applied, the elementary dipoles have the tendency to be oriented according to the direction of the field. The stronger the field, the larger the number of elementary dipoles that switch; increasing their contribution to the macroscopic polarization by the same extent. This is diagrammatically explained in Figure 1.19, across the hysteresis loop presented by the macroscopic polarization according to an applied electric field.

The aspect of a perovskite lattice is represented in Figure 1.19 for the two possible stable states when the electric field is null. For these two states, the barycenter of the positive charges (Ti^{4+} or Zr^{4+}) in the cubic lattice is shifted in relation to the barycenter of the negative charges (O^{2-}). We will resume these notions through a thermodynamic development, enabling us to properly understand what happens from an energy point of view.

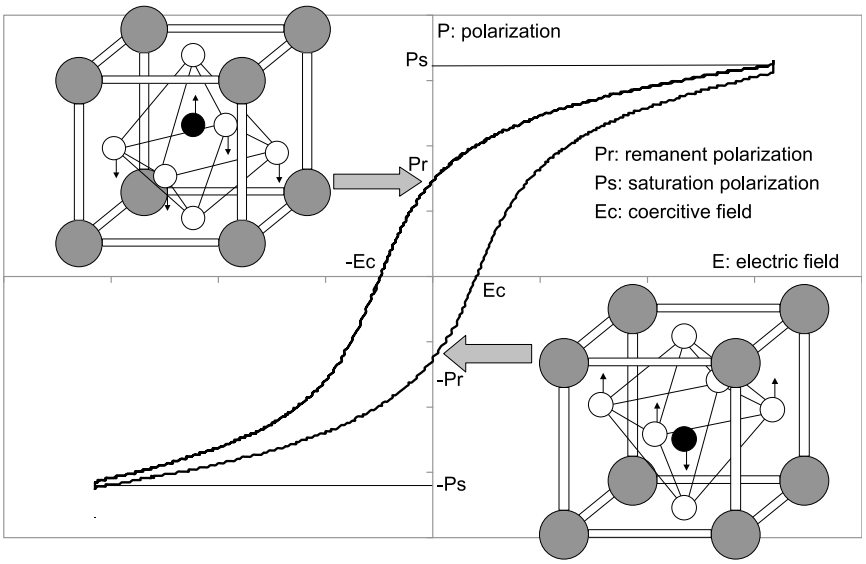

Figure 1.19. *Polarization of a ferroelectric material according to the electric field applied. The two diagrams represent the perovskite lattice in the two possible states of remnant polarization (P_r and $-P_r$)*

1.4.3.3. *Piezoelectricity of the perovskite phase*

The piezoelectric phenomenon appears through the mechanical strain of the elementary dipole of the lattice. In the case of ferroelectric materials, remanent polarization is more important and piezoelectric coefficients are higher. This happens if the elementary dipoles are oriented in the same direction in order to give a non-null macroscopic dipole. A so-called preliminary stage of polarization, called poling, is thus mandatory for aligning all the ferroelectric domains in the same direction or at least in a way sufficient to cause a non-null macroscopic polarization to appear. This is true whether the materials are single crystals or poly crystals. Figure 1.20 is a diagrammatic illustration of this mandatory stage of polarization in the case of a polycrystalline material. For a single crystal, the main difference is that only certain directions are authorized by the structure. The aim of the poling stage is always the same, however: to make non-null macroscopic polarization appear.

Finally, we will note that a polarized polycrystalline PZT thin film has an infinite axis following the axis of polarization. This structure is equivalent to point group *6mm*.

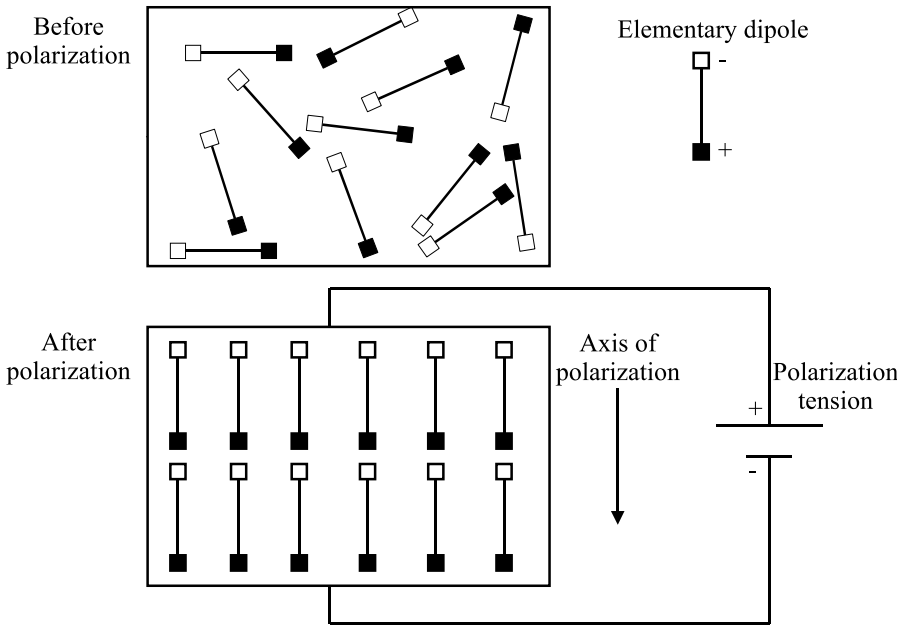

Figure 1.20. *Stage of polarization of electric dipoles through the application of an electric field in the case of polycrystalline ferroelectric ceramics like PZT*

1.5. Bibliography

[CUR 80] CURIE P., CURIE J., *Bulletin de minéralogie*, t. III, p. 90, 1880.

[CUR 81] CURIE P., CURIE J., "Contractions et dilatations produites par des tensions électriques dans les cristaux hémièdres à faces inclines", *Comptes rendus de l'Académie des Sciences*, vol. XCIII, p. 1137, 1881.

[ESN 94] ESNOUF C., Cours de Caractérisation Structurale, INSA de Lyon, 1994.

[EYR 67] EYRAUD L., *Diélectriques solides anisotropes et ferroélectricité*, Gauthier-Villars, Paris, p. 183, 1967.

[JAF 71] JAFFE B., COOK W.R., JAFFE H., *Piezoelectric Ceramics*, Academic Press Limited, New York, 1971.

[JON 62] JONA F., SHIRANE G., *Ferroelectric Crystals*, chapter 4, Barium titanate, p. 108-110, Pergamon Press, New York, 1962.

[LIP 81] LIPPMANN G., *Annales de chimie et de physique*, 5th series, t. XXIV, p. 145, 1881.

[MIT 69] MITSUI T., *Landolt-Bornstein: Numerical Data and Functional Relationships in Science and Technology*, *vol. 3*, *Ferro and Antiferroelectric Substances*, p. 308, Spinger Verlag, Berlin, 1969.

[NOH 99] NOHEDA B., COX D.E., SHIRANE G., GUO R., JONES B., CROSS L.E., "A monoclinic ferroelectric phase in the Pb(Zr1 – xTix)O3 solid solution", *Applied Physics Letters*, vol. 74, 2059, 1999.

Chapter 2

Thermodynamic Study: a Structural Approach

2.1. History

Despite several dozen years of microscopic modeling, no theory is yet reliable enough to completely explain and anticipate the behavior of thin film perovskites, although the *ab initio* or first principles approach is beginning to give very good results [JUN 03]. The thermodynamics-based phenomenological approach, which is a statistical view of the problem, enables us to explain a very large number of the many perovskite behaviors. Although the case of thin films is more delicate because of extrinsic effects such as residual stresses, interfaces, composition inhomogeneities, effects of crystalline orientation or domain walls, it is often possible to understand, at least qualitatively, how a mechanism that integrates a perovskite material will behave using the thermodynamic formalism.

For this reason, we will develop the equations that allow us to use this formalism. This energy method is very structured for understanding the many possible couplings originating in perovskites. The general idea is to have the greatest possible breadth in describing the system and to thus quantify the conversions of thermal, mechanical, electrostatic and even magnetic energy.

This theory is often called LGD for Landau-Ginzburg-Devonshire, all three having sequentially contributed to developing it in the first part of the 20th Century. Landau's work focused on phase transitions of the second order, i.e. not involving

---

Chapter written by Emmanuel DEFAŸ.

the latent heat of transition. This can be a ferromagnetic or ferroelectric close to the Curie temperature, a superconductor close to its transition, or a fluid close to its critical point. All these transitions can have behaviors with many similarities (the notion of "universality") and are called "critical phenomena" in the literature, which has been studied in detail since Landau's precursory works [LIN 77].

In 1950, Landau and Ginzburg adapted Landau's initial theory to the study of the transition of a superconductor. In 1949, Devonshire took inspiration from this formalism to apply it to a ferroelectrics study [DEV 49]. This global energy approach achieved huge success and is still used today for bulk and thin films. It is therefore possible to take domain walls and stresses due to the substrate and many couplings into consideration.

In this approach, the notion of symmetry is important as, almost all the time, there is loss of symmetry during a phase transition (liquid-solid, ferromagnetic-paramagnetic, ferroelectric-paraelectric). It is fundamental to be able to quantify the symmetry change induced during transition using a characteristic parameter of the system, which is called the *order parameter*. Therefore, in the case in which we are interested, it is polarization that represents the order parameter for describing the transition between the paraelectric and ferroelectric states. Landau assumes that free energy of the system undergoing the transition can be described using an analytical function of the order parameter and, more specifically, through an even power development of the latter.

For ferroelectrics, this hypothesis means that the energy of the phase with the highest symmetry is the same regardless of the sign of the applied field strength associated with the order parameter. This is the case because polarization is always aligned with the electric field strength applied in the paraelectric phase. The dielectric contribution to energy is therefore the same regardless of the sign of field strength. A phase transition is also characterized by a transition temperature. This temperature is introduced by Landau in his formalism so that the order parameter is null in the high temperature phase of high symmetry and non-null in the low temperature phase of low symmetry. This is specified upon entering thermodynamic formalism in the next section.

2.2. Revisiting statistical thermodynamics

2.2.1. *Introduction*

The link between the macroscopic thermodynamic approach and statistical physics enables us to specifically define and quantify the notion of the thermodynamic equilibrium of a thermodynamic system. It also enables us to define

the difficult notion of entropy, which is closely linked to that of equilibrium. In this section, we suggest revisiting the foundations of statistical physics in order to better understand what thermodynamic equilibrium and its implications on the macroscopic values accessible through experiments mean. Entropy and absolute thermodynamic temperature are defined, which enables us to arrive at the term *thermal energy* (in other words heat), used in the thermodynamic formalism we wish to use. An excellent introduction to statistical physics is the 5th volume of Berkeley's physics course written by Frederick Reif [REI 65].

2.2.2. *Notion of equilibrium, statistical postulate*

Each macroscopic system (for example a thin film with its electrodes) is made up of atoms linked to each other. Today, from discoveries of the beginning of the 20th Century, we know that it is quantum mechanics that governs the energy state of each of these atoms. The fundamental concept of quantum theory is that energy levels of each atom are quantified and very well defined. The generalization of these microscopic quantum laws to macroscopic systems is not within our scope, given the enormous number of parameters to take into consideration that are in the order of magnitude of the number of particles that make up the macroscopic system. An order of magnitude of this quantity is the Avogadro number equal to $6.02.10^{23}$ particles. This is the number of particles contained in one mole of a substance (it corresponds exactly to the number of particles contained in 12g of carbon).

At each moment a macroscopic system is in a given microscopic state. This means that each atom in this system is in a given energy state, which can change with time. As the number of parameters to determine is colossal, we make our argument in statistical terms. It is easier to look for the probability of occurrence of this or that microscopic state of the system as a function of external macroscopic parameters. To do this, for an isolated macroscopic system it is necessary to determine the degrees of freedom at the microscopic level. These degrees of freedom numbering, l, define the amount of independent data necessary for microscopic description of the system. Therefore, a full set of these given l degrees of freedom determine a possible microscopic state of the system.

If we consider an isolated system (i.e. without the possibility of energy exchange with the external environment), and we know the external macroscopic parameters (temperature, electric field strength and mechanical stresses, for example) and the initial quantity of energy contained in the system, we can define all the possible microscopic states in which the system can be found. It therefore becomes conceivable to carry out a statistical analysis through calculations of the probability of occurrence of this or that state compared to the set of possible states.

2.2.2.1. *Statistical postulate*

This statistical postulate enables us to define the state of equilibrium of a macroscopic system from microscopic statistical considerations. Let us take the isolated macroscopic system above and assume that it is in equilibrium. At the microscopic level, movement of particles always exists (we are not placed at absolute zero) and it is a dynamic situation that prevails (for example Brownian movement). Particles continuously go from one state of energy to another.

If we assume that macroscopic equilibrium exists, it is legitimate to consider that all the microscopic states that follow are equiprobable at equilibrium. Conversely, it is said that *if all the microscopic states of a system are equiprobable, then the system is in equilibrium*. This postulate is the basis of notions of thermodynamic equilibrium and irreversibility. Indeed, according to this postulate, a non-equilibrium system will naturally go towards a situation where all microscopic states are equiprobable.

2.2.2.2. *Remarks on relaxation time*

It is important to note that the establishment of coupling equations presented in section 3.4 assumes that thermodynamic equilibrium has been achieved. The duration of the experiment is therefore implicitly assumed to be very long in relation to the thermodynamic relaxation time of the system. The dielectric relaxation evoked above is an example illustrating the fact that certain physical contributions (e.g. ferroelectric domain walls) have a relaxation time that can be of the order of magnitude of the experiment time. Here, we are still assuming that equilibrium is established, but the physical constants of the system, like the dielectric constant or the piezoelectric coefficients, become variable with the frequency of excitation. It is therefore necessary to consider the losses that are often introduced by transforming the physical constants of the problem into a complex number.

2.2.3. *Numbers of accessible states of a system*

If we place ourselves at equilibrium, according to the statistical postulate, we can independently argue about the time. As all states are equiprobable, the probability of occurrence, p_i, of a given microscopic state, i, is simply the opposite of the total number of accessible states, N, of the system in this equilibrium: $P_i = 1/N$.

Let us now turn our interest to the macroscopic parameters of this system, for example the electric field. This field takes a given value for each microscopic state of the system. Therefore, at equilibrium the probability, $P(E_i)$, of the occurrence of an electric field of given intensity, E_i, corresponds to the number of microscopic states, $N(E_i)$, that have this electric field value over the total number of accessible

states of the system. Therefore: $P(E_i) = N(E_i)/N$. The value taken by the electric field at equilibrium, E_{eq}, is therefore:

$$E_{eq} = \sum_i P(E_i)E_i = \frac{\sum_i N(E_i)E_i}{N} \qquad [2.1]$$

This probability calculation is simple when the system is also simple, but it can quickly become very complex in the case of real systems that have an extremely high number of accessible states. In this situation it is interesting to estimate the number of accessible states, as this will enable us to define the entropy of the system.

For a given isolated macroscopic system and for a given energy, E, let $N(E)$ be the number of accessible microscopic states included between E and $E+\delta E$. δE represents a small quantity of energy at the macroscopic level that enables us to say that $N(E)$ is proportional to δE (as if we were making a first-order expansion). On the other hand, δE is assumed to be very large at the microscopic level so that it has a very large number of microscopic states. This property enables us to consider $N(E)$ as a continuous function of energy (N does not see the quantum leaps). Mathematically, $N(E)$ can be defined as the difference between the number of microscopic states of energy less than $E + \delta E$ ($\sum(E + \delta E)$) and the number of microscopic states of energy less than E ($\sum(E)$). This is translated by the following equation, always of the first order:

$$N(E) = \Sigma(E+\delta E) - \Sigma(E) = \frac{\partial \Sigma}{\partial E}\delta E \qquad [2.2]$$

This formalism will enable us to estimate the change in the number of states as a function of energy. We saw before that an energy value must be given to each of the f degrees of freedom of the system to determine a microscopic state. In other words, each degree of freedom of each particle in the system has a quantified energy, e, which is well-defined for each microscopic state of the system. Therefore, for each degree of freedom, i, let us define the number of possible states, $s(e)$, whose energy is less than e. We can note that $s(e_{min}) = 1$. If we place ourselves at a higher energy than the minimum energy, we can make a first-order assumption that $s(e)$ is proportional to $e - e_{min}$. The total energy of the system must be the sum of all these small energies corresponding to each of the degrees of freedom of the system, which gives:

$$E = l\left(e - e_{\min}\right) + E_{\min} \qquad [2.3]$$

where E_{min} corresponds to the minimum energy state of the system.

To go further, we can determine the number of possible states of the complete system whose energy is less than E as a function of the number of possible states of each degree of freedom whose energy is less than e. In statistical terms, this is translated simply by:

$$\Sigma(E) = (s(e))^l \qquad [2.4]$$

As $s(e)$ is proportional to $e - e_{min}$, we have:

$$\Sigma(E) \propto (e - e_{\min})^l \qquad [2.5]$$

This estimation enables us to reconsider equation [2.2], which then gives:

$$N(E) = \frac{\partial \Sigma}{\partial E}\delta E \propto \left(\frac{E - E_{\min}}{l}\right)^{l-1}\delta E \qquad [2.6]$$

As l is of the order of the Avogadro number, this equation tells us that the number of accessible states, $N(E)$, increases very strongly as soon as the energy of the system increases a little. This is because of the dependence of the term $E - E_{min}$ in powers of l, which produces a huge number.

To refine the estimation, let us take the logarithm $N(E)$, noting that $\partial e/\partial E = 1/l$:

$$\ln(N(E)) = \ln\left(ls^{l-1}\frac{\partial s}{\partial E}\delta E\right) = \ln\left(ls^{l-1}\frac{\partial s}{\partial e}\frac{1}{l}\delta E\right) = (l-1)\ln s + \ln\left(\frac{\partial s}{\partial e}\delta E\right) \qquad [2.7]$$

s is the number of possible states of energy less than e. If we consider e to be higher than e_{min}, then s is strictly greater than 1. We just assumed that s was proportional to $e - e_{min}$. Even if the constant of proportionality is very large, $ln(s)$ is in the order of the unit. $(l-1)ln(s)$ is therefore in the order of l. For the rightmost term of equation [2.7], even if $\partial s/\partial e\delta E$ is extremely high, its logarithm will never reach l because this term is linked to the change in the number of states of a single degree of freedom of the system. The term that prevails in equation [2.7] is of the order of magnitude of the degree of freedom of the system. In this way, we therefore obtain the following result:

$$\ln(N(E)) \approx l \qquad [2.8]$$

The logarithm of the number of accessible states of a system is of the same order of magnitude as the number of the degree of freedom of this system.

NOTE ON IRREVERSIBILITY.– This type of argument enables us to grasp the notion of irreversibility. Let us take an enclosure, isolated from the external environment and separated into two equal parts by a sealed wall. At the initial state, a gas is contained in one of the enclosure parts. This gas, which contains a number of molecules in the order of the Avogadro number, $\aleph$, is in equilibrium. At a given moment, the wall is removed. Each molecule therefore has access to more possible states throughout the increase in volume. It could be shown that the number of accessible states is doubled for each molecule. The number of accessible states for the complete system at equilibrium after withdrawing the wall is therefore multiplied by $2\aleph$. Thus, the probability of finding the initial state of the system in which all the gas molecules are one side of the enclosure is equal to $1/2\aleph$, which is extremely low. This transformation is therefore irreversible.

2.2.4. *Energy variation – work and heat*

We saw before that a system at equilibrium enabled us to calculate the average value of macroscopic parameters with the help of probability calculations. This calculation can be applied to the internal energy, U, of a system at equilibrium. We refer to internal energy to the exclusion of the possible macroscopic kinetic and potential energies of the system. For example, if the system is a gas enclosure, we assume that the enclosure is not displaced and does not have potential energy in the mechanical sense (it will not recover energy from a potential drop). Thus, we can say that the macroscopic internal energy, $\bar{U}$, of a system at equilibrium is, according to equation [2.1]:

$$\overline{U} = \sum_i P(U_i)U_i = \sum_i P_i U_i \qquad [2.9]$$

where $P(U_i) = P_i$ is the probability of finding a microscopic state, i, with macroscopic internal energy, U_i.

We want to calculate the energy change in the system during an interaction with the external environment. In order to conserve the possibility of carrying out probability calculations, we must assume that this change does not result in the system being out of equilibrium. Therefore, we consider an infinitesimal quasistatic change. The total differential of the average internal energy takes the following form:

$$d\overline{U} = \sum_i \left(dP_i U_i + P_i dU_i\right) \qquad [2.10]$$

This equation reveals that there are two possibilities for changing the internal energy of a system, whatever it may be: either the probability of occupying an energy state changes or the level of energy itself changes while at the same time conserving the same probability of occurrence. These two possibilities are none other than the infinitesimal heat, δQ, and work, δW, respectively, quantities transferred by the system:

$$\delta Q = \sum_i U_i dP_i \qquad [2.11]$$

$$\delta W = \sum_i P_i dU_i \qquad [2.12]$$

and we therefore get:

$$d\overline{U} = \delta Q + \delta W \qquad [2.13]$$

This relation, synonymous with the first principle of thermodynamics, is of utmost importance as it states, first and foremost, that heat and work are both energies. It is possible to transfer them in a system. In other words, it must be possible to find a system that enables us to transform heat into work. Furthermore, it says that the microscopic nature of heat and work is different. An increase in heat in a system implies that the microscopic energy levels are not modified. On the other hand, the probability of elevated energy levels being occupied increases. Furthermore, if work is received by a system, it is the energy level of the states that increases, while at the same time conserving the same probability of occurrence of each one of these states.

On the other hand, the first principle assumes that there is always a function called *internal energy* that depends on experimental variables describing the system whose change is indicative of all the energy transfers carried out by the system considered during a transformation. In other words, this principle translates energy conservation. A function capable of translating this conservation is a *function of state*. Its value only depends on the initial and final states of the system during transformation because all transfers are considered in this function. It must be noted that generally, transferred work and heat are not functions of state since part of work can be transformed into heat and vice versa. Experimental conditions make it such that this transfer can be different depending on the path followed [BER 84].

We will see, in section 2.3, that there are several possible functions of state depending on the experimental variables (or variables of state) considered. The choice of the correct function of state to describe system equilibrium is fundamental for a successful thermodynamic study.

2.2.5. *Heat transfer: entropy and absolute temperature*

2.2.5.1. *Heat transfer*

The aim of this section is to formalize the heat transfer of a system, S, of energy, E, with the external environment. To do this, we consider the system in contact with another system S_e of energy E_e that represents the external environment. These two systems are assumed to be isolated in order to consider the sum of their energy as being constant ($E + E_e = E_0 = constant$). The two systems are in equilibrium. The probability, $P_S(E)$, that system S will have energy E is equal to the ratio between the number of states accessible by S that have an energy $E(N_S(E))$ over the total number of states accessible by S. However, this last number is difficult to find as S is not isolated. It is wiser to place ourselves in the system $S + S'$ that is itself isolated. Thus, if S has an energy E, then S' has an energy $E' = E_0 - E$. $P(E)$ is therefore the product of states accessible to S of energy E ($N_S(E)$) and states accessible to S' of energy $E_0 - E((N_{S'}(E_0 - E))$ divided by the total number of states accessible by the two systems ($N_{S+S'}(E_0)$). As $S + S'$ is of constant energy and is isolated, $N_{S+S'}(E_0)$ is a constant:

$$P_S(E) = \frac{N_S(E) N_{S'}(E_0 - E)}{N_{S+S'}(E_0)} \qquad [2.14]$$

We previously saw that the number of accessible states of a system is a function that increases extremely rapidly with energy (see equation [2.6]). According to equation [2.14], the probability $P_S(E)$ is the product of a function $N_s(E)$ that increases very quickly with E, with another function $N_{S'}(E_0 - E)$ that reduces very quickly with E. We can therefore expect a very marked maximum of $P(E)$ as a function of E. In other words, when the two systems are in equilibrium, E takes an extremely probable particular value E_m, to the detriment of all other possible values. We can calculate this value by noting that the derivative of $P(E)$ in relation to E must be null when $E = E_m$:

$$\frac{\partial P(E)}{\partial E} = 0 \text{, which gives } \frac{1}{N}\frac{\partial N}{\partial E} = \frac{1}{N'}\frac{\partial N'}{\partial E'} \qquad [2.15]$$

with $N' = N_{S'}(E')$.

This equation can also be written:

$$\frac{\partial \ln N(E)}{\partial E} = \frac{\partial \ln N'(E')}{\partial E'} \qquad [2.16]$$

This relation, verified when $E = E_m$, translates the conditions for thermal equilibrium between the two systems.

2.2.5.2. *Entropy*

It is possible to define the macroscopic thermodynamic parameter called *entropy*, σ, from this last relation by writing:

$$\sigma = k \ln N(E) \qquad [2.17]$$

where k is the Boltzmann constant, whose presence will be explained a bit later. It is noteworthy that entropy is often expressed as S in the literature. Here we choose σ, as S corresponds to mechanical strain.

According to the thermodynamic postulate, the number of accessible states is at a maximum at equilibrium, which is translated by the fact that *entropy is at its maximum at equilibrium*. This notion of entropy is therefore particularly important, as knowing it enables us to determine the state of equilibrium of a thermodynamic system. Usually, entropy is associated with disorder. In other words, it is often evoked that the state of equilibrium is reached when maximum disorder is reached. This notion of disorder is not necessarily very intuitive and it is certainly preferable to associate entropy with its core definition, which makes it proportional to the number of microscopic states that the system involved can reach.

2.2.5.3. *Absolute temperature*

Let us note that equation [2.16] can be written using entropy:

$$\frac{\partial \sigma}{\partial E} = \frac{\partial \sigma'}{\partial E'} \qquad [2.18]$$

This equation enables us to define another thermodynamic parameter. This parameter is such that at thermal equilibrium between two systems it takes the same value in both. It is the absolute temperature, T, defined by the relation:

$$\frac{1}{T} = \frac{\partial \sigma}{\partial E} \qquad [2.19]$$

With this definition, it is possible to translate the thermal equilibrium condition between S and S' using the well-known relation:

$$T = T' \qquad [2.20]$$

Thus, at equilibrium the absolute temperature of the two systems is identical. This is obvious from a practical point of view, but here we have shown it using properties of entropy.

2.2.5.4. *Average energy per degree of freedom*

It is possible to estimate the average energy per degree of freedom at equilibrium by returning to the definition of absolute temperature as well as the estimation of the number of accessible states (see equation [2.7]):

$$\frac{1}{T} = \frac{\partial \sigma}{\partial E} = k \frac{\partial \ln N}{\partial E} \approx k \frac{l}{E - E_{\min}} \qquad [2.21]$$

Thus, at the equilibrium for which energy is equal to E_m we get:

$$kT \approx \frac{E_m - E_{\min}}{l} \qquad [2.22]$$

The average energy per degree of freedom is of kT order of magnitude. This enables us to understand why the Boltzmann constant was introduced in the definition of entropy. This constant is a macroscopic parameter defined using microscopic entities.

2.2.6. *Thermal energy: heat transfer*

To get a particularly useful form to thermal energy, it is wise to consider a quasistatic heat transfer between the system we are interested in and the external environment. This term quasistatic means that the equilibrium of the system is never broken and that the change in macroscopic parameters happens slowly enough to continuously conserve a state of equilibrium. This equilibrium evolves but is always present. Thus, an important change in a macroscopic parameter can be broken down into a series of infinitesimal changes that can be placed end-to-end without breaking equilibrium.

Here we are placing ourselves in the case of the infinitesimal heat transfer, δQ, of a system S' into a system S, without work transfer. We assume that the quantity of heat transferred is negligible compared to the average energy, E_0, of the system S. In other words, the transfer of this heat leads to a negligible change in the temperature, T, of S. Let us calculate the change in the logarithm of the number of accessible system states S before and after heat transfer ($lnN_S(E_0+\delta Q)-lnN_S(E_0)$). As δQ is very low with respect to E_0, it is legitimate to carry out a first-order expansion, which gives:

$$\ln N_e(E_0+\delta Q)-\ln N_e(E_0)=\delta Q\frac{\partial \ln N_e(E_0)}{\partial E}=\delta Q\frac{1}{kT} \qquad [2.23]$$

If we multiply the left term of this equation by k, we get the entropy change $\Delta\sigma$ of S, as defined previously. As we are considering an infinitesimal quantity of heat, the entropy change is also infinitesimal. $\Delta\sigma$ can therefore be expressed as $d\sigma$. Finally we get the following expression, which is valid in the case of infinitesimal heat transfer:

$$d\sigma=\frac{\delta Q}{T} \qquad [2.24]$$

By extension, this relation remains valid in the case of quasistatic heat transfer.

We must differentiate the affected differential, d, from the entropy of the affected infinitesimal quantity, δ, of heat. Indeed, heat is a quantity of transferred energy and not a function variation. Entropy is itself well defined before and after the transfer. $d\sigma$ is a true differential.

In the case of a system that transfers solely heat, work transfer is null.

According to equation [2.13] (the first principle of thermodynamics), we get:

$$dU_{thermal}=\delta Q \qquad [2.25]$$

Inserting the quasistatic relation (see equation [2.24]), the relation above becomes:

$$dU_{thermal}=Td\sigma \qquad [2.26]$$

This energy contribution corresponds to the thermal energy to be taken into consideration in the thermodynamic approach. It is therefore important to have a physical understanding of what entropy and absolute temperature are.

2.2.6.1. *Heat capacity*

We experimentally have access to heat. It is therefore very useful to define the heat capacity, C, of a system. This is the quantity of heat absorbed by the system during an increase in temperature:

$$C=\frac{\delta Q}{dT} \qquad [2.27]$$

In the case of a pure heat transfer (no work transferred), this relation can be combined with equation [2.26]:

$$dU_{thermal} = Td\sigma = \delta Q = CdT \qquad [2.28]$$

It is therefore possible, from heat transfer measurement, to calculate entropy using the relation:

$$d\sigma = C\frac{dT}{T} \qquad [2.29]$$

2.2.7. *Quasistatic transformation with work and heat transfer*

Now let us assume that the system above can exchange energy and work with the external environment. To simplify the calculation, we imagine that there is only one single external parameter, x, that influences the system. The energy, E, of the system therefore depends on the value of x. The number of microscopic states, N, accessible by the system depends both on E and x at the same time: $N=N(E,x)$.

If x varies from an infinitesimal quantity dx, a microscopic state i of energy E_i will vary from the value dE_i, such that:

$$dE_i = \frac{\partial E_i}{\partial x}dx = X_i dx = \delta W_i \qquad [2.30]$$

Here we have assumed that the change in heat was null. X_i corresponds to the conjugate variable of x. For example, if we consider electric displacement, D, as a controlled external parameter (i.e. x), then X is the electric field strength (we will see the different forms of work in more detail in the following chapters). In other words, the change in energy corresponds to the external work exchanged by the system with the external environment.

2.2.7.1. *Change in the number of accessible states as a function of x*

Although x often modifies each of the microscopic states in a different way when it changes from dx, to simplify the calculation we assume that all the accessible states are modified from the same energy when x becomes $x + dx$. The consideration of these different changes finally returns to the average, $\overline{X}$, of X_i over all the accessible states. All states are equiprobable as we are at equilibrium.

$N(E,x)$ is the number of accessible states of the system when its energy is between E and $E + \delta E$ and the external parameter takes the value x. In other words,

the number of states per unit of energy (which could be called the *energy state density*) is equal to $N(E,x)/\delta E$.

The next step is to calculate the number of states $\sum(E)$ that move from an energy below E to an energy greater than E when the external parameter moves from x to $x+dx$ (we assume that the change in x induces a positive change in energy). $\sum(E)$ is therefore the energy state density multiplied by the change in energy due to the change in the external parameter. We therefore get:

$$\Sigma(E) = \frac{N(E,x)}{\delta E}\overline{X}dx \qquad [2.31]$$

We can now calculate the change in the number of states when x varies in an infinitesimal way. As this variation induces a change in the energy of states, we must include the difference between the states that enter the $E + \delta E$ interval and those that leave it (from the top, as we are considering an increase in energy).

Thus we get:

$$\frac{\partial N(E,x)}{\partial x}dx = \Sigma(E) - \Sigma(E+\delta E) = -\frac{\partial \Sigma(E)}{\partial E}\delta E \qquad [2.32]$$

Using the expression $\sum(E)$ in the equation above, we get:

$$\frac{\partial N(E,x)}{\partial x} = -\frac{\partial\left(N(E,x)\overline{X}\right)}{\partial E} = -\overline{X}\frac{\partial N}{\partial E} - N\frac{\partial \overline{X}}{\partial E} \qquad [2.33]$$

Dividing by N, the previous equation becomes:

$$\frac{\partial \ln(N)}{\partial x} = -\overline{X}\frac{\partial \ln(N)}{\partial E} - \frac{\partial \overline{X}}{\partial E} \qquad [2.34]$$

We saw before that the change in the number of states as a function of energy is extremely high (see equation [2.6]). The first term of the right member of the equation above therefore generally dominates compared to the second term.

The change in the logarithm of N compared to E is known as $(1/kT)$, which enables us to write:

$$\frac{\partial \ln(N)}{\partial x} = -\overline{X}\frac{1}{kT} \qquad [2.35]$$

We will now be able to calculate the relationships between the different entities constituting the energy during a general quasistatic change with heat and energy transfer.

2.2.7.2. *Work and heat transfer through quasistatic transformation*

In our example with a single external parameter, x, we can write:

$$d\ln N = \frac{\partial \ln N}{\partial E} dE + \frac{\partial \ln N}{\partial x} dx \qquad [2.36]$$

According to what we have just seen, we get:

$$d\ln N = \frac{1}{kT} dE - \frac{\overline{X}}{kT} dx \qquad [2.37]$$

Modifying the place of kT, we cause the entropy change and the quantity of heat transferred to appear, which gives:

$$Td\sigma = dE - \overline{X}dx = \delta Q \qquad [2.38]$$

Finally, we can re-write the previous equation:

$$dE = Td\sigma + \overline{X}dx = \delta Q + \delta W \qquad [2.39]$$

The generalization to several external parameters is immediate because we just have to add a term to the quantity of work transferred, δW.

Equation [2.39] enables us to generalize the first principle in the case of a quasistatic transfer. It is possible to calculate the heat and work terms as well as entropy. This relation is very important as we saw that entropy enabled us to find the state of equilibrium of the system. Taking this general quasistatic change into consideration enables us to express the microscopic relations of the statistical postulate in equations that are useful for applications by causing measurable macroscopic parameters to appear.

2.2.8. *Example of a constant pressure and temperature experiment*

We will end these recollections on statistic thermodynamics with the classic situation of an experiment taking place at constant pressure and temperature. This example enables us to make the conditions of equilibrium stemming from entropy stand out for the function of state adapted to this situation. It is this very argument

that we will then use to systematically choose the correct function of state that will decide the condition of equilibrium through an extremum as a function of the external parameters chosen.

We therefore assume we have an isolated system, S_T, which can be for example an isolated room. This system is made up of two sub-systems: a source, S_0, which can be the surrounding air at a temperature T_0 and pressure P_0 that can interact with the system S in which we are interested. We assume that the work and heat transfers are so low for the source that P_0 and T_0 remain constant. This induces a quasistatic transformation for the system S_0.

The number of states accessible to S_T is equal to the product of the states accessible to S_0 and S. Therefore, the total entropy of the system is the sum of the entropies of the two sub-systems (as $\sigma = klnN$):

$$\sigma_T = \sigma_0 + \sigma \qquad [2.40]$$

As the source undergoes an infinitesimal transformation, we can use the entropy expression given by equation [2.38], considering a transferred heat Q_0 that gives:

$$\Delta\sigma_0 = \frac{Q_0}{T_0} \qquad [2.41]$$

It must be noted that the changes given can be important for the system S (hence the use of Δ instead of d and the omission of δ), but the source remains in the conditions of a quasistatic transformation. On the other hand, we assume that S_0 exchanges mechanical work with S through the application of pressure P_0. Thus, the work W_0 transferred is:

$$W_0 = P_0 \Delta V \qquad [2.42]$$

where ΔV is the change in the volume of system S (indeed, the product PV is homogeneous to the work).

The total energy of the system is constant, which leads to $\Delta E_0 + \Delta E = 0$. We therefore have:

$$Q_0 = \Delta E_0 - P_0 \Delta V = -\Delta E - P_0 \Delta V \qquad [2.43]$$

We can express the complete entropy change of the system as a function of the only variables of system S:

$$\Delta\sigma_T = \Delta\sigma_0 + \Delta\sigma = \frac{-\Delta E - P_0\Delta V + T_0\Delta\sigma}{T_0} = -\frac{\Delta G}{T_0} \qquad [2.44]$$

Here we have defined a new function $G = E + PV - T\sigma$. This function is homogeneous with an energy that gives the following formula because of the stability of P and T:

$$\Delta G = \Delta E + P_0\Delta V - T_0\Delta\sigma \qquad [2.45]$$

We have seen that the state of equilibrium corresponds to the maximum entropy. When the energy transfer occurs between S and the source S_0, entropy evolves until it reaches its maximum value. ΔS is thus maximum at equilibrium. Equation [2.44] indicates that the equilibrium condition is translated by ΔG minimum at equilibrium in the experimental conditions defined here: constant pressure and temperature.

In section 2.3 we will see the different possible functions describing the internal energy of the system, considered as a function of the experimental variables that are accessible.

2.3. State functions

This formalism has largely been described in the literature. Here we gather together the different approaches proposed in order to ensure coherence in the notations that can be found. This part is largely inspired by the articles by Devonshire [DEV 49] and Damjanovic [DAM 98], as well as the work by Lines and Glass [LIN 77].

The fact that several energy couplings are possible in many cases leads to several physical domains being mixed *a priori* without a link in the elaboration of their respective models. In thermodynamics, as we were able to see, the microscopic state of a system is described by breaking down its internal energy into several distinct contributions: mechanical, electrical, thermal, magnetic and chemical. All these contributions correspond to global, statistical values independently of any microscopic description of the state of the material of the system considered. If we are capable of writing the expression for this internal energy, then we can determine the state of the system as a function of independent macroscopic variables (for example, pressure or the electric field) and it becomes possible to determine its equilibrium as a function of these variables, as we saw in the previous section.

In the internal energy expression, the infinitesimal work quantity, δW, depends on the nature of the system's interactions with the external environment. Here, we will consider two types of interactions that can be applied to the solids considered:

mechanical and electric. Generalizing to other forms of energy (especially magnetic) can be done in the same way. So-called conjugate variable couples to be considered are: strains S and stresses T for the mechanical part, the electric field E and displacement D for the electric part, as we will see in the next chapters. In this book, we deliberately choose to describe the mechanical and electric works and their associated variables after the exposition of thermodynamic formalism. For what follows, we choose θ to describe the temperature in order to avoid all ambiguity with mechanical stress T.

Thus, for these two types of work, by virtue of the first principle and its validity in the case of a quasistatic transformation, the infinitesimal change in internal energy is:

$$dU = \theta d\sigma + TdS + EdD \qquad [2.46]$$

We recall that internal energy constitutes a *state function*, i.e. that it completely describes the energy transfers undergone by the system. Its changes therefore only depend on the initial and final states of the system during a transformation. dU is a total differential.

It is fundamental to note that the external parameters, defined as variables in this internal energy expression (S and D), correspond to a *choice*. Thus, to estimate the infinitesimal change in mechanical energy (TdS), the stress is fixed and we look at the change in strain. For electrical energy, E is considered to be fixed and we look at the change in electrical displacement (therefore charges). The contribution to dU is therefore EdD. To calculate dU, intensive variables are chosen as constants during the change (temperature, stress and electric field strength) whereas the extensive variables vary (entropy, strain and electric displacement). An extensive variable has a value that changes depending on the size of the system. According to what we saw when revisiting statistical physics, the main interest in the use of internal energy is in characterizing the equilibrium of the system at fixed electric entropy, strain and displacement. Indeed, we then have $dU = 0$, according to the equation above, which corresponds to an extremum of U. We can show that this extremum is a minimum [REI 65]. We then say that U represents the *thermodynamic potential* of this system for the transformation considered.

Experimentally, the parameters over which it is possible to intervene are not always the same. It is therefore interesting to be able to change the thermodynamic potential. This is can be done by carrying out a *Legendre transform* of internal energy, which refers to adding terms homogeneous to energy that are the product of conjugated variables. This operation transforms the internal energy into another state function. It is therefore possible to define a thermodynamic potential adapted to each experiment.

We commonly work at constant temperature rather than at constant entropy. On the other hand, to describe the ferroelectric-paraelectric phase transition, it is interesting to make polarization (and by extension, electric displacement) appear rather than the electric field, as it involves the order parameter of the transition. For the mechanical part, boundary conditions depend on the geometry of the sample. For the case of thin films, it is common to set different boundary conditions for stresses and strains. The most common thermodynamic potentials for the study of thin films are the following:

– Helmholtz free energy (F or A, depending on authors):

$$F = A = U - \sigma\theta \qquad [2.47]$$

– Gibbs energy:

$$G = U - \sigma\theta - TS - ED \qquad [2.48]$$

– Gibbs elastic energy:

$$G_1 = U - \sigma\theta - TS \qquad [2.49]$$

– Gibbs electric energy:

$$G_2 = U - \sigma\theta - ED \qquad [2.50]$$

NOTE.– By definition, mechanical stresses are positive when they are tensile and negative when they are compressive.

The total differentials obtained are:

$$\begin{aligned} dF &= dA = -\sigma d\theta + TdS + EdD \\ dG &= -\sigma d\theta - SdT - DdE \\ dG_1 &= -\sigma d\theta - SdT + EdD \\ dG_2 &= -\sigma d\theta + TdS - DdE \end{aligned} \qquad [2.51]$$

The three variables appearing in differential form in the second term of each equation correspond to the *natural* variables of each thermodynamic potential. Also, the minimum Gibbs elastic energy, G_1, is achieved at the equilibrium of a system for which temperature, stresses and electric displacement are constant. These three parameters represent the natural variables of G_1.

As we have seen, all these thermodynamic potentials are functions of state. Their differential is total because all possible contributions to energy change are considered. From a mathematical point of view, they are analytical functions depending on several variables. They have the property of being able to be broken

down into a Taylor series of different variables, provided that successive derivatives exist up to the order in which we are interested. If the second derivatives are continuous (which is true most of the time in physics), we get an important property: there is equality of cross derivatives. This enables us to obtain the *Maxwell relations of thermodynamics* that play a key role in thermodynamic potentials. For example, the equality of crossed derivatives for G_1 gives the following relations:

$$\left.\frac{\partial\sigma}{\partial T}\right)_{D,\theta} = \left.\frac{\partial S}{\partial\theta}\right)_{D,T} \qquad \left.\frac{\partial\sigma}{\partial D}\right)_{T,\theta} = -\left.\frac{\partial E}{\partial\theta}\right)_{T,D} \qquad \left.\frac{\partial S}{\partial D}\right)_{\theta,T} = -\left.\frac{\partial E}{\partial T}\right)_{\theta,D} \qquad [2.52]$$

Another translation of this property is that the order of derivation for the multiple derivatives is of no importance. Taking the example of G_1 again, we have:

$$\left.\frac{\partial G_1}{\partial T}\right)_{\theta,D} = -S \quad \left.\frac{\partial G_1}{\partial D}\right)_{\theta,T} = E \qquad [2.53]$$

which, by derivation with the crossed variable for each relation, gives:

$$\left.\frac{\partial\left(\left.\frac{\partial G_1}{\partial T}\right)_{\theta,D}\right)}{\partial D}\right)_{\theta,T} = -\left.\frac{\partial S}{\partial D}\right)_{\theta,T} \quad \left.\frac{\partial\left(\left.\frac{\partial G_1}{\partial D}\right)_{\theta,T}\right)}{\partial T}\right)_{\theta,D} = \left.\frac{\partial E}{\partial T}\right)_{\theta,D} \qquad [2.54]$$

This property can be represented in a diagram by the expression $\frac{\partial^2 G_1}{\partial D\partial T} = \frac{\partial^2 G_1}{\partial T\partial D}$. We will see that this property enables us to simplify the characteristic tensors of materials studied.

One final important note is that work and heat are not generally functions of state. Indeed, the first principle tells us that it is their sum that represents internal energy. Their differential is therefore not total. For energy balances, it is fundamental to work with state functions.

2.4. Linear equations – piezoelectricity

From these definitions, it is now possible to define state equations from different thermodynamic potentials. The simplest equations correspond to a hypothesis of linearity of all effects.

Let us continue our Gibbs elastic energy example. To go into detail, we must describe each conjugate variable according to the three axes, knowing that stresses and strains are described by rank 2 tensors, whereas electric field strength and displacement are described by vectors (rank 1 tensors). dG_1 becomes:

$$dG_1 = -\sigma d\theta - S_{ij} dT_{ij} + E_i dD_i \qquad [2.55]$$

Therefore, Gibbs elastic energy function of state can be mathematically written in the form of a Taylor series.

Stopping at second order, we get:

$$\begin{aligned}\Delta G_1 = G_1(\theta,T,D) - G_1(\theta_0,0,0) &= \left.\frac{\partial G_1}{\partial \theta}\right)_{T,D}(\theta-\theta_0) + \left.\frac{\partial G_1}{\partial T_{ij}}\right)_{\theta,D} T_{ij} + \left.\frac{\partial G_1}{\partial D_i}\right)_{T,\theta} D_i + \frac{1}{2}\left.\frac{\partial^2 G_1}{\partial \theta^2}\right)_{T,D}(\theta-\theta_0)^2 \\ &+ \frac{1}{2}\left.\frac{\partial^2 G_1}{\partial T_{ij}^2}\right)_{\theta,D} T_{ij}^2 + \frac{1}{2}\left.\frac{\partial^2 G_1}{\partial D_i^2}\right)_{\theta,T} D_i^2 + \frac{1}{2}\left(2\left.\frac{\partial^2 G_1}{\partial \theta \partial T_{ij}}\right)_D (\theta-\theta_0)T_{ij} + 2\left.\frac{\partial^2 G_1}{\partial \theta \partial D_i}\right)_T (\theta-\theta_0)D_i + 2\left.\frac{\partial^2 G_1}{\partial D_i \partial T_{jk}}\right)_\theta T_{jk} D_i\right) \\ &+ \textit{terms of greater order}\end{aligned} \qquad [2.56]$$

It is also possible to describe each non-natural variable by breaking them down following a Taylor series of natural variables.

Stopping at the first order, we get the following linear equations:

$$\begin{aligned} d\sigma &= \left.\frac{\partial \sigma}{\partial \theta}\right)_{T,D} d\theta + \left.\frac{\partial \sigma}{\partial T_{ij}}\right)_{\theta,D} dT_{ij} + \left.\frac{\partial \sigma}{\partial D_i}\right)_{\theta,T} dD_i \\ dS_{ij} &= \left.\frac{\partial S_{ij}}{\partial \theta}\right)_{T,D} d\theta + \left.\frac{\partial S_{ij}}{\partial T_{kl}}\right)_{\theta,D} dT_{kl} + \left.\frac{\partial S_{ij}}{\partial D_k}\right)_{\theta,T} dD_k \\ dE_i &= \left.\frac{\partial E_i}{\partial \theta}\right)_{T,D} d\theta + \left.\frac{\partial E_i}{\partial T_{jk}}\right)_{\theta,D} dT_{jk} + \left.\frac{\partial E_i}{\partial D_j}\right)_{\theta,T} dD_j \end{aligned} \qquad [2.57]$$

Each of the partial derivatives appearing in these equations represents a given distinct physical effect for particular conditions. Therefore $\left.\frac{\partial S_{ij}}{\partial D_k}\right)_{\theta,T}$ and $\left.\frac{\partial E_i}{\partial T_{jk}}\right)_{\theta,D}$ correspond, respectively, to the indirect piezoelectric effect at fixed temperature and stress on one hand, and the direct piezoelectric effect at fixed temperature and electric displacement on the other. Moreover, according to the Maxwell relations of thermodynamics applied to Gibbs free energy (see

equation [2.52]), these two coefficients are equal to a type of sign. *They are therefore energy considerations that prove that the direct and indirect piezoelectric effects are identical*.

In the end, it is possible to write linear equation [2.57] using the denominations of standards of piezoelectricity [IEE 87]. To do this, the changes in X variables are supposedly low, which allows the approximation $dX = X - X_0$ [LIN 77]. We get:

$$\Delta\sigma = \frac{c^{T,D}}{\theta}\Delta\theta + \alpha_{ij}^{D} T_{ij} - p_i^{*T} D_i \qquad [2.58]$$

$$S_{ij} = \alpha_{ij}^{D}\Delta\theta + s_{ijkl}^{\theta,D} T_{kl} + g_{kij}^{\theta} D_k \qquad [2.59]$$

$$E_i = p_i^{*T}\Delta\theta - g_{ikl}^{\theta} T_{kl} + \beta_{ik}^{\theta,T} D_k \qquad [2.60]$$

where:

$c^{T,D}$: heat capacity of the system with fixed T and D – scalar;

α_{ij}^{D} : coefficients of thermal dilation with fixed D – rank 2 tensor;

p_i^{*T} : pyroelectric coefficients of field strength with fixed T – rank 1 tensor;

$s_{ijkl}^{\theta,D}$: coefficients of elastic compliance with fixed θ and D – rank 4 tensor;

g_{kij}^{θ} : piezoelectric coefficients with fixed θ – rank 3 tensor;

$\beta_{ij}^{\theta,T}$: dielectric impermittivity coefficients with fixed θ and T – rank 2 tensor.

The coefficients that appear are tensors of various ranks between 0 and 4. It is noteworthy that piezoelectricity appears in the form of a tensor of third order. The indices chosen allow optimum accounting with the four possible forms of piezoelectric formalism (see Chapter 6). To end, it is noteworthy that the coupling coefficients, i.e. those that link variables of different natures (α_{ij}^{D}, p_i^{*T} and g_{kij}^{θ}), are identical in their direct and indirect effects by virtue of the thermodynamic Maxwell relations, as we explained for piezoelectricity. They are therefore given for a single fixed variable: the one that is not part of the coupling (for example, θ for piezoelectricity).

2.5. Non linear equations – electrostriction

The Taylor series development of free energies can occur at greater orders to take into consideration the nonlinear effects common in perovskites, such as the hysteretic relation between polarization and electric field or electrostrictive phenomena. A very good example of this development was given by Mason in 1950 to explain the electrotrictive effect of barium titanate ceramics [MAS 50]. It must be noted that this approach is independent of the description of the paraelectric-ferroelectric phase transition and that all the insulating materials can in theory be described in this way.

If we continue with our example based on Gibbs elastic energy, disregarding heat terms, the third-order expansion for energy and second-order expansion for non-natural variables gives the following equations:

$$S_{ij} = s_{ijkl}T_{kl} + g_{nij}D_n + \frac{1}{2!}\left[\frac{\partial^2 S_{ij}}{\partial T_{kl}\partial T_{qr}}T_{kl}T_{qr} + 2\frac{\partial^2 S_{ij}}{\partial T_{kl}\partial D_n}T_{kl}D_n + \frac{\partial^2 S_{ij}}{\partial D_n \partial D_o}D_n D_o\right] \quad [2.61]$$

$$E_m = -g_{mkl}T_{kl} + \beta_{mn}D_n + \frac{1}{2!}\left[\frac{\partial^2 E_m}{\partial T_{kl}\partial T_{qr}}T_{kl}T_{qr} + 2\frac{\partial^2 E_m}{\partial T_{kl}\partial D_n}T_{kl}D_n + \frac{\partial^2 E_m}{\partial D_n \partial D_o}D_n D_o\right] \quad [2.62]$$

We get $\frac{\partial^2 S_{ij}}{\partial D_n \partial D_o} = -\frac{\partial^3 G_1}{\partial D_n \partial D_o \partial T_{ij}} = -\frac{\partial^3 G_1}{\partial T_{ij}\partial D_n \partial D_o} = -\frac{\partial^2 E_o}{\partial T_{ij}\partial D_n} = 2Q_{noij}$ with Q_{noij}, the electrostrictive coefficients. Electrostriction is therefore represented by a tensor of fourth order. Term $\frac{\partial^2 S_{ij}}{\partial T_{kl}\partial T_{qr}}$ corresponds to the change in flexibility as a function of stress, $\frac{\partial^2 S_{ij}}{\partial T_{kl}\partial D_n}$ to the change in flexibility as a function of the electric displacement, $\frac{\partial^2 E_m}{\partial T_{kl}\partial T_{qr}}$ to the change in piezoelectric coefficients as a function of stress, and $\frac{\partial^2 E_m}{\partial D_n \partial D_o}$ to the change in the reverse of dielectric permeability as a function of electric displacement.

As can be seen in this example, complexity increases very quickly and the number of experiments required to determine all these coefficients can become impossible. It is necessary to make assumptions on the preponderance of certain effects in relation to others. For the case of perovskites, the higher-order terms involving electric variables are often preponderant compared to those related to mechanical variables. This comes from the fact that the dielectric constant is very sensitive to all the experimental variables. For other materials, such as AlN (another

notable piezoelectric), the changes in coefficients as a function of variables are much more homogeneous and it is harder to disregard the mechanical terms.

2.6. Bibliography

[BER 84] BERTIN M., FAROUX J.-P., RENAULT J., *Cours de Thermodynamique*, Dunod University of Paris, 1984.

[DAM 98] DAMJANOVIC D., "Ferroelectric, dielectric and piezoelectric properties of ferroelectric thin films and ceramics", *Rep. Prog. Phys.*, 61, 1267-1324, 1998.

[DEV 49] DEVONSHIRE A.F., *Philosophical Magazine*, 40, 1040, 1949.

[IEE 87] IEEE Standard on Piezoelectricity, ANSI/IEEE Std, 176, 1987.

[JUN 03] JUNQUERA J., GHOSEZ P., *Nature*, 422, 506, 2003.

[LIN 77] LINES M.E., GLASS A.M., *Principles and Applications of Ferroelectrics and Related Materials*, Clarendon Press, Oxford, 1977.

[MAS 50] MASON W.P, *Piezoelectric Crystals and their Application to Ultrasonics*, D. Van Nostrand Company, New Jersey, 289, 1950.

[REI 65] REIF F., *Statistical Physics*, Berkeley Physics Course, vol. 5, McGraw-Hill, New York, 1965.

Chapter 3

Ferroelectric-paraelectric Phase Transition Thermodynamic Modeling

3.1. Hypothesis on Gibbs' elastic energy

Ferroelectric-paraelectric transition appears at a given temperature called the Curie temperature, T_C, which is analogous to ferromagnetics. Thus, above T_C the lattice is centrosymmetric (simple cubic for perovskites) and therefore no polarization can appear if the electric field strength is null. Below T_C, a polarization can appear even at null field strength because the crystal lattice loses its center of symmetry. For barium titanate ($BaTiO_3$ called BTO), one of the most frequently studied perovskites, it is the tetragonal phase that appears below T_C. Polarization in this phase follows direction <001>, often called the c-axis.

As specified before, the thermodynamic description does not require knowledge of microscopic phenomena. It is an energy description that relies on the identification of "good" macroscopic "variables", chosen as a function of experimental conditions undergone by the system described. The choice of an adapted free energy that takes a minimum value when equilibrium is reached by virtue of thermodynamic principles results from this. The usual hypothesis is therefore to describe this energy using a polynomial that involves the order parameter. This is an experimental parameter whose value is null in one of the phases and non-null in the other. It is therefore representative of this transition. In the case of ferroelectric-paraelectric transition, the order parameter is polarization. Indeed, in the cubic phase, no polarization can appear in the absence of an electric field, or cubic symmetry would no longer be respected [NYE 61]. On the other

---

Chapter written by Emmanuel DEFAŸ.

hand, in the ferroelectric phase just below T_C (tetragonal phase for BTO), the loss of symmetry enables the appearance of a non-null polarization in the absence of an electric field.

The order of the polynomial depends on the degree of nonlinearity necessary for the phenomenological description of transition. An additional clever hypothesis is suggested by Landau: the same polynomial can describe the high- and low-temperature phase. For ferroelectrics, this is justified by the fact that, though non-centrosymmetric, the low-temperature lattice is very similar to the high-temperature one. For example, the strain of the lattice parameter undergone by BTO during phase transition is of the order of one percent. Thus, centrosymmetric high-temperature phase modeling, called the prototype phase, must enable us to describe the system above but also below T_C. The main limitation of this hypothesis is that it does not allow a perfect description of critical phenomena that appear in second-order transitions (without phase transition of latent heat) [LIN 77]. This approach gives very satisfying results for describing the greater part of perovskite behaviors, however, whether in bulk form or in thin films.

Cubic phase symmetry enables us to simplify the polynomial. Indeed, the odd terms of the order parameter are excluded from the polynomial. If there were such terms, the energy would not be the same in the cubic lattice following different direction of polarization, which is impossible. Regarding the order parameter, the accessible experimental variable is not polarization, *P*, but electric displacement, *D*, whose derivative in time gives electric current. However, polarization is the order parameter, as this variable enables us to better understand what happens on the crystal lattice scale during the transition. As $D = \varepsilon_0 E + P$ and transition intervenes when *P* becomes non-null for a null electric field *E*, it is equivalent to the thermodynamic sense of considering *P* or *D* as a conjugated variable of *E* when describing transition.

Lines and Glass, in their description of ferroelectric materials in 1977 [LIN 77], point out that it is not correct to use the *(P,E)* couple to describe the electric contribution in the different free energies. Actually, it is not possible to experimentally control polarization, which results in an uncertainty in the definition of constants defined at constant *P*. On the other hand, using *P* in the energy balance results in electric displacement being neglected in the vacuum, $\varepsilon_0 E$. Nevertheless, most of the time this ambiguity does not play a very important role. This is because perovskite permittivity is very high compared to that of vacuum, which means *D* and *P* exhibit extremely similar values. We will, however, adopt the thermodynamic orthodox approach by using the (*D,E*) couple of conjugated variables to describe the electric contribution of free energies.

Thus, the classic way to describe ferroelectric-paraelectric transition is to use temperature, mechanical stresses and electric displacement as variables. The natural variables are therefore (θ,T,P), which corresponds to Gibbs' elastic energy G_1. G_1 is therefore the thermodynamic potential whose minimum will define equilibrium. To simplify things, we place ourselves in the one-dimensional case where polarization can only take a single direction in the non-centrosymmetric phase, a direction that corresponds to that of the electric field. In these conditions, G_1 can take the form of the following polynomial [UCH 97]:

$$G_1(\theta,T,D)-G_1(\theta_0,0,0)=\frac{1}{2}\alpha D^2+\frac{1}{4}\alpha' D^4+\frac{1}{6}\alpha'' D^6-\frac{1}{2}sT^2-QD^2T \qquad [3.1]$$

Order 6 is generally sufficient to reveal first- and second-order transitions for most materials. More recently, Vanderbilt *et al.* suggested keeping the terms up until order 12 to correctly predict $Pb(Zr_{0.52}Ti_{0.48})O_3$ (PZT) behavior in the morphotropic region of its phase diagram where several monoclinic phases appear [VAN 01]. The fourth term from the right corresponds to elastic energy (with $S = sT$) and the last term is the electrostriction term that can appear in the centrosymmetric phase. The thermal term does not appear explicitly but the temperature dependence is found in the α coefficients.

At first sight, this equation does not seem well-adapted for describing the low-temperature phase as piezoelectricity does not explicitly appear. We will, however, see that this linear property can be described by the presence of a remanent polarization associated with the electrostrictive effect. In addition, this approach turns out to be a lot closer to experience as it highlights the significant influence of the dielectric constant in piezoelectric coefficients.

On the other hand, the choice of signs in equation [3.1] is not, *a priori*, of importance as it is enough to correct these signs in the different coefficients *(α, s, Q)*. Despite this, it is wiser to choose signs that enable us to define positive elastic compliances, s_{ii}, and positive electrostrictive coefficients, Q_{iijj}, by respecting the "natural" signs of the total differential of Gibbs' elastic energy. Actually, s_{ii} is the reverse of Young's modulus in an isotropic material, and electrostriction is often defined simply by the relation between the strain S induced by the electrostrictive effect and electric displacement D by $S = QD^2$. Experimentally, in the one-dimensional case (for example, depending on thickness) and for ceramic materials, Q is always positive, which means that the material experiences an increase in thickness when D is non-null.

To characterize the transition, we must follow electric displacement as a function of temperature at null electric field strength. This means that thermodynamic

potential is not G_1 but G Gibbs' energy such that $G = G_1 - ED$. This change in thermodynamic potential can seem strange, but it enables us to have an expression that depends on order parameter D and set the electric field to a null value at the same time, which is necessary for observing this transition. Therefore, it is $G(\theta, T, E)$ that is minimum at equilibrium. The expression of E is given by the derivative of G_1 in relation to D:

$$\left.\frac{\partial G_1}{\partial D}\right|_{T,\theta} = E = \alpha D + \alpha' D^3 + \alpha'' D^5 - 2QDT \qquad [3.2]$$

3.2. Second-order transition

To describe the transition in the simplest way possible, let us place ourselves at null stress and take α' to be positive and α'' to be null. This scenario corresponds to transitions called second-order transitions for which there is no latent heat associated with phase change. Here the order parameter continuously changes until it reaches zero as temperature increases until it reaches T_C. The transition appears when there is a null-field electric displacement, which gives:

$$0 = D(\alpha + \alpha' D^2) \qquad [3.3]$$

Non-null D is possible if solution $D^2 = -\frac{\alpha}{\alpha'}$ exists. Following Landau's example, Devonshire introduced temperature in the α term in the simplest possible way by suggesting a linear dependence of the form $\alpha = \frac{\theta - \theta_C}{C}$, with θ_C and C being the Curie temperature and Curie constant, respectively. This dependence is physically explained by the thermal expansion that appears when temperature changes. Therefore, above θ_C, D is null and below θ_C, $D = \sqrt{\frac{\theta_C - \theta}{C\alpha'}}$. Let us note that the form of α is not completely the same if α'' is non-null as we will see later. In this simple model, the energy's temperature dependence only appears in the α coefficient. α' and α'' are considered constants.

The expression of β, the reverse dielectric susceptibility χ, is obtained by deriving equation [3.2] according to D, which gives:

$$\left.\frac{\partial E}{\partial D}\right|_{T,\theta} = \beta^{T,\theta} = \left.\frac{1}{\chi}\right|_{T,\theta} = \alpha + 3\alpha' D^2 + 5\alpha'' D^4 - 2QT \qquad [3.4]$$

Taking the same hypotheses as before (null *T (stress)*, null α'' and positive α'), the values of χ on both sides of the transition become:

$$\begin{aligned} \theta > \theta_C &\longrightarrow \chi_{T,\theta} = \varepsilon_{T,\theta} - 1 = \frac{1}{\alpha} = \frac{C}{\theta - \theta_C} \\ \theta < \theta_C &\longrightarrow \chi_{T,\theta} = \varepsilon_{T,\theta} - 1 = \frac{1}{\alpha + 3\alpha' D^2} = \frac{C}{2(\theta_C - \theta)} \end{aligned} \qquad [3.5]$$

These expressions, widely described in the literature, highlight the fact that the dielectric constant ε diverges when $\theta = \theta_C$, that ε follows Curie-Weiss law in the paraelectric phase, and that the gradient of ε as a function of $1/\theta$ is twice as low and in the opposite direction in the ferroelectric phase as in the paraelectric phase.

To illustrate these properties, we take the example of a ferroelectric that could be compared to *PZT*. The description that follows is, however, more qualitative than quantitative because of many extrinsic effects that can appear during the synthesis of a real material and which, in addition, is in a thin film (interfaces, crystal defects, space charges, grains). To do this, we take $\theta_C = 400$ °C, $C = 10^5.\varepsilon_0$ F/(m.K), $\alpha' = 8.10^9$ m^5/(F^{3}V^2), $s = 1/(100\text{GPa}) = 10^{-11}$m²/N and $Q = 0.1$m^4/C².

Figure 3.1a represents Gibbs' elastic energy calculated according to equation [3.1] as a function of electric displacement at different temperatures on both sides of transition (400°C). The minimums of each of the curves correspond to the state of equilibrium. We observe that below θ_C, there are two possible symmetrical states of equilibrium in relation to null D, and that we continuously get closer to the state of equilibrium for null D when θ tends towards θ_C. This equilibrium is reached when $\theta = \theta_C$ and remains the same when the temperature increases again. The absolute value of electric displacement D at equilibrium is illustrated in Figure 3.1b, in accordance with equation [3.3]. D continuously decreases as temperature increases until it is cancelled at 400°C, which is characteristic of a second-order transition.

The change in the dielectric constant ε as a function of temperature is easily obtained with equation [3.5] and is not represented here. ε tends towards infinity as temperature gets closer to 400°C. This phenomenon is sometimes called *polarization catastrophe* as in this case a very low electric excitation induces an infinite polarization, only limited by nonlinearities. Physically, it is a very low frequency transverse optical phonon (the soft mode) that originates in the ferroelectric material and explains the extremely high polarizability [KIT 04].

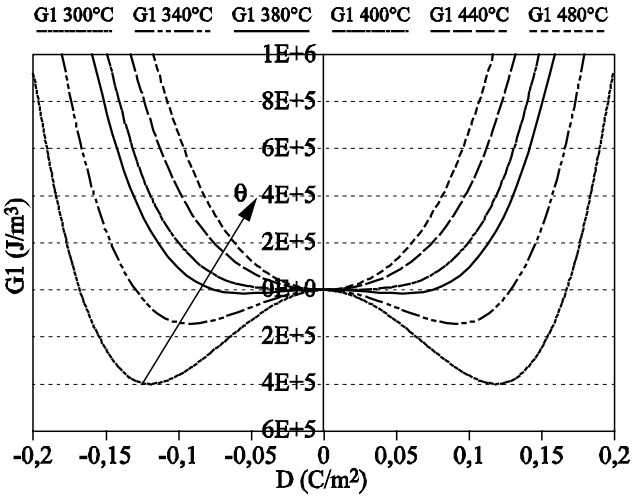

a)

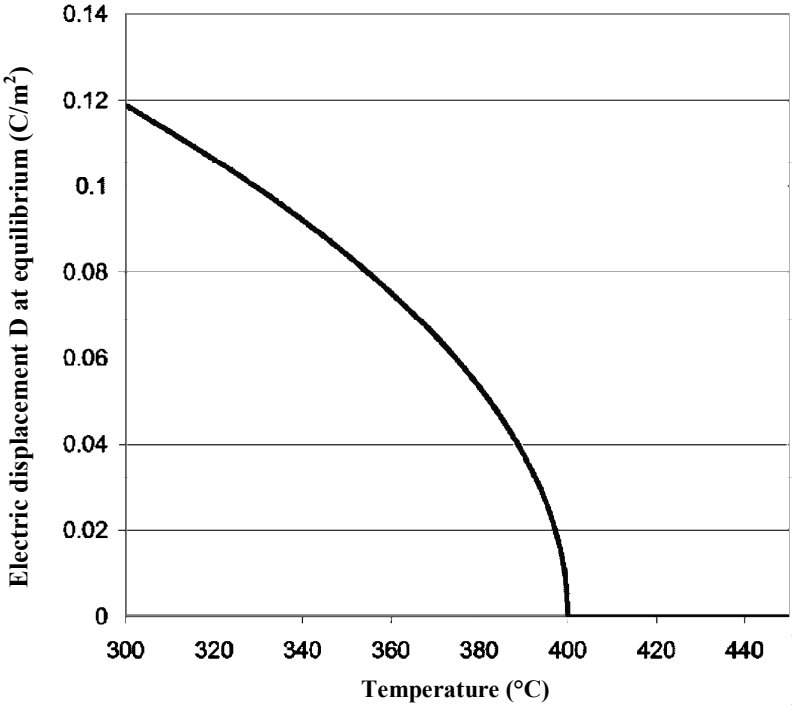

b)

Figure 3.1. *a) Gibbs' elastic energy calculated as a function of electric displacement for a second-order transition; and b) electric displacement at equilibrium as a function of temperature*

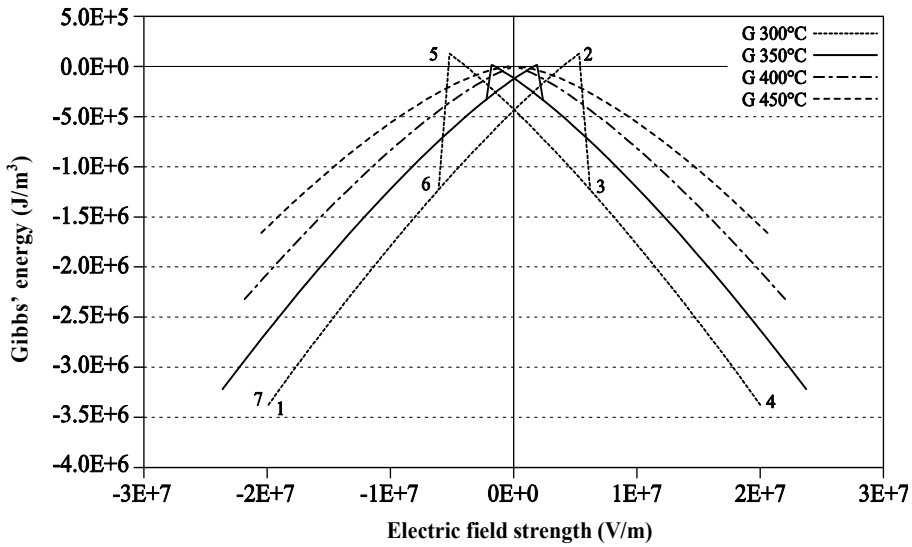

Figure 3.2. *Gibbs' energy, G, as a function of electric field strength applied to different temperatures for a second-order transition*

In accordance with the above remarks, it is often wiser to represent the functions describing transition as a function of electric field E, hence the use of G in place of G_1. Thus, Figure 3.2 represents the change in G as a function of E at different temperatures around transition, calculated with equation [3.1], as well as $G = G_1 - ED$. The change in field strength begins at the most negative values, reaches its maximum value, and then re-descends to its minimum value.

The curve reveals a hysteresis when the temperature is located below θ_C. To describe these hystereses, it is good to rely on D's curve obtained as a function of E based on equation [3.2]. D is therefore copied to Figure 3.3 and also reveals a hysteresis characteristic of ferroelectric materials. The description of the cycle is identical to that of G and is marked off based on numbers 1 to 7, included in Figures 3.2 and 3.3.

To get a rough understanding of these hystereses, we can propose a macroscopic description of a single crystal ferroelectric material in which several ferroelectric domains can be formed. A ferroelectric domain is a part of the material in which the polarization value is identical and no two adjacent domains have the same polarization value. In this explanation, we will lump together electric displacement and polarization, which is legitimate for ferroelectrics given their dielectric constant.

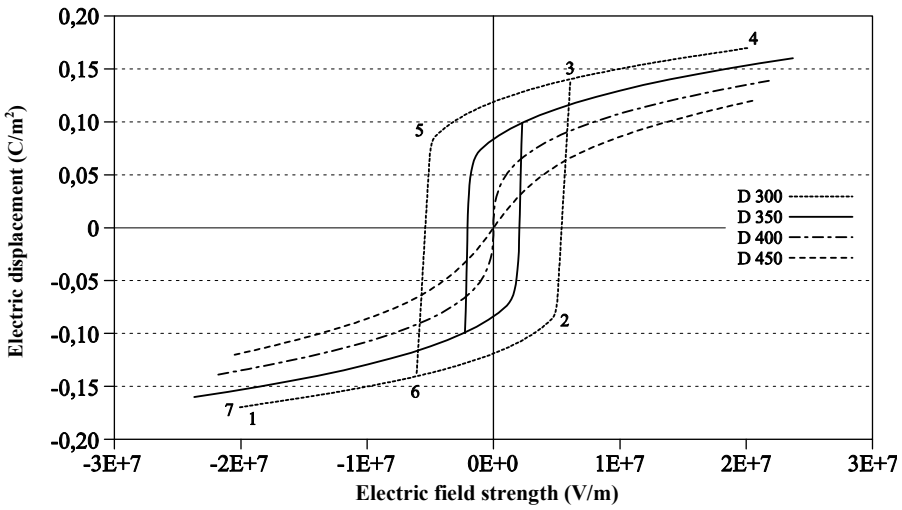

Figure 3.3. *Electric displacement as a function of electric field strength applied to different temperatures for a second-order transition*

Therefore, for a strong and negative field strength, polarization follows the field strength and is therefore also negative because we are located beyond the coercive field (point 1 of Figure 3.3). When field strength tends towards positive values, G increases because the absolute value of ED decreases and polarization decreases because several ferroelectric domains successively tip over in the positive direction. This progressive overbalancing is illustrated by the nonlinear term α'. At point 2, the coercive field is almost reached and is therefore the maximum of G since $| ED |$ is minimum at that time. At point 3, the coercive field is reached and all the domains that have not yet tipped over do so to give a positive polarization. $| ED |$ becomes important again and therefore decreases G (leading to a more stable state).

Energy further decreases as field strength increases because $| ED |$ increases. Polarization increases slightly still by pure dielectric effect (point 4). When the electric field strength decreases, the situation is exactly symmetrical, with a gradual decrease in polarization correlated with the increase in free energy until negative coercivity (point 5). There is a sudden overbalancing of polarization and energy to negative coercivity (point 6) and a gradual decrease in energy with a gradual increase in polarization as the field strength decreases (point 7).

When temperature increases, this hysteresis effect decreases to completely disappear at the Curie temperature, beyond which the nonlinear effect subsists. The microscopic origin of this nonlinear effect is located in the decrease in polarizability as electric field strength increases.

It is also possible to plot the evolution of the relative dielectric constant ε_r as a function of field strength at different temperatures (see Figure 3.4). Hysteresis is visible in the evolution of ε_r when temperature is below 400°C. The maximum of ε_r appears at coercive fields (points 2 and 5) corresponding to the polarization overbalancing, which brings a very important contribution to material polarizability (infinite in the case of our model).

The coercivity value decreases during the increase in temperature to be cancelled at θ_C, at which ε_r reaches an infinite value at null field strength. It is interesting to note that at null field strength, the change in ε_r as a function of temperature is in accordance with equation [3.5] because the values of ε_r are identical at 350°C and 500°C (factor on both sides of the transition). At high field strength, all the ε_r decrease as the polarizability of the material decreases. In physical terms, this corresponds to soft mode hardening, i.e. to an increase in its resonance frequency. Another way of seeing things is to consider one of the equalities of cross derivatives of G, which gives:

$$\left.\frac{\partial \sigma}{\partial E}\right|_{T,\theta} = \left.\frac{\partial D}{\partial \theta}\right|_{T,E} \qquad [3.6]$$

We saw that D decreases with temperature at null stress and field strength. According to equation [3.6], this means that entropy decreases as a function of the field strength applied at given stress and temperature. In other words, the number of accessible microscopic states of the system decreases with field strength. The ease of movement of charged spaces contributing to material polarization therefore decreases with field strength as does the dielectric constant.

On the other hand, Figure 3.4 shows that ε_r has a tendency to be higher at a strong field strength when the temperature is greater – although at higher temperatures the effect is cancelled (unrepresented). This comes from competition between terms α and $3\alpha' D^2$. Actually, α increases with temperature, whereas $3\alpha' D^2$ decreases because for a given E. D is lower when the temperature is high. This last remark can seem paradoxical as if D, which is often defined as $D = \varepsilon E$, is lower this means that ε is also lower, whereas the reverse is observed. The reason for this comes from the fact that the phenomenological definition of ε is $\partial D / \partial E$, which implies that it is the change in D as a function of E that matters.

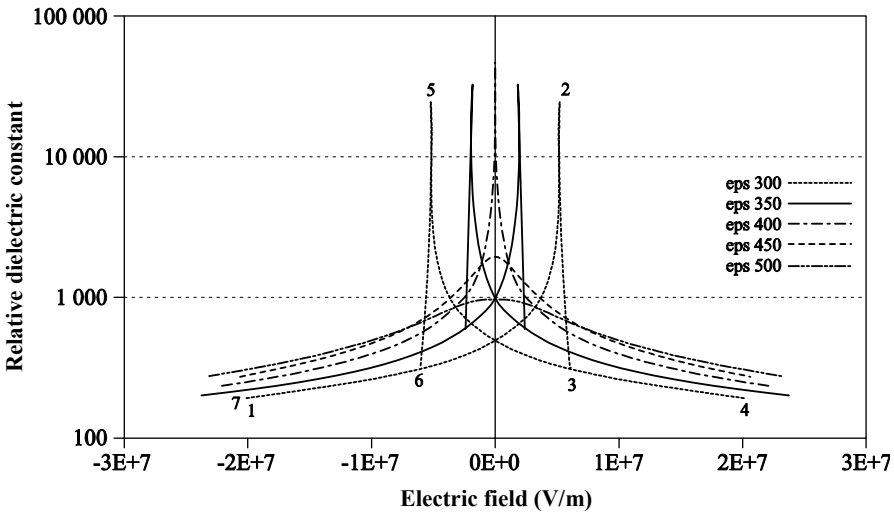

Figure 3.4. *Relative dielectric constant as a function of electric field strength applied at different temperatures for a second-order transition*

3.3. Effects of stresses

Comparing this model to experience gives very good results for bulk materials. For thin films, non-negligible differences can appear, especially due to extrinsic parameters such as stresses.

Therefore, if we place ourselves at fixed but non-null stress, equation [3.2] (still with positive α' and null α'', therefore for a second-order transition) becomes:

$$E = D\left(\alpha + \alpha' D^2 - 2QT\right) \qquad [3.7]$$

This gives a transition when the following expression is cancelled:

$$D^2 = \frac{2QT - \alpha}{\alpha'} = \frac{2QT - \frac{\theta - \theta_C}{C}}{\alpha'} \qquad [3.8]$$

The temperature θ_{CT} at which a non-null electric displacement appears for a null electric field when a stress is applied is therefore:

$$\theta_{CT} = \theta_C + 2QCT \qquad [3.9]$$

Therefore, for the PZT example above, the term *2QCT* is equal to 35.4°C for a typical stress for thin films of 200 MPa. Figure 3.5 illustrates the impact of different stresses on Gibbs' elastic energy, G_1, plotted as a function of D at 420°C, i.e. above the θ_C of the unstressed material. For null or negative stresses (compression), there is only one minimum located at null D, therefore the material is paraelectric. A tensile stress of 100 MPa induces a G_1 curve that is very close to transition and a stress of 200 MPa clearly causes two minima to appear, a tendency that is further supported for 300 MPa. Thus, in accordance with equation [3.9], tensile stresses (applied along sample thickness) stabilize the ferroelectric phase by shifting the transition towards high temperatures.

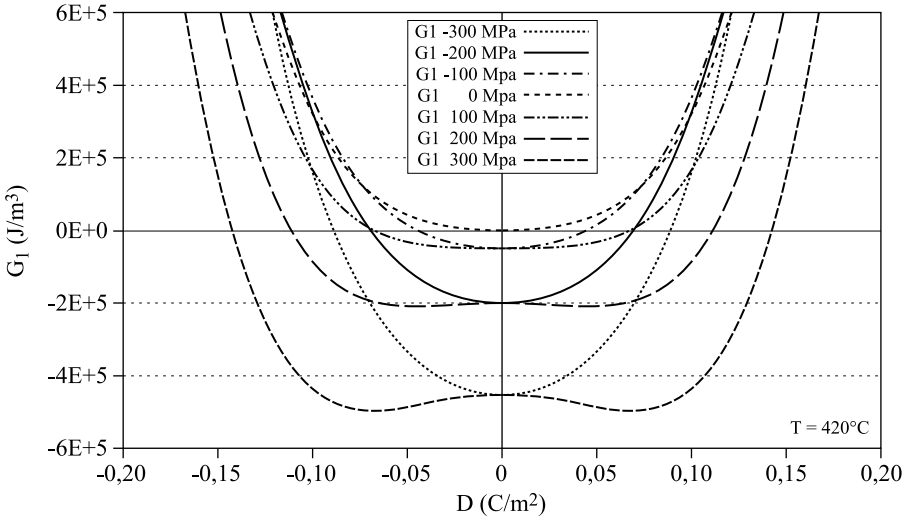

Figure 3.5. *Gibbs' elastic energy at 420°C as a function of electric displacement at different applied stress values*

Qualitatively, for the configuration of a plane capacitance vertically polarized by two electrodes, this means that an out-of-plane lattice traction helps to maintain polarization at null field strength. In the case of BTO, which is tetragonal just below transition, it is easy to imagine that this traction helps with the establishment of the out-of-plane *c*-axis, as this axis carries the polarization. It must be noted that most discussions focusing on stresses in thin films concern stresses in the plane and not the out-of-plane.

3.4. First-order transition

To end this description of transition, we must consider the case where α' is negative and α'' non-null in equation [3.1]. This corresponds to a first-order transition for which electric displacement presents a discontinuity for transition. The presence of phase transition latent heat, unlike second-order transitions, must be noted. At null stress, G_1 is expressed as follows:

$$G_1(\theta,0,D)-G_1(\theta_0,0,0)=\frac{1}{2}\alpha D^2+\frac{1}{4}\alpha' D^4+\frac{1}{6}\alpha'' D^6 \qquad [3.10]$$

where α is defined a bit differently than for a second-order transition by $\alpha = (\theta - \theta_0)/C$, with θ_0 being the *Curie-Weiss* temperature. This is not entirely the same as θ_C for a first-order transition, as we will see. α' and α'' are considered constants.

At equilibrium, when E is defined as null, $G = G_1 - ED$ is the minimum. At null stress, we get the relation:

$$0=D\left(\alpha+\alpha' D^2+\alpha'' D^4\right) \qquad [3.11]$$

There is a solution to equation [3.11] for non-null D corresponding to a minimum:

$$D^2=\frac{-\alpha'+\sqrt{\alpha'^2+4\alpha''\frac{\theta_0-\theta}{C}}}{2\alpha''} \qquad [3.12]$$

The other solution, with a minus in front of the square root, exists between θ_0 and θ_1. The latter is the temperature that cancels the square root. However, this solution corresponds to a maximum and is therefore not a position of equilibrium. θ_1 also corresponds to the maximum temperature for which D can be non-null, even beyond θ_C. Thus, between θ_C and θ_1, metastable states of non-null D can exist, as we will see in Figure 3.6. θ_1 is represented by the following formula:

$$\theta_1=\theta_0+\frac{C\alpha'^2}{4\alpha''} \qquad [3.13]$$

In the paraelectric phase, if E is null, D is null and according to equation [3.10] G_1 is also null. Therefore, solutions to non-null D correspond to the absolute minimum of G_1 if G_1 is less than zero for these values of D.

Thus, transition intervenes at θ_C when we have null G_1 and $\partial G_1/\partial D$ simultaneously for non-null D. We must therefore cancel equation [3.10] and equation [3.11] for non-null D. The solution to the system gives:

$$D^2(\theta_C) = \frac{4(\theta_0 - \theta_C)}{C\alpha'} = \frac{-3\alpha'}{4\alpha''} \qquad \theta_C = \theta_0 + \frac{3C\alpha'^2}{16\alpha''} \qquad [3.14]$$

The reverse dielectric susceptibility $1/\chi$ is obtained by deriving equation [3.10] twice in relation to D:

$$\frac{1}{\chi} = \alpha + 3\alpha' D^2 + 5\alpha'' D^4 = \frac{\theta - \theta_0}{C} + 3\alpha' D^2 + 5\alpha'' D^4 \qquad [3.15]$$

Beyond transition ($\theta > \theta_C$), null D is the most stable solution and $\chi = \varepsilon - 1 = C/(\theta - \theta_0)$ follows Curie-Weiss law.

Getting closer to θ_C from high temperatures, we get:

$$\frac{1}{\chi}\left(\theta_C^+\right) = \frac{\theta - \theta_0}{C} = \frac{\theta - \theta_C}{C} + \frac{3\alpha'^2}{16\alpha''} \qquad [3.16]$$

Getting closer to θ_C from low temperatures, we can estimate the value and gradient of $1/\chi$ by doing a first-order expansion, which gives:

$$\frac{1}{\chi}\left(\theta_C^-\right) \overset{1^{st}\,order}{\approx} \frac{8(\theta - \theta_C)}{C} + \frac{3\alpha'^2}{4\alpha''} \qquad [3.17]$$

The gradient of $1/\chi$ as a function of θ is thus eight times greater before transition than after it (ignoring the sign change). $1/\chi$ remains finite around transition and the relationship between the values before and after transition is equal to 4.

To illustrate these formulae, we return to the numerical example above, using the following parameters: $\theta_0 = 400°C$, $C = 10^5.\varepsilon_0$ F/(m.K), $\alpha' = -8.10^9$ m^5/(F^{3}V^2), and $\alpha'' = 6.10^{11}$ m^9/(F^{5}V^4). The characteristic magnitudes stemming from the model above are therefore $\theta_C = 417.7°C$, $D(\theta_C) = 0.10$ C/m² and $\theta_1 = 423.6°C$.

Figure 3.6 represents Gibbs' elastic energy, G_1, as a function of D for different temperatures for a null mechanical stress. Up to 417.7 °C (θ_C), there are two absolute minima for G_1 that correspond to the two possible states for polarization in the ferroelectric phase (same modulus but different meaning). At 417.7°C, there are three absolute minima for which G_1 and its derivative in relation to D are cancelled. This is transition.

Between 417.7°C and 423.6°C (θ_1), the minima of non-null D still exist but are no longer absolute minima: they correspond to metastable equilibriums. We also observe that between 400°C (θ_0) and 417.7°C, the solution $D = 0$ is a minimum, but not absolute. They are the metastable states of the paraelectric phase below transition. For θ >417.7°C, only one absolute equilibrium still exists – that of null D. Thus, at transition D suddenly moves from a non-null value to a null value.

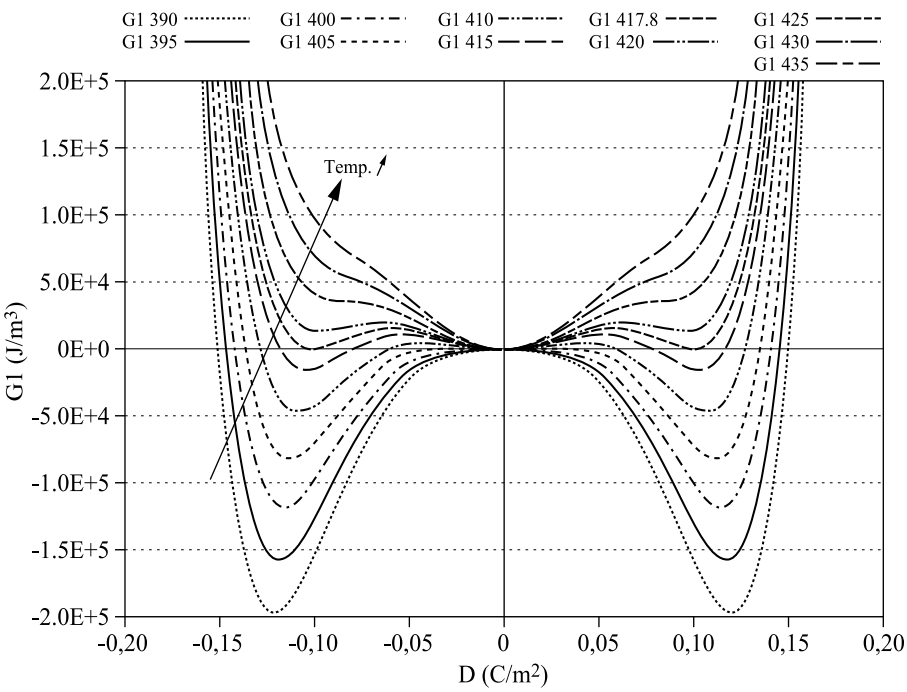

Figure 3.6. *Gibbs' elastic energy G_1 as a function of electric displacement at different temperatures around a first- order transition*

To make this last remark more specific, Figure 3.7 presents both metastable D and G_1 at equilibrium at the same time in the transition region. Metastable D corresponds to non-null values of D for which $G_1(D)$ is a local minimum, as seen in

Figure 3.6. Therefore, a reduction in D correlates with an increase in G_1 when transition is approaching. When G_1 is cancelled, absolute equilibrium is at null D, hence transition that takes place here at 417.7°C. The curve also informs us of the values of D for the metastable states of equilibrium at non-null D between θ_C and θ_1 (423.6°C).

These metastable states induce an experimental difficulty in pinpointing transition since there is a range of about 20°C ($\theta_1 - \theta_0$) in the example presented in which the two cases of polarization (null and non-null) can coexist.

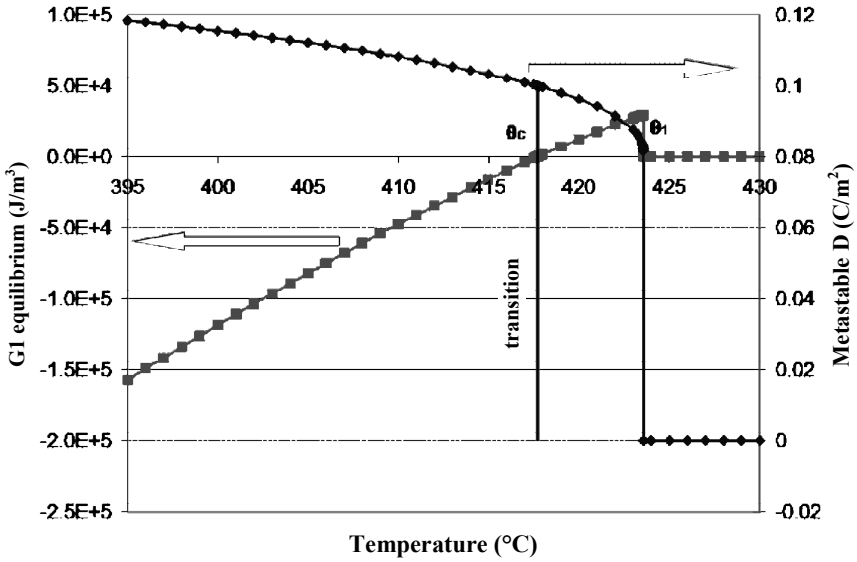

Figure 3.7. *Representation of electric displacement, D, and Gibbs' elastic energy, G_1, at equilibrium around transition. Case of a first-order transition*

Figure 3.8 finally presents the reverse dielectric susceptibility $1/\chi$ as well as the relative dielectric constant ε_r as a function of temperature. The most noticeable element in relation to a second-order transition is the fact that ε_r is finite on both sides of the transition, although there is a discontinuity.

The representation of $1/\chi$ lets us compare the gradients and boundary points of transition. The gradient ratio is -7.53 and the ratio of values of $1/\chi$ just before and after transition gives 3.92, in accordance with the simplifications suggested in equations [3.16] and [3.17]. ε_r moves from 1,420 just before transition to 5,620 just after, and therefore conserves the finite values.

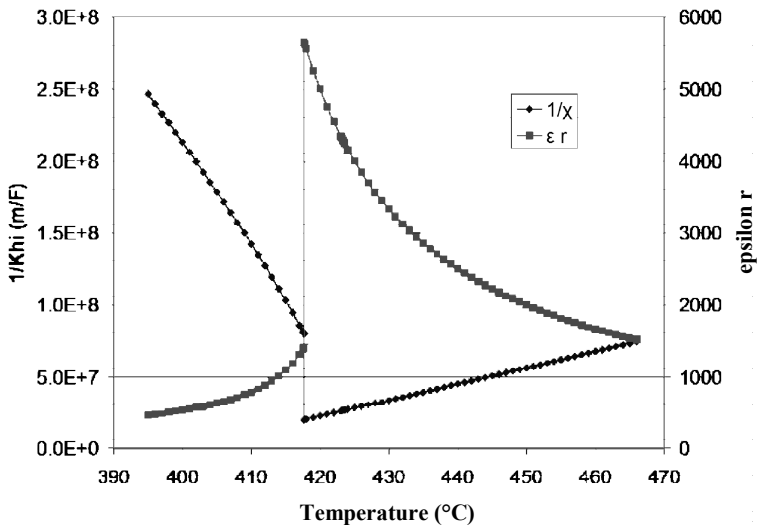

Figure 3.8. *Reverse dielectric susceptibility, χ, and relative dielectric constant, ε_r, as a function of temperature for a first-order transition*

We will not go into detail about the relationships between *D* and *E* for first-order transitions, as the latter are rare in the case of thin films. The interested reader should refer to Lines and Glass' book [LIN 77, p. 78].

To end this part, we must note that the thermodynamic formalism enables us to give the phase transition latent heat value from the value of electric displacement of the transition. Entropy, σ, is given by $-\partial G_1/\partial\theta$ at fixed *T* and *D*.

Therefore, according to equation [3.10] and the definition of α:

$$\sigma = -\frac{D^2}{2C} \qquad [3.18]$$

Therefore, on both sides of the transition, as *D* moves from $D(\theta_{C-})$ to 0, $\Delta\sigma$ is given by:

$$\Delta\sigma(\theta_C) = \sigma(\theta_{C+}) - \sigma(\theta_{C-}) = \frac{D^2(\theta_C)}{2C} = \frac{-3\alpha'}{8C\alpha''} = \frac{L_t}{\theta_C} \qquad [3.19]$$

with L_t being the latent heat of transition. The numerical example gives $L_t = 2.36.10^6$ J/m^3.

3.5. Conclusion

In this chapter, we saw how the microscopic thermodynamic approach could be implemented in order to explain the behavior of coupled materials, especially perovskites. The microscopic approach is itself much harder to implement. Electric, mechanical and thermal energies are all taken into consideration in this formalism. It must be noted that all the energy contributions can be considered using this formalism (especially magnetic) but we did not look at this magnetic energy in detail. This thermodynamic approach enables us to describe ferroelectric-paraelectric transition, but it can also be used to describe other transitions between ferroelectric phases. It is also possible to preview the dielectric, ferroelectric, piezoelectric and electrostrictive behaviors of materials.

3.6. Bibliography

[KIT 04] KITTEL C., *Introduction to Solid State Physics*, 8th edition, Wiley, Oxford, 2004.

[LIN 77] LINES M.E., GLASS A.M., *Principles and Applications of Ferroelectrics and Related Materials*, Clarendon Press, Oxford, 1977.

[NYE 61] NYE J.F., *Propriétés physiques des cristaux*, Dunod, Paris, 1961.

[UCH 97] UCHINO K., *Piezoelectric Actuators and Ultrasonic Motors*, Kluwer Academic Publishers, Norwell, 1997.

[VAN 01] VANDERBILT D., COHEN M.H., "Monoclinic and triclinic phases in higher-order Devonshire theory", *Phys. Rev. B*, 63, 094108, 2001.

Chapter 4

Mechanical Formalism

4.1. Introduction

One of the features of thin films displayed or reported on a substrate in relation to bulk materials and ceramic perovskites is the influence of mechanical energy in transitions or in the very values of the characteristic coefficients. Indeed, the boundary conditions imposed on perovskite active films by the substrate or by certain free structures in the case of microsystems, induce a coupling between several effects and/or directions. It is often impossible to obtain intrinsic coefficients for thin films, but rather effective values as a result of several mixed effects. It is therefore necessary to have a description of the systems studied taking into consideration the contribution of "internal" mechanical energy declined in terms of stresses and strains.

These notions originating from the mechanics of deformable media are widely described in specialized books. Experience shows that it is necessary to properly master these notions in order to understand how a perovskite thin film functions in a microsystem. Thus, this chapter includes the indispensable definitions of the mechanics of deformable media in the context of interest to us.

4.2. Hooke's law

The origin of the mechanics of deformable media is Hooke's law, which signifies the proportionality between the force applied on a solid body, F, and the

---

Chapter written by Emmanuel DEFAŸ.

extension, x, that results from it. In fact, it is the same law as that of the extension of a spring of stiffness k, such that $F = kx$. This law is valid in the elastic field of the solid body studied. It is a field where the effect is reversible in such a way that the body returns to its initial position if the force is no longer applied. If the force becomes too great, we enter the irreversible plastic field where, if the force increases again, the material breaks. The elastic field is the only one that will be discussed here as on one hand it enables us to describe a very large majority of situations encountered and on the other hand the other fields need the implementation of a much heavier formalism that is the intention of this book.

It is interesting to try and define the characteristic values of the system independently of the dimensions of the body studied to be able to give a local description. This very simple description is inspired by that made by Feynman in Chapter 38 on elasticity from his physics courses [FEY 99].

Thus, let us take a given body displayed in the form of an elongated cylinder that is L long and of section A, for example. According to Hooke's law, applying a force F in the lengthwise direction induces an elongation ΔL and the latter is proportional to F according to the relation $F = k\,\Delta L$, with k being the characteristic stiffness of the barrel. If we now use a body of the same nature, the same section, but that is mL long (m integer >1) and the same force is applied, the force is constantly felt all along the body. If, in our mind, we divide the body into elements that are L long, each is subjected to force F and is elongated from ΔL. The body therefore undergoes a total elongation equal to $m\Delta L$. Thus it is more interesting to consider the relative elongation that is the relationship between the length and the elongation that gives, in the two cases, $\Delta L/L$ – a value independent of length. It is this relative elongation that is called "strain S". This strain is unitless. In the case of perovskites, the order of maximum strain magnitude is less than 1%.

Now let us assume that the section of the cylindrical barrel L long is multiplied by a factor n (n integer >1). If the force applied is the same, the strain on the barrel will be weaker. Dividing the barrel into n barrels of section A, we find ourselves in the case of n springs in parallel. The stiffness of each spring is added together, which makes the final strain equal to $\Delta L/nL$.

It is therefore wiser to define the force applied in terms of applied "pressure" by calculating the force over surface ratio: F/A. This value is independent of the section. It is homogeneous with a pressure (N/m²) and is defined as being the effort, but more often the *stress* T, applied to the body. The order of magnitude of the stresses undergone by thin film perovskites is typically located in the [-1G Pa/+1 GPa] range. We recall that usual convention is to consider the tensile stresses as positive and compression stresses as negative.

Based on the relations above, we get:

$$T = \frac{Lk}{A} S = YS \qquad [4.1]$$

Value Y is the Young's modulus of the material making up the body (often designated by the letter E in mechanics books). It is independent of the dimensions of the body and is expressed in N/m². It is a characteristic that belongs to each material. The typical value of Y for perovskites is 100 GPa (1 GPa of stress divided by 1% of strain – let us note that these values, T and S, are very high).

To make a link with the next section, let us note that if the barrel is embedded on one edge ($x = 0$) and free on the other ($x = L$), the displacement u_x in the lengthwise direction of a solid particle located in x during the application of the force is equal to $x\Delta L/L$, i.e. xS. In other words, strain can be defined by the relation $S = \partial u_x / \partial x$.

This presentation enables us to simply introduce the notions of stresses and strains through an example where the latter are homogeneous throughout the body. Generalizing the concept is a bit more complex and necessitates a more detailed approach that will enable us to describe anisotropic materials and above all to have a local definition of stresses and strains.

4.3. Definitions of local strains

4.3.1. *Local strains in small strains hypothesis*

To introduce local strains, we can take an orthonormal reference system (O, X_1, X_2, X_3), as in Figure 4.1. In this reference system, a deformable solid undergoes the application of stresses. These stresses will induce a deformation of the solid. Let us take a point P of the solid before the stresses are applied, which is changed to point P' once the stresses have been applied. The definition of the displacement vector u is:

$$\vec{U} = \vec{OP'} - \vec{OP} = \vec{X'} - \vec{X} \qquad [4.2]$$

To provide a local definition of strains, we choose an element of the solid materialized by vector dX that is infinitely small around P and which is transformed into dX' after the application of stress. Having an infinitely small element enables us to ensure a local definition of strain. dX points along n and dX' along n', where n and

n' length is unit. It must be noted that n is chosen. The lengths of dX and dX' are respectively ds and ds', such that we have:

$$\vec{dX} = ds\,\vec{n} \qquad \vec{dX}' = ds'\,\vec{n}' \qquad [4.3]$$

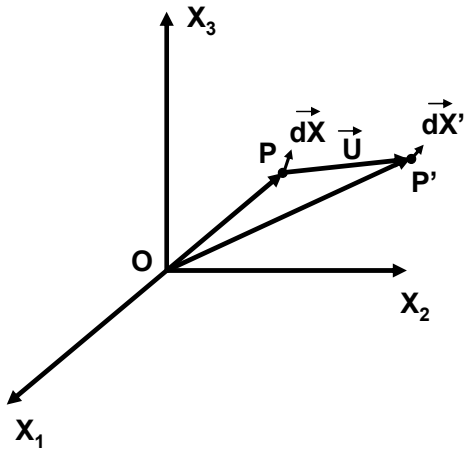

Figure 4.1. *Definition of displacement U during the strain of a body*

One way of measuring strains is to look at the difference in the squares of the lengths of the infinitesimal element before and after strain, i.e. ds'^2-ds^2. Thus, a translation of the solid is not interpreted as a strain.

With Cartesian coordinates, we have:

$$ds^2 = \sum_i dX_i^{\,2} \qquad ds'^2 = \sum_i dX_i'^2 \qquad [4.4]$$

Furthermore, based on equation [4.2] we know that:

$$X_i' = X_i + U_i \qquad [4.5]$$

For each direction i, the differentiation of this equation to the first order gives:

$$dX_i' = dX_i + \sum_j \frac{\partial U_i}{\partial X_j} dX_j + \frac{\partial U_i}{\partial t} dt \qquad [4.6]$$

In the continuation of this exposition, we take the quasistatic case in which time is not involved, i.e. the solid is considered to be at equilibrium all the time. Therefore, the last term on the right is considered null. The square of equation [4.6] gives:

$$dX_i'^2 = dX_i^2 + 2\sum_j \frac{\partial U_i}{\partial X_j} dX_j dX_i + \sum_j \sum_l \frac{\partial U_i}{\partial X_j} \frac{\partial U_i}{\partial X_l} dX_j dX_l \qquad [4.7]$$

The last term on the right is a second-order displacement term. It is disregarded so that we only keep the first order, which is legitimate in the case of small strains. In the previous section, we saw that the maximum strains considered in the case of thin film perovskites are of the order of 1%, which justifies the small strains hypothesis in most cases.

Thus, summing up all *i* directions, the previous equation becomes:

$$\sum_i \left(dX_i'^2 - dX_i^2 \right) = 2\sum_i \sum_j \frac{\partial U_i}{\partial X_j} dX_j dX_i \qquad [4.8]$$

To properly understand the form chosen to express strains, it is interesting to develop the above expression:

$$\frac{\sum_i \left(dX_i'^2 - dX_i^2 \right)}{2} = \frac{\partial U_1}{\partial X_1} dX_1^2 + \frac{\partial U_2}{\partial X_2} dX_2^2 + \frac{\partial U_3}{\partial X_3} dX_3^2 + \left(\frac{\partial U_1}{\partial X_2} + \frac{\partial U_2}{\partial X_1} \right) dX_1 dX_2 + \left(\frac{\partial U_1}{\partial X_3} + \frac{\partial U_3}{\partial X_1} \right) dX_1 dX_3 + \left(\frac{\partial U_2}{\partial X_3} + \frac{\partial U_3}{\partial X_2} \right) dX_2 dX_3 \qquad [4.9]$$

Thus we see that it is not possible to distinguish the cross effects $\partial U_i / \partial X_j$ and $\partial U_j / \partial X_i$ from the difference of the squares. It is therefore logical to associate them to define what will become strains, S_{ij}. We will see later that it is in fact important to not distinguish the cross effects if we do not want to take rotations into consideration.

Therefore, we choose $S_{ij} = \frac{1}{2}\left(\frac{\partial u_i}{\partial X_j} + \frac{\partial u_j}{\partial X_i}\right)$, which based on equation [4.9] gives:

$$\sum_i \left(dX_i'^2 - dX_i^2\right) = 2\sum_i \sum_j S_{ij} dX_j dX_i \qquad [4.10]$$

Not distinguishing cross effects to a certain extent refers to separating $\partial U_i / \partial X_j$ into two distinct contributions: strains, S_{ij}, and rotations, $w_{ij} = \frac{1}{2}\left(\frac{\partial u_i}{\partial X_j} - \frac{\partial u_j}{\partial X_i}\right)$. The fact that S_{ij} describe strains is discussed later. To produce the nature of rotations, w_{ij}, let us take two-dimensional example. Let us imagine a square of side a, initially leaning against the reference system (X_1, X_2), as represented in Figure 4.2. This square undergoes a pure rotation of angle θ without any strain. There is therefore no elastic energy stored in the square. As we are interested in small strains, we also assume that the rotation is weak.

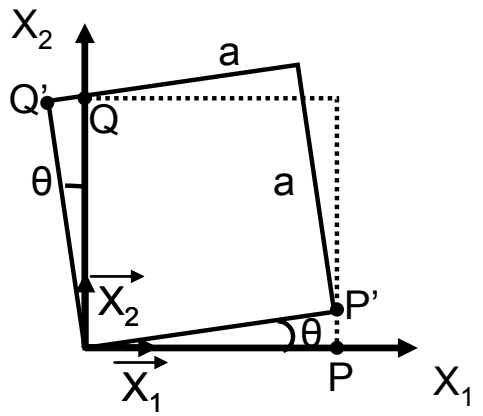

Figure 4.2. *Illustration of the rotation of a square in two dimensions*

Points P and Q that are at the end of the square on the X_1 and X_2 axes, respectively, are displaced by P' and Q'. We therefore have:

$$\overrightarrow{OP'} = a\left(\cos\theta\,\overrightarrow{X_1} + \sin\theta\,\overrightarrow{X_2}\right)$$
$$\overrightarrow{OQ'} = a\left(-\sin\theta\,\overrightarrow{X_1} + \cos\theta\,\overrightarrow{X_2}\right) \qquad [4.11]$$

The fact that the rotation is weak enables us to approximate to the first-order $cos\theta$ at *1* and $sin\theta$ at θ. As *P* and *Q* are coordinates (a, 0) and (0, a), respectively, equation [4.11] can be expressed:

$$\overrightarrow{OP'} - \overrightarrow{OP} = a\theta\,\overrightarrow{X_2} \text{ and } \overrightarrow{OQ'} - \overrightarrow{OQ} = -a\theta\,\overrightarrow{X_1} \qquad [4.12]$$

In addition, the left-hand terms of equations [4.12] are by definition displacement vectors $\overrightarrow{U_1}$ and $\overrightarrow{U_2}$ along X_1 and X_2. Assuming the change in linear displacement on the square (small displacements), equations [4.12] can be expressed as:

$$\overrightarrow{U_1} = a\theta\,\overrightarrow{X_2} = a\frac{\partial U_1}{\partial X_2}\overrightarrow{X_2} \text{ and } \overrightarrow{U_2} = -a\theta\,\overrightarrow{X_1} = a\frac{\partial U_2}{\partial X_1}\overrightarrow{X_1} \qquad [4.13]$$

Thus, we see that in a pure rotation, there are non-null $\partial U_i / \partial X_j$ terms.

The link between these terms and the angle of rotation is therefore based on the equation above:

$$\frac{\partial U_1}{\partial X_2} = -\frac{\partial U_2}{\partial X_1} = \theta \qquad [4.14]$$

Thus, we see that the definition of w_{ij} terms given in equation [4.9] corresponds to a pure rotation term. We note that the matrix composed of w_{ij} terms is antisymmetric.

The fact that S_{ij} corresponds to a strain, as we defined it in the case of Hooke's law, is not obvious. We will see that in the case of small strains, identification becomes natural. The left-hand term of equation [4.8] is none other than $(ds'^2 - ds^2)$. For the next calculation, we define the relative change in length $S_l = (ds' - ds)/ds$, sometimes called unitary extension in accordance with the definition of a strain in Hooke's law:

$$ds'^2 - ds^2 = \frac{(ds' - ds)(ds' + ds)}{ds^2} ds^2 = S_l \frac{ds' - ds + 2ds}{ds} ds^2$$
$$= S_l (S_l + 2) ds^2 = 2ds^2 \left(S_l + \frac{S_l^2}{2} \right) \quad [4.15]$$

In the case of small strains, S_l is small so we can cancel the S_l^2 term in order to keep just the first order to get:

$$\frac{ds'^2 - ds^2}{2ds^2} \approx S_l \quad [4.16]$$

and therefore, combining equation [4.10] and equation [4.16], we get to the first-order equation:

$$S_l = \frac{\sum_i \sum_j S_{ij} dX_j dX_i}{ds^2} \quad [4.17]$$

Furthermore, based on equation [4.3], we have:

$$n_i = \frac{dX_i}{ds} \quad [4.18]$$

hence:

$$S_l = \sum_i \sum_j S_{ij} n_i n_j \quad [4.19]$$

where S_{ij} defines a matrix $\overline{\overline{S}}$ that describes the state of strain of a solid at each point. The state of strain does not depend on the reference system from which the solid is observed. We say that matrix $\overline{\overline{S}}$ is a rank 2 tensor (see the note below).

$$\overline{\overline{S}} = \begin{pmatrix} S_{11} & S_{12} & S_{13} \\ S_{21} & S_{22} & S_{23} \\ S_{31} & S_{32} & S_{33} \end{pmatrix} \quad [4.20]$$

In accordance with the definition of the S_{ij} terms, tensor $\overline{\overline{S}}$ is symmetric.

NOTE ON TENSORS.– This strain matrix of second order defines a local property of the material that must be the same regardless of the reference system from which we are looking at the solid described. This property can be compared to that of a vector (characterizing, for example, a force) that keeps the same direction, way and intensity when the reference system is changed. We say that this vector is a rank 1 tensor. Similarly, the strain matrix is a rank 2 tensor. A tensor is therefore fundamentally different to a change in reference system as it defines a property of the material: it always represents the same entity no matter what the reference system chosen.

The exact definition of a tensor is given by Nye [NYE 61] and is linked to the laws of transformation for moving from one reference system to another. Thus, let a_{ij} be the coefficients that enable us to move from reference system $R = (X_1, X_2, X_3)$ to reference system $R' = (X'_1, X'_2, X'_3)$ such that $X'_i = a_{ij}X_j$. Any rank 2 matrix $\overline{\overline{S}}$ is a tensor if its components are transformed according to the following law for going from R to R': $S'_{ij} = a_{ik}a_{jl}S_{kl}$. For a rank 1 tensor vector V, the law is the following: $V'_i = a_{ij}V_j$. A rank n Z tensor in R is transformed into Z' in R' by the relation:

$$Z'_{\ldots ijk\ldots} = \ldots a_{il}a_{jm}a_{kn}\ldots Z_{\ldots lmn\ldots} \qquad [4.21]$$

A rank zero tensor is a scalar, whatever the reference system. Another way of characterizing a rank 2 tensor $\overline{\overline{S}}$ is to show a linear-type relation between two rank 1 tensor vectors (U and V, for example) through the use of $\overline{\overline{S}}$. Thus, if $V = \overline{\overline{S}}\,U$, then $\overline{\overline{S}}$ is a rank 2 tensor.

4.3.2. *Meaning of matrix* $\overline{\overline{S}}$

Equation [4.22] represents the product of a matrix with two vectors. It is a scalar that can be expressed as:

$$S_l\left(\vec{n}_1, \vec{n}_2\right) = \vec{n}_2 . \overline{\overline{S}}\,\vec{n}_1 \qquad [4.22]$$

Physically, this value is the relative change in length observed along the direction of the unit vector $\vec{n}_2$ of an infinitesimal element initially carried by vector $\vec{n}_1$ at point P. In other words, vector $\overline{\overline{S}}\,\vec{n}_1$ represents the strain vector of an

infinitesimal element initially carried by vector $\vec{n_1}$ at point P. This affirmation proves the tensor nature of $\overline{\overline{S}}$, in accordance with the note above on rank 2 tensors.

Vectorially, returning to the notations defined in Figure 4.1, we can write:

$$\vec{dX}' = \vec{dX} + ds\overline{\overline{S}}\,\vec{n} \qquad [4.23]$$

Let $\vec{n_1} = \begin{pmatrix} 1 & 0 & 0 \end{pmatrix}$ and $\vec{n_2} = \begin{pmatrix} 1 & 0 & 0 \end{pmatrix}$. This means that we are observing the strain at point P along direction X_1 of an element that also points along X_1. Equation [4.22] gives S_{11}, which is equal to:

$$S_{11} = \frac{\partial U_1}{\partial X_1} \qquad [4.24]$$

S_{11} corresponds to the relative change in length along direction 1 as was obtained in Hooke's law.

In addition, let $\vec{n_1} = \begin{pmatrix} 1 & 0 & 0 \end{pmatrix}$ and $\vec{n_2} = \begin{pmatrix} 0 & 1 & 0 \end{pmatrix}$. The initial element is always along X_1 but the strain is observed along X_2. The result is $S_{21} = S_{12}$ and gives:

$$S_{12} = \frac{1}{2}\left(\frac{\partial U_1}{\partial X_2} + \frac{\partial U_2}{\partial X_1}\right) \qquad [4.25]$$

This coefficient corresponds to shear. Figure 4.3 illustrates the two coefficients S_{11} and S_{12} graphically. To do this, we choose an element dX at point P that points along X_1. P is transformed into P' after strain and dX becomes dX'. As only local strains matter, we superimpose P and P' on the graph. $S_{11}ds$ represents the longitudinal local extension. $S_{12}ds$ represents the displacement of dX along X_2. Graphically, we define angle θ between dX and dX'. As we are dealing with small strains, this angle is low and so is S_{11}. We therefore have the following relation:

$$\theta \approx \tan\theta = \frac{S_{12}ds}{ds\left(1 + S_{11}\right)} \approx S_{12} \qquad [4.26]$$

S_{12} is therefore about equal to the angle between the unstrained vector and the strained vector. If we place ourselves in a plane for the case of a pure shear for a square, we can show with the same argument that the change in right angle is equal to 2 times θ. It is for this reason that S_{12} is often called the half-distortion of the right

angle. Let us also note that the definition of shear strains (i.e. S_{ij} with $i \neq j$) implies that $S_{ij} = S_{ji}$ and therefore $S_{12}ds$ is also the displacement along X_1 of a vector dY; an infinitesimal vector along X_2. In the example given, $S_{12}ds$ is positive and therefore there is an angle θ in the clockwise direction between X_2 and the deformed vector dY'. The strain due to shear is therefore not a simple rotation.

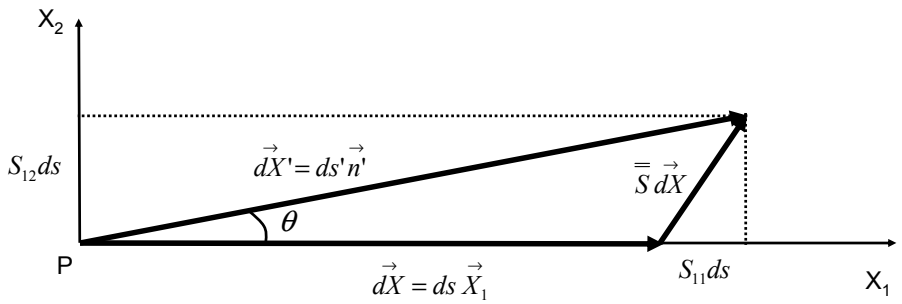

Figure 4.3. *Representation of shear and local longitudinal strains of an infinitesimal element dX carried by X_1*

To end this part on strains, we must note that as the small strains tensor is symmetric, it is diagonalizable. This means that it is always possible to define the main directions that are the directions for which displacement is only longitudinal. In other words, if we consider an infinitely small sphere around point P before strain, the strain will become ellipsoid after a strain whose major axis corresponds to a main direction.

4.4. Definition of local strains

4.4.1. *The strain tensor*

To define local strains in a deformable solid, the challenge is to locally translate the influence of external strains undergone by the solid. These solicitations can be of two natures: volumic (weight, inertia force) and surface. Punctual strains pose a problem in solving equations. Their influence is replaced by an unpunctual distribution with the same effects on the solid far from the point on which this solicitation is applied, by virtue of St. Venant's principle.

The concept of strains is introduced by taking a deformable solid in equilibrium. In our minds, we cut this solid into two parts, P_1 and P_2, separated by a virtual interface. For each one of the interfaces to remain at equilibrium, the influence of one on the other must be replaced by a surface force density that is exercised on the

cut part. This surface force density is therefore homogeneous to a pressure, as in the simple case of Hooke's law developed above. In this way, it is possible at each point of the solid to define an infinitesimal surface on which a force resulting from external strains acting on the solid will be applied. Figure 4.4 illustrates the suggested definitions. At point *M*, a surface force density called local stress $\vec{T}$ can be defined. This is the result of external strains of which the solid is the subject. $\vec{n}$ is the surface element normal *dS* on which the stress is applied. $\vec{n}$ is directed towards the exterior of volume P_1, since a tensile stress is defined as being positive. $\vec{T}$ depends on point *M* and the orientation of the surface element, therefore on $\vec{n}$. It is possible to construct a rank 2 tensor, called a stress tensor, from these definitions. This enables us to find $\vec{T}$ at any point *M* regardless of what $\vec{n}$ may be.

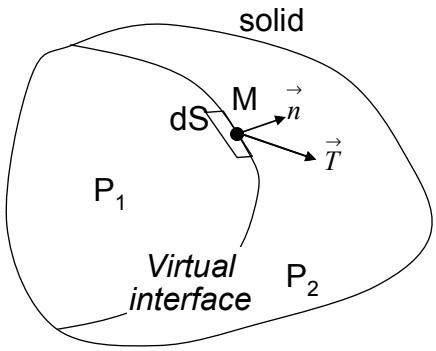

Figure 4.4. *Illustration of the definition of local stresses in a deformable solid resulting from external strains to which the solid is exposed*

To define this stress tensor, let us write that a small element of volume δV defined around point *M* on which $\vec{T}$ is applied is at equilibrium.

The environment of point *M* is returned in an orthonormal Cartesian reference system (X_1, X_2, X_3), with center *O*, as in Figure 4.5. So we define the small surface dS_{123} equal to the area of triangle $M_1M_2M_3$ around *M* (M_i, intersection between the x_i axis and the surface). The forces that are exerted on this small volume element are the surface forces on the four faces of the tetrahedron as well as the volume forces

characterized by $\vec{f}$ (weight, inertia). As the volume δV is very small, we can consider the stresses that are applied to it as being characterized by $\vec{T}$ (M).

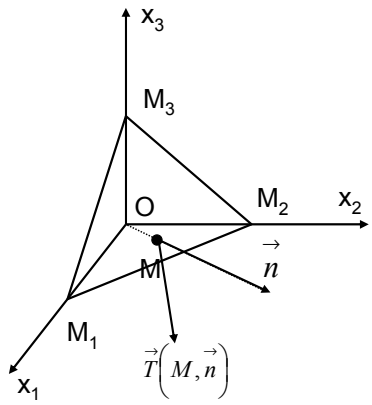

Figure 4.5. *Definition of point M undergoing stress vector $\vec{T}(M)$ surrounded by the small volume element δV made up of the surfaces of triangles OM1M2- OM1M3- OM3M2- M1M2M3*

Thus, the equilibrium of the forces, with dS_{oij} being the surface of triangle OM_iM_j gives:

$$\vec{T}\left(M,\vec{n}\right)dS_{123}+\vec{T}\left(M,-\vec{X}_1\right)dS_{023}+\vec{T}\left(M,-\vec{X}_2\right)dS_{013}+\vec{T}\left(M,-\vec{X}_3\right)dS_{012}+\vec{f}\,\delta V=\vec{0} \qquad [4.27]$$

As $\vec{n}$ is the normal to the surface element dS, we have relations $dS_{oij} = dS.n_k$, with i, j and k all being different from each other. Thus, equation [4.22] becomes:

$$\vec{T}\left(M,\vec{n}\right)+\vec{T}\left(M,-\vec{X}_1\right)n_1+\vec{T}\left(M,-\vec{X}_2\right)n_2+\vec{T}\left(M,-\vec{X}_3\right)n_3=\vec{0} \qquad [4.28]$$

The volume force disappears because, as the lengths are infinitely small, the surfaces are of second order magnitudes and third order volumes. As f is a datum independent of the size of the volume, since it is homogeneous to a volumic mass through acceleration, the term of the volume force is of third order, negligible in front of that of surface forces.

Thus, according to equation [4.28] and by virtue of the note on tensors given in the section on strains, a rank 2 tensor $\overline{\overline{T}}(M)$ called a local stress tensor can be defined as:

$$\vec{T}\left(M,\vec{n}\right)=\overline{\overline{T}}(M)\,\vec{n} \qquad [4.29]$$

with:

$$\overline{\overline{T}}(M)=\begin{pmatrix} T_{11}(M) & T_{12}(M) & T_{13}(M) \\ T_{21}(M) & T_{22}(M) & T_{23}(M) \\ T_{31}(M) & T_{32}(M) & T_{33}(M) \end{pmatrix} \qquad [4.30]$$

Thus, by developing equation [4.29], we get:

$$\vec{T}\left(M,\vec{n}\right)=\begin{pmatrix} \sum_{j=1}^{3} T_{1j}n_j \\ \sum_{j=1}^{3} T_{2j}n_j \\ \sum_{j=1}^{3} T_{3j}n_j \end{pmatrix}=\begin{pmatrix} T_{11} \\ T_{21} \\ T_{31} \end{pmatrix}n_1+\begin{pmatrix} T_{12} \\ T_{22} \\ T_{32} \end{pmatrix}n_2+\begin{pmatrix} T_{13} \\ T_{23} \\ T_{33} \end{pmatrix}n_3= \qquad [4.31]$$

$$\vec{T}\left(M,\vec{X}_1\right)n_1+\vec{T}\left(M,\vec{X}_2\right)n_2+\vec{T}\left(M,\vec{X}_3\right)n_3$$

and so, the passage from equation [4.31] to equation [4.28] is clear by simply applying the sign change of the unit vectors.

This definition of the local stress tensor $\overline{\overline{T}}(M)$ therefore enables us to define constraints that are applied to M at any point of a deformable solid subjected to external solicitations of the volumic or surface type, no matter the direction in which we are looking (i.e. regardless of what $\vec{n}$ is).

4.4.2. *Physical meaning of T_{ij}*

Figure 4.6 illustrates the meaning of T_{ij}. In the deformable solid, a cube of infinitesimal volume $\delta V = dX_1 dX_2 dX_3$ is defined from some point O of the solid. If the cube is assumed to be sufficiently small, the knowledge of $\overline{\overline{T}}(O)$ can be considered to be enough to completely define the state of forces being applied to the faces of the cube. Thus, in accordance with equation [4.31], three forces are applied in the middle of each face of the cube. For the face of the cube parallel to plane OX_2X_3 which cuts the X_1 axis into dX_1, these three forces are $dX_2dX_3T_{11}(O)\,\vec{X}_1$. This corresponds to a longitudinal force directed in the same direction as the surface normal (here along X_1), $dX_2dX_3T_{21}(O)\,\vec{X}_2$ and $dX_2dX_3T_{31}(O)\,\vec{X}_3$, which both correspond to shear forces contained in the plane supporting the surface on which they are applied (see Figure 4.6). Therefore, in element T_{ij} of the stress tensor, i indicates the direction of the force being applied to the surface whose normal is given by j. Although this has no great physical sense in the hypothesis of a local definition of stresses, T_{ij} is equivalent to the force being applied along direction X_i in the middle of the normal unit surface along X_j.

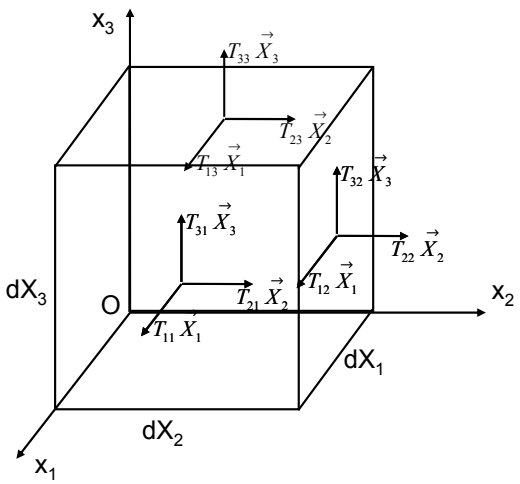

Figure 4.6. *Description of forces being applied to a volume $\delta V = dX_1dX_2dX_3$ of a deformable solid, defined by the components of the stress tensor*

Furthermore, the stress tensor is symmetric, just like the strains tensor. To show this, let us consider the cube in Figure 4.6 seen from above (X_3 perpendicular to the sheet), as in Figure 4.7. The cube is considered to be in equilibrium. Here, only the

moment along X_3 is observed. If we go around the cube, four forces contribute to establishing this moment. In the middle of the cube, each force imposes a moment along X_3. The sum of these moments gives:

$$2dX_2dX_3T_{21}\frac{dX_1}{2} - 2dX_1dX_3T_{12}\frac{dX_2}{2} = 0 \qquad [4.32]$$

This equation therefore implies that $T_{21} = T_{12}$. The argument can be made in the same way along the X_1 and X_2 axes and we show finally that $T_{ij} = T_{ji}$ the stress tensor is symmetric.

Thus, this property implies that the tensor is still diagonalizable. It is therefore still possible to find the main directions for which the stresses are longitudinal, to the exclusion of any shear.

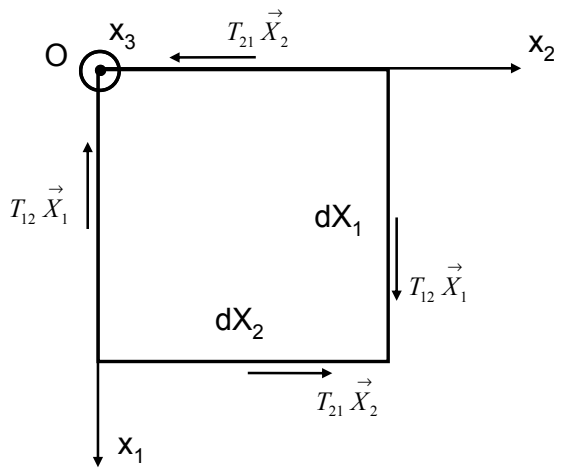

Figure 4.7. *Infinitesimal cube on which stresses are applied, inducing a moment along X_3 and illustrating symmetry of the stress tensor*

4.4.3. *Equations of motion in a deformable solid*

Figure 4.6 enables us to simply produce equations of motion of the solid's particles during dynamic external solicitations. To do this, we must produce a difference between the stresses applied to the faces for a non-null global effort to exist. Let us consider what happens at the first order along direction X_1. The sum of the forces $\sum F_1$ along this direction is:

$$\sum F_1 = dX_2 dX_3 \left(T_{11}\left(dX_1\right) - T_{11}\left(0\right)\right) + dX_1 dX_3 \left(T_{12}\left(dX_2\right) - T_{12}\left(0\right)\right) + dX_1 dX_2 \left(T_{13}\left(dX_3\right) - T_{13}\left(0\right)\right) \quad [4.33]$$

Development to the first order of each difference gives:

$$\sum F_1 = dX_1 dX_2 dX_3 \left(\sum_{j=1}^{3} \frac{\partial T_{1j}}{\partial X_j}\right) \quad [4.34]$$

In accordance with the fundamental relation of the dynamics, if we only consider as volume force the product of acceleration $\vec{a}$ of a_i components with the mass of the cube $\delta V \rho$ (ρ being the supposedly constant volumic mass), we get the following relation by generalizing the two equations above to the three dimensions:

$$\rho a_i = \sum_j \frac{\partial T_{ij}}{\partial X_j} \quad [4.35]$$

4.5. Stress-strain relation

4.5.1. *Hooke's generalized law*

The relationship between stresses and strains in the framework of the elastic field and small strains considered goes back to a generalization of Hooke's law. This enables us to linearly link the rank 2 tensors, $\overline{\overline{S}}$ and $\overline{\overline{T}}$, with a rank 4 tensor, called the stiffness tensor, $\overline{\overline{C}}$. The components of these three tensors are thus linked by the following linear relation:

$$T_{ij} = \sum_{kl} c_{ijkl} S_{kl} \quad [4.36]$$

There is the reverse relationship between $\overline{\overline{S}}$ and $\overline{\overline{T}}$, involving the s_{ijkl} coefficients, which are called the compliance coefficients:

$$S_{ij} = \sum_{kl} s_{ijkl} T_{kl} \quad [4.37]$$

In practice, it is useful to be able to express elastic tensors in the form of a 6x6 matrix. To do this, stress and strain tensors are first of all transformed into a 6x1 vector, thanks to their symmetry, by using the following contracted notations:

$$T_{ii} = T_i \quad T_{ij} = T_{9-(i+j)} \text{ for } i \neq j \qquad [4.38]$$

In other words, for the non-diagonal terms, we have $T_{12} = T_6$, $T_{13} = T_5$ and $T_{23} = T_4$.

For strains, in order to be coherent with the uncontracted values when the above convention on strains is chosen, the piezoelectricity standards recommend the following notation:

$$S_{ii} = S_i\,,\ 2S_{ij} = S_{9-(i+j)} \text{ for } i \neq j \qquad [4.39]$$

These relations induce others on stiffness coefficients:

$$\begin{aligned} c_{iikk} &= c_{ik} \\ c_{ijkl} &= c_{9-(i+j)\ \ 9-(k+l)} \end{aligned} \qquad [4.40]$$

and other more complicated ones for the compliance coefficients:

$$\begin{aligned} &s_{ijkl} = s_{mn} \quad si \quad i = j \quad \text{and} \quad k = l \quad \text{with} \quad m,n = 1,2,3 \\ &2s_{ijkl} = s_{mn} \quad si \quad i = j \quad \text{and} \quad k \neq l \quad \text{with} \quad m = 1,2,3 \quad \text{and} \quad n = 4,5,6 \\ &4s_{ijkl} = s_{mn} \quad si \quad i \neq j \quad \text{and} \quad k \neq l \quad \text{with} \quad m,n = 4,5,6 \end{aligned} \qquad [4.41]$$

4.5.2. *Dynamic relation*

For applications that bring acoustic phenomena such as piezoelectric or electrostrictive resonators into play, there is propagation of elastic energy. It is therefore necessary to have a dynamic relation that brings stresses and strains into play in order to produce a propagation equation. This equation stems from linear relations between stresses and strains, as well as from the dynamic equation linking stress gradients to the acceleration of points of the solid, as detailed above.

4.5.2.1. *Elastic material*

To simplify calculations, the material considered here is not piezoelectric. Acceleration a_i in equation [4.35] is none other than $\partial^2 U_i / \partial t^2 = \ddot{U}_i$. On the other hand, the term containing the stress gradient of equation [4.35] can be modified by

introducing stiffness coefficients and strain. Thus, these modifications lead to the following equation:

$$\rho \frac{\partial^2 U_i}{\partial t^2} = \sum_j \sum_{k,l} c_{ijkl} \frac{\partial S_{kl}}{\partial X_j} \qquad [4.42]$$

According to the relation that links strains to displacements, we get:

$$\rho \frac{\partial^2 U_i}{\partial t^2} = \frac{1}{2} \sum_j \sum_{k,l} c_{ijkl} \left(\frac{\partial^2 U_k}{\partial X_l \partial X_j} + \frac{\partial^2 U_l}{\partial X_k \partial X_j} \right) \qquad [4.43]$$

Due to the symmetry of the tensor $\overline{\overline{C}}$ ($c_{ijkl} = c_{ijlk}$), the equation above is simplified to give:

$$\rho \frac{\partial^2 U_i}{\partial t^2} = \sum_{j,k,l} c_{ijkl} \frac{\partial^2 U_k}{\partial X_j \partial X_l} \qquad [4.44]$$

4.5.2.2. *Piezoelectric material*

In the case of piezoelectric material, we must add the contribution of the coupling that appears in the stress gradients term. To do this, we use the linear equations encountered in Chapter 2. Most of the time, the effect of temperature is neglected when describing this propagation equation and the coefficients are assumed to be the same, as the experiment conditions are isothermal or adiabatic. Two equations are therefore most often used to describe piezoelectricity (equivalent to equations [2.59] and [2.60]). In the case of propagation, it is necessary to express stresses as a function of strains and the electric field. To simplify the equations, we choose Einstein's notation (no summation sign) for which the doubled variables indicate a summation.

This linear equation is the following:

$$T_{ij} = c^E_{ijkl} S_{kl} - e_{kij} E_k \qquad [4.45]$$

The e_{kij} factors are the piezoelectric coefficients in this formalism where strains and field strength are the independent (or natural) variables. The exponent E over the factors c indicates that the stiffness coefficients are measured at constant electric field.

As $\vec{E} = -\overrightarrow{grad}\, V$, the combination of equations [4.35] and [4.45] gives:

$$\rho \frac{\partial^2 U_i}{\partial t^2} = c_{ijkl}^{E} \frac{\partial^2 U_k}{\partial X_j \partial X_l} + e_{kij} \frac{\partial^2 V}{\partial X_j \partial X_k} \qquad [4.46]$$

The second linear equation is the following:

$$D_j = \varepsilon_{jk} E_k + e_{jkl} S_{kl} \qquad [4.47]$$

where ε_{jk} constitutes the terms of the dielectric permittivity matrix.

For a dielectric, it is often considered that the conductivity is very low, which implies the absence of charges inside of the dielectric.

According to the (electromagnetic) Maxwell relations, the divergence of D is therefore null ($div\, \vec{D} = 0$), which finally imposes:

$$\sum_j \frac{\partial D_j}{\partial X_j} = -\varepsilon_{jk} \frac{\partial^2 V}{\partial X_j \partial X_k} + e_{jkl} \frac{\partial^2 U_l}{\partial X_j \partial X_k} = 0 \qquad [4.48]$$

4.6. Elastic energy density

4.6.1. *Expression of elastic energy density*

We can ask ourselves what the quantity of elastic energy stored in an infinitely small cube, like the one in Figure 4.6, is? The answer must enable us to give a local definition of elastic energy density. As a starting point, we can choose a non-null state of stress and strain.

The idea is then to determine the change in elastic energy when a force f is applied to the infinitely small cube. Here f is small enough for the small strains hypothesis to be valid. The effect of this force on the cube can be replaced by the stress tensor $\overline{\overline{T}}$ that is applied on the faces of the cube in accordance with what was detailed above.

Elastic energy is equal to the work of the force exerted in the solid.

Thus, if we only look in direction X_1 (see Figure 4.6), this work δW_1 is by definition equal to the force (therefore the stress multiplied by the surface area) that is applied on the center of each of the six faces multiplied by the small displacement δU_1 resulting in direction X_1.

The sum of these contributions is therefore:

$$\begin{aligned}\delta W_1 &= T_{11} dX_2 dX_3 \left(\delta U_1 \left(dX_1, \frac{dX_2}{2}, \frac{dX_3}{2} \right) - \delta U_1 \left(0, \frac{dX_2}{2}, \frac{dX_3}{2} \right) \right) \\ &+ T_{12} dX_1 dX_3 \left(\delta U_1 \left(\frac{dX_1}{2}, dX_2, \frac{dX_3}{2} \right) - \delta U_1 \left(\frac{dX_1}{2}, 0, \frac{dX_3}{2} \right) \right) \\ &+ T_{13} dX_1 dX_2 \left(\delta U_1 \left(\frac{dX_1}{2}, \frac{dX_2}{2}, dX_3 \right) - \delta U_1 \left(\frac{dX_1}{2}, \frac{dX_2}{2}, 0 \right) \right)\end{aligned} \quad [4.49]$$

We must see that the stress is considered to be constant on the cube but the displacement is necessarily different depending on the localization in the cube, or the latter would not be deformed but simply displaced. There would therefore not be elastic energy stored.

Considering the first order in the equation above, δW_1 becomes:

$$\delta W_1 = dX_1 dX_2 dX_3 \left(T_{11} \frac{\partial \delta U_1}{\partial X_1} + T_{12} \frac{\partial \delta U_1}{\partial X_2} + T_{13} \frac{\partial \delta U_1}{\partial X_3} \right) \quad [4.50]$$

Summing their three spatial directions, elastic work δW of the force f becomes:

$$\delta W = d\tau \sum_{i,j} T_{ij} \frac{\partial \delta U_i}{\partial X_j} = d\tau \sum_{i,j} T_{ij} \frac{1}{2} \left(\frac{\partial \delta U_i}{\partial X_j} + \frac{\partial \delta U_j}{\partial X_i} \right) = d\tau \sum_{i,j} T_{ij} \delta S_{ij} \quad [4.51]$$

with $d\tau = dX_1 dX_2 dX_3$.

Thus, the change in elastic energy density that is involved in the calculation of internal energy is equal to the work produced by the force f in the solid. To make a direct link with the sections above on energy considerations, we can say that in the adiabatic case (without heat exchange), if we neglect electric energy, the internal energy change is equal to the elastic work. Thus, considering the energy density per unit of volume, we get:

$$dU_{adiab.} = \delta W = \sum_{i,j} T_{ij} dS_{ij} \qquad [4.52]$$

It is important to note that stress is the intensive variable, like pressure in the case of a gas. Strain, which is considered here as the consequence of stress, is an extensive variable (just like volume for a gas). As the internal energy U by definition differentiates extensive variables, we have $dU = TdS$.

Finally, we note that Nye suggests a calculation that is slightly different by looking only at the strain of the cube by blocking it in the middle. The result is identical [NYE 61].

4.6.2. *Symmetry of the elasticity tensor*

By deriving internal energy in relation to T_{ij}, we get:

$$\frac{\partial U}{\partial T_{ij}} = S_{ij} = \sum_{kl} s_{ijkl} T_{kl} \qquad [4.53]$$

A second derivation in relation to T_{kl} gives us:

$$\frac{\partial^2 U}{\partial T_{ij} \partial T_{kl}} = \frac{\partial S_{ij}}{\partial T_{kl}} = s_{ijkl} \qquad [4.54]$$

In addition, we saw in Chapter 2 that cross second derivatives are identical for state functions, which is the case of internal energy. This therefore leads to:

$$s_{ijkl} = \frac{\partial^2 U}{\partial T_{ij} \partial T_{kl}} = \frac{\partial^2 U}{\partial T_{kl} \partial T_{ij}} = s_{klij} \qquad [4.55]$$

If we move on to the matrix notation, we therefore have:

$$s_{mn} = s_{nm} \qquad [4.56]$$

The compliance tensor $\overset{=}{s}$ is therefore symmetric. We saw that the independent terms of $\overset{=}{s}$ were up to the number of 36 because of the symmetries of stress and

strain tensors. As $\overline{\overline{s}}$ is also symmetric, it no longer has only 21 independent coefficients. By virtue of the relationship between s_{ijkl} and c_{ijkl}, the stiffness tensor $\overline{\overline{c}}$ is also symmetric.

4.7. Expression of the elasticity tensor as a function of elements of symmetry

With tensors $\overline{\overline{S}}$ and $\overline{\overline{T}}$ being symmetric, they each contain six independent coefficients, which induce 36 independent coefficients c_{ijkl} (or s_{ijkl}). According to energy considerations, we just saw that $\overline{\overline{c}}$ is also symmetric, which results in a maximum of 21 independent coefficients.

In the case of single crystals or epitaxial films, the anisotropic character is present and the number of independent stiffness coefficients depends on the crystal studied. Thus, it is the point group of the crystal studied that sets the number of independent coefficients. These symmetry elements enable us to highlight relations that must be verified by the coefficients. Thus, the higher the level of symmetry, the more relations between coefficients there are and the fewer independent coefficients. The interested reader can refer to one of the following excellent references: *Elastic Waves in Solids* by Dieulesaint and Royer (Springer-Verlag Berlin) [DIE 74] and *Physical Properties of Crystals* (Oxford University Press) by Nye [NYE 61]. For a triclinic lattice, 21 coefficients are necessary, whereas the paraelectric cubic lattice has only three independent coefficients. In the case of amorphous or polycrystalline materials with random orientation, only two coefficients are necessary to describe this elastic isotropic state.

As an example let us take the monoclinic point group *2*.

If we apply the change in reference system relation for the elasticity tensor that is of rank 4, and this change in reference system corresponds to a symmetry element of the point group, we get:

$$c_{ijkl} = a_{im}a_{jn}a_{ko}a_{lp}c_{mnop} \qquad [4.57]$$

In point group *2*, if we choose axis 3 parallel to the axis of order 2, the elasticity tensor must be invariant for the following reference system:

$$a = \begin{pmatrix} -1 & 0 & 0 \\ 0 & -1 & 0 \\ 0 & 0 & 1 \end{pmatrix} \qquad [4.58]$$

Throughout the diagonal nature of matrix *a*, equation [4.57] becomes:

$$c_{ijkl} = a_{ii}a_{jj}a_{kk}a_{ll}c_{ijkl} \qquad [4.59]$$

Thus, each time index 3 appears an odd number of times, we have $c_{ijkl} = -c_{ijkl} = 0$.

Therefore, the stiffness tensor of point group 2 is expressed:

$$\overline{\overline{C}}_2 = \begin{pmatrix} c_{11} & c_{12} & c_{13} & 0 & 0 & c_{16} \\ c_{12} & c_{22} & c_{23} & 0 & 0 & c_{26} \\ c_{13} & c_{23} & c_{33} & 0 & 0 & c_{36} \\ 0 & 0 & 0 & c_{44} & c_{45} & 0 \\ 0 & 0 & 0 & c_{45} & c_{44} & 0 \\ c_{16} & c_{26} & c_{36} & 0 & 0 & c_{66} \end{pmatrix} \qquad [4.60]$$

This form is valid for all point groups of the monoclinic crystal system.

Proceeding in the same way, we can construct the stiffness tensors of all point groups by including the different symmetry elements.

For point group *6mm* of AlN, the stiffness tensor shows five independent coefficients:

$$\overline{\overline{C}}_{6mm} = \begin{pmatrix} c_{11} & c_{12} & c_{13} & 0 & 0 & 0 \\ c_{12} & c_{11} & c_{13} & 0 & 0 & 0 \\ c_{13} & c_{13} & c_{33} & 0 & 0 & 0 \\ 0 & 0 & 0 & c_{44} & 0 & 0 \\ 0 & 0 & 0 & 0 & c_{44} & 0 \\ 0 & 0 & 0 & 0 & 0 & \frac{c_{11}-c_{12}}{2} \end{pmatrix} \qquad [4.61]$$

Piezoelectric thin films integrated on silicon frequently show a preferential orientation in the out-of-plane direction, but random orientation in plane.

We say that these materials have an axis of symmetry of infinite order. This is the typical case for polycrystalline PZT and AlN.

In this case, these materials have the same behavior as those of the *6mm* hexagonal crystal class. All the hexagonal point groups have the same stiffness tensor form.

Point group *3m* ($LiNbO_3$) has the following stiffness tensor (six independent coefficients).

It is also valid for point groups 32 (quartz) and $\bar{3}m$ (high temperature $LiNbO_3$):

$$\overline{\overline{C}}_{3m} = \overline{\overline{C}}_{32} = \begin{pmatrix} c_{11} & c_{12} & c_{13} & c_{14} & 0 & 0 \\ c_{12} & c_{11} & c_{13} & -c_{14} & 0 & 0 \\ c_{13} & c_{13} & c_{33} & 0 & 0 & 0 \\ c_{14} & -c_{14} & 0 & c_{44} & 0 & 0 \\ 0 & 0 & 0 & 0 & c_{44} & c_{14} \\ 0 & 0 & 0 & 0 & c_{14} & \dfrac{c_{11}-c_{12}}{2} \end{pmatrix} \qquad [4.62]$$

For this matrix, contraction of the index for compliance tensor s imposes a different value for coefficients $s_{65} = s_{56}$ that are equal to $2s_{14}$ (and not s_{14}).

Point group *4mm* (tetragonal $BaTiO_3$, PZT) has the following stiffness tensor:

$$\overline{\overline{C}}_{4mm} = \begin{pmatrix} c_{11} & c_{12} & c_{13} & 0 & 0 & 0 \\ c_{12} & c_{11} & c_{13} & 0 & 0 & 0 \\ c_{13} & c_{13} & c_{33} & 0 & 0 & 0 \\ 0 & 0 & 0 & c_{44} & 0 & 0 \\ 0 & 0 & 0 & 0 & c_{44} & 0 \\ 0 & 0 & 0 & 0 & 0 & c_{66} \end{pmatrix} \qquad [4.63]$$

For the simple case of cubic lattice of paraelectric phase perovskites (point group *m3m*) for dielectric, electrostrictive or variable capacitor applications the stiffness matrix is the following:

$$\overline{\overline{C}}_{cubic} = \begin{pmatrix} c_{11} & c_{12} & c_{12} & 0 & 0 & 0 \\ c_{12} & c_{11} & c_{12} & 0 & 0 & 0 \\ c_{12} & c_{12} & c_{11} & 0 & 0 & 0 \\ 0 & 0 & 0 & c_{44} & 0 & 0 \\ 0 & 0 & 0 & 0 & c_{44} & 0 \\ 0 & 0 & 0 & 0 & 0 & c_{44} \end{pmatrix} \quad [4.64]$$

In the isotropic case, the stiffness tensor has the same form as in the cubic case by adding the relation:

$$c_{44} = \frac{c_{11} - c_{12}}{2} \quad [4.65]$$

For isotropic materials it is more common to define the two independent coefficients E (or Y to avoid confusion with the electric field in problems involving electromechanical coupling) and ν, which are respectively Young's modulus and Poisson's ratio. These two coefficients are often given to the detriment of coefficients c_{ijkl}, as they are simpler to measure experimentally. Returning to the example of the stretched cylinder in the case of an isotropic material (see section 4.2 on Hooke's law), we saw that Y links stress to longitudinal strain in the case of a longitudinal stretch.

Poisson's ratio quantifies the decrease in the transverse lengths for a longitudinal stress. Translated into equations, here is what the stress-strain relations give in the case of a longitudinal stress along axis 1 applied on a free isotropic material to be deformed:

$$S_1 = \frac{1}{Y} T_1 = s_{11} T_1 \quad S_2 = -\frac{\nu}{Y} T_1 = s_{12} T_1 \quad S_3 = -\frac{\nu}{Y} T_1 = s_{12} T_1 \quad [4.66]$$

Identification between equations enables us to obtain a simple relation between compliance coefficients on one hand and Y and ν on the other, namely:

$$Y = \frac{1}{s_{11}} \qquad \nu = -\frac{s_{12}}{s_{11}} \quad [4.67]$$

Relationships between stiffness and compliance coefficients are obtained through the following relation, where I is the unit matrix:

$$c_{ijkl} s_{ijkl} = I \quad [4.68]$$

4.8. Bibliography

[DIE 74] DIEULESAINT E., ROYER D., *Elastic Waves in Solids*, Springer-Verlag, Berlin, (Translated in 1999), 1974.

[FEY 99] FEYNMAN R., *Le cours de Physique de Feynman – électromagnétisme 2*, Chapter 38, Dunod, Paris, 1999.

[NYE 61] NYE J.-F., *Physical Properties of Crystals*, Oxford University Press, UK, 1961.

Chapter 5

Dielectric Formalism

5.1. Introduction

In this chapter we introduce well-established notions about the electric variables of an insulating material. These variables are clear enough for people who know about the physics of solids, but experience shows that the concepts are more difficult to understand in the microsystems community. It therefore seems important to us to dwell at length, just like we did for mechanical energetics, on the electric part in order to introduce the indispensable notions:

– the average and local electric field;

– electric displacement and polarization;

– the relation between field strength and polarization;

– the polarization catastrophe phenomenon that appears in perovskites;

– dielectric relaxation and the different contributions to polarization characteristic of perovskites; and finally

– electric energy density which contributes to internal energy.

5.2. The dielectric effect seen by Faraday

Electric charges cross a conductor when a potential difference is applied. In the case of a perfect insulator, charges cannot cross. The dielectric effect observed for

---

Chapter written by Emmanuel DEFAŸ.

the first time by Faraday corresponds to the mutual influence of opposite charges contained in the two electrodes of a plane capacitor. The most telling experiment of this dielectric effect is illustrated in Figure 5.1. This shows the decrease in potential difference observed between the electrodes of a pre-charged isolated plane capacitor (see Figure 5.1a) when a dielectric material is introduced in the space between the electrodes (see Figure 5.1b). This effect is perfectly reversible and the potential difference recovers its initial value after the dielectric is withdrawn from the inter-electrode space (when losses are negligible).

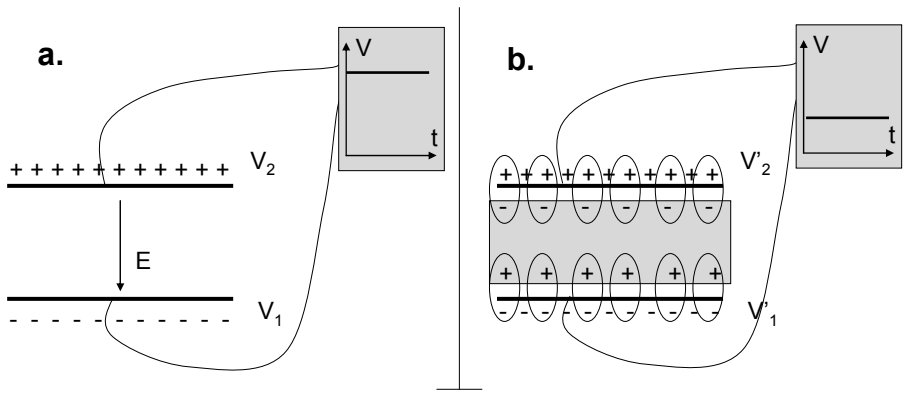

Figure 5.1. *Illustration of Faraday's experiment on the revelation of the dielectric capacitance of insulator: a) voltage, V, measured at the terminals of a pre-charged isolated plane capacitor; and b) decrease in voltage, V, when a dielectric is introduced between the electrodes*

Thus, for a given charge, the difference in potential observed between electrodes will be lower when a dielectric is present between the electrodes. It is experimentally possible to quantify this effect through the definition of dielectric capacitance, C. Capacitance is such that it linearly links the charge, Q, of a capacitor to the potential difference, V, between its electrodes. We therefore have $Q = CV$. As the potential difference depends on the geometry of the capacitor, it is very often with the macroscopic average electric field, E, that we work. The field can be determined at each point in the space. It is defined by:

$$\vec{E} = -\overrightarrow{grad}\,(V) \qquad [5.1]$$

This definition of field based on the knowledge of the potential difference at the terminals of the capacitor corresponds to an *average field*. This field is different from the field that is exerted at each point of the dielectric, called the *local field*, which will be defined a bit later on. In the case of a plane capacitor of inter-

electrode distance, d, and with z the coordinate perpendicular to the electrode plane, equation [5.1] simply gives:

$$\vec{E} = -\frac{\partial V}{\partial z}\vec{z} = -\frac{V}{d}\vec{z} \qquad [5.2]$$

It is useful to go into more detail on what happens inside of the capacitor, between the electrodes. In Figure 5.1a, the charges on the electrodes exhibit an opposing polarity: the negatives attract the positives and vice versa. It is a purely electrostatic effect. The dielectric in Figure 5.1b is also sensitive to this electrostatic effect, since it consists of atoms in which the nucleus and electron charges will not behave in the same way. In passing, let us note that this effect, called the polarization effect, can have various origins but the presence of atoms is enough to understand the physical phenomenon. Simply taking into consideration the electrostatic effect enables us to see that the surface charges on the dielectric have opposite signs to that of the electrode opposite, as seen in Figure 5.1b. These charges will therefore create another electric field that is opposite to the first. It is called the depolarizing field, E_d. According to equation [5.1], the potential difference is the integral along direction z of the electric field. As in the dielectric, two electric fields of opposing directions are superimposed, it is easy to understand that the potential difference decreases in the presence of the dielectric.

Another way of seeing things is to introduce the concept of *linked charges*. If we go back to Figure 5.1b, it is possible to associate with each elementary charge on the surface of the dielectric, a charge with the opposite sign on the electrode facing it. When the potential difference is measured, this charge cannot contribute as it is almost invisible to the voltmeter since it cannot move. Everything happens as if the charge measured by the voltmeter were smaller than it really is. We say that these charges that do not contribute are *linked charges*. This particular notion sometimes blurs comprehension of the polarization phenomenon, but suggests a different physical clearing.

It is possible to go further in the description by using laws of electrostatics on the capacitor. Figure 5.2 is a close-up view of a slice of the capacitor.

Gauss' theorem tells us that the flux of the electric field on a closed surface is equal to the charge inside the volume defined by the closed surface, divided by the permittivity of the vacuum. By applying this theorem to the surface, a, in Figure 5.2, we get:

$$\oiint \vec{E}.\vec{dS} = \frac{Q_{\text{int}}}{\varepsilon_0} = E_0 \delta S = \frac{Q_{free}}{\varepsilon_0} \qquad [5.3]$$

In this equation, δS represents the plane surface parallel to the electrodes. As the field beyond the electrodes is considered to be null (far from the edges of the capacitor), the only field E_0 that contributes is the one under the electrode, which is identical to the field when the dielectric is absent. Q_{free} represents the charges on the surface, δS, of the electrode. These charges were brought during the dielectric charge. They can therefore be determined, for example, by measuring the current necessary for charging the capacitor.

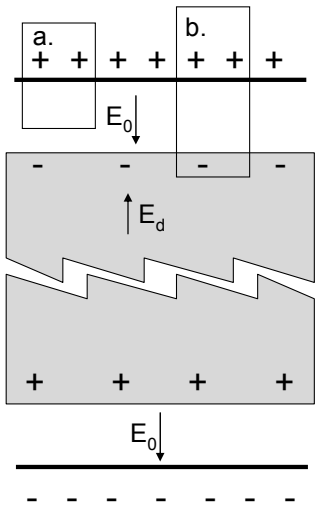

Figure 5.2. *Close-up view of a slice of the capacitor. Letters a and b represent the two surfaces on which laws of electrostatics (Gauss' theorem) are applied*

Now, let us apply Gauss' theorem on surface *b* of Figure 5.2. We get:

$$E\delta S = \left(E_0 - E_d\right)\delta S = \frac{Q_{free} - Q_{pol}}{\varepsilon_0} \qquad [5.4]$$

E is the average macroscopic field in the dielectric, therefore the difference between the field E_0 produced by free charges minus the depolarizing field E_d. Q_{pol} corresponds to surface charges (called polarization surface charges) created in the dielectric through the influence of free charges on the electrodes. This phenomenon is called *polarization* of the dielectric material. A bit later we will see how these polarization surface charges are linked to the polarized state of any dielectric volume. As this notion of surface charge dominates, we use the ratio $Q/\delta S$, usually called σ. We should take care not to confuse this with entropy, as defined in this book.

Thus, equation [5.4] becomes:

$$E = \frac{\sigma_{free} - \sigma_{pol}}{\varepsilon_0} \qquad [5.5]$$

We will note that in this simple case of a plane capacitor, the depolarizing field, E_d, is equal to $-\sigma_{pol}/\varepsilon_0$.

5.3. Electric polarization and displacement

It is possible to link these notions of surface charges with fields at each point of the dielectric in the same way as the electric field. It is this stage that enables us to define an electric energy density at each point of the dielectric, independently of the form taken by the capacitance. To do this, we must look at what is happening at the microscopic level.

As we said, there are charges inside the dielectric. If we imagine an atom in the dielectric, applying an electric field will induce a displacement of the electrons that carry the negative charge in one direction and the displacement of the nucleus that carries the positive charge in the opposite direction. This separation of centers of inertia of the charges therefore by definition creates an elementary electric dipole that is the product of the charge by the distance between these charges.

Thus, inside the dielectric, a succession of dipoles, p, follow each other in the direction of the electric field, as illustrated in Figure 5.3b. We can therefore macroscopically define a dipole density called *polarization P* that corresponds to the average of the dipole per unit of volume.

If n is the number of dipoles per unit of volume, P can be expressed:

$$\vec{P} = n\,\vec{p} = nq\,\vec{\delta} \qquad [5.6]$$

Here, q is the charge of each elementary dipole and δ is the distance between the conjugated charges of each elementary dipole. We are assuming that all the dipoles are identical.

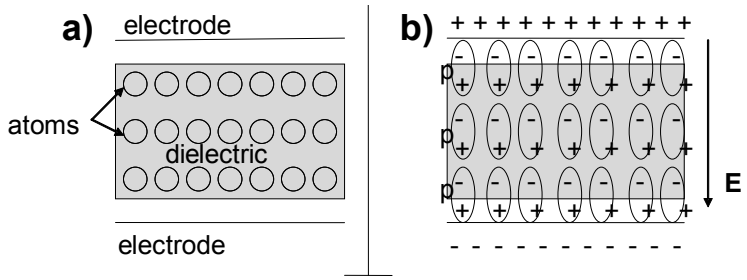

Figure 5.3. *Diagram of the microscopic behavior of a dielectric: a) no electric field applied; and b) an applied electric field, separation of charges in each atom and creation of dipoles in the direction of the electric field*

In terms of units, the elementary dipole p is in C.m whereas polarization P is in C/m². We must also note that P is in the same direction as the ps. In this example, the direction and way are the same as those of the applied electric field.

NOTE.– Here, we must distinguish the spontaneous polarization that is found in the pyroelectric materials (and ferroelectrics *a fortiori*) of polarization, which can be qualified as dynamic. This last is directly linked to the polarizability of the dielectric, and therefore to its capacitance to store charges for a given electric field. Polarizability will be defined more specifically a bit later. Spontaneous polarization corresponds to the presence of non-null dipoles without any applied electric field. If the sum of all these dipoles leads to a non-null polarization, we say that a spontaneous polarization is formed in the dielectric. The spontaneous polarization can only appear in certain crystalline lattices (with no center of symmetry and a unique polar axis). Furthermore, this is the definition of pyroelectric materials. It is this spontaneous polarization that is found in all perovskite materials in the ferroelectric phase (therefore for a temperature below the Curie temperature) and also in AlN, which also has a spontaneous polarization along the *c*-axis (although AlN is only pyroelectric, not ferroelectric, unlike perovskites). This does not, however, prevent these materials from having dielectric properties in the other directions. A dynamic polarization can develop in a direction perpendicular to spontaneous polarization. For example, bulk $BaTiO_3$ (often considered the standard perovskite material) in the tetragonal phase has a dynamic polarization 10 times greater in the direction perpendicular to the spontaneous polarization (*c*-axis) than in the direction of the latter. Spontaneous polarization is not necessarily in the same direction as the electric field as not all directions of polarization are allowed (the polar axis concept). In ferroelectric dielectrics, spontaneous polarization always tries to align itself with the field in order to decrease the free energy. This leads to a hysteresis phenomenon as we saw in Chapter 2. In the case of non-ferroelectric

pyroelectric materials like AlN, spontaneous polarization cannot evolve (to the first order) with the electric field, regardless of its intensity and direction.

To go further, we must find a solution to link the surface charge density to polarization, which is not obvious. In the case of a plane capacitor uniformly polarized in the vertical direction (*z*-axis), one of the ways of doing this is to virtually separate the dielectric into very fine columns of section, *dS*. Each element of volume $d\tau = dSdz$ contains a large number of dipoles (to be able to use the value of macroscopic polarization *P*), but remains very small in relation to the capacitor in order to integrate. This means that the elementary entities that we are summing up can be limited to the first order.

Thus, each element $d\tau$ has a dipole moment equal to $dp = PdSdz$. We can now look at the electric field or (simpler!) at the potential created by each column at a point *M* outside the capacitor, as illustrated in Figure 5.4.

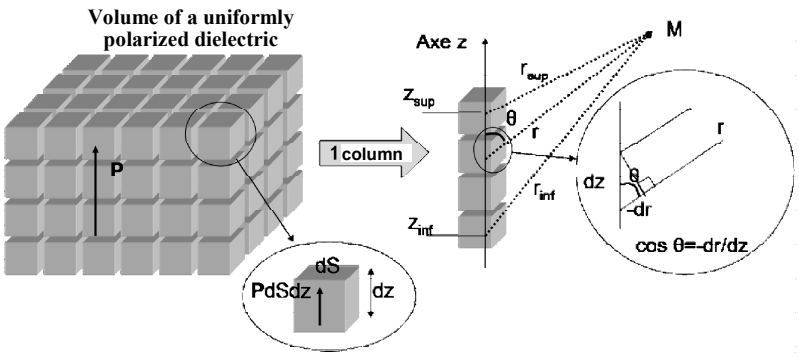

Figure 5.4. *Illustration of the argument used for calculating the potential created at point M by a column of section dS of the uniformly polarized dielectric*

Here, we are not seeking to find the sources that polarize the material but only that which induce its polarized state on a point external to the dielectric. The contribution, $dV_{d\tau(z)}(M)$, to the electric potential at *M* of the dipole moment, *dp*, of each element, $d\tau$, according to electrostatic laws is:

$$dV_{d\tau(z)}(M) = \frac{1}{4\pi\varepsilon_0}\frac{\vec{dp}.\vec{r}}{r^3} \qquad [5.7]$$

Here, *r* is the vector between element $d\tau$ and point *M*.

If we consider the angle θ between the z-axis and r, equation [5.7] becomes:

$$dV_{d\tau(z)} = \frac{1}{4\pi\varepsilon_0}\frac{P\cos\theta dSdz}{r^2} \qquad [5.8]$$

Summing up all the contributions between z_{inf} and z_{sup}, respectively, the z coordinates of the lowest and highest points of the dielectric, the potential at M due to the column (see Figure 5.4) becomes:

$$V(P) = \int_{z_{\inf}}^{z_{\sup}} dV_{d\tau(z)} = \frac{1}{4\pi\varepsilon_0}PdS\int_{z_{\inf}}^{z_{\sup}}\frac{\cos\theta dz}{r^2} = \frac{1}{4\pi\varepsilon_0}PdS\int_{r_{\inf}}^{r_{\sup}}\frac{-dr}{r^2} = \frac{PdS}{4\pi\varepsilon_0}\left(\frac{1}{r_{\sup}} - \frac{1}{r_{\inf}}\right) \qquad [5.9]$$

The change in variable between dz and dr is explained in Figure 5.4. For the potential created at M, everything happens as if the uniformly polarized column were replaced by a dipole of the dipole moment, $zPdS$. The influence of the column on point M external to the dielectric is the same as a dipole with a $+PdS$ charge in z_{sup} and $-PdS$ in z_{inf}. P is therefore equivalent to a surface charge density that is none other than σ_{pol}.

We must not lose sight, however, of the fact that this is only the effect of a dielectric column on a point located outside the dielectric. On the inside, the effect could be completely different. The condition that will enable us to generalize is the fact that the rotational of the electric field is null in electrostatics. This leads to the existence of the electric potential. Canceling the rotational results in the circulation of the electric field being independent of the path traveled. We place one end of the line on which we calculate the circulation of the electric field on each electrode. Thus, whether the line of circulation passes on the outside or the inside of the dielectric, the circulation of the field is identical. As the circulation of the field is equal to the potential difference, we deduce that the average macroscopic interior field created by uniform polarization, P, of a dielectric is the same as the one created by a surface charge distribution, σ_{pol}, such that:

$$P = \sigma_{pol} \qquad [5.10]$$

This equation enables us to link P, a field that can be defined at each point of the dielectric, to σ_{pol} a measurable quantity thanks to equation [5.5]. Returning to this equation, we get:

$$\sigma_{free} = \varepsilon_0 E + P \qquad [5.11]$$

σ_{free} is, by definition, equal to the *electric displacement field D*. It is a measurable experimental datum as it is the integral at the time of the charge or discharge current of the capacitor. The most physical definition of D is, however, given in relation to E and P, which we can link to microscopic entities of the material. Although historically D was introduced before P, Feynman suggests not using D, which is always linked to E and P. As most texts focusing on dielectrics use D, let us write the general vector formula linking E, P and D according to equation [5.11]:

$$\vec{D} = \varepsilon_0 \vec{E} + \vec{P} \qquad [5.12]$$

We can generalize the formula linking σ_{pol} to P in the case where P is not perpendicular to the surface. With the argument made around Figure 5.3, we understand that the surface charges surpass the dielectric in the direction of polarization. Thus, if we choose a surface parallel to polarization, there are no polarization charges. If n is the normal to surface S, the polarization charges created on this surface by the polarization dielectric P are:

$$\sigma_{pol} = \vec{P} . \vec{n} \qquad [5.13]$$

It is interesting to see what happens when polarization is not uniform, which happens frequently at interfaces or in the case of inhomogeneous materials. In the case of a homogeneous polarization, such as in Figure 5.3b, the global charge emitted from the dielectric is null as there are as many positive as negative charges. Thus, the average charge inside the dielectric remains null. According to equation [5.13], charge ΔQ_{pol} that is emitted from a dielectric volume delimited by the surface S and having a polarization P at each point is:

$$\Delta Q_{pol} = \oiint_S \vec{P} . \vec{n} \, dS = \iiint_V \vec{\nabla} . \vec{P} \, dV \qquad [5.14]$$

We used Gauss' theorem to go from the surface integral to the volume integral.

Thus, if P is not uniform and therefore presents a gradient in the dielectric, ΔQ_{pol} is not null. If a charge comes out of the volume, V, a charge with an opposite sign is found inside the volume considered as globally no charge is created or suppressed. In this case, there is a *polarization volume* charge density ρ_{pol} in the dielectric. We therefore have:

$$\Delta Q_{pol} = -\iiint_V \rho_{pol} dV \qquad [5.15]$$

Finally, by combining equations [5.14] and [5.15], we get the relation:

$$\rho_{pol} = -\vec{\nabla}.\vec{P} = -div\,\vec{P} \qquad [5.16]$$

5.4. The dielectric constant

Now that the fields governing electrostatic energy have been described, we can introduce a relation between them like Hooke's law for mechanical energy. The initial hypothesis is that the higher the field, the greater the polarization. This is understandable, since polarization depends on each elementary dipole and each one of them is sensitive to the field (watch out for the local field, see later). As a first approximation, we assume that this relation is linear. Thus, the dielectric susceptibility χ links polarization to the average electric field according to:

$$\vec{P} = \varepsilon_0 \overline{\overline{\chi}}\,\vec{E} \qquad [5.17]$$

As P and E are vectors, χ is a rank 2 tensor. The use of χ is less common than that of the dielectric constant ε, however, which links electric displacement to the field:

$$\vec{D} = \varepsilon_0 \overline{\overline{\varepsilon_r}}\,\vec{E} = \overline{\overline{\varepsilon}}\,\vec{E} \qquad [5.18]$$

According to this definition, $\overline{\overline{\varepsilon}}$ is the rank 2 tensor of the dielectric constant whereas $\overline{\overline{\varepsilon_r}}$ is the tensor of the relative dielectric constant.

It is important to note that a spontaneous polarization is often present in the materials in which we are interested. This polarization is not directly involved in the dielectric effect. The clearest definition of the dielectric constant is therefore the *derivative* of electric displacement in relation to the electric field.

In the most general case, the unambiguous definition of element ε_{ij} of tensor $\overline{\overline{\varepsilon}}$ is:

$$\varepsilon_{ij} = \frac{\partial D_i}{\partial E_j} \qquad [5.19]$$

In the same way as for the stiffness tensor, the dielectric constant tensor has a number of independent coefficients that depend on the point group of the crystal studied. The *6mm* (polycrystalline AlN and lead zirconate titantate [PZT]) and *3m* (niobate and lithium tantalate) crystal classes, and all the tetragonal crystal classes (for example, bulk single crystal $BaTiO_3$ between 5°C and 120°C) present a dielectric constant tensor with solely diagonal elements and with $\varepsilon_{11} = \varepsilon_{22}$. For a perovskite cubic lattice, only diagonal elements exist and they are all equal. The dielectric constant tensor is reduced to a scalar. The letter *K* is therefore often used to designate the dielectric constant.

With all these definitions, the expression of the capacitance, *C*, of a surface plane capacitor, *S*, and of dielectric thickness, *e*, is:

$$C = \frac{Q_{free}}{V} = \frac{DS}{Ee} = \frac{\varepsilon ES}{Ee} = \frac{\varepsilon S}{e} = \frac{\varepsilon_0 \varepsilon_r S}{e} \qquad [5.20]$$

We must note that to end up with this simple and very useful formula it was necessary to assume that the space between the electrodes is entirely occupied by the dielectric, in such a way that the electric field is simply *V/e*. The space between the electrodes and the dielectric that we used for the argument is neglected (see Figure 5.2).

5.5. The local field in dielectrics: polarization catastrophe

We now take up a rather complex concept of dielectric media: the local electric field, E_l. It is a particularly important point for perovskite materials as it enables us to explain, at least qualitatively, why the dielectric constant takes a very high value at ferroelectric-paraelectric transition. The issue is in quantifying the electric field that produces the dipoles.

As happens at the macroscopic level, the microscopic dipole moment at first glance presents a linear dependence with the field it is in. We must therefore find this field, which is applied to each dipole and that we call the *local field*.

This field corresponds to the sum of the macroscopic field with all the fields stemming from neighboring dipoles, with the exception of itself. E_l therefore evolves as a function of the crystal structure of the dielectric considered. We must

note that in the case of perovskites, the local phenomena are not all completely understood yet.

The *ab initio* approach is certainly the one that is best to describe what happens at this scale and the works developing this approach are currently very numerous. It is interesting, however, to give the classic expression of the local field valid for ionic gases, liquids and solids of cubic structure. This actually enables us to obtain the Clausius-Mossoti law, which suggests the possibility of divergence of dielectric constant.

The approaches for obtaining the local field are not always the same, depending on the authors. Kittel's work [KIT 04] remains the reference and constitutes the view that is most generally observed. He suggests decomposing the local field into four contributions:

– the field due to free charges;

– the depolarization field;

– the field called the Lorentz field calculated by removing a sphere that is fictionally cut up in the dielectric; and

– the field due to the closest dipoles contained in the sphere (see Figure 5.5).

The idea in this *a priori* complicated decomposition is to have the most generic calculation possible based on crystal structures.

Indeed, if the sphere is big enough (typically a few crystalline lattices in diameter), the direct influence of each dipole beyond the sphere is negligible and therefore the contribution of the dipoles beyond this limit corresponds to the third configuration of the right "term" represented in Figure 5.5. It corresponds to the *Lorentz* field and is equal to $P/3\varepsilon_0$ (see Kittel for the classic electrostatics calculation decomposing the surface of the corona sphere [KIT 04]). The field in the sphere, produced by the sphere, is therefore calculated in a specific way depending on the structures.

Using the field created by all the neighboring dipoles on the central site in which we are interested, we can show that this field is null in the case of a cubic lattice.

This is also true in liquids or gases and, in general, in all cases for which there is no dipole other than the one in the central site in the sphere.

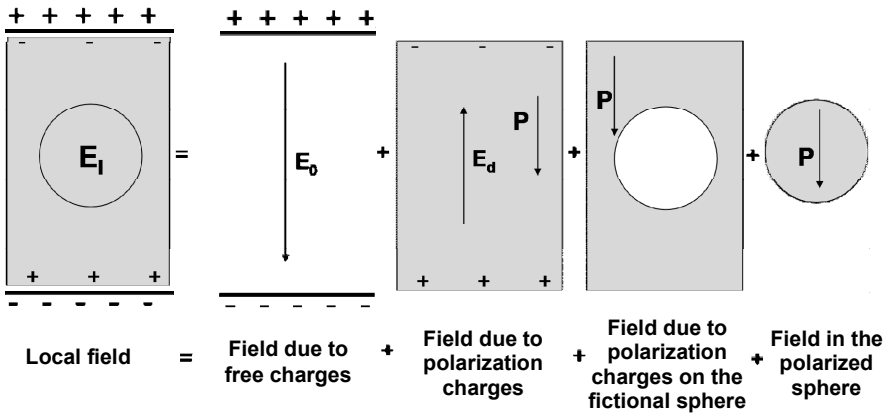

Figure 5.5. *Illustration of the calculation of the local electric field in a uniformly polarized medium*

Thus, the formula for the local field in relation to the Lorentz field is the following:

$$E_l = E + \frac{P}{3\varepsilon_0} \qquad [5.21]$$

with $E = E_0 - E_d$.

Now that the expression of the local field is known (in the case of the Lorentz field), it is possible to specify the local dipole moment p by assuming a linear relation between p and E_l: the stronger E_l, the more important p. Thus, we define polarizability, α, which is the proportionality coefficient between p and E_l: this is none other than a first-order estimate. Polarizability is homogeneous to a volume and is such that:

$$p = \varepsilon_0 \alpha E_l \qquad [5.22]$$

Using equations [5.6], [5.21] and [5.22], we get the following expression linking polarization and the macroscopic field:

$$P = \frac{n\varepsilon_0 \alpha}{1 - \frac{n\alpha}{3}} E \qquad [5.23]$$

Thus, in this Lorentz field hypothesis, the expression of the relative dielectric constant is:

$$\varepsilon_r = \frac{n\alpha}{1-\frac{n\alpha}{3}} + 1 \qquad [5.24]$$

This is the Clausius-Mossotti relation, which can be found in different forms. It is a good explanation of the behavior of materials that have polarizability with a strong electronic contribution. In the case of perovskites and wurtzites (AlN), there are other contributions to polarizability, as we will explain in detail in the next section. Let us also note that this relation is only valid for materials without spontaneous polarization. Therefore, it is not applied for AlN and perovskites in the ferroelectric phase. The Clausius-Mossotti relation, however, enables us to understand the particular behavior of perovskites in phase transition, since in the paraelectric phase these materials are in cubic phase, a condition using the Lorentz field for crystalline materials.

Equation [5.24] suggests that if $n\alpha$ nears 3, the dielectric constant can diverge. This divergence is called the *polarization catastrophe*. It highlights looping between the local field and the dipole moment in the paraelectric phase. Indeed, E_l produces p. If p increases, P also increases and therefore also E_l by virtue of equation [5.21]. This positive loop therefore gives the possibility of a divergence. It is what happens during ferroelectric-paraelectric transition.

When the temperature decreases, the density of the paraelectric increases because the coefficient of dilatation is positive (around 10 ppm/°C). Therefore, n increases and $n\alpha$ also increases, assuming α is constant in this temperature range. We can therefore make the hypothesis that in certain materials, around a temperature θ_C, $n\alpha$ can present, to the first order, a linear variation with the temperature such that:

$$n\alpha = 3 - \lambda(\theta - \theta_C) \qquad [5.25]$$

Replacing this expression in the Clausius-Mossotti relation, keeping only the dominant term we get:

$$\varepsilon_r = \frac{9}{\lambda(\theta - \theta_C)} \qquad [5.26]$$

Here we find another form of equation [3.5], which was the phenomenological expression of Curie-Weiss law. We must take note, however, that although it is approximative, equation [5.26] gives a microscopic explanation of the phenomenological behavior. When the temperature is less than θ_C, the dielectric constant cannot become negative due to nonlinear effects. The crystal then undergoes a phase transition that enables stabilization of dipole moments even in the absence of a macroscopic field. It is the appearance of spontaneous polarization that is seen, for example, in the tetragonal phase of $BaTiO_3$ below 120°C.

The continuation of this discussion focuses on the polarizability that is particular to perovskites, of which the sum of the different contributions (electronic, ionic and domain walls) enables the condition of polarization catastrophe to be achieved. Through their different natures, these contributions have different frequencies of relaxation.

5.6. Dielectric relaxation

5.6.1. *The various relaxations*

The dielectric property of materials that links electric displacement to the field is not independent of frequency. This change in the dielectric constant as a function of work frequency is called *dielectric relaxation*. It is a phenomenon that is found in all dielectrics and depends on the various contributions of the charged species present in the material: trapped charges, dipoles, ions and electrons.

Generally speaking, there is a lot of information about this field in the literature. For perovskites, dielectric relaxation has certain specificities. The most original contribution to the dielectric constant in the case of perovskites comes from domain walls. In the case of PZT, it can constitute more than half of the dielectric constant [ZHA 94]. This is also the case for piezoelectric properties.

Figure 5.6 is a typical representation of relaxation in the case of perovskites by being limited in frequency to THz (10^{12} Hz). In this diagram, we are limited to phenomena of dielectric relaxation by removing those of atomic resonance (around 10^{12} Hz, corresponding to phonons and the soft mode) and those of electronic resonance near visible frequencies (around 10^{15} Hz). We will simply note that at optical frequencies, only the contribution of electrons subsists. At these frequencies, the typical dielectric constant is in the order of 6 and is equal to the square of the optical index n.

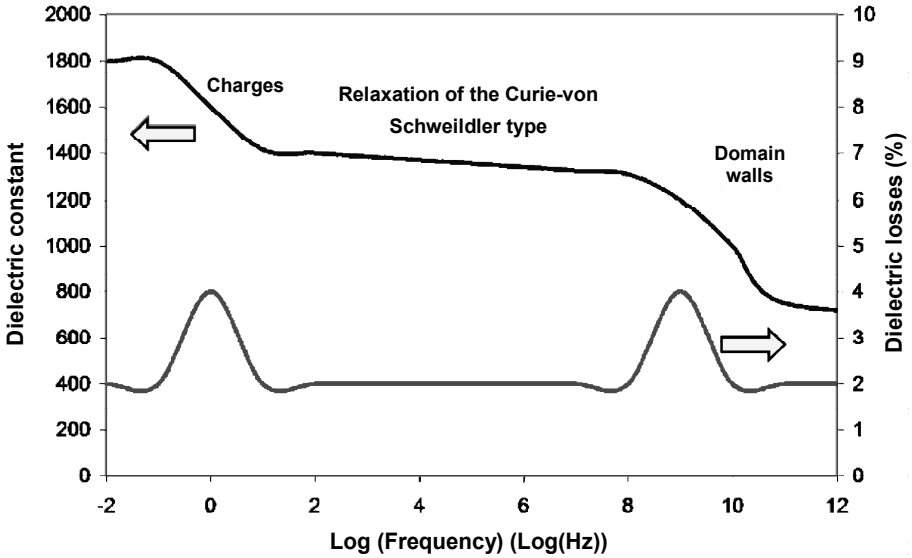

Figure 5.6. *Typical representation of the behavior of the dielectric constant and dielectric losses in frequency of PZT in thin films. Only dielectric relaxation phenomena are plotted*

In Figure 5.6, three relaxation phenomena are represented as a function of the frequency of excitation. Other contributions can relax in this frequency range (between 10^{-2} and 10^{12} Hz) but the three represented are present almost all of the time, regardless of the perovskite characterized.

The first contribution corresponds to charges: it can be electrons, vacancies (often oxygen vacancies) that are linked to the material and that can, at low frequency, move from one trap to the other. This movement contributes to the dielectric constant, which subsides as soon as the frequency becomes too high. Indeed, typically beyond a few Hz or dozens of Hz, these charges no longer have the time to move from one trap to the next. It is this phenomenon that is called *dielectric relaxation*: when it starts and frequency increases, the losses also begin to increase because the dielectric effect of this contribution becomes less efficient. The dielectric constant decreases little by little until the relaxing contribution completely vanishes. The losses then find a lower level.

This very general description of dielectric relaxation corresponds to the functioning of a low-pass filter and is therefore often modeled by an RC cell. This is what is called the Debye model. The different contributions are often more subtle but the Debye model enables us to properly seize the phenomenon. The

characterization of low-frequency relaxation is done through the use of a specific analyzer, called a *low frequency spectrometer*. It is also possible to observe these relaxations by measuring the current that crosses a capacitor excited by a voltage step.

The second contribution is distributed over a large frequency range. This is called *Curie-Von Schweidler* relaxation. It is found in most dielectrics in a more or less marked way. Its physical origin is still not well-known, although the phenomenon was identified more than a century ago. In temporal space, it corresponds to a power law as a function of the time of the relaxation current density, J_r, such that $J_r = Kt^{-n}$, with K and n being constants.

The third contribution corresponds to domain walls. Today we know that these walls play a dominant role in the dielectric effect of ferroelectrics. Indeed, when work temperature is reduced, the mobility of domain walls decreases, as does their influence. Zhang *et al.* showed that in this way permittivity loses about 50% of its value to ambient temperature [ZHA 94]. Let us note that this relaxation only concerns materials in the ferroelectric phase, since it is they that are susceptible to presenting domain walls. Paraelectrics, devoid of domains since there is no remanent polarization, do not present this particular relaxation. The phenomenon of losses associated with domain walls corresponds to the generation of shear acoustic waves inside the material [ARL 93]. The losses thus correspond to the conversion of the electric energy of excitation into acoustic energy. We will return to this phenomenon when we go into the details of the radiofrequency properties of these materials.

Another phenomenon that can be compared to dielectric relaxation can be observed in the case of electrode-dielectric-electrode film configurations at frequencies in the region of GHz. These are acoustic resonances that come from the piezoelectric effect induced by ferroelectricity. When the ferroelectric thin film is excited by an alternative signal, there is a frequency that corresponds to the mechanical resonance of the resonator made up of the ferroelectric with its electrodes. This mechanical movement in the ferroelectric film induces a current produced by the piezoelectric effect. At resonance, this current is in phase with the excitation signal that is translated by a drop in the real part of impedance. The capacitance gets closer to a short circuit at this particular frequency. If we look at this system as a capacitance and not an acoustic resonator, this fall in the real part of impedance is interpreted as an increase in dielectric losses. In the case of a capacitive application (fixed or variable), this resonance can be a problem because the effect can be very strong. Resonance is typically located at a few GHz for thicknesses of a few hundred nm. We must also note that this resonance can be observed in the case of paraelectrics polarized by a continuous voltage. The material then behaves like a piezoelectric induced by the electrostrictive effect, which is

particularly strong in the case of perovskites. We will return to this effect and spend a lot of time on it in Chapter 8, due to it being very advantageous for acoustic resonators.

5.6.2. *Kramers-Kronig relations*

We cannot speak of dielectric relaxation without bringing up *Kramers-Kronig relations*. Indeed, these relations that are obtained by purely mathematical calculations enable us to prove that the dielectric constant and dielectric losses are interdependent. It is even possible to calculate one in relation to the other, if one of the two is known throughout the entire frequency range. In this section, we sum up the main part of the procedure necessary for understanding how these relations are established, largely inspired by Jonscher's reference book on dielectric relaxation, *Dielectric Relaxation in Solids* [JON 99].

Let us consider dielectric susceptibility, χ, as a complex value such as $\chi = \chi' - i\,\chi''$. We recall that χ links polarization to the electric field through the relation $P = \chi E$. When the electric field suddenly changes value in the dielectric, typically by applying a voltage step to the terminals of a capacitor, the polarization of the material evolves, but not instantaneously. Actually, the various contributions to the dielectric constant implicate entities that have a mass (with the exception of the vacuum, whose permittivity is ε_0). They therefore all have a non-null response time. Let us therefore consider this dielectric response $f(t)$ as a function of time when an electric field dirac of amplitude E_0 is applied to the dielectric. This function can only take a non-null value from the time the excitation dirac is applied. This evident remark is called the *principle of causality* and means that a consequence cannot precede the cause that produced it. In response to this dirac applied at $t = 0$, polarization at time t is equal to $\varepsilon_0 f(t) E_0$. Now, if the electric field evolves, the resultant polarization will be the sum of the responses at all diracs of the electric field applied over time. In other words, if the electric field is decomposed into parts of infinitesimal duration $d\tau$ and variable amplitude over time $E(t)$, polarization will be the sum of all these contributions distributed over time.

It is the principle of superposition that is applied here. Translated into equations, the existence of $f(t)$ refers to writing:

$$P(t) = \varepsilon_0 \int_0^{+\infty} f(\tau) E(t-\tau)\, d\tau \qquad [5.27]$$

To properly understand this equation, we must first place ourselves at time t. The field then takes the value $E(t)$. The contribution of $E(t)$ is "felt" by polarization after

a delay. This is translated by the term $\varepsilon_0 E(t)f(0)$ added to polarization. If we take the field that was applied at time $t - \Delta t$, its contribution to polarization is $\varepsilon_0 E(t - \Delta t)f(\Delta t)$. And so on and so forth until $t = 0$. As soon as $t - \tau$ is <0, E is null. Next, according to the principle of causality, we can extend the integral to -∞. Thus, in mathematical terms, the integral of equation [5.27] corresponds to the convolution of $f(t)$ and $E(t)$.

We can apply equation [5.27] when a voltage (or field) step is applied. This field step is such that E is null when t <0 and $E = E_0$ when t >0. If we look at the polarization that results from this voltage step at the end of infinite time, we get:

$$P(+\infty) = \varepsilon_0 E_0 \int_0^{+\infty} f(t)\,dt \qquad [5.28]$$

This corresponds to the purely dielectric response of the material. The contribution of leakage current is not taken into consideration. Physically, this dielectric response comes from the movement of charges that remain inside the dielectric. These charges cannot escape from the dielectric. Furthermore, the leakage current comes from the movement of free charges that themselves completely cross the dielectric. These two physically very different contributions are sometimes difficult to distinguish, especially when high field strengths are applied to the terminals of the dielectric. The frequency study enables us to distinguish the leakage current from the purely dielectric part.

Equation [5.28] also enables us to see that the integral of $f(t)$ up to infinity must be finite, as the polarization of a material always keeps a finite value (even in the case of polarization catastrophe where nonlinear phenomena limit the divergence of polarization).

From an experimental point of view, we must note that the measurement of depolarization current (the applied field suddenly goes from E_0 to 0) is more appropriate for determining $f(t)$, given that the leakage current does not exist in the absence of an applied field. We must, however, be sure to have achieved the permanent state of polarization as defined by equation [5.28].

5.6.2.1. *Frequency range*

The hypothesis of the existence of $f(t)$ will enable us to link the real and imaginary parts of χ' and χ''. To do this, we must first express the Fourier transform of equation [5.27]. Let us recall that the Fourier transform $f(w)$ of the time range to the frequency range of a function $f(t)$ is given by the equation:

$$f(w) = \frac{1}{2\pi}\int_{-\infty}^{+\infty} f(t)e^{-iwt}dt \qquad [5.29]$$

Thus, by applying this transformation to equation [5.27], (for the mathematical demonstration, see [JON 99]) we get:

$$P(w) = \varepsilon_0 f(w)E(w) \qquad [5.30]$$

In this expression, *f(w)* is identical to the definition of dielectric susceptibility *χ(w)*. We can therefore write:

$$\chi(w) = \chi'(w) - i\chi''(w) = \int_{-\infty}^{+\infty} f(t)e^{-iwt}dt \qquad [5.31]$$

The real part χ' corresponds to the amplitude of polarization in phase with the field of excitation E whereas the imaginary part χ'' corresponds to the amplitude of polarization in quadrature with the field E (in other words, the part that enables us to quantify dielectric losses). Decomposing the exponential in sine and cosine, equation [5.31] gives:

$$\begin{aligned} \chi'(w) &= \int_{-\infty}^{+\infty} f(t)\cos(wt)dt \\ \chi''(w) &= \int_{-\infty}^{+\infty} f(t)\sin(wt)dt \end{aligned} \qquad [5.32]$$

As χ' and χ'' both depend on *f(t)*, it seems that it must be possible to determine one in relation to the other. Actually, the reverse Fourier transform of χ' or χ'', enables us to extract *f(t)*. We kept the integral between minus and plus infinity in order to give a stronger mathematical meaning. Indeed, it seems that χ' is an even function of w, whereas χ'' is an odd function of w.

From these properties, after several mathematical manipulations not detailed here (see [JON 99]), Kramers-Kronig relations take the following form:

$$\chi'(w) = \frac{2}{\pi}\int_0^{+\infty} \frac{x\chi''(x)}{x^2 - w^2}dx$$
$$\chi''(w) = -\frac{2w}{\pi}\int_0^{+\infty} \frac{\chi'(x)}{x^2 - w^2}dx \qquad [5.33]$$

These relations are not specific to dielectrics. Indeed, they are valid for any passive linear system that has losses. In mathematical terms, for Kramers-Kronig relations to be applied this system must respect the principle of causality, must have a response that tends towards zero when frequency tends towards infinity, and must have one even real part in w and one odd imaginary part in w (see [KIT 04]). Thus, these relations are also applied for magnetic permeability or the optical index.

An initial consequence of these relations is the following. If we take a null frequency, i.e. if we are interested in permittivity taking into consideration all polarization phenomena (even those at low frequency), equation [5.33] gives:

$$\chi'(0) = \frac{2}{\pi}\int_0^{+\infty} \frac{\chi''(x)}{x}dx = \frac{2}{\pi}\int_{-\infty}^{+\infty} \chi''(x)d(\ln x) \qquad [5.34]$$

Thus, a very high dielectric susceptibility necessarily implies significant dielectric losses that will appear in a given frequency range. Said in another way, it is not possible to find a good quality dielectric without dielectric losses. These losses are intrinsic to the material and this is so regardless of the leakage current. The dielectric relaxation phenomenon is therefore closely linked to the dielectric effect and the stronger this effect, the more significant the associated losses will be. Physically, the frequency range in which the losses are important corresponds to the moment a dielectric mechanism stops contributing (domain walls, movement of ions, trapped charges, etc.).

5.7. Electric energy density

To take up the calculation of electric energy density, we will use the example of the plane capacitor, which is the case predominantly found for thin films. This is not the general case but generalizing the calculation of energy density does not modify the formulae obtained for the plane capacitor, although the demonstration is quite complex.

Thus, for the capacitor we choose a reference point in which axes 1 and 2 are in plane and axis 3 is out-of-plane. Electric voltage is applied along axis 3, i.e. perpendicularly to the electrodes, and we neglect the boundary effects. Everything therefore happens along axis 3 and the problem is one-dimensional. The energy stored in the capacitor corresponds to the work necessary to bring charges to the electrodes. An uncharged capacitor (i.e. without energy) has its two electrodes at the same potential. When a constant difference in potential, V, is applied between the electrodes with the help of a battery, if the leakage current is neglected for example the current that circulates in the circuit is exclusively there to charge the capacitor. In energy terms, everything happens as if charges were transferred from one electrode to another. The necessary work, δW, for this transfer from a small charge quantity, δQ, under the difference in potential V is $V\ \delta Q$. The thickness, h, of the dielectric in the capacitor is constant. The absolute value of the applied electric field, E, in the dielectric is therefore V/h. Thus, δW is equal to δQE x h. δQE is the electrostatic force that is applied on the charge, δQ, and this force is applied over the distance h. δW is therefore homogeneous to work in which we can make the electric field, but also the electric displacement D, appear:

$$\delta W = V\delta Q = Eh\delta Q = E\delta DhS \qquad [5.35]$$

In this expression, S is the surface of the electrodes facing the dielectric and δD is the small change in electric displacement due to the application of the electric field E. The infinitesimal change in electric energy density per unit of volume, dU_{el}, in the case where a constant electric field is applied is therefore:

$$dU_{el}\left(plane\ \ capacitor\right) = EdD \qquad [5.36]$$

In the general case, the expression of this electric energy density is:

$$dU_{el} = \sum_{i=1}^{3} E_i dD_i \qquad [5.37]$$

If electric displacement is expressed as a function of the dielectric constant (see equation [5.19]) and the field, equation [5.37] becomes:

$$dU_{el} = \sum_{i,j} \varepsilon_{ij} E_i dE_j \qquad [5.38]$$

5.8. Bibliography

[ARL 93] ARLT G., BÖTTGER U., WITTE S., *Applied Physics Letters*, vol. 63, 602, 1993.

[KIT 04] KITTEL C., *Introduction to Solid State Physics*, 8th edition, Wiley, Oxford, 2004.

[JON 99] JONSCHER A.K., "Dielectric relaxation in solids", *J. Phys. D: Appl. Phys.,* vol. 32, R57-R70, 1999.

[ZHA 94] ZHANG Q.M., WANG H., KIM N., CROSS L.E., "Direct evaluation of domain wall and intrinsic contributions to the dielectric and piezoelectric response and their temperature dependence on lead zirconate titanate ceramics", *J. Appl. Phys.* vol. 75, 454, 1994.

Chapter 6

Piezoelectric Formalism

6.1. Thermodynamic equations

We saw before that piezoelectricity and electrostriction appear easily from energy considerations (see Chapter 2). This is the most natural method of defining them, even if there are microscopic models that enable us to better "appreciate" these phenomena.

The thermodynamic method is used to define piezoelectric equations of any material. The method is found in the reference document *Standards on Piezoelectricity* [IEE 87]. Most of the time, these equations leave out the heat term by assuming that the constant (adiabatic) entropy or constant temperature (isothermal) coefficients are very similar. It is possible to develop free energies for the four different configurations of natural variables (*(T,D)*, *(T,E)*, *(S,D)* and *(S,E)*) and obtain four matrix equation couples that describe the same piezoelectric system, but considered based on different boundary conditions.

To do this, it is enough to change the free energy in which we are interested into a function of the natural variables we wish to use. Therefore, for the *(T,D)* formalism already discussed, which uses Gibbs' elastic energy (G_1), we can re-write equations [2.59] and [2.60] by dropping the heat term, which gives:

$$S_{ij} = s^{D}_{ijkl} T_{kl} + g_{kij} D_k \qquad [6.1]$$

$$E_i = -g_{ikl} T_{kl} + \beta^{T}_{ik} D_k \qquad [6.2]$$

Chapter written by Emmanuel DEFAŸ and Mathieu PIJOLAT.

We saw that the Maxwell thermodynamic relations enable us to conclude that the piezoelectricity tensor is the same in both equations.

After discovery of the direct piezoelectric effect in 1880 by the Curie brothers (equation [6.2]), using these thermodynamic considerations (in other words, energy conservation), Lippmann anticipated that the reverse effect should exist (see equation [6.1]) and should be equivalent in intensity to the direct effect [LIP 81].

As the piezoelectric tensor is of order 3, it has 27 coefficients. This tensor gathers an electric tensor of first order (three coefficients) to a symmetrical mechanical tensor of order 2 (six independent coefficients). It therefore has 18 independent coefficients. Following the example of what was done for stress and strain tensors (see Chapter 4), it is possible to contract the indices, respecting certain rules of conversion based on those chosen for strains.

As $g_{kij} = \left.\frac{\partial S_{ij}}{\partial D_k}\right)_T$ (therefore with S_{ij}), the particular contraction rule is applied to g, which gives:

$$g_{kp} = g_{kij} \text{ for } i = j \text{ and } p = 1,2,3 \qquad [6.3]$$

$$g_{kp} = 2g_{kij} \text{ for } i \neq j \text{ and } p = 4,5,6$$

The other forms of the formalism appear by taking other free energies. If we place ourselves at constant temperature, the four free energies to take into consideration are F, G, G_1 and G_2.

Doing the same calculation as the one specified for G_1, for G, F and G_2 respectively, we get:

$$\begin{aligned} S_{ij} &= s^E_{ijkl} T_{kl} + d_{kij} E_k \\ D_i &= d_{ikl} T_{kl} + \varepsilon^T_{ik} E_k \end{aligned} \qquad [6.4]$$

$$\begin{aligned} T_{ij} &= c^D_{ijkl} S_{kl} - h_{kij} D_k \\ E_i &= -h_{ikl} S_{kl} + \beta^S_{ik} D_k \end{aligned} \qquad [6.5]$$

$$\begin{aligned} T_{ij} &= c^E_{ijkl} S_{kl} - e_{kij} E_k \\ D_i &= e_{ikl} S_{kl} + \varepsilon^S_{ik} E_k \end{aligned} \qquad [6.6]$$

The four piezoelectric tensors are therefore *g*, *d*, *h* and *e*. We can use contracted notations for these four formalisms. Thus, *d* behaves like *g* and respects equation [6.3]. As *e* and *h* function with T_{ij}, the contracted forms are simpler and give $e_{kij} = e_{kp}$ and $h_{kij} = h_{kp}$. The nature of the index giving the blocked variable does not influence the contraction rule.

These four equivalent formalisms induce relationships between all these terms. To obtain them, the equations must be crossed; for example, we can place S_{ij} from equation [6.4] in equation [6.6] and identify the terms. These equations are given in the *Standards on Piezoelectricity* [IEE 87]. Here are some of the equations (the terms are considered to be matrices and X^t represents the transpose of matrix X):

$$\begin{aligned} &c^E s^E = 1 && \\ &c^D s^D = 1 && \varepsilon^S = \varepsilon^T - d c^E d^t \\ &s^D = s^E - d^t \beta^t d && g = \beta^t d \\ &c^D = c^E + e^t h && e = c^E d \\ &\beta^T \varepsilon^T = 1 && h = \beta^S e \end{aligned} \qquad [6.7]$$

6.2. Reducing coefficients using crystal symmetry

In the same way we proceeded to reduce independent coefficients for the elastic tensor, we can reduce the independent coefficients of piezoelectric tensors by looking at the symmetries of the different point groups. In particular, as piezoelectricity is represented by a tensor of third order, we can quickly see why crystal classes, with one center of symmetry, have a null piezoelectric tensor. Actually, the center of symmetry gives the following relations for coefficients d_{ijk}, for example:

$$d_{ijk} = (-1)^3 d_{mno} \text{ hence } d_{ijk} = 0 \qquad [6.8]$$

Thus, for crystal classes with one center of symmetry, there cannot be a piezoelectric effect.

For the crystal classes in which we are mainly interested, piezoelectric tensors (*e* taken as an example here) are given in Table 6.1, after taking into consideration the different symmetries.

e is taken as an example as it does not pose any problems of conversion between the indices, just like *h*. For matrices *d* and *g*, we must take conversion into

consideration. In trigonal classes, this induces a doubling of the coefficients found in the sixth column (*-2d*$_{22}$ for *3m* and *-2d*$_{11}$ for *32*).

We will note that for changes in reference system, it is a lot more accurate to work on un-reduced coefficients to avoid all ambiguity.

6mm	*4mm*
$\begin{pmatrix} 0 & 0 & 0 & 0 & e_{15} & 0 \\ 0 & 0 & 0 & e_{15} & 0 & 0 \\ e_{31} & e_{31} & e_{33} & 0 & 0 & 0 \end{pmatrix}$	$\begin{pmatrix} 0 & 0 & 0 & 0 & e_{15} & 0 \\ 0 & 0 & 0 & e_{15} & 0 & 0 \\ e_{31} & e_{31} & e_{33} & 0 & 0 & 0 \end{pmatrix}$
3m	*32*
$\begin{pmatrix} 0 & 0 & 0 & 0 & e_{15} & -e_{22} \\ -e_{22} & e_{22} & 0 & e_{15} & 0 & 0 \\ e_{31} & e_{31} & e_{33} & 0 & 0 & 0 \end{pmatrix}$	$\begin{pmatrix} e_{11} & -e_{11} & 0 & e_{14} & 0 & 0 \\ 0 & 0 & 0 & 0 & -e_{14} & -e_{11} \\ 0 & 0 & 0 & 0 & 0 & 0 \end{pmatrix}$

Table 6.1. *Piezoelectric tensor e for point group 6mm, 4mm, 3m and 32*

6.2.1. *Example of a calculation: point group 3m*

In the case of materials from class *3m*, one of the symmetry operations is the 120° rotation about the *c*-axis (axis 3 here). The rotation matrix can be expressed in space:

$$A = \begin{bmatrix} \cos\theta & \sin\theta & 0 \\ -\sin\theta & \cos\theta & 0 \\ 0 & 0 & 1 \end{bmatrix}$$

$$A\left(\frac{2\pi}{3}\right) = \begin{bmatrix} -1/2 & \sqrt{3}/2 & 0 \\ -\sqrt{3}/2 & -1/2 & 0 \\ 0 & 0 & 1 \end{bmatrix} = \begin{bmatrix} a_{11} & a_{12} & a_{13} \\ a_{21} & a_{22} & a_{23} \\ a_{31} & a_{32} & a_{33} \end{bmatrix} \qquad [6.9]$$

Thus, e_{33} is not modified by a rotation of *2π/3* about the *c*-axis. Using the transformation formula, we get:

$$e'_{33} = e'_{333} = \sum_{m,n,o} a_{3m} a_{3n} a_{3o} e_{mno} = a_{33} a_{33} a_{33} e_{333} = e_{33} \qquad [6.10]$$

First of all, let us find the shape of matrix e (non-null coefficients):

$$\begin{bmatrix} e_{11} & e_{12} & e_{13} & e_{14} & e_{15} & e_{16} \\ e_{21} & e_{22} & e_{23} & e_{24} & e_{25} & e_{26} \\ e_{31} & e_{32} & e_{33} & e_{34} & e_{35} & e_{36} \end{bmatrix}$$

In class *3m*, the plane (YZ) that contains the c-axis is a plane of symmetry, as defined by the piezoelectric standards [IEE 87]:

$$[e]='e']=[Sym].[e] \text{ with } [Sym]=\begin{bmatrix} -1 & 0 & 0 \\ 0 & 1 & 0 \\ 0 & 0 & 1 \end{bmatrix}$$

Thus, $e_{111} = (-1)^3\, e_{111} = -\, e_{111} = 0$ and $e_{112} = (-1)^2\, e_{112} = e_{112}$. To generalize, all the coefficients including an odd number of index 1s are therefore null. Thus:

$$e_{111} = e_{122} = e_{123} = e_{132} = e_{133} = e_{212} = e_{213} = e_{221} = e_{231} = e_{312} = e_{313} = e_{321} = e_{331} = 0$$

In contracted notation: $e_{11} = e_{12} = e_{14} = e_{13} = e_{26} = e_{25} = e_{36} = e_{35} = 0$.

Matrix e was therefore simplified into: $\begin{bmatrix} 0 & 0 & 0 & 0 & e_{15} & e_{16} \\ e_{21} & e_{22} & e_{23} & e_{24} & 0 & 0 \\ e_{31} & e_{32} & e_{33} & e_{34} & 0 & 0 \end{bmatrix}$.

6.2.1.1. *Coefficients e_{23} and e_{34}*

Let us use matrix A for an angle of 120° and for coefficient 23 (233 in extended notation):

$$e_{23}' = e_{233}' = \sum_{m,n,o} a_{2m} a_{3n} a_{3o} e_{mno} = \sum_{m} a_{2m} a_{33} a_{33} e_{m33} =$$

$$a_{21} a_{33} a_{33} e_{133} + a_{22} a_{33} a_{33} e_{233} = \frac{1}{2} e_{233}$$

as $e_{133} = 0$, $\Rightarrow e_{23}' = e_{233}' = e_{23} = 0$.

The same argument is applicable to $e_{34} = e_{323} = 0$.

6.2.1.2. *Coefficient e_{16}*

Let us calculate coefficient e_{16}, which poses a problem in some publications.

Let us find the relation between e_{16}, e_{21} and e_{22}.

Still using the rotation of $2\pi/3$, we have:

$$e_{16}' = e_{112}' = \sum_{m,n,o} a_{1m}a_{1n}a_{2o}e_{mno} = a_{11}a_{11}a_{22}e_{112} + a_{11}a_{12}a_{21}e_{121} + a_{12}a_{11}a_{21}e_{211} + a_{12}a_{12}a_{22}e_{222}$$

because $e_{111} = e_{122} = e_{212} = e_{221} = 0$ and $a_{23} = a_{13} = 0$.

$$e_{112}' = \left(-\frac{1}{2}\right)\cdot\left(-\frac{1}{2}\right)\left(-\frac{1}{2}\right)e_{112} + \left(-\frac{1}{2}\right)\left(\frac{\sqrt{3}}{2}\right)\left(-\frac{\sqrt{3}}{2}\right)e_{112} + \left(\frac{\sqrt{3}}{2}\right)\left(-\frac{1}{2}\right)\left(-\frac{\sqrt{3}}{2}\right)e_{211} + \left(\frac{\sqrt{3}}{2}\right)\left(\frac{\sqrt{3}}{2}\right)\left(-\frac{1}{2}\right)e_{222}$$

$$e_{112}' = e_{112} = \left(-\frac{1}{8} + \frac{3}{8}\right)e_{112} + \frac{3}{8}e_{211} - \frac{3}{8}e_{222} = \frac{2}{8}e_{112} + \frac{3}{8}e_{211} - \frac{3}{8}e_{222}$$

hence:

$$2e_{112} = \left(e_{211} - e_{222}\right) \qquad [6.11]$$

Similarly, for coefficient e_{21}:

$$e_{21}' = e_{211}' = \sum_{m,n,o} a_{2m}a_{1n}a_{1o}e_{mno} = a_{21}a_{11}a_{12}e_{112} + a_{22}a_{11}a_{11}e_{211} + a_{22}a_{12}a_{12}e_{222} + a_{21}a_{12}a_{11}e_{121}$$

$$e_{211}' = \left(-\frac{\sqrt{3}}{2}\right)\cdot\left(-\frac{1}{2}\right)\left(\frac{\sqrt{3}}{2}\right)e_{112} + \left(-\frac{1}{2}\right)\left(-\frac{1}{2}\right)\left(-\frac{1}{2}\right)e_{211} + \left(-\frac{1}{2}\right)\left(\frac{\sqrt{3}}{2}\right)\left(\frac{\sqrt{3}}{2}\right)e_{222} + \left(-\frac{\sqrt{3}}{2}\right)\left(\frac{\sqrt{3}}{2}\right)\left(-\frac{1}{2}\right)e_{112}$$

$$e_{211}' = e_{211} = \left(\frac{3}{8} + \frac{3}{8}\right)e_{112} - \frac{1}{8}e_{211} - \frac{3}{8}e_{222} = \frac{6}{8}e_{112} - \frac{1}{8}e_{211} - \frac{3}{8}e_{222}$$

hence:

$$3e_{211} = \left(2e_{112} - e_{222}\right) \qquad [6.12]$$

Similarly, for coefficient e_{22}:

$$e_{22}' = e_{222}' = \sum_{m,n,o} a_{2m}a_{2n}a_{2o}e_{mno} = a_{21}a_{21}a_{22}e_{112} + a_{22}a_{21}a_{21}e_{211}$$
$$+a_{22}a_{22}a_{22}e_{222} + a_{21}a_{22}a_{21}e_{121}$$

$$e_{222}' = \left(-\frac{\sqrt{3}}{2}\right).\left(-\frac{\sqrt{3}}{2}\right)\left(-\frac{1}{2}\right)e_{112} + \left(-\frac{1}{2}\right)\left(-\frac{\sqrt{3}}{2}\right)\left(-\frac{\sqrt{3}}{2}\right)e_{211}$$
$$+\left(-\frac{1}{2}\right)\left(-\frac{1}{2}\right)\left(-\frac{1}{2}\right)e_{222} + \left(-\frac{\sqrt{3}}{2}\right)\left(-\frac{1}{2}\right)\left(-\frac{\sqrt{3}}{2}\right)e_{112}$$

$$e_{222}' = \left(-\frac{3}{8}-\frac{3}{8}\right)e_{112} - \frac{3}{8}e_{211} - \frac{1}{8}e_{222} = -\frac{6}{8}e_{112} - \frac{3}{8}e_{211} - \frac{1}{8}e_{222}$$

hence:

$$3e_{222} = \left(-2e_{112} - e_{211}\right) \qquad [6.13]$$

By linear combinations:

– equation [6.11]-equation [6.12] :

$$\Leftrightarrow 4e_{112} = 4e_{211} \Leftrightarrow e_{112} = e_{211} \Leftrightarrow e_{16} = e_{21};$$

– equation [6.11]-equation [6.13] :

$$\Leftrightarrow 2e_{112} - 3e_{222} = e_{211} - e_{222} + 2e_{112} + e_{211} \Leftrightarrow -2e_{222} = 2e_{211} \Leftrightarrow e_{22} = -e_{21}$$

The final relation is therefore: $e_{16} = e_{21} = -e_{22}$.

However, because of the contraction rules for strain tensor indices that are also applied to the piezoelectric tensor *d*, we have: $d_{16} = 2d_{21} = -2d_{22}$.

6.2.1.3. *Coefficient e_{31}*

The *2π/3* rotation is applied to e_{322}:

$$e_{322}' = e_{322} = \sum_{m,n,o} a_{3m}a_{2n}a_{2o}e_{mno} = \sum_{n,o} a_{2n}a_{2o}e_{3no} = a_{21}a_{21}e_{311} + a_{21}a_{22}e_{312}$$
$$+a_{22}a_{21}e_{321} + a_{22}a_{22}e_{322}$$

$$e_{322} = \frac{3}{4}e_{311} + \frac{1}{4}e_{322} \Rightarrow e_{322} = e_{311} \Rightarrow e_{32} = e_{31}$$

6.2.1.4. *Coefficient e_{15}*

Still for a rotation of 120°, we have:

$$e_{15}' = e_{15} = e_{113} = \sum_{m,n,o} a_{1m}a_{1n}a_{3o}e_{mno} = \sum_{m,n} a_{1m}a_{1n}e_{mn3}$$

Only components e_{113} and e_{223} contribute to the result:

$$e_{15} = e_{113} = a_{11}a_{11}e_{113} + a_{12}a_{12}e_{223} = \left(-\frac{1}{2}\right)^2 e_{113} + \left(\frac{\sqrt{3}}{2}\right)^2 e_{223} = \frac{1}{4}e_{113} + \frac{3}{4}e_{223}$$

hence: $e_{15} = e_{113} = e_{223} = e_{24}$.

6.2.1.5. *For class 3m*

The matrices to use here are:

$$e_{3m} = \begin{bmatrix} 0 & 0 & 0 & 0 & e_{15} & -e_{22} \\ -e_{22} & e_{22} & 0 & e_{15} & 0 & 0 \\ e_{31} & e_{31} & e_{33} & 0 & 0 & 0 \end{bmatrix}$$

and $$d_{3m} = \begin{bmatrix} 0 & 0 & 0 & 0 & d_{15} & -2d_{22} \\ -d_{22} & d_{22} & 0 & d_{15} & 0 & 0 \\ d_{31} & d_{31} & d_{33} & 0 & 0 & 0 \end{bmatrix}$$

6.3. One-dimensional microscopic model

To get a more local idea of what piezoelectricity represents at the atomic level, the simplest thing is undoubtedly to take a linear chain made up of two successive ions joined by strings of *different stiffness*, as suggested by Royer and Dieulesaint [DIE 74] and Uchino [UCH 97].

This representation of a spring is quite close to reality as the position of atoms is balanced between Coulombic force and the Pauli principle repulsion. Having two

springs of different stiffness is also logical, since piezoelectricity only appears in crystals that do not have a center of symmetry.

This chain of ions is represented in Figure 6.1. As we assume a one-dimensional ionic crystal, the elementary dipole moment p, which corresponds to that of one section, can be calculated, for example from one positive ion to another, separated by a distance a.

The key is to consider the charges carried by each ion as belonging half to the right dipole and half to the left dipole.

Thus, it results in:

$$p = \frac{q}{2}(a-b) - \frac{q}{2}b = \frac{q}{2}(a-2b) \qquad [6.14]$$

Therefore we immediately see that if the distance between the ions is different (a-$b \neq b$), then p is not null and there is a spontaneous polarization (we have a pyroelectric crystal). It is noteworthy that polarization (only ionic in this model) is obtained, by definition, by multiplying p by n, the dipole number per unit of volume. If the initial lengths of the springs are the same ($a - b = b$), the crystal is either non-pyroelectric piezoelectric (if $k_1 \neq k_2$) or centrosymmetric.

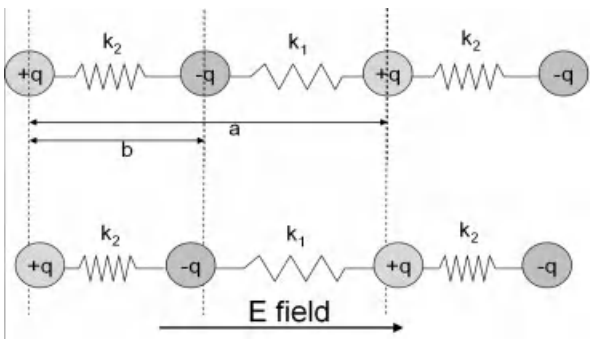

Figure 6.1. *Model of a chain of two ions linked by springs of different stiffness. The bottom diagram represents the chain when an electric field is applied*

Applying an electric field, E, in the direction of the chain, the ions move in the opposite direction, like in the bottom part of Figure 6.1. A change in dipole moment, δp, ensues so that:

$$\delta p = \frac{q}{2}(\delta a - 2\delta b) \qquad [6.15]$$

The static equilibrium of the ions imposes the following relation (here we take the example of a positive ion) that enables us to link δa and δb. Only the first order is considered (the spring is linear):

$$qE - k_1\delta(a-b) + k_2\delta(b) = 0 \qquad [6.16]$$

To go further, one possibility is to calculate the internal energy of a section of the chain, for example between two positive ions. We will therefore be able to derive this internal energy as a function of natural variables to make a piezoelectric microscopic formalism emerge. The natural variables chosen are the strain, $\delta a/a = S$, and the electric field, E. Internal energy is therefore similar to Gibbs' electric energy G_2 (see Chapter 2, however here we are looking at the microscopic scale). δG_2 takes the following form, by summing up the elastic and electric contributions:

$$\delta G_2 = \frac{1}{2}k_1\left[\delta(a-b)\right]^2 + \frac{1}{2}k_2\left[\delta(b)\right]^2 - \delta pE \qquad [6.17]$$

Inserting the expressions S, δb (from equation [6.16]) and δp (from equation [6.15]) into the equation, and after several simplifications, δG_2 becomes:

$$\delta G_2 = \frac{1}{2}\frac{k_1k_2}{k_1+k_2}a^2S^2 - \frac{1}{2}\frac{q^2}{k_1+k_2}E^2 - \frac{qa}{2}\frac{k_2-k_1}{k_1+k_2}SE \qquad [6.18]$$

In this one-dimensional model, t is defined as the lineic mechanical stress, and p the polarization, such that:

$$t = \left.\frac{\partial \delta G_2}{\partial S}\right)_E \qquad p = -\left.\frac{\partial \delta G_2}{\partial E}\right)_S \qquad [6.19]$$

Thus we get:

$$\begin{aligned} t &= \frac{k_1k_2}{k_1+k_2}a^2S - \frac{qa}{2}\frac{k_2-k_1}{k_2+k_1}E \\ p &= \frac{qa}{2}\frac{k_2-k_1}{k_2+k_1}S + \frac{q^2}{k_1+k_2}E \end{aligned} \qquad [6.20]$$

We must note that p and t are not homogeneous, respectively to the polarization P (or the electric displacement D) and the stress T. To get homogeneity, we must multiply t and p by the dipole number per unit of volume n.

Finally, we therefore get:

$$\begin{aligned} T &= n\frac{k_1k_2}{k_1+k_2}a^2S - \frac{nqa}{2}\frac{k_2-k_1}{k_2+k_1}E \\ P &= \frac{nqa}{2}\frac{k_2-k_1}{k_2+k_1}S + \frac{nq^2}{k_1+k_2}E \end{aligned} \qquad [6.21]$$

Assuming that the piezoelectric effect is only due to the influence of the ions (we take the polarization P defined here, and not D), we can identify this equation with the one that comes from the piezoelectric formalism (see equation [6.6]) with the following parameters:

$$c^E = n\frac{k_1k_2}{k_1+k_2}a^2 \quad \chi_{ion}{}^S = \frac{nq^2}{k_1+k_2} \quad e = \frac{nqa}{2}\frac{k_2-k_1}{k_2+k_1} \qquad [6.22]$$

This expression confirms the fact that piezoelectricity only exists if the two springs are different ($k_1 \neq k_2$). Therefore, e is not null. $\chi_{ion}{}^S$ corresponds to the ionic susceptibility of this crystal to constant strain. c^E corresponds to the stiffness constant of the crystal at a constant electric field. It is also possible to define the electromechanical coupling coefficient k_{em}, which determines the quantity of energy that can be transferred between mechanical and electric energies. To produce this, we sometimes use the following definition (equivalent to the one we give in the next section) based on a translation of the energy, E, of the crystal in the form:

$$k_{em}^2 = \left|\frac{E_{coupling}^2}{E_{mech}E_{elec}}\right| \qquad [6.23]$$

The expressions of mechanical, electrical and coupling energies are identified with the expression of δG_2 (see equation [6.18]) so that $\delta G_2 = E_{mech}+E_{elec}+2E_{coupling}$. Thus, $k^2{}_{em}$ takes the following form:

$$k_{em}^2 = \frac{e^2}{c^E\chi_{ion}^S} = \frac{(k_2-k_1)^2}{4k_1k_2} \qquad [6.24]$$

Making the ratio $r = k_2/k_1$ vary, we get Figure 6.2.

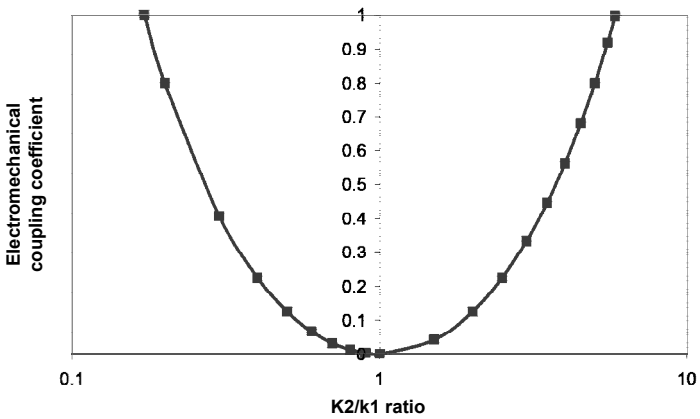

Figure 6.2. *Electromechanical coupling coefficient k_{em}^2 from the static one-dimensional model as a function of the ratios of the two springs*

When the springs are equal ($k_2/k_1 = 1$), we see that coupling is null, which is logical since there is no piezoelectricity. When r tends towards 0 or infinity, coupling increases indefinitely, which is not physical beyond $k_{em}^2 \geq 1$. Actually, the transformed energy cannot be greater than the invested energy. The crystal envisioned, in this case, has a much more flexible spring than the other one, which explains the very strong coupling, but this also induces an instability that the model does not translate. The mathematical limit translated by $k_{em}^2 < 1$ is that the ratio of the greatest stiffness over the least stiffness must not be greater than 5.82 (more specifically $3+2\sqrt{2}$).

6.4. Electromechanical coupling coefficient

The coupling coefficient (often written squared and called k^2) is a concept that is often used in relation to piezoelectric materials as it enables us to quantify the amount of energy that can pass through one form to another (mechanical to electric). There are several possible definitions and ways of producing this coefficient as a function of use: static, transformer and resonator. For resonators, it changes, depending on the modes of resonance used and the boundary conditions. We will go into the details of two ways of producing the coupling coefficient.

Taking a piezoelectric material, we can imagine applying a cycle that enables us to recover electric energy from mechanical energy. To do this, we can carry out a discharge at constant strain based on the cycle described in Figure 6.3. We assume that everything happens in one single direction, which enables us to work on a one-dimensional model.

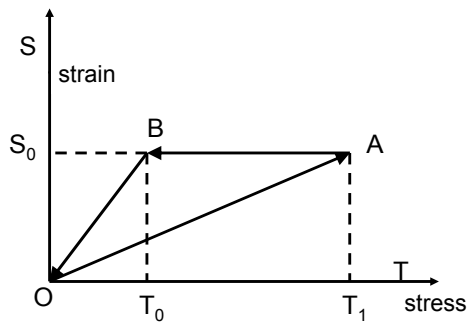

Figure 6.3. *Electromechanical cycle of a piezoelectric material during a discharge at constant strain*

A stress T_1 is applied to an open circuit piezoelectric material initially at rest (point O) to reach point A of the cycle. At A, the piezoelectric material is short-circuited at constant strain. Experimentally, we observe a decrease in stress from T_1 to T_0 to reach point B. Finally the stress is relaxed to reach point O. This cycle can be described using equations, as follows:

– from O to A the circuit is open, therefore D is constant. The formalism (T,D) therefore gives $S = s^D T$. The mechanical work supplied is:

$$W_{OA} = \int_O^A TdS = \int_O^A s^D TdT = \frac{1}{2} s^D T_1^2$$

– from A to B the circuit is closed, therefore E is constant. As experimentally stress decreases from T_1 to T_0 at constant strain, there is a transfer of mechanical energy into electric energy, W_{elec}, during the passage from A to B;

– at constant E, stress is relaxed to move from B to 0. Untransformed mechanical energy is therefore:

$$W_{OB} = \frac{1}{2} s^E T_0^2$$

W_{elec} is the difference between the mechanical energy supplied to the material (W_{OA}) and the untransformed mechanical energy (W_{OB}):

$$W_{elec} = W_{OA} - W_{OB} = \frac{1}{2} s^D T_1^2 - \frac{1}{2} s^E T_0^2 \qquad [6.25]$$

Electromechanical coupling, k^2, is defined as the relationship between transformed energy and supplied energy:

$$k^2 = \frac{W_{elec}}{W_{OA}} = 1 - \frac{W_{OB}}{W_{OA}} = 1 - \frac{s^E T_0^2}{s^D T_1^2} = 1 - \frac{s^D}{s^E} \qquad [6.26]$$

For the last conversion, we must note, on Figure 6.3, that $S_0 = s^E T_0 = s^D T_1$.

k^2 is always <1 as $s^D < s^E$. It is often simpler to speak of stiffness coefficients c^E and c^D. As we saw that $sc = 1$, we can say that $c^D > c^E$. In other words, the open circuit stiffness of a piezoelectric material is always higher than in a closed circuit. This is why we often speak of stiffened coefficients.

From this expression, it is possible to find another practical expression of k^2. The idea is to mix the two piezoelectric formalisms (*T,D)* and (*T,E*) in order to eliminate s^D. Returning to equation [6.4] and assuming that there is only one dimension for all variables, we can insert the expression of *E* from the last equation into the first equation, which becomes:

$$S = \left(s^E - \frac{d^2}{\varepsilon^T} \right) T + \frac{d}{\varepsilon^T} D \qquad [6.27]$$

Identifying the term in front of *T* in equation [6.27] with the term in front of *T* of equation [6.1], we get:

$$s^D = s^E - \frac{d^2}{\varepsilon^T} \qquad [6.28]$$

Inserting this equation in equation [6.26], k^2 becomes:

$$k^2 = \frac{d^2}{s^E \varepsilon^T} \qquad [6.29]$$

This expression is very general (square piezoelectric coefficient divided by the product of the mechanical coefficient with the electric coefficient) and can be found with the other formalisms as a function of the cycle applied. k^2 is always transformed energy over implied energy, whether these energies are electric or mechanical.

It is interesting to carry out a cycle based on the reverse principle: an initial electric energy, one part of which is transformed into mechanical energy. In Figure 6.4, a piezoelectric, always considered based on one single dimension, describes the following cycle:

– from O to A, the piezoelectric is charged by applying an electric field E_1. This charge happens at constant strain (the material is prevented from moving);

– from A to B, the material is mechanically released, and this is done in an open circuit (constant D). This is the stage during which the material supplies mechanical energy. The field moves from value E_1 to E_0;

– from B to O, still at constant stress, the field returns to a null value.

It is the electric displacement change that is considered here. Indeed, the value of spontaneous polarization does not matter here. We also assume that the field change does not change the orientation of the dipoles in the material.

The energy balance of each of the phases gives:

– O–A: $D_0 = \varepsilon^S E_1$ therefore $W_e^{O-A} = \frac{1}{2}\varepsilon^S E_1^2$;

– B–O: $D_0 = \varepsilon^T E_0$ therefore $W_e^{B-O} = \frac{1}{2}\varepsilon^T E_0^2$.

Energy conservation in the cycle gives the mechanical energy recovered during a cycle:

$$W_m^{A-B} = W_e^{O-A} - W_e^{B-O} = \frac{1}{2}\varepsilon^S E_1^2 - \frac{1}{2}\varepsilon^T E_0^2$$

The coupling coefficient k^2 here is the ratio between the recovered mechanical energy and the "invested" electrical energy.

Using the two forms of D_0, k^2 becomes:

$$k^2 = \frac{W_m^{A-B}}{W_e^{O-A}} = 1 - \frac{\varepsilon^S}{\varepsilon^T} \qquad [6.30]$$

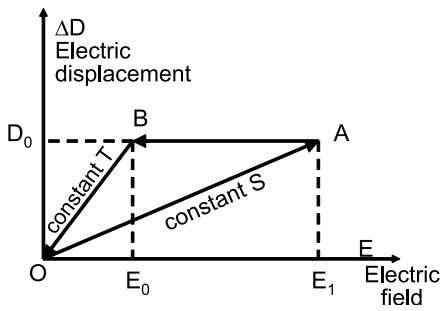

Figure 6.4. *Electromechanical cycle of a piezoelectric material during a change in thickness at constant charge*

Experimentally, ε^S is always less than ε^T, which induces a k^2 between 0 and 1. This is physically understandable because the dielectric effect is always greater when all the contributions can participate. If the material is blocked (therefore S is fixed), some contributions can no longer be added to the dielectric effect.

In the same way as before, another form can be given for equation [6.30] by combining the equations of two piezoelectric formalisms. Using formalisms *(T,E)* and *(S,E)*, we get:

$$k^2 = 1 - \frac{\varepsilon^S}{\varepsilon^T} = \frac{d^2}{\varepsilon^T s^E} \qquad [6.31]$$

This formula is identical to the one we found for the electromechanical cycle of discharge at constant strain (see Figure 6.3).

This means that the piezoelectricy transforms the same way as mechanical energy into electric energy in the same and vice versa. This is completely logical as the piezoelectric effect is linear.

A similar form is found for k^2 in the case of acoustic resonances, as we will see in Chapter 7. The expression can vary depending on the boundary conditions and resonance mode considered.

6.5. Piezoelectric coefficients of key materials

In thin films, piezoelectric coefficients can be quite different from bulk materials, whether this is in single crystals or in ceramics. It is therefore often much more reliable to proceed to a direct measurement of coefficients through an adapted method.

On the other hand, the materials deposited are often polycrystalline, with variable crystalline orientations. The piezoelectric coefficients as well as the dielectric constants and stiffness coefficients therefore have effective values that can be difficult to determine other than through direct measurement. Moreover, the substrate presence adds a difficulty for the measurement of intrinsic coefficients.

Despite this, it is good to have some orders of magnitude for the materials most often used: $Pb(ZrTi)O_3$, AlN, $LiNbO_3$, $LiTaO_3$.

Material	**LiNbO3**	**LiTaO3**	**Bulk PZT 52/48 (Motorola 3203HD)**	**Single crystal AlN**
Point group	*3m*	*3m*	*6mm*	*6mm*
Ref	[KOV 90]	[KOV 90]	[SHE 97]	[TSU 85]
εS11/ε0	45.6	40.9		8.0
εS33/ε0	26.3	42.3		9.5
εT11/ε0	84.45	52.51	2417	
εT33/ε0	28.85	44.12	3332	
CE11 (GPa)	198	2.33		345
CE12 (GPa)	55	0.465		125
CE13 (GPa)	65	0.836	101	120
CE14 (GPa)	7.9	-0.105		-
CE33 (GPa)	228	2.760	141	395
CE44 (GPa)	59	0.949		118
sE11 (10-12m²/N)			15.6	3.53
sE12 (10-12m²/N)			-4.2	-1.02
sE13 (10-12m²/N)			-8.2	-0.76
sE33 (10-12m²/N)			18.9	2.99
sE44 (10-12m²/N)				8.47
d13 (pm/V)			-295	-2
d33 (pm/V)			564	5
d15 (pm/V)			560	-4.07
e15 (C/m²)	3.69	2.64		-0.48
e22 (C/m²)	2.42	1.86	-	-
e31 (C/m²)	0.3	-0.22	-12.2	-0.58
e33 (C/m²)	1.77	1.71	19.3	1.55
ρ (kg/m²)	4,628	7,454	7,850	3,260

Table 6.2. *Stiffness constants, dielectric and piezoelectric coefficients of $LiNbO_3$, $LiTaO_3$, PZT and AlN*

6.6. Calculating coupling as a function of crystal orientation

In the case of single crystal materials, cut simulations can be carried out with the help of tensor theory. This is typically the case for surface wave resonators, but is also possible in thin films for volume waves in the case of films bonded on a substrate. The techniques used to do this are bonding-thinning or implantation-bonding separation (called *Smart Cut*, Chapter 1). Thus, using the change in reference system formulae, it is possible to calculate the most favorable crystal orientations for one property or another. For example, optimal electromechanical coupling can be previewed through calculation, once all the constants of the material are known. Let us take the case of coupling of one longitudinal wave ($k_{t\ longi}^2$) and two shear waves ($k_{t\ shear1}^2$ and $k_{t\ shear2}^2$) for a thin film from the *3m* point group. The thickness is much smaller than the lateral dimensions and the lateral strains are very weak. On the other hand, if we place ourselves in the configuration of an electric field perpendicular to the plane of films, it can be wise to use *D* as the electric variable because $divD = 0$. The natural variables in this problem are therefore *(S,D)*.

Thus, the electromechanical couplings are:

$$k_{t\ longi}^2 = \frac{h_{33}^2}{c_{33}^D \beta_{33}^S} \quad k_{t\ shear1}^2 = \frac{h_{34}^2}{c_{44}^D \beta_{33}^S} \quad k_{t\ shear2}^2 = \frac{h_{35}^2}{c_{44}^D \beta_{33}^S} \qquad [6.32]$$

It is common to use different but absolutely equivalent expressions for these couplings. Indeed, we prefer to use the piezoelectric coefficients *e* and permittivity ε. Using conversion formulae, we get:

$$k_{t\ longi}^2 = \frac{e_{33}^2}{c_{33}^D \varepsilon_{33}^S} \quad k_{t\ shear1}^2 = \frac{e_{34}^2}{c_{44}^D \varepsilon_{33}^S} \quad k_{t\ shear2}^2 = \frac{e_{35}^2}{c_{44}^D \varepsilon_{33}^S} \qquad [6.33]$$

IMPORTANT NOTE.– These expressions are not equivalent to the couplings we get by using the formalism *(S,E)*, in which coefficient *e* appears. In this case, the stiffness coefficient is at fixed *E* and not *D*. The expression of k^2 corresponds to another experimental configuration for which the mechanism considered is, for example, a cylinder in direction *3* (and no longer a plate). This coefficient is called k_{33}^2. We will return to this discussion in Chapter 7.

The three-dimensional rotation matrix depends on three successive rotations of angles *a* (from 0 to 360°), *b* (from 0 to 360°) and *c* (from 0 to 180°), respectively, around the *z* axis from the new *x′* and from the new *z′* axes.

These three rotations enable us to sweep all the possible reference systems (this is different from all possible directions, which only need two angles). In the case of the *3m* structure, considering the symmetries we vary *a* until 120° and *b* until 180°.

Actually, the last rotation about *z′* does not change coefficient *33* and therefore does not have an influence on k_t^2. The successive rotations are applied to matrices *e*, c^D and ε^S, which are therefore used to calculate $k_{t\ longi}^2$, $k_{t\ shear1}^2$ and $k_{t\ shear2}^2$.

Angle *b* is the most important one for this *3m* crystal class. Figure 6.5 gives the coupling calculated from rotation about the *x* axis as a function of angle $\theta = b - 90°$ for $LiNbO_3$ and $LiTaO_3$. This angle is used by substrate manufacturers. We also note that a single rotation is applied in this case.

In addition, a single shear wave is presented for all these cuts because coefficient e_{35} is cancelled, regardless of what angle θ is. This is because the rotation about *x* does not modify the orientation in relation to the plane of symmetry *YZ*. This means that this shear wave is not coupled, although it can exist. It cannot simply be excited in this configuration.

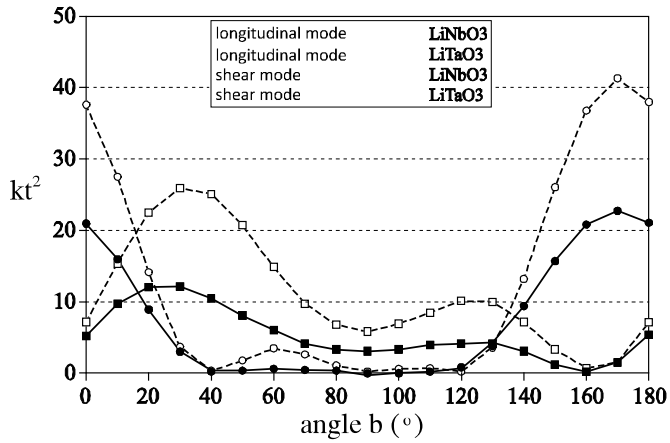

Figure 6.5. *Maximum longitudinal coupling according to angle b for $LiNbO_3$ and $LiTaO_3$*

Several functioning points can turn out to be interesting:

– the longitudinal maximum coupling with a null shear for avoiding parasite modes of resonance ($\theta = 36°$);

– a shear maximum coupling for a null longitudinal mode ($\theta = 163°$).

It is noteworthy that X-cut is obtained through a rotation of -90° about the z axis (angle a) followed by a rotation of 90° about the new axis x' (which corresponds to the old y axis).

Similarly, Y-cut is obtained through a rotation of 90°about the x axis.

6.7. Piezoelectric coefficients in the case of ferroelectric materials

For ferroelectric materials, it is interesting to use the thermodynamic formalism to translate piezoelectricity in a more "fundamental" form.

Indeed, in the paraelectric-ferroelectric phase transition analysis, we saw that it was possible to use a simplified form of free energy that describes this transition well (see Chapter 3). This expression of free energy is also well-adapted to the description of piezoelectricity of these materials.

Actually, when the temperature is lower than the Curie temperature, there is a remanent polarization P_r in the ferroelectric phase. So let us take the total polarization P_t as the sum of P_r and P ($P_t = P_r+P$). Piezoelectricity appears when free energy is derived in relation to the natural variables of this energy.

In equation [3.1], it is G_1 that is used. It is therefore T and D that are the natural variables. To simplify the expressions, we identify D with P_t.

Therefore we get:

$$\frac{\partial G_1}{\partial D} = E_t = \alpha P_t - 2QP_tT \quad -\frac{\partial G_1}{\partial T} = S_t = sT + QP_t^2 \qquad [6.34]$$

Decomposing P_t in the coupled term, these expressions become:

$$\begin{aligned} E_t &= \alpha P_r + \alpha P - 2QP_rT - 2QPT \\ S_t &= sT + QP_r^2 + QP^2 + 2QP_rP \end{aligned} \qquad [6.35]$$

It is possible to decompose E_t and S_t into one remanent term and one dynamic term, as for polarization. Keeping only the linear dynamic term (no P^2 term), we get:

$$\begin{aligned} E &= \alpha P - 2QP_rT = \beta^T P - gT \\ S &= sT + 2QP_rP = s^D T + gP \end{aligned} \qquad [6.36]$$

We see that these equations can be interpreted as a piezoelectric formalism identical to equations [6.1] and [6.2]. Identifying the piezoelectric term, we have:

$$g = 2QP_r \qquad [6.37]$$

Therefore, in the case of ferroelectric piezoelectrics, the piezoelectric coefficients, g, are equivalent to the product between an electrostrictive coefficient and remanent polarization.

We often have the habit of translating the piezoelectric effect through the relationship between strain, S, and the electric field, E. At first approximation, we get:

$$S = gP = 2QP_r.P = 2QP_r\varepsilon E = dE \qquad [6.38]$$

Coefficient d is therefore equal to $2QP_r\varepsilon$.

6.8. Relation between piezoelectric formalism and matter

As a final paragraph, it is noteworthy to develop some aspects of piezoelectric formalism with respect to what happens actually in matter once an external stimulus is applied to a piezoelectric material. This approach is very similar to what we showed in Chapter 5 about the dielectric effect. This highlights the permanent dielectric nature of all piezoelectric and pyroelectric materials.

To do so, we take a piezoelectric slab as shown in Figure 6.5a. We disregard first the electrodes as they are not required to understand properly what happens. Moreover, we consider that there is no current circulation, which means that D (electric displacement) is kept constant during this experiment. The piezoelectric material used here is pyroelectric. Therefore, it exhibits a spontaneous polarization P_S. This last is supposed to be constant during the experiment, like in the case of a non ferroelectric material as Aluminum Nitride. But this is valuable for ferroelectric materials as well; if one considers that the applied mechanical stimulus does not modify P_S.

We first calculate the electric field E_{SP} induced by P_{SP} in the piezoelectric slab by using Gauss theorem on surface 1, as depicted in figure 6.6a (see Chapter 5 and equation [5.3] for Gauss theorem). Then, we obtain:

$$-E_{sp} = \frac{\sigma_{pol}}{\varepsilon_0} = \frac{P_{sp}}{\varepsilon_0} \qquad [6.39]$$

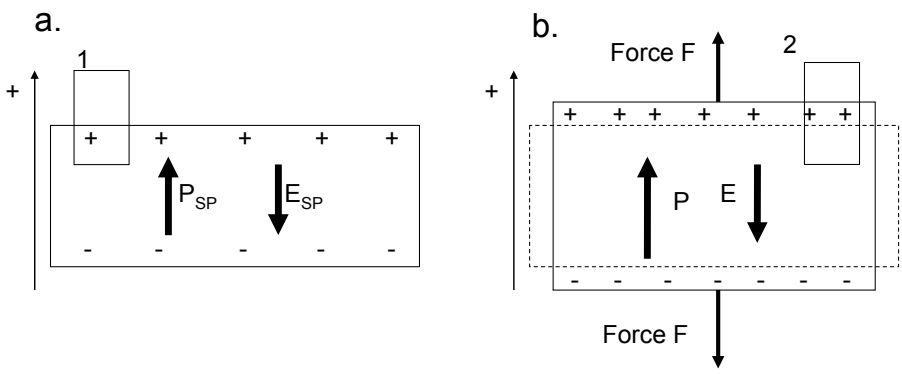

Figure 6.6. *Charges on a piezoelectric slab by using Gauss theorem: a- initial state with a spontaneous polarization; b- final state after applying force F inducing strain S. The dashed line shows the initial shape of the slab before applying force*

Then, we add an out-of-plane force F to the piezoelectric slab which induces strain S as observed in Figure 6.6b. Here, S is positive as thickness increases. As the material is piezoelectric, polarization P changes together with the internal electric field E. This can be expressed in an equation by considering surface 2 in Figure 6.6b and applying once again Gauss theorem, which gives:

$$-E = \frac{\sigma_{pol}}{\varepsilon_0} = \frac{P_{sp} + P_{piezo} + P_{dielectric}}{\varepsilon_0} \qquad [6.40]$$

Two new terms actually appear in polarization: the first one P_{piezo} coming from the piezoelectric effect and $P_{dielectric}$ appearing as the dielectric response to the polarization variation. Indeed, this last induces an electric field variation which in turn induces a dielectric response, exactly as it was figured out in chapter 5 for a pure dielectric material (see equation [5.11]). According to the piezoelectric formalism (see equation [6.6]), as a strain is applied, we get $P_{piezo}=eS$ with e: longitudinal piezoelectric coefficient. It is important to note that even if D (electric displacement) is involved in the piezoelectric formalism, this piezoelectric term is actually a polarization variation. There is no approximation here. In addition, $P_{dielectric}=(\varepsilon-\varepsilon_0)(E-E_{sp})$. Indeed, $(\varepsilon-\varepsilon_0)$ appears by combining equations [5.12], [5.17] and [5.18] and $(E-E_{sp})$ corresponds to the variation of electric field induced by strain S. Therefore, by using these expressions in equation [6.40], one eventually obtains:

$$-\varepsilon_0 E = P_{sp} + eS + (\varepsilon - \varepsilon_0)(E - E_{sp}) \qquad [6.41]$$

And by using equation [6.39]:

$$E - E_{sp} = \frac{-eS}{\varepsilon}$$

The electric field variation when strain is applied is proportional to the piezoelectric coefficient, to strain and inversely proportional to the dielectric constant. This last statement is actually important as it means that the higher the dielectric constant, the lower the measured voltage. As an example, let us compare the behaviors of Aluminum Nitride (AlN) and lead zirconate titanate (PZT) materials. PZT exhibits a dielectric constant 100 times greater than AlN. Besides, its piezoelectric coefficients are roughly 10 times greater than AlN. Therefore, for a given strain S, output electric field is 10 times lower for PZT than for AlN. This is quite surprising but does not mean that AlN is a "better" piezoelectric material than PZT. Indeed, the converted energy is still much higher in the case of PZT. But for sensors applications, it can make sense to use AlN instead of PZT especially when one wants to use voltage as the output parameter.

Adding electrodes to the model described in Figure 6.6 does not change the results. This allows us to compensate for the initial electric field by screening the initial polarization charges if one lets charges circulate before the force is applied. The initial electric field becomes zero, thanks to a new term coming from free charges on the electrodes.

In the case of piezoelectric non-pyroelectric materials, the only difference is that there is no spontaneous polarization. Therefore, $E_{sp}=0$.

Finally, if one considers the pyroelectric effect instead of the piezoelectric effect for this pyroelectric slab, the treatment is exactly the same. If p is the pyroelectric coefficient, for a given temperature variation ΔT, and if we still consider an experiment at constant D (free charges), we obtain:

$$E - E_{sp} = \frac{-p\Delta T}{\varepsilon} \qquad [6.42]$$

6.9. Bibliography

[DIE 74] DIEULESAINT E., ROYER D., *Ondes élastiques dans les solides*, Masson, Paris, 1974.

[IEE 87] IEEE Standard on Piezoelectricity, ANSI/IEEE Std 176, 1987.

[KOV 90] KOVACS G., ANHOM M., ENGAN H.E., VISINTINI G., RUPPEL C.C.W., "Improved material constants for LiNbO3 and LiTaO3", *Proc. 1990 IEEE Ultrason. Symp.*, p. 435-438, December 1990.

[LIP 81] LIPPMANN G., *Annales de chimie et de physique*, 5th series, t. XXIV, p. 145, 1881.

[SHE 97] SHERRIT S., WIEDERICK H.D., MUKHERJEE B.K., "A complete characterization of the piezoelectric, dielectric, and elastic properties of Motorola PZT 3203 HD, including losses and dispersion", *SPIE Proceedings*, vol. 3037-22, p. 158-169, 1997.

[TSU 85] TSUBOUCHI K., MIKOSHIBA N., "Zero temperature coefficients SAW devices on AlN epitaxial films", *IEEE Transactions UFFC*, vol. 32, n° 5, p. 634-644, 1985.

[UCH 97] UCHINO K., *Piezoelectric Actuators and Ultrasonic Motors*, Kluwer Academic Publishers, Norwell, 1997.

Chapter 7

Acoustic Formalism

7.1. Propagation of bulk waves

7.1.1. *Propagation of bulk waves in an elastic medium*

In Chapter 4, we have already established the equation for acoustic waves in an elastic medium:

$$\rho \frac{\partial^2 U_i}{\partial t^2} = \sum_{j,k,l} c_{ijkl} \frac{\partial^2 U_k}{\partial X_j \partial X_l} \qquad [7.1]$$

We consider monochromatic plane wave solutions in the simplest form possible:

$$\vec{U}\left(\vec{X},t\right) = \vec{U}_0 e^{j\left(\omega t - \vec{k}.\vec{X}\right)} = \vec{U}_0 e^{j\omega\left(t - \vec{s}.\vec{X}\right)} \qquad [7.2]$$

where ω is the angular frequency, t the time coordinate, $\vec{s}$ the propagation slowness vector and $\vec{X}$ the position vector. It is actually more convenient, even if less intuitive *a priori*, to argue in terms of propagation slowness than in terms of velocity. These two quantities are nevertheless linked by the relation:

$$\vec{s} = \frac{1}{v}\vec{n} = s\vec{n} \qquad [7.3]$$

Chapter written by Alexandre REINHARDT.

where v is the velocity of wave propagation and $\vec{n}$ the direction of propagation. The wave vector normally associated with propagating this plane wave can then be defined as:

$$\vec{k} = \omega\vec{s} \qquad [7.4]$$

Having chosen the form of plane waves given in equation [7.2], time and spatial coordinate derivation operators can be replaced, respectively, by multiplications by $j\omega$ and by $-j\omega s_i$. Equation [7.1] then becomes:

$$\rho U_i = \sum_{j,k,l} c_{ijkl} s_j s_l U_k \qquad [7.5]$$

Including propagation velocity and the Kronecker symbol, δ, defined as:

$$\delta_{ij} = 1, \text{ if } i = j; \ \delta_{ij} = 0, \text{ otherwise,} \qquad [7.6]$$

we end up with the Christoffel equation:

$$\sum_k \left(\sum_{j,l} c_{ijkl} n_j n_l - \rho v^2 \delta_{ik} \right) U_k = \sum_k \left(\Gamma_{ik} - \rho v^2 \delta_{ik} \right) U_k = 0 \qquad [7.7]$$

Equation [7.7], in practice, refers to solving an eigenvalue problem. Matrix Γ, whose coefficients are defined by:

$$\Gamma_{ik} = \sum_{j,l} c_{ijkl} n_j n_l \qquad [7.8]$$

only depends on the elastic tensor of the medium and on the direction of propagation.

Solving the eigenvalues problem enables us to determine the phase velocity, v, of plane waves propagating in direction, $\vec{n}$. Eigenvectors $\vec{U}^{(m)}$ associated with these consequently provide the acoustic polarizations of these plane waves. This term exists for all types of vector waves and was initially defined for electromagnetic waves. For the latter, the polarization vector corresponds to the direction of polarization induced in a medium by wave propagation (direction of the electric field). In the case of an acoustic wave, this vector has nothing to do with any polarization of the material, as discussed more widely in the remainder of this book.

This vector corresponds, rather, to the direction of particle displacements of the elastic medium considered.

With Γ in the case of a lossless medium being a symmetric real matrix, by virtue of elastic tensor symmetry that we demonstrated in Chapter 2, its eigenvectors are orthogonal. Physically, this means that three plane waves with orthogonal polarizations can propagate simultaneously in the same direction. As velocity is defined apart from its sign, since it is its square that is given by the Christoffel equation solution, propagation in direction $\vec{n}$ and in the opposite direction will be considered in the same way. Therefore, in all there are six plane waves that are solutions to propagation equation [7.1] at the same time *for a given direction of propagation*.

Once the phase velocities and associated polarizations have been determined, the solutions to the propagation equation are generally expressed as a linear combination of the six plane waves determined by the Christoffel equation:

$$\vec{U}(\vec{X},t) = \sum_m \left(A_m e^{-j\omega\vec{s}^{(m)}\vec{X}} + B_m e^{j\omega\vec{s}^{(m)}\vec{X}} \right) \vec{U}^{(m)} e^{j\omega t} \qquad [7.9]$$

To calculate stress field strength, we return to Hooke's law. Inserting the expression that links strains to displacements, as well as the properties of elastic tensor symmetry into this law, we arrive at the relation between stress and displacement:

$$T_{ij} = \sum_{k,l} c_{ijkl} \frac{\partial U_k}{\partial X_l} \qquad [7.10]$$

After derivation of displacement fields, we get:

$$T_{ij} = -j\omega \sum_m \left(\sum_{k,l} c_{ijkl} s_l^{(m)} U_k^{(m)} \right) \left(A_m e^{-j\omega\vec{s}^{(m)}\vec{X}} - B_m e^{j\omega\vec{s}^{(m)}\vec{X}} \right) e^{j\omega t} \qquad [7.11]$$

For the elastic wave propagation analysis, it is often useful to consider the forces applied to an orthogonal surface in the direction of propagation. It is expressed as:

$$\vec{F} = -\vec{T}(\vec{X},t) = -\overline{\overline{T}}(\vec{X},t).\vec{n} \qquad [7.12]$$

The "–" sign in equation [7.12] comes from the fact that, in Chapter 4, we considered stress as tensile and therefore vector $\vec{T}$ pointing outside the volume element considered, whereas the wave exerts an external force on this very volume element.

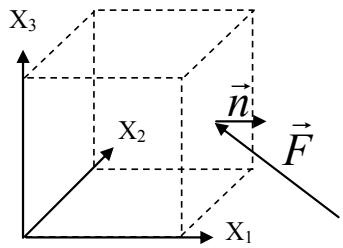

Figure 7.1. *Geometric representation of the force applied to an orthogonal surface in the direction of propagation (here, X_1)*

Its components are therefore expressed as:

$$F_i = -\sum_j T_{ij} n_j = j\omega \sum_{j,k,l} c_{ijkl} n_j s_l U_k A e^{-j\omega \vec{s}\vec{X}} \qquad [7.13]$$

if equation [7.11], limited to a single plane wave solution to the Christoffel equation, is inserted into equation [7.12].

To reveal the components of the Christoffel matrix Γ, we use the colinearity of the slowness vector with $\vec{n}$:

$$T_i = -j\omega \sum_{j,k,l} c_{ijkl} n_j n_l s U_k A e^{-j\omega \vec{s}\vec{X}} = -j\omega s \sum_k \Gamma_{ik} U_k A e^{-j\omega \vec{s}\vec{X}} \qquad [7.14]$$

With the polarization vector being, by definition, an eigenvector of matrix Γ for eigenvalue ρv^2, we get:

$$T_i = -j\omega s \rho v^2 U_i A e^{-j\omega \vec{s}\vec{X}} = -Z V_i \qquad [7.15]$$

where the acoustic impedance was revealed as:

$$Z = \rho v \qquad [7.16]$$

and the particle velocity defined by:

$$\vec{V} = \frac{\partial \vec{U}}{\partial t} = j\omega\vec{U} \qquad [7.17]$$

The acoustic impedance is therefore the scalar quantity that links the force generated by the wave over a volume element in the direction of propagation to the particle velocity. This particle velocity is the instantaneous velocity of a point of the medium (not to be confused with the propagation velocity of the acoustic wave). The unit of acoustic impedance is the Rayleigh, abbreviated as "Rayl".

As an example, let us consider the propagation of a wave in an isotropic medium. As all the directions are *a priori* equivalent, without losing the general character of our example, we can take $\vec{n} = \begin{pmatrix} 1 & 0 & 0 \end{pmatrix}^T$. So the Christoffel relation is expressed:

$$\begin{pmatrix} c_{11} - \rho v^2 & 0 & 0 \\ 0 & c_{44} - \rho v^2 & 0 \\ 0 & 0 & c_{44} - \rho v^2 \end{pmatrix} U_k = 0 \qquad [7.18]$$

With the matrix being directly diagonal, the solutions to the eigenvalue problem is immediate. We therefore find three velocities, two of which are identical:

$$\begin{aligned} v^{(1)} &= \pm\sqrt{\frac{c_{11}}{\rho}} \\ v^{(2)} = v^{(3)} &= \pm\sqrt{\frac{c_{44}}{\rho}} \end{aligned} \qquad [7.19]$$

The associated polarization vectors are respectively:

$$\begin{aligned} \vec{U}^{(1)} &= \begin{pmatrix} 1 & 0 & 0 \end{pmatrix}^T \\ \vec{U}^{(2)} &= \begin{pmatrix} 0 & 1 & 0 \end{pmatrix}^T \\ \vec{U}^{(3)} &= \begin{pmatrix} 0 & 0 & 1 \end{pmatrix}^T \end{aligned} \qquad [7.20]$$

These different vectors are represented in Figure 7.2. The first wave has a polarization colinear with the propagation direction: we therefore speak of a *pure longitudinal* wave. The two others have polarizations orthogonal to the propagation direction: we therefore speak of *pure transverse* waves.

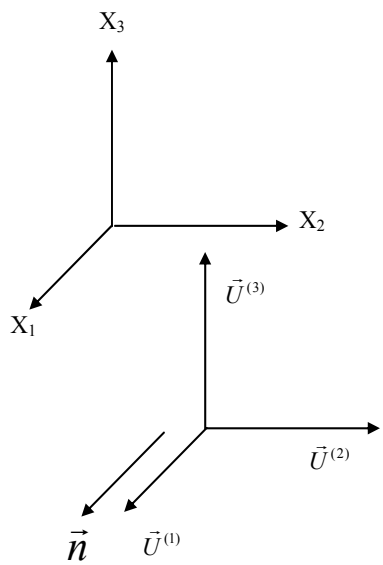

Figure 7.2. *Geometric representation of direction and polarization vectors for the propagation of a wave along the X_1 axis of an isotropic medium*

We will now seek to calculate the mechanical field strengths associated with the propagation of a single one of these waves. If we start with the longitudinal wave:

$$\vec{U}(\vec{X},t) = \begin{pmatrix} 1 \\ 0 \\ 0 \end{pmatrix} Ae^{j\omega\left(t - s^{(1)}X_1\right)} \qquad [7.21]$$

using equation [7.11], we can calculate the stresses associated with the propagation of the longitudinal waves:

$$\overline{\overline{T}}(\vec{X},t) = -j\omega \begin{pmatrix} c_{11} & 0 & 0 \\ 0 & c_{12} & 0 \\ 0 & 0 & c_{12} \end{pmatrix} s^{(1)} Ae^{j\omega\left(t - s^{(1)}X_1\right)} \qquad [7.22]$$

As can be seen, the stress tensor is diagonal, which is characteristic of compression of the medium. This is why this wave is also sometimes called a *compressional wave*. In the same way, displacements associated with the propagation of the first transverse wave are expressed:

$$\vec{U}(\vec{X},t) = \begin{pmatrix} 0 \\ 1 \\ 0 \end{pmatrix} Ae^{j\omega\left(t - s^{(2)}X_1\right)} \qquad [7.23]$$

The resultant strains of these displacements are expressed by:

$$\bar{\bar{S}}(\vec{X},t) = -\frac{1}{2} j\omega s^{(2)} \begin{pmatrix} 0 & 1 & 0 \\ 1 & 0 & 0 \\ 0 & 0 & 0 \end{pmatrix} Ae^{j\omega\left(t - s^{(2)}X_1\right)} \qquad [7.24]$$

The only non-zero terms are those in S_{12} and S_{21}. In the same way, for the second transverse wave, we could show that only terms S_{13} and S_{31} are non-zero. This wave only generates shear strains, and this is why it is also known as a *shear wave*.

Let us note that in the general case of an anisotropic material, the velocities of the two transverse waves are not necessarily equal. To illustrate this point, let us consider propagation in direction [110] of a material that has a cubic crystal lattice. This direction corresponds to the diagonal of one of the faces of the cube and is represented in Figure 7.3. The direction of propagation is therefore defined by the normalized vector $\vec{n} = \begin{pmatrix} 1/\sqrt{2} & 1/\sqrt{2} & 0 \end{pmatrix}^T$. In this case, the Christoffel relation is expressed:

$$\frac{1}{2}\begin{pmatrix} c_{11} + c_{44} - \rho v^2 & c_{12} + c_{44} & 0 \\ c_{12} + c_{44} & c_{11} + c_{44} - \rho v^2 & 0 \\ 0 & 0 & 2c_{44} - \rho v^2 \end{pmatrix} U_k = 0 \qquad [7.25]$$

The first solution is immediate:

$$v^{(3)} = \pm\sqrt{\frac{c_{44}}{\rho}} \qquad [7.26]$$

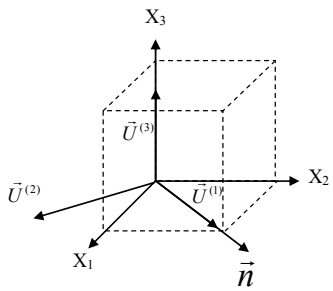

Figure 7.3. *Geometric representation of direction and polarization vectors for the propagation of a wave along the diagonal of one of the faces of the elementary lattice of a cubic symmetry material*

It presents a polarization $\vec{U}^{(3)} = \begin{pmatrix} 0 & 0 & 1 \end{pmatrix}^T$. This is the vertically polarized transverse wave.

The two other solutions to the Christoffel equation are coupled. To determine them, we must calculate the zeros of the characteristic determinant:

$$\begin{vmatrix} c_{11} + c_{44} - \rho v^2 & c_{12} + c_{44} \\ c_{12} + c_{44} & c_{11} + c_{44} - \rho v^2 \end{vmatrix} = 0 \qquad [7.27]$$

After some algebraic manipulations, we get:

$$v^{(2)} = \pm\sqrt{\frac{c_{11} - c_{12}}{\rho}} \qquad [7.28]$$

$$v^{(1)} = \pm\sqrt{\frac{c_{11} + c_{12} + 2c_{44}}{\rho}} \qquad [7.29]$$

To get the polarizations associated with these waves, we re-insert the velocity values in the characteristic equation. For example, for $v^{(2)}$, the following system is solved:

$$\begin{pmatrix} c_{11} + c_{44} - \rho v^{(2)2} & c_{12} + c_{44} \\ c_{12} + c_{44} & c_{11} + c_{44} - \rho v^{(2)2} \end{pmatrix} \begin{pmatrix} U_1 \\ U_2 \end{pmatrix} = \begin{pmatrix} 0 \\ 0 \end{pmatrix} \qquad [7.30]$$

This is a system of two equations with two unknowns. With its determinant being zero, it reduces to the relation between the components of the displacement vector:

$$U_1 + U_2 = 0 \qquad [7.31]$$

The vector that generates the set of these solutions, if we add the fact that component U_3 is zero is therefore:

$$\vec{U}^{(2)} = \frac{1}{\sqrt{2}}\begin{pmatrix}1 & -1 & 0\end{pmatrix}^T \qquad [7.32]$$

This vector is perpendicular to the direction of propagation: it is therefore the transverse wave with a horizontal polarization. Let us note that unlike the previous example, its velocity of propagation is *a priori* different to that of the vertically polarized transverse wave. Intuitively, this result is understandable given that geometrically the conditions of propagation, and in particular the effective stiffness of the medium, are different in the direction perpendicular to that of propagation. Nevertheless, for an isotropic material, the relation between elastic constants renders the phase velocities of the two transverse waves equal.

Using a similar procedure, we search for the last polarization. The system of two equations with two unknowns formed by substituting $v^{(1)}$ in the characteristic equation reduces to:

$$U_1 - U_2 = 0 \qquad [7.33]$$

The vector that generates the solution set is therefore:

$$\vec{U}^{(1)} = \frac{1}{\sqrt{2}}\begin{pmatrix}1 & 1 & 0\end{pmatrix}^T \qquad [7.34]$$

With this vector being equal to the direction of propagation, we now have to deal with the pure longitudinal wave.

The two sections above gave examples of propagation where acoustic polarizations were always perpendicular or collinear to the direction of propagation. If we now consider, for example, propagation in some direction in the X_1X_2 plane, for example, of the same cubic symmetry material, we expect to obtain the same transverse vertical wave, given that we did not modify the vertical component of propagation direction. In this case, however, equation [7.27] becomes more complex to solve, because it takes the form:

$$\begin{vmatrix} c_{11}n_1^2 + c_{44}\left(1-n_1^2\right) - \rho v^2 & \left(c_{12}+c_{44}\right)n_1 n_2 \\ \left(c_{12}+c_{44}\right)n_1 n_2 & c_{11}n_2^2 + c_{44}\left(1-n_2^2\right) - \rho v^2 \end{vmatrix} = 0 \qquad [7.35]$$

One of the consequences of the difference that appears between the two diagonal terms is that the eigenvectors for the two waves with an acoustic polarization in the propagation plane are no longer exactly collinear or orthogonal with the direction of propagation. We therefore speak of *quasi-longitudinal* and *quasi-transverse waves*. The orthogonality of the three polarizations is nevertheless always assured, since the symmetry of the Christoffel matrix is independent of the symmetry properties of the medium and of the direction of propagation.

To conclude this part on elastic waves, we are interested in the elastic energy density brought by the wave's transit.

The expression of this density was provided in Chapter 4 and is adapted here for complex fields:

$$U_{elastic} = -\frac{1}{2}\sum_{i,j} T_{ij} S_{ij}^{\ *} \qquad [7.36]$$

Resuming the expression of displacements associated with an acoustic wave given by equation [7.9], we can express the strain tensor in the form:

$$\begin{aligned} S_{ij}\left(\vec{X},t\right) = \ & -j\omega\sum_m \frac{1}{2} \left(s_j^{(m)}U_i^{(m)} + s_i^{(m)}U_j^{(m)}\right) \\ & \left(A_m e^{-j\omega\vec{s}^{(m=}\vec{X}} - B_m e^{j\omega\vec{s}^{(m=}\vec{X}}\right)e^{j\omega t} \end{aligned} \qquad [7.37]$$

Adding the form of stress fields calculated in equation [7.11], using the elastic tensor symmetry and the fact that the slowness and polarization vectors are all real (since the Christoffel matrix is real symmetric), we get:

$$\begin{aligned} U_{elastic} = & \frac{\omega^2}{2}\sum_{i,j,k,l,m,n} c_{ijkl} s_i^{(n)} s_l^{(m)} U_j^{(n)} U_k^{(m)} \\ & \left(A_m e^{-j\omega\vec{s}^{(m)}\vec{X}} - B_m e^{j\omega\vec{s}^{(m)}\vec{X}}\right)\left(A_n e^{-j\omega\vec{s}^{(n)}\vec{X}} - B_n e^{j\omega\vec{s}^{(n)}\vec{X}}\right)^* \end{aligned} \qquad [7.38]$$

In the case of a monochromatic plane wave of amplitude A (*a priori* complex), this expression is considerably simplified. Using the identities used to reveal the acoustic impedance between equations [7.14] and [7.15], we get:

$$U_{elastic} = \frac{\omega^2 s^2}{2} \sum_i \rho v^2 U_i^2 |A|^2 \qquad [7.39]$$

With the polarization vectors being normalized, we finally get:

$$U_{elastic} = \frac{\rho\omega^2}{2} |A|^2 \qquad [7.40]$$

Furthermore, calculation of kinetic energy density is expressed:

$$U_{kinetic} = \frac{1}{2}\rho |V|^2 = \frac{\rho\omega^2}{2} \left| \sum_i U_i^2 |A|^2 \right| = \frac{\rho\omega^2}{2} |A|^2 \qquad [7.41]$$

We therefore have equality between elastic and kinetic energy for a monochromatic plane wave. With strains and particle velocity being in opposition, in practice we have a constant transfer of energy from one form to the other [ROS 45].

7.1.2. *Elastic wave propagation in a piezoelectric medium*

Having analyzed wave propagation in an elastic medium, let us now consider propagation in a piezoelectric medium. The fundamental difference between this type of material and a purely elastic material originates in the coupling between electric and mechanical quantities. We showed that, in a piezoelectric medium, the equations of piezoelectricity were substituted in Hooke's law.

Integrating the dynamic behavior of the material electrically through the quasistatic approximation of the Maxwell-Gauss equation, and mechanically through the fundamental relation of dynamics, we get:

$$\rho \frac{\partial^2 U_i}{\partial t^2} = \sum_{j,k,l} c_{ijkl} \frac{\partial^2 U_k}{\partial X_j \partial X_l} + \sum_{j,l} e_{lij} \frac{\partial^2 V}{\partial X_j \partial X_l} \qquad [7.42]$$

$$\sum_j \frac{\partial D_j}{\partial X_j} = -\sum_{j,k} \varepsilon_{jk} \frac{\partial^2 V}{\partial X_j \partial X_k} + \sum_{j,k,l} e_{jkl} \frac{\partial^2 U_l}{\partial X_j \partial X_k} = 0 \qquad [7.43]$$

Let us note that, unlike in section 7.1.1, V designates the electric potential and not the particle velocity.

As before, we consider solutions in the form of monochromatic plane waves. All the fields being linearly linked by the linear equations of piezoelectricity, we expect them to follow a similar dependence on electric and mechanical displacements at the same time, as well as for the electric potential.

Under these assumptions, equations [7.36] and [7.37] are re-written in the forms:

$$\rho U_i = \sum_{j,l} \left(\sum_k c_{ijkl} U_k + e_{lij} V \right) s_j s_l \qquad [7.44]$$

$$\sum_{j,k} \varepsilon_{jk} s_j s_k V = \sum_{j,k,l} e_{jkl} s_j s_k U_l \qquad [7.45]$$

Equation [7.45] enables us to express the electric potential in terms of displacement fields, provided that the pathological case of a zero $\vec{s}$ vector (which corresponds to uniform fields in the entire space) is eliminated:

$$V = \frac{\sum_{j,k,l} e_{jkl} s_j s_k U_l}{\sum_{p,q} \varepsilon_{pq} s_p s_q} \qquad [7.46]$$

Inserting this expression in equation [7.38], electric potential is eliminated to arrive at the mechanical displacements propagation equation:

$$\rho U_i = \sum_{j,k,l} \left(c_{ijkl} + \frac{\sum_{m,n} e_{lij} e_{mnk} s_m s_n}{\sum_{p,q} \varepsilon_{pq} s_p s_q} \right) s_j s_l U_k \qquad [7.47]$$

As in the purely elastic case, this matrix equation is revised in order to reproduce the Christoffel equation:

$$\sum_k \left(\sum_{j,l} \bar{c}_{ijkl} n_j n_l - \rho v^2 \delta_{ik} \right) U_k = 0 \qquad [7.48]$$

where *stiffened elastic constants* are used, i.e. the elastic constants are modified by the presence of piezoelectricity and coupling with a quasielectric wave (of infinite slowness in the quasistatic approximation):

$$\bar{c}_{ijkl} = c^E_{ijkl} + \frac{\sum_{m,n} e_{lij} e_{mnk} n_m n_n}{\sum_{p,q} \varepsilon_{pq} n_p n_q} = c^E_{ijkl}\left(1 + k^2_{ijkl}\right) \qquad [7.49]$$

in which we introduced a correction factor $k_{ijkl}{}^2$ that takes into consideration the increase in wave propagation velocity compared to the purely elastic case.

As an example, let us consider the propagation of an acoustic wave in direction X_3 of a material of hexagonal class *6mm*. For such a material, the elastic tensor was given in Chapter 4, equation [4.61].

As for its piezoelectric and dielectric tensors, they are expressed as:

$$\bar{\bar{e}} = \begin{pmatrix} 0 & 0 & 0 & 0 & e_{15} & 0 \\ 0 & 0 & 0 & e_{15} & 0 & 0 \\ e_{31} & e_{31} & e_{33} & 0 & 0 & 0 \end{pmatrix} \qquad [7.50]$$

$$\bar{\bar{\varepsilon}} = \begin{pmatrix} \varepsilon_{11} & 0 & 0 \\ 0 & \varepsilon_{11} & 0 \\ 0 & 0 & \varepsilon_{33} \end{pmatrix} \qquad [7.51]$$

For a vector $\vec{n} = \begin{pmatrix} 0 & 0 & 1 \end{pmatrix}^T$, the Christoffel equation is expressed:

$$\begin{pmatrix} c_{44} - \rho v^2 & 0 & 0 \\ 0 & c_{44} - \rho v^2 & 0 \\ 0 & 0 & c_{33} + \frac{e_{33}{}^2}{\varepsilon_{33}} - \rho v^2 \end{pmatrix} U_k = 0 \qquad [7.52]$$

The three solutions to the equation are:

$$v^{(1)} = v^{(2)} = \pm\sqrt{\frac{c_{44}}{\rho}} \qquad [7.53]$$

with respective polarizations:

$$\vec{U}^{(1)} = \begin{pmatrix} 1 & 0 & 0 \end{pmatrix}^T \qquad [7.54]$$

$$\vec{U}^{(2)} = \begin{pmatrix} 0 & 1 & 0 \end{pmatrix}^T \qquad [7.55]$$

These are the two transverse waves that can propagate vertically. The last solution is:

$$v^{(3)} = \pm\sqrt{\frac{c_{33} + {e_{33}}^2 / \varepsilon_{33}}{\rho}} \qquad [7.56]$$

with polarization:

$$\vec{U}^{(3)} = \begin{pmatrix} 0 & 0 & 1 \end{pmatrix}^T \qquad [7.57]$$

As can be seen, the solution to the Christoffel equation is identical to the purely elastic case at all points. In our example, the two shear waves found exhibit propagation velocities identical to those we encountered in a non-piezoelectric medium. On the other hand, for the longitudinal wave we note an increase in the propagation velocity caused by hardening of the elastic constants effectively involved in the Christoffel equation.

The displacement fields are formally identical to those encountered in the purely elastic case:

$$\vec{U}(\vec{X},t) = \sum_m \left(A_m e^{-j\omega\vec{s}^{(m)}\vec{X}} + B_m e^{j\omega\vec{s}^{(m)}\vec{X}} \right) \vec{U}^{(m)} e^{j\omega t} \qquad [7.58]$$

To calculate the electric potential, we use equation [7.37] that, after double derivation and double integration of the mechanical displacements, gives us:

$$V(\vec{X},t) = \sum_m \frac{\sum_{j,k,l} e_{jkl} s_j^{(m)} s_k^{(m)}}{\sum_{p,q} \varepsilon_{pq} s_p^{(m)} s_q^{(m)}} \left(A_m e^{-j\omega \vec{s}^{(m)} \vec{X}} + B_m e^{j\omega \vec{s}^{(m)} \vec{X}} \right) U_l^{(m)} e^{j\omega t} + \sum_i V_i^0 X_i + V^0 \qquad [7.59]$$

where V_i^0 and V^0 are integration constants that are possibly time-dependant. Since the slowness vector and direction of propagation are colinear, it is possible to eliminate the value of the slowness in the first term and express the electric potential in the form:

$$V(\vec{X},t) = \sum_m \frac{\sum_{j,k,l} e_{jkl} n_j n_k U_l^{(m)}}{\sum_{p,q} \varepsilon_{pq} n_p n_q} \left(A_m e^{-j\omega \vec{s}^{(m)} \vec{X}} + B_m e^{j\omega \vec{s}^{(m)} \vec{X}} \right) e^{j\omega t} + \sum_i V_i^0 X_i + V^0 \qquad [7.60]$$

We therefore see that electric potential appears in the form of an electrostatic potential solution of Poisson's equation $\Delta V = 0$ (the second term involving integration constants V_i^0 and V^0) on which the electric contributions of each of the plane waves that can propagate in the medium are superimposed. We can note that these contributions are in phase with mechanical displacements and involve piezoelectric and dielectric properties of the medium at the same time.

To calculate the stresses generated in the medium, we use the first piezoelectricity equation in which the electric field is expressed as a gradient of the electric potential and strains in terms of mechanical displacements:

$$T_{ij}\left(\vec{X},t\right) = \sum_{k,l} c_{ijkl}^E \frac{\partial U_k}{\partial X_l} + \sum_k e_{kij} \frac{\partial V}{\partial X_k} \qquad [7.61]$$

After inserting the mechanical displacement and the electric potential expressions given by equations [7.58] and [7.60], we get:

$$T_{ij}\left(\vec{X},t\right)= -j\omega\sum_{m}\left(\sum_{k,l}c_{ijkl}^{E}s_{l}^{(m)}U_{k}^{(m)}+\frac{\sum_{k,l,m,n}e_{kij}e_{lmn}n_{l}n_{m}U_{n}^{(m)}s_{k}^{(m)}}{\sum_{p,q}\varepsilon_{pq}n_{p}n_{q}}\right)$$
$$\left(A_{m}e^{-j\omega\vec{s}^{(m)}\vec{X}}-B_{m}e^{j\omega\vec{s}^{(m)}\vec{X}}\right)e^{j\omega t}+\sum_{k}e_{kij}V_{k}^{0} \qquad [7.62]$$

Through the symmetry of the elastic tensor, we can produce hardened elastic constants in the first term and thus write:

$$T_{ij}\left(\vec{X},t\right)= -j\omega\sum_{m}\left(\sum_{k,l}\bar{c}_{ijkl}s_{l}^{(m)}U_{k}^{(m)}\right)$$
$$\left(A_{m}e^{-j\omega\vec{s}^{(m)}\vec{X}}-B_{m}e^{j\omega\vec{s}^{(m)}\vec{X}}\right)e^{j\omega t}+\sum_{k}e_{kij}V_{k}^{0} \qquad [7.63]$$

This expression is close to the one obtained for a purely elastic medium in equation [7.11], except that here we must consider hardened elastic constants instead of purely elastic factors.

Furthermore, the second term corresponds to the stress generated in the medium by compressing or expanding the material, due to the electric field established by the electrostatic field existing in the medium. Similarly to an elastic medium, it becomes possible to introduce the notion of acoustic impedance associated with a plane wave as being the product of propagation velocity (taking into consideration piezoelectric hardening) by the density of the medium.

To calculate electric displacement, we proceed in the same way, but this time using the second piezoelectricity equation:

$$D_{j}=-\sum_{k}\varepsilon_{jk}\frac{\partial V}{\partial X_{k}}+\sum_{k,l}e_{jkl}\frac{\partial U_{k}}{\partial X_{l}} \qquad [7.64]$$

which, after inserting the expressions of electric potential and the mechanical displacements given in [7.58] and [7.60], gives us:

$$D_j = j\omega \sum_m \sum_{k,l} \left(\varepsilon_{jl} \frac{\sum_{o,p} e_{opk} n_o n_p}{\sum_{r,s} \varepsilon_{rs} n_r n_s} - e_{jkl} \right) s_l^{(m)} U_k^{(m)} \left(A_m e^{-j\omega \vec{s}^{(m=} \vec{X}} - B_m e^{j\omega \vec{s}^{(m=} \vec{X}} \right) - \sum_i \varepsilon_{ji} V_i^0 \quad [7.65]$$

We can note that in particular cases, such as the example of propagation along the *c*-axis of a material from crystal class *6mm* (which we saw before), the coefficients of the first term cancel each other out. In this case:

$$D_j = -\varepsilon_{jj} V_j^0 \quad [7.66]$$

Through the symmetry of the dielectric tensor, the electric displacement associated with propagation of the acoustic wave vanishes and this electric displacement is therefore uniquely electrostatic. Similar to a non-piezoelectric medium, we can calculate the elastic and kinetic energies associated with a plane wave. For this we use the stress expression [7.63], without the term corresponding to a static stress and equation [7.58]. Thanks to the use of stiffened elastic constants, we find the same expressions as for a non-piezoelectric medium:

$$U_{elastic} = U_{kinetic} = \frac{\rho\omega^2}{2} |A|^2 \quad [7.67]$$

However, if we go back to the definition of elastic energy density (equation [7.36]) and insert the first piezoelectricity relation in it, elastic energy can be decomposed into two terms:

$$\begin{aligned} U_{elastic} &= -\frac{1}{2} \sum_{ijkl} c_{ijkl}^E S_{ij}^* + \frac{1}{2} \sum e_{mij} E_m S_{ij}^* \\ &= U_{mm} + U_{em} \end{aligned} \quad [7.68]$$

The first term corresponds to the elastic energy encountered in a classic dielectric medium. It is a purely mechanical energy.

The second term, itself, contains electric and mechanical terms at the same time. It represents the portion of elastic energy that has an electric origin; the conversion being implemented through the use of piezoelectricity.

In the same way, the electric energy can be decomposed into two terms:

$$\begin{aligned} U_{electric} &= \frac{1}{2}\sum_i E_i D_i^* \\ &= \frac{1}{2}\sum_{ij} \varepsilon_{ij} E_i E_j^* + \frac{1}{2}\sum_{mij} e_{mij} E_m S_{ij}^* \\ &= U_{ee} + U_{em} \end{aligned} \qquad [7.69]$$

The first term corresponds to the electrostatic energy density in a classic dielectric medium. It is therefore purely electric energy.

For the second term, it corresponds to the portion of electric energy that has an elastic origin, which is equal to the electromechanical term for elastic energy.

Calculation of the purely mechanical energy associated with a plane wave is done by using the relation between strains and displacement, as well as the expression for displacements in a piezoelectric medium (equation [7.58]):

$$U_{mm} = \frac{\omega^2}{2}\sum_{ijkl} c_{ijkl}^E s_j s_l U_i U_k |A|^2 = \frac{\omega^2}{2v^2}\sum_{ijkl} c_{ijkl}^E n_j n_l U_i U_k |A|^2 \qquad [7.70]$$

If the medium were non-piezoelectric, with the wave being a solution to the Christoffel equation [7.48], we could produce the propagation velocity, which would be simplified with slowness. We would therefore find the result of equation [7.36]. Due to the piezoelectric stiffening, this is no longer true.

The calculation of purely electric energy is done using the expression for U_{ee} and the electric potential expression [7.60], which is derived to produce the electric field:

$$\begin{aligned} U_{ee} &= \frac{\omega^2}{2}\left(\frac{\sum_{klm} e_{klm} n_k n_l U_m}{\sum_{pq} \varepsilon_{pq}^S n_p n_q}\right)^2 \sum_{ij} \varepsilon_{ij}^S s_i s_j |A|^2 \\ &= \frac{\omega^2}{2v^2}\frac{\left(\sum_{klm} e_{klm} n_k n_l U_m\right)^2}{\sum_{pq} \varepsilon_{pq}^S n_p n_q}|A|^2 \end{aligned} \qquad [7.71]$$

Finally, the coupled term is calculated from the derivatives of the electric potential and displacements:

$$U_{em} = \frac{\omega^2}{2}\sum_{mij} e_{mij} s_m s_i U_j \left(\frac{\sum_{klo} e_{klo} n_k n_l U_o}{\sum_{pq} \varepsilon^S_{pq} n_p n_q} \right) |A|^2$$

$$= \frac{\omega^2}{2v^2} \frac{\left(\sum_{klm} e_{klm} n_k n_l U_m \right)^2}{\sum_{pq} \varepsilon^S_{pq} n_p n_q} |A|^2 \qquad [7.72]$$

We can note that terms U_{ee} and U_{em} are equal, which means that the density of energy stored in electrostatic form is equal to that stored in electromechanical form.

From these expressions, we can form the ratio of electrostatic (or electromechanical) and mechanical energy density:

$$\frac{U_{ee}}{U_{mm}} = \frac{U_{em}}{U_{mm}} = \frac{\left(\sum_{klm} e_{klm} n_k n_l U_m \right)^2}{\left(\sum_{pq} \varepsilon^S_{pq} n_p n_q \right)\left(\sum_{ijkl} c^E_{ijkl} n_j n_l U_i U_k \right)} = k^2 \qquad [7.73]$$

This ratio is called the *piezoelectric coupling coefficient* [ROS 45]. It provides information about the proportion of electromechanical energy, compared to the mechanical energy, brought by the plane wave during its propagation. To the extent that the direction of propagation and polarization of the wave are involved in its calculation, the term is specific to a polarization and a given direction. For this reason, it is often written in several variations. As an example, for the longitudinal wave propagating along the X_3 axis of a material of *6mm* crystal symmetry, this coefficient is normally expressed as $k_{33}{}^2$ [IEE 87]:

$$k_{33}{}^2 = \frac{e_{33}{}^2}{\varepsilon^S_{33} c^E_{33}} \qquad [7.74]$$

Resuming relation [7.47], it is possible to re-write the plane wave velocity propagation expression in terms of the piezoelectric coupling coefficient:

$$\rho v^2 U_i = \sum_{jkl} c_{ijkl}^E n_j n_l U_k + \frac{\sum_{jklmn} e_{lij} e_{mnk} n_j n_l n_m n_n U_k}{\sum_{pq} \varepsilon_{pq}^S n_p n_q} \qquad [7.75]$$

With the polarization vector being normalized and, for each value of i, multiplying this last expression by U_i and summing up all these expressions, we end up with:

$$\rho v^2 = \left(\sum_{ijkl} c_{ijkl}^E n_j n_l U_i U_k \right) \left(1 + k^2 \right) \qquad [7.76]$$

This seems as though the piezoelectric stiffening effect is directly proportional to the piezoelectric coupling coefficient.

In the particular case of the longitudinal wave propagating along axis X_3 of a material from crystal class *6mm*, coefficient $k_{33}{}^2$ is clearly related to hardened elastic constants, since according to equation [7.56], we similarly have:

$$\bar{c}_{33} = c_{33}^E \left(1 + k_{33}{}^2 \right) \qquad [7.77]$$

The second relation that it is possible to form is that between energy density in electromechanical form and the sum of pure mechanical and electrostatic energy densities.

This relation is expressed as:

$$\frac{U_{em}}{U_{mm} + U_{ee}} = \frac{k^2}{1 + k^2} = K^2 \qquad [7.78]$$

and is called the *electromechanical coupling coefficient* [ROS 45]. This expression provides information about the proportion of energy that can be exchanged between the mechanical and the electric forms.

If we return to the example of a longitudinal wave propagating along axis X_3 of a material from crystal class *6mm*, we get:

$$K^2 = \frac{k_{33}{}^2}{1 + k_{33}{}^2} = \frac{e_{33}{}^2}{\bar{c}_{33} \varepsilon_{33}^S} \qquad [7.79]$$

7.2. Bulk wave resonator

Now that we have presented a formalism enabling us to describe acoustic wave propagation in an elastic or piezoelectric medium, we will use these results to analyze the vibration of a piezoelectric plate on a thickness mode.

7.2.1. *Piezoelectric plate vibrations*

In its simplest form, a bulk wave resonator is solely composed of a piezoelectric plate, which we will initially assume to be excited solely by infinitely thin electrodes, so that the electrodes only have an electric influence. This geometry is represented in Figure 7.4. Furthermore, we will assume that the lateral dimensions of the plate are very large compared to its thickness, so it is possible to assume it to be of infinite lateral extent and thus neglect all transverse effects. This means that all X_1 and X_2 coordinate derivatives are zero. The propagation slowness vector, and consequently the direction of propagation, can only therefore be vertical and thus colinear to the X_3 axis, i.e. to the thickness of the plate. In addition, regarding the electric potential, only integration constants V_3^0 and V^0 are *a priori* non-zero.

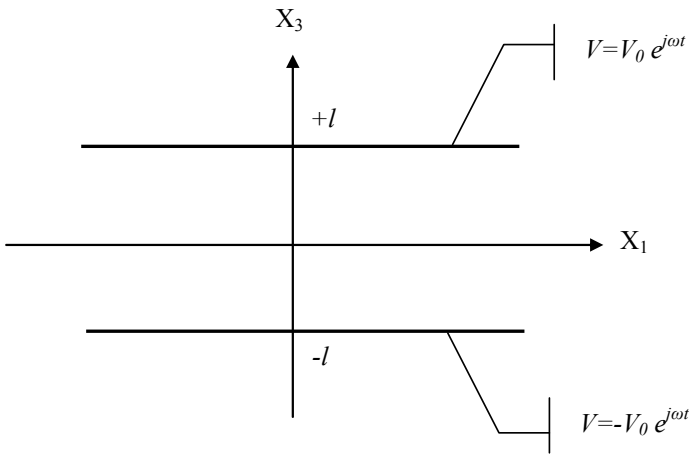

Figure 7.4. *Geometry used for analyzing vibration with the thickness mode of a piezoelectric plate that is 2l thick*

With the direction of propagation being fixed, we can calculate the solutions to plane waves propagating in the medium by using the Christoffel equation. We can consequently consider electromechanical fields of the form established in equations [7.58], [7.60], [7.63] and [7.65].

With the plate being assumed to be isolated in a vacuum, no mechanical force is applied. This is translated by cancelling the surface normal stresses at the edges of the plate. With the electric potential being imposed on these very faces, we find the value this potential at the level of planes $X_3 = \pm l$, if we assume that the plane is of $2l$ thick. The expression of these boundary conditions therefore provides the following set of equations:

$$\begin{aligned} V(X_3 = \pm l) = & \frac{e_{33}}{\varepsilon_{33}}\left(A_L e^{\mp j\omega s_L l} + B_L e^{\pm j\omega s_L l}\right)e^{j\omega t} \\ & + \frac{e_{35}}{\varepsilon_{33}}\left(A_{S1} e^{\mp j\omega s_{S1} l} + B_{S1} e^{\pm j\omega s s_{S1} l}\right)e^{j\omega t} \\ & + \frac{e_{34}}{\varepsilon_{33}}\left(A_{S2} e^{\mp j\omega s_{S1} l} + B_{S2} e^{\pm j\omega s_{S1} l}\right)e^{j\omega t} \pm V_3{}^0 l + V^0 \\ & = \pm V_0 e^{j\omega t} \end{aligned} \quad [7.80]$$

$$\begin{aligned} T_{13}(X_3 = \pm l) = & -j\omega\Big(\bar{c}_{53} s_L \left(A_L e^{\mp j\omega s_L l} - B_L e^{\pm j\omega s_L l}\right)e^{j\omega t} \\ & + \bar{c}_{55} s_{S1}\left(A_{S1} e^{\mp j\omega s_{S1} l} - B_{S1} e^{\pm j\omega s_{S1L} l}\right)e^{j\omega t} \\ & + \bar{c}_{54} s_{S2}\left(A_{S2} e^{\mp j\omega s_{S2} l} - B_{S2} e^{\pm j\omega s_{SL} l}\right)e^{j\omega t}\Big) + e_{35} V_3^0 \\ & = 0 \end{aligned} \quad [7.81]$$

$$\begin{aligned} T_{23}(X_3 = \pm l) = & -j\omega\Big(\bar{c}_{43} s_L \left(A_L e^{\mp j\omega s_L l} - B_L e^{\pm j\omega s_L l}\right)e^{j\omega t} \\ & + \bar{c}_{45} s_{S1}\left(A_{S1} e^{\mp j\omega s_{S1} l} - B_{S1} e^{\pm j\omega s_{S1L} l}\right)e^{j\omega t} \\ & + \bar{c}_{44} s_{S2}\left(A_{S2} e^{\mp j\omega s_{S2} l} - B_{S2} e^{\pm j\omega s_{SL} l}\right)e^{j\omega t}\Big) + e_{34} V_3^0 \\ & = 0 \end{aligned} \quad [7.82]$$

$$\begin{aligned} T_{33}(X_3 = \pm l) = & -j\omega\Big(\bar{c}_{33} s_L \left(A_L e^{\mp j\omega s_L l} - B_L e^{\pm j\omega s_L l}\right)e^{j\omega t} \\ & + \bar{c}_{35} s_{S1}\left(A_{S1} e^{\mp j\omega s_{S1} l} - B_{S1} e^{\pm j\omega s_{S1L} l}\right)e^{j\omega t} \\ & + \bar{c}_{34} s_{S2}\left(A_{S2} e^{\mp j\omega s_{S2} l} - B_{S2} e^{\pm j\omega s_{SL} l}\right)e^{j\omega t}\Big) + e_{33} V_3^0 \\ & = 0 \end{aligned} \quad [7.83]$$

Thus we have a set of eight equations with eight unknowns. This enables us to determine amplitudes A_L, B_L, A_{S1}, B_{S1}, A_{S2} and B_{S2}, corresponding to longitudinal waves, transverse waves polarized along the X_1 axis, and transverse waves polarized along the X_2 axis, respectively, at the same time.

In the general case, the symmetry of the piezoelectric material leads to a number of elastic and piezoelectric constants appearing in this set of equations being cancelled. Calculations therefore end up being considerably simplified. If we take the case, for example, of an aluminum nitride (AlN) film, which is a material of crystal class *6mm*, the non-diagonal elastic and piezoelectric terms are cancelled. In this case, it seems that each of the shear waves is mechanically decoupled from the other waves and that the longitudinal wave is coupled to the electric potential through the piezoelectric constant e_{33}.

If we are interested in the first shear wave (called "S1"), the problem is limited to the matrix relation:

$$\begin{pmatrix} e^{-j\omega s_{S1}l} & -e^{j\omega s_{S1}l} \\ e^{j\omega s_{S1}l} & -e^{-j\omega s_{S1}l} \end{pmatrix} \begin{pmatrix} A_{S1} \\ B_{S1} \end{pmatrix} = \begin{pmatrix} T_{13}\left(X_3 = l\right) \\ T_{13}\left(X_3 = -l\right) \end{pmatrix} = \begin{pmatrix} 0 \\ 0 \end{pmatrix} \qquad [7.84]$$

The solutions to this equation are uniformly zero in the general case, except when the matrix determinant of the left-hand side cancels out. This condition is satisfied when:

$$\sin 2\omega s_{S1} l = 0 \qquad [7.85]$$

or when the frequency is equal to:

$$f = \frac{p}{4 s_{S1} l} \qquad [7.86]$$

where p is an integer indicating the order of the solution. At these frequencies, the amplitudes of waves that can propagate in the film are non-zero and satisfy the relation $A_{S1} = B_{S1}$. The waves are therefore totally reflected at the interface and the mechanical displacements are expressed in the form:

$$\vec{u}\left(X_3\right) = \begin{pmatrix} A_{S1} \cos \omega s_{S1} X_3 e^{j\omega t} \\ 0 \\ 0 \end{pmatrix} \qquad [7.87]$$

When condition [7.85] is satisfied, the mechanical displacements exhibit a profile corresponding to a multiple of a half-wavelength established in the thickness of the film. The vibration amplitude, given by A_{S1}, nevertheless remains undetermined for lack of an explicit condition of excitation. The plate considered can therefore vibrate on an eigen mode, but disregarding the electric excitation.

The same analysis can be carried out for the study of the second shear wave and leads to the same types of results: only the frequencies of resonance and the direction of mechanical displacements are potentially different.

Regarding the longitudinal wave, on the other hand, the coupling of electric and mechanical fields leads to a matrix equation:

$$\begin{pmatrix} \frac{e_{33}}{\varepsilon_{33}} e^{j\omega(t-s_L l)} & \frac{e_{33}}{\varepsilon_{33}} e^{j\omega(t+s_L l)} & l & 1 \\ \frac{e_{33}}{\varepsilon_{33}} e^{j\omega(t+s_L l)} & \frac{e_{33}}{\varepsilon_{33}} e^{j\omega(t-s_L l)} & -l & 1 \\ -j\omega Z_L e^{j\omega(t-s_L l)} & j\omega Z_L e^{j\omega(t+s_L l)} & e_{33} & 0 \\ -j\omega Z_L e^{j\omega(t+s_L l)} & j\omega Z_L e^{j\omega(t-s_L l)} & e_{33} & 0 \end{pmatrix} \begin{pmatrix} A_L \\ B_L \\ V_3^0 \\ V^0 \end{pmatrix} = \begin{pmatrix} V_0 e^{j\omega t} \\ -V_0 e^{j\omega t} \\ 0 \\ 0 \end{pmatrix} \qquad [7.88]$$

where the acoustic impedance $Z_L = s_L \bar{c}_{33}$ was used to simplify the expressions a bit. The amplitudes of longitudinal waves, the electric field and the electric potential can thus be obtained in terms of electric and mechanical boundary conditions by inverting the matrix of equation [7.88].

This can, for example, be carried out by calculating the transpose of the comatrix. With a few calculations, we get:

$$\begin{pmatrix} A_L \\ B_L \\ V_3^0 \\ V^0 \end{pmatrix} = \begin{pmatrix} A & -A & B & -C \\ -A & A & C & -B \\ D & -D & E & E \\ F & F & G & -G \end{pmatrix} \begin{pmatrix} V_0 e^{j\omega t} \\ -V_0 e^{j\omega t} \\ 0 \\ 0 \end{pmatrix}, \qquad [7.89]$$

in which:

$$
\begin{aligned}
A &= \frac{je_{33}\varepsilon_{33}e^{-j\omega t}}{4\left(l\omega\varepsilon_{33}Z_L\cos\omega s_L l - e_{33}{}^2\sin\omega s_L l\right)}\\
B &= \frac{\left(e_{33}{}^2 + jl\omega\varepsilon_{33}Z_L - l\omega e_{33}Z_L\cot\omega sl\right)e^{-j\omega t}}{4Z_L\omega\left(l\omega\varepsilon_{33}Z_L\cos\omega s_L l - e_{33}{}^2\sin\omega s_L l\right)}\\
C &= \frac{\left(e_{33}{}^2 - jl\omega\varepsilon_{33}Z_L - l\omega e_{33}Z_L\cot\omega sl\right)e^{-j\omega t}}{4Z_L\omega\left(l\omega\varepsilon_{33}Z_L\cos\omega s_L l - e_{33}{}^2\sin\omega s_L l\right)}\\
D &= \frac{Z_L\varepsilon_{33}\omega\cos\omega s_L l}{2\left(l\omega\varepsilon_{33}Z_L\cos\omega s_L l - e_{33}{}^2\sin\omega s_L l\right)}\\
E &= \frac{-e_{33}\sin\omega s_L l}{2\left(l\omega\varepsilon_{33}Z_L\cos\omega s_L l - e_{33}{}^2\sin\omega s_L l\right)}\\
F &= \frac{l}{2}\\
G &= \frac{e_{33}\cot\omega s_L l}{2Z_L\varepsilon_{33}\omega}
\end{aligned}
\qquad [7.90]
$$

The unknowns that enable us to express the electromechanical fields in the film are deduced from this:

$$A_L = -B_L = 2AV_0e^{j\omega t} = \frac{je_{33}\varepsilon_{33}V_0}{2\left(l\omega\varepsilon_{33}Z_L\cos\omega s_L l - e_{33}{}^2\sin\omega s_L l\right)} \qquad [7.91]$$

$$V_3^0 = 2DV_0e^{j\omega t} = \frac{Z_LV_0\varepsilon_{33}\omega\cos\left(\omega s_L l\right)e^{j\omega t}}{l\omega\varepsilon_{33}Z_L\cos\omega s_L l - e_{33}{}^2\sin\omega s_L l} \qquad [7.92]$$

$$V^0 = 0 \qquad [7.93]$$

Equation [7.91] enables us to notice that acoustic wave amplitudes are proportional to the voltage applied upon the two electrodes surrounding the piezoelectric film. They are also proportional to the dielectric constant involved as well as the coupling coefficient, which establishes the link between the electric and mechanical quantities. Finally, let us note that the amplitudes of the two waves propagating in opposite directions are equal, apart from their sign. This is the consequence of a perfect reflection of these waves at the interface between the piezoelectric solid and vacuum.

Once the unknowns of the problem have been determined, it is possible to arrive at the expressions for the mechanical and electrical fields in the piezoelectric film:

$$\vec{U}(\vec{X},t) = \frac{e_{33}\varepsilon_{33}\sin\omega s_L X_3}{l\omega\varepsilon_{33}Z_L\cos\omega s_L l - e_{33}{}^2\sin\omega s_L l} V_0 e^{j\omega t}\begin{pmatrix}0\\0\\1\end{pmatrix} \qquad [7.94]$$

$$V\left(\vec{X},t\right) = \frac{e_{33}{}^2\varepsilon_{33}\sin\omega s_L X_3 + X_3 Z_L\varepsilon_{33}\omega\cos\omega s_L l}{l\omega\varepsilon_{33}Z_L\cos\omega s_L l - e_{33}{}^2\sin\omega s_L l} V_0 e^{j\omega t} \qquad [7.95]$$

$$T_{33}\left(\vec{X},t\right) = \frac{Z_L e_{33}\varepsilon_{33}\omega\left(\cos\omega s_L l - \cos\omega s_L X_3\right)}{l\omega\varepsilon_{33}Z_L\cos\omega s_L l - e_{33}{}^2\sin\omega s_L l} V_0 e^{j\omega t} \qquad [7.96]$$

$$D_3\left(\vec{X},t\right) = \frac{\varepsilon_{33}{}^2 Z_L\omega\cos\omega s_L l}{l\omega\varepsilon_{33}Z_L\cos\omega s_L l - e_{33}{}^2\sin\omega s_L l} V_0 e^{j\omega t} \qquad [7.97]$$

On the one hand, we can note that all these fields have the same denominator and therefore tend towards infinity when the denominator is canceled. This condition is satisfied from the moment that:

$$\frac{\omega s_L l}{k_t{}^2} = \tan\omega s_L l \qquad [7.98]$$

where we find again the electromechanical coupling coefficient expression defined in equation [7.79]: $k_t{}^2 = K^2 = \frac{e_{33}{}^2}{\varepsilon_{33}\bar{c}_{33}}$. Tiersten and Onoe obtained a similar equation for a thickness shear mode in a quartz plate [ONO 69, TIE 69], which proves that the approach presented here can be similarly applied to other polarizations. Due to the periodicity of the function $\tan x$, this relation has an infinite number of non-analytical solutions. It is nevertheless possible to solve this equation numerically or even graphically because the solutions are given by the intersection of the function $\tan\omega s_L l$ and $\omega s_L l / k_t{}^2$. As can be seen in Figure 7.5, for a coefficient k_t^2 in the order of a few per cent, as is normally the case for most piezoelectric materials, this condition is close to the one where the tangent diverges. It diverges from this, however, when the coefficient is increased, i.e. the material has significant piezoelectric properties. In comparison with the behavior of piezoelectrically uncoupled waves, for which mechanical resonance occurs when

condition [7.85] is satisfied, which corresponds to a divergence of the tangent function, we experience a frequency offset in the mechanical resonance.

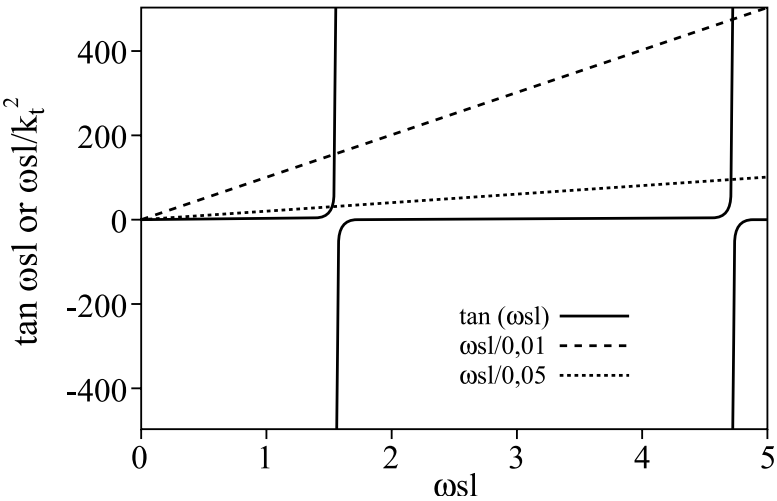

Figure 7.5. *Graphical representation of the resonance condition for free piezoelectric plate vibration*

If we now turn our interest to the behavior of the plate at the frequency that corresponds to the mechanical resonance in the absence of the offset caused by piezoelectricity, we get:

$$\vec{U}(\vec{X},t) = -\frac{\varepsilon_{33}}{e_{33}} V_0 e^{j\omega t} \sin \omega s_L X_3 \qquad [7.99]$$

This shows that the displacement field in the film presents a sinusoidal form with maximums at the interfaces delimiting this film. In practice, therefore, at this frequency the thickness is equal to an odd integer multiple of the half wavelength. The higher the piezoelectric coefficient; the lower the amplitude of vibration at this frequency.

If we now turn our interest to the electric response of the component, it is necessary to calculate the current circulating in the electrodes obtained as a response to the voltage applied. This current is obtained by deriving the surface charge density accumulated at the interfaces delimiting the plate, themselves equal to the normal electric displacement value:

$$Y(\omega) = \frac{I}{2V_0 e^{j\omega t}} = \frac{1}{2V_0 e^{j\omega t}} \left(\frac{\partial D_3(l,t)}{\partial t} \right) = j\omega \frac{\varepsilon_{33}}{2l} \frac{1}{1 - k_t^2 \frac{\tan \omega s_L l}{\omega s_L l}} \qquad [7.100]$$

This admittance is given per surface unit. It is represented in Figure 7.6 in the case of a 2 µm-thick plate of aluminum nitride (AlN), the characteristics of which are provided in Table 7.1. This is the typical behavior of a plane capacitor on which a pole centered on the frequency of mechanical resonance is superimposed. When the tangent diverges, admittance, on the other hand, tends to cancel. Therefore this frequency is called the *antiresonance frequency*. It corresponds to the frequency at which all fields reach their minimum value.

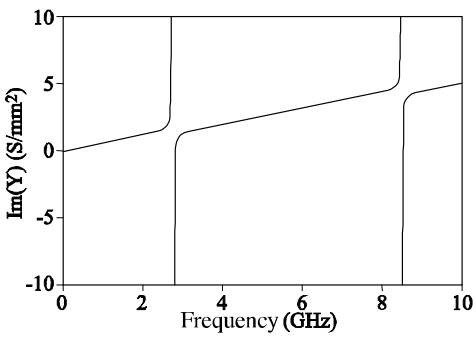

Figure 7.6. *Electric response of a 2 µm-thick plate of AlN vibrating on a thickness mode*

Velocity of propagation of the longitudinal wave	11.1 km/s
Dielectric constant	82.6 pF/m
Electromechanical coupling coefficient	6.5%

Table 7.1. *Acoustic properties of AlN*

Using a graphic construction, we showed that the deviation between the resonance and antiresonance frequencies depends on the piezoelectric coupling coefficient. To evaluate the relation that links these three quantities, let us consider the condition of antiresonance:

$$\omega_A s_L l = \frac{2n+1}{2}\pi \qquad [7.101]$$

with n being an integer number, from which we extract:

$$s_L l = \frac{2n+1}{4f_A} \qquad [7.102]$$

If we insert this in the condition of resonance [7.98], we get:

$$\frac{(2n+1)\omega_R}{4f_A} = k_t^2 \tan\frac{(2n+1)\omega_R}{4f_A}, \qquad [7.103]$$

which finally leads to the expression of the piezoelectric coupling coefficient as a function of the spacing between resonance and antiresonance frequencies:

$$k_t^2 = \frac{(2n+1)\pi}{2}\frac{f_R}{f_A}\tan\left(\frac{(2n+1)\pi}{2}\frac{f_A - f_R}{f_A}\right) \qquad [7.104]$$

The most commonly used form of this relation is given for the fundamental mode of resonance ($n = 0$), for which we get:

$$k_t^2 = \frac{\pi}{2}\frac{f_R}{f_A}\tan\left(\frac{\pi}{2}\frac{f_A - f_R}{f_A}\right) \qquad [7.105]$$

From this, and as can be seen in Figure 7.5, the deviation between resonance and antiresonance decreases when the order of resonance increases. To quantify this effect more accurately, we will assume *a priori* that the spacing between the two frequencies is low.

We can therefore simplify the tangent to the first order into:

$$k_t^2 \approx \frac{(2n+1)^2\pi^2}{4}\frac{f_R}{f_A}\frac{f_A - f_R}{f_A} \approx (2n+1)^2\frac{\pi^2}{4}\frac{f_A - f_R}{f_A} \qquad [7.106]$$

This simplified expression proves to be useful for relating the electromechanical coupling coefficient to the frequency spacing between resonance and antiresonance.

7.2.2. *Plate delimited by arbitrary acoustic impedance media*

In the previous section, we studied the behavior of a plate delimited by a vacuum. These boundary conditions had the effect of cancelling the stresses on the

borders of the plate. We will now generalize this concept, by assuming that the borders of the plate present a linear relation between displacements and stresses.

As we saw before, this corresponds to assuming that the adjacent medium presents an acoustic impedance Z. According to equation [7.15], this refers to saying that when we only consider the propagation of a single plane wave, for example the longitudinal wave from the example in the previous section, we get:

$$T_{33}\left(X_3 = l\right) = -j\omega Z_t U_3(X_3 = l) \qquad [7.107]$$

$$T_{33}\left(X_3 = -l\right) = -j\omega Z_b U_3(X_3 = -l) \qquad [7.108]$$

where Z_t and Z_b are the acoustic impedances presented at the top and bottom of the plate, respectively. These new boundary conditions lead us to re-write the matrix relation [7.88] in the form:

$$\begin{pmatrix} \frac{e_{33}}{\varepsilon_{33}} e^{j\omega(t-s_L l)} & \frac{e_{33}}{\varepsilon_{33}} e^{j\omega(t+s_L l)} & l & 1 \\ \frac{e_{33}}{\varepsilon_{33}} e^{j\omega(t+s_L l)} & \frac{e_{33}}{\varepsilon_{33}} e^{j\omega(t-s_L l)} & -l & 1 \\ -j\omega\left(Z_L - Z_t\right) e^{j\omega(t-s_L l)} & j\omega\left(Z_L + Z_t\right) e^{j\omega(t+s_L l)} & e_{33} & 0 \\ -j\omega\left(Z_L - Z_b\right) e^{j\omega(t+s_L l)} & j\omega\left(Z_L + Z_b\right) e^{j\omega(t-s_L l)} & e_{33} & 0 \end{pmatrix} \begin{pmatrix} A_L \\ B_L \\ V_3^0 \\ V^0 \end{pmatrix} = \begin{pmatrix} V_0 e^{j\omega t} \\ -V_0 e^{j\omega t} \\ 0 \\ 0 \end{pmatrix}$$

[7.109]

Through a derivation analogous to the free plate case, we can calculate the electric admittance of the resonators as a function of the acoustic impedances applied to the boundaries of the piezoelectric film. Thus we get [LAK 90]:

$$Y(\omega) = \frac{j\omega \frac{\varepsilon_{33}}{2l}}{1 - k_t^2 \frac{\tan(\omega s_L l)}{\omega s_L l} \frac{\frac{Z_t + Z_b}{Z_L} \cos^2 \Phi + j \sin 2\Phi}{\frac{Z_t + Z_b}{Z_L} \cos 2\Phi + j\left(1 + \frac{Z_t Z_b}{Z_L^2}\right) \sin 2\Phi}} \qquad [7.110]$$

where $\Phi = \omega s_L l$ is the dephasing of the wave experiences when it travels across half the plate.

We find a form analogous to the one obtained for the ideal plate in section 7.2.1. A correction factor, depending on the frequency and the acoustic impedances of the adjacent media, nevertheless modifies the form of the admittance.

As for the ideal plate, the resonance condition is obtained by canceling the admittance denominator. Conversely, the frequency of antiresonance is obtained when this denominator is at a minimum. In these two cases, searching for an analytical solution becomes difficult because of the complexity of the denominator. We will nevertheless consider a few particular cases.

7.2.3. *Bimorph plate*

Here, the piezoelectric plate is considered as being positioned on a substrate e_S thick, density ρ_S and exhibiting a wave velocity V_S (for shear or longitudinal, depending on the type of waves generated in the piezoelectric film) as represented in Figure 7.7.

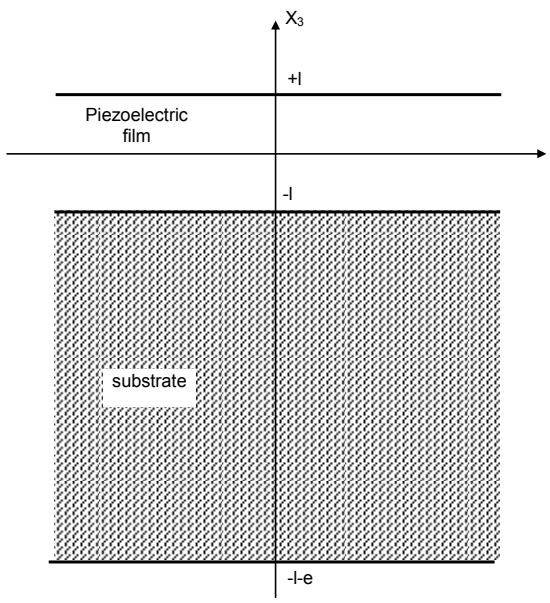

Figure 7.7. *Piezoelectric plate positioned on a substrate*

In the substrate, we assume that mechanical displacements and stresses are expressed in the form:

$$U_3 = A_S e^{j\omega(t - s_S X_3)} + B_S e^{j\omega(t + s_S X_3)} \quad [7.111]$$

$$T_{33} = j\omega Z_S \left(A_S e^{j\omega(t - s_S X_3)} - B_S e^{j\omega(t + s_S X_3)} \right) \quad [7.112]$$

A free surface condition is applied to the bottom surface of the substrate. Cancelling the stresses therefore leads to:

$$B_S = A_S e^{2j\omega s_S (l+e)} \quad [7.113]$$

If this relation is now re-inserted into the expression of displacements, and then in the expression of stresses on the upper surface of the substrate we get:

$$U_3 \left(X_3 = -l \right) = 2 A_S e^{j\omega s_S l} \cos \omega s_S e \quad [7.114]$$

$$T_{33} \left(X_3 = -l \right) = 2\omega Z_S A_S e^{j\omega s_S l} \sin \omega s_S e \quad [7.115]$$

The effective acoustic impedance at the level of the interface between the piezoelectric plate and substrate can therefore be calculated:

$$Z_b = j Z_S \tan \omega s_S e \quad [7.116]$$

By continuity of stresses and displacements at the interface between the two media, this is also the impedance "seen" on the bottom surface of the piezoelectric film. Furthermore, the upper surface of the piezoelectric film is free of stress, therefore $Zt = 0$. Electric admittance is consequently expressed:

$$Y(\omega) = j\omega \frac{\varepsilon_{33}}{2l} \frac{1}{1 - k_t^2 \dfrac{\tan(\Phi)}{2\Phi} \left(1 + \dfrac{Z_L \tan 2\Phi + Z_S \dfrac{\tan(\omega s_S e)}{\cos 2\Phi}}{Z_L \tan 2\Phi + Z_S \tan(\omega s_S e)} \right)} \quad [7.117]$$

We thus find an expression similar to the expression for the electric admittance of a simple piezoelectric plate vibrating on a thickness mode, but including a correction factor that takes into consideration the interaction with the additional film. Another expression commonly encountered is Sittig's expression [SIT 72]:

$$Y(\omega) = j\omega \frac{\varepsilon_{33}}{2l} \frac{1}{1 - \frac{k_t^2}{2\Phi} \frac{\frac{Z_S}{Z_L} \tan \omega s_S e + 2 \tan \Phi}{1 + \frac{Z_S}{Z_L} \frac{\tan \omega s_S e}{\tan 2\Phi}}} \qquad [7.118]$$

The condition for obtaining a resonance frequency always corresponds to the cancellation of the admittance denominator, namely:

$$\tan 2\Phi + \frac{Z_S}{Z_L} \tan \omega s_S e = \frac{k_t^2}{2\Phi} \left(2 \tan \Phi + \frac{Z_S}{Z_L} \tan \omega s_S e \right) \tan 2\Phi \qquad [7.119]$$

Similarly, the condition of antiresonance corresponds to the frequency at which this very denominator tends towards infinity, i.e.:

$$\tan 2\Phi + \frac{Z_S}{Z_L} \tan \omega s_S e = 0 \qquad [7.120]$$

Initially, we will assume that the added film is thin compared to the piezoelectric film. This is translated by condition $\omega s_S e << \Phi$. Using this approximation, admittance is simplified into:

$$Y(\omega) = j\omega \frac{\varepsilon_{33}}{2l} \frac{1}{1 - k_t^2 \frac{\tan \Phi}{\Phi} - R k_t^2 \tan^2 \Phi} \qquad [7.121]$$

where R is the mass ratio between substrate and piezoelectric film.

For an added film of low mass, the ratio, R, is low and the resonance condition, which corresponds to cancellation of the admittance denominator, is therefore close to the one obtained for a single plate. In these conditions, the change in resonance frequency is also low. We can then develop the denominator of equation [7.121] around Φ_0, which is the resonance frequency of the plate only, which is the solution to equation [7.98]. By a perturbation analysis, we express the relative frequency change due to the added mass as:

$$\frac{\Phi - \Phi_0}{\Phi_0} = -R \qquad [7.122]$$

This expression lets us show that the relative change in resonator mass leads to a relative change in frequency. It is on this principle that piezoelectric microbalances are realized. On the other hand, adding mass leads to a decrease in frequency. A more general approach reveals that the mass effect is, in practice, caused by a change in the resonator kinetic energy [YAN 04].

If we now consider the substrate to be very thick compared to the piezoelectric film, it becomes possible to consider the $\tan\Phi$ or $\tan 2\Phi$ terms as having an extremely slow change compared to the $\tan \omega s_S e$ terms. In practice, we can therefore consider them to be constants.

The conditions of resonance and antiresonance given by relations [7.119] and [7.120] are therefore solely conditioned by substrate thickness and by the velocity of propagation of waves in the latter. Neglecting even the change in $\tan\Phi$, we can see that the conditions of resonance and antiresonance present a periodicity related to that of the tangent function. The frequency period at which these conditions are satisfied is:

$$\Delta\omega s_S e = \pi \qquad [7.123]$$

i.e.:

$$\Delta f = \frac{1}{2 s_S e} = \frac{V_S}{2e} \qquad [7.124]$$

where V_S is the velocity of wave propagation in the substrate. This goes back to saying that a new resonance and antiresonance pair arises with each additional half wavelength in the thickness of the substrate.

7.2.4. *Piezoelectric plate between two electrodes*

In a manner similar to the bimorph plate, we will assume that the piezoelectric plate is sandwiched between two metal electrodes that we will assume to be symmetric in order to simplify the expressions. The acoustic impedance expression brought to the lower surface of the piezoelectric film is still given by equation

[7.116]. A similar calculation leads to an acoustic impedance brought to the upper surface of the piezoelectric film of:

$$Z_t = jZ_S \tan \omega s_S e \qquad [7.125]$$

The electric admittance of this resonator is consequently expressed:

$$Y(\omega) = \frac{j\omega \dfrac{\varepsilon_{33}}{2l}}{1 - \dfrac{k_t^2}{\left(1 - \left(\dfrac{Z_S}{Z_L}\right)^2 \tan^2 \omega s_S e\right)} \dfrac{\tan(\omega s_L l)}{\omega s_L l}} \qquad [7.126]$$

The condition of resonance is therefore expressed:

$$\tan(\omega s_L l) = \frac{1 - \left(\dfrac{Z_S}{Z_L}\right)^2 \tan^2 \omega s_S e}{k_t^2} \omega s_L l \qquad [7.127]$$

The graphic construction providing the frequency of resonance is similar to that obtained for the ideal plate, except that the presence of a correction factor on the right hand side, which is lower than 1, and which causes a decrease of the $y = \dfrac{1 - \left(\dfrac{Z_S}{Z_L}\right)^2 \tan^2 \omega s_S e}{k_t^2} x$ curve, thus causing a decrease of the resonance frequency compared to the unelectroded plate, as represented in Figure 7.8. This decrease is either much stronger than the acoustic impedance or the electrodes are very thick.

The expression for the admittance of the device (equation [7.126]) reveals admittance in the same form as for the ideal plate, but with an effective electromechanical coupling coefficient close to the frequency of antiresonance, which can be estimated as:

$$k_{eff}{}^2 \approx \frac{k_t{}^2}{1-\left(\frac{Z_S}{Z_L}\right)^2 \tan^2\left(\omega_R s_S e\right)} \qquad [7.128]$$

where ω_R is the angular frequency of the frequency of resonance.

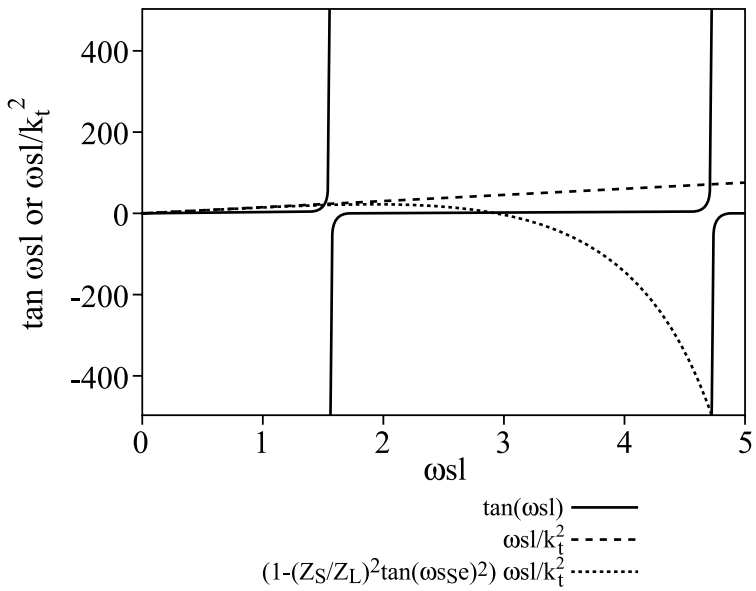

Figure 7.8. *Graphic representation of the condition of resonance for the vibration of a piezoelectric plate sandwiched between two electrodes*

We can therefore note that this effective coupling coefficient increases with the acoustic impedance of the metal film.

As with the case of the piezoelectric plate charged by a very thin film, if we assume that electrodes are very thin compared to the thickness of the piezoelectric film, we can transform the condition of resonance (equation [7.127]) into:

$$\frac{\tan \omega s_L l}{\omega s_L l} = \frac{1}{k_t{}^2}\left(1 - R^2\left(\omega s_L l\right)^2\right) \qquad [7.129]$$

where R is the ratio between the total mass of the electrodes and the mass of the piezoelectric film. A perturbation analysis enables us to retrieve the expression we have already established for the frequency change due to a small added mass:

$$\frac{\Phi_R - \Phi_0}{\Phi_0} = -R \qquad [7.130]$$

where, as before, Φ_0 is the phase change undergone by the acoustic wave when it crosses half the piezoelectric film at the resonance frequency of the piezoelectric film only, and Φ_R is the phase change undergone at the resonance frequency of the film sandwiched between two electrodes.

Re-inserting this result in the expression of the effective electromechanical coupling coefficient results in:

$$k_{eff}{}^2 = \frac{k_t{}^2}{1 - \left(\frac{Z_S}{Z_L}\right)^2 \tan^2\left(\omega_0 s_S e(1-R)\right)} \qquad [7.131]$$

Returning to the expression of the deviation between resonance and antiresonance frequencies for the ideal plate, and remembering that the antiresonance frequency is related to the plate thickness and the velocity of acoustic wave propagation in the piezoelectric material, the effective coupling coefficient can be expressed as a function only of the acoustic impedances of the materials and of the mass ratio:

$$k_{eff}{}^2 = \frac{k_t{}^2}{1 - \left(\frac{Z_S}{Z_L}\right)^2 \tan^2\left(\frac{\pi}{2}\left(1 - \frac{4k_t{}^2}{\pi}\right)\frac{Z_L}{Z_S} R(1-R)\right)} \qquad [7.132]$$

For a fixed acoustic impedance ratio, the effective coupling coefficient no longer only depends on the mass ratio, R. In this case it is at a maximum when the term $\tan^2\left(\frac{\pi}{2}\left(1 - \frac{4k_t{}^2}{\pi}\right)\frac{Z_L}{Z_S} R(1-R)\right)$ is also at its maximum. A first scenario bringing this term to be at maximum corresponds to the one where the tangent diverges, its argument being a multiple of $\pi/2$. To do this, R must be a second-order solution of the following equation:

$$R^2 - R + \frac{Z_S}{Z_L\left(1 - \frac{4k_t^2}{\pi}\right)} = 0 \qquad [7.133]$$

This is only possible if the discriminant of this equation is positive or zero, i.e. if:

$$Z_S \leq Z_L \frac{1 - \frac{4k_t^2}{\pi}}{4} \qquad [7.134]$$

This goes back to saying that the acoustic impedance of the metal used for electrodes must be extremely low. Most of the piezoelectric materials have acoustic impedances of the order of 20–50 MRayl. Condition [7.134] is therefore satisfied with difficulty, even when using aluminum, the common metal with the lowest acoustic impedance (except silver), as shown by Table 7.2.

Metal	**Acoustic impedance (MRayl)**
Aluminum	17
Silver	17
Copper	40
Nickel	52
Gold	62
Molybdenum	63
Tantalum	65
Ruthenium	73
Tungsten	94
Platinum	99
Iridium	120

Table 7.2. *Acoustic impedance of the most common metals*

In practice, therefore, the effective coupling coefficient never diverges. It is at a maximum when $R(1 - R)$ is maximum, i.e. for a mass ratio of ½. At that moment, we get a maximum effective coupling coefficient of:

$$k_{eff,\max}{}^2 = \frac{k_t{}^2}{1-\left(\frac{Z_S}{Z_L}\right)^2 \tan^2\left(\frac{\pi}{8}\left(1-\frac{4k_t{}^2}{\pi}\right)\frac{Z_L}{Z_S}\right)} \qquad [7.135]$$

7.2.5. *Equivalent electric circuit*

The form of the electric admittance of a bulk wave resonator (equation [7.100]) reveals a correction factor that corresponds to the plate capacitor formed by the piezoelectric medium sandwiched between a set of electrodes. An acoustic term is superimposed over this capacitance. Throughout the 7.2.4, we saw that this term depended on the considered structure. Nevertheless, it can still be mathematically represented by a pole appearing over the admittance. This admittance can therefore generally be expressed in the form:

$$Y = jC_0\omega\left(1+\frac{K}{1-\left(\frac{\omega}{\omega_0}\right)^2}\right) \qquad [7.136]$$

If we look for an equivalent electric circuit, superimposing a mathematical pole over the admittance of a capacitor is equivalent to considering a circuit in which a perfect capacitance C_0 is connected in parallel with a resonant circuit. The simplest of these circuits is a resonator composed of a capacitor and an inductor in series (an LC resonator). Indeed, such an assembly exhibits an admittance:

$$Y = jC_0\omega\left(1+\frac{C/C_0}{1-LC\omega^2}\right) \qquad [7.137]$$

with $\omega_0 = \frac{1}{\sqrt{LC}}$ and K the ratio between capacitances C and C_0. We thus find a circuit presenting the form of expression [7.136]. In practice, to better correspond with electric measurements, it is often useful to take dissipative phenomena into consideration and therefore add a resistance to the LC resonator. Thus we get the electric equivalent circuit, called the Butterworth-Van Dyke circuit represented in Figure 7.9. In this circuit, we distinguish the electric branch, which includes static capacitance C_0, and the motional branch corresponding to purely mechanical terms [VAN 28].

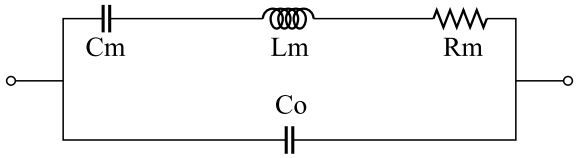

Figure 7.9. *Butterworth-Van Dyke circuit*

The admittance expression of this electric circuit is slightly more complicated than the one presented in the lossless case:

$$Y_{BVD} = jC_0\omega\left(1+\frac{K}{1-\left(\frac{\omega}{\omega_0}\right)^2+j\frac{\omega}{Q\omega_0}}\right) \qquad [7.138]$$

where the adimensional quantities traditionally used for an RLC resonant circuit, made of a resistor, an inductor and a capacitor in series, were introduced:

$$K = \frac{C_m}{C_0} \qquad [7.139]$$

$$\omega_0 = \frac{1}{\sqrt{L_m C_m}} \qquad [7.140]$$

$$Q = \frac{1}{R_m}\sqrt{\frac{L_m}{C_m}} \qquad [7.141]$$

To link the parameters of this equivalent circuit to the physical parameters of a bulk wave resonator, like those studied in section 7.2.4, we identify the specific characteristics of the frequency response. Thus, the resonance frequency corresponds to cancelling the denominator of equation [7.138], i.e.:

$$\omega = \frac{\omega_0}{2Q}\left(\sqrt{4Q^2-1}+j\right) \approx \omega_0\left(1+\frac{j}{2Q}\right) \qquad [7.142]$$

for large Q (i.e. a small motional resistance R_m and therefore low losses).

The mathematical effect of adding losses is that it shifts the admittance pole out of the real frequencies axis. Resonance is therefore generally defined as the projection of this pole onto the real frequencies axis, therefore $\omega_R = \omega_0$: the frequency of the resonator is the same as that of the equivalent RLC series circuit. At this frequency, most of the current crosses the RLC branch. Most of the electric energy is therefore concentrated in the motional branch, which is analogous to the observation made earlier, that at resonance most of the energy is concentrated in mechanical form in the resonator. The antiresonance frequency is given by the cancellation of admittance. This goes back to cancelling the numerator of equation [7.138], i.e.:

$$\left(\frac{\omega}{\omega_0}\right)^2 - j\frac{\omega}{Q\omega_0} - (K+1) = 0 \qquad [7.143]$$

and therefore:

$$\omega = \frac{\omega_0}{2Q}\left(\sqrt{4Q^2(K+1)-1} + j\right) \approx \omega_0\left(\sqrt{K+1} + \frac{j}{2Q}\right) \qquad [7.144]$$

Similarly to resonance, antiresonance is obtained by projecting the zero-admittance frequency onto the real axis, which leads to:

$$\omega_A = \omega_0\sqrt{K+1} \qquad [7.145]$$

Returning to the expression of ω_0 and K in terms of equivalent circuit parameters (equations [7.139] and [7.140]), we get:

$$\omega_A = \sqrt{\frac{C_m + C_0}{L_m C_m C_0}} = \frac{1}{\sqrt{L_m C_{eq}}} \qquad [7.146]$$

where the equivalent resistance "seen" at antiresonance is that given by theoretically putting C_0 and C_m in series. This shows that at this frequency, the current circulates in the motional branch and re-loops through the purely electric branch, producing an overall minimization of the current crossing the whole circuit.

In the perspective of equation [7.145], it is possible to link the effective electromechanical coupling coefficient to the ratio of the capacitances of the motional branches:

$$k_{eff}{}^2 \approx \frac{\pi^2}{4}\frac{\omega_A - \omega_R}{\omega_A} = \frac{\pi^2}{4}\frac{\sqrt{1+K}-1}{\sqrt{1+K}} \qquad [7.147]$$

hence the expression of the capacitance ratio:

$$K = \frac{1}{\left(1-\frac{4k_{eff}{}^2}{\pi^2}\right)^2} - 1 \approx \frac{8k_{eff}{}^2}{\pi^2}, \qquad [7.148]$$

for a small effective electromechanical coupling coefficient. In other words, the ratio of motional and static capacitances directly corresponds to half the relative spacing between resonance and antiresonance frequencies. As we were able to express the parameters of the equivalent circuit in terms of physical characteristics of the resonator (again, apart from the quality coefficient), we can re-write the admittance expression in terms of the latter:

$$Y_{BVD} = jC_0\omega\left(1+\frac{\frac{8k_{eff}{}^2}{\pi^2}}{1-\left(\frac{\omega}{\omega_R}\right)^2 + j\frac{\omega}{Q\omega_R}}\right) \qquad [7.149]$$

Maximum admittance is obtained at the resonance frequency:

$$Y_{\max} = \frac{8Qk_{eff}{}^2 C_0}{\pi^2}\omega_R + jC_0\omega_R \qquad [7.150]$$

Conversely, maximum impedance is obtained at the antiresonance frequency:

$$Z_{\max} = \frac{KQ}{C_0\omega_A\sqrt{K+1}} + \frac{1}{jC_0\omega_A} \approx \frac{8Qk_{eff}{}^2}{\pi^2 C_0\omega_A} + \frac{1}{jC_0\omega_A} \qquad [7.151]$$

in which we assumed again that the effective coupling coefficient was small. These last two relations reveal that the amplitudes of the real part of admittance at resonance or impedance at antiresonance are directly proportional to the product of the quality factor by the electromechanical coupling factor and by the admittance or impedance of the static capacitance at the frequency considered. As for the imaginary part, it corresponds each time to that of the static capacitance alone.

7.3. Bulk acoustic waves filter

Section 7.2 dealt in detail with how to form an electric resonator by exploiting the resonance of bulk acoustic waves in a piezoelectric medium. Expressions [7.150] and [7.151] show in particular that for resonators exhibiting high quality and electromechanical coupling factors, changes in electrical impedance can reach several orders of magnitude. It is consequently common to use these components as elements of variable impedance as a function of frequency. At first glance, it is indeed possible to consider the resonator as behaving like a closed switch at resonance (its electric impedance becomes very small) and like an open switch at antiresonance (its electric impedance becomes very large). The most frequent use consists of associating bulk acoustic wave resonators in band-pass filter circuits. The most common of these circuits is the ladder structure, as represented in Figure 7.10, where some resonators are placed in series between the input and output of the filter, and another set of resonators is placed in parallel arms. This structure was initially proposed by Espenschied of AT&T to synthesize filters using quartz bulk acoustic wave resonators [BER 78].

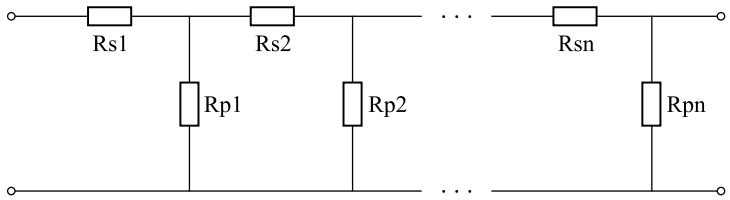

Figure 7.10. *Ladder structure of a filter*

In general, all resonators displayed on the series arm have the same resonance frequency, while all resonators displayed on parallel arms have a different frequency.

To obtain a circuit allowing a signal to pass through at the center frequency of the filter, we arrange for the series resonators to be at their resonance frequency, in such a way that they behave like closed switches. Meanwhile parallel resonators must be at their antiresonance frequency, in order to behave like open switches, so that it looks like the diagram in Figure 7.11a. When this happens, the filter behaves like a completely conducting circuit, since current and voltage are transferred practically unchanged from the entrance to the exit.

At the frequency of resonance of the parallel resonator, which is lower than the center frequency, the connection behaves like a short circuit, as illustrated in Figure 7.11b. This prevents the signal from being transmitted.

Conversely, at the antiresonance frequency of the parallel resonators, which is higher than the center frequency, the connection presents open switches near the entrance and exit of the filter, as represented in Figure 7.11c. Here again, the electric signal can no longer be transmitted.

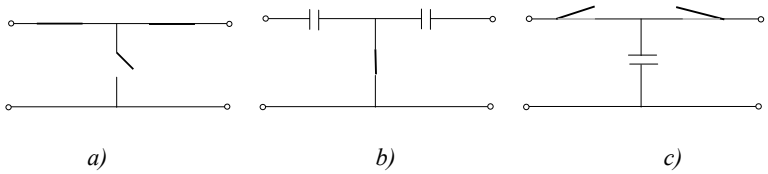

Figure 7.11. *Principle of operation of a ladder filter: a) at center frequency; b) at the resonance of parallel resonators; and c) at antiresonance of series resonators*

To simplify the calculations, let us consider a filter composed of only one series resonator and one parallel resonator. We calculate the transmission of the two-port network formed by a ladder section.

$$S_{21} = \left.\frac{b_2}{a_1}\right|_{a_2=0} = \left.\frac{V_2 - Z_0 I_2}{V_1 + Z_0 I_1}\right|_{V_2=-Z_0 I_2} \qquad [7.152]$$

where the currents and voltages are defined as illustrated in Figure 7.12.

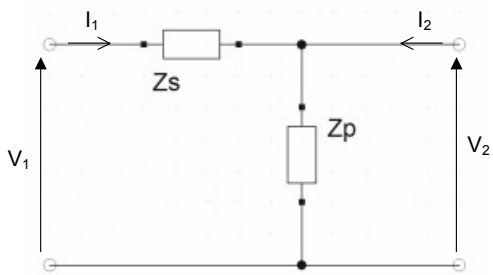

Figure 7.12. *Definition of the currents and voltages used for the filter analysis*

By classically applying Kirchhoff's laws, we express all the currents and voltages as a function of the input current:

$$I_2 = -\frac{Z_p}{Z_0 + Z_p} I_1$$
$$V_2 = \frac{Z_0 Z_p}{Z_0 + Z_p} I_1 \qquad [7.153]$$
$$V_1 = \frac{Z_0 Z_p + Z_s Z_0 + Z_s Z_p}{Z_0 + Z_p} I_1$$

Finally, we form the relation giving the transmission of a single filter section:

$$S_{21} = \frac{2 Z_0 Z_p}{Z_0^2 + Z_s Z_p + Z_s Z_0 + 2 Z_0 Z_p} = \frac{2 Z_0 Y_s}{1 + Z_0 Y_p + 2 Z_0 Y_s + Z_0^2 Y_s Y_p} \qquad [7.154]$$

The transfer function obtained is illustrated in Figure 7.13.

At antiresonance of the series resonator and resonance of the parallel resonator, transmission tends towards 0. It is high, however, at the center frequency f_0, which was chosen as corresponding to the resonance of the series resonator and the antiresonance of the parallel resonator.

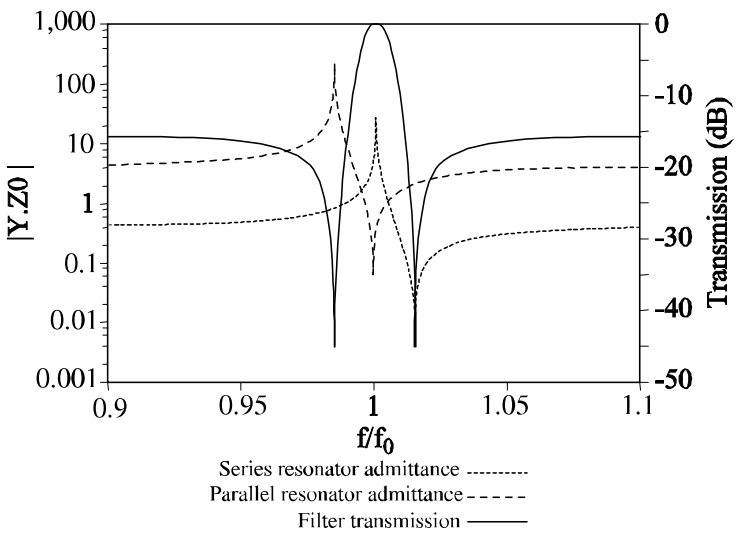

Figure 7.13. *Resonator admittances and associated filter transmission*

Several frequencies are particularly interesting.

At *resonance of the parallel resonator*, filter transmission is equal to:

$$S_{21} \approx \frac{2Z_0 Y_s}{Z_0\left(1+Z_0{}^2 Y_s\right)Y_p} \qquad [7.155]$$

since Y_p becomes dominant compared to Y_s and Z_0. Transmission, as we said before, tends towards 0.

At *antiresonance of the series resonator*, the contribution of admittance of this resonator becomes negligible and so:

$$S_{21} \approx \frac{2Z_0 Y_s}{1+Z_0 Y_p} \qquad [7.156]$$

and the transmission also tends towards 0, as we expect from more practical considerations.

Far from resonances, we can compare Y_s and Y_p solely through the expression of their capacitances, i.e. at low frequency:

$$\begin{aligned} Y_s &\approx jC_{0s}\omega\left(1+K_s{}^2\right) \\ Y_p &\approx jC_{0p}\omega\left(1+K_p{}^2\right) \end{aligned} \qquad [7.157]$$

and at high frequency:

$$\begin{aligned} Y_s &\approx jC_{0s}\omega \\ Y_p &\approx jC_{0p}\omega \end{aligned} \qquad [7.158]$$

In these conditions, at high frequency, the transmission module is expressed:

$$|S_{21}| \approx \frac{\omega C_{0s} Z_0}{\sqrt{1+4\left(\omega C_{0s} Z_0\right)^2 + R^2\left(\left(\omega C_{0s} Z_0\right)^2 + \left(\omega C_{0s} Z_0\right)^4\right)}} \qquad [7.159]$$

where R was introduced as being the ratio between static capacitance of the series resonator and that of the parallel resonator. An equivalent expression is obtained by replacing the value of the series resonator capacitance at high frequency with the value it presents at low frequency: $C_{0s}\left(1+K_s{}^2\right)$. This relation shows that

transmission is approximately inversely proportional to the capacitance ratio of both types of resonator. This is illustrated in Figure 7.14. Hence, to increase the rejection of such a filter, it is necessary to increase the ratio of the static capacitances.

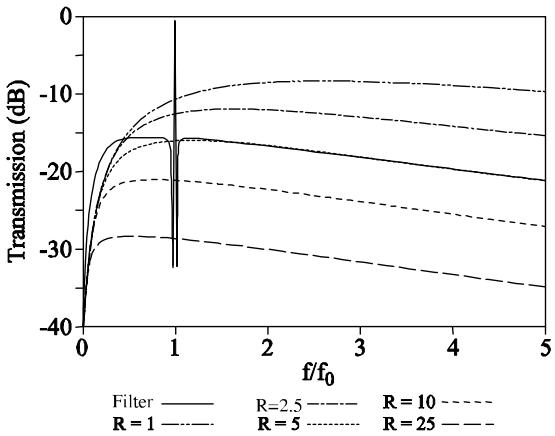

Figure 7.14. *Influence of the ratio of static capacitances of series and parallel resonators on out-of-band rejection*

At *center frequency*, the series resonator presents its maximum admittance, while the parallel resonator presents its maximum impedance. Assuming that the two types of resonators have approximately the same electromechanical coupling coefficients and quality factors, it results that:

$$S_{21} = \frac{2Z_0 Y_{s\max}}{1+\frac{Z_0}{Z_{p\max}}+2Z_0 Y_{s\max}+\frac{Z_0^{\,2} Y_{s\max}}{Z_{p\max}}}$$

$$= \frac{2jZ_0\left(1+K^4Q^2\right)C_{0s}\omega_0}{jC_{0p}\omega_0 Z_0+\left(1+jK^2Q\right)+2jC_{0s}\omega_0 Z_0\left(1+K^4Q^2\right)-C_{0p}C_{0s}\omega_0^{\,2}Z_0^{\,2}\left(1-jK^2Q\right)} \quad [7.160]$$

For AlN thin film-based bulk wave resonators, the quality factors are in the order of 1000 for electromechanical coupling coefficients bringing $K^2 = 5\%$, which gives a product K^2Q in the order of 50, which we will assume to be large compared to 1. In other words, we assume that at this frequency the effect of static capacitances of resonators is completely masked by resonances and antiresonances. Under these conditions:

$$S_{21} \approx \frac{1}{1+\dfrac{C_{0p}C_{0s}\omega_0{}^2 Z_0{}^2 K^2 Q}{2C_{0s}\omega_0 Z_0 K^4 Q^2}} \approx 1-\frac{C_{0p}\omega_0 Z_0}{2K^2 Q} \qquad [7.161]$$

This simplified expression makes it seem that filter losses, i.e. the maximum level of transmission, originate in two distinct causes: the impedance of the static capacitance of the parallel resonator at center frequency, compared to the characteristic impedance of the external circuit. The higher this capacitance, the more important the losses are. A comparison with relation [7.159] shows that at this level, a compromise must be found between maximizing the capacitance of the parallel resonator to provide a high rejection and minimizing this rejection to maximize the filter transmission. Insertion losses are highly dependent on the figure of merit QK^2, i.e. finally on the amplitude of impedance changes of the resonators. Therefore, for filter applications, we look towards simultaneously maximizing the quality factors and electromechanical coupling coefficients of resonators.

7.4. Bibliography

[BER 78] BERTÉ M. and HARTEMANN P., "Quartz resonators at fundamental frequencies greater than 100 MHz", *Proceedings of the 1978 IEEE Ultrasonics Symposium*, p. 148, 1978.

[IEE 87] IEEE Standard on Piezoelectricity, ANSI/IEEE Std 176-1987.

[LAK 90] LAKIN K.M., "Fundamental properties of thin film resonators", *Proceedings of the 45th Annual Symposium on Frequency Control*, p. 201, 1990.

[ONO 69] ONOE M., "Thickness-twist vibrations of a piezoelectric plate", *Trans. Inst. Electr. & Comm. Engr. Japan*, vol. 52-A(10), p. 38-43, 1969.

[ROS 45] ROSENBAUM J.F., *Bulk Acoustic Waves Theory and Devices*, Artech House, 1945.

[SIT 72] SITTIG E.K., "Design and technology of piezoelectric transducers for frequencies above 100 MHz", in *Physical Acoustics vol. IX*, MASON W.P. and THURSTON R.N. (eds.), Academic Press, 1972.

[TIE 69] TIERSTEN H.F., *Linear Piezoelectric Plate Vibrations: Elements of the Linear Theory of Piezoelectricity and the Vibration of Piezoelectric Plates*, Plenum, 1969.

[VAN 28] VAN DYKE K.S., "The piezo-electric resonator and its equivalent network", *Proceedings of the IRE*, 1928

[YAN 04] YANG J., "Frequency shifts in a piezoelectric body due to small amounts of additional mass on its surface", *IEEE. Transactions on Ultrasonics, Ferroelectrics and Frequency Control*, vol. 51, n°10, p. 1199, 2004.

Chapter 8

Electrostrictive Formalism

8.1. Foundations of electrostriction

Electrostriction appears in all dielectric materials. Whereas the indirect piezoelectric effect induces a linear dependence on mechanical strain due to the imposed electric field, electrostriction induces a quadratic change in it. The piezoelectric effect only appears in non-centrosymmetric crystal lattices, whereas electrostriction appears in all dielectric materials. For these non-centrosymmetric lattices, the electrostrictive effect is often negligible compared to the piezoelectric effect and therefore rarely considered. The quadratic character of electrostriction made it less frequently studied than piezoelectricity. However, the study of PMN ($Pb(Mg,Nb)O_3$), an electrostrictive relaxor material (in a Relaxor, whether we consider the temperature at which the dielectric constant maximum takes place depends on the frequency) proved that strain could reach the same values as the best piezoelectrics, of the order of a few tenths of a per cent without the inconvenience of hysteresis [DAM 92]. Many books therefore have been produced about these quadratic, electroactive materials, mainly based on Pb around PMN. It was, above all, ceramics and single crystals that were studied, especially to better understand how these relaxor materials work.

Electrostriction is often defined with the following formula, linking strain, S, to polarization, P, with the electrostrictive term Q. The relationship between P and the electric field E (ε_r: relative permittivity, ε_0: vacuum permittivity) is added:

$$S = QP^2 = Q\varepsilon_0^2\varepsilon_r^2 E^2 \qquad [8.1]$$

Chapter written by Emmanuel DEFAŸ.

If a constant field strength E_0 is applied to an alternative field e that is negligible compared to E_0, to the first order the term E^2 becomes $E_0^2 + 2E_0e$.

The strain therefore becomes:

$$S = Q\varepsilon_0^2\varepsilon_r^2 E_0^2 + 2Q\varepsilon_0^2\varepsilon_r^2 E_0 e \qquad [8.2]$$

On the right part of this equation, the left term describes the static strain whereas the right term can be qualified as piezoelectric induced with coefficient $d_{induced}$ such that:

$$d_{induced} = 2Q\varepsilon_0^2\varepsilon_r^2 E_0 \qquad [8.3]$$

This coefficient therefore shows that, in an electrostrictive material (and therefore a paraelectric perovskite), an induced piezoelectric effect can be generated. The intensity of this effect varies linearly with the continuous electric field applied. This change in piezoelectric coefficient results in a change in the electromechanical coupling coefficient.

This electrostrictive solution forces us to conserve a constant voltage while operating, especially in the case of an acoustic resonator. If the dielectric losses are low, the consumption that results from this mode of operation must be negligible because work is null.

It can be interesting to remain in the paraelectric phase to make a tunable frequency resonator with a continuous voltage: there are no domain walls so there is a decrease in losses and no hysteresis due to the continuous field applied.

The most studied materials are principally $SrTiO_3$, $(Ba,Sr)TiO_3$ (BST) and $Pb(Mg,Nb)TiO_3$ because they are available in thin films and can present a Curie lower than ambient temperature. Let us recall, however, that all dielectrics present an electrostrictive effect.

8.2. Thermodynamic model of electrostriction – case of the resonator

For this model, it is imperative that the approaches are distinguished according to the paraelectric case and the piezoelectric case. Indeed, in the first case, the lattice considered is centro-symmetric. Therefore, no terms with an odd order electric contribution can exist, so they are directly eliminated. In the pure piezoelectric case like quartz or the pyroelectric case like AlN, the material is non centro-symmetric. This forces us to leave the odd terms and especially the piezoelectric term. In the case of ferroelectrics, even when the working temperature is lower than Curie

temperature, we can use an even development in free energy similar to the paraelectric case. Adding the spontaneous polarization in the formalism induces apparition of the piezoelectric term. We already addressed the formalism in Chapter 3. Here, we will provide a few extra details.

The way to deal with this problem has been suggested in the literature by several authors [NÖT 07, VEN 08, VOL 08]. Here, we propose to summarize these works, which all have the same basis. The key to this calculation is to find the dominant parameters that enable us to explain the change in frequencies of resonance and antiresonance of the resonators due to the continuous voltage applied. Electrostriction can explain the coupling change observed (therefore the separation between resonance and antiresonance); whereas the quadratic mechanical change in stiffness due to the voltage applied gives the correct order of magnitude of the drift of the two frequencies due to the continuous voltage. The very significant change in the dielectric constant due to voltage is part of the development. The choice of electric variable used in the free energy is the electric displacement D, because it is this displacement that has the most physical sense. Indeed, we saw before that paraelectric-ferroelectric transition could be described by the same form of free energy using polarization as the order parameter. This choice also gives us the opportunity to use coefficients already identified and quantified in the literature. We will note that certain authors make the distinction between polarization and electric displacement in this method. Actually, Nöth says that only one part of the paraelectric is susceptible to polarizing, like a ferroelectric, whereas it remains a part of the material that can be considered as a much less polarizable dielectric (a notion called *background permittivity*) [NOT 09]. The effect is very weak, however, because typically the relative constant of this not very polarizable permittivity is 7 in BST for a "ferroelectric" constant around 300, which represents a bit more than 2%. Today, experimental results do not need this degree of finesse to understand and anticipate the behaviors of these resonators. We will therefore neglect this not very polarizable permittivity and we will consider a free energy that uses electric displacement as a variable.

For the mechanical variable, the simplest thing is to choose the strain, especially in the case of a thin film resonator. Indeed, as the films are placed on a rigid substrate, the thin film hypothesis imposes a null strain in the plane ($S_1 = S_2 = 0$). Thus, only the out-of-plane strain S_3 is non-zero. Dealing with the equations therefore looks like a problem with a single dimension (the axis perpendicular to the film's plane), which is very practical.

The free energy to consider is the one that uses (D,S) as variables, in other words *Helmholtz free energy*, F. We assume that we are working at constant temperature, which eliminates the heat term, $\sigma d\theta$, in the expression of the total differential, dF. The terms introduced in this energy are:

– the electric terms in D^2 and D^4 (necessary for taking into consideration the strong change in permittivity) and then its nonlinearity;

– the mechanical term in S^2;

– the electrostrictive coupling term in SD^2; and

– the nonlinear electrostriction term in S^2D^2.

This development does not take into consideration the other terms that it would be *a priori* logical to add to conserve the same orders of power. Thus, the change in stiffness due to strain (the energy term in S^3 and S^4) is not considered as its change is extremely small compared to the other terms. It is very important to note that this argument is *valid for materials with a very large change in polarization due to the electric field* (such as perovskites).

We recall that $dF = TdS + EdD - \sigma d\theta$. F therefore takes the following form:

$$F - F_0 = \frac{1}{2}c_0^D S^2 + \frac{1}{2}\beta^S D^2 + \frac{1}{4}\gamma^S D^4 + GD^2 S + \frac{1}{2}MS^2 D^2 \qquad [8.4]$$

We will note that the fractions in front of each term are determined by use more than by a perfect logic. The initial idea is to no longer have any multiplying term after derivation, but this does not apply for the electrostrictive term for which we assume a stress of the form GD^2. The term ½ is added in front of the nonlinear electrostriction term for a state-of-the-art conforming. These factors are not fundamentally useful but must be treated with precision as they are often subject to error when the various books are compared.

In this expression, S and D are considered as referring to the out-of-plane component, in other words, S_3 and D_3 respectively. As $S_1 = S_2 = 0$ for a thin film on a substrate and we neglect all shear; only S_3 is non-null. For D, we also consider $D_1 = D_2 = 0$ (plane capacitor), therefore only D_3 is non-zero. The problem is one-dimensional. It is possible to express F with all its components, but we choose to keep this simple model to highlight the most important points of this electrostrictive approach.

At the level of coefficients appearing in equation [8.4]:

– c_0^D is the coefficient of rigidity c^D_{33} at fixed D;

– β^S is the dielectric impermittivity constant β^S_{33} at fixed S;

– γ^S is the coefficient γ^S_{3333} of the nonlinear tensor of dielectric impermittivity at fixed S;

– G is the coefficient G_{3333} of the electrostriction tensor in the formalism *(S,D)*; and

– M is the coefficient M_{3333} of the nonlinear electrostriction tensor.

It is noteworthy that the electrostriction tensor is a tensor of fourth order.

With this formalism, the conjugate variables S and D are obtained by the following partial derivatives of F:

$$\left.\frac{\partial F}{\partial S}\right)_D = T \qquad \left.\frac{\partial F}{\partial D}\right)_S = E \qquad [8.5]$$

Thus we have:

$$\begin{aligned} T &= c_0^D S + GD^2 + MSD^2 \\ E &= \beta^S D + \gamma^S D^3 + 2GSD + MS^2 D \end{aligned} \qquad [8.6]$$

8.3. The electrostriction tensor

Similarly to piezoelectricity, several formalisms are possible for electrostriction depending on the natural variables chosen. Each time a fourth-order tensor is involved. Two other formalisms are often presented in the literature; these formalisms are different to the one presented before ($T = GD^2$): $S = ME^2$ and $S = QD^2$ (or QP^2 identifying P with D in strong permittivity dielectrics).

Using the index representation and not omitting the eventual presence of a piezoelectric effect, we have:

$$S_{ij} = d_{kij} E_k + M_{klij} E_k E_l \qquad S_{ij} = g_{kij} D_k + Q_{klij} D_k D_l \qquad [8.7]$$

In the same way as for the elasticity tensor, it is possible to move on to a contracted notation by respecting the following rule for Q and M, which are defined in relation to S, which is subject to the conversion rule:

$$\begin{aligned} &Q_{mn} = Q_{ijkl} \ \ (m, n = 1,2,3) \\ &Q_{mn} = 2Q_{ijkl} \ \ (m \text{ or } n = 4,5,6) \\ &Q_{mn} = 4Q_{ijkl} \ \ (m \text{ and } n = 4,5,6) \end{aligned} \qquad [8.8]$$

On the other hand, G is not subject to this rule because it is defined in relation to T.

Respecting symmetries enables us to decrease the independent coefficients based on the point groups considered. In the same way that we presented for piezoelectric crystals, the most useful electrostrictive tensors are given in Table 8.1 (see [UCH 97] for the other point groups). It must be noted that the electrostriction tensor is not necessarily symmetric, unlike the elasticity tensor.

6mm	*4mm*
$\begin{pmatrix} Q_{11} & Q_{12} & Q_{31} & 0 & 0 & 0 \\ Q_{12} & Q_{11} & Q_{31} & 0 & 0 & 0 \\ Q_{13} & Q_{13} & Q_{33} & 0 & 0 & 0 \\ 0 & 0 & 0 & Q_{44} & 0 & 0 \\ 0 & 0 & 0 & 0 & Q_{44} & 0 \\ 0 & 0 & 0 & 0 & 0 & 2(Q_{11}-Q_{12}) \end{pmatrix}$	$\begin{pmatrix} Q_{11} & Q_{12} & Q_{31} & 0 & 0 & 0 \\ Q_{12} & Q_{11} & Q_{31} & 0 & 0 & 0 \\ Q_{13} & Q_{13} & Q_{33} & 0 & 0 & 0 \\ 0 & 0 & 0 & Q_{44} & 0 & 0 \\ 0 & 0 & 0 & 0 & Q_{44} & 0 \\ 0 & 0 & 0 & 0 & 0 & Q_{66} \end{pmatrix}$
3m and *32*	*m3m*
$\begin{pmatrix} Q_{11} & Q_{12} & Q_{31} & Q_{41} & 0 & 0 \\ Q_{12} & Q_{11} & Q_{31} & -Q_{41} & 0 & 0 \\ Q_{13} & Q_{13} & Q_{33} & 0 & 0 & 0 \\ Q_{14} & -Q_{14} & 0 & Q_{44} & 0 & 0 \\ 0 & 0 & 0 & 0 & Q_{44} & 2Q_{14} \\ 0 & 0 & 0 & 0 & Q_{41} & 2(Q_{11}-Q_{12}) \end{pmatrix}$	$\begin{pmatrix} Q_{11} & Q_{12} & Q_{12} & 0 & 0 & 0 \\ Q_{12} & Q_{11} & Q_{12} & 0 & 0 & 0 \\ Q_{12} & Q_{12} & Q_{11} & 0 & 0 & 0 \\ 0 & 0 & 0 & Q_{44} & 0 & 0 \\ 0 & 0 & 0 & 0 & Q_{44} & 0 \\ 0 & 0 & 0 & 0 & 0 & Q_{44} \end{pmatrix}$
Isotropic	
$\begin{pmatrix} Q_{11} & Q_{12} & Q_{12} & 0 & 0 & 0 \\ Q_{12} & Q_{11} & Q_{12} & 0 & 0 & 0 \\ Q_{12} & Q_{12} & Q_{11} & 0 & 0 & 0 \\ 0 & 0 & 0 & 2(Q_{11}-Q_{12}) & 0 & 0 \\ 0 & 0 & 0 & 0 & 2(Q_{11}-Q_{12}) & 0 \\ 0 & 0 & 0 & 0 & 0 & 2(Q_{11}-Q_{12}) \end{pmatrix}$	

Table 8.1. *Electrostrictive tensors of point groups 6mm, 4mm, 3m, 32, m3m and isotropic materials*

We must note that the most useful tensors are *m3m* and isotropic materials because electrostriction is most often used without piezoelectric effect, as for

example with $(Ba,Sr)TiO_3$ or $Pb(Mg,Nb,Ti)O_3$ perovskite films in the paraelectric phase (*m3m*).

These formulae are valid for Q and M. For G, the $2(Q_{11} - Q_{12})$ terms must be changed into $(G_{11} - G_{12})/2$ and finally, term $2Q_{14}$ into tensors *3m,* and *32* is replaced by G_{14}.

8.4. Microscopic model of electrostriction

8.4.1. *One-dimensional model*

Just as for piezoelectricity, it is possible to suggest a one-dimensional model based on the succession of two ions of opposite sign, joined by springs. In the case of electrostriction, to suppress piezoelectricity the springs chosen are identical to each other (see Figure 8.1). For this example, we also use a method based on an energy balance to reveal the electrostrictive term. In the piezoelectric case, we saw that it was imperative that the springs have different stiffnesses for electromechanical coupling to appear.

In the electrostrictive case, the springs are identical. To produce coupling, it is therefore imperative to reveal nonlinearities in the model. The most natural thing is to include a nonlinear stiffness for each spring. In other words, we assume that the springs are easier to stretch than to compress. Therefore, this nonlinearity allows us to see that the stiffness of the two adjacent springs is not exactly the same, as one of the springs is compressed when the other is stretched. Indeed, it is harder to get closer to an ion than to move away from it (which is modeled by the Born Mayer potential in statistical physics). The stiffness, k, of the springs is therefore defined as:

$$k = k_1 - k_2 \delta a \qquad [8.9]$$

We will see that this method enables us to produce an electromechanical coupling.

The dipole moment is null in the absence of an electric field, E. When E is present, δp is equal to $q/2(\delta a - 2\delta b)$. The equilibrium of each ion is still valid and, taking into consideration the nonlinearity of the springs, we have:

$$\frac{-qE}{2k} + \frac{\delta a}{2} = \delta b \qquad [8.10]$$

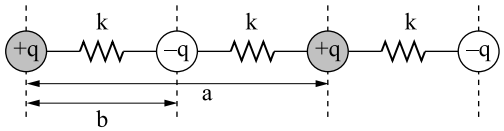

Figure 8.1. *One-dimensional model of an electrostrictive chain of ions*

The different energy contributions to local Gibbs' electric energy, G_2, for one section (from one positive ion to another) are the elastic energy stored in the two springs and the dipole energy $-pE$. G_2 is always the energy that translates system equilibrium since the natural variables are strain ($S = \delta a/a$) and electric field. δG_2 is therefore:

$$\delta G_2 = \frac{1}{2}k\left[\delta(a-b)\right]^2 + \frac{1}{2}k\left[\delta(b)\right]^2 - \delta pE \qquad [8.11]$$

If k is not developed, δG_2 takes the following form:

$$\delta G_2 = \frac{1}{4}k(\delta a)^2 - \frac{q^2E^2}{4k} \qquad [8.12]$$

If k is simply equal to k_1, we see that there is no coupling term in this energy, in accordance with what we expected. The first term corresponds to mechanical energy and the second to dipole energy. Nonlinearity is then introduced in the stiffness. To give a form that is easily exploitable, we can assume a weak nonlinearity, which enables us to make a first-order expansion. δG_2 becomes:

$$\delta G_2 = \frac{1}{4}k_1(\delta a)^2 - \frac{1}{4}k_2(\delta a)^3 - \frac{q^2E^2}{4k_1\left(1-\frac{k_2}{k_1}\delta a\right)} \approx \frac{1}{4}k_1(\delta a)^2 - \frac{1}{4}k_2(\delta a)^3 - \frac{q^2E^2}{4k_1} - \frac{q^2k_2}{4k_1^2}\delta aE^2$$

[8.13]

Returning to the definition of strain, $S = \delta a/a$, δG_2 takes the following form:

$$\delta G_2 \approx \frac{1}{4}a^2k_1S^2 - \frac{1}{4}k_2a^3S^3 - \frac{q^2E^2}{4k_1} - \frac{q^2ak_2}{4k_1^2}SE^2 \qquad [8.14]$$

This form of energy clearly highlights a quadratic mechanical energy term, another of the third order, a quadratic dipole energy term and the SE^2 electromechanical coupling term. In the same way as those defined for the

microscopic piezoelectric model, the S and E derivatives (respectively, lineic strain t and polarization p) give:

$$\left.\frac{\partial \delta G_2}{\partial S}\right)_E = t = \frac{1}{2}a^2 k_1 S - \frac{3}{4}k_2 a^3 S^2 - \frac{q^2 a k_2}{4k_1^2}E^2$$
$$-\left.\frac{\partial \delta G_2}{\partial E}\right)_S = p = \frac{q^2 E}{2k_1} + \frac{q^2 a k_2}{2k_1^2}SE \qquad [8.15]$$

This form is very similar to the electrostrictive thermodynamic formalism highlighted in equation [8.6]. The various terms are therefore:

$\frac{1}{2}a^2 k = c_0^E$: linear stiffness;

$\frac{3}{4}k_2 a^3 = c_1^E$: nonlinear stiffness;

$\frac{q^2}{2k_1} = \chi_{ion}^S$: dielectric susceptibility; and

$\frac{q^2 a k_2}{4k_1^2} = g$: the electrostrictive coefficient that enables electromechanical coupling.

We get:

$$t = \left(c_0^E - c_1^E S\right)S - gE^2$$
$$p = \chi_{ion}^S E + 2gSE \qquad [8.16]$$

We see that if the nonlinear stiffness coefficient (k_2) is null, there is no longer coupling.

8.4.2. *Origin of spontaneous polarization in perovskite crystals*

It is possible to suggest a simple microscopic model enabling us to arrive at an energy expression, highlighting the presence of spontaneous polarization in materials such as perovskites. Actually, we could think that they should conserve a non-polar stable state, like when temperature is above Curie temperature (point group *m3m*). Taking into consideration dipole and elastic energies enables us to

produce this spontaneous polarization. This model is interesting as it enables us to create a local idea of the meaning of spontaneous polarization. We must, however, note that in the case of perovskites, the true microscopic model is quite far from this ion-related view. Indeed, at the end of the 1980s, Cohen showed that it was the covalent nature of the B-O combination that is responsible for the ferroelectric character of this structure [COH 92].

To simplify things, let us assume a crystal structure in which the dipole moment, p, is due to the displacement of one single type of A ion in the crystal lattice. The presence of all the dipole moments induces a polarization, P, which creates a local electric field, E_l, even in the absence of a macroscopic field (as discussed in Chapter 5, dealing with the electric term of energy). If ion A has a polarizability α, we see that $p = \varepsilon_0 \alpha E_l$. In the Lorentz field hypothesis (isotropic case) with $E_{ext} = 0$, the local field takes expression $E_l = P/3\varepsilon_0$, which gives:

$$p = \frac{\alpha P}{3} \qquad [8.17]$$

The energy of this dipole moment, w_{dip}, is:

$$w_{dip} = -p.E_l = -\frac{\alpha P^2}{9\varepsilon_0} \qquad [8.18]$$

If there are N ions per unit of volume, the energy per unit of volume W_{dip} is therefore:

$$W_{dip} = -\frac{N\alpha P^2}{9\varepsilon_0} \qquad [8.19]$$

The displacement, u, of A ions is limited by the repulsion between the ions. The elastic energy of the crystal lattice must therefore increase. Let us assume that this repulsion is described by a spring with a linear term (k) and a quadratic term (k') essential here. The expression of elastic energy per unit of volume, W_{el}, is:

$$W_{el} = N\left(\frac{1}{2}ku^2 + \frac{1}{4}k'u^4\right) \qquad [8.20]$$

On the other hand, polarization P is none other than Nqu, where q is the charge carried by the A ion. Substituting u for P, total energy W_{tot} becomes:

$$W_{tot} = W_{el} + W_{dip} = N\left(\frac{1}{2}k\frac{P^2}{N^2q^2} + \frac{1}{4}k'\frac{P^4}{N^4q^4}\right) - \frac{N\alpha P^2}{9\varepsilon_0}$$
$$= \left(\frac{k}{2Nq^2} - \frac{N\alpha}{9\varepsilon_0}\right)P^2 + \frac{k'}{4N^3q^4}P^4 \qquad [8.21]$$

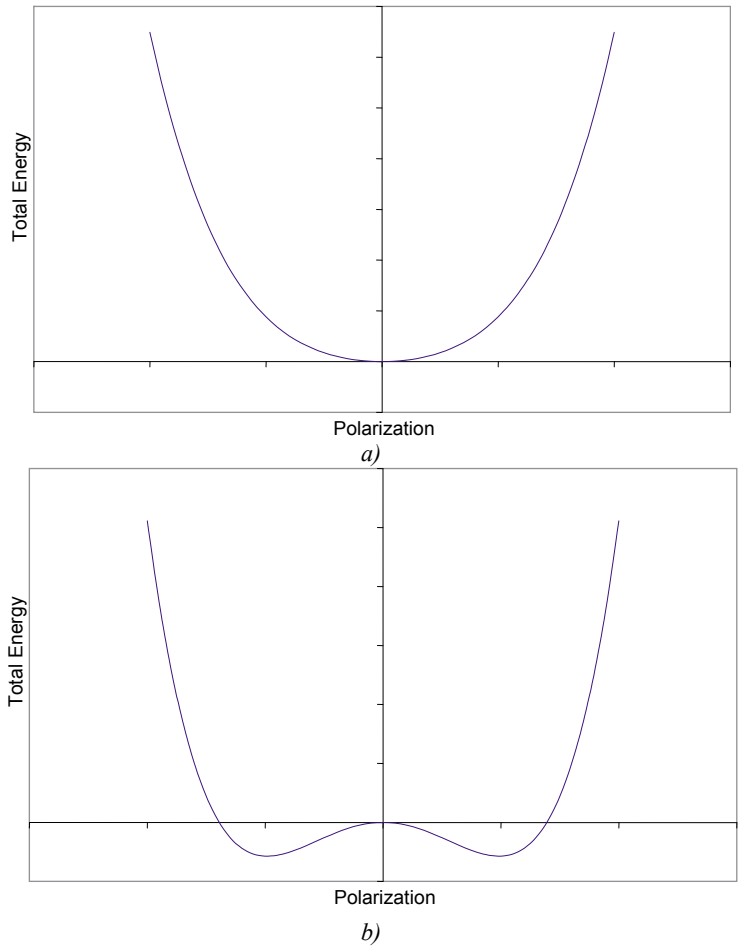

Figure 8.2. *Illustration of the total energy of a crystal lattice taking into consideration the dipole and elastic energies: a) quadratic elastic energy term > dipole energy; and b) quadratic elastic energy term < dipole energy*

Looking at this equation, we see that the sign of the P^2 term determines whether or not there are two different stable positions of $P = 0$. Indeed, deriving W_{tot} in relation to P, we get a solution for non-zero P:

$$P_S^2 = \frac{8N^3q^4}{k'}\left(\frac{N\alpha}{9\varepsilon_0} - \frac{k}{2Nq^2}\right) \qquad [8.22]$$

In the case where the harmonic elastic term (k) is greater than the dipole term, there is only one stable position in $P = 0$; whereas when the dipole term is greater than the elastic harmonic term, the stable position corresponds to a non-zero polarization given by equation [8.22]: it is the spontaneous polarization. This is illustrated in Figure 8.2. We find the same shapes of curves as in the macroscopic thermodynamic formalism but on a local scale.

8.5. Electrostrictive resonator

We saw that electrostriction induces an equation pair that is more complex than those of the piezoelectric formalism (see equation [8.6]). It is however possible to find a more customary form with which the same acoustic approach can be used to deal with the resonances of a resonator. To do this, we assume that a continuous voltage is added to the resonator. This induces a field E_{dc} and an electric displacement D_{dc}, as well as a strain S_{dc} and a stress T_{dc}. We immediately note that T_{dc} is zero because T_3 is zero in the thin film hypothesis (the film can freely deform in the out-of-plane direction). These *DC* parameters are assumed to be large compared to the variable values, which we will call *AC*. This hypothesis will enable us to implement a first-order expansion in equation [8.6] and reduce it to an equivalent piezoelectric formalism. Thus, eliminating the continuous term (in which only *DC* terms appear), equation [8.6] becomes:

$$\begin{aligned} T_{ac} &= \left(c_0^D + MD_{dc}^2\right)S_{ac} + \left(2GD_{dc} + 2MS_{dc}D_{dc}\right)D_{ac} \\ E_{ac} &= \left(\beta^S + 3\gamma^S D_{dc}^2 + 2GS_{dc} + MS_{dc}^2\right)D_{ac} + \left(2GD_{dc} + 2MS_{dc}D_{dc}\right)S_{ac} \end{aligned} \qquad [8.23]$$

The terms between brackets do not depend on dynamic *AC* variables but on *DC* fields. The general form of this equation pair is identical to the piezoelectric formalism *(S,D)* for which we recall that:

$$\begin{aligned} T &= c^D S - hD \\ E &= \beta^S D - hS \end{aligned} \qquad [8.24]$$

It is enough to identify the terms between the two equation pairs. We can progress a bit further in the calculation by expressing S_{dc} in terms of D_{dc}, using the fact that T_{dc} is zero. Replacing T_{dc} in equation [8.6], neglecting to the first order the influence of M (the experimental results show that its influence is lower than 1%, which justifies neglecting it) we get the following result:

$$S_{dc} = -\frac{GD_{dc}^2}{c_0^D} \qquad [8.25]$$

The coupling term of equation [8.23] becomes:

$$2GD_{dc} + 2MS_{dc}D_{dc} = 2GD_{dc}\left(1 - \frac{MD_{dc}^2}{c_0^D}\right) \qquad [8.26]$$

We could explain the other terms of equation [8.23] containing S_{dc} but, for the case of paraelectric perovskites, the change in the dielectric constant due to the electric field is such that the electric term in β and γ is dominant in relation to the G and M terms. As impermittivity is the inverse of permittivity, it is often the latter that we prefer to model. This permittivity can be modeled thanks to the *LGD* formalism when working temperature is below Curie temperature. It is therefore about solving the following third-degree equation:

$$\varepsilon \approx \frac{1}{\alpha + 3\alpha' D^2} = \frac{1}{\alpha + 3\alpha' \varepsilon^2 E_{DC}^2} \qquad [8.27]$$

Starting with equation [8.27], Chase *et al.* suggested a practical sort of equation for modeling the behavior of the dielectric constant of the paraelectrics and of BST in particular [CHA 05]. They got the following equation, which is an exact solution to equation [8.27]:

$$\varepsilon(E) = \frac{\varepsilon_{\max}}{2\cosh\left(\frac{2}{3}\sinh^{-1}\left(2\frac{E}{E_{1/2}}\right)\right) - 1} \qquad [8.28]$$

The two parameters to be extracted from the experimental data are ε_{max} and $E_{1/2}$, this last corresponding to the field value for which $\varepsilon = \varepsilon_{max}/2$.

With these remarks and using $D_{dc} = \varepsilon E_{dc}$, the formalism for equation [8.23] becomes:

$$T_{ac} = \left(c_0^D + M\varepsilon^2 E_{dc}^2\right) S_{ac} + \left(2G\varepsilon E_{dc}\left(1 - \frac{M\varepsilon^2 E_{dc}^2}{c_0^D}\right)\right) D_{ac}$$
$$E_{ac} = \left(\frac{1}{\varepsilon}\right) D_{ac} + \left(2G\varepsilon E_{dc}\left(1 - \frac{M\varepsilon^2 E_{dc}^2}{c_0^D}\right)\right) S_{ac} \qquad [8.29]$$

We can therefore identify each of the terms with equation [8.24]:

$$-h = 2G\varepsilon E_{dc}\left(1 - \frac{M\varepsilon^2 E_{dc}^2}{c_0^D}\right) \qquad c^D = c_0^D + M\varepsilon^2 E_{dc}^2 \qquad \beta^S = \frac{1}{\varepsilon} \qquad [8.30]$$

We notice that an index "0" is added to $c^D{}_0$ to indicate that it is a constant that does not depend on any parameters; whereas c^D depends on the *DC* electric field.

In the *(S,D)* formalism, the coupling coefficient k_t^2 of the piezoelectric thin film only is equal to $h^2/\beta^S c^D$. Assuming that the correction factor of stiffness is low and making a first-order expansion, k_t^2 is equal to:

$$k_t^2 \approx \frac{4G^2\varepsilon^3 E_{dc}^2}{c_0^D}\left(1 - \frac{2M\varepsilon^2 E_{dc}^2}{c_0^D}\right) \qquad [8.31]$$

We can simplify the k_t^2 expression by eliminating the term between brackets (experimentally this term represents a maximum of 5% of the value of *h*).

This gives the following formula:

$$k_t^2 \approx \frac{4G^2\varepsilon^3 E_{dc}^2}{c_0^D} \qquad [8.32]$$

This expression is very interesting as it shows that coupling depends on the cube of the dielectric constant and on the square of the electric field *DC*. It is therefore favorable to work with materials that have a very strong dielectric constant and at strong electric field. We also note that the electrostrictive coefficient is squared at the numerator. This coefficient depends little on the ferroelectric, antiferroelectric or paraelectric nature of the material. It is also relatively insensitive to temperature. On the other hand, it is very sensitive to the notion of disorder in the structure. In perovskites (ABO_3), many substitutions are possible on the cationic sites A and B. These substitutions can be made with atoms that have different valences and sizes. This induces varying degrees of disorder in the structure. Uchino reported that the

electrostrictive coefficient Q (such as $S = QP^2$) increases when that order increases in the structure. He noticed that these same materials exhibit an opposite change to the Curie constant. We recall that the Curie constant, C, is such that $\varepsilon = C/(\theta-\theta_C)$ when temperature is above Curie temperature, θ_C, which is the case of electrostrictive materials. It is worth noting that Uchino empirically observed that electrostrictive materials exhibit an almost constant QC product [UCH 97]. For bulk materials in which he was interested, he reports $QC \approx 3.10^3 m^4 C^{-2} K$.

An intuitive way of understanding why QC is just about constant involves returning to the phenomenological approach. Referring to Chapter 2, we saw that we had:

$$\left.\frac{1}{\varepsilon}\right|_{T,\theta} \approx \left.\frac{1}{\chi}\right|_{T,\theta} = \alpha + 3\alpha' D^2 + 5\alpha'' D^4 - 2QT \qquad [8.33]$$

with $\alpha = \dfrac{\theta - \theta_C}{C}$.

Placing ourselves above θ_C, the terms with D are cancelled and we can write:

$$\frac{\partial\left(\frac{1}{\varepsilon}\right)}{\partial\theta} = \frac{1}{C} \qquad \frac{\partial\left(\frac{1}{\varepsilon}\right)}{\partial T} = -2Q \qquad [8.34]$$

If we accept that the sensitivity of the dielectric constant of these materials is comparable versus both mechanical stresses (T) and temperature (θ) – which is true from the experimental point of view – we can imagine from equation [8.34] that QC can be roughly constant.

A microscopic view also enables us to understand this property. A material with a lot of cationic disorder enables its cations to move easily without moving the oxygen octahedron. Therefore, during the application of an electric field, these cations can move a lot, which induces a big change in local charges and so a strong dielectric constant. As the octahedron is weakly moved, the exchange of mechanical energy is weak and therefore the induced strain is also weak. For this reason, the electrostrictive coefficient cannot be high. We can make the reverse argument for a material with a weak disorder that exhibits a weaker dielectric constant, but a higher electrostrictive coefficient.

This means that it is more interesting to choose materials with a high dielectric constant, since this last constant appears to the power of three, whereas G is only squared in the simplified expression of k_t^2.

To end, stiffness is the numerator of equation [8.32] which indicates that the more flexible the material, the more important its coupling. It is likely, however, that a flexible material presents a more important mechanical viscosity and therefore more significant acoustic losses, which tends to degrade the quality factor of the resonators.

8.6. Bibliography

[CHA 05] CHASE D.R., CHEN L.Y., YORK R.A., "Modeling the capacitive non linearity in thin film BST varactors", *IEEE Transactions on Microwave Theory and Techniques*, vol. 53 (10), p. 3215, 2005.

[COH 92] COHEN R.E., "Origin of ferroelectricity in perovskite oxides", *Nature*, 358, p. 136-138, 1992.

[DAM 92] DAMJANOVIC D., NEWHNAM R.E., "Electrostricitve and piezoelectric materials for actuator applications", *J. Intel. Mat. Struct.*, vol. 3, 190, 1992.

[NÖT 07] NÖTH A., YAMADA T., SHERMAN V.O., MURALT P., TAGANTSEV A.K., SETTER N., "Tuning of direct current bias-induced resonances in micromachined Ba0.3Sr0.7TiO3 thin-film capacitors", *Journal of Applied Physics 102*, 114110, 2007.

[NÖT 09] NÖTH A., Micromachined tunable devices based on silicon integrated BaxSr1-xTiO3, PhD Thesis, Ecole polytechnique de Lausanne, 2009.

[UCH 97] UCHINO K., *Piezoelectric Actuators and Ultrasonics Motors*, Kluwer Academic Publishers, Norwell, 1997.

[VEN 08] VENDIKA I.B., TURALCHUK P.A., VENDIK O.G., BERGE J., "Modeling tunable bulk acoustic resonators based on induced piezoelectric effect in BaTiO3 and Ba0.25Sr0.75TiO3 films", *Journal of Applied Physics 103*, 014107, 2008.

[VOL 08] VOLATIER A., DEFAŸ E., AID M., NHARI A., ANCEY P., DUBUS B., "Switchable and tunable strontium titanate electrostrictive bulk acoustic wave resonator integrated with a Bragg mirror", *Applied Physics Letters*, 92(3):032906, 2008.

Chapter 9

Electric Characterization

9.1. Static piezoelectric characterization of thin films

9.1.1. *Notion of effective coefficients*

The characterization of the piezoelectricity of thin films is not very simple and specific systems must be developed to arrive at them. The main difficulty comes from the fact that a well-defined stress or strain must be applied to the piezoelectric film, or we must be able to measure a very low displacement.

There are several techniques in the literature. Some of them tend to be standardized, especially for determining coefficient d_{33} and, more recently, coefficient e_{31} (aixAcct company in Germany). We will note that the most sophisticated technique enables us to characterize d_{33} by using a double interferometer that measures the difference in thickness of a sample when the piezoelectric thin film is excited by a known electrical signal. A beam is reflected on the front and another on the back of the sample to suppress the contribution of bending, often of the same order of magnitude as the useful measurement. This technique is extremely precise (10^{-4} A) but necessitates a very elaborate slotted line [KHO 96].

For transverse coefficient measurements, the simplest techniques are based on mechanical excitation of a bar of Si 1 cm long on which a piezoelectric film with its electrodes is placed. This much lighter technique enables us to find coefficient e_{31}, to within a few percent, with a careful calibration of the experimental connection

---

Chapter written by Emmanuel DEFAŸ, Gwenaël LE RHUN and Emilien BOUYSSOU.

[DES 92]. It is also possible to obtain coefficient d_{31} through the use of the reverse piezoelectric effect, which induces a mechanical strain when an electric field is applied. To have a consequent strain, however, it is often imperative to produce a micromanufactured beam, which induces a much more complicated process than the characterization of e_{31}.

Let us note that speaking of e_{31} or d_{33} is a misuse of language here because it more precisely involves effective coefficients due to particular boundary conditions applied to the film. Indeed, with the substrate being a lot thicker than the thin film, it is the former that imposes on the strain. Thus, if there is no substrate motion, in-plane film strains are zero ($S_1 = S_2 = 0$). Moreover, the stress perpendicular to the plane of films is zero ($T_3 = 0$). Using the piezoelectric formalisms previously detailed with these mechanical boundary conditions, we get the following effective coefficients:

$$d_{33eff} = d_{33} - 2\frac{s_{13}^E}{s_{11}^E + s_{12}^E} d_{31} \qquad e_{31eff} = e_{31} - \frac{c_{13}^E}{c_{33}^E} e_{33} \qquad [9.1]$$

Coefficient d_{33eff} is therefore lower than d_{33} because s_{13}^E is negative and d_{31} and d_{33} have opposite signs. As for e_{31eff}, it is higher than e_{31} because c_{13}^E and c_{33}^E are positive and e_{31} and e_{33} have opposite signs. It is common to see $d_{33} > 0$ and $d_{31} < 0$. This depends on the orientation of polarization in the material. We must be vigilant on this point in the case of ferroelectrics such as PZT, for which polarization can be reversed by an intense electric field. This is also the case with wurtzites such as AlN, for which the deposition process can generate the start of A1 or N growth and therefore a downward- or upward-oriented polarization.

We will now go into the details of one of the techniques for measuring coefficient e_{31eff}. There are several of them but they all rely on the same basis.

9.1.2. *Piezoelectric characterization of coefficient e_{31eff}*

The original idea, published for the first time by Deschanvers *et al.* in 1992 [DES 92], consists of placing a piezoelectric thin film in MIM (metal-insulator-metal) configuration on a Si substrate, dividing a test sample that is longer than it is wide, and applying a uniaxial stress to it by blocking one end and causing the free-clamped bar thus obtained to vibrate at its first bending mode. Charges are then created on electrodes and can be received on an oscilloscope. A variation of this technique is to apply a periodical mechanical excitation to the bar, which improves the quality of the signal received by using a lock-in [DUB 99].

It is possible to shape the signal by adding an impedance-match circuit between the oscilloscope and the piezoelectric film. This matching enables us to extract coefficient e_{31eff} as well as the leakage current of the piezoelectric film without other electric measurements. A complete description of the set up is given in Figure 9.1 [DEF 06].

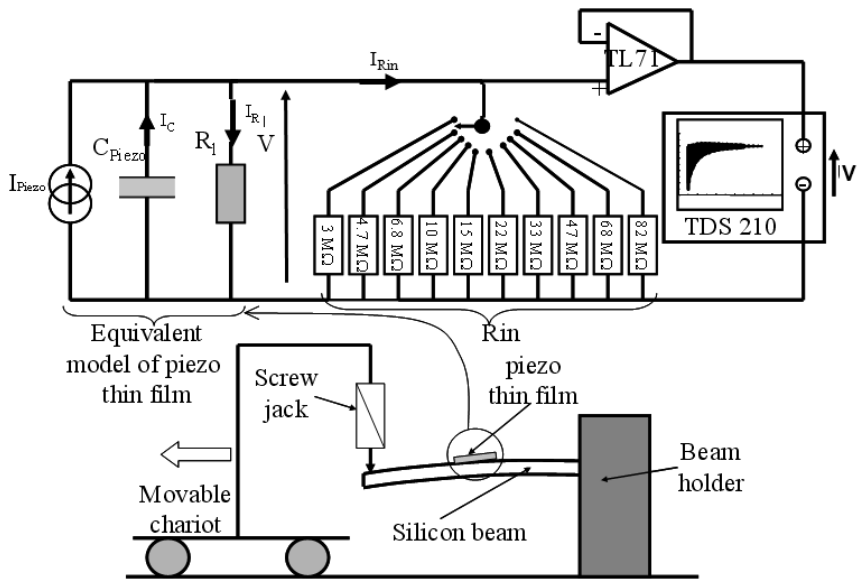

Figure 9.1. *Experimental connection for measuring coefficient e_{31} of piezoelectric thin films*

The Si bar is typically 4 cm long by 1 cm wide. It is clamped on a fixed support. A jack enables a known initial arrow to be applied to the free end of the bar. The jack is mounted on a wheeled carriage that enables the bar to be released. At that time, the bar is vibrating mainly in its bending dominant mode if there is enough clamping (observed by optical profilometric method). Si transmits its strain to the piezoelectric film, which then creates charges. The piezoelectric film is modeled by a current source in parallel with static capacitance and a leakage resistance that includes dielectric losses. The electric signal then enters an amplifier, which has an input impedance of several GΩ. The input impedance of this amplifier is therefore fixed by a parallel resistance whose value is between 3 and 82 MΩ. The amplifier is mounted as a voltage follower. Its output voltage is therefore equal to its input voltage. This connection enables us to model the signal received and to eventually extract coefficient e_{31eff} and the leakage resistance of the piezoelectric film.

9.1.3. *Model*

The Si substrate has a thickness (typically 725 µm for a substrate 200 mm in diameter) that is larger than the thin films of the stack. It is therefore the substrate that imposes its in-plane strain on all other layers. The piezoelectric film does not undergo any out-of-plane T stress and the shear stress is neglected. Thus, the mechanical formalism allows us to find the strain, S, applied to the piezoelectric film. Furthermore, it is the voltage that we will follow experimentally. It would therefore be logical to take the electric field, E, as the electric parameter. However, the model is not further simplified by using E or D (electric displacement) because neither of the two is cancelled in the experiment. E is therefore used as the electric parameter for having access to parameter e_{31} rather than g_{31}. The piezoelectric formalism chosen is therefore *(S,E)*.

Direction 1 is based on the length of the bar; direction 3 is the upward-directed normal to the surface of the film; and direction 2 completes the right-handed trihedron. Based on these definitions, the working hypothesis gives:

$$E_1 = E_2 = 0 \qquad D_1 = D_2 = 0 \qquad T_3 = 0 \qquad [9.2]$$

The piezoelectric equations become, for a material from the 6mm point group:

$$T_3 = c_{13}{}^E (S_1 + S_2) + c_{33}{}^E S_3 - e_{33} E_3 \qquad [9.3]$$

$$D_3 = e_{31}(S_1 + S_2) + e_{33} S_3 + \varepsilon_{33}{}^S E_3 \qquad [9.4]$$

The combination of equations [9.2] and [9.4] gives:

$$D_3 = e_{31eff}(S_1 + S_2) + \varepsilon^S{}_{33eff} E_3 \qquad [9.5]$$

with $\varepsilon^S{}_{33eff} = \varepsilon_{33}{}^S + \dfrac{e_{33}{}^2}{c_{33}{}^E}$ [9.6]

Time differentiation of equation [9.5] gives the dielectric and piezoelectric current density. Multiplying by A the surface of the top electrode (supposedly the smallest one), we are dealing with current contributions of the capacitance, I_C, and the current source, I_{piezo}.

In this calculation, we assume that the electrode is short enough to be able to neglect any change in the physical parameters along axis 1. Typically, the electrode is 0.5 mm long for a 30 mm long beam:

$$\frac{A\partial D_3}{\partial t} = Ae_{31eff}\frac{\partial(S_1+S_2)}{\partial t} - \frac{A\varepsilon^S{}_{33eff}}{d}\frac{\partial V}{\partial t} \qquad [9.7]$$

With the conventions chosen in Figure 9.1, we get:

$$I_{piezo} = Ae_{31eff}\frac{\partial(S_1+S_2)}{\partial t} \qquad I_C = -\frac{A\varepsilon^S_{33eff}}{d}\frac{\partial V}{\partial t} \qquad [9.8]$$

We have to add the contribution of the leakage current or losees of the piezoelectric material. This is modeled by the equivalent resistance, R_l. Therefore, the effective resistance R_{eff} has to be taken into account, and the parallel association of R_l and R_{in}, the so-called input resistance (see Figure 9.1). This contribution is not directly taken into consideration by the piezoelectric formalism (except when complex matrices are applied with a losses term). According to Figure 9.1, we have:

$$I_{piezo} + I_C = I_{Rl} + I_{Rin} \qquad [9.9]$$

By combining these equations, we obtain:

$$V = -R_{eff}C^S\frac{dV}{dt} + R_{eff}Ae_{31eff}\frac{\partial(S_1+S_2)}{\partial t} \qquad [9.10]$$

with $C^S = \frac{A\varepsilon^S{}_{33eff}}{d}$.

In-plane strains are obtained by static calculation of a bent bar [FEY 99]. The bar is considered to be vibrating in its first bending mode and the influence of other modes is considered to be negligible:

$$S_1 + S_2 = \left(1 + \frac{s_{21Si}}{s_{11Si}}\right)\frac{3d_{Si}(L-l_m)}{2L^3}\delta = k\delta \qquad [9.11]$$

with:

– s_{ijSi}: Si compliance coefficients;

– d_{Si} : Si thickness;

– L: vibrating length;

– l_m: average position of electrodes in direction 1; and

– δ: deflection of the free end of the bar. k is introduced to simplify the following expressions.

NOTE:– $S_1 + S_2$ is positive when the film is under tensile stress.

It is interesting then to integrate the voltage V measured at the terminals of the oscilloscope over the time between 0 and infinity.

$$\int_0^{+\infty} V dt = -R_{eff} C^S \left[V(+\infty) - V(0)\right] + R_{eff} A e_{31eff} k \left[\delta(+\infty) - \delta(0)\right] \qquad [9.12]$$

$V(+\infty)$ is zero as well as $V(0)$ because the charges created during the initial strain are left to leak out into the resistance before letting the beam escape. Furthermore, $\delta(+\infty)$ is also zero. The previous equation therefore becomes:

$$\frac{1}{\int_0^{+\infty} V dt} = -\frac{1}{A e_{31eff} k \delta(0)} \left(\frac{1}{R_l} + \frac{1}{R_{in}} \right) = p \frac{1}{R_{in}} + Y_0 \qquad [9.13]$$

Thus, the reverse integral of the voltage V over the voltage time, linearly depends on the tracking input resistance, R_{in}. The slope, p, of this straight line depends on coefficient e_{31eff} whereas the ordinate at origin Y_0 depends on the leakage resistance of the piezoelectric thin film. The final values of e_{31eff} and R_l extracted from the model are:

$$e_{31eff} = -\frac{1}{A k \delta(0) p} \text{ and } R_l = \frac{p}{Y_0} \qquad [9.14]$$

The data required to extract these values are the surface area of the top electrode, the initial deflection, the elastic parameters and the thickness of the substrate (Si), the vibrating length and the distance between the clamped-end and the top electrode. We must note that it is not necessary to get the capacitance value, nor the thickness

of the film. The most delicate value is the vibrating length, L, because it appears to the power of three in the denominator and once in the numerator, which in theory produces an error twice as big in determining e_{31eff}. The quality of clamping is therefore particularly sensitive. Estimating the influence of errors in parameter measurement entering the calculation of e_{31eff} (2% per parameter), the accuracy of the estimation is in the order of +/-15%. With the losses, R_l, the precision is a lot less as the curve cuts the ordinates axis very close to zero, as we will see. This method enables us to measure the leakage resistance in leaky films. Having an ordinate at the origin close to zero proves that the film has a negligible leakage resistance compared to input resistances used in the set up.

Determining e_{31eff} does not necessarily require the calculation of the slope as a single datum obtained with one single input resistance can be enough, in accordance with equation [9.13] provided that R_l is found or neglected, which is possible in most cases. The slope method, however, is more accurate and checks the value of R_l.

9.1.4. *Example of characterization: PZT films*

The films characterized here are PZT films. The stack used is the following: Si substrate, SiO_2 0.5µm (antidiffusion film in Si), TiO_2 10nm (adhesion layer), Pt 100 nm (lower electrode), sputtered PZT (piezoelectric) of variable thickness and Pt 100 nm (upper electrode). Only the top Pt film is patterned by lift-off technique (lithography performed before Pt deposition). Access to the bottom electrode is via wet etching of PZT.

The sample presented here is 265 nm thick and was annealed at 700 °C. It is poled under a field of 200 kV/cm at room temperature for 40 seconds. The top electrode therefore has negative potential during poling. The initial deflection is 150 µm (downwards) for a beam 26 mm-long and an electrode placed at 5.5 mm from the clamped edge. The substrate is 532 µm thick. The surface of the top electrode is 480 x 550 µm². Figure 9.2a shows the curve for the reverse voltage integral measured in terms of the reverse input resistance used. The maximum resistance used is 10 MΩ and the minimum resistance is that of the oscilloscope (1 MΩ), which gives a rather weak signal with more uncertainty than the other resistances.

Using the slope of the curve in Figure 9.2a, e_{31eff} is equal to -4.0 C/m² +/- 15%. The sign is negative because the remanent polarization of the sample is in the direction of increasing z. This value corresponds to a rather modest coefficient whose low value is principally explained by low thickness. The best results published deal with sol-gel PZT films that reach a e_{31eff} of -18 C/m² for a thickness of 2 µm with an optimized polarization (100 kV/cm, 10 minutes at 150°C)

[CAL 07]. The best sol-gel films between 100 and 200nm thick reach an e_{31eff} of -6.5 C/m² for a polarization field of 200 kV/cm applied over a few seconds.

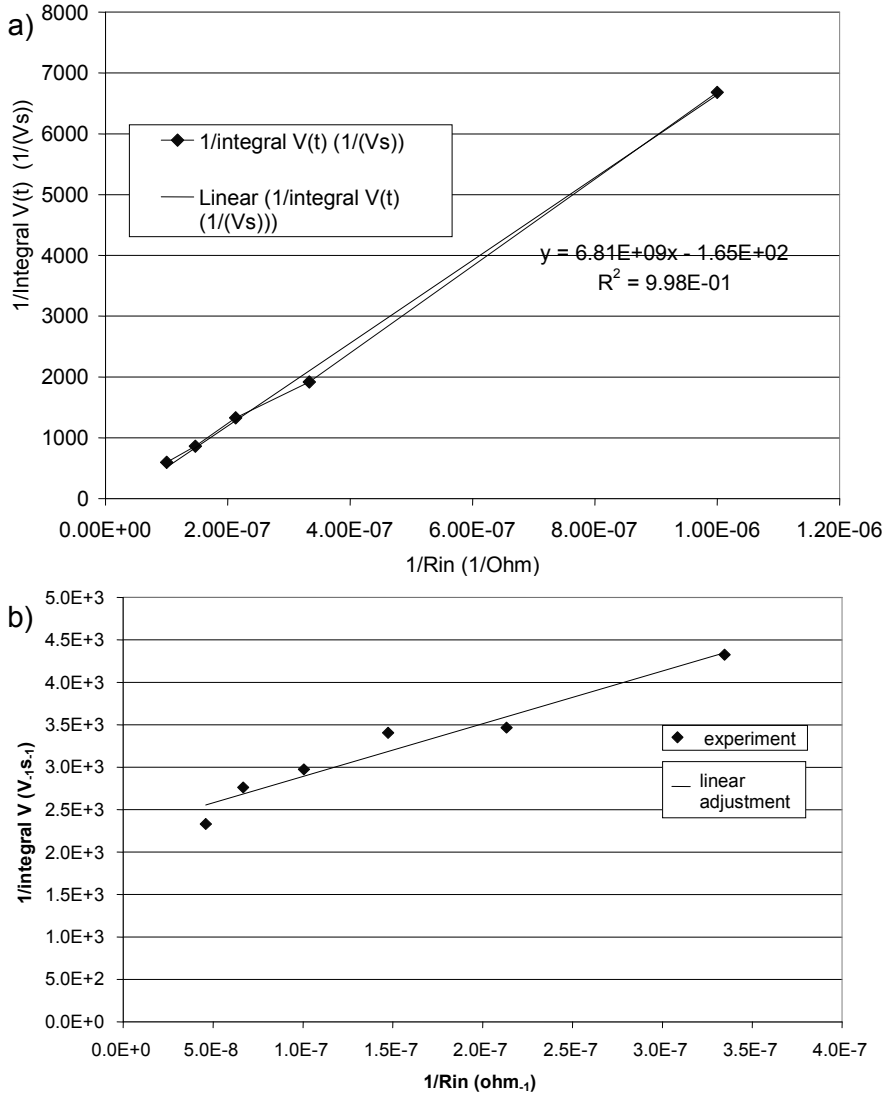

Figure 9.2. *Reverse integral of the voltage versus time measured for two PZT samples: a) reference sample N°9; and b) poor quality sample using the vibrating beam method according to the reverse of different input resistances*

The linear fit extracted from Figure 9.2a gives an ordinate at the negative origin inducing a negative leakage resistance that is not physical. This is the typical case for a very high film resistance compared to the input resistances of the set up. To test the measurement method suggested, Figure 9.2b shows the piezoelectric characterization of a poor quality film (Pb deficiency, significant porosity). The value of e_{31eff} extracted is -1.68 C/m². Intersection with the ordinate axis is very clear here and enables us to extract a leakage resistance of 2.7 MΩ. This measurement has good precision because R_f is close to the input resistance values used in this experiment (3–22 MΩ).

9.2. Piezoelectric and atomic force microscopy

The atomic force microscope in piezoresponse mode is the piezoresponse force microscope (PFM). This is part of the family of scanning probe microscopes, the general principle of operation of which relies on interaction between a point of nanometric dimensions and a surface. The scanning tunneling microscope (STM) invented in 1982 by Binnig and Rohrer, two researchers from the Zurich IBM laboratory, is the precursor of this family of instruments [BIN 82], while the atomic force microscope (AFM), from which PFM is derived, is among the most frequently used of these near-field microscopes. This was invented by Binnig in 1986 [BIN 86]. The piezoresponse mode was introduced in 1991 by Birk *et al.* with the aim of measuring the piezoelectric coefficient of a ferroelectric polymer film [BIR 91]. Although initially adapted to an STM, the piezoresponse mode is most often coupled with an AFM today. We will therefore present AFM and PFM.

9.2.1. *Atomic force microscope*

Atomic force microscopy is a near-field technique, the basic principle of which consists of scanning the surface of an object with a very fine tip and detecting the effect of forces interacting with the surface. AFM is therefore a very high resolution profilometer enabling us to map forces at the atomic scale, thus revealing the surface topography of an object. A simplified schematic of an AFM is presented in Figure 9.3.

The most important element of an AFM is the tip (see Figure 9.4). This tip is mounted at the end of a cantilever, which is comparable to a spring with a stiffness varying between 0.01 and 50 N/m. The shape and size of the tip are crucial parameters for an AFM. It must be as fine as possible, while being sufficiently mechanically robust to obtain an atomic resolution of the measurement. AFM tips are most often made of silicon nitride or crystalline silicon and have a radius of curvature of 10 nm. However, this radius deteriorates a bit after a certain number of

scans of the sample. This deterioration happens more or less quickly, depending on the roughness of the surface of the object analyzed and the mode of AFM operation (contact or intermittent contact).

Deflections of the cantilever are detected through a laser diode and a photodetector. A laser beam is thus focused on the end of the cantilever, the surface of which is covered by a thin reflecting film. The beam is reflected in the direction of a photoelectric cell made of four photodiodes. The latter are illuminated in a different way due to reflections of the beam. Voltage differences generated are converted into units of length following fine calibration adjustments. Sample displacement along the x, y and z axes is obtained thanks to piezoelectric translators (generally PZT) that enable micro-displacements of a few angstroms up to one hundredth of a micrometer. The piezoelectric scanner can be located under the sample or in contact with the cantilever.

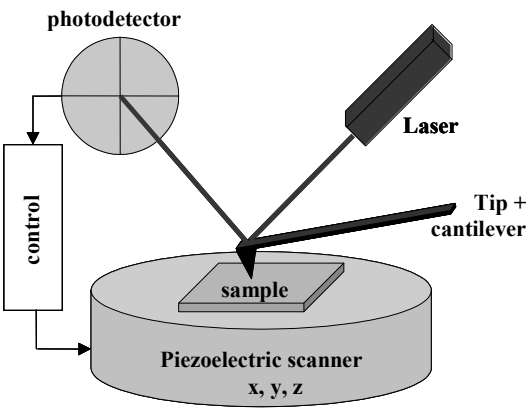

Figure 9.3. *Diagram of a simplified AFM*

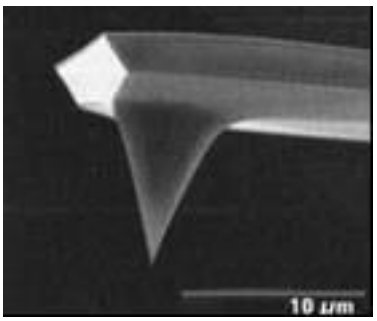

Figure 9.4. *Scanning electron microscope image of an AFM tip*

During an AFM analysis, the cantilever on which the tip is mounted will move very close to the surface of the object to be studied (a few angstroms), initially undergoing attractive forces, then repulsive ones. Figure 9.5 represents the evolution of the force of interaction between the tip and the surface of the sample in terms of the distance separating them. From this force curve, three modes of detection can be used to map the surface topography of a sample: the contact mode, the non-contact mode and the tapping mode.

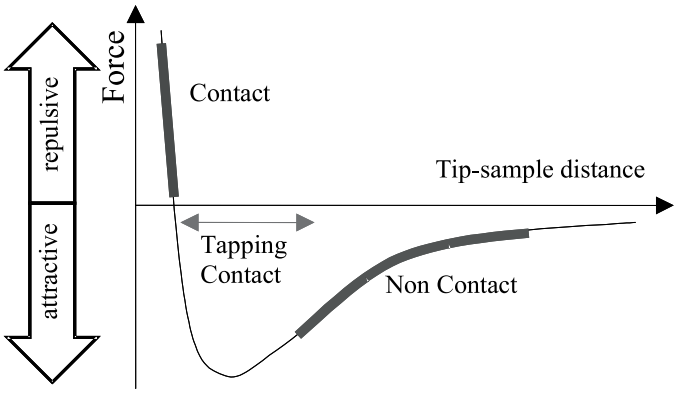

Figure 9.5. *Curve of the interaction force as a function of the tip-sample distance*

In contact mode, the main interaction between the tip and the sample involves repulsive forces of very short reach (a few nanometers at maximum). The changes in these forces imposed by the topography are used to record an image. There are two principle modes of imagery: constant deflection mode and constant height mode.

In the first case, deflection of the cantilever is kept constant while the tip sweeps the surface, thanks to a control loop that monitors displacement along z of the piezoelectric scanner under the sample. Changes in z of 0.01 nm can be measured. Isoforce lines are interpreted as the topography of the sample and the contrast of the image results solely from the z displacement of the sample.

In the second case, the height of the sample is fixed and the changes in bending of the cantilever are measured. The origin of image contrast here is fluctuations in forces related to tip-sample interactions. Figure 9.6 is a topographical image of an epitaxial PZT (20/80) film, with a domain structure *c/a/c*, obtained in contact mode [VRE 06].

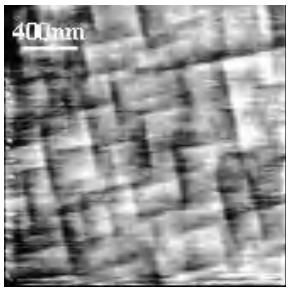

Figure 9.6. *Topographical image of a PZT (20/80) film*

In tapping contact mode, the surface is imaged by making the cantilever oscillate at or near its frequency of resonance. Each cantilever has a resonance frequency that depends especially on the geometry and on the mass of the cantilever. These oscillation frequencies typically go from a few tens of kHz to several hundreds of kHz. The height of the cantilever is adjusted in such a way that the tip only ends up touching the sample periodically. The gradient of forces modifies the frequency response and the amplitude of oscillation of the cantilever. We can therefore measure the displacement of the frequency of resonance, i.e. the change in amplitude of oscillation. It is this last detection technique that is most often used. Amplitude (or frequency) modulation is exploited in the control loop to follow the topography of the surface. Resolution is not quite as good as in contact mode, but the resonant mode enables us to avoid deterioration of the tip and/or surface of the (fragile) sample.

The non-contact mode is comparable to the tapping mode. The tip detects attractive forces. The control loop will be created by a shift in the frequency of resonance in order to follow the surface topography. This mode is preferentially used when we are working under a vacuum. The drawback is that the acquisition time of an image is relatively long.

9.2.2. *Piezoresponse force microscope*

AFM in piezoresponse mode is a near-field microscopy technique based on the reverse piezoelectric effect, which corresponds to a linear coupling between the electrical and mechanical properties of a material. This technique was initially developed to visualize the polar regions in ferroelectric films [GUT 92]. With ferroelectrics also being piezoelectric, they deform when subjected to applied voltage.

Let us take the simple case of a material with two opposite polarization fields perpendicular to the surface of the sample. In the PFM technique, the tip is used as an electrode that can be swept over the surface of the sample. At equilibrium, i.e. without applied voltage, the two domains will have the same dimension along Z (see Figure 9.7a). Now, if a voltage, V, is applied between the tip and the lower electrode, the electric field E generated in the sample will produce an extension of the field whose polarization is parallel to the electrical field and the contraction of the domain at the opposite polarization (see Figures 9.7b and 9.7c). This corresponds to the piezoelectric response of the ferroelectric material.

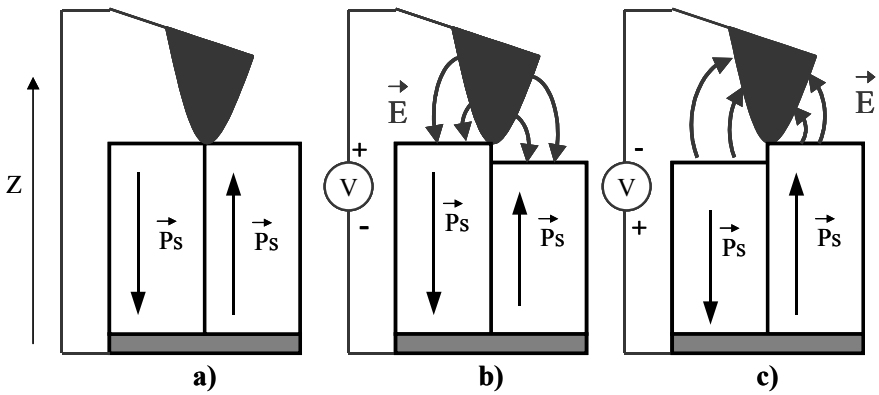

Figure 9.7. *Basic principle of PFM: a) without voltage; b)positive voltage applied to the tip; c) negative voltage applied to the tip*

The measurement device has the same sensitivity as AFM, except that a synchronous detection amplifier is used to detect piezoelectric oscillations. A sinusoidal voltage, V_{ac}, is applied between the tip and the lower electrode, thus necessitating the use of the microscope in contact mode. This voltage must not exceed the coercive voltage of the ferroelectric material with the risk of modifying the state of polarization of ferroelectric domains. It is also possible to apply a continuous voltage, V_{dc}, in order to polarize the material. Just as for AFM, the most important element is the tip. It must be conducting. The tips are most often made from strongly doped silicon or even silicon covered with a metal coating (Pt/Ir, WC_2, Rh, Au). The cantilever generally has a high stiffness constant (>>1 N/m) so that the effects of electrostatic interaction between the cantilever/tip couple and the lower electrode of the sample are limited [CHR 98].

Applying a voltage V_{ac} sin(ωt) produces a sample vibration at the same frequency ω due to the reverse piezoelectric effect. Assuming that displacement of

the surface of the sample is solely linked to induced piezoelectric vibrations, the vertical displacement of point, $\Delta z(t)$, is then expressed:

$$\Delta z(t) = d_{zz} V_{ac} \sin(\omega t + \varphi) \qquad [9.15]$$

with d_{zz} being the effective piezoelectric coefficient and $\varphi = 0$ or π depending on the orientation of the domains. Ferroelectric domains with opposite orientations will therefore lead to piezoresponse signals in phase opposition. This will be translated by a strong contrast on the piezoresponse image (see Figure 9.8).

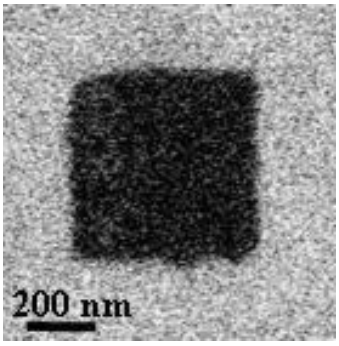

Figure 9.8. *Piezoresponse image of a PZT (20/80) film with domains at 180°*

Ferroelectric domains can be viewed by analyzing the first harmonic signal. The piezoresponse signal (PRS) thus detected is directly linked to the phase and amplitude of surface vibrations via the sensitivity of the detector, δ:

$$\text{PRS} = \delta d_{zz} V_{ac} \cos(\varphi) \qquad [9.16]$$

The piezoresponse signal thus contains information about the orientation of polarization via dephasing φ and about the amplitude of the piezoelectric coefficient, provided that φ can only take the value 0 or π.

It is also possible to determine an in-plane component of the polarization vector. If the polarization vector is perpendicular to the electric field, there will be no piezoelectric strain, depending on the direction of the field. On the other hand, there will be a strain in the plane of the sample. This can lead to the cantilever twisting, which can be detected by the four quadrants of the photodiode.

As seen before in the case of out-of-plane domains, applying a voltage V_{ac} will induce piezoelectric oscillation in the plane of the sample with a dephasing of 180° between the domains of opposite polarization.

Figure 9.9 shows a topographical image and the associated piezoresponse image, both obtained simultaneously for a polycrystalline PZT (40/60) film. The topographical image informs us that the film is made up of grains between 50 nm and 200 nm. It is also possible to determine the roughness of the film surface. As for the piezoresponse image, it is quite a bit more complicated than the one presented in Figure 9.8. Indeed, the image reveals a structure that is rather complex and composed mainly of 90° domains (*c/a/c* structure) [ROY 76]. Nevertheless we can distinguish a few domains at 180° for which the contrast is very marked (black or white).

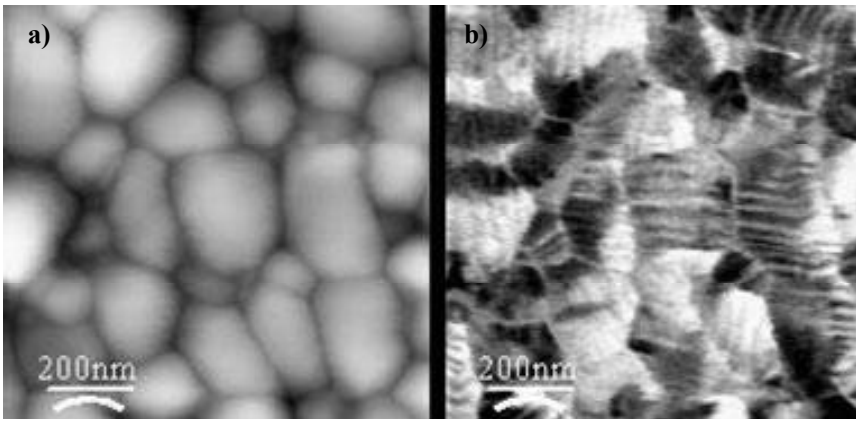

Figure 9.9. *a) Topography images and b) piezoresponse of a polycrystalline PZT film*

One of the main uses of PFM is local characterization of the electromechanical properties of the material with the help of the conducting tip [HAR 00]. This tip is positioned at the location we want to analyze. The piezoresponse signal must be calibrated beforehand with the use of a test sample, the piezoelectric coefficient of which is known (generally, X-cut quartz for which d_{33} = 2.17 pm/V). We can therefore determine the effective piezoelectric coefficient by varying the voltage amplitude V_{ac} between 0 V and the coercive voltage of the sample. We then get a straight line (see Figure 9.10a). The piezoelectric constant can be calculated from the slope of this straight line, which is expressed by the following equation:

$$\text{PRS} = \delta d_{33} V_{ac} \qquad [9.17]$$

where PRS is the piezoresponse signal measured for a PZT (20/80) film with tetragonal structure and δ the conversion factor between displacement of the tip and the deflection electric signal (sensitivity of the optical detector). In this case, PZT is oriented according to the *c*-axis so well that the piezoelectric coefficient detected is d_{33}. It is also possible to measure piezoelectric hysteresis cycles. We then use a voltage source, V_{dc}, in series with the voltage, V_{ac}. The hysteresis cycles are obtained by recording the piezoresponse signal while varying V_{dc}. An example of a hysteresis loop $d_{33}(V)$ is presented in Figure 9.10b. Finally, it is theoretically possible to estimate the coefficient of electrostriction from the second harmonic signal, provided that the noise is sufficiently low. The strain measured is then proportional to E_{ac}^2, but forces us to find the local dielectric permittivity of the material.

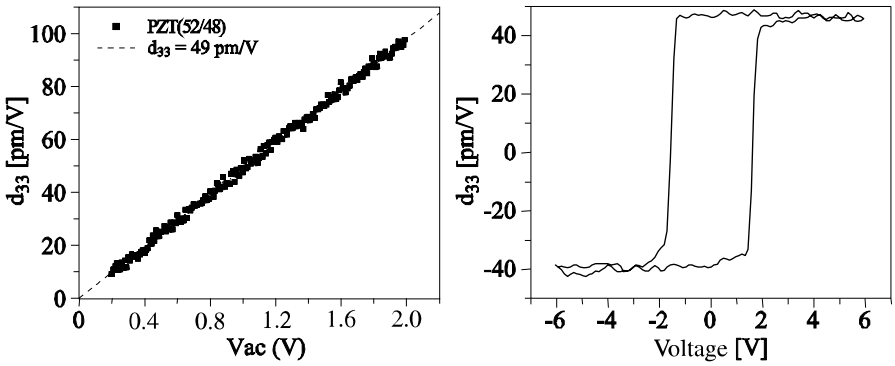

Figure 9.10. *a) Measurements of the effective piezoelectric coefficient d_{33}; and b) associated piezohysteresis cycle implemented on a PZT(20/80) film*

One particularity of the PFM technique is that the electric field in the sample is strongly non-uniform due to the asymmetry between the two electrodes [HAR 01]. According to Harnagea calculations, 90% of the voltage applied between the AFM tip and the lower electrode is confined to 30% of the thickness of the material [HAR 04]. So it is possible to observe phenomena that we could not see in the case of a plane capacitor. It is this way, for instance, that it is possible to visualize the movement of domain walls at 90° in a continuous PZT (20/80) film [LER 06]. These 90° domains are said to be ferroelastic as they present two states of stable polarization orientation (ferroelectric) and it is possible to move from one to another of these states by applying a mechanical stress. The question of mobility of these ferroelastic domains was long the object of controversial discussions. The electric field that is developed under the tip has a non-negligible component in the plane, which can represent a certain mobile force for displacing the 90° domains. The images in Figure 9.11 were obtained after having swept the surface of the sample

with an AFM tip while applying a polarization voltage, V_{dc}. We clearly see that certain ferroelastic domains (vertical and horizontal lines) are mobile.

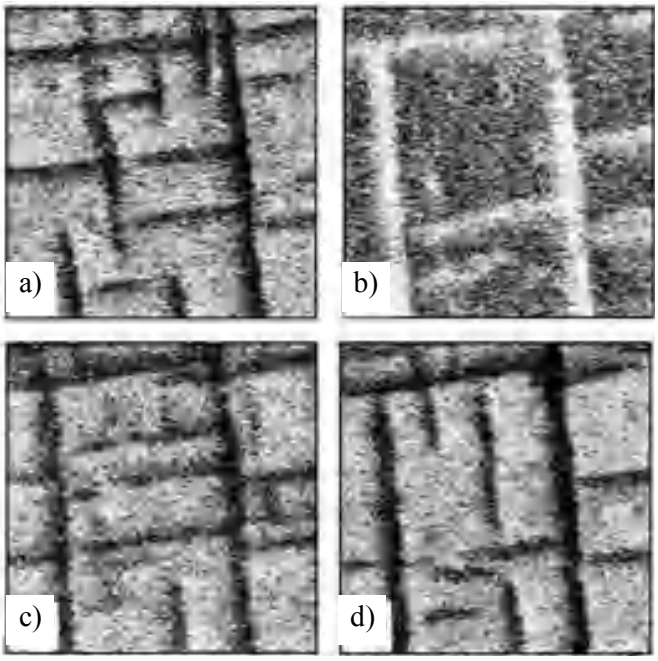

Figure 9.11. *Movement of c/a/c domain walls following the application of a voltage V_{dc}: a) initial state; b) after –6 V; c) after +3 V; and d) after +6 V*

Movement of these ferroelastic domains is translated by a local change in piezoelectric response. Figure 9.12 presents two piezoelectric hysteresis cycles measured on a PZT (20/80) film presenting a *c/a/c* structure as in Figure 9.11, where one is registered on a *c* domain and the other on an *a* domain (in-plane *c*-axis). The first cycle is completely classical and takes into consideration the reversal of polarization in a 180° domain. The second loop itself is completely distorted. The piezoelectric response at equilibrium ($V_{dc} = 0$ V) is close to zero because the polarization vector is in the plane of the sample.

We therefore distinguish two loops depending on whether a positive or negative voltage is applied. Figure 9.12b enables us to understand the form of the cycle. For positive voltages, the volume probed by the tip is a mix of *a* and *c* domains. At saturation ($V_{dc} = +5$ V), the only contribution to the piezoelectric signal comes from the 180° domain. For negative voltages, the piezoelectric response remains constant

up to –4 V (domain *a* does not move), then quickly increases due to the expulsion of *a* domain under the tip. Furthermore, we note that the movement of ferroelastic domains is reversible because the piezoelectric signal returns to zero at equilibrium.

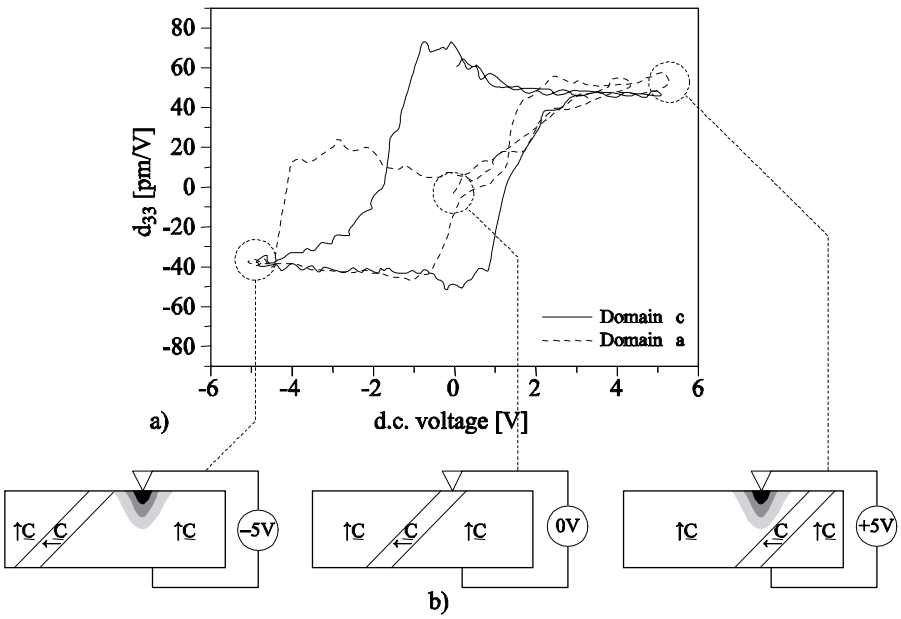

Figure 9.12. *The effect of movement of a 90° domain on the piezo-hysteresis cycle: a) comparison of cycles measured on a* c *domain and* a *domain (in-plane c axis). During measurement, voltage is swept in the following way: 0 → +5V → -5V → +5V; and b) a schematic representation of the movement of the ferroelastic domain under the tip during cycle measurement*

It is also possible to probe the piezoelectric response of a sample across a plane electrode. The electric contact between the tip and the surface therefore ends up being dramatically improved. This enables us to obtain more precise and reliable quantitative results. Figure 9.13 presents three piezoelectric hysteresis cycles recorded across a plane platinum electrode over a PZT film, as presented in Figure 9.11. Curve □ was obtained in a region without ferroelastic domain. As for curves Δ and o, they were measured near a 90° domain. A d_{33} coefficient that is twice as large as the one obtained for a *c* domain is observed locally. The strong spatial change in the piezoelectric coefficient d_{33} is explained by a localized movement of the ferroelastic domains [LER 07]. Although the quality of the piezoresponse images has deteriorated due to the presence of the platinum electrode, it is possible to distinguish the zones where the piezoelectric coefficient is strongly excited, i.e. along the 90° domains (white lines on the piezoresponse image). This

study enabled us to experimentally prove the increase in polarization near 90° domains, in accordance with Ishibashi *et al.*'s predictions [ISH 05].

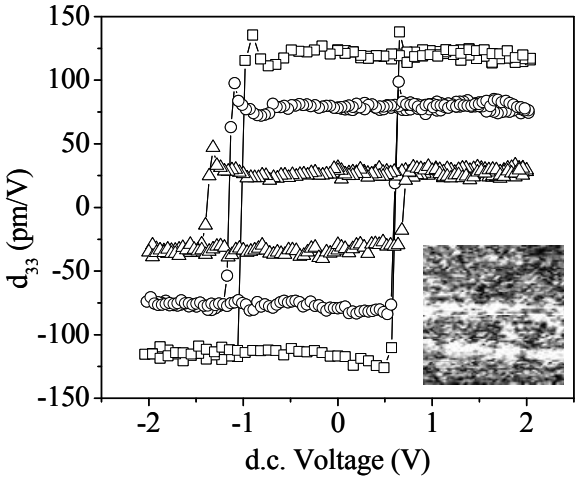

Figure 9.13. *Piezohysteresis measured near a 90° domain (curves o and Δ) and over a* c *domain (curve □) across a plane electrode*

The PFM technique is now a standard method of characterization of ferroelectric materials [ALE 04a]. It is widely used for studying nanostructures in all genres [ALE 04b] such as nanotubes [YUN 03], nanowires [FAN 06] and nanodiscs [HAN 09]. PFM has also contributed to the understanding fatigue mechanisms in ferroelectric films [COL 98] and reversals of ferroelectric domains [GRU 08]. Recently, the Kalinin group in the United States, which is very active in PFM instrumentation and its use for studying materials, developed a spectroscopy mode for PFM called switching spectroscopy PFM [JES 06]. This mode enables recording of a hysteresis loop at any point of an image during its acquisition.

Thus we have access to a panel of data (coercive fields, imprint voltage and amplitude of piezoelectric response), which can be correlated with surface topography and can be very useful for representing spatial variations in the piezoelectric properties of a ferroelectric capacitor [JES 06].

9.3. Ferroelectric measurement

The characteristic property of ferroelectric materials is that the change in polarization due to the electric field presents a hysteresis cycle. The term *ferroelectricity* was chosen by Muller in 1935, due to the analogy between the

hysteretic behavior of electric polarization as a function of the electric field and that of magnetization as a function of the magnetic field in ferromagnetic materials.

At the structural level, the presence of a spontaneous polarization in a ferroelectric compound is due to the existence of dipole moments, the barycenter of positive and negative charges no longer coinciding. A ferroelectric material consists of domains within which the dipoles are oriented in the same direction. Under the application of a sufficient electric field, the material is polarized: domains oriented in the direction of the field grow to the detriment of the others. This contributes to the rise in total polarization. Unlike "ordinary" dielectrics in which polarization, P, linearly varies with the electric field, E, this phenomenon is manifested for ferroelectric materials by a hysteresis cycle, $P(E)$, presented in Figure 9.14. Saturation polarization $\pm P_s$ is obtained when all electric dipoles of the material are oriented parallel to the applied electric field. Remanent polarization $\pm P_r$ is the value of polarization at zero electric field. The coercive field, E_c, is the electric field necessary for cancelling polarization in the material.

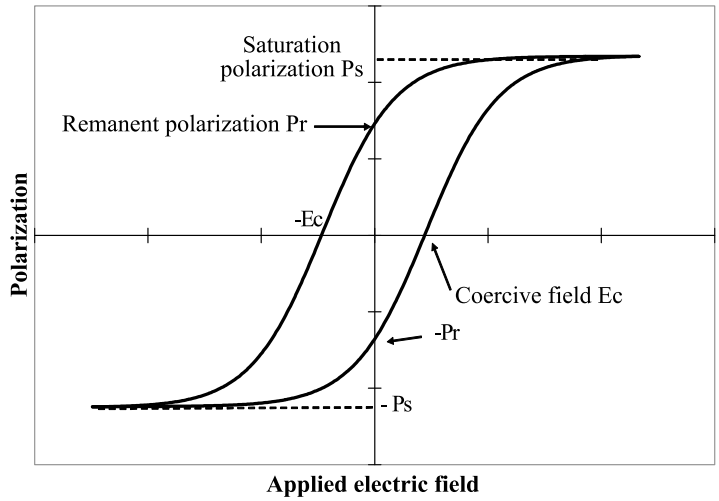

Figure 9.14. *Ferroelectric hysteresis loop*

In the absence of an applied electric field, a ferroelectric material can present two stable states of polarization with opposite signs. Non-volatile memories, the operating principle of which is based on switching between these two states of polarization, are a direct application of ferroelectricity in thin films [SCO 89].

Measurement of the change in polarization with the electric field E can be done with the so-called Sawyer-Tower circuit or the "virtual ground" circuit. These two types of measurement are described below.

9.3.1. *Sawyer-Tower circuit*

The Sawyer-Tower circuit, see Figure 9.15, mainly uses a reference capacitor of known value, C_n, in series with the ferroelectric capacitor, C_{FE}, to be characterized, both being subject to an alternative voltage [SAW 30].

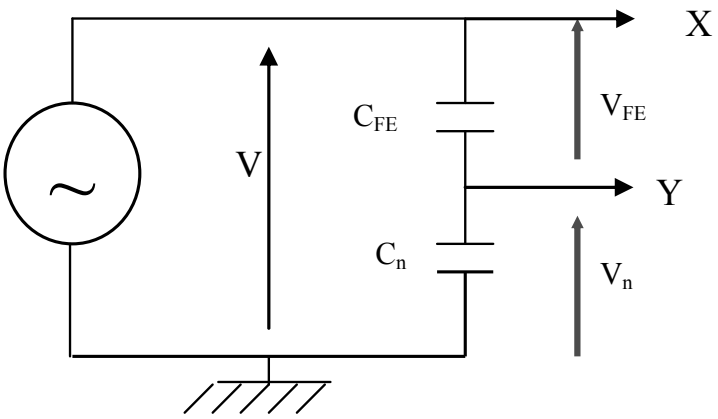

Figure 9.15. *Sawyer-Tower circuit*

It allows us to measure the surface charge density D (D: normal electric displacement in the electrode plane) accumulated at the electrodes. This surface charge density is expressed by:

$$D = \varepsilon_0 E + P \qquad [9.18]$$

with ε_0 being vacuum permittivity, E the electric field applied to the ferroelectric film and P the total polarization of the ferroelectric film. The hysteresis cycle $D(E)$ therefore translates the nonlinear character of domain polarization due to the applied electric field.

By measuring the voltage V_n at the terminals of the standard capacitor C_n in series with the film, we can determine the charge Q_{FE} of the film. Actually, considering two capacitors in series and neglecting the conduction currents in each

of them (the ideal capacitive circuit), the electric charge accumulated by each of the two capacitors is the same.

So we write:

$$Q_{FE} = Q_{n,} \text{ with } Q_{FE} = D.S_{FE} \text{ and } Q_n = Cn$$

S_{FE} being the surface of the ferroelectric capacitor. We then get:

$$D = \frac{C_n \cdot V_n}{S_{FE}} \approx P \qquad [9.19]$$

The measurement of V_n (path Y of the oscilloscope) therefore enables us to access the surface charge density D. In the case of ferroelectrics, the contribution of polarization is much greater than that of the electric field in equation [9.18]. D can therefore be compared to P. The electric field measurement E in the ferroelectric film happens via the X path of the oscilloscope. The voltage V of the generator is expressed:

$$V = V_{FE} + V_n \qquad [9.20]$$

In practice, a sufficiently big C_n is chosen compared to C_{FE} so that its impedance is negligible compared to that of the ferroelectric capacitor. This enables us to write $V \approx V_{FE}$.

In the hypothesis of a uniform electric field in the film, with d being the thickness of the film, E is expressed:

$$E = \frac{V_{FE}}{d} \qquad [9.21]$$

A major drawback of ferroelectric measurement via the Sawyer-Tower circuit is that the ferroelectric capacitor is continuously cycled during measurement time (a few seconds). For films with a precocious fatigue (from 10^4 polarization cycles, for example), we can see the hysteresis cycle progressively vanish (polarization tends to be cancelled) [LER 04]. Fatigue represents the loss of remanent polarization of the ferroelectric material subject to writing/reading cycles. This circuit is therefore not adapted to the study of the fatigue of ferroelectric materials. The “virtual ground”

circuit, which will be presented hereafter, enables us to carry out this type of study because a single period of the signal is applied to the film to make the polarization measurement.

9.3.2. *Virtual ground circuit*

In the method called the *virtual ground* circuit, the reference capacitor is replaced by an operational amplifier A_1 (see Figure 9.16). With the differential input voltage ε being null (where A_1 is ideal), the output voltage U of A_1 is directly proportional to the displacement current i_{dis} crossing the ferroelectric sample ($U = R.i_{dis}$). The current displacement density J_{dis} is then expressed:

$$J_{dis} = \frac{\partial D}{\partial t} = \frac{U}{R.S_{FE}} \qquad [9.22]$$

Current density J_{dis} is then integrated and leads to the value of electric displacement D and therefore to polarization P:

$$P = \int_t \frac{U}{R.S_{FE}} dt \qquad [9.23]$$

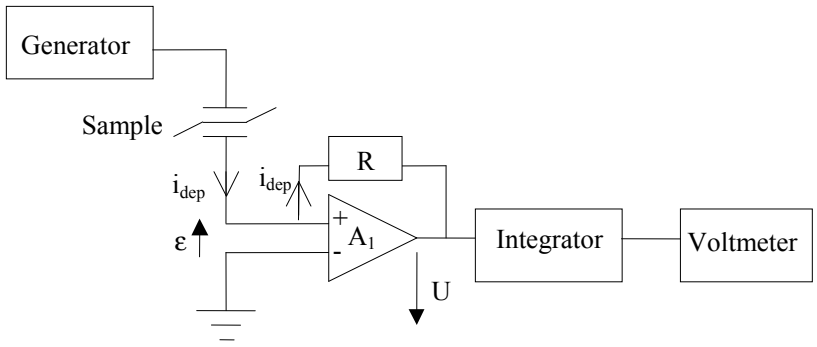

Figure 9.16. *Virtual ground circuit*

In the Sawyer-Tower circuit, when input voltage is rigorously zero and if C_n is not high enough compared to C_{FE} (C_n must be at least 10 times bigger than C_{FE}), the sample undergoes a non-negligible voltage. This residual voltage applied to the

sample is called *back voltage* and does not allow the sample to completely relax. The way to minimize the effect of back voltage consists of choosing $C_n >> C_{FE}$. In this case, however, the voltage levels measured at the terminals of C_n become very low and reduce the accuracy of the measurement of D. On the other hand, with the "virtual ground" circuit, the ferroelectric sample is never subjected to back voltage because ideally $\varepsilon = 0$ (in reality, a few microvolts). That is why this circuit is said to be at "virtual ground" since the ferroelectric capacitor is at mass potential without being materially linked to it.

Moreover, the virtual ground system minimizes the effect of parasitic capacitors inherent to the measurement circuit (cables, ~7 to 10 pF). In the Sawyer-Tower circuit, the error introduced by the parasitic capacitor can be significant if C_n is not sufficiently big compared to the parasitic capacitor. On the other hand, in the virtual ground circuit, the parasitic effect is eliminated due to the fact that the input potential of amplifier A_1 is null.

It is important to specify that the measurements of hysteresis loops only enable us to determine a charge quantity, Q:

$$Q = 2P_rA + \sigma EAt \qquad [9.24]$$

with P_r being the remanent polarization, A the surface area of the capacitor, σ electric conductivity, E the applied electric field and t measurement time. With dielectric losses being proportional to conductivity, σ, these losses can contribute to the apparent polarization of the hysteresis cycle. One of Scott's recent articles shows that the results of ferroelectric polarization loop measurement are too often misinterpreted due to the presence of measurement artifacts such as leakage currents [SCO 08]. Figure 9.17, which represents D–E cycles for non-ferroelectric dielectrics, illustrates this last remark [LIN 77].

Radiant Technologies suggests two methods for measuring remanent polarization. The first one is the method called the virtual ground method, seen above, which allows a hysteresis cycle measurement. The second method, called the *Positive Up, Negative Down* (PUND) method, consists of applying a sequence of five pulses (see Figure 9.18). The first (preset) pulse allows the ferroelectric domains to be oriented in a specified direction and make measurements with comparable initial conditions from one sample to the next. The four others lead the sample to a state of polarization and retain this state during the duration of the pulse. This PUND signal is characterized by three parameters:

– applied voltage, the amplitude of which is identical for each of the five pulses;

– the duration of the pulses;

– the time interval between two consecutive pulses.

Eight polarization values are recorded during this sequence.

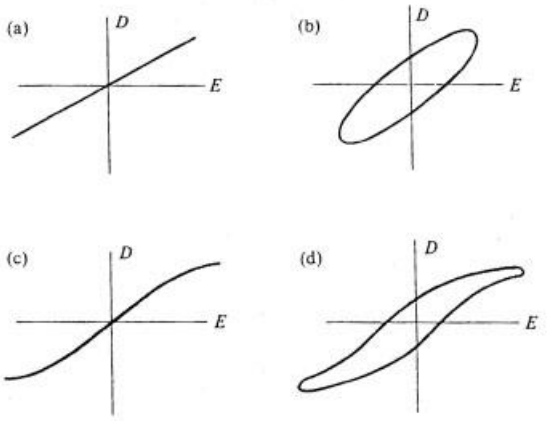

Figure 9.17. *Cycles D–E for: a) lossless linear dielectric; b) linear dielectric with losses; c) nonlinear lossless dielectric; and d) nonlinear dielectric with losses*

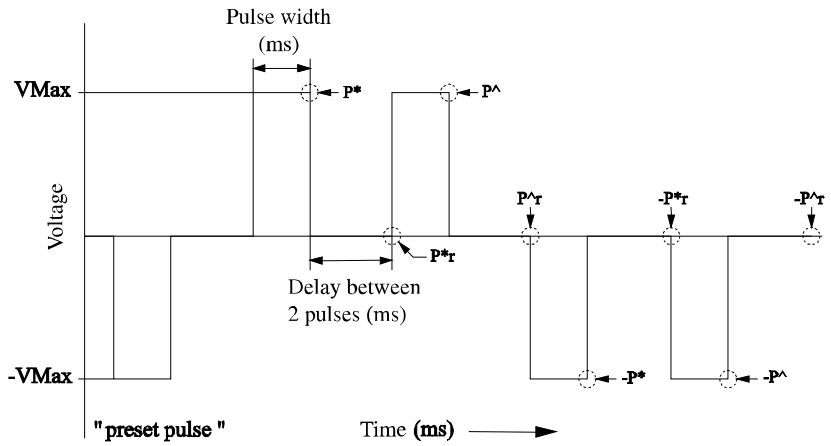

Figure 9.18. *Polarization found during PUND measurement*

The second pulse switches polarization to the opposite state and measures the associated polarization P^* (switched polarization). In this case, P^* contains the sum of two out-of-equilibrium polarization components (remanent + non-remanent). A second measurement is carried out at zero volts just before the third pulse is applied and it gives P^*_r. The time interval between pulses must be sufficient to eliminate the

non-remanent component before the measurement (sample relaxation). The third pulse is identical to the second, except that in this case polarization is not switched.

The two measurements, called $P^\wedge$ and $P^\wedge_r$, contain solely non-remanent polarization components. The fourth and fifth pulses correspond to the second and third pulses, but with opposite sign.

From these different polarization values, also plotted on an arbitrary hysteresis cycle (see Figure 9.19), the term ΔP is defined as follows:

$$\Delta P = P^* - P^\wedge = (\text{remanent} + \text{non- remanent}) - \text{non- remanent}$$

$$= \text{remanent polarization } (2P_r).$$

Similarly we define $\Delta P_r = P^*_r - P^\wedge_r$ so well that we have $\Delta P = \Delta P_r = 2\ P_r$.

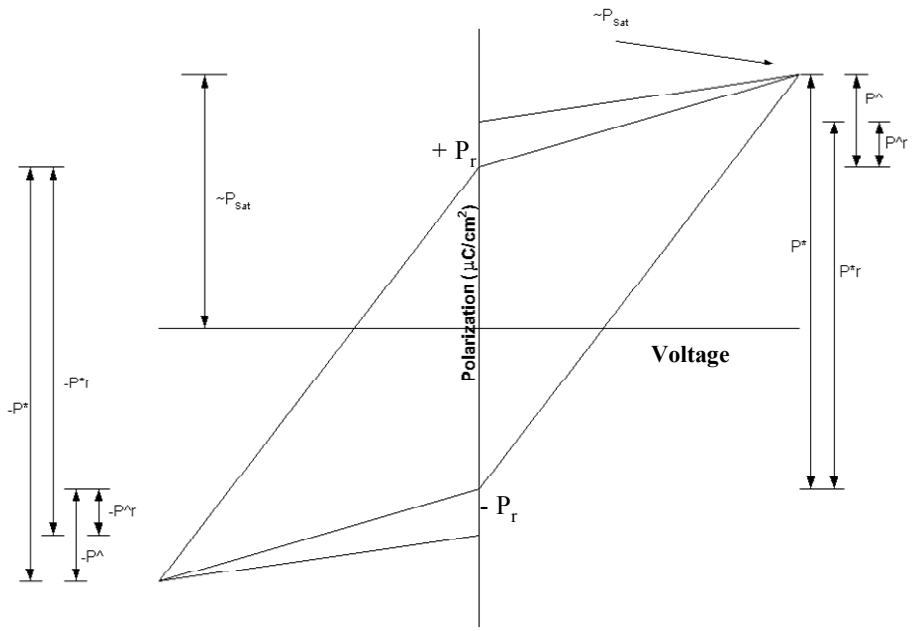

Figure 9.19. *View of the different polarizations on a hysteresis cycle*

9.4. Dielectric measurement

A dielectric is an insulating material that is characterized by the presence of a dipole moment induced by application of an electric field. Such a material placed in

between two electrodes forms a capacitor. When a voltage V is applied to it, the energy stored by the capacitor is given by:

$$W = \frac{CV^2}{2} \qquad [9.25]$$

For a plane capacitor, the capacitance C is expressed as follows:

$$C = \frac{\varepsilon_0 \varepsilon_r S}{d} \qquad [9.26]$$

with ε_0 vacuum permittivity, ε_r relative permittivity, S the surface area of the electrodes and d the thickness.

Two quantities enable us to characterize a dielectric material: its dielectric constant and its dielectric losses. The relative dielectric constant ε_r is defined as being the ratio of the charge stored in a given volume of the material over the charge for an identical volume placed between two electrodes separated by a vacuum. Thus, it indicates the capacity of the material to store electrostatic energy. The dielectric losses correspond to the existence of a dephasing between the displacement current and the alternative voltage applied to the material. They therefore indicate the behavior of the material under an alternative voltage.

A dielectric material can contain mobile and linked electric charges. In the dynamic regime, the total current crossing a capacitor made of a real dielectric is the sum of two contributions: the conduction current and the displacement current. In the case of a plane capacitor, quantities are uniformly distributed (perpendicular to the planes formed by the electrodes) and the current density crossing it is given by:

$$J = \sigma E + \frac{\partial D}{\partial t} \qquad [9.27]$$

with J the current density, σ the conductivity, E the electric field applied and D the electric displacement. In the sinusoidal regime, expression [9.27], with $D = \varepsilon_0 \varepsilon_r E$, becomes:

$$J = \sigma E + j\omega\varepsilon_0\varepsilon_r E \qquad [9.28]$$

with ω the angular frequency of electric quantities. In order to take into consideration dielectric losses appearing in the material when the frequency of the electric signal increases, permittivity is put in complex form:

$$\varepsilon_r = \varepsilon' - j\varepsilon'' \qquad [9.29]$$

with ε' characterizing the faculty of the material to store electrostatic energy and 'characterizing the possible dissipation of part of this energy (in the form of dielectric losses). From this, there results:

$$J = (\sigma + \omega\varepsilon_0\varepsilon'')E + j\omega\varepsilon_0\varepsilon' E \qquad [9.30]$$

In the hypothesis of a uniform electric field perpendicular to the electrodes, $E = \frac{V}{d}$, hence:

$$I = \frac{V}{R_c} + \frac{V}{R_d} + j\omega CV \qquad [9.31]$$

with I the electric current, $R_c = d/(\sigma.S)$ the resistance due to the conduction current, $R_d = d/(\omega\varepsilon_0\varepsilon''S)$ the resistance due to dielectric losses and $C = \varepsilon_0\varepsilon' S/d$ the capacitance of the plane capacitor. In fact, the total current is the sum of two resistive terms, therefore in phase with V and a capacitive term in advanced quadrature with V.

In practice and under dynamic conditions, for a sufficiently insulating material dielectric losses are typically dominant compared to losses by Joule effect, and the equivalent electric circuit of the capacitor is represented in Figure 9.20.

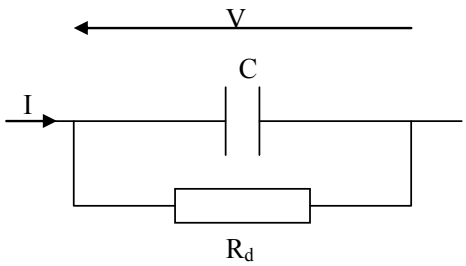

Figure 9.20. *Equivalent circuit of the capacitor considering dielectric losses*

Total impedance can be given by the vector diagram in Figure 9.21, in which $\omega = 2\pi f$.

From this we can deduce:

$$\tan\delta = \frac{1}{\omega R_d C} = \frac{\varepsilon''}{\varepsilon'} \qquad [9.32]$$

tan δ is called the energy loss in the insulator or the dielectric loss tangent. This function characterizes the relation between the current at the origin of dielectric losses and the one that would cross the capacitor in the absence of these losses. It therefore translates the absorption of energy by the material or the deviation presented by this material in comparison to a perfect insulator. A good dielectric therefore has a loss tangent that tends towards zero.

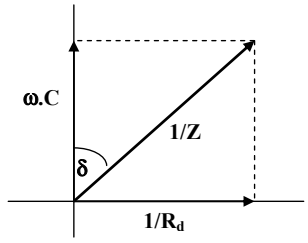

Figure 9.21. *Vector diagram of a capacitor*

The capacitance and loss tangent of films due to the applied electric field and the frequency are measured with the help of an impedance meter. The capacitance of a capacitor is defined as the variation in the charge stored when this charge is subjected to a potential difference, i.e.:

$$C = \frac{\partial Q}{\partial V} \qquad [9.33]$$

The measurement is therefore carried out under dynamic conditions of small signals, i.e. by superimposing a sinusoidal signal $V(t)$ of very low amplitude (10–100 mV) and controllable frequency at a continuous voltage V_0.

Given that $Q = D.S$ and $V = E.d$, it happens that:

$$C \cong \frac{S}{d} \cdot \frac{\partial D}{\partial E} \qquad [9.34]$$

Capacitance is therefore given by variations in electric displacement due to the electric field.

Given that $D = \varepsilon_0.\varepsilon_r.E$, then:

$$C \cong \frac{S}{d}\ \varepsilon_0.\varepsilon_r \qquad [9.35]$$

It is therefore possible to determine the dielectric constant of the material. This constant varies with the applied electric field as shown in Figure 9.22 in the case of a paraelectric material (a) and a ferroelectric material (b). This property of permittivity tunability due to the applied electric field is the basis for agile microwave applications [GEV 09].

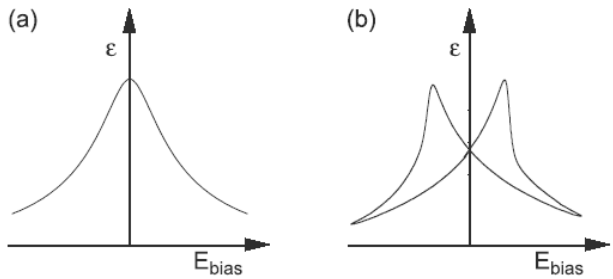

Figure 9.22. *a) Dependence on the electric field of the dielectric constant of a paraelectric material; and b) a ferroelectric material*

9.5. Leakage current in metal/insulator/metal structures

Before any interpretation of capacitors electrical characterization results, a description of the classical mechanisms for leakage current conduction in metal/insulator/metal structures is proposed, as well as a few notions concerning metal/insulator contact.

9.5.1. *Metal/insulator contact: definitions*

9.5.1.1. *Fermi level, work function and electronic affinity*

In a crystal, electrons are located on energy levels separated by forbidden bands. At $T = 0\ K$, all levels located below Fermi level E_F are filled.

If $f_n(E)$ is the probability that a given energy level E is occupied, we have:

$f_n(E) = 1$ if $E < E_F$;

$f_n(E) = 0$ if $E > E_F$.

When the temperature increases, for $T > 0\ K$, electronic distribution loses its "binary" nature. The probability that an energy level E is occupied is then determined by the Fermi-Dirac statistic:

$$f_n(E) = \frac{1}{1 + \exp(\frac{E - E_F}{k_B T})} \qquad [9.36]$$

In the case of metals, the Fermi level E_F is located inside the conduction band. The work function of metal Φ_M represents the energy necessary for extracting an electron from the conduction band towards the vacuum level. The vacuum level is defined as the reference energy of an electron isolated in a vacuum.

For an insulator or a semiconductor, the Fermi level E_F is located inside the forbidden band. The energy necessary to extract an electron from the conduction band to the vacuum level is, in this case, represented by electronic affinity χ. The work function Φ_S necessary to extract an electron from the Fermi level to the vacuum level is then equal to $\chi + \xi$, with ξ defined by the difference between $E_C - E_F$, as represented in Figure 9.23.

When a metal and an insulator or a semiconductor, come into contact, and after thermodynamic equilibrium is reached, the Fermi levels of the two materials are aligned. The band structure in the vicinity of the interface is therefore conditioned by the eventual difference in work function of the two materials.

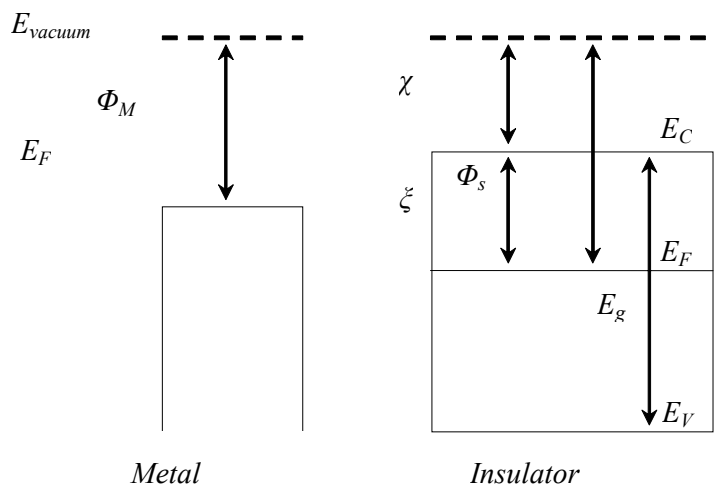

Figure 9.23. *Out of contact metal/insulator energy level diagram*

9.5.1.2. *Neutral contact*

If the work functions are equivalent, $\Phi_M = \Phi_S$, the alignment of Fermi levels does not lead to any a band curvature in the insulator, as shown in Figure 9.24. The height of the interface barrier is then equal to $\Phi_0 = \Phi_M - \chi = \xi$.

This barrier height represents the energy required by an electron to make it move from the Fermi level of the metal to the conduction band of the insulator.

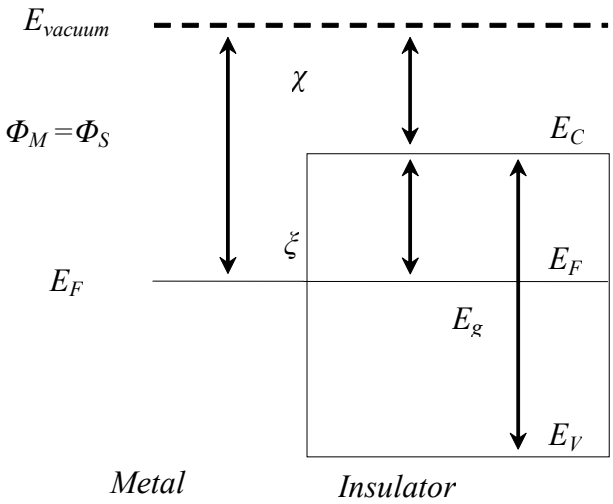

Figure 9.24. *Energy level diagram of a metal/insulator neutral contact*

9.5.1.3. *Blocking contact*

If $\Phi_M > \chi + \xi$, in the case of an insulator or a semiconductor of type *n*, the alignment of Fermi levels leads to an upward band curvature, as indicated in Figure 9.25. Indeed, the work function of the metal is in this case greater than the work function of the insulator. Hence, the electrons move from the insulator to the metal, leading to the creation of a depleted layer in the insulator and the appearance of a positive space charge zone. In the metal, an accumulation of electrons is observed at the interface, to ensure the electrical neutrality condition. The energy contact obtained in this scenario is qualified as a "blocking" contact, because the passage of carriers of metal to the insulator is conditioned by the bringing of a certain quantity of energy determined by the height of the barrier $\Phi = \Phi_M - \chi$. The blocking contact can also be observed when $\Phi_M < \chi + \xi$ in the case of a semiconductor of type *p* [BAR 86].

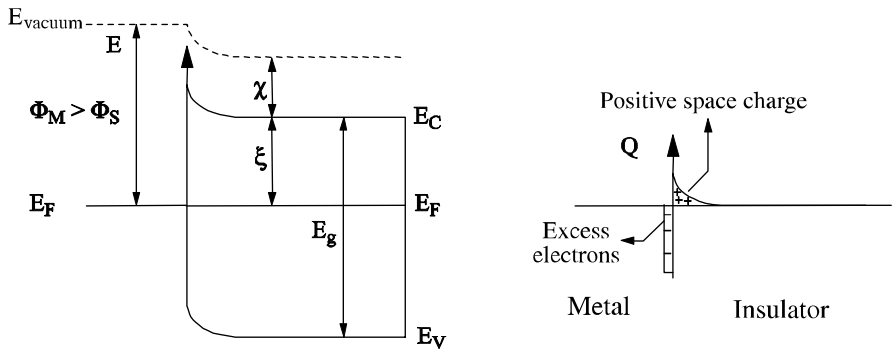

Figure 9.25. *Diagram of the energy bands of a metal/insulator blocking contact*

9.5.1.4. *Ohmic contact*

If $\Phi_M < \chi + \xi$, in the case of an insulator or a semiconductor of type *n*, the alignment of Fermi levels is accompanied by a downward band curvature, as represented in Figure 9.26.

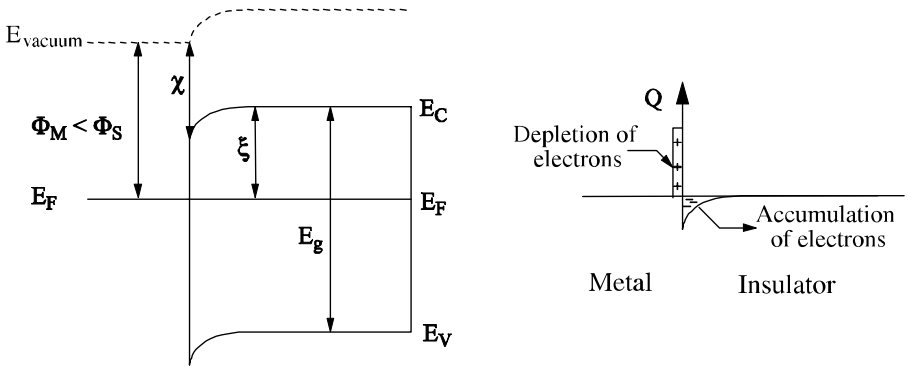

Figure 9.26. *Diagram of energy bands of a metal/insulator ohmic contact*

Actually, with the work function of the metal being lower than that of the insulator, electrons are extracted from the metal to the insulator. A layer of electrons is formed at the interface of the insulator, while a layer of depletion appears in the side of the metal. When the width of accumulation reaches a dimension close to that of the insulator thickness, the electronic density greatly exceeds the intrinsic density of the carriers.

A perfect injection at the interface is hence obtained and the current is then only limited by the material bulk. This type of contact called *ohmic contact* is also observed when $\Phi_M > \chi + \xi$ in the case of an insulator or a semiconductor of type *p* [BAR 86].

9.5.1.5. *Intrinsic and extrinsic carriers*

Carriers are called "intrinsic" when they come from the insulating material itself and "extrinsic" when they are injected by electrodes. Above a certain voltage level, conduction is ensured by extrinsic carriers and the transport mechanisms are then divided into two main families:

– the injection of carriers is *limited by interfaces* and the electrons freely cross through the insulator bulk once they are injected (Schottky emission, tunnel conduction); or

– the electrodes behave like infinite sources of carriers and the current is *limited by the bulk* of the insulator (Poole-Frenkel effect, conduction by carriers jumping from trap to trap, current limited by the space charge).

9.5.2. *Conduction mechanisms limited by the interfaces*

Conduction mechanisms limited by the interfaces are observed when metal/insulator contact is either neutral or blocking.

9.5.2.1. *Schottky emission*

In the case of Schottky emission or thermoionic emission, the current is generated by the carriers flowing above the potential barrier at the interface (see Figure 9.27). With Φ_m being the height of the energy barrier to be crossed by the carriers to be injected, the thermoionic current expression is given by:

$$J = A^* T^2 \exp\left(\frac{-\Phi_m}{k_B T}\right) \qquad [9.37]$$

where A^* represents the Richardson constant modified by the introduction of m^*, the effective mass of the electrons, which replaces m_0, the free mass of the electrons:

$$A^* = \frac{4\pi m^* q k_B{}^2}{h^3} = 120\frac{m^*}{m_0} \qquad [9.38]$$

The term Φ_m corresponds to the maximum of the potential energy curve of injected carriers, $\Phi(x)$. This evolution of potential energy in the thickness of the film

is described by equation [9.39], in which Φ_0, $\Phi_{im}(x)$ and E_{ext} represent, respectively, the energy difference between the Fermi level of the metal and the conduction band of the insulator, the lowering of the barrier resulting from the force image [BAR 86] and the applied field:

$$\Phi(x) = \Phi_0 - \Phi_{im}(x) - E_{ext}x \qquad [9.39]$$

Using the approximation of the lowering $\Phi_{im}(x)$ valid for regions close to the interface [BAR 86], we have:

$$\Phi_{im}(x) = \frac{q^2}{4\pi\varepsilon_0\varepsilon_i} \cdot \frac{1}{4x} \qquad [9.40]$$

The maximum Φ_m is reached for the value x_m that verifies the condition $d\Phi(x)/dx = 0$. By inserting equation [9.40] into equation [9.39], after derivation we get:

$$x_m = \frac{q}{(16\pi\varepsilon_0\varepsilon_i E_{ext})^{1/2}} \qquad [9.41]$$

The energy barrier Φ_m at the metal/insulator interface is therefore obtained by taking $x = x_m$ in equation [9.39], i.e.:

$$\Phi_m = \Phi_0 - \left(\frac{qE_{ext}}{4\pi\varepsilon_0\varepsilon_i}\right)^{1/2} \qquad [9.42]$$

The final expression giving the evolution of thermoionic current as a function of temperature and applied electrical field E_{ext} is obtained by implementing the Φ_m expression in equation [9.37]:

$$J = A^* T^2 \exp\left[-\frac{\Phi_0 - (qE_{ext}/4\pi\varepsilon_0\varepsilon_i)^{1/2}}{k_B T}\right] \qquad [9.43]$$

At constant temperature, the semi-logarithmic representation $ln(J) = f(E_{ext}^{1/2})$ of a Schottky current is a linear characteristic, with a slope controlled by the constant ε_i, defined as the square of the optical refraction index of the material: $\varepsilon_i = n^2$.

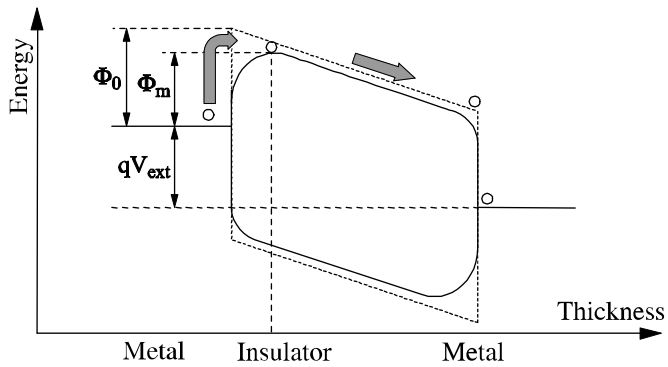

Figure 9.27. *Diagram of energy bands of a metal/insulator/metal structure under the effect of an applied voltage V_{ext}: illustration of the Schottky injection mechanism*

9.5.2.2. *Tunnel conduction*

Tunnel conduction is observed when the carriers have insufficient energy to cross above the potential barrier at the interface. The only way for these carriers to be injected in the oxide is to cross the barrier using the tunnel effect. The current density therefore depends on the quantity of electrons likely to cross through the barrier by tunnel effect. It also depends on their energy distribution given by the Fermi-Dirac statistic *f(E)*, as well as the transparence *T(E)* that represents the probability that an electron might cross the energetic barrier of the oxide [BAR 86].

Depending on the level of the electric field applied, two possibilities represented in Figures 9.28a and 9.28b, respectively, can be distinguished:

– the direct tunnel effect;

– the Fowler-Nordheim tunnel effect.

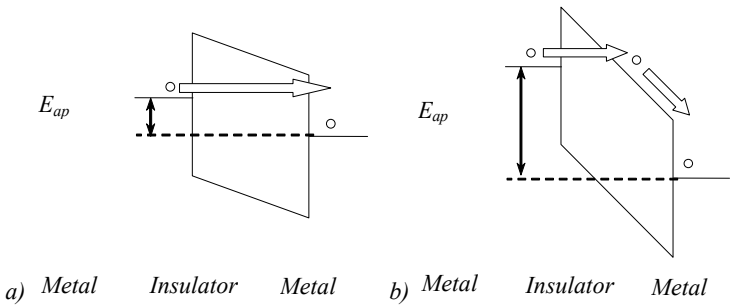

Figure 9.28. *Illustration of: a) direct tunnel effect; and b) Fowler-Nordheim tunnel effect*

The direct tunnel effect corresponds to a trapezoidal barrier configuration that is observed for low electric field strengths. In this case, the carriers are injected directly from one electrode to the other without passing through the conduction band of the insulator.

The Fowler-Nordheim tunnel effect is observed for higher field strengths, in the case of a triangular barrier configuration. After having crossed the barrier, the carriers pass through the conduction band of the insulator before joining the other interface. In this last case, the simplified expression of the Fowler-Nordheim current density is expressed by [BAR 86]:

$$J = \frac{q^2 E_{ext}^2}{8\pi h \Phi_0} \exp\left[\frac{4\sqrt{2m^*}\,(\Phi_0)^{3/2}}{3\hbar q E_{ext}}\right] \qquad [9.44]$$

9.5.3. *Bulk-limited conduction mechanisms*

In the case of an ohmic contact, the injection from interfaces is considered to be perfect and the leakage current depends only on electronic properties of the insulator. The conduction of carriers in the insulator relies on trapping/untrapping mechanisms by shallow trap levels N_t, as well as by donor levels N_D localized from a few tens of eV to a few eV, respectively, under the conduction band.

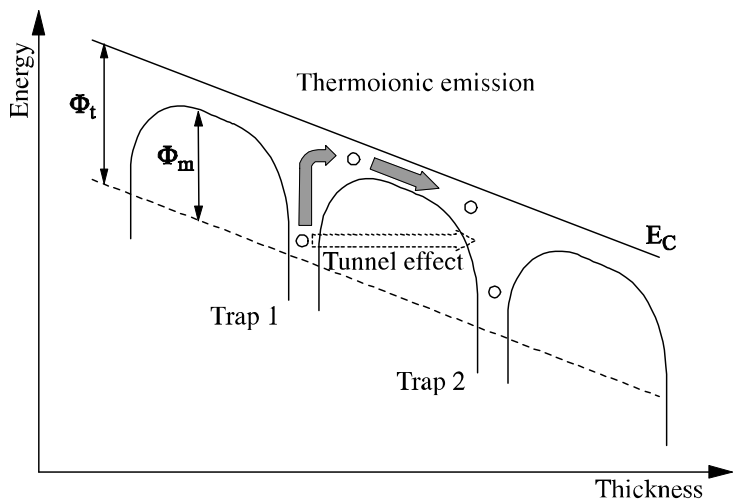

Figure 9.29. *Diagram of the potential energy of an insulator, containing trap levels subjected to an applied voltage V_{ext}. Thermoionic emission is produced the Poole-Frenkel-type mode of conduction, whereas the tunnel effect corresponds to hopping mode*

As long as trap levels are not saturated, electronic conduction is ensured by the transfer of carriers from trap to trap. Considering the energy diagram in Figure 9.29, two conduction mechanisms can be observed: *Poole-Frenkel emission* (thermoionic effect) and *hopping* (tunnel effect from trap to trap). When the injection becomes strong, a space charge is established in the film due to the accumulation of charges in the insulator. We are entering the regime of *conduction limited by space charge*.

9.5.3.1. *Poole-Frenkel emission*

Poole-Frenkel emission takes place when carriers have enough energy to cross the potential barrier through thermoionic emission ($E_{carriers} > \Phi_m$). For a given trap site, the height of the barrier Φ_m to cross over is calculated by taking into consideration the decrease in potential energy due to Coulombic interactions of the carriers trapped in neighboring sites. Assuming that the trapping sites are sufficiently spread, evolution of the height of the energy barrier with the applied field E_{ext} can be approximated by equation [9.45]:

$$\Phi_m = \Phi_t - \left(\frac{qE_{ext}}{\pi\varepsilon_0\varepsilon_i} \right)^{1/2} \qquad [9.45]$$

In the case of a thin film for which the width of the zone where electrons accumulate at the interface is large in comparison with the film width, the evolution of Poole-Frenkel current is given by:

$$J = q\mu E_{ext} N_C \exp\left[-\frac{\Phi_t - (qE_{ext} / \pi\varepsilon_0\varepsilon_i)^{1/2}}{k_B T} \right] \qquad [9.46]$$

In this equation, we find the general expression for the transport of charges in a material, with μ being the mobility of the carriers, E_{ext} the electric field applied and q the elementary charge. The term $N_C \exp\left[-\frac{\Phi_t - (qE_{ext} / \pi\varepsilon_0\varepsilon_i)^{1/2}}{k_B T} \right]$ represents the density of carriers coming from trapping levels and passing through the conduction band.

9.5.3.2. *Hopping conduction*

When the energy of the carriers is too low to cross the potential barrier ($E_{carriers} < \Phi_m$), conduction can be ensured by tunnel effect. This is called hopping conduction. The current is then directly proportional to the field applied, and also depends on the density of trapped electrons and the frequency of jumps between two sites. A simplified mathematical expression of the current density obtained by this mechanism is:

$$J = \frac{q^2 a^2}{k_B T \tau_0} n^* E_{ext} \exp\left(-\frac{4\pi m^* \Phi_m a}{h}\right) \quad [9.47]$$

where τ_0 is a time constant, a represents the distance between two traps and n^* is the density of trapped carriers.

9.5.3.3. *Space-charge-limited conduction*

In the two mechanisms limited by bulk – Poole-Frenkel and hopping conduction – the electric field is assumed to be constant across the thickness of the insulator. This hypothesis becomes false when the injection of carriers becomes too strong, due to the space charge that is established in the film. The distribution of potential is therefore modified according to Poisson's law and the evolution of space-charge-limited current density is given by:

$$J = \frac{9\varepsilon_0 \varepsilon_i \mu \theta}{8d^3} V_{ext}^2 \quad [9.48]$$

where θ represents the rate at which the traps are filled, μ is the electronic mobility of the carriers, d represents the thickness of the film and V_{ext} is the applied voltage.

A *very strong injection regime* is achieved when all the traps are filled ($\theta = 1$). The transition between the strong and very strong injection regime is characterized by the trap filled limit voltage:

$$V_{TFL} = \frac{qN_t d^2}{2\varepsilon_0 \varepsilon_i}$$

where N_t represents the trap density.

9.6. Bibliography

[ALE 04a] ALEXE M., GRUVERMAN A., (Eds.), *Ferroelectrics at Nanoscale: Scanning Probe Microscopy Approach*, Springer, New York, 2004.

[ALE 04b] ALEXE M., HARNAGEA C., HESSE D., *Journal of Electroceramics,* vol. 12, 69-88, 2004.

[BAR 86] BARBOTTIN G., VAPAILLE A., *Instabilities in Silicon Devices*, *Silicon Passivation and Related Instabilities*, vol. I, North Holland, Amsterdam, 1986.

[BIN 82] BINNIG G., ROHRER H., GERBER CH., WEIBEL E., *Applied Physics Letters,* vol. 40, 178-180, 1982.

[BIN 86] BINNIG G., QUATE F.C., GERBER CH., *Physical Review Letters*, vol. 56, 930-933, 1986.

[BIR 91] BIRK H., GLATZ-REICHENBACH J., JIE L., SCHRECK E., DRANSFELD K., *Journal of Vaccum Science Technology*, vol. B 9, 1162-1165, 1991.

[CAL 07] CALAME F., MURALT P., *Applied Physics Letters*, vol. 90, no. 6, 62907, 2007.

[CHR 98] CHRISTMAN J.A., WOOLCOTT R.R., KINGON A.I., NEMANICH R.J., *Applied Physics Letters,* vol. 73, 3851-3853, 1998.

[COL 98] COLLA E.L., HONG S., TAYLOR D.V., TAGANTSEV A.K., SETTER N., NO K., *Applied Physics Letters*, vol. 72, 2763-2765, 1998.

[DEF 06] DEFAŸ E., ZINCK C., MALHAIRE C., BABOUX N., BARBIER D., "Modified free vibrating beam method for characterization of effective e31 coefficient and leakage resistance of piezoelectric thin films", *Review of Scientific Instrument*, vol. 77, p. 103903-7, 2006.

[DES 92] DESCHANVRES J.L., REY P., DELABOUGLISE G., LABEAU M., JOUBERT J.C., PEUZIN J.C., *Sens. Actuators A*, vol. 33, 43, 1992.

[DUB 99] DUBOIS M.A., MURALT P., *Sensors and Actuators A*, vol. 77, 106, 1999.

[ELI 01] ELLISALDE C., RAVEZ J., *Journal of Materials Chemistry*, vol. 11, 1957-1967, 2001.

[FAN 06] FAN H.J., LEE W., HAUSCHILD R., ALEXE M., LE RHUN G., SCHOLZ R., DADGAR A., NIELSCH K., KALT H., KROST A., ZACHARIAS M., GOESELE U., *Small 4*, 561-568, 2006.

[FEY 99] FEYNMAN R., *Le cours de Physique de Feynman – électromagnétisme 2*, Dunod, Paris, 1999.

[GEV 09] GEVORGIAN S., *IEEE Microwave Magazine*, 93-98, 2009.

[GRU 08] GRUVERMAN A., WU D., SCOTT J.F., *Physical Review Letters*, vol. 100, 097601, 2008.

[GUT 92] GUTHNER P., DRANSFELD K., *Applied Physics Letters*, vol. 61, 1137-1139, 1992.

[HAN 09] HAN H., JI R., PARK Y.J., LEE S.K., LE RHUN G., ALEXE M., NIELSCH K., HESSE D., GOESELE U., BAIK S., *Nanotechnology*, vol. 90, no. 8, 2009.

[HAR 00] HARNAGEA C., PIGNOLET A., ALEXE M., HESSE D., GOESELE U., *Applied Physics A,* vol. 70, 261-267, 2000.

[HAR 01] HARNAGEA C., PhD Dissertation, Halle, Germany, 2001.

[HAR 04] HARNAGEA C., PIGNOLET A., in ALEXE M. and GRUVERMAN A. (eds.), *Ferroelectrics at nanoscale: scanning probe microscopy approach*, Springer, New York, 45-85, 2004.

[ISH 05] ISHIBASHI Y., IWATA M., SALJE E.K.H., *Japanese Journal of Applied Physics*, Part 1 vol. 44, 7512-7517, 2005.

[JES 06a] JESSE S., BADDORF A.P., KALININ S.V., *Applied Physics Letters,* vol. 88, 062908, 2006.

[JES 06b] JESSE S., LEE H.-N., KALININ S.V., *Review of Scientific Instruments*, vol. 77, 073702, 2006

[KHO 96] KHOLKIN A.L., WUTCHRICH CH., TAYLOR D.V., SETTER N., *Review of Scientific Instruments*, vol. 67, no. 5, 1935, 1996.

[LER 06] LE RHUN G., VREJOIU I., PINTILIE L., HESSE D., ALEXE M., GOESELE U., *Nanotechnology*, vol. 17, 3154-3159, 2006.

[LER 07] LE RHUN G., VREJOIU I., ALEXE M., *Applied Physics Letters*, vol. 90, 012908, 2007.

[LER 04] LE RHUN G., POULLAIN G., BOUREGBA R., LECLERC G., *J. Eur. Ceram. Soc*., vol. 25, 2281-2284, 2004.

[LIN 77] LINES M.E., GLASS A.M., *Principles and Applications of Ferroelectrics and Related Materials*, Clarendon Press, Oxford, 1977.

[ROY 76] ROYBURD A.L., *Physica Status Solidia*, vol. 37, 329, 1976.

[SAW 30] SAWYER C.B., TOWER C.H., *Physical Review*, vol. 35, 269-273, 1930.

[SCO 89] SCOTT J.F., PAZ DE ARAUJO C.A., *Science*, vol. 246, 1400-1405, 1989.

[SCO 08] SCOTT J.F., *Journal of Physics: Condensed Matter*, vol. 20, 021001, 2008.

[VRE 06] VREJOIU I., LE RHUN G., ZAKHAROV N.D., HESSE D., PINTILIE L., ALEXE M., *Philosophical Magazine*, vol. 86, 4477-4486, 2006.

[YUN 03] YUN L., SZAFRANIAK I., ZAKHAROV D., NAGARAJA V., STEINHART M., WHERSPOHN R.B., WENDORFF J.H., RAMESH R., ALEXE M., *Applied Physics Letters*, vol. 83, 440-442, 2003.

Chapter 10

Piezoelectric Resonators and Filters

10.1. Acoustic resonators: principle and history

10.1.1. *Quartz resonators*

In practice, the first bulk acoustic wave resonators were produced using quartz plates. Longitudinal waves were initially used in this type of component, but these waves quickly proved to be temperature-sensitive, leading to frequency shifts of resonators with temperature changes.

Crystal cuts enabling the generation of waves with reduced temperature sensitivities were therefore investigated. The AT cut, obtained by rotating the plate 35.15° around the crystallographic X axis proves to be nearly insensitive to temperature changes close to the ambient temperature, with only a second-order frequency versus temperature derivative. This cut is still used today. Here, only slow transverse waves are piezoelectrically coupled.

In the 1980s, other cuts appeared. These cuts were obtained by two successive rotations around the crystallographic axes. These cuts, called FC, IT or SC, exhibit a third-order temperature derivative only, but around a temperature higher than the ambient temperature (55°C for the FC cut, or even 95°C for the SC cut).

Another major problem with these resonators is the arrangement of their support. During packaging, quartz crystals must be mechanically maintained without their vibrations being disturbed. For high-quality factor resonators, the geometries of the

---

Chapter written by Alexandre REINHARDT and Christophe BILLARD.

resonators are optimized: the plates are generally chamfered or one (or two) of their faces is convex, which geometrically forces a confinement of acoustic energy to the center of the resonator and enables the plate to be fixed by its edges.

In 1965, Newell described a way to transform the acoustic impedance of the mechanical support of a resonator in such a way that it was comparable to that of air or a vacuum and therefore provide a robust mechanical solution to the problem of mounting resonators in a package [NEW 65]. For this, Newell suggested stacking quarter-wavelength layers of materials with very different acoustic impedances above the substrate. This way, very low impedance can be obtained and vibration of the resonator is no longer transmitted into the substrate, which therefore no longer disturbs its operation. In practice, acoustic waves generated in the resonator are reflected by a Bragg lattice, which prevents the resonator from radiating into its support.

Another interesting effect, as Newell showed, is that this also makes the complete structure more rigid and so decreases the amplitude of parasitic resonances produced by parasitic plate modes [NEW 65]. This idea has however never been implemented, because it forces us to stack a certain number of plates together while guaranteeing excellent mechanical contact at each interface. This invention is to be noted, however, as it will be reused for resonators based on piezoelectric thin films operating at high frequency, as we will see later.

The solution finally retained was suggested in 1977 by Besson. He presents an architecture of suspensions that are used to fabricate the resonators with the highest quality factors [BES 77]: the central part, the only one to vibrate, is supported by four bridges, as represented in Figure 10.1. The bridges are oriented according to the direction of minimum sensitivity to stresses. The structure is monolithically determined by chemical etching of a single crystal disc.

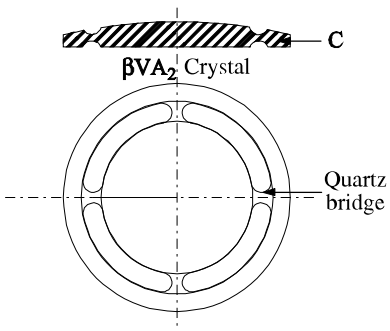

Figure 10.1. *Architecture of the resonator suspended by bridges, also called self-suspended quartz [BES 77]*

Frequency stability was further improved by no longer placing electrodes on quartz, but on the encapsulation placed on both sides of the resonator. The space between the quartz crystal and its electrodes is only a few microns, so that the electric field generated in the quartz crystal is hardly modified compared to a classic resonator. The absence of contact between electrodes and the piezoelectric medium suppresses metal diffusion phenomena in the quartz, which guarantees the long-term stability of the resonator. This structure is designed like BVA: improved ageing packaging and is represented in Figure 10.2.

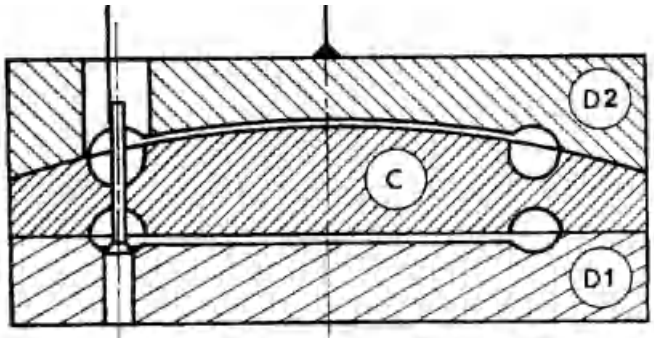

Figure 10.2. *Quartz improved ageing packaging [BES 77]*

Such very high spectral purity resonators are used for time-frequency metrology applications where very great frequency stability is necessary. Atomic clocks are a typical example of this: atomic time references (such as, for example, Cesium fountains) are, in practice, enslaved by quartz resonators to ensure their long-term stability [BES 95].

10.1.2. *High-frequency operation of resonators*

The theoretical analysis of bulk wave resonators in Chapter 7 showed that resonance frequency is directly related to the thickness of the piezoelectric material. In other words, the increase in operation frequency is obtained by thinning the piezoelectric substrates used. For a long time this has limited quartz resonator operation to a few hundreds of MHz. One way of pursuing the increase in frequency while keeping thicknesses compatible with classic quartz machining techniques was, initially, to make resonators work in harmonic modes. Nevertheless, as we saw, operating on a harmonic p leads to a decrease in the effective electromechanical coupling coefficient of p^2, which seriously limits their use for filtering applications. In order to keep an effective coupling coefficient that is compatible with filter synthesis, in 1971 Roberts had the idea of using a cadmium sulfide (CdS) thin film

sandwiched between two electrodes and placed atop a quartz substrate [ROB 71], as represented in Figure 10.3. He showed that harmonic modes of a composite structure can exhibit effective coupling factors higher than the dominant vibration mode. He therefore ended up reaching effective coupling coefficients of 5% at 234 MHz, on the ninth harmonic, which is unattainable with quartz alone.

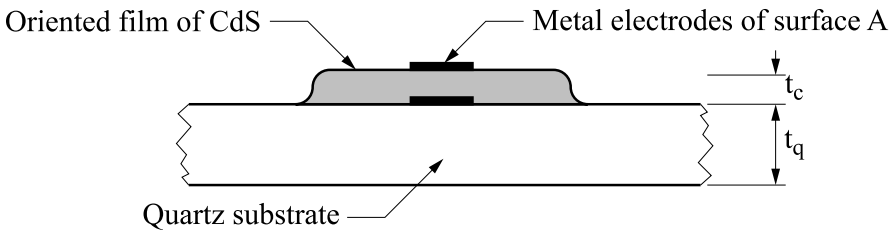

Figure 10.3. *CdS/quartz resonator [ROB 71]*

Another method, suggested in 1974 by Coussot [COU 74], is to locally thin a piezoelectric substrate made, for example, of lithium niobate in such a way as to form a membrane that is then metalized on its two faces. For mechanical reasons, the thickness of these membranes was initially limited to 10–20 µm, which only lead to frequencies of 100–200 MHz. In 1978, based on same idea, Berté [BER 78] created resonators made of 3 µm thick quartz membranes and he obtained a dominant mode at 525 MHz.

In 1980, Grudkowski [GRU 80] and Lakin [LAK 80] combined the two approaches above to create composite resonators made of piezoelectric thin films supported by a silicon membrane obtained by a local etching of the substrate. These devices are represented in Figure 10.4. Their works take advantage of advances in the fields of piezoelectric thin film deposition and silicon etching. The advantage of using a silicon substrate is the possibility of co-integration with active circuits or with MEMS components.

In order to precisely control the membrane thickness, the two authors implanted the silicon substrate with boron over the membrane. Etching of the substrate is based on a chemical attack that has a strong etching selectivity between the intrinsic and doped silicon, in such a way as to form almost an etch stop layer.

With the piezoelectric film, the two candidates initially studied were zinc oxide (ZnO) and aluminum nitride (AlN), the first having slightly better piezoelectric properties than the second, but a lower bulk wave propagation velocity (11 km/s for AlN compared to 6.4 km/s for ZnO). This forces the use of thinner films at equivalent frequency and therefore is less suited to operation at higher frequencies.

In addition, AlN exhibits lower variations of its acoustic properties with temperature. This is why it is this material that is currently almost the only one used in industrial production.

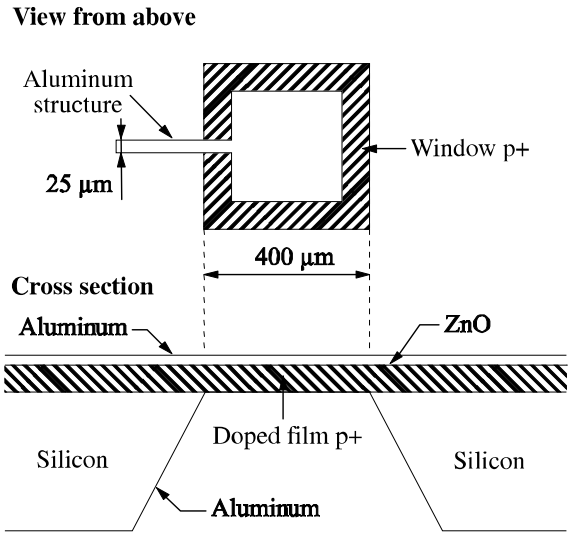

Figure 10.4. *Composite ZnO/Si resonator [LAK 82]*

These two materials are of hexagonal crystal structure. Naturally, deposition of these materials on textured electrodes or an amorphous plane surface leads to the crystallographic axis of symmetry being perpendicular to the surface of the substrate. For this reason, when metalizing the two faces of the piezoelectric film, longitudinal waves are naturally excited across its width. The principal mode of vibration of these resonators is therefore different from the shear mode used in classic quartz resonators and bulk wave filters. Nevertheless, as shown by theoretical calculations, this has no fundamental impact on the operation of these components.

The first resonators of this type, called thin film resonators (TFR), have a dominant mode at frequencies of several hundred MHz. In order to be able to increase operation frequency while trying to preserve the use of the fundamental vibration mode, it proved necessary to further reduce the resonator thickness. To this end, as soon as deposition processes enabled low-stress films to be obtained, support membranes proved to be useless. Resonators became then only composed of a self-suspended piezoelectric film sandwiched between two electrodes, coming closer to the ideal resonator, as represented in Figure 10.5. In practice, such a structure does not enable temperature compensation as the piezoelectric films used do not present

intrinsic compensation. The temperature derivative is nevertheless similar to the one displayed by surface acoustic wave resonators (SAWs), which is the technology that is principally used for radio frequency filtering. Due to the polycrystalline character of the films deposited and defects in these films, suppressing a single crystal support leads to a more fragile structure and a decrease in its coefficient of quality at the same time. Nevertheless, it enables a clear increase in resonance frequency and in electromechanical coupling factor. These defects initially noticed have not been shown to be unacceptable for the use of these resonators in radiofrequency filters.

As represented in Figures 10.4 and 10.5, the chemical etching of silicon originally used produces inclined grooves corresponding to the crystal planes with the lowest etching velocity. These grooves force us to foresee that etching openings will be considerably larger than the resonator, which strongly reduces the om-wafer integration. From an industrial point of view, therefore, this solution is not very profitable. Processes for dry deep etching of silicon were used to supply almost vertical grooves. Such a stage nevertheless remains expensive, as it requires a double-side alignment and relatively long etching times.

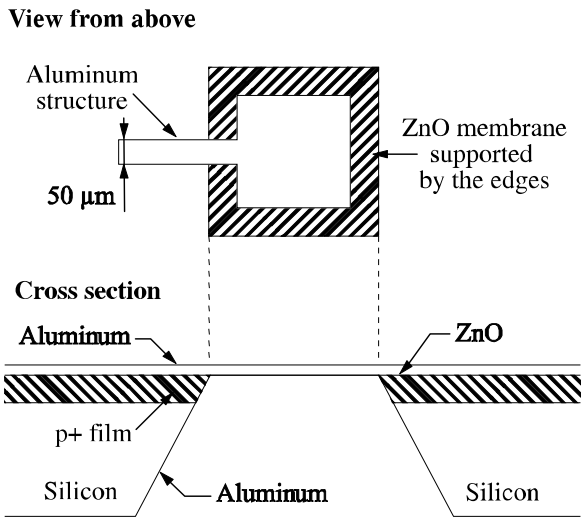

Figure 10.5. *Resonator with self-suspended piezoelectric film [LAK 82]*

To overcome these limitations, Satoh *et al.* [SAT 85] developed a process flow for obtaining a suspended piezoelectric membrane offering a high integration density, relying entirely on operations carried out on the top face of the substrate: the resonator is built on top of a sacrificial film. This film is removed by chemical etching or plasma etching across liberation orifices. At the end of this process, a

membrane suspended above an air gap is obtained, as represented in Figure 10.6. This new type of component is called a film bulk acoustic resonator (FBAR).

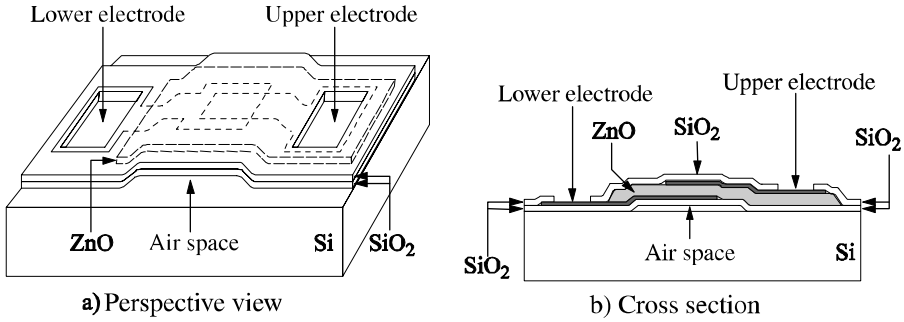

Figure 10.6. *Air gap resonator [SAT 85]*

Piezoelectric membranes, whether they are produced by backside etching of the substrate or by the use of a front face sacrificial layer, remain very flexible and mechanically fragile. In addition, they exhibit a reduced path for evacuation of the heat generated in the resonator during operation, which can be the source of power-related problems. This is why Lakin, in 1995, suggested a new resonator concept based on piezoelectric thin films [LAK 95a]. Returning to Newell's idea of using an acoustic Bragg mirror to isolate a quartz resonator from its support [NEW 65], he suggested applying this idea to resonators using piezoelectric thin films. At frequencies of a few GHz, the quarter-wavelength films necessary for forming a Bragg mirror have thicknesses accessible to thin film deposition techniques, just like the piezoelectric film. For this reason, a mirror can be simply produced by a succession of thin film depositions. Such a device has been baptized a solidly mounted resonator (SMR) and is represented in Figure 10.7.

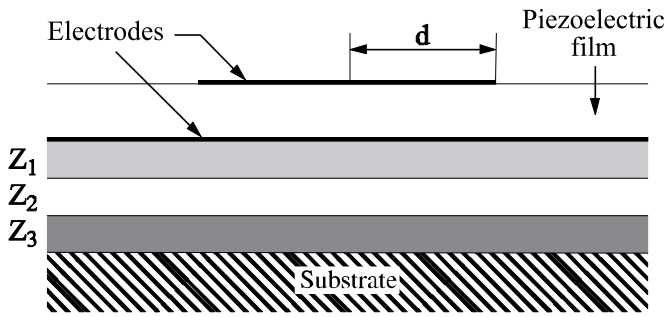

Figure 10.7. *Diagram of a SMR [LAK 95b]*

10.1.3. *Perfecting FBAR and SMR resonators*

Specifications of standards involving FBAR or SMR resonators require filters with relative pass bands varying between 3 and 4% of their center frequency. This requires resonators with electromechanical coupling factors in the order of 6–8% in order to allow a spacing between resonance and antiresonance frequencies sufficient to limit the insertion losses and ripple of the transmission function. AlN, almost exclusively used industrially for these applications, has an electromechanical coupling coefficient of 6.5%. It therefore fulfills the specification of only the least critical standards. Even for these standards, however, taking into consideration the frequency shifts caused by temperature changes requires filters with wider bands to be designed, which finally require electromechanical coupling coefficients approaching 7%. To be able to synthesize these filters, it is therefore necessary to prevent deterioration of this coupling coefficient and to seek to improve the intrinsic performances of the material used [KAI 07].

Furthermore, filter specifications exhibit a double constraint: minimizing filter insertion losses, i.e. maximizing in-band transmission; but at the same time, the filters must reject signals localized in adjacent frequency bands that end up, with the increase in spectral congestion, being ever closer. For this, it is necessary to maximize the quality of resonators, in order to offer maximum impedance variations with frequency.

Section 10.1.2 showed the evolution of bulk wave resonators in the 1980s and 1990s, ending up with the two current industrial solutions: FBARs, commercialized since the end of the 1990s, and SMRs. The basic structures are now determined and a large number of improvements have appeared over the last 10 years. These improvements aimed at increasing electromechanical coupling coefficients and quality factors. They have led to great complication of the conception and fabrication of these components. Thus, industrial SMR resonators currently involve no less than 15 mask levels: the technological complexity of these components comes close to that of integrated circuits [AIG 08].

10.1.3.1. *Electrodes*

The simplest functional resonator, in terms of technological realization, is a SMR, all the films of which are deposited. Only the layer corresponding to the upper electrode needs to be patterned, as illustrated in Figure 10.8. It is therefore practical to have two resonators in series to be able to recover the electric contacts on the upper level. If the mass connection exhibits an area considerably larger than the other electrode, we end up with two strongly different series capacitors, which in the end behave like the smaller of the two capacitors. Such a device can already be used to characterize material stacks and estimate the performances of a resonator. This

only provides an estimation, however, as such geometries generally provide electrical parasitics, especially an increase in static capacitance caused by lines of electric fields leaving the upper electrode to reach the large overflow of the lower electrode.

When it becomes critical to limit these parasitic capacitances, the overflow of the lower electrode compared to the upper electrode must be minimal. Indeed, piezoelectric resonators are very sensitive to a parasitic capacitance. If we return to the expression of the admittance of a resonator from the equivalent Butterworth-Van Dyke (BVD) model and add a parallel capacitor, we get the effective admittance:

$$Y = jC_p\omega + jC_0\omega\left(1 - \frac{\frac{8k^2}{\pi^2}}{1-\left(\frac{\omega}{\omega_R}\right)^2 + j\frac{\omega}{Q\omega_R}}\right) = j\left(C_0 + C_p\right)\left(1 - \frac{\frac{8k^2}{\pi^2}\frac{C_0}{C_p + C_0}}{1-\left(\frac{\omega}{\omega_R}\right)^2 + j\frac{\omega}{Q\omega_R}}\right) \quad [10.1]$$

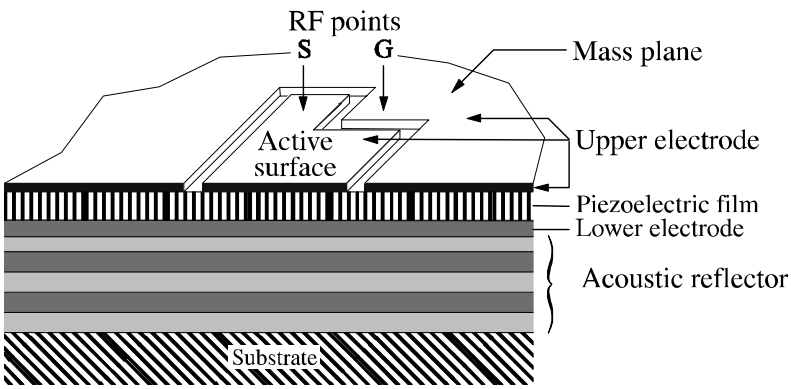

Figure 10.8. *Diagram of the simplest possible resonator, using only one step of photolithography [AIG 08]*

From this, it results that this capacitance leaves the frequency of resonance stable, but on the other hand it decreases the effective electromechanical coupling coefficient:

$$k_{eff}{}^2 = \frac{C_0}{C_0 + C_p}k^2 \quad [10.2]$$

Therefore, to prevent the effective coupling coefficient deteriorating, it is necessary to limit these parasitic capacitances: a parasitic capacitance of 10% of the static capacitance (i.e. 0.1 pF for typical resonators of 1 pF) leads to a 10% decrease in the electromechanical coupling coefficient (or a drop from 6.5 to 6% of this factor).

Nevertheless, a definition of the two metal levels with identical masks can be problematic from a technological point of view because with the slightest misalignment, it is the entire surface of the resonator and, therefore its static capacitance, which is modified. Despite the big lateral dimensions of the resonators (of about 100 μm), the lithography processes used should provide the maximum alignment precision to allow for reducing the extension of the bottom electrode from underneath the top electrode, and so to not substantially deteriorate the effective electromechanical coupling coefficient. With this structure, it becomes necessary to define contacts on the two electrode levels, which forces the formation of openings through the piezoelectric film and imposes extra photolithography and etching steps.

Furthermore, the choice of electrode material is critical. Originally, low resistivity metals were used, typically aluminum, or even gold. Very quickly, studies on piezoelectric thin film deposition showed that the nature of the lower electrode had a strong impact on the quality of piezoelectric films and their piezoelectric properties. Metal films in particular must be strongly textured, i.e. they must clearly exhibit a crystal orientation, but at the same time their atoms must be positioned at the surface of the electrode to present a lattice parameter compatible with a quasi-hepitaxial growth of the piezoelectric film.

This constraint requires the use of a seed layer, which serves both as an adhesion layer between the substrate and the metal film, and as a layer enhancing the electrode texturation. In addition, it forces the use of a metal deposition process almost as critical as that of piezoelectric film deposition.

The constraint of crystallographic compatibility between the metal and the piezoelectric film forces the use of specific metals. The best candidate is platinum oriented along its [111] crystallographic axis. But this metal has the disadvantages of exhibiting a high resistivity and being very expensive. Molybdenum (with a [110] orientation) is therefore usually preferred.

Electrodes also have an influence on the propagation of acoustic waves in the layer stack of a resonator. In the section on the principles of operation of a bulk-wave resonator, we saw that the presence of electrodes leads to a decrease in the resonance frequency caused by the mass loading effect. This loading can be compensated for by a decrease in the thickness of the piezoelectric film. At constant frequency, it is therefore possible to show that the thickness and nature of electrodes

influence the effective electromechanical coupling coefficient of the resonator. Very thick electrodes tend to uniformly deteriorate the electromechanical coupling coefficient. However, for small thicknesses, they allow it to increase. This gain is that much stronger than the acoustic impedance of the metal is high, as illustrated in Figure 10.9.

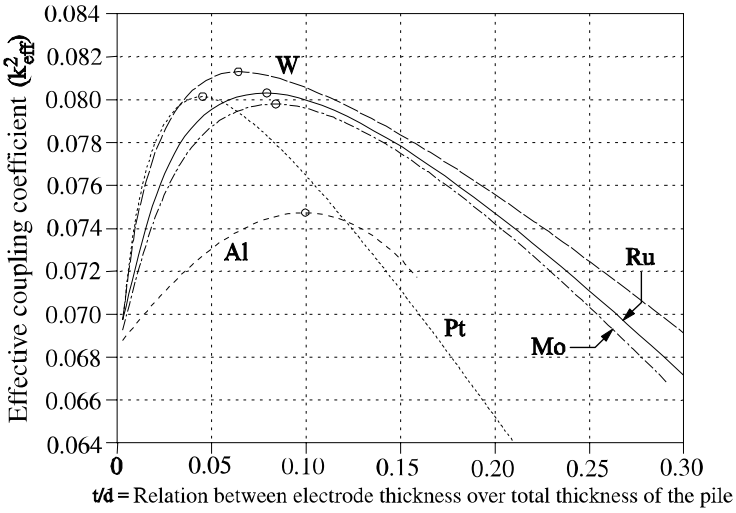

Figure 10.9. *Electromechanical coupling in terms of the relation between electrode thickness and that of the piezoelectric material for materials most normally used (Al, Pt, Mo, W, Ru)[KAI 07]*

The inconvenience is that metals with high acoustic impedance generally also exhibit a large resistivity, as shown in Figure 10.10. A compromise therefore needs to be found between resistive losses and improvement of the electromechanical coupling coefficient. It is in this way that molybdenum long remained the best compromise. More recently, iridium was suggested as an interesting alternative [IBO 08] because it exhibits a relatively low resistivity associated with extremely high acoustic impedance, as represented in Figure 10.10.

The improvement in the electromechanical coupling coefficient is, in practice, due to acoustic waves being confined in the piezoelectric film and to a reduction of the amplitude of vibrations in metal films [REI 02], as represented in Figure 10.11. Lakin suggested an alternative to the usual compromise, which involves using electrodes made of two distinct metals: one with a strong acoustic impedance, generally tungsten, in contact with the piezoelectric film and the other with a strong conductivity, generally aluminum [LAK 01a], as represented in Figure 10.12.

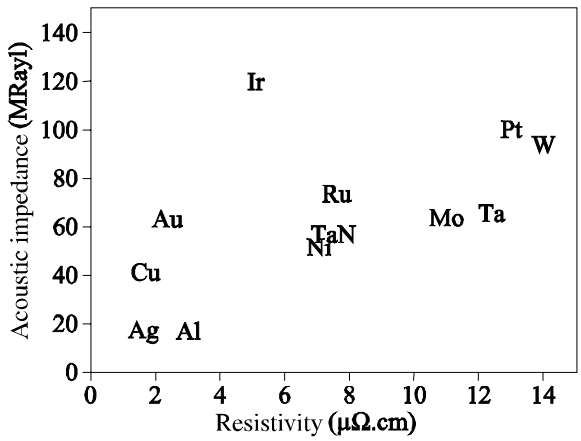

Figure 10.10. *Acoustic impedance and resistivity of most metals that can be used as bulk-wave resonator electrodes [REI 09]*

Varying the relative thicknesses of the two metals, we succeed in globally obtaining a resonator whose coupling coefficients and access resistances are located anywhere between the extremes formed by the use of each metal. This solution, although it needs to deposit and control more films (in terms of thickness and texture), offers greater freedom to filter designers.

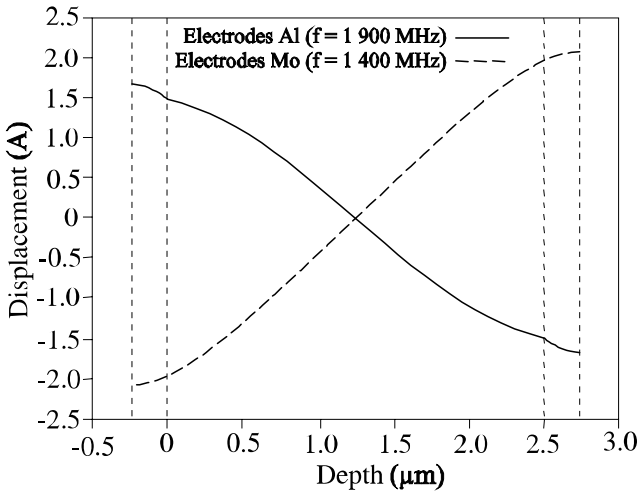

Figure 10.11. *Displacement profiles in a resonator for a structure made up of 2.5 μm AlN and Al or Mo electrodes 250 nm thick, corresponding to piles presenting a maximum electromechanical coupling coefficient in two cases [REI 02]*

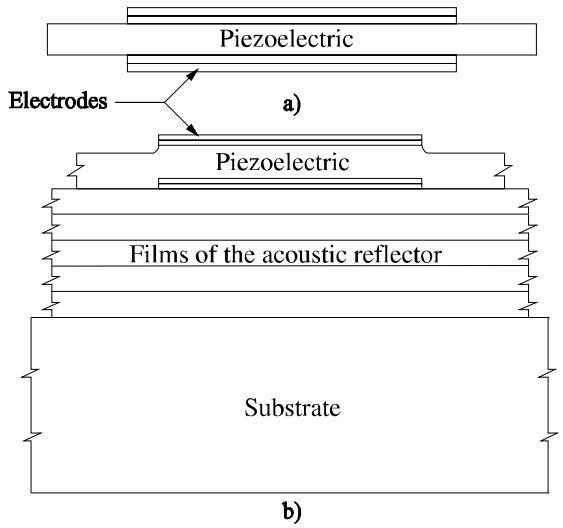

Figure 10.12. *Configuration of two-layer electrodes on: a) FBAR; and b) SMR resonators*

10.1.3.2. *Bragg mirror*

For the first applications, Bragg mirrors made up of AlN and SiO_2, for which seven layers are necessary, were used [LAK 01a]. Later, the use of silicon nitride (SiN) and silicon oxycarbide (SiOC) was suggested [CAR 05]. Although the acoustic impedance of each of these two materials is relatively low, their impedance ratio is nevertheless extremely high. Thus, only three pairs of quarter-wavelength films are necessary for ensuring transmission of acoustic waves of -35 dB (or a reflection of 99.9%) from the resonator towards the substrate, which is the condition of sufficient acoustic isolation.

In comparison, Infineon suggested using mirrors made of layers of tungsten (W) and silica (SiO_2), exhibiting equivalent performances [AIG 03]. The inconvenience of this type of mirror is that it uses a metal that risks forming inter-resonator parasitic connections, forming an electric path that crosses capacitors formed by the silica layers. With this effect being unacceptable for filtering applications as it directly short-circuits the whole device, it is necessary to limit tungsten layers and to localize them only under resonators. This necessitates extra lithography and etching steps. In some implementations, a planarization step aims to suppress the topology induced by the patterning of tungsten films.

Initially, all these films had thicknesses equal to a quarter-wavelength of the longitudinal wave, to obtain a maximum reflection coefficient. However, with this

type of arrangement, the maximum quality coefficients reached in the first applications were approximately 700, which was insufficient for the synthesis of filters satisfying radio frequency (RF) specifications in terms of losses. Characterizations by optical interferometry showed that despite mirrors with coefficients of reflection >99.9%, vibrations could still be detected on the back of the substrate, providing evidence of energy leakage through the mirror [KAI 07]. In reality these vibrations are produced by shear waves crossing the mirror. As the propagation velocities of this type of wave are close to half those of longitudinal waves, the quarter-wavelength mirror presents a very weak reflection, as shown in Figure 10.13.

These waves originate in the finite lateral dimensions of the resonators. In the acoustic formalism, we always assumed a resonator with infinite lateral dimensions, which forced a purely vertical propagation. In reality, this hypothesis is no longer respected and excited waves have a lateral propagation component that is low, but not zero. Mathematically, it is possible to show that a linear combination of longitudinal vibrations and shear vibrations must be considered to correctly describe the vibrations of the resonator. Even if <1% of acoustic energy is made up of shear vibrations, the leakage of this from the resonator towards the substrate is sufficient to limit quality coefficients to a value of 700–900 [MAR 05].

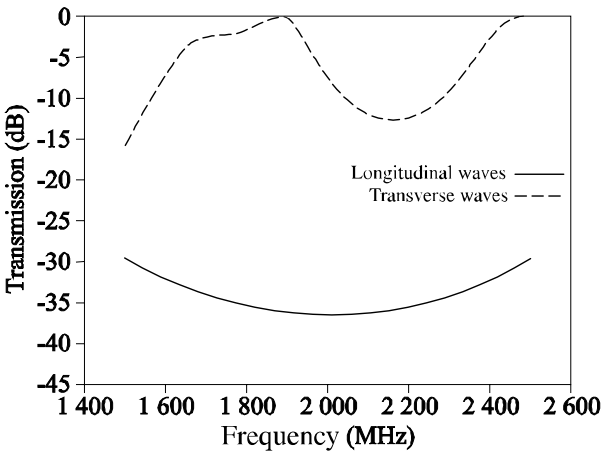

Figure 10.13. *Transmission coefficients for a SiN/SiOC Bragg mirror composed of three pairs of quarter-wave films*

Recent resonators integrate Bragg mirrors designed to ensure a reflection of both longitudinal waves and transverse waves at the same time, in order to keep most of the energy inside the resonator. The transmission spectra of such a mirror are

represented in Figure 10.14. In practice, this implies that quarter-wavelength films should no longer be used and so there is a decrease in the coefficient of reflection of longitudinal waves.

The very low deterioration of the maximum attainable coefficient of quality, however, due to a slightly reduced reflection coefficient is more than outweighed by the decrease in shear wave leakage and the corresponding increase in quality coefficient.

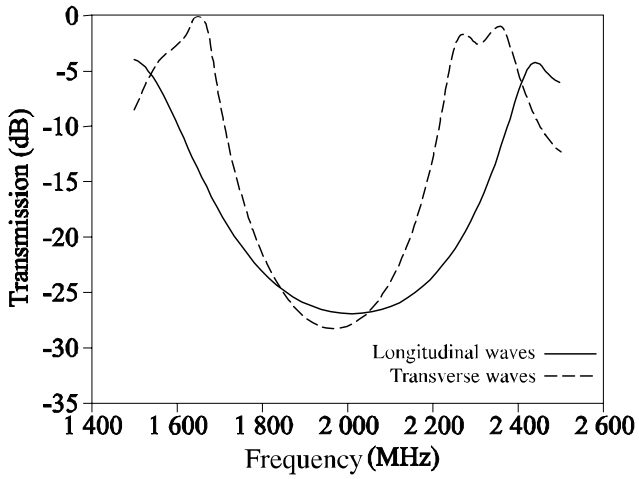

Figure 10.14. *Coefficients of transmission for a SiN/SiOC Bragg mirror with three pairs of films optimized for reflecting longitudinal and shear waves at the same time*

Optimization of the Bragg mirror enables us to confine vibrations vertically. For its effect to be fully beneficial, we must also ensure a lateral confinement. Naturally, in an aluminum nitride thin film resonator, this confinement is not assured: vibrations of the resonator initiate vibrations in its vicinity that manifest in the form of waves propagating away from the resonator and therefore taking energy away with them, again producing losses through lack of lateral confinement. This behavior is explained by the fact that the waves exploited have a negative group velocity: the relation between frequency and wave vector, called the *dispersion curve*, has a negative slope, as illustrated in Figure 10.15. Thus, at resonance (i.e. at the frequency where the wave vector of the resonator is null), wave vectors can exist in the area surrounding the resonator.

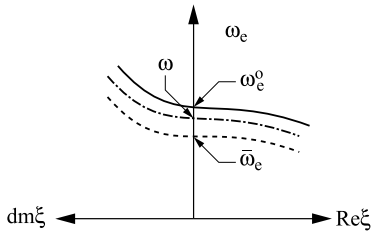

Figure 10.15. *Shape of dispersion curves for the thickness extensional mode in a stack, where it exhibits a negative group velocity [TIE 83]. The continuous line represents the area surrounding the resonator, and the dotted line the metalized area inside the resonator*

Group velocity is in practice influenced, in a homogeneous plate at least, by the Poisson's ratio of the material. As a function of this coefficient, group velocity can even change sign and become positive [MIN 57]. The transition from one behavior to the other takes place for a Poisson's ratio of 1:3, as illustrated in Figure 10.16.

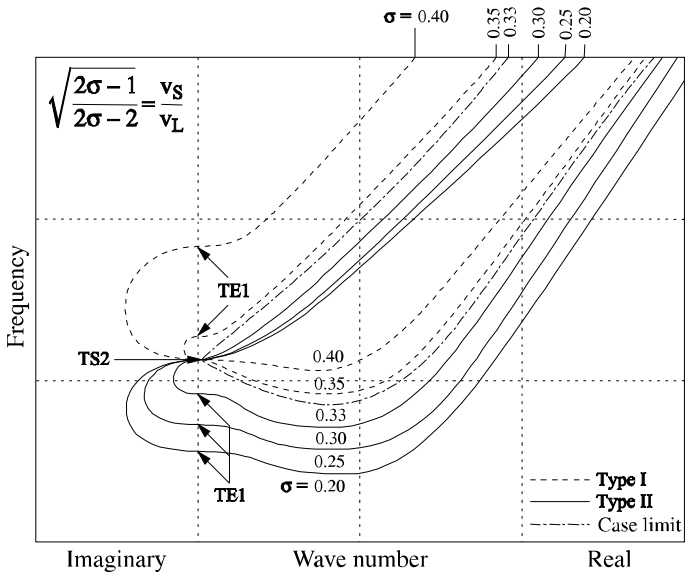

Figure 10.16. *Influence of Poisson's ratio on the dispersion curves of an isotropic material plate [FAT 05a]*

For a resonator, the same effect is obtained by artificially modifying the effective Poisson's ratio of the material stack, causing the proportion of materials presenting a low Poisson's ratio (typically SiO_2) to vary as well as those presenting a large ratio

(for example AlN). In practice, this effect is obtained by increasing the thickness of the upper layer of the Bragg mirror and compensating for this by reducing the thickness of the piezoelectric film [FAT 05a] to keep the same resonance frequency. With a positive group velocity, there can no longer be real solutions to the propagation equation outside the resonator at the resonance frequency: waves are laterally confined in the resonator. The drawback of this method is that it leads to a slight decrease in the effective electromechanical coupling coefficient, but it is the price that has to be paid to optimize the quality factor.

10.1.3.3. *Lateral loading of a resonator*

Whereas a three-dimensional confinement of waves in the resonator largely suppresses acoustic leakage, it also results in the appearance of a large number of parasitics on the electric response. These parasitics reduce the spectral purity of the resonator and can even be the cause of extra ripples in the in-band transmission of a filter. The parasitics are produced by the resonance of laterally propagating waves reflected at the edges of the resonator by their inability to propagate outside it [KAI 07].

With these parasitics being related to the lateral dimensions of electrodes, the techniques used to suppress them aim at making a resonator appear to be virtually infinite. A first method, suggested for FBAR resonators by Avago, consists of adopting electrodes with non-symmetric shapes [LAR 01], as illustrated in Figure 10.17.

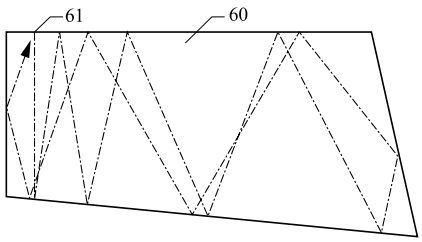

Figure 10.17. *Shape of non-symmetric electrodes and path of a laterally propagating wave inside of the resonator [LAR 01]*

Without parallel sides, standing waves form with more difficulty. In practice, the resonance condition for these laterally propagating waves is spatially smeared out, which leads to a deterioration of their quality factor and spreading them out on the spectrum. The parasitics are therefore smoothed out rather than truly suppressed.

A second method, suggested by Nokia, is analogous to the conditions of adaptation of radiofrequency transmission lines by adding localized loading at the

edges of the resonators, as illustrated in Figure 10.18. Such a localized loading has a well-chosen thickness and width, for which it ends up imposing an impedance matching condition between laterally propagating waves inside the resonator and the outside environment [KAI 04]. The reflection of these waves is therefore suppressed. In addition, the boundary conditions for these waves become the same as those that would be presented by an infinite resonator: these waves are simply not excited. It is therefore possible to reach quality factors >2,000.

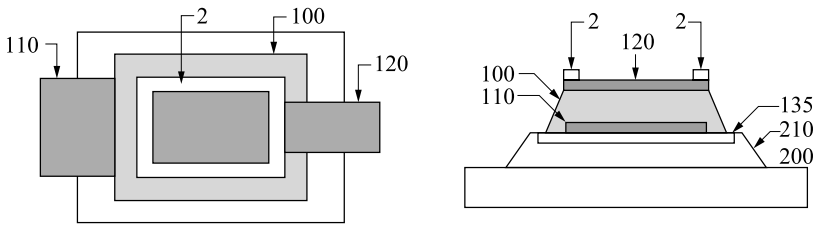

Figure 10.18. *Top view (left) and cross-section (right) of a resonator with lateral loading over its electrodes [KAI 04]*

10.1.3.4. *Mass loading*

To synthesize a filter, we saw in Chapter 7 that two types of resonators operating at different frequencies are necessary. In theory, this necessitates a specific material stack for each resonator, with its own set of thicknesses. This is not a profitable approach, however, in terms of area requirements or technological complexity. Instead, the two resonators are made in the same way and the frequency of resonators located in the parallel arms is slightly lowered by adding a mass loading. This loading takes the form of an extra layer patterned to cover the parallel resonators only.

The first approaches consisted of using insulating films, which additionally protected the surface of the resonators. The one chosen at CEA LETI involves etching the upper electrodes to reduce their thickness over the series resonators. The interest in doing this is two-fold. First, electrical connections are slightly thicker than if they were made for the series resonators. This contributes to reducing the resistivity of these electrodes. Second, when using electrodes with high acoustic impedance, the effective electromechanical coupling coefficient is increased compared to solutions based on a dielectric layer, which usually exhibit lower acoustic impedance.

10.1.3.5. *Passivation*

Due to the small volume of a bulk acoustic wave (BAW) resonator, the power densities present are extremely high, even in the presence of an excitation in the

order of a Watt. This corresponds to the maximum level of the output signal of an amplifier in an RF chain. This power is mainly dissipated in the form of the Joule effect taking place in the electrodes and the warming caused by alternating compression and expansion of the piezoelectric film. During operation, a resonator can reach a temperature between 40 and 180°C, depending on its geometry and fabrication process [IVI 08]. Under the effect of temperature, the surfaces of electrodes tend to oxidize if exposed to air, which facilitates their destruction when the resonator is subjected to a strong electric stress. Resonators therefore need to be encapsulated by a layer serving as a barrier to oxygen diffusion. For the BAW technology developed at CEA LETI, for example, a thin film of SiN is used. This top layer influences the characteristics of the resonator in terms of resonance frequency and effective electromechanical coupling coefficient. It especially tends to deteriorate the latter. Thus, a minimum thickness is sought to maximize the properties of the resonator, but a limit is imposed by the need for a sufficiently thick barrier.

The second advantage of this passivation layer is that the resonance and antiresonance frequencies vary almost linearly with thickness. The passivation layer can therefore be used to compensate for production errors and ensure that the frequency targets are reached at the end of their fabrication. With the appearance of etching equipment using ion beams or beams made of clusters of atoms, it has become possible to locally adjust the frequency of components and thus to correct frequency dispersions encountered on the same substrate, caused by the cumulating deposition inhomogeneity profiles of each film. This step is critical for an industrial process because it ensures a sufficient yield to ensure the industrial profitability of the process [REI 07].

10.1.3.6. *Encapsulation*

After being manufactured, resonators must be able to be introduced into a ceramic package or be mounted on a substrate through a classic assembly technique:

– wire-bonding (sticking it onto a substrate and connecting it by soldering gold or aluminum wires); or

– flip-chip (a connection with the resonator flipped over with its face directed towards the substrate, and connections and mechanical assembly by solder balls).

In the end, the assembly is generally sealed in a resist or polymer, before being encapsulated by molding of a plastic top. During these steps, it is necessary to protect the surface of the resonators to prevent contact between the surface and any other material, which would disturb the mechanical vibrations of resonators during operation.

The package connection covered by a metal cap is the simplest solution, but it has the drawback of providing a very bulky final component and necessitates cutting and unit manipulation of the chips. Collective capping techniques have therefore been developed. Avago and Infineon developed techniques based on forming silicon caps by etching dedicated wafers to form cavities, then bonding these wafers on the substrates that served to produce resonators. Finally, holes are etched through these caping substrates and filled with metal to form the electrical vias used to create an electric contact towards the filter electrodes, see Figure 10.19.

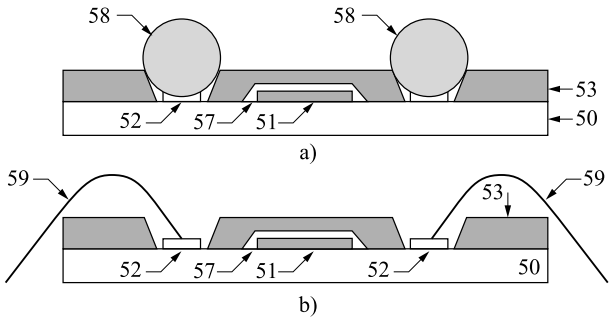

Figure 10.19. *Protection of a BAW resonator by encapsulation through a substrate in which a cavity and crossing pathways were made [TIM 04]*

CEA LETI developed a process based on using a resist forming a sacrificial layer, deposition of a mineral cap, etching the sacrificial layer through openings formed in the caps and finally sealing these sacrificial layer etching holes with a polymer. This solution has the advantage of being relatively cheap and not presenting significant topology, since the cavities formed above the resonators are only a few microns thick, as illustrated in Figure 10.20. In addition, electric measurements proved that the deposition then removal of the resist sacrificial layer does not disturb the electric response of a resonator: its resonance and antiresonance frequencies are unaffected.

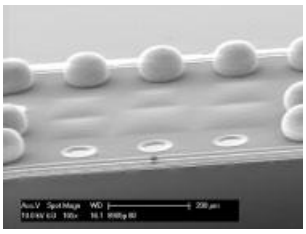

Figure 10.20. *Protection of resonators from a BAW resonator by a thin film encapsulation according to [POR 07]*

10.2. BAW technology

10.2.1. *Introduction*

The first publications on BAWs date from the beginning of the 1980s [GRU 80, LAK 82]. Worldwide research activity then increased until the beginning of the 1990s. At this moment the enthusiasm aroused by this new technology decreased, especially because of the difficulty in developing a stabilized fabrication process.

One of the most critical components of RF architecture of a mobile terminal is the duplexer. A duplexer is the assembly of two filters with the same input point (the antenna). It filters the RF signal going to the reception path (Rx filter) and the RF signal coming from the transmission path (Tx filter). With low insertion loss at the filter stage, you can relax the requirements on the LNA (low noise amplifier) of the RX path and on the PA (power amplifier) of the TX path, and that means having less consumption and thus a longer battery life. They must also have significant levels of out-of-band rejection to reject eventual interferers, such as GPS signals (1,575 MHz) and Bluetooth (2,400 MHz), but also to avoid leakage of the Tx signal into the Rx path. These filters must also remain linear. Finally, the Tx filter must support the RF output power levels of the power amplifier. It is often placed next to this amplifier; it must not shift with temperature.

At the beginning of the 2000s, duplexers were based on ceramic filters for the Tx path and SAW filters for the Rx path. The first duplexers had acceptable performance but were very cumbersome while the second ones were limited to the Rx path because of their low power-handling capabilities. The first BAW duplexers introduced in 2001 by Agilent [RUB 99, RUB 01] to cover the personal communications service (PCS) band truly revolutionized the duplexer market (Agilent's BAW team became Avago Technologies in 2005). Their much smaller size, very low insertion losses, excellent RF power-handling capabilities and electrostatic discharge (ESD) robustness, enabled them to cover most of the market.

Since this era, BAW technology has extended to other types of RF filter and other standards (especially Universal Mobile Telecommunications System (UMTS)). Recently, a new application for this technology appeared in the literature [PET 08, PET 09]: BAW resonators dedicated to time reference applications. The possibility of replacing quartz with a component that can be integrated into silicon opened unimaginable perspectives in terms of complete RF system integration.

In section 10.2.2, we will present a review of BAW technology by introducing the principle of BAW resonator and filter operation. We will identify the key parameters of resonators and explain what impacts they have on filter performances. We will then discuss a BAW from CEA LETI technology in detail and will give a

few examples of realizations. Section 10.2.3 will be devoted to an extension of BAW technology, which consists of producing acoustically coupled filters (coupled resonator filter, CRF) thanks to the vertical stacking of two piezoelectric resonators.

10.2.2. *BAW filter topology*

To build a BAW filter, we use the electric assembly of several resonators. The topologies are the same as those found in SAW filters; the most common topology is ladder topology, as can be seen in Figure 10.21a.

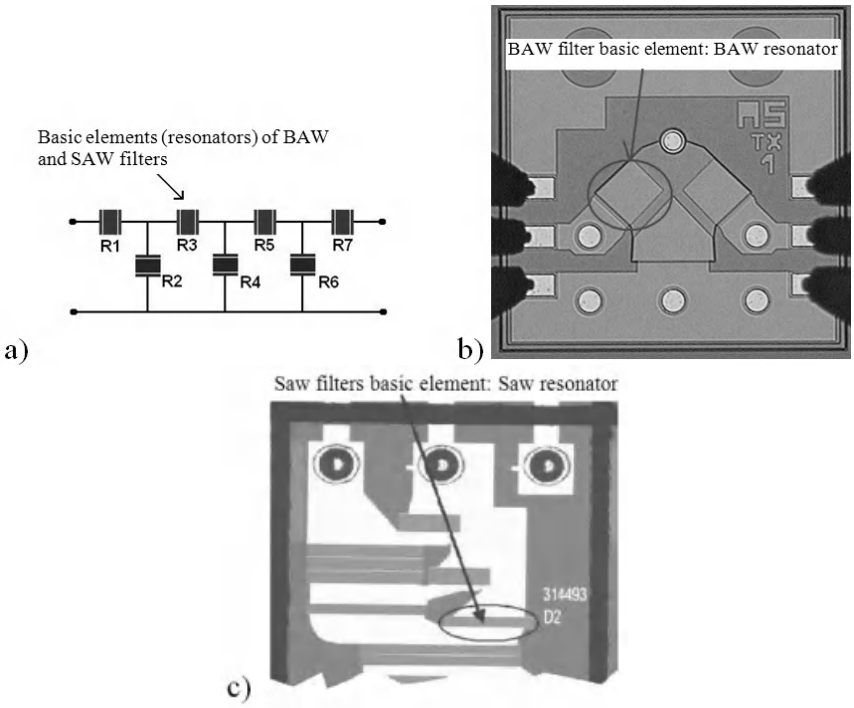

Figure 10.21. *a) Ladder topology; b) layout of a ladder BAW filter; and c) a ladder SAW filter*

A ladder filter is made up of several L sections; the number of sections determines the order of the filter. One L section is based on the electrical connection of two resonators: one in series and the other in parallel. The impedance of each of these two resonators, taken separately, presents two frequencies of resonance. At series resonance, impedance is minimal and is typically equal to <1 ohm to a few ohms. At parallel resonance, impedance is maximal and is equal to several thousand

ohms. For frequencies far from resonances, resonators behave like capacitors. In one L section, resonances of the parallel resonator are shifted slightly in relation to those of the series resonator, see Figure 10.22. Between frequencies fp2 and fs1, impedance is very low between the input and output of the L section and it is very high between the output and the ground. The L section acts as a band pass filter. At frequency fs2, all the current crossing the section is shorted towards the ground because the impedance of the parallel resonator is very low. This leads to zero transmission in the frequency response of the L section. At frequency fp1, impedance between the input and output of the section is very high (open circuit) on the series path and all the current is reflected to the input, this determines another transmission zero. Far from resonances of the two resonators, the L section behaves like a combination of two capacitors and it gives a certain level of rejection across a large frequency band.

By cascading several L sections, a better out-of-band rejection can be obtained, but this also leads to an increase of the in-band insertion losses. It is also common to add one or more series elements, such as an inductor, or parallel ones, such as a capacitor. This enables the in-band ripple to be smoothed or the rejection to be optimized by shifting the transmission zero of the L section to a desired frequency. The specifications of the L section are entirely determined by the parameters of these constitutive elements, i.e. by BAW resonator parameters. They set the bandwidth, insertion losses and in-band ripple, out-of-band rejection, or even the level of in-band impedance matching.

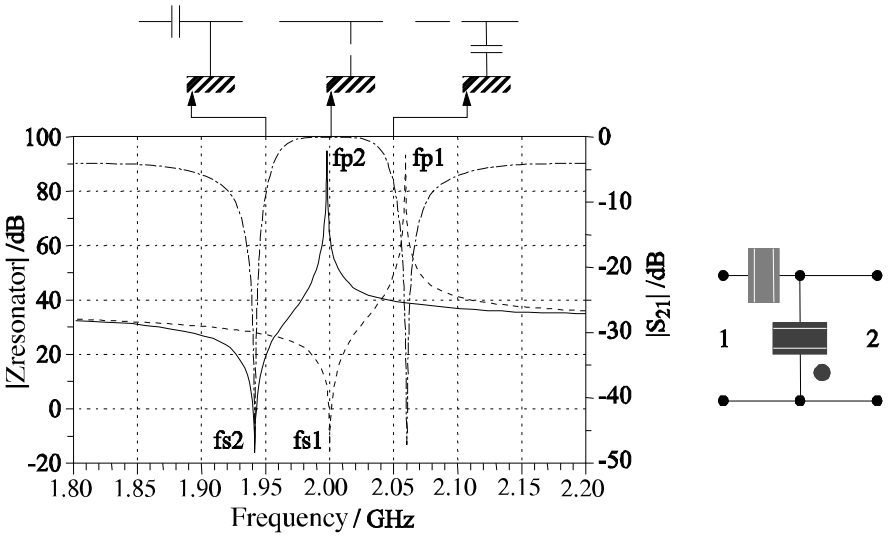

Figure 10.22. *Operating principle of an L cell [TIL 07]*

Another topology used to build BAW filters is lattice topology, which can be seen on the left in Figure 10.23. As in ladder topology, two types of resonators are connected together: series resonators (X1) and parallel resonators (X2). The frequencies of these two types of resonator are chosen to be slightly different to get a band pass filter. Several lattice cells can be cascaded to improve out-of-band rejection. This, on the other hand, leads to an increase in insertion losses in the pass band. The specificity of this topology in relation to ladder topology is its differential excitation mode. The filter has inputs and outputs that are not referenced in relation to the ground. This differential mode ensures a better noise immunity, thanks to the fact that signals are no longer referenced to a supply potential (often the ground), which is susceptible to being particularly noisy.

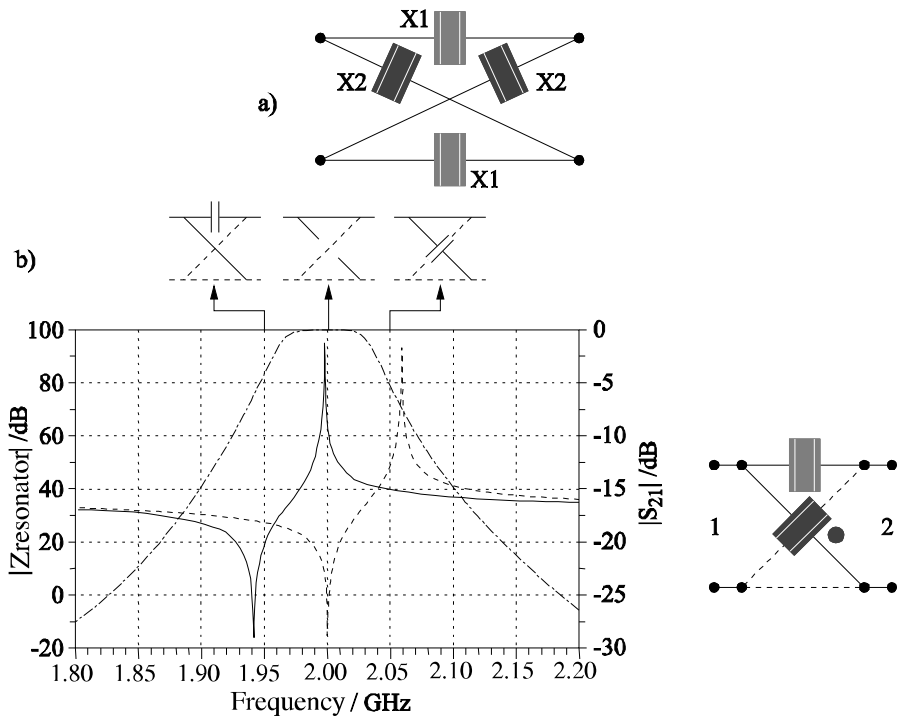

Figure 10.23. *a) Lattice filter topology; and, b) operating principle*

10.2.3. *Parameters of the BAW resonator and their impact on filter response*

The main electrical parameters of a BAW resonator are:

– *fs*: series resonance;

– *fp*: parallel resonance;

– *Qs*: quality factor at series resonance;

– *Qp*: quality factor at parallel resonance;

– *kt2*: piezoelectric coupling coefficient;

– Z_{min}: impedance at series resonance;

– Z_{max}: impedance at parallel resonance;

– *Co*: static capacitance.

Figure 10.24 gives an example of parameter extraction from measurement of a SMR-type BAW resonator. On the left, we notice impedance in dB and on the right a Smith chart.

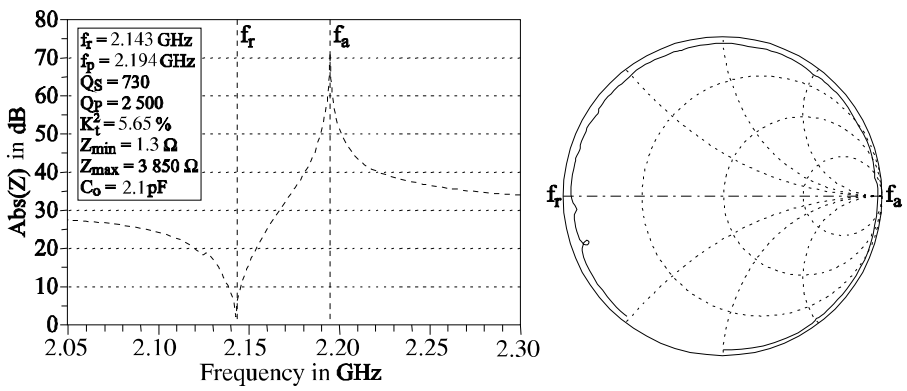

Figure 10.24. *Main electrical parameters of a BAW resonator*

Other complementary parameters are sometimes extracted [BIF 08], such as:

– Z_c: impedance of static capacitance *Co* at $(fs + fp)/2$;

– Z_{max}/Z_{min}: ratio between min and max impedances;

– $FOM = k_t^{2} \times Q$: factor of merit for filter design.

10.2.3.1. *Frequencies of resonance*

Frequencies of resonance are fixed by the thickness of the piezoelectric material and the electrodes. The technological limitations for etching thick films or those for

controlling deposition of very thin films give minimum and maximum frequencies of resonance that can be reached with a BAW resonator. In the literature, different definitions for frequencies of resonance are found [IEE 87, LAR 00, STA 10]. We sum these up below. For series resonance we have:

– f_r: susceptance zero, i.e. fr = zero(Im(Y));

– f_s: conductance maximum, i.e. fs = max(Re(Y));

– f_m: impedance minimum, i.e. $fm = min$(|Z|);

– f_{s_mbvd}: resonance of the mechanical arm of the Modified Butterworth-Van Dyke (MBVD) model;

and for parallel resonance:

– f_a: reactance zero, i.e. fa = zero(Im(Z));

– f_p: resistance maximum, i.e. $fp = max$(Re(Z));

– f_n: impedance maximum, i.e. $fn = max$(|Z|);

– f_{p_mbvd}: resonance of the two arms of the MBVD model.

In most acoustic resonators, quartz as well as BAW, these four frequencies are close enough to not distinguish them [STA 10]:

$$f_r \approx f_s \approx f_m \approx f_{s_MBVD} \qquad\qquad f_a \approx f_p \approx f_n \approx f_{p_MBVD}$$

From a practical point of view, it is the couple (f_r,f_a) that is extracted. These two frequencies correspond to phase cancellation:

$$\mathrm{f}r = zero(Im(\mathrm{Y})) \Leftrightarrow Im(\mathrm{Y}) = 0 \Leftrightarrow \text{phase (Y)} = 0;$$

$$\mathrm{f}a = zero(\mathrm{Im(Z)}) \Leftrightarrow Im(\mathrm{Z}) = 0 \Leftrightarrow \text{phase (Z)} = \text{- phase(Y)} = 0.$$

The frequency f_r corresponds to the first time the admittance phase passes through zero and frequency f_a for the second time, see Figure 10.25. Determining the phase zeros is a much more robust method and is much easier to automate than looking for peaks on the real parts of admittance and impedance.

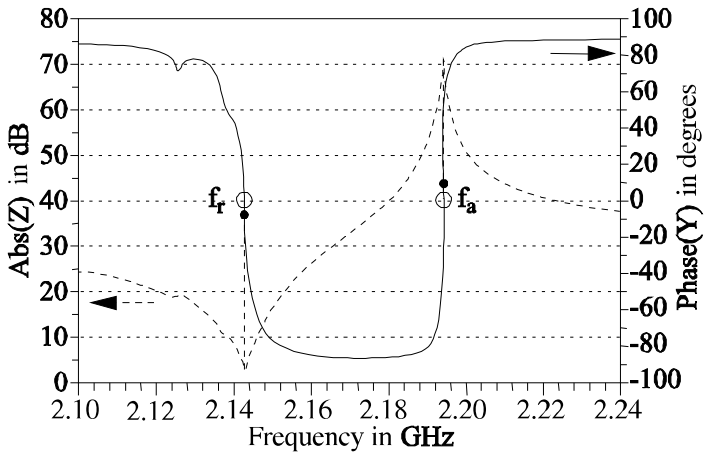

Figure 10.25. *Impedance and admittance phase module of a BAW resonator between two resonances*

10.2.3.2. *Coupling coefficient*

The piezoelectric coupling coefficient determines the degree of energy transferred between the mechanical and electric domains. It is mainly linked to the piezoelectric material, electrodes and interfaces with electrodes (roughness, orientations, etc) during deposition. Currently, the most commonly used piezoelectric material for BAW resonators and filters is AlN. With a good mastery of deposition and adequate electrodes, coupling coefficient values of 7% are obtained for AlN. This parameter is one of the most important for BAW resonators as it determines the bandwidth that can be reached by the filters.

In Figure 10.26, on the left, transmission parameter S21 is represented and on the right, reflection parameter S11 for a ladder-type BAW filter. Parameter S21 gives the frequency response of the filter, i.e. the in-band insertion losses and the out-of-band rejection. Parameter S11 gives the in-band impedance matching of the filter. We can see that the coupling coefficient has an influence on the bandwidth of the filter, generally calculated at -3 dB. It also has an effect on the insertion losses in the middle of the band and on the impedance matching in the middle of the band. The "hole" that appears on the curve of S21 in the middle of the pass band is called the *ripple*. For RF receivers using code-division multiple-access schemes, it is a critical point to watch. A maximum ripple value is often specified over the entire band (<0.5 dB for a band of 80 MHz, for example) but also in each transmission channel (<0.2 dB for each channel of 5 MHz, for example).

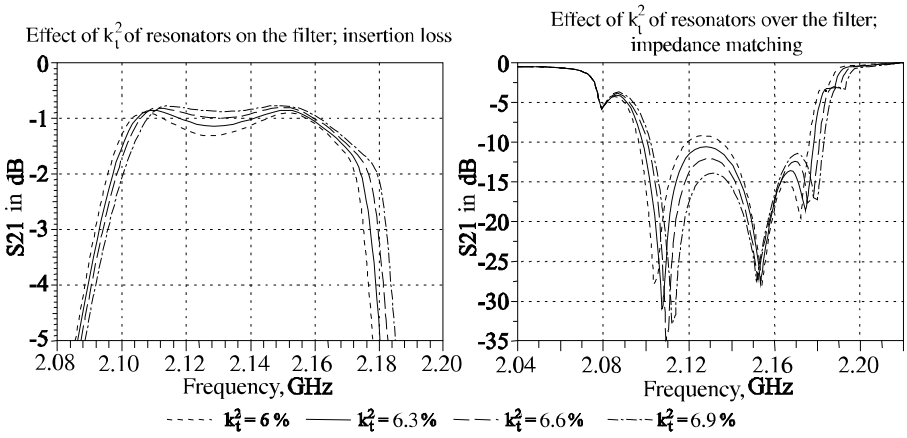

Figure 10.26. *Effect of the k_t^2 coupling coefficient of resonators on the frequency response of a ladder-type filter*

A strong coupling coefficient therefore enables us to get larger bandwidth with less ripple. We must note that to increase industrial yield the coupling coefficient will have to be as uniform as possible over the wafer.

For radiofrequency applications, such as UMTS duplexers or low-power radio filters (Zigbee or 802.11), the required bandwidths are around 80 MHz centered at 2.14 GHz or 2.45 GHz. These values are reachable with coupling coefficients of at least 6.5%.

There is a great interest in maximizing the coupling coefficient. A larger bandwidth is a way of ensuring that, even with temperature drifts, the filter will verify RF standard specifications. Secondly, a strong coupling coefficient gives an extra degree of freedom for compromises with other filter parameters.

For example, the series quality factor *Qs*, which determines insertion losses of the filter, depends to a large extent on the resistive losses in electrodes. These losses can be reduced by thickening the electrodes, but this also has the effect of reducing the coupling coefficient.

Another example is the use of a thicker passivation layer that reduces the hermeticity requirement of the final packaging, but which also has the effect of lowering the coupling coefficient [BIF 08]. The coupling coefficient can be extracted from a physical characterization of the material, but the bulk material often has a different behavior to the thin film. In addition to this its electrodes and other layers have an influence on this coupling coefficient.

It is generally preferred to deduce this parameter from a measurement of frequencies of series and parallel resonance. According to the admittance equation of a BAW resonator introduced before, the k_t^2 coefficient is directly linked to the frequency deviation between the two frequencies of resonance.

We therefore speak more of the effective coupling coefficient. More or less accurately approximated formulae are found in the literature [AIG 07, BIF 08, IEE 87]:

$$k_{eff}^2 = \frac{\pi}{2}\frac{f_s}{f_p}\tan\left(\frac{\pi}{2}\frac{f_p - f_s}{f_p}\right) \qquad [10.3]$$

or Taylor approximation of the second order:

$$k_{eff}^2 = \frac{\pi^2}{4} \times \frac{f_s}{f_p} \times \frac{f_p - f_s}{f_p} \qquad [10.4]$$

or Taylor approximation of the first order:

$$k_{eff}^2 = \frac{\pi^2}{4} \times \frac{f_p - f_s}{f_p} \qquad [10.5]$$

The first formula is the definition of k^2_{eff} given in the IEEE standards [IEE 87], but it is not currently used. The Taylor series second-order approximation, which gives a good approximation and is simple to manipulate, is preferred.

The last formula is sometimes used but it must be known that it overestimates the values of k_t^2.

10.2.3.3. *Quality factor*

With the coupling coefficient, the quality factor is the most important parameter. It determines the insertion losses and selectivity that will be obtained with BAW filters.

Two quality factors are defined:

– Q_s, or *series quality factor*, is the quality factor calculated at series resonance f_s; and

– Q_p, or *parallel quality factor*, is the quality factor calculated at parallel resonance f_p.

Figure 10.27 represents the frequency response of a ladder-type BAW filter for different quality factor couples (Q_s, Q_p). We notice that the quality factors Q_s and Q_p have a direct impact on the insertion losses of the filter. The series quality factor is acting more on the left-hand side of the band and the parallel quality factor more on the right side. A value of 1,000 for Q_s and Q_p is a minimum when designing filters with good performance. Suppliers of BAW filters, like Avago or Triquint, use values > 2,000.

The extraction of quality factors is particularly critical. It is very sensitive to measurement noises and acoustic parasites over the response of resonators. Several methods are currently used. Depending on the type of BAW resonator, they lead to sometimes very different results [AIG 07].

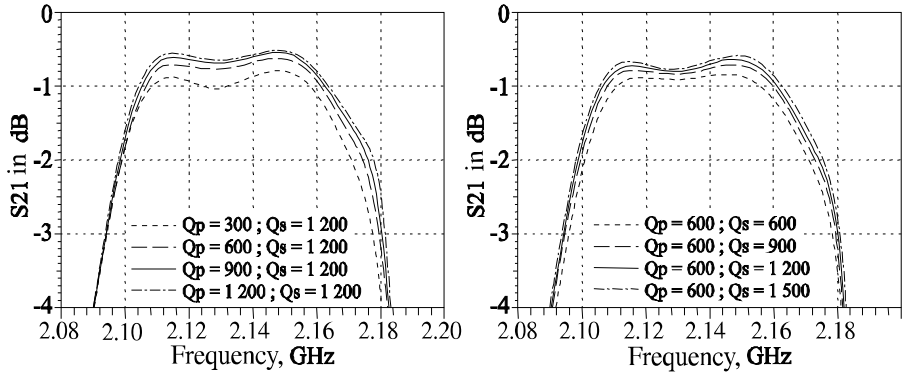

Figure 10.27. *Effect of series and parallel quality factors of resonators on the frequency response of a ladder-type filter*

10.2.3.3.1. The -3 dB method

Here $Q_s = \dfrac{f_s}{\Delta f_{-3dB}}$ with Δf_{-3dB}, the width of the impedance peak Z at half the maximum and $Q_p = \dfrac{f_p}{\Delta f_{-3dB}}$ with Δf_{-3dB}, the width of the admittance peak Y at half of the maximum.

This classic method does not seem to be used anymore because it is too dependent on the frequency step and the number of points used during measurement

and also because it is sensitive to the parasites over the response of the resonator. The data must be smoothed out and this is an important source of error.

10.2.3.3.2. Phase derivative method

From the phase derivative

$$Q_s = \frac{1}{2} \times f_s \times \left. \frac{d\Phi(Y)}{df} \right|_{series} \qquad [10.6]$$

with $\Phi(Y)$ admittance phase and:

$$Q_p = \frac{1}{2} \times f_p \times \left. \frac{d\Phi(Y)}{df} \right|_{parallel} \qquad [10.7]$$

This method is also very sensitive to the frequency step of measurement *df*. For a similar resonator at 2 GHz, a *Q* value of 1,500 is extracted with *df* = 0.25 MHz and a value of 2,000 with *df* = 0.5 MHz in [BIF 08]. This method is increasingly being replaced by methods based on the extraction of parameters of the MBVD model that are much more robust in the case of parasitic responses. Another argument for not using this and the -3 dB method is that they are only valid around resonances and therefore they do not enable us to trace the frequency-change in *Q* on the Smith chart, which is necessary for modeling, for example, pass band filters.

10.2.3.3.3. Fitting with a MBVD model

To not rely on the response of the resonator or a step of measurement that is too big. The idea is to derive a MBVD model that fits the electric response measured on the operating band of the resonator and then, either to use the formulas [10.6] and [10.7], or calculate the energy stored in each reactance of the model and divide it by the energy lost by the cycle in the resistances, i.e. by the term $I^{2*}R$ [AIG 07]. This last method gives the value of the quality factor at all frequencies.

10.2.3.3.4. Bode's method

Another method, called Bode's method, was published in 2007 by the Avago team [RUB 07] to overcome the limitations of the first two methods. One of its advantages is to give the quality factor at all frequencies using the following equation:

$$Q(f) = 2\pi f \tau(f) \frac{mag(S_{11})}{\left(1-(mag(S_{11})^2\right)} \qquad [10.8]$$

with $\tau(f) = -\frac{dPhase(\omega)}{d\omega}$, the group delay of S_{11} and $mag(S_{11})$ the S_{11} module.

The group delay and S_{11} module are read directly on the vector analyzer during RF measurement. This method is sensitive to the frequency step of measurement, like the phase derivative method, and so we need to take a sufficient number of measurement points to extract a correct value of the quality factor. Another drawback of this method is its sensitivity to digital noises linked to the group delay method of calculation by the vector analyzer [BIF 08].

This method is an approximation and it only gives correct results if the mechanical losses are low in the resonator. In this case, the results obtained are identical to those of the fit method of the MBVD model.

10.2.4. *Examples of realizations*

Here we give a few examples of filters produced in the clean rooms at LETI in collaboration with STMicroelectronics Crolles.

10.2.4.1. *Lattice filters*

The first example is a filter with a double lattice-type topology (see Figure 10.28). The targeted application is the filtering of the reception path (Rx) for W-CDMA standard. For this standard, the specifications are the following:

– a central frequency of 2.14 GHz;

– maximal insertion losses of 2.7 dB;

– a useful bandwidth of 60 MHz between 2,110 MHz and 2,170 MHz; and

– differential input and output impedances of 100 ohms.

The filter created fulfills the specifications set. The quality factors of the resonators are estimated here at Q_s = 1,800 and Q_p = 1,400. These “not optimized” values prevent us obtaining very low insertion losses.

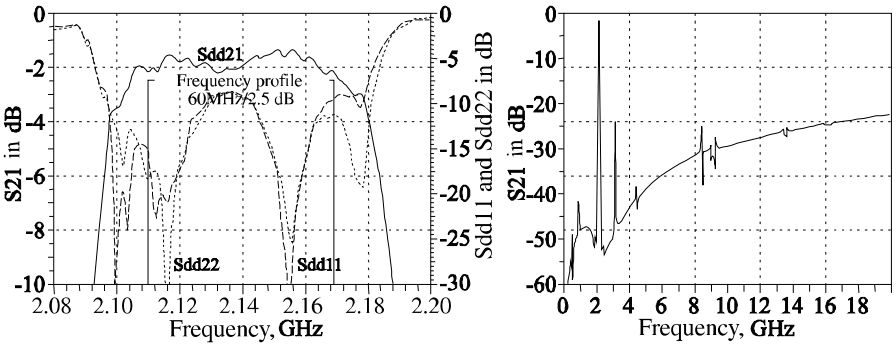

Figure 10.28. *RF performances of a SMR-type double-lattice BAW filter*

The filter design (see Figure 10.23b) could be further optimized by working on the lengths and thickness of RF access paths in order to limit series losses. The double lattice topology enables us to obtain a good out-of-band rejection, greater than 20 dB up to 20 GHz.

10.2.4.2. *Ladder filters*

The second example is a filter with a simple ladder-type topology consisting of three resonators: two in series and one in parallel. The out-of-band rejection shown on the right in Figure 10.29 is, here, limited to –10 dB because of the reduced number of resonators. This filter is destined to be assembled in a W-CDMA duplexer to filter the transmission path (Tx).

The idea is to obtain the lowest possible insertion losses. The out-of-band rejection is finally optimized by adding external elements (capacitors and inductors) at the input and output of the filter.

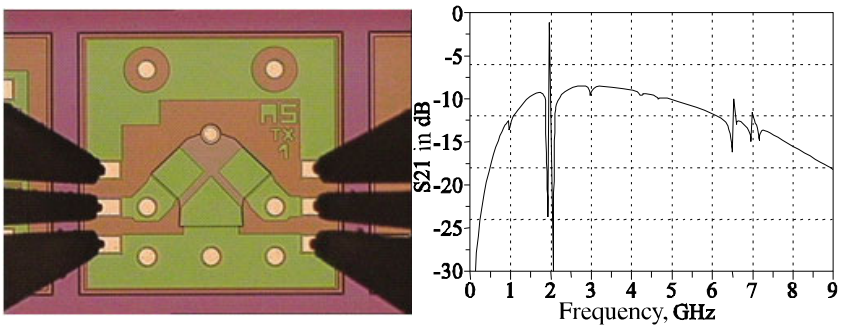

Figure 10.29. *SMR-type ladder, BAW filter produced at LETI*

10.2.4.3. *Temperature-compensated resonators*

The last example of technological realization is a temperature-compensated resonator. Here, the thicknesses of the Bragg mirror, the electrode and the piezoelectric layer are jointly optimized, not only to obtain the desired frequency of resonance but also to get minimal temperature sensitivity.

To do so, we are playing on the thermal expansion coefficients of opposing signs between the different layers. A compromise must often be made because cancellation of temperature sensitivity occurs, most times, to the detriment of the quality factor.

Figure 10.30a shows an example of a temperature-compensated BAW resonator produced at LETI. Thermistors that will serve to calibrate the oscillating circuit in which the resonator will be integrated are around the resonator. The resonator does not respect the specifications in itself; it is therefore necessary to make an extra compensation thanks to an external circuit consisting of switched capacitors.

Finally, we get a temperature derivative of the frequency of resonance that is <± 20 ppm over a temperature range between -40°C and +80°C, see Figure 10.30b. More details can be found in [PET 08] and [PET 09].

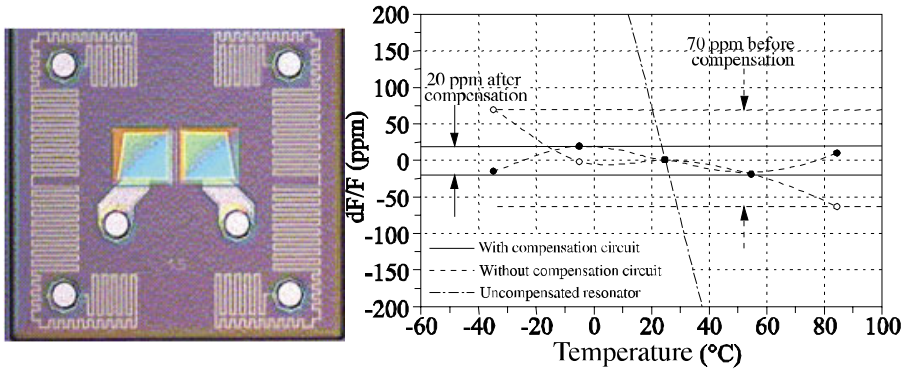

a) *b)*

Figure 10.30. *a) Temperature-compensated SMR-type BAW resonator produced at LETI; and b) frequency derivative versus temperature of the oscillator with and without calibration circuit*

10.3. CRF technology

10.3.1. *Introduction*

CRF technology is an evolution of BAW technology that consists of vertically stacking two BAW resonators and acoustically coupling them, see Figure 10.31. This technology appeared at the beginning of the 2000s [LAK 01b], and has aroused increasing interest because it allows the combination of the advantages of SAW and BAW filters. A galvanic isolation between the input and output is obtained thanks to the acoustic coupling layers and it makes impedance and mode conversions possible. This is also possible in SAW filters but not in BAW filters. In addition, CRFs keep the advantages of BAW filters compared to SAW filters, i.e. a better RF power-handling capability and ESD robustness, a lower sensitivity to temperature and a compatibility with classic silicon technologies.

Finally, CRF filters are potentially much more compact than their SAW and BAW homologues. After the precursory works of TFR Technologies, Inc. [LAK 01b], other groups began to develop CRFs. Readers may wish to refer to the Infineon publications [FAT 04, FAT 05b], LETI/ST Microelectronics [VOL 06, BIL 09] and finally Avago [SMA 07, JAM 09]. Nevertheless, commercial applications will certainly wait a while because the economic viability of such a technology does not seem so clear due the significant number of steps and the drastic control on thicknesses of layers that are necessary to obtain an acceptable final yield.

Below, we will go into the details of the operating principle of CRF filters by giving a few examples of realizations.

10.3.2. *Operating principles of CRF filters*

Figure 10.31 shows a cross-section of a four-pole CRF filter with two sections. One section is made up of the vertical stacking of two BAW resonators acoustically coupled by a Bragg mirror between them. As in classic BAW resonators, substrate-acoustic isolation is obtained either by a Bragg mirror (as is the case in this diagram), or by a membrane forming an air gap. We therefore speak, respectively, of SMR- or FBAR -type CRFs.

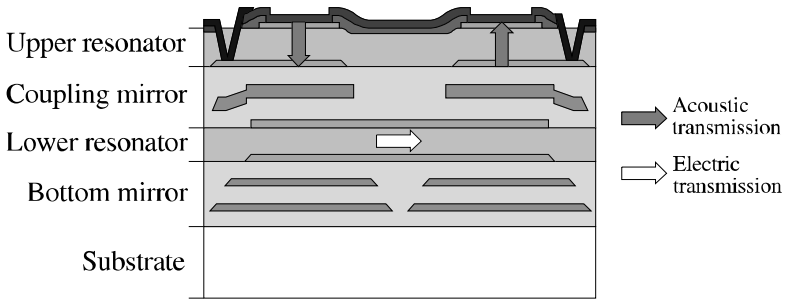

Figure 10.31. *Cross-section of a CRF filter*

The application of an electric field at the input upper resonator generates an acoustic wave that propagates at the lower resonator through the coupling layer. At the bottom resonator, the acoustic wave is inversely converted into an electric field that passes to the lower resonator of the second section. This electric field generates an acoustic wave that goes back up to the upper resonator of the second section that finally converts the acoustic wave into an electric field.

The coupling Bragg mirror plays a very important role by fixing the bandwidth of the filter, as seen in Figure 10.32. Decoupling the two resonators enables us to make them vibrate partly independently and to form two more or less spaced out frequencies of resonance. Acoustic coupling also determines the ripple in the pass band and in part the insertion losses. It also influences the out-of-band rejection by offering a relatively strong galvanic isolation between the input and output of the filter. To optimize the Bragg mirror, the number of layers and their nature can be modified. Classically, this Bragg mirror is made up of three layers of very different acoustic impedance materials. Infineon [FAT 04, FAT 05b] and LETI/ST Microelectronics [BIL 09, VOL 06] used a layer of W sandwiched between two layers of SiO_2. LETI/ST Microelectronics showed that we could use a purely dielectric SiN and SiOC tri-layer, which avoids to engraving the conducting W layer, which is necessary to avoid inter-resonator parasitic electric couplings. More recently, Avago showed very promising results by using a single polymer or CDO (Carbon Doped Oxide) coupling layer [SMA 07, JAM 09]. This last solution simplifies the process, but at the cost of a decrease in out-of-band rejection.

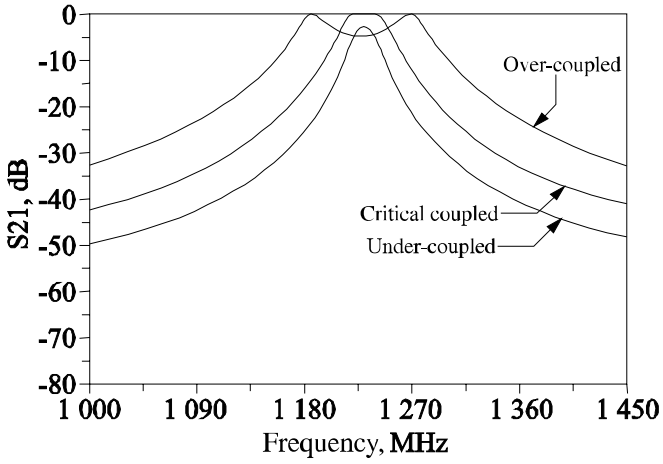

Figure 10.32. *Acoustic coupling of two CRF resonators to form a pass band filter*

The main advantage of CRF filters over BAW filters is the possibility of having an impedance conversion and a mode conversion at the level of the filter. The mode conversion is obtained quite simply by placing two CRF filtering paths side-by-side and connecting them together. For a differential-to-differential mode excitation (see Figure 10.33a), the two filtering paths are linked at level of the bottom electrode of the upper resonator; the four top electrodes of the upper resonator are left floating and they constitute differential inputs/outputs. For a single-to-differential excitation (see Figure 10.33b), the architecture is identical, except that one of the top electrodes is referenced on the ground at the input. We must note that we can also obtain this mode conversion with a single filtering path, as in Figure 10.33c. In this case it is the bottom electrodes of the upper resonators that are referenced on the ground (at the input level) or left floating (at the output level).

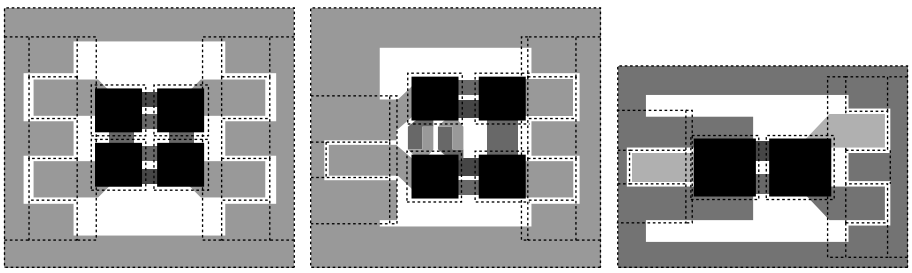

a) b) c)

Figure 10.33. *Mode conversion principle*

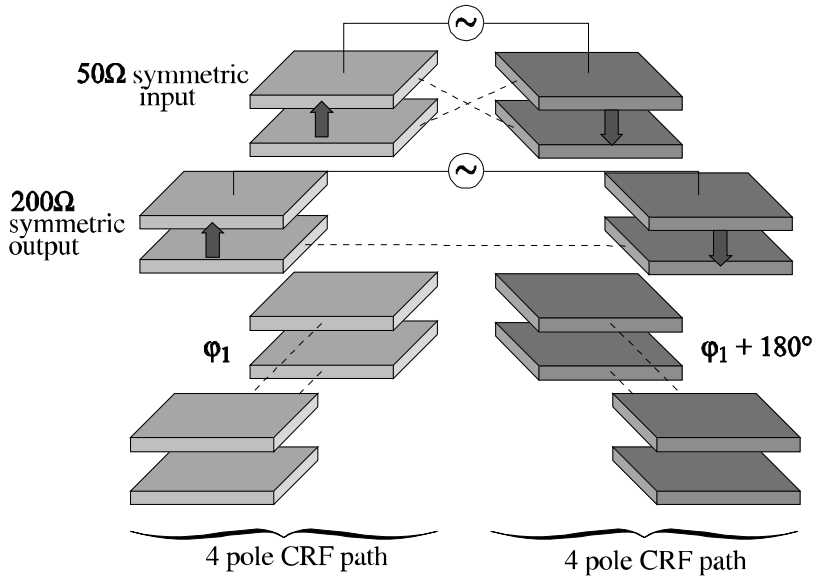

Figure 10.34. *Impedance conversion of factor 4 obtained by electric connections [VOL 06]*

There are two approaches by which to obtain the impedance conversion. The first is based on specific electric connections (see Figure 10.34) and the second is based on the combination of CRF sections of different surface areas (see Figure 10.35). Figure 10.34 gives an example of 50–200 ohm impedance conversion based on the first principle. The differential to differential filter is obtained by placing to CRF filtering paths side-by-side. The surface area of the resonators of each of the two filtering paths is calculated for input/output impedance to be 100 ohms. At the input level, the two resonators are connected in an anti-parallel way, which leads to an impedance of 50 ohms. At the output level the two resonators are connected in series: this gives an impedance of 200 ohms. This approach is particularly effective for obtaining an impedance conversion by a factor of 4. To obtain a factor of 2, three CRF filtering paths will have to be connected, and for a factor of 3, four CRF filtering paths will be needed. As a result a 50 ohms-input filter with a conversion factor of 2 will need three filtering paths side-by-side designed to have an input impedance of 150 ohms; this can be done with resonators with very small surface areas that are more sensitive to acoustic parasitics and difficult to optimize.

Figure 10.35 illustrates the second method of obtaining an impedance conversion, this time being based on CRF sections with different surface area. Therefore an impedance relation of a factor of 2 is easily obtained with a single CRF

filtering path: conversion from 50 to 25 ohms and from 50 to 100 ohms is presented in Figure 10.35a. This method can be applied to all types of filters. The filter in Figure 10.35b is a single-to-differential filter with an impedance conversion of 50 ohms to 100 ohms. One of the advantages of this approach is that it enables us to obtain low input/output impedances by using resonators with a large surface area that are less sensitive to acoustic parasitics. The impact of this method on insertion losses of the filter is quite low, at about 0.5 dB. On the other hand, it produces a reduction in the impedance matching of the filter in the pass band. The in-band impedance match is often a critical parameter for certain RF standards, which is why this method is generally confined to impedance conversion by a factor of less than three.

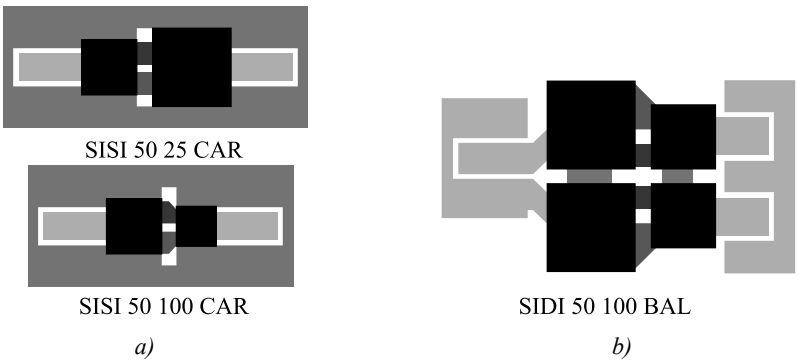

Figure 10.35. *a) Impedance conversion of factor 2 obtained by a change in surface area; and b) impedance conversion of factor 2 obtained by change in surface area coupled to a mode conversion*

10.3.3. *Example of implementations*

Below we give a few examples of CRF filters produced in the clean rooms at LETI [BIL 09].

10.3.3.1. *Two port filters*

The first example is a 50 ohms to 50 ohms two-port filter centered at 2.14 GHz. Figure 10.36 shows two versions of this filter: the first (a) is the basic version with square resonators; the second (b) is an optimized version in which the resonators are apodized to limit acoustic parasitics.

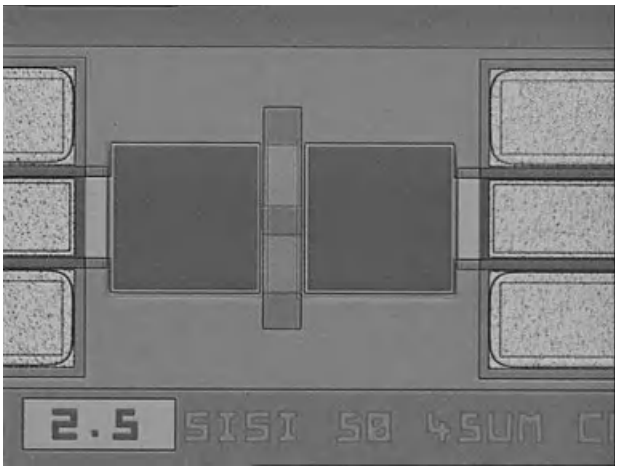

a)

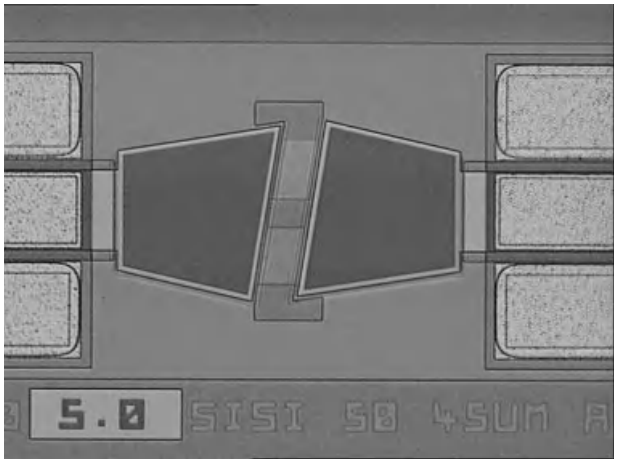

b)

Figure 10.36. *Examples of two-port CRF filters*

The filter fulfills the requirements of the application, see Figure 10.37a: it is centered at 2.14 GHz with 60 MHz of bandwidth and has <3 dB of losses. The bandwidth of the filter extracted at -3 dB is 81.6 MHz. Insertion losses in the band are at minimum -1.86 dB and at maximum -3 dB. In-band matching, S22 in Figure 10.37a, is greater than -8 dB, which is just enough. Out-of-band rejection is >-40 dB from 0–9 GHz, see Figure 10.37b. This first example shows the potential of

CRF technology: this filter with a much reduced size, of around 0.16 mm^2, has remarkable performance.

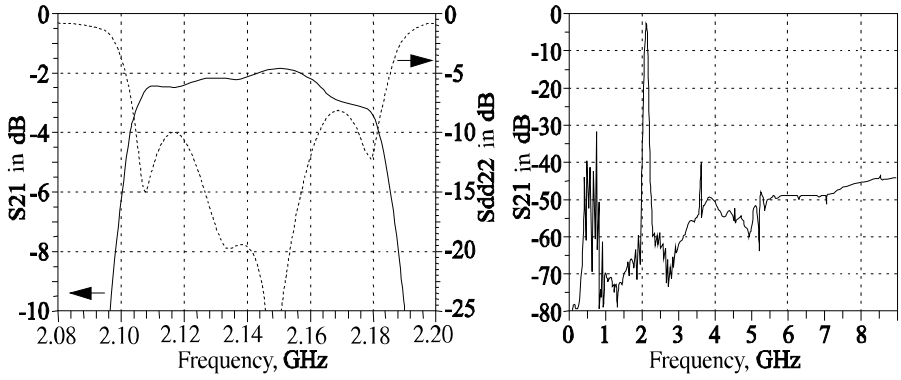

a) *b)*

Figure 10.37. *a) In-band response of a two port CRF filter; and b) wideband filter response*

10.3.3.2. *Three-port filters*

Below is an example of a three-port CRF filter. The mode conversion is obtained by using two CRF filtering paths side-by-side and connecting one of the input ports to the ground. Impedance conversion from 50 ohms to 200 ohms is based on the use of anti-parallel and series electric connections between the two filtering paths. Each of the resonators is of identical size and has an impedance of 100 ohms. In Figure 10.38, we can observe the pathways between the two resonators of the first sections that have the anti-parallel connection between the top and bottom electrodes of the upper resonators.

In this photograph, the apodization of the resonators that aims to limit the acoustic parasitics can also be seen. Extraction at -3 dB gives a central frequency of 2.131 GHz and a bandwidth of 73 MHz. In-band insertion losses are at minimum -2.6 dB and at maximum -4.2 dB. Input and output impedance matches, respectively, S11 and Sdd in Figure 10.38a, are >-8 dB into the pass band. For this parameter, this impedance conversion solution is better than the having different surface areas. Out-of-band rejection is excellent and >40 dB up to 9 GHz.

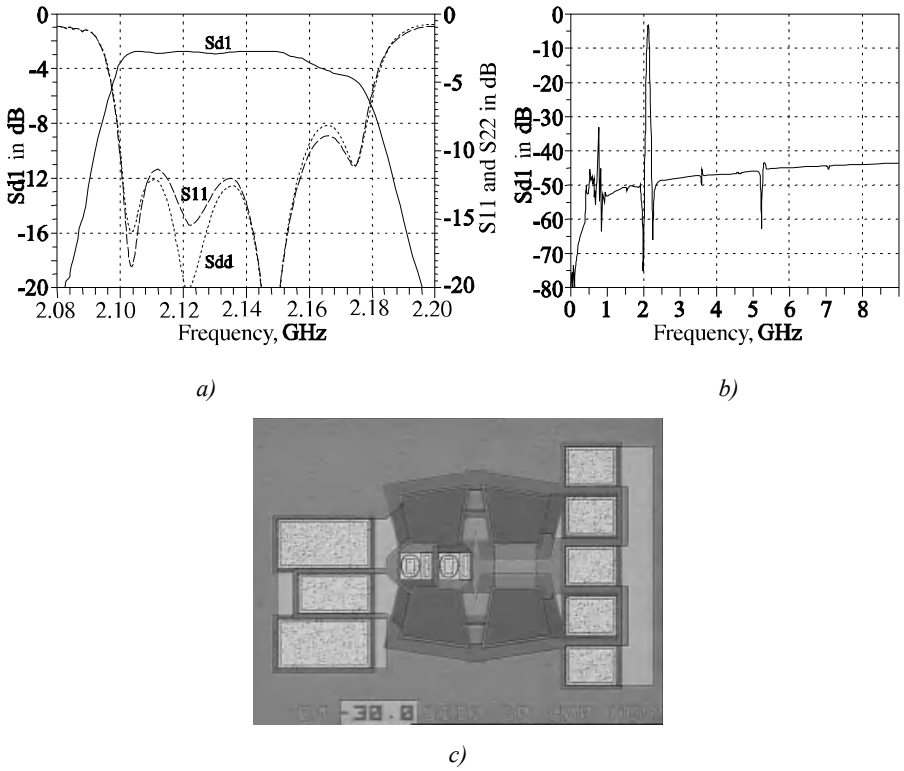

Figure 10.38. *Second example of a three-port CRF filter: a) in-band response; b) wide band response; and c) photograph of the filter*

10.3.3.3. *Four-port filters*

The final example is a four-port differential-to-differential filter with an impedance conversion from 50 ohms to 12 ohms based on anti-parallel and series electric connections; the resonators are of identical size. Each resonator shows an impedance of 25 ohm. This filter is dedicated to an output filtering application of a power amplifier, which explains its low output impedance.

The version of this filter presented in Figure 10.39 is the one that was divided and reported by flip-chip. In Figure 10.39c, the circular pads that will receive the flip-chip balls are observed. In Figure 10.39d, we can see the thin-film packaging on each of the four upper resonators. This packaging is not hermetic and therefore does not serve as final packaging. On the other hand, it is robust enough to protect the resonators during the sawing and reporting phases. Extraction at -3 dB gives a central frequency of 2.134 GHz and a pass band of 82 MHz. In-band insertion losses

are at minimum -1.9 dB and at maximum -3.4 dB. In-band impedance matching is not so good (>8 dB) for differential input and output. Out-of-band rejection is around 30 dB up to 20 GHz.

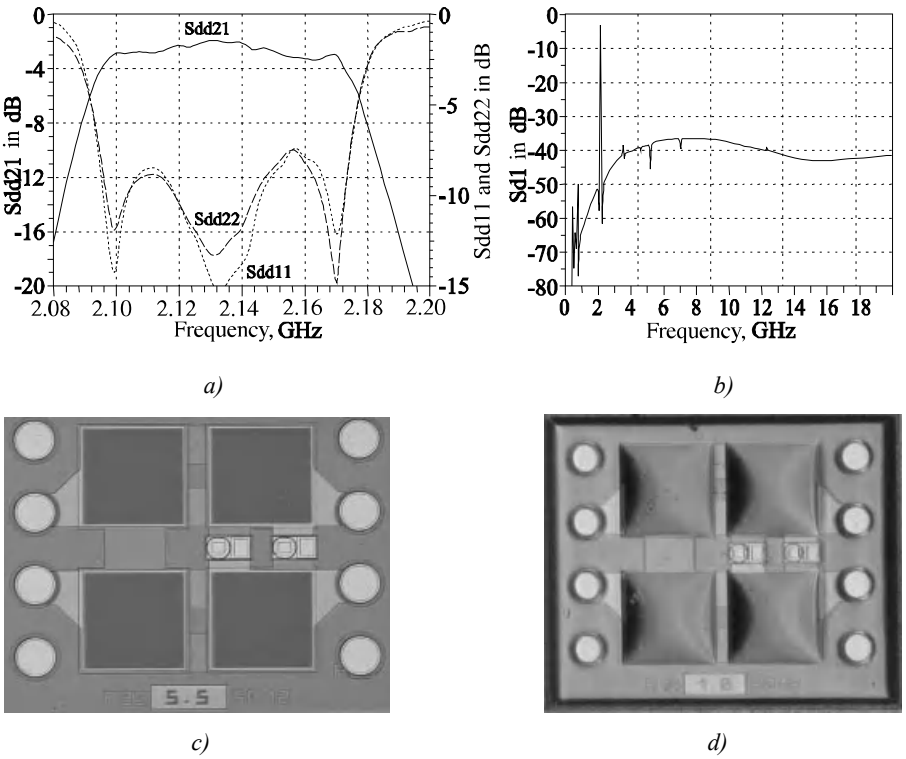

Figure 10.39. *Example of a four-port CRF filter: a) in-band response; b) wideband response; c) photograph before thin-film packaging; and d) photograph after thin-film packaging*

10.4. Bibliography

[AIG 03] AIGNER R., KAITILA J., ELLÄ J., ELBRECHT L., NESSLER W., HANDTMANN M., HERZOG T.R., MARKSTEINER S., "Bulk acoustic wave filters: performance optimization and volume manufacturing", *IEEE MTT-S Digest*, p. 2001, 2003.

[AIG 07] AIGNER R., "Bringing BAW technology into volume production: the ten commandments and the seven deadly sins", *3rd International Symposium on Acoustic Wave Devices for Future Mobile Communication Systems*, 2007.

[AIG 08] AIGNER R., "SAW and BAW technologies for RF filter applications: a review of relative strengths and weaknesses", *Proceedings of the 2008 IEEE International Ultrasonics Symposium*, p. 582, 2008.

[BER 78] BERTÉ M., HARTEMANN, P., "Quartz resonators at fundamental frequencies greater than 100 MHz", *Proceedings of the 1978 IEEE Ultrasonics Symposium*, p. 148, 1978.

[BES 77] BESSON R.J., "A new 'electrodeless' resonator design", *Proceedings of the 31st Annual Frequency Control Symposium*, p. 147, 1977.

[BES 95] BESSON R.J., BOY J.J., MOUREY M.M., "BVA resonators and oscillators: a review. Relation with space requirements and quartz material characterization", *Proceedings of the 1995 IEEE International Frequency Control Symposium*, p. 590, 1995.

[BIF 08] FRANCK Z.B., BRADLEY P.B., "Bulk Acoustic Wave RF Technology", *IEEE Microwave Magazine*, October 2008.

[BIL 09] BILLARD C., BUFFET N., JOBLOT S., REINHARDT A., PARAT G., BAR P., "200 mm manufacturing solution for coupled resonator filters", *ESSDERC2009*, Athens, Greece, 14-18 September 2009.

[CAR 05] CARUYER G., DEVOS A., CARPENTIER J.F., VÉLARD R., CASANOVA N., LEFEVRE A., DUMONT F., PARAT G., ANCEY P., "Design of bulk acoustic wave RF resonators and filters based on advanced Bragg reflector", *Proceedings of the 2005 IEEE Ultrasonics Symposium*, 2005.

[COU 74] COUSSOT G.J., "Bulk wave resonator for the 100-300 MHz range", *Proceedings of the 1974 Ultrasonics Symposium*, p. 590, 1974.

[FAT 04] FATTINGER G.G., KAITILA J., AIGNER R., NESSLER W., "Single-to-balanced Filters for Mobile Phones using Coupled Resonator BAW Technology", *IEEE Ultrasonics Symposium 2004*, p. 416-419, 2004.

[FAT 05a] FATTINGER G.G., FATTINGER M.R., DIEFENBECK K., MIILLER P., AIGNER R., "Spurious Mode Suppression in Coupled Resonator Filters", *IEEE IMS Proceedings 2005*, 2005.

[FAT 05b] FATTINGER G.G., MARKSTEINER S., KAITILA J., AIGNER R., "Optimization of acoustic dispersion for high performance thin film BAW resonators", *Proceedings of the 2005 IEEE Ultrasonics Symposium*, p. 1175, 2005.

[GRU 80] GRUDKOWSKI T.W., BLACK J.F., REEDER T.M., "Fundamental mode VHF/UHF bulk acoustic wave resonators and filters on silicon", *Proceedings of the 1980 Ultrasonics Symposium*, p. 829, 1980.

[ESP 31] ESPENSCHIED L., *Electrical wave filter*, US patent 1795204, 1931.

[IBO 08] IBORRA E., OLIVARES J., GONZALEZ-CASTILLA S., SANGRADOR J., RIMMER N., RASTOGI A., IVIRA B., REINHARDT A., "BAW resonators base don AlN with Ir electrodes for digital gíreles transmissions", *Proceedings of the 2008 IEEE Ultrasonics Symposium*, 2008.

[IEE 87] IEEE Standard on Piezoelectricity, ANSI/IEEE Std 176, 1987.

[IVI 08] IVIRA B., FILLIT R.Y., NDAGIKIMANA F., BENECH P., PARAT G., ANCEY P., "Self-heating study of bulk acoustic wave resonators under high RF power", *IEEE Transactions on Ultrasonics, Ferroelectrics and Frequency Control*, vol. 55, n° 1, p. 139, January 2008.

[JAM 09] JAMNEALA T., KOELLE U.B., SHIRAKAWA A., GILBERT S.R., NIKKEL P., FENG C., RUBY R., "Ultra-miniature coupled resonator filter with single-layer acoustic coupler", *IEEE Trans. on UFFC*, vol. 56, p. 2553-2558, 2009.

[KAI 04] KAITILA J., YLILAMMI M., ELLÄ J., "Resonator structure and a filter comprising such a resonator structure", Brevet US 6,812,619, 2004.

[KAI 07] KAITILA J., "Review of wave propagation in BAW thin film devices: progress and prospects", *Proceedings of the 2007 Ultrasonics Symposium*, p. 120, 2007.

[LAK 80] LAKIN K.M., WANG J.S., "UHF composite bulk wave resonators", *Proceedings of the 1980 Ultrasonics Symposium*, p. 834, 1980.

[LAK 82] LAKIN K.M., WANG J.S., KLINE G.R., LANDIN A.R., CHEN Y.Y., HUNT J.D., "Thin film resonators and filters", *Proceedings of the 1982 Ultrasonics Symposium*, p. 466, 1982.

[LAK 90] LAKIN K.M., "Fundamental properties of thin film resonators", *Proceedings of the 45th Annual Symposium on Frequency Control*, p. 201, 1990.

[LAK 95a] LAKIN K.M., KLINE G.R., MCCARRON K.T., "Development of miniature filters for wireless applications", *IEEE Transactions on Microwave Theory and Techniques*, vol. 43, n° 12, p. 2933, 1995.

[LAK 95b] LAKIN K.M., MCCARRON K.T., ROSE R.E., "Solidly mounted resonators and filters", *Proceedings of the 1995 IEEE Ultrasonics Symposium*, p. 905, 1995.

[LAK 01a] LAKIN K.M., BELSICK J., MCDONALD J.F., MCCARRON, K.T., "Improved bulk wave resonator coupling coefficient for wide bandwidth filters", *Proceedings of the 2001 IEEE Ultrasonics Symposium*, p. 827, 2001.

[LAK 01b] LAKIN K.M., BELSICK J., MCDONALD J.F., MCCARRON K.T., "High performance stacked crystal filters for GPS and wide bandwidth applications", *IEEE Ultrasonics symp. 2001*, p. 833-838, 2001.

[LAR 00] LARSON J.D., BRADLEY P.D., WARTENBERG S., RUBY R., "Modified Butterworth-Van Dyke circuit for FBAR resonators and automated measurement system", *IEEE Ultrasonics Symposium*, p. 863-868, 2000.

[LAR 01] LARSON III J.D., RUBY R.C., BRADLEY P., "Bulk acoustic wave resonator with improved lateral mode suppression", US patent 6,215,375, 2001.

[MAR 05] MARKSTEINER S., KAITILA J., FATTINER G.G., AIGNER R., "Optimization of acoustic mirrors for solidly mounted BAW resonators", *Proceedings of the 2005 IEEE Ultrasonics Symposium*, p. 329, 2005.

[MIN 57] MINDLIN R.D., "Mathematical theory of vibrations of elastic plates", *Proceedings of the 11th Annual Frequency Control Symposium*, 1957.

[NEW 65] NEWELL W.E., "Face-mounted piezoelectric resonators", *Proceedings of the IEEE*, vol. 53, p. 575, 1965.

[ONO 69] ONOE M., "Thickness-twist vibrations of a piezoelectric plate", *The Transactions the Institute of Electronics Information and Communication Engineers of Japan*, vol. 52-A(10), p. 38-43, 1969.

[PET 08] PETIT D., CÉSAR E., BAR P., JOBLOT S., PARAT G., BERCHAUD O., BARBIER D., CARPENTIER J.F., "Thermally stable oscillator at 2.5 GHz using compensated BAW resonator and its integrated temperature sensor", *2008 IEEE International Ultrasonics Symposium (IUS)*, Beijing, China, 2-5 November 2008.

[PET 09] PETIT D., CÉSAR E., BAR P., JOBLOT S., PARAT G., BERCHAUD O., VERDIER J., CARPENTIER J.F., "Temperature compensated BAW resonator and its integrated thermistor for a 2.5 GHz electrical thermally compensated oscillator", *International Microwave Symposium MTT-IMS 2009*, Boston, 7-12 June 2009.

[POR 07] PORNIN J.L., GILLOT C., PARAT G., JACQUET F., LAGOUTTE E., SILLON N., POUPON G., DUMONT F., "Wafer level thin film encapsulation for BAW RF MEMS", *Proceedings of the 57th ECTC*, 2007.

[REI 02] REINHARDT A., LAUDE V., PASTUREAUD T., BALLANDRAS S., "Numerical simulation and comparison of membrane and solidly mounted FBAR's", *Proceedings of the 2002 IEEE Ultrasonics Symposium*, p. 497, 2002.

[REI 07] REINHARDT A., BUFFET N., SHIRAKAWA A., DAVID J.B., PARAT G., AÏD M., JOBLOT S., ANCEY P., "Simulation of BAW resonators frequency adjustment", *Proceedings of the 2007 IEEE Ultrasonics Symposium*, p. 1444, 2007.

[REI 09] REINHARDT A., PORNIN J.L., AÏD M., CLEMENT LORENZO M., OLIVARES M., IBORRA, E., RIMMER N., BURGESS S., ANCEY, P., "BAW technology for advanced RF architectures, workshop on advanced BAW-enabled wireless transceivers: from devices to system architectures", *2009 IEEE MTT-S International Microwave Symposium*, 2009.

[ROB 71] ROBERTS D.A., "CdS-quartz monolithic filters for the 100-500 MHz frequency range", *Proceedings of the 25th Annual Frequency Control Symposium*, p. 251, 1971.

[ROS 45] ROSENBAUM J.F., *Bulk Acoustic Waves Theory and Devices*, Artech House, Boston, 1945.

[RUB 99] RUBY R., BRADLEY P., LARSON J., OSHMYANSKY Y., "PCS 1900 MHz duplexer using thin film bulk acoustic resonator (FBARs)", *Electron. Letters*, vol. 35, p. 794-795, 1999.

[RUB 01] RUBY R., BRADLEY P., LARSON J., OSHMYANSKY Y., FIGUEREDO D., "Ultra-miniature high-Q filters and duplexers using FBAR technolgy", *International Solid-State Circuits Conference*, p. 120-121, 2001.

[RUB 07] RUBY R., "Review and comparison of bulk acoustic wave FBAR, SMR technology", *2007 IEEE Ultrasonics Symposium*, p. 1029-1040, 2007.

[SAT 85] SATOH H., EBATA Y., SUZUKI H., NARAHARA C., "An air-gap type piezoelectric composite thin film resonator", *Proceedings of the 39th Annual Frequency Control Symposium*, p. 361, 1985.

[SMA 07] SMALL M.K., JAMNEALA T., CALLAGHAN L.A., LARSON III J.D. (FELLOW), RUBY R.C., "A de-coupled stacked bulk acoustic resonator (DSBAR) filter with 2 dB bandwidth > 4%", *IEEE Ultrasonics Symp. 2007*, p. 604-607, 2007.

[SIT 72] SITTIG E.K., "Design and technology of piezoelectric transducers for frequencies above 100 MHz", in MASSON W.P. and THURSTON R.N. (eds.) *Physical Acoustics*, vol. IX, Academic Press, New York, 1972.

[STA 10] SOCIÉTÉ STATEK, Note technique n°32, The Quartz Crystal Model and its Frequencies, available at: http://www.statek.com, 2010.

[TIE 69] TIERSTEN H.F., *Linear Piezoelectric Plate Vibrations: Elements of the Linear Theory of Piezoelectricity and the Vibration of Piezoelectric Plates*, Plenum, New York, 1969.

[TIE 83] TIERSTEN H.F., STEVENS D.S., "An analysis of thickness-extensional trapped energy resonators with rectangular electrodes in the zinc-oxide thin film on silicon configuration", *Proceedings of the 37th Annual Frequency Control Symposium*, p. 325, 1983.

[TIL07] TILHAC C., Développement d'architectures de filtres à base de résonateurs à ondes acoustiques de volume et contribution à l'intégration dans une technologie avancée silicium industrielle pour des applications radio-fréquences, Thesis, July 2007.

[TIM 04] TIMME H.J., AIGNER R., ELBRECHT L., ELLA J.S., POHJONEN K.H., TIKKA P., Filter device and method for fabricating filter devices, Patent number US 2004/0029356, 2004.

[VAN 28] VAN DYKE K.S., "The piezo-electric resonator and its equivalent network", *Proceedings of the IRE*, 1928.

[VOL 06] VOLATIER A., DEFAŸ E., N'HARI A., CARPENTIER J.F., ANCEY P., DUBUS B., "Design, elaboration and characterization of coupled resonator filters for WCDMA applications", *IEEE Ultrasonics Symp. 2006*, p. 829-832, 2006.

[YAN 04] YANG J., "Frequency shifts in a piezoelectric body due to small amounts of additional mass on its surface", *IEEE Transactions on Ultrasonics, Ferroelectrics and Frequency Control*, vol. 51, n° 10, p. 1199, 2004.

Chapter 11

High Overtone Bulk Acoustic Resonator (HBAR)

11.1. About HBAR

Among elastic wave components, high-overtone bulk acoustic resonators occupy a place apart from the main stream of radio frequency (RF) acoustic-electric devices. Indeed, these components whose structural simplicity might be compared with that of classic surface and bulk wave components are affected, as indicated by their name, by a spectral density that is not very compatible with the specifications of RF components generally used for single-mode filtering or filtering with controlled spectral density, which allow out-of-band signal rejections that conform to the needs of the electronic systems concerned. They are not currently a solution regularly implemented at the industrial level. They nevertheless represent a path for the development of future components exploited for sensors of various physico-chemical quantities. They are also sources of high stability and spectral purity that can potentially be integrated into direct synthesis, consequently eliminating frequency multiplications that artificially increase the phase noise of corresponding oscillators. As such, they enable us to obtain the highest coefficients of quality of all acousto-electric devices and show extremely low volume. For certain specific applications, it is also possible to exploit them for narrowband and average filtering functions (between 1/1000 and 1/10 of the relative bandwidth).

Here we will present the important points characterizing these components by first recalling the great lines of their operation, their modalities of implementation

---

Chapter written by Mathieu PIJOLAT, Chrystel DEGUET and Sylvain BALLANDRAS.

and the associated technologies and materials. Finally, we will show examples of implementation and characterization of such resonators through several applications in the domain of sources of frequency and remote access sensors.

11.1.1. *Generalities*

HBAR (high overtone bulk acoustic resonators) or OMR (overmoded resonators) are composite structures made of a thin piezoelectric film over a substrate whose thickness is largely greater than that of the film above. A characteristic figure of merit of these resonators is the frequency – quality factor product, greater by at least one order of magnitude than that of bulk or surface elastic wave resonators on fundamental mode. This figure of merit is consequently greater for HBAR than for film bulk wave resonators (FBAR) or solidly-mounted resonator (SMR).

Thanks to these outstanding coefficients of quality, HBARs can be used in oscillation loops to develop high-stability frequency sources with high spectral purity. These structures originate from the first bulk wave delay lines and constitute reflective delay lines as such, (the transducer emits a bulk wave package that propagates in the substrate, reflects on its back, and returns to the transducer that reconverts it into an electric signal).

Their use in applications as resonators was revealed as soon as their implementation techniques were improved. These resonators, first studied towards the end of the 1970s [LAK 93], re-gained in interest in the 1990s and 2000s. This success was due partly to the enormous progress in developing piezoelectric thin films on substrates of high crystalline quality as well as the new uses generated by the multiplication of standards and their associated frequency sources.

State-of-the-art HBAR resonators correspond to a record $Q.f$ product of 1.1×10^{14} Hz obtained by Lakin *et al.* in 1993 with AlN on sapphire [LAK 93]. In comparison, the best FBAR solutions have a quality factor of 3,500 at 1.9 GHz or a $Q.f$ product of 7.10^{12} Hz [RUB 09] and bulk wave resonators on quartz reach 1.5×10^{13} Hz. Intensifying work in the field enables us to expect new improvements in these devices in years to come and the establishment of new operational limits in terms of functional characteristics (electromechanical coupling, quality factor, frequency control, etc.).

11.1.2. *Principle*

A bulk elastic wave is generated in the (classic) piezoelectric thin film electrode stack and then propagates into the substrate. The distinctive characteristic of HBAR

is that it uses the substrate as a cavity resonator for the acoustic wave. Actually, contrary to FBAR or SMR encountered in the previous chapters, the substrate is in no way decoupled from the piezoelectric stack. It is even thanks to the cavity resonator that the *Q.f* product of HBARs can reach the 10^{14} Hz range. This cavity must, nevertheless, respond to quality criteria. A simple HBAR example will be used in this part: an aluminum nitride (AlN) thin film surrounded by two electrodes, all placed on a silicon substrate.

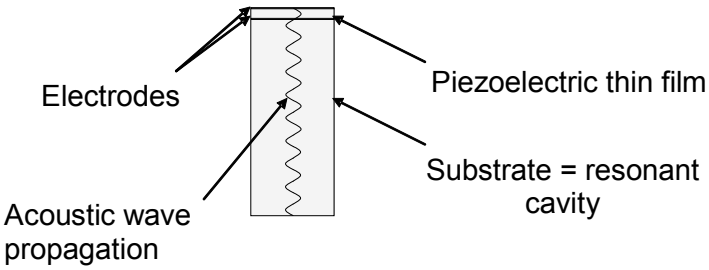

Figure 11.1. *Schematic of an HBAR*

11.1.3. *Description of the spectrum*

In order to understand the spectrum of HBAR resonances, the resonance conditions defined in Chapter 7 on acoustic formalism can be reused:

$$Y(\omega) = j\omega \frac{\varepsilon_{33}}{2l} \frac{1}{1 - \frac{k_t^2}{2\Phi} \frac{\frac{Z_S}{Z_L}\tan\omega s_S e + 2\tan\Phi}{1 + \frac{Z_S}{Z_L}\frac{\tan\omega s_S e}{\tan 2\Phi}}} \qquad [11.1]$$

Once again, taking the case where the piezoelectric film is of negligible thickness compared to that of the substrate, the conditions of resonance of the cavity are actually provided by the $\tan(\omega s_S e)$ terms. Yet, these resonances cannot be dissociated from the change, though slow, in response of the piezoelectric film contained in the Φ terms. Two views of an HBAR resonator are then distinguished: the influence of the substrate (cavity resonator) and the influence of the piezoelectric film (the transducer).

11.1.3.1. *Influence of the substrate*

The frequency of resonance of the fundamental mode of the cavity (the substrate) is $f_0 \approx v/2s$, with v being the velocity of the elastic wave in the substrate and s the thickness of the substrate. The periodicity of the tangent function explains the resonances of the following or harmonic modes, with a frequency separation of $\Delta f_0 \approx f_0$.

Frequencies of resonance and antiresonance can be extracted from the real parts of admittance and impedance, respectively. These frequency-real parts are presented as Dirac peaks in the absence of intrinsic losses of the materials, in the perfectly parallel planes of reflection hypothesis and in the absence of power flow angles (deviation between the direction of propagation and power flow in the thickness of the substrate, also called beam-steering angle).

In the case where these accumulated losses turn out to be low, the peaks are no longer infinitely thin spectrally but are close to a Lorentzian function, from which it is possible to extract quality factors with the *full width at half maximum* (see Figure 11.2) based on the formula $Q = f/\Delta f$.

In addition, effective coupling of the mode considered can be extracted thanks to the electromechanical coupling formula.

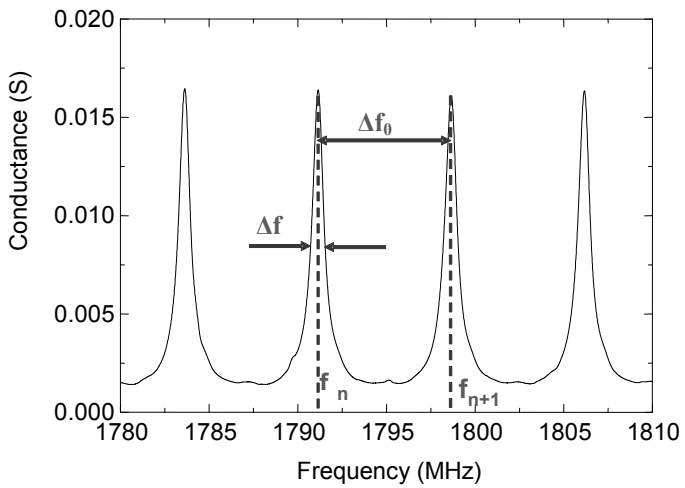

Figure 11.2. *Frequency separation $\Delta f_0 \approx f_0$ of two successive harmonics, f_n and f_{n+1}, for an AlN/Si HBAR. Δf is used to extract the quality factor Q*

11.1.3.2. *Influence of the transducer: the piezoelectric film*

When the piezoelectric thin film is placed on a substrate of semi-infinite thickness or made of absorbent material, only the influence of the thin film is visible in the electric response. Coupled energy is maximal when the frequency resonance corresponds to the resonance of the piezoelectric thin film. This condition is fulfilled when a half-wavelength gets close to the thickness of the piezoelectric film. As soon as the substrate is of finite thickness, however, the response is modulated by the effects of resonance in this cavity and the response of the piezoelectric layer is an envelope of all the harmonics due to the substrate. The comparison is shown in Figure 11.3, where the response stimulated by an AlN film on a semi-infinite silicon substrate is shown in gray, the experimental response of an HBAR in black, and the mathematical evaluation per average of adjacent points to the HBAR response enclosure in light gray.

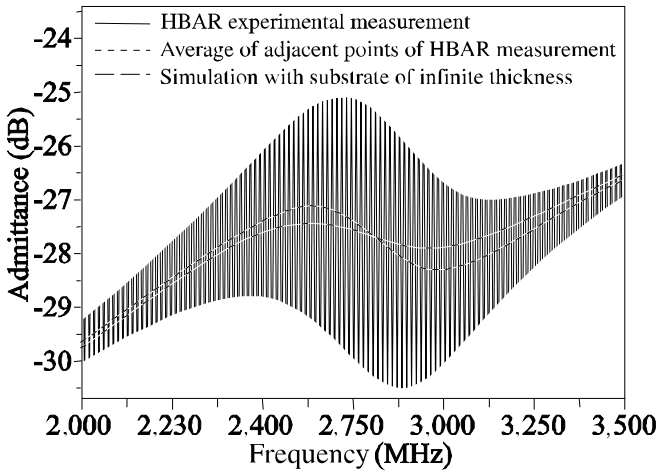

Figure 11.3. *Comparison of the resonance spectrum of an AlN/SI HBAR with a representation of the average of 100 adjacent points and a simulation of an HBAR, the substrate of which has an infinite thickness*

Depending on the ratio of thickness of the thin film to that of the substrate, resonances will generally be in this zone of strong coupling. The goal in the framework of an oscillator is stability: the lower the ratio, the more spectral purity is favored and the more stable the oscillation loop. In addition to the oscillator applications, this envelope turns out to be useful for evaluating the electromechanical coupling of a piezoelectric film. Indeed, as soon as frequency corresponds to the response of the piezoelectric film, we can wonder about the properties of the film from which HBAR electric responses can be extracted. This is

so much more important that the technological process for obtaining an HBAR can be reduced to a one-level mask, unlike FBAR or SMR technologies which are largely more complex (we speak of at least five levels of lithography). The standard formula due to frequencies of resonance and antiresonance can be used with the peaks of the envelope. The coupling constant extracted is, however, overvalued by 10% to 20%. From the experimental measurement of an AlN HBAR on silicon (see Figure 11.4), the frequencies of resonance and antiresonance, f_r and f_a, respectively, are extracted from the envelope. The extracted electromechanical coupling factor is about 10%. Once again, the systematic overvaluation enables us to deduce that electromechanical coupling of the AlN piezoelectric film is close to the value obtained by simulating the same stack, i.e. 7% (the theoretical AlN thickness coupling value is also 7%).

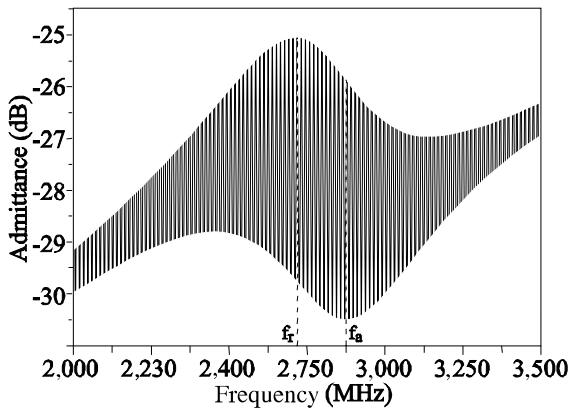

Figure 11.4. *Extraction of resonance and antiresonance frequencies to obtain the electromechanical coupling constant of the film*

The electromechanical coupling constant extraction will be justified later for a technological implementation of an HBAR, followed by a deep etching, in order to obtain the corresponding FBAR. The electromechanical couplings extracted from the HBAR's electrical response and that of the FBAR will then be compared.

11.2. Technology

11.2.1. *Technological constraints*

While the main figure of merit of an HBAR is its *Q.f* product and its propensity to favor high-frequency operating, any parameter that is not in favor with this figure of merit must be minimized or even avoided. With the piezoelectric stack, the

demands are the same as for an FBAR or a SMR. For the substrate (the resonant cavity), the key parameters are:

– the parallelism of the two faces in order to avoid acoustic energy leakage at the sides of the resonator;

– polishing of the two faces with a mirror quality. Indeed, the reflection of the acoustic wave on the rear face of the substrate must be perfect so it does not lose energy;

– the recommended thickness for inserting an HBAR in the oscillation loop does not have to be very large. When it is inserted in an oscillation loop, the resonance peak on which the oscillator is stabilized must be detached from the other peaks. Indeed, the frequency separation of the peaks that corresponds to the first mode is directly inversely proportional to the thickness of the substrate. Decreasing the thickness then returns to favoring the presence of one single peak in the most coupled zone of the envelope [MAS 07] but it leads to technological difficulties inherent to this type of operation.

11.2.2. *Choice of materials*

11.2.2.1. *Substrate*

The substrate used for HBARs must limit dielectric as well as viscoelastic losses. With the goal of an HBAR being to obtain the highest possible frequency – quality factor products, it is necessary to use single-crystal plates composed of materials known for their low viscoelastic and dielectric losses, such as YiG or YaG (see [LAK 93]), sapphire (Al_2O_3), lithium niobate (LNO or $LiNbO_3$), lithium tantalate ($LiTaO_3$) or even quartz (SiO_2). Quartz also has crystal orientations compensated for temperature effects for bulk waves such as AT or BT cuts. With the aim of integration and stability, choosing quartz can enable us to develop oven-controlled crystal oscillators (OCXO) without temperature regulation systems. This generally responds to the heat stability demands of systems controlled in this way.

11.2.2.2. *Piezoelectric material*

The choice of a piezoelectric material depends on the final use. The HBAR is clearly not suited for wide RF bandwidth filtering, *a contrario* to BAW and SAW filters. We could think, on first consideration, that electromechanical coupling of the piezoelectric film is not critical. However, an HBAR will be much easier to integrate in an oscillator loop if resonance peaks exhibit a significant dynamic, i.e. the admittance module peak is big compared to the noise floor. Therefore, the material must show a sufficiently high electromechanical coupling to effectively couple the HBAR harmonics, still keeping in mind that the strong couplings can result in an

increase in electric losses (ohmic losses in metallic and contact films). A second issue, just as for BAWs, will be the crystal quality of the material. LNO is an excellent choice, especially for its unique bulk wave cuts, such as the Y+36°cut, with the longitudinal wave with a coupling coefficient $k_t^2 \approx 26\%$ as the only coupled wave and Y+163° cut, with a shear wave with a coupling coefficient $k_t^2 \approx 40\%$ as the only coupled wave.

11.2.3. *Geometry of resonators*

Although they allow the use of longitudinal or shear polarization bulk elastic waves, depending on the nature and properties of the transducer film, resonators of the HBAR type are often conceived in a similar way to resonators on thin films (FBAR and SMR). They also give rise to the same electrode geometries, although they are not subjected to the same low-frequency parasitic-mode rejection issues that modulate the response of the mode exploited.

The resonators tested next will be those with one or two ports, as described in Figures 11.5a and 11.5b. The most common and most intuitive configuration consists of the *simple port structure*, which pertains to classic bulk wave resonators. This can be represented by a lumped elements diagram with two parallel branches:

– one linked to the static capacitance made up of the two electrodes facing each other separated by the transducer material (in majority dielectric);

– the other linked to the motional effects describing the resonances (as with many motional branches, resonance branches will then be compared to the HBAR resonator described).

Nevertheless we do know the structures of bulk wave monolithic filters for which we exploit mode couplings, allowing energy exchange between the input and output ports of the component.

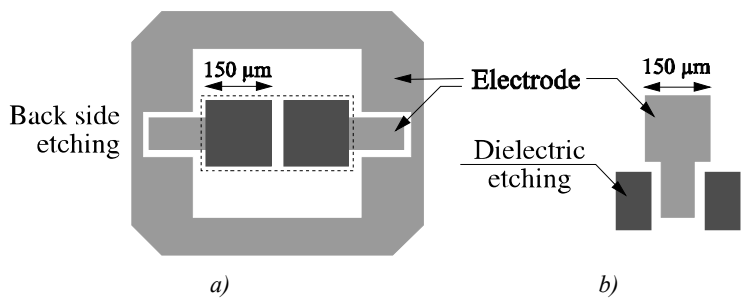

Figure 11.5. *Geometry of resonators: a) two ports; and b) one port*

11.3. Examples of implementations

In this part, two examples of HBAR realizations will be developed and characterized. The first example concerns an HBAR that includes a single crystal thin film of LNO and its electrode reported on a substrate of LNO through Smart Cut™ technology. The second example is a LNO-based HBAR stuck to a silicon substrate then mechanically thinned, with an FBAR obtained from a similar stack thanks to a deep etching of the substrate backside to obtain electrode–LNO–electrode membranes. The RF measurements are produced through pre-calibrated reflection (one-port measurements) or transmission (two-port measurements) with vector network analyzers (*short open load thru* calibration).

11.3.1. *LNO on LNO*

11.3.1.1. *Experimental process*

LNO is one of the most frequently used materials for SAW technology. Existing in the form of single crystal wafers 10 cm in diameter, the industry uses more than 100,000 wafers per year, mainly to produce surface elastic wave RF filters for mobile telephony applications. Its use in bulk wave configuration dates from the 1960s, as a delay line.

Attempts at integration with the film report and polishing were also carried out [GAC 08, HUA 74, UCH 73], but among the other outstanding LNO applications, we will cite acoustic imaging and acousto-electric modulators that also drain a large part of global annual production. With LNO being strongly anisotropic, crystal orientation must be chosen in terms of the object we wish to produce and the mode of propagation we seek to exploit. In addition, the coupling efficiency of elastic waves depends especially on orientation, as well as the principal physical characteristics of the corresponding waves: mode polarization (longitudinal, shear), phase velocity and the intrinsic losses that are related to the material. In this section, HBARs are produced by transferring an X-cut submicronic single crystal thin film of $LiNbO_3$ thanks to Smart Cut™ Technology. This X orientation based on the normal to the plate was chosen for the two coupled shear waves that it allows to be exploited. The most coupled wave shows an electromechanical coupling reaching $k_t^2 = 45\%$, i.e. seven times more than aluminum nitride coupling. In order to create HBAR test vehicles, the following steps are carried out:

– Metal deposit, which will form the buried electrode.

– Ionic implantation in a LNO substrate. The average depth of implantation is imposed by the energy given to the ions during acceleration, a platinum deposit playing the role of buried electrode, a SiO_2 deposit on this same substrate, as well as another “B” LNO substrate.

– Direct bonding of the two plates together after specific preparation of these two wafers followed by a heat treatment: a fracture at the level of the zone that is mainly implanted is realized. A single crystal thin film is therefore transferred onto the B substrate, a platinum deposit (the top electrode) followed by a photolithography aimed at defining the planar patterns of the resonators. Finally, the LNO thin film is etched to create RF access points at the bottom electrode.

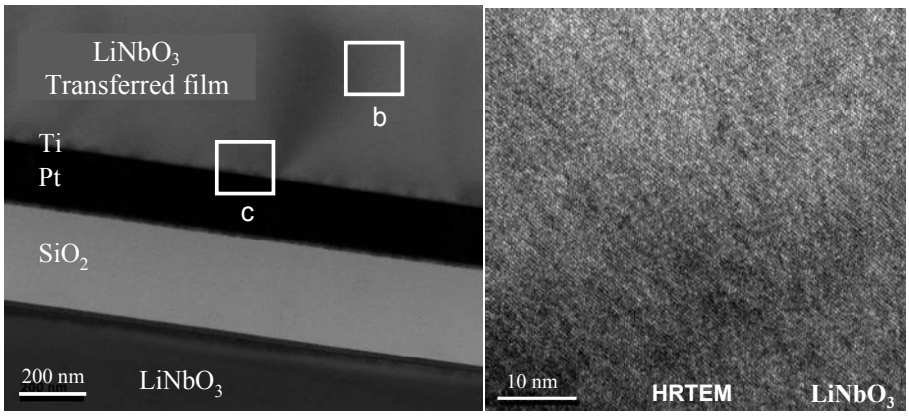

a) *b)*

Figure 11.6. *a) Transmission electron microscopy (TEM) picture after film transfer; and b) high-resolution TEM picture in the transferred LNO film: the crystal lattice is visible and no clear defect is detected*

Physical characterizations are performed after these technological steps in order to verify the single-crystal character of the transferred film [MOU 08].

The high-resolution transmission electron microscopy image enables us to see that there are no clear defects visible in the crystal lattice (see Figures 11.6a and 11.6b).

This observation is confirmed by an X-ray diffraction study showing a crystalline quality that is comparable to the LNO substrate, although of slightly poorer quality.

11.3.1.2. *Electric results*

11.3.1.2.1. Broadband measurement

In broadband measurement, the influence of the piezoelectric film, i.e. its resonance modulated by the HBAR resonance peaks is observed.

In Figure 11.7, two contributions of the admittance module can be distinguished:

– a very broad band contribution, from which the frequencies of resonance and antiresonance due to the piezoelectric film (the carrier) are extracted, i.e. the curve of the average over 100 points of experimental data;

– a slightly narrower contribution that is in reality solely a measurement artifact. Indeed, in broadband measurement, the number of points per measurement is too low to correctly describe them and thus a periodicity artificially appears (aliasing phenomenon).

The contribution of the piezoelectric film is extracted from the response envelope and an electromechanical coupling of around 40% is thus determined. This value is partially comparable to theoretical couplings of LNO bulk waves based on elastic, dielectric and piezoelectric constants, i.e. 45%.

This strong electromechanical coupling enables us to envisage broadband RF filtering applications [MOU 08].

Taking into consideration the low quality factors of the envelope, the validity of the extraction of an electromechanical coupling can be discussed. This extraction will be validated in section 11.3.2.

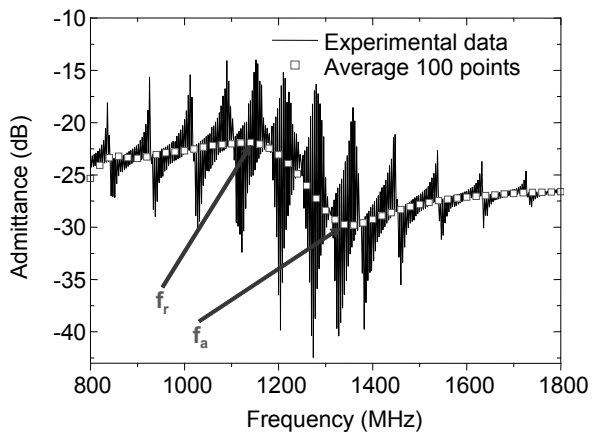

Figure 11.7. *Broadband measurement of the HBAR admittance module versus frequency*

In Figure 11.8, the envelope of the third harmonic due to the piezoelectric film is observed. The second harmonic is not visible because it does not satisfy the coupling conditions, as described in Chapter 8, for a single piezoelectric plate. The coupling of this third harmonic is around 4% i.e. $3^2 = 9$ times less than the first harmonic, a

phenomenon that is explained by the average energy ratio in the piezoelectric film for the two harmonics (see Chapter 7, equation [7.106]). This further confirms the coupling extracted. Moreover, such a coupling for harmonic 3 lets the possibility of an increase in frequency by exploiting odd harmonics of the piezoelectric film (we can expect 2% for harmonic 5).

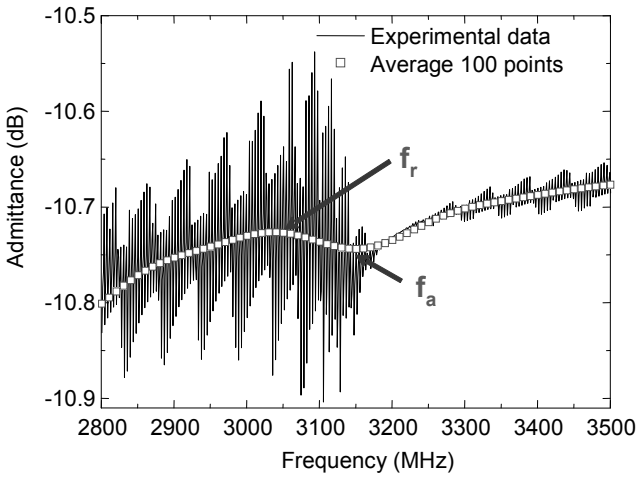

Figure 11.8. *Modulation of the third harmonic of the piezoelectric film by the acoustic cavity resonators*

11.3.1.2.2. Narrowband measurement

After the overview provided by broadband measurements, narrowband measurement is performed on a frequency sweep of 16 MHz covering four HBAR resonances. Simulations based on an admittance calculation exploiting Green's function of the medium considered [PIJ 08, PIJ 09, REI 03] enable correspondence of the experimental and simulated data, especially by adjusting key parameters such as acoustic and dielectric losses, and velocities (through the use of elastic constants) [PIJ 08].

In Figure 11.9, the real part of admittance is plotted in terms of frequency: the peaks observed are the HBAR resonances studied for which quality factors of around 45,000 are extracted at 1.95 GHz, i.e. $Q.f = 8.8\ 10^{13}$ Hz. This results in perfect coherence with other results obtained based on an alternative resonator manufacturing technology that is more rudimentary than the Smart Cut™ method used here [GAC 08].

The reader can see the presence of two sets of peaks with different amplitudes and spectral distances.

It is in fact the harmonics of the two shear waves coupled in the LNO: the frequency-distribution deviation between the two waves comes from the difference in their phase velocities (slow and fast shear) and amplitude is dependant on the coupling of each wave.

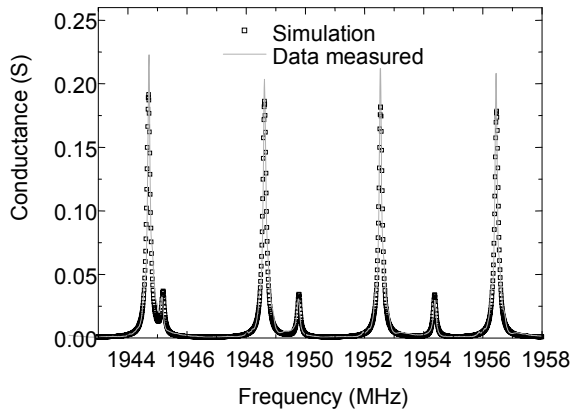

Figure 11.9. *Comparison of resonances between experimental and simulated data, conductance versus frequency*

11.3.2. *Validation of parameter extractions: LNO on HBAR/FBAR Si*

This second HBAR example corresponds to the relation of an X-cut LNO substrate on a silicon substrate (100). The goal of this experiment is to compare the HBAR results with the FBAR results coming from a similar structure. By deep etching silicon, we get a FBAR with a piezoelectric stack, which is the same as that in the HBAR tested before [PIJ 09].

11.3.2.1. *First stage: HBAR manufacturing*

The first stages of implementation concern the bonding of a lithium substrate on a silicon plate followed by its thinning.

HBAR is thus obtained by successively performing:

– an AlCu deposit on the X-cut LNO substrate: this will be the bottom HBAR electrode after the layer transfer;

– an SiO_2 deposit on this same substrate as well as on a "B" silicon substrate, the two faces of which are polished;

– direct bonding of the two wafers;

– thinning of the LNO substrate by the back side, first roughly to a thickness of about 50 µm;

– the application of a CMP type process in order to reduce the LNO thickness to <10 µm. Thus we get a LNO film ranging from 4–8 µm in thickness;

– an aluminum deposit followed by photolithography in order to pattern the resonators.

The stack thus created constitutes an HBAR, the piezoelectric transducer of which is successively composed of AlCu, X-cut LNO and aluminum. Narrowband measurements are not shown – on one hand because of quality factors that are too weak, and on the other hand because of the goal of the experiment: broadband measurements and the extraction of HBAR then FBAR electromechanical coupling coefficients.

Thus, from Figure 11.10, the frequencies of resonance and antiresonance are extracted from the envelope relative to the single-crystal piezoelectric film. The k_t^2 coupling extracted is evaluated as being somewhere around 40%, very close to the theoretical coupling of LNO for this cut.

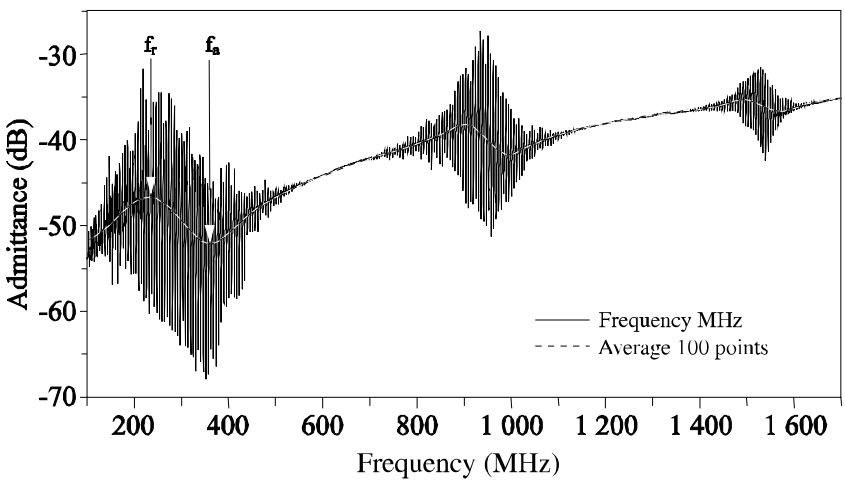

Figure 11.10. *Broadband spectrum of the HBAR response showing the first three modulated harmonics of the transferred and thinned piezoelectric film*

11.3.2.2. *Second stage: FBAR*

After HBAR RF characterizations, the additional steps are performed on the same stack in order to obtain the FBAR, i.e.:

– photolithography on the rear face with a front side/back side alignment in order to correctly position the membranes with respect to the top electrodes delimiting the resonators;

– deep etching following the Bosch process, which alternates SF_6 anisotropic etching cycles and C_4F_8 passivation. The 550 µm of the silicon substrate is thus removed; the SiO_2 film stopping the etching.

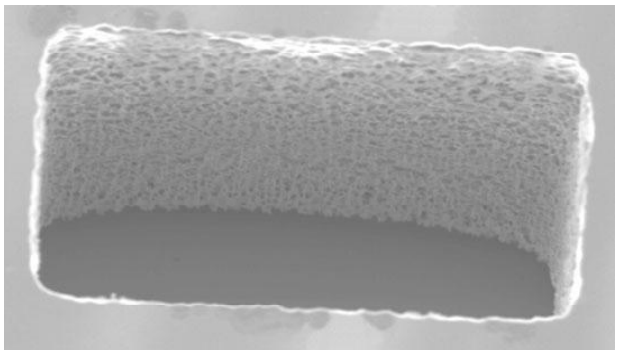

Figure 11.11. *Image obtained by scanning electron microscopy of the deep etching of silicon from the back side*

The final FBAR structure is thus obtained: SiO_2 (400 nm)/AlCu (120 nm)/ LNO (4–8 µm)/Al (200 nm). Figure 11.11 is a view of the back side opening obtained by scanning electron microscopy. Relatively straight, though slightly porous, grooves are observed, the cause probably being linked to insufficient groove passivation stages. Nevertheless, the membranes obtained do not break and the RF tests can be carried out under the proper conditions.

On broadband measurements, shown in Figure 11.12, we find the three resonances of the piezoelectric film present in the form of envelopes in the case of HBAR (see Figure 11.11). These resonances correspond to FBAR harmonics 1, 3 and 5. Frequencies of resonance and antiresonance do not change for the first harmonic: the electromechanical coupling coefficient of the single crystal film of LNO is directly measured so that $k_t^2 = 43\%$. The HBAR and FBAR results correspond with each other, enabling us to justify the previously detailed HBAR approach for first-approximation extraction of electromechanical couplings of piezoelectric films.

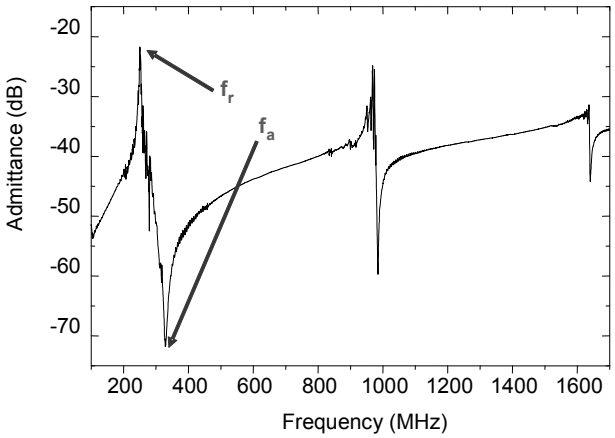

Figure 11.12. *First three FBAR resonances and antiresonances; k_t^2 electromechanical coupling extracted is 43%, close to the 40% evaluated after extracting HBAR measurements*

This study on FBARs is taken further in an article [PIJ 09] dealing with the problem of the limited quality factor observed on these FBARs.

11.4. Conclusions about HBAR

HBARs are resonators that are, at first sight, difficult to exploit because of the strong density of resonance peaks presented by their spectrum. Yet, they can turn out to be perfectly adapted for oscillator stabilization applications for the development of ultra-stable frequency sources. The quality factor frequency product can reach 10^{14} and then exceed that of FBAR or SMR technologies by more than one order of magnitude, naturally improving the frequency stability of the oscillators thus stabilized.

In addition, it is possible to extract the electromechanical coupling coefficient k_t^2 from the envelope corresponding to the response of the piezoelectric film. Though limited in precision, this technique is very useful for evaluating the adequacy of a piezoelectric thin film for RF signal processing applications by passive components.

Finally, to the extent that the spectral density of these resonators is measured and we are shown to be capable of accurately adjusting the resonance frequency, we can exploit them as elements of wireless and batteryless measurement systems, instead of surface elastic wave resonators. We can therefore draw part of their strong

coefficients of quality to improve their operational characteristics [MAS 07, MAS 09].

11.5. Bibliography

[GAC 08] GACHON D., COURJON E., MARTIN G., GAUTHIER-MANUEL L., JEANNOT J.-C., DANIAU W., BALLANDRAS S., "Fabrication of high, frequency bulk acoustic wave resonator using thinned single−crystal lithium niobate layers", *Ferroelectrics*, vol. 362, n° 1, p. 30-40, 2008.

[HUA 74] HUANG H.C., KNOX J.D., TURSKI Z., WARGO R., HANAK J.J., "Fabrication of submicron $LiNbO_3$ transducers for microwave acousitc (bulk) delay lines", *Applied Physics Letters*, vol. 24, 109, 1974.

[LAK 93] LAKIN K.M., KLINE G.R., MCCARRON K.T., "High-Q microwave acoustic resonators and filters", *IEEE Transactions on Microwave Theory and Techniques*, vol. 41, n° 12, p. 2139-2146, 1993.

[MAS 07] MASSON J., ARTIEDA A., MARTIN G., BOUDOT R., GRUSON Y., BELGACEM B., CHOMMELOUX L., MURALT P., BALLANDRAS S., "On the dispersive behaviour of AlN/Si High Overtone Bulk Acoustic Resonators", *Proceeding of the Joint EFTF-IFCS (TimeNav 07)*, Geneva, 2007.

[MAS 09] MASSON J., STEICHEN W., FAGOT-REVURAT L., ARTIEDA A., MURALT P., BALLANDRAS S., "Hybrid resonant structures for wireless sensor applications", *Proceeding of the joint IEEE IFCS – EFTF*, Besançon, 2009.

[MOU 08] MOULET J.S., PIJOLAT M., DECHAMP J., MAZEN F., TAUZIN A., RIEUTORD F., REINHARDT A., DEFAŸ E., DEGUET C., GHYSELEN B., CLAVELIER L., AÏD M., BALLANDRAS S., MAZURÉ C., "High piezoelectric properties in $LiNbO_3$ transferred layer by the Smart Cut™ technology for ultra wide band BAW filter applications", *IEEE IEDM*, 2008.

[PIJ 08] PIJOLAT M., MOULET J.S., REINHARDT A., DEFAŸ E., DEGUET C., GACHON D., GHYSELEN B., AÏD M., BALLANDRAS S., *IEEE Ultrasonics Symposium*, 201, 2008.

[PIJ 09] PIJOLAT M., LOUBRIAT S., QUESTE S., MERCIER D., REINHARDT A., DEFAŸ E., DEGUET C., CLAVELIER L., MORICEAU H., AÏD M., BALLANDRAS S., *Applied Physics Letters*, 95, 18, 182106, 2009.

[REI 03] REINHARDT A., PASTUREAUD TH., LAUDE V., BALLANDRAS S., *Journal of Applied Physics*, 94, 10, 6923, 2003.

[RUB 09] RUBY R., "Future Extensions of FBAR Technology", in "WSE: advanced BAW-enabled wireless transceivers: from devices to system architecture", *IEEE Radio Frequency Integrated Circuits Symposium, RFIC 2009*, 7-9 June 2009.

[UCH 73] UCHIDA N., FUKUNISHI S., SAITO S., "Performance of single-crystal $LiNbO_3$, transducers operating above l GHz", *IEEE Transaction on Sonics and Ultrasonics*, SU20, 3, p. 285-287, 1973.

Chapter 12

Electrostrictive Resonators

12.1. Introduction

In this chapter, we will deal mainly with the case of acoustic resonators that use or undergo the electrostrictive phenomenon. The latter corresponds to a mechanical strain that depends on the square of the electric field or displacement. It is therefore a quadratic phenomenon that enables us to control coupling properties by a continuous electric field, as we will explain. This phenomenon is also used for actuators to eliminate the hysteresis phenomenon observed in piezoelectric materials, such as PbZrTiO3 (PZT). The price we pay is the continuous application of a voltage to the terminals of the electrostrictive material to emulate a piezoelectric effect.

After a state-of-the-art rapid survey of devices using this quadratic effect, we will go into the details of the thermodynamic model and the devices referring to BaSrTiO3 (BST)- or SrTiO3 (STO)-type paraelectric perovskite resonators that today constitute most of the research on the subject. We will then close this chapter with the behavior of AlN, a permanent piezoelectric (even pyroelectric), when under a continuous electric field. The nonlinear phenomenon appears here and dealing with this situation enables us to suggest a few applications. It also helps us to properly understand the phenomenological development that underlies this entire book.

Chapter written by Alexandre VOLATIER, Brice IVIRA, Christophe ZINCK, Nizar BEN HASSINE and Emmanuel DEFAŸ.

12.2. State of the art

12.2.1. *Introduction*

Technological research in the domain of thin-film electrostrictive resonators is very active today. This domain is not as accomplished as that of piezoelectric resonators because the first results only appeared in the literature at the beginning of the 2000s. Scientific articles relating to thin-film electrostrictive resonators are good to follow because each advancement is notable: first resonances yielded, first modeling, first acoustic insulation, first adapted Bragg mirror, comparison of materials (all of the perovskite type), first coupling greater than that of AlN (7%), electric field-change in antiresonance frequency, and maximum quality factor discussion. This last point is the ultimate step for convincing the majority of the scientific community of the value of this alternative approach. These results are now imminent.

In this section we will go into the details of the state of the art of electrostrictive resonators. From this domain, we entirely exclude ferroelectric phase resonators, such as PZT. Although PZT could be considered an electrostrictive material with a spontaneous polarization, the presence of domain walls is unacceptable with regard to the possibility of producing a resonator with low acoustic losses. It is admitted in the literature that these domain walls induce acoustic losses by generating shear waves, hence the low intrinsic quality factor of PZT [MUR 05]. Single crystal growth is, however, a serious way to obtain PZT, the nature of the domains of which could be much better mastered, thus reducing their negative effect on the quality factor.

There are a few examples of electrostrictive resonators in the literature. It seems that Morito *et al.*, in 2003, were the first to specifically study electromechanical resonators induced by a continuous field biasing a STO metal-insulator-metal or MIM capacitor [MOR 03]. In 2004, Tappe *et al.* presented similar observations on a BST MIM capacitor with a more acoustic approach than Morito, but considering a constant induced piezoelectric constant, thus neglecting the frequency change with the constant electric field applied [TAP 04].

In 2006, Gevorgian *et al.* analyzed the change in frequency of resonance on STO- and BST-based electrostrictive stacks [GEV 06]. The acoustic model developed identify the various modes of resonance and prove that the frequency for which dielectric losses are maximal corresponds to an electrostrictive effect, and more specifically to the resonance frequency. Despite this, there is no information about the antiresonance frequency for which it would have been necessary to follow the real part of admittance. Although they demonstrate the concept, experimental results of all these works show many spurious parasitic resonances as acoustic

insulation is not implemented. In 2007, during the IEEE Microwave Symposium conference, Zhu *et al.* presented a free-standing membrane using BST [ZHU 07]. The spurious resonances were then suppressed and the k_t^2 extracted reached 7% (under 25 V bias), which is equivalent to AlN. Their model predicted a quality factor of 1,000 for BST after extraction of the influence of electrodes. This result seems to prove that paraelectric materials, devoid of domain walls, present acoustic losses that are much lower than perovskites in the ferroelectric phase. In this article, there are unfortunately no exploitable data on change in frequencies of resonance and antiresonance with applied voltage.

In 2008, Vendik suggested an attractive acoustic model taking the antiresonance frequency into consideration independently of the electromechanical coupling. The resonators developed are made of BST and $BaTiO_3$ (BTO). This approach is in very good agreement with experience [VEN 08]. Still in the same year, Volatier *et al.* presented the first STO resonator that was acoustically insulated from the substrate through the use of an acoustic W/SiO_2 Bragg mirror [VOL 08]. The main difficulty with this approach is mastering the thermal budget that is mandatory for STO crystallization, but which in turn tends to destroy the Bragg mirror. It has been proven that an annealing temperature of 450°C enabled STO to crystallize while preserving the Bragg mirror. The maximum coupling is 3% at 30 V and the maximum change in the frequency of resonance reaches 1.6% towards the low frequencies. Due to the material not being optimized, the quality factor is only about 50, which is not enough for radio frequency (RF) filtering applications. Improvement in intrinsic properties of the material is required. One of the most advanced pieces of research in the domain is that reported in Nöth's PhD work at EPFL held in 2009 [NÖT 09]. The basic structure on which he worked is a BST resonator on membrane. Maximum coupling is 4%, the best quality factor reaches 200 and the changes in resonance and antiresonance frequencies reach -2.4% and -0.6%, respectively. More recently, Gevorgian *et al.* showed that hot sputtered BST can reach quality factor as high as 350, which is very promising for the field [GEV 10].

In view of these results considered as state of the art in 2010, the progress that is still necessary to overtake typical AlN results is measured (k_t^2 AlN = 7%, Q AlN = 2,000). There are still many paths available for improving these values. The possibility of adding commutation and frequency adjustment functions controlled by voltage at existing resonators has aroused vibrant interest.

12.2.2. *Formalism of the electrostrictive resonator*

The implementation of this formalism enables us to construct an acoustic model from the parameters of the electrostrictive material. We will first deal with the case

of the electrostrictive film alone. We will therefore speak about the real case in which we have to take the electrodes and the acoustic Bragg mirror into consideration. This mirror is used to confine acoustic energy in the resonator. This way of confining energy is similar to what we saw in the case of piezoelectric resonators (see Chapter 7).

12.2.2.1. *Acoustic model of the electrostrictive film alone*

To build this model, we rely on Figure 12.1. The acoustic influence of the electrodes is neglected. In other words, we assume that their acoustic impedance is negligible as it involves an interface with air. However, the electric role of the electrodes is retained. The electrostrictive film is t thick. Acoustic propagation of the longitudinal wave takes place perpendicularly to the planes of the films (along the z axis). In other words, it is the thickness mode that is considered. P_{DC} and E_{DC} are in the direction of positive z. The surface of the in-plane resonator is A.

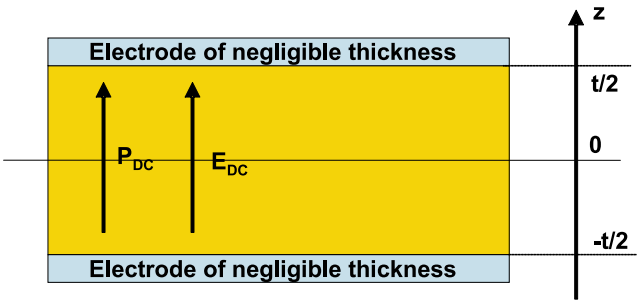

Figure 12.1. *Scheme of the structure modeled only considering the electrostrictive material*

We will calculate the electric impedance of this electrostrictive film in order to determine the analytic expressions of the resonance and antiresonance frequencies in terms of E_{DC}. We must note that we will consider a film without dielectric or acoustic losses, which prevents from looking at the quality factor. This analysis allows to discuss electromechanical coupling as well as the shift in characteristic frequencies in terms of the DC voltage applied.

We saw that the acoustic propagation equation is of the following form, with u the mechanical displacement so that $S = \partial u/\partial z$:

$$\rho \frac{\partial^2 u}{\partial t^2} = \frac{\partial T}{\partial z} \qquad [12.1]$$

Taking the piezoelectric formalism *(S, D)* (see Chapter 7), we get:

$$\rho \frac{\partial^2 u}{\partial t^2} = \frac{\partial \left(c^D S - hD \right)}{\partial z} = c^D \frac{\partial S}{\partial z} = c^D \frac{\partial^2 u}{\partial z^2} \qquad [12.2]$$

The derivative of D in relation to z is zero. As there are no free charges in the electrostrictive dielectric (ideal case), divergence from D must be zero according to the Maxwell equation. Since the only non-zero contribution of D is along z, we have:

$$divD = \partial D/\partial z = 0 \;\; => \;\; D = D_0 e^{jwt} \qquad [12.3]$$

where D_0 is a constant. We then make the hypothesis that u takes the following form:

$$u = e^{jwt} \left(A \sin kz + B \cos kz \right) \qquad [12.4]$$

where k is the wave vector. Inserting equation [12.4] into the propagation equation (equation [12.2]) induces the formula for k:

$$k = \frac{w}{v^D} = \frac{w}{\sqrt{\frac{c^D}{\rho}}} \qquad [12.5]$$

where v^D is the acoustic velocity of the wave considered at constant D.

The boundary conditions are used to determine A and B. Indeed, the mechanical stresses vanish at the interfaces. Therefore, in $z = t/2$ and $z = -t/2$, we get:

$$\begin{aligned} T\left(\frac{t}{2}\right) &= 0 = c^D S - hD = c^D \frac{\partial u}{\partial z}\left(\frac{t}{2}\right) - hD \\ T\left(-\frac{t}{2}\right) &= 0 = c^D \frac{\partial u}{\partial z}\left(-\frac{t}{2}\right) - hD \end{aligned} \qquad [12.6]$$

Thus:

$$\begin{aligned} A &= \frac{hD_0}{kc^D} \frac{1}{\cos\left(kt/2\right)} \\ B &= 0 \end{aligned} \qquad [12.7]$$

Including this expression in equation [12.4], u and S take the following forms:

$$u = Ae^{jwt}\sin kz = \frac{hD}{kc^D\cos(kt/2)}\sin kz$$
$$S = \frac{hD}{c^D\cos(kt/2)}\cos kz \qquad [12.8]$$

Electric impedance Z_e is the ratio between voltage V and the current I generated by the electrostrictive film. To simplify, we will take a positive voltage for this calculation, so that V is defined as $E = +gradV$.

V is calculated by integrating E along z:

$$V = \int_{-t/2}^{t/2} Edz = \int_{-t/2}^{t/2}\left(\beta^S D - hS\right)dz = \beta^S Dt - \frac{h^2 D}{c^D\cos(kt/2)}2\frac{1}{k}\sin(kt/2) \qquad [12.9]$$

Then we get:

$$V = \beta^S Dt\left(1 - \frac{h^2}{c^D\beta^S\cos(kt/2)}2\frac{1}{kt}\sin(kt/2)\right)$$
$$= \beta^S Dt\left(1 - \frac{h^2}{c^D\beta^S}\frac{\tan(kt/2)}{kt/2}\right) = \beta^S Dt\left(1 - k_t^2\frac{\tan(kt/2)}{kt/2}\right) \qquad [12.10]$$

The electromechanical conversion coefficient k_t^2 is $h^2/c^D\beta^S$.

Current I is the change in charge Q versus time across the dielectric:

$$I = \frac{dQ}{dt} = A\frac{dD}{dt} = jwAD \qquad [12.11]$$

As $Z = V/I$, the expression of Z is:

$$Z = \frac{\beta^S t}{jwA}\left(1 - k_t^2\frac{\tan(kt/2)}{kt/2}\right) = \frac{1}{jC_0 w}\left(1 - k_t^2\frac{\tan(kt/2)}{kt/2}\right) \qquad [12.12]$$

where C_0 represents the blocked capacitance (at constant S) of the resonator defined by the formula of the planar capacitor, in which the dielectric constant at fixed displacement is involved:

$$C_0 = \frac{A}{\beta^S t} = \frac{\varepsilon^S A}{t} \qquad [12.13]$$

The antiresonance frequency is defined as the frequency for which impedance is infinite. In this model, we assumed that the resonator is ideal, and therefore lossless. The definition of the characteristic frequencies is therefore not ambiguous. As soon as acoustic losses are introduced (often through the quality factor, see Chapter 7), it is important to clearly determine the conditions for which the frequencies are defined. We choose to follow the Standards on Piezoelectricity, that recommend using frequencies of resonance f_s and antiresonance f_p, which are defined as being, respectively, the frequencies for which the real parts of admittance and impedance are maximal [IEE 87].

For f_p, we get this condition when the tangent of equation [12.12] tends towards infinity, which happens for the first mode of resonance when:

$$\frac{kt}{2} = \frac{\pi}{2} \qquad [12.14]$$

$$kt = \frac{2\pi f_p t}{\sqrt{\frac{c^D}{\rho}}} = \pi \quad => \quad f_p = \frac{1}{2t}\sqrt{\frac{c^D}{\rho}} \qquad [12.15]$$

This expression is an exact solution. Unfortunately, the exact analytical solution for resonance does not exist because it involves solving the following transcendental equation originating from the cancellation of impedance at the resonance frequency (equation [12.12]):

$$kt/2 = k_t^2 \tan\left(kt/2\right) \qquad [12.16]$$

It is very important to see that coupling can be experimentally calculated from frequencies of resonance and antiresonance, from an exact formula that we will get by combining equation [12.15] and equation [12.16], which gives:

$$k_t^2 = \frac{\pi}{2}\frac{f_s}{f_p}\frac{1}{\tan\left(\frac{\pi}{2}\frac{f_s}{f_p}\right)} \qquad [12.17]$$

In the case of resonators that are weakly coupled (a few per cent), it is possible to give an approximate expression of f_s. According to equation [12.17], if coupling is low, the difference between f_p and f_s is low. Therefore $k_t/2$ is equal to almost $\pi/2$ at resonance (resonance takes place before antiresonance). We can therefore make an approximation near the tangent pole just before $\pi/2$ which gives:

$$\tan\frac{kt}{2} \approx \frac{4kt}{\pi^2 - (kt)^2} \qquad [12.18]$$

By inserting this approximation into equation [12.16], we get:

$$f_s = f_p\sqrt{1 - \frac{8k_t^2}{\pi^2}} \qquad [12.19]$$

This approximation becomes too inaccurate for coupling of a few per cent. It is generally more secure to use the exact definitions of f_p and k_t.

This analytical analysis, which applies to piezoelectric resonators, can be used for the electrostrictive case by replacing the piezoelectric coefficient h by its electrostrictive counterpart, as discussed in Chapter 8 and more specifically in equation [8.30]. We also give the approximate value for the resonance frequency for low couplings:

$$\begin{aligned} f_p &= \frac{1}{2t}\sqrt{\frac{c_0^D + M\varepsilon^2 E_{dc}^2}{\rho}} \\ f_s &= \frac{1}{2t}\sqrt{\left(\frac{c_0^D + M\varepsilon^2 E_{dc}^2}{\rho}\right)\left(1 - \frac{32G^2\varepsilon^3 E_{dc}^2}{c_0^D \pi^2}\right)} \end{aligned} \qquad [12.20]$$

12.2.2.2. *Model of the electrostrictive film charged by the electrodes, Bragg mirror and substrate*

In the case of a real thin film structure, the electrodes play an important role in the values of the characteristic frequencies of the resonator and also in the value of electromechanical coupling, as we saw in the case of the piezoelectric resonator.

Acoustic insulation is influenced by electrodes, the Bragg mirror and the substrate. Modeling the behaviors of the resonator requires to take these different contributions into consideration. To do this, we proceed in a similar way to the film alone by calculating the electric impedance of the charged resonator. This calculation was explained in the section on piezoelectric materials and gives the following result (slightly adapted here):

$$Z_{charged} = \frac{1}{jC_0 w}\left(1 - k_t^2 \frac{\tan\varphi}{\varphi} \frac{\left(z_{top} + z_{bot}\right)\cos^2\varphi + j\sin 2\varphi}{\left(z_{top} + z_{bot}\right)\cos 2\varphi + j\left(z_{top} z_{bot} + 1\right)\sin 2\varphi}\right)$$

[12.21]

with $\varphi = kt/2$, k and t, the wave vector and the thickness of the electrostrictive film, respectively, k_t^2 the stiffened electromechanical coupling $h^2/c^D\beta^S$, z_{top} and z_{bot} the normalized acoustic impedances of the mechanical loads on both sides of the piezoelectric film.

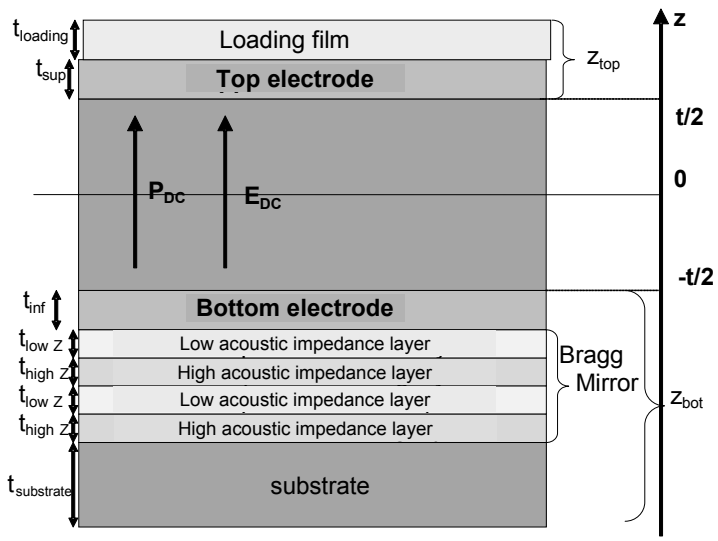

Figure 12.2. *Description and notation of an acoustically-loaded electrostrictive resonator with electrodes and Bragg mirror*

These impedances, z_{top} and z_{bot}, are normalized by the acoustic impedance of the electrostrictive material, $Z_e^0 = \sqrt{\rho_e c^D}$, so that:

$$z_{top} = \frac{Z_{top}}{Z_e^0} \qquad z_{bot} = \frac{Z_{bot}}{Z_e^0} \qquad [12.22]$$

where Z_{top} and Z_{bot} are the acoustic impedances resulting from the layers above and below the electrostrictive material, respectively, as shown in Figure12.2. These impedances are not solely a combination of impedances of materials making up the stack because they include phase information. Indeed, acoustic propagation takes place across the entire structure, like a line of electromagnetic propagation. For a given wave, passing from one material to another one the acoustic and electric transfer relations are respected. If the electrically inactive layers above and below the electrostrictive film are considered alone, these transfer relations at the interfaces are purely mechanical and therefore boil down to the equality of normal stresses on one hand and displacement of particles on the other. As acoustic impedance is defined as the ratio between the mechanical stress (negatively counted) and the velocity of displacement, the transfer relations can be translated as the equality of acoustic impedances at the level of the interface between two films in contact. We will now explain the acoustic impedance of an electrically-inactive mechanical film included in a complex stack.

12.2.2.3. *Acoustic impedance of an electrically-inactive mechanical film*

Let us focus on the case of an electrically-inactive acoustic film for which the stress and strain of the particles are considered in accordance with Figure 12.3.

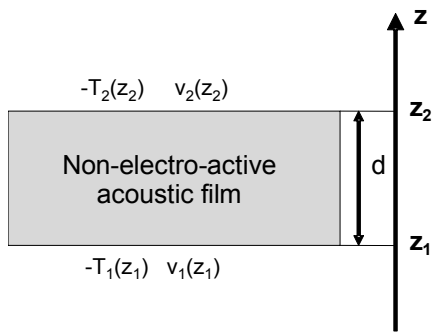

Figure 12.3. *Diagram and notation of a non-electro-active acoustic film*

As in the case of an electro-active film, acoustic propagation induces a displacement u of the particles as follows: $u = e^{jwt}\left(Ae^{-jkz} + Be^{jkz}\right) = ae^{-jkz} + be^{jkz}$.

The e^{jwt} time term is placed into terms *a* and *b*. For the velocity of displacement *v*, this gives:

$$v = \frac{\partial u}{\partial t} = jw\left(ae^{-jkz} + be^{jkz}\right) \qquad [12.23]$$

with *c* being the mechanical stiffness coefficient for the propagation mode considered, stress *T* is defined as:

$$T = c\frac{\partial u}{\partial z} = jkc\left(-ae^{-jkz} + be^{jkz}\right) \qquad [12.24]$$

writing *T* and *v* in z_1 and z_2 and combining the equations, we get:

$$-T_1 = Z^0\left(\frac{v_1}{j\tan kd} - \frac{v_2}{j\sin kd}\right) \text{ and } -T_2 = Z^0\left(\frac{v_1}{j\sin kd} - \frac{v_2}{j\tan kd}\right) \qquad [12.25]$$

By definition, $Z_2 = -T_2 / v_2$ and $Z_1 = T_1 / v_1$. Stress is counted negatively in Z_2 because it is the wave compression that is considered, therefore the stress directed towards the material. In equation [12.25], we divide $-T_1$ by v_1 and $-T_2$ by v_2. We then eliminate the ratio v_2/v_1 by combining the two equations obtained, which finally gives:

$$Z_1 = Z^0\left(\frac{Z_2\cos kd + jZ^0\sin kd}{Z^0\cos kd + jZ_2\sin kd}\right) \qquad [12.26]$$

If we want to generalize this formula in the case of a stack of three materials $n-1$, n and $n+1$, we get:

$$Z_n = Z_n^{\,0}\left(\frac{Z_{n-1}\cos kd + jZ_n^{\,0}\sin kd}{Z_n^{\,0}\cos kd + jZ_{n-1}\sin kd}\right) \qquad [12.27]$$

where:

– $Z_n^{\,0}$ is the impedance of the material making up the film *n* (therefore $Z_n^{\,0} = \sqrt{\rho_n c_n}$);

– Z_{n-1} is the impedance of the film $n-1$ supposedly known at the level of the interface between films $n-1$ and *n*;

– Z_n is the impedance of film n at the level of the interface between films n and $n+1$;

– d is the thickness of material n;

– k is the wave vector in material n;

– kd represents the wave phase considered in the material n.

For this calculation, we always start from an interface with air and step-by-step, we reach the electroactive material from the top (normalized impedance, z_{top}) and by the bottom (normalized impedance, z_{bot}). Thus, the acoustic impedance of the entire stack can be determined.

12.3. Experimental implementations

We will now implement these models on three experimental devices using an electrostrictive material: a resonator without acoustic insulation, another on a Bragg mirror and the last one on a released membrane.

12.3.1. *70/30 BST resonator without acoustic insulation*

12.3.1.1. *Structure*

For this first example, the device is simply a MIM capacitor like the one in Figure 12.4. The implementation is simplified to the maximum by structuring only the last film corresponding to the top electrode. The RF test for measuring resonances is therefore carried out by placing the GSG (ground-signal-ground) RF probes directly on the structure. Tip S is on a central ring with a diameter of 50 µm whereas the G probes are placed on the circumference, the surface area of which is more than 1,000 times greater than that of the central ring. The equivalent diagram is therefore two MIM capacitors in series. One corresponds to the BST between the central ring and the lower electrode, whereas the other is made up of the BST between the circumference and the bottom electrode. The potential measured at the terminals of the tips between G and S therefore corresponds to < 0.1% of that applied between the top electrode of the central ring and the buried bottom electrode. This configuration is therefore very close to the one which has a direct contact with the bottom electrode and enables us to avoid etching the BST. This is the simpler structure for gauging the coupling potential of an electroactive film.

We will see, however, that this structure only gives a rough estimate of the intrinsic quality factor of the electrostrictive film because of the significant influence of the substrate on the electric response of the resonator.

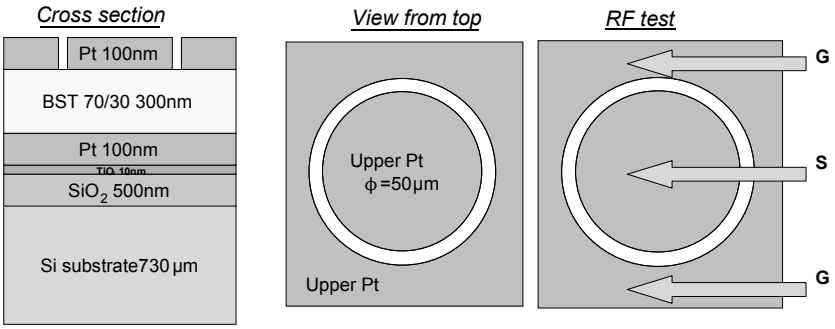

Figure 12.4. *Configuration of the acoustically uninsulated BST electrostrictive resonators*

12.3.1.2. *Technology*

In this example, silicon 200 mm in diameter and 730 µm thick is thermally oxidized in order to form 500 nm of SiO_2. A 5 nm Ti film is then deposited by sputtering, then stabilized by oxidization at 700°C for three minutes (rapid thermal annealing by halogen lamps). A 100 nm Pt film is deposited at 450°C using sputtering. 70/30 BST is deposited using the sol-gel technique. The composition Ba/Sr = 70/30 is chosen because its Curie temperature is close to room temperature, which induces a strong dielectric constant and a strong change in this constant in terms of the continuous voltage that will be applied. The counterpart is an important influence of temperature. BST thickness is 300 nm, obtained after the deposition of eight successive films of around 40 nm each. Each coating is followed by a calcination annealing at 400°C for 10 minutes and crystallization at 700°C for two minutes under air. A top Pt electrode is deposited, then structured by ion milling in accordance with the top view in Figure 12.4. A final polishing stage of the back of the substrate is carried out to improve resonances in the substrate. Although these resonances are not desired most of the time, they can enable to characterize the properties of the electroactive film that generates these waves (structure for a High overtone Bulk Acoustic wave Resonator, or HBAR). Polishing is carried out by a chemico-mechanical process.

12.3.1.3. *RF measurements and discussion*

Figure 12.5 shows the impedance module measured on the BST resonator for different continuous voltages applied during measurement. At 0 V, the change in impedance conforms to that of a 1/Cw capacitance. A very slight inflection is noticed around 3.5 GHz, a sign of low piezoelectric activity in the BST without continuous voltage. Although the BST composition is supposed to be paraelectric, the residual stresses in BST can introduce a change in Curie temperature as we saw

in Chapter 3. It is therefore likely to have a weak piezoelectric phenomenon due to the ferroelectricity of BST.

This low piezoelectric activity is neglected in the model. When the bias voltage increases, two phenomena appear. The first is the very clear resonance followed by antiresonance, which is characteristic of any electromechanical coupling. The second phenomenon is the increase in out-of-resonance impedance, which is due to the BST dielectric constant sensitivity to the voltage. We also note an important "line width" on the high voltage curves. This is due to the presence of numerous parasites of the substrate, as we will see in more detail hereafter.

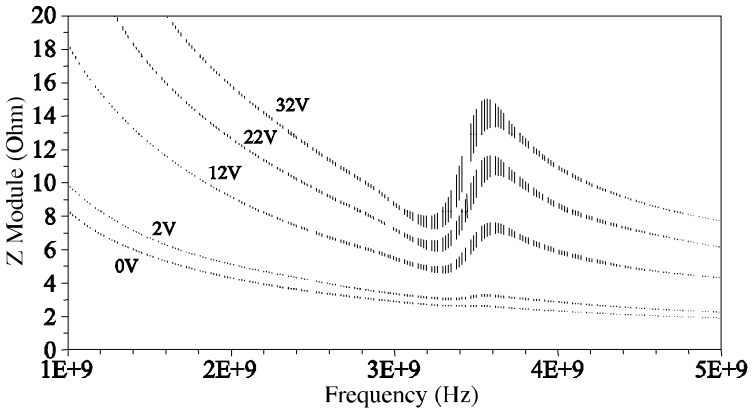

Figure 12.5. *Impedance module of the BST resonator in terms of frequency for different continuous voltages applied during the measurement*

To go further in the extraction of characteristic values of the resonator, it is more accurate to work on the real parts of impedance and admittance. Figure 12.6 shows the real parts of impedance and admittance for the BST resonator with a DC voltage of 32 V. The frequency range is reduced to between 3.2 and 3.6 GHz in order to produce tighter resonances corresponding to harmonics of high orders in the acoustic cavity (silicon substrate in this case). Actually, these 6 MHz-spaced resonances correspond to harmonics of order n of the thickness mode in the silicon based on the formula $nv_{Si}/2d$, with n integer, v_{Si} the acoustic velocity of the longitudinal mode in silicon and d silicon thickness.

We already discussed about these HBAR devices in Chapter 11. Here, however, the quality factor is much lower than in the case of optimized HBARs. Moreover, Figure 12.6 enables us to appreciate the difference in frequency between the maximum of the real parts of impedance and admittance corresponding, respectively, to the antiresonance and resonance frequencies of the complete

resonator. To extract the coupling coefficient, it is much more precise and complete to apply the model detailed above in the chapter on electrostrictive formalism and to find the characteristic values of the resonator (ε^S, k_t^2, c^D). Comparing the different voltages, we will thus be able to extract the characteristic values of BST that are parameters G, M and c_0^D.

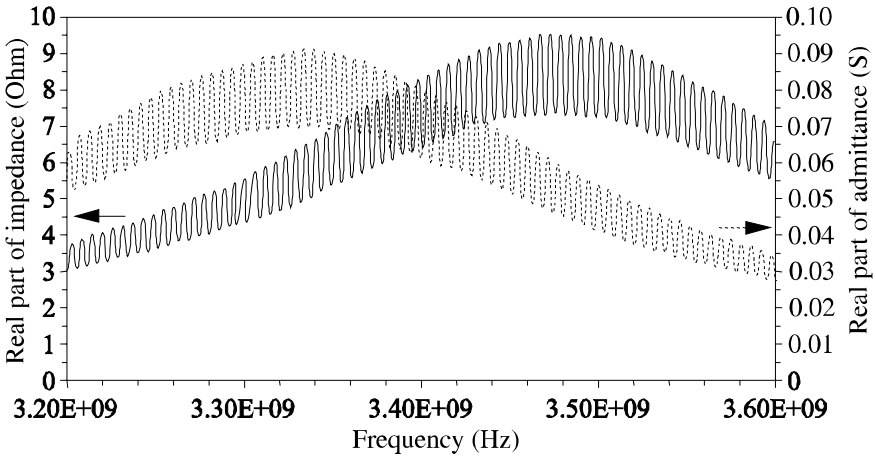

Figure 12.6. *Real parts of impedance and admittance of the BST resonator in terms of frequency for a direct current voltage of 32 V*

Figure 12.7 presents the experimental curves and those of the model for the real parts of admittance and impedance for two different continuous voltages: 32 V and 2 V. The model is based on the above use of impedance in series with a resistance that mainly corresponds to the resistivity of Pt electrodes. The order of magnitude of this resistance is around 1 Ω. The model is adjusted to the experimental curves by playing on the quality factors of silicon Q_{Si} and BST Q_{BST} and on the values of c^D, ε and k_t^2. The value of series resistance is also slightly adjusted between 0.9 and 1.2 Ω depending on the DC voltage.

We observe that the model explains, with remarkable precision, the behavior of this electrostrictive resonator in terms of the DC voltage applied, in accordance with what it is possible for a piezoelectric resonator. It is worth noting that the quality factor of silicon Q_{Si} can be extracted with the model. We get 750, which is quite modest compared to what we can get building our capacitor on an optimized double sided polished substrate. In this case, we can reach a value of 2000. It is worth noting that this HBAR configuration does not enable us to correctly extract Q_{BST}. The model only indicates a minimum value of Q_{BST} of 50.

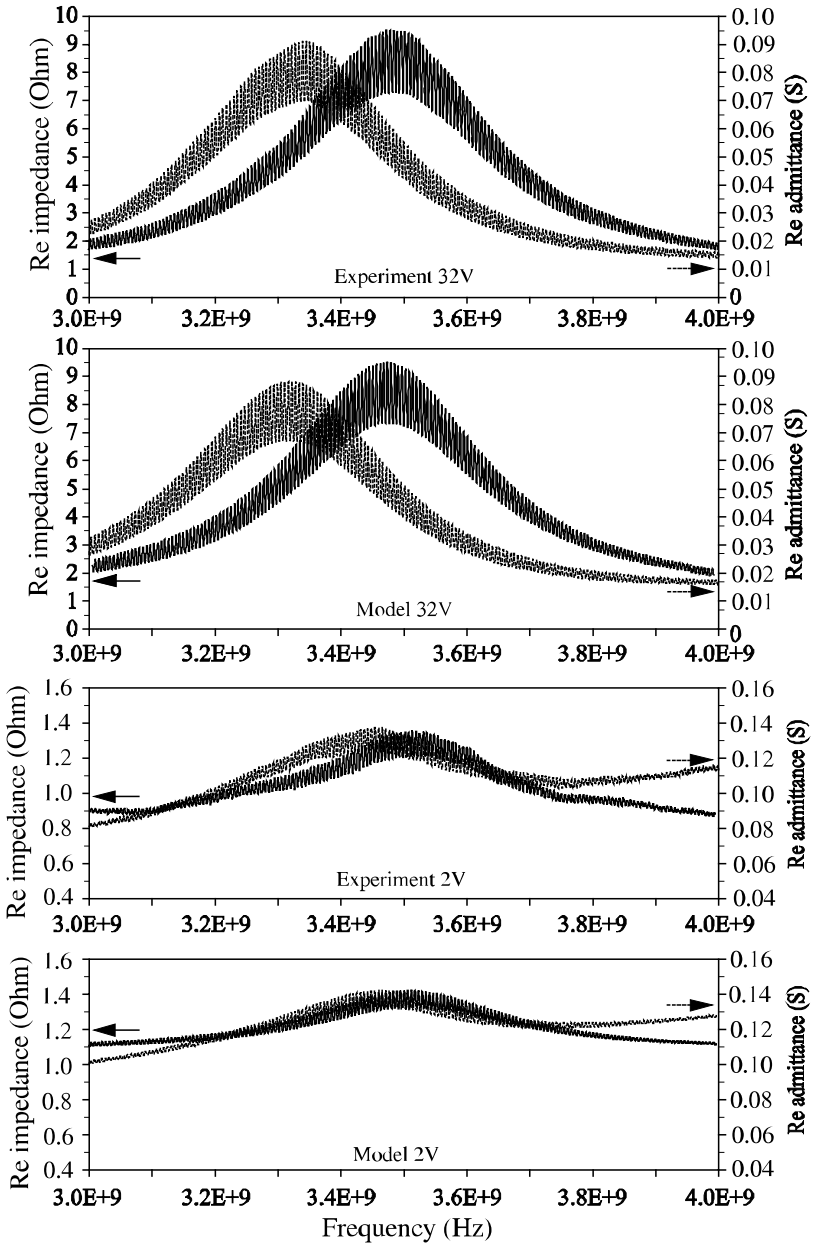

Figure 12.7. *Comparison of experimental curves and modeled curves of the real parts of admittance and impedance of the BST resonator for two DC voltages: 32 V (strong field) and 2 V (low field)*

The values of c^D, ε and k_t^2 extracted from the experimental curves from the impedance model are respectively plotted in Figures 12.8, 12.9 and 12.10. The curves of the adjusted electrostrictive model on these experimental curves are also plotted on these figures.

In the case of c^D (see Figure 12.8), a decrease due to the applied DC voltage is observed. This is the case for BST and STO in their paraelectric phase, but can be a hysteresis curve for PZT [ZIN 04] and BTO [VEN 08]. The fit of the electrostrictive model is not very accurate but it gives the correct trend. This imprecision comes from the fact that the curve of the real part of impedance is modulated by the tightened resonances due to the harmonics of the thickness mode of the substrate. In addition, as the effective quality factor of the curve is low (around 11), the maximum is not very sharp, which adds to the imprecision. The extracted values are $c_0^D = 1.52.10^{11}$ N/m² and $M = -8.10^{11}$ N.m²/C².

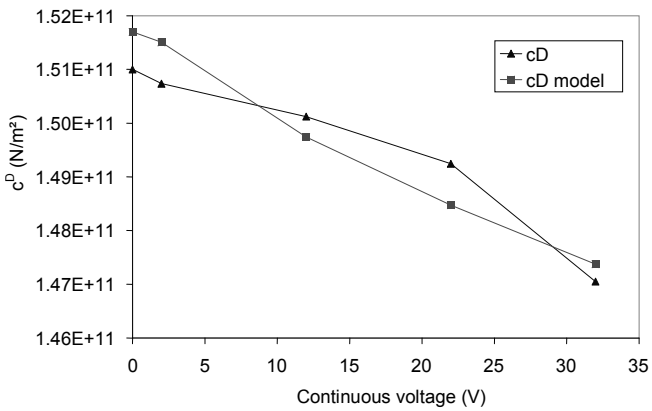

Figure 12.8. *c^D extracted from experimental data (triangles) from the charged impedance model and c^D extracted from the electrostrictive model (squares) after adjustment of the experimental values*

For ε, the decrease due to DC voltage is in accordance with the usual behavior of perovskites in the paraelectric phase. We will note a very large change in the value of ε, which moves from 320 to 80, for a DC voltage of 0 V and 32 V respectively. The corresponding relative change in ε is 75% for an electric field of 1.07 MV/cm. This change is the main driving force of the electrostrictive effect.

In this example, the experimental curve and the model are represented in Figure 12.9 with $\varepsilon_{max} = 320$ and $E_{1/2} = 3.5\ 10^7$ V/m. The small discrepancy observed at low voltage can be due to not taking the parasitic capacitors into consideration (a

delicate RF problem) or to the fact that the RF signal is not negligible compared to the DC electric field.

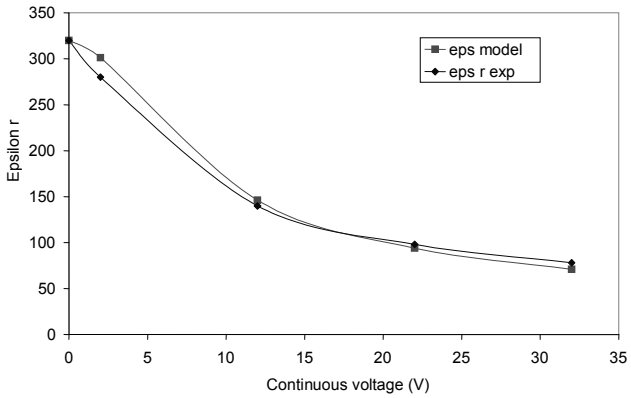

Figure 12.9. *ε extracted from experimental data (rhombuses) from the loaded impedance model and ε extracted from the LGD model (squares) after adjustment of the experimental values*

Finally, the correspondence between the model and experimentation for k_t^2 coupling presented Figure 12.10 is of good quality, which proves that the foremost effects in the model are taken into consideration. The curve seems to have two rising slopes according to DC voltage: a first one is quite high up to 12 V; then a second is much less marked. This behavior comes from the competition between the increase in the electric field and the decrease in the dielectric constant, as suggested by the model.

We will note that taking into consideration the change in stiffness is only responsible for 3% of the calculation of k_t^2. Everything else comes from the change of the dielectric constant with the electric field. The coefficient of electrostriction, G, extracted from the model reaches 2.8 x 10^{10} m/F.

We must notice that k_t^2 reaches 8.5%, which is about one third greater than AlN. Although this figure is encouraging, we must temper this value by not taking into consideration the BST quality factor and by the fact that the necessary electric field is of the order of 1 MV/cm, which is close to the breakdown field of BST.

These two observations highlight the paths we need to improve to make this electrostrictive solution a realistic alternative to broadband RF filters for telecoms applications.

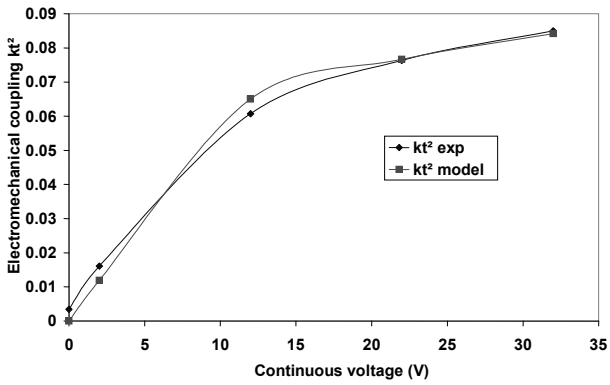

Figure 12.10. *k_t^2 extracted from experimental data (rhombuses) from the loaded impedance model and k_t^2 extracted from the electrostrictive model (squares) after adjustment of the experimental values*

This thermodynamic model uses a fit of the parameters over the experimental values. It is theoretically possible to do better by using the linear and nonlinear electrostriction coefficients coming from *ab initio* calculation, as suggested by Nöth in his thesis. The very nature of the material, however, like its degree of porosity, exact composition or stress level can greatly affect these coefficients. It is eventually more efficient to proceed to a fit of the model parameters. The first step before the prediction is to ensure the reproducibility of the material. This represents an indispensable task for confirming its capability to generate acoustic waves of very good quality. We must note that the quality required for an electroacoustic material is more drastic than for a dielectric material because the material must exhibit very good dielectric and mechanical properties at the same time. Using BST as a strong permittivity dielectric for decoupling capacitors or variables has been validated at the industrial level, but not yet for electrostrictive applications.

12.3.2. *STO resonator on Bragg mirror*

In the previous example, we discussed the results of a resonator not insulated from the substrate. Parasitic resonances induced by the substrate impede the use of these resonators in oscillators or filters. The implementation suggested here uses the principle of the Bragg mirror as acoustic insulation. The same model as before is used to take into consideration the stack of all the films in the acoustic behavior of the resonator. The main difficulty of this technological job is mastering the thermal budget supported by the Bragg mirror. Indeed, the electrostrictive material (here STO) requires crystallization annealing at 450°C, which can induce cracks in the

underlying films. Ion beam sputtering (IBS) deposition plays a dominant role here because it enables this low temperature crystallization of STO.

12.3.2.1. *Structure*

Figure 12.11 is a diagram of the implemented stack: Si (525 µm)/[Ti (20 nm)/W (610 nm)/SiO2 (710 nm)] x 2/Ti (40 nm)/Pt (140 nm)/STO (400 nm)/Pt (80 nm)/Ti (20 nm)/Au (100 nm) substrate.

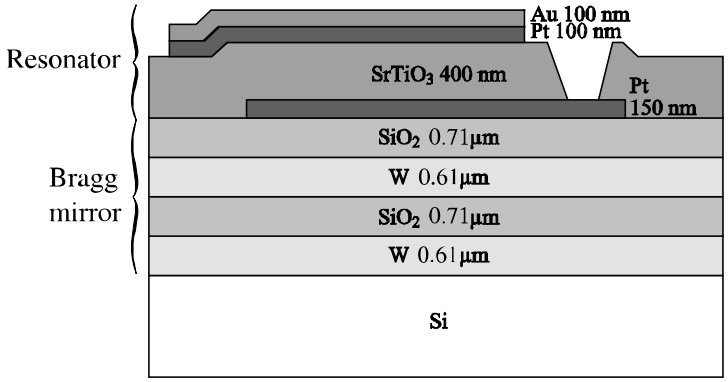

Figure 12.11. *Diagram of the stack of the electrostrictive resonator with a Bragg mirror [VOL 06]*

The Bragg mirror consists of a double stack of W (strong acoustic impedance)/SiO_2 (low acoustic impedance). Pt is kept in contact with STO because it improves its electrical characteristics. Gold is finally added in order to reduce contact resistance during RF tests. Ti films improve adhesion. After deposition, STO is air-annealed at 450°C, without deteriorating the Bragg mirror.

X-ray diffraction shows that the perovskite phase is alone and that the film does not exhibit any preferential orientation. The design is based on a one-port resonator with remote contacts. The active surface area is 30 x 80 µm². The measurements are performed using a vector network analyzer (HP8753E). As for BST HBAR, a DC voltage is added to the device during the test. The contribution of RF plots is extracted thanks to correction patterns (de-embedding).

12.3.2.2. *RF characterization and discussion*

Figure 12.12 represents the broadband impedance response of the STO resonator with and without DC voltage. No resonance is observed at 0 V, whereas with 20 V the impedance shape is characteristic of a resonance with electromechanical coupling. We can therefore imagine a switching function. The resonance frequency

is around 2.2 GHz for a target at 2.14 GHz. Thanks to the one-dimensional model, we know that this value corresponds to the half-wavelength-thickness mode resonance of the stack made up of STO with its electrodes (Pt and Pt/Au). The parasitic resonances induced by the substrate are not present here, which proves the efficiency of the Bragg mirror. We can also note a global increase in impedance under DC voltage because of the decrease in dielectric constant under electric field, as for BST. Finally, we see that the impedance module is of the order of a few Ω. To be around 50 Ω, it would be necessary to reduce the capacitor surface. Typically, a surface of 25 x 25 µm² would ensure 50 Ω at 2 GHz.

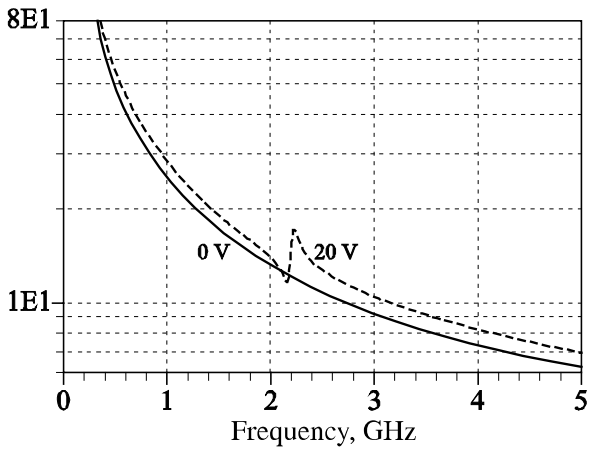

Figure 12.12. *Impedance module in terms of frequency with and without DC voltage of the STO resonator around the thickness mode of the stack (STO + electrodes)*

Figures 12.13a and 12.13b, respectively, show conductance and resistance of the resonator near principle resonance with a DC voltage varying between 0 and 30 V. The resonance frequency, f_s (conductance maximum), decreases when voltage increases (-1.62% at 30 V, compared to 0 V). The antiresonance frequency f_p (resistance maximum) also decreases, but more modestly (-0.59% at 30 V). No hysteresis is observed, which is evidence of the electrostrictive state of the material.

Figure 12.14 represents the resistance (Real part of impedance) and conductance (Real part of admittance) curves stemming from the previous model applied to this example of the STO resonator near the thickness mode. The similarity of the experimental and modeled curves attests to the quality of the electrostrictive model. To account for the electrodes resistance, a series resistance of 2.5 Ω was added to the resonator model. The quality factor extracted is low for the two characteristic frequencies because it is around 30. We will return to the reasons for this low value.

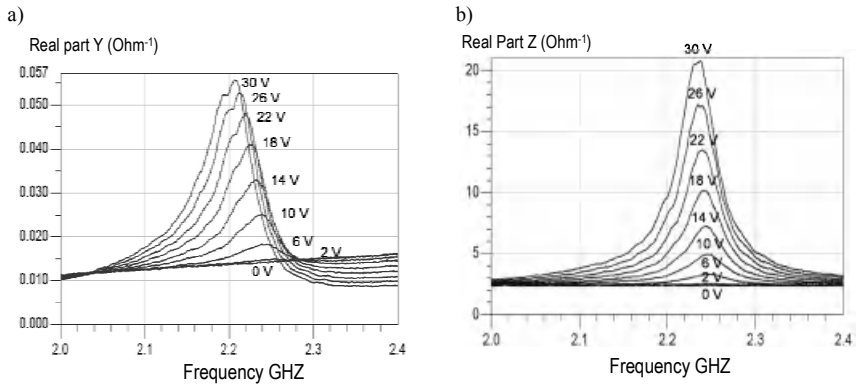

Figure 12.13. *a) Conductance; and b) resistance of the STO resonator around the thickness mode [VOL 08]*

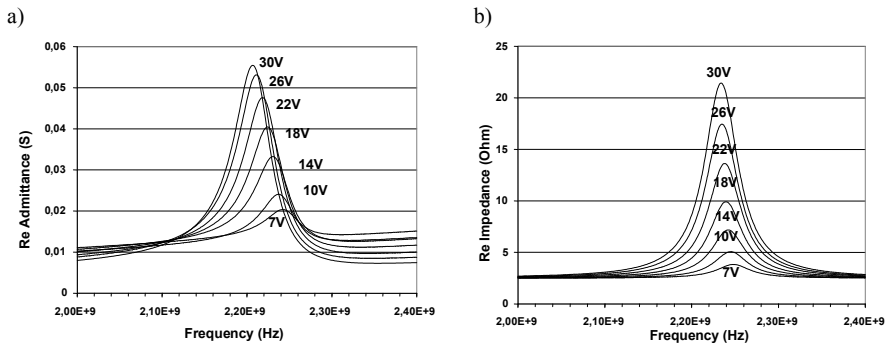

Figure 12.14. *a) Modeled conductance; and b) modeled resistance of the STO resonator around thickness mode*

As in the HBAR case above, it is possible to extract the characteristic values of the phenomenological model from the impedance of the resonator. The relative dielectric constant of STO varies here between 100 at 7 V and 76 at 30 V, which represents a maximum applied electric field of 0.75 MV/cm. The behavior is similar to that of BST, but the maximum value for STO is lower. For the stiffness coefficient, returning to the electrostrictive formalism and fitting the parameters with the experimental curve (as represented in Figure 12.15a), the values extracted are $c_0^D = 1.56 \times 10^{11}$ N/m² and $M = -1.2 \times 10^{12}$ Nm²/C². For the coupling coefficient, k_t^2, the experimental values of the model are plotted in Figure 12.15b. A linear coefficient of electrostriction $G = 2.5 \times 10^{10}$ m/F is extracted.

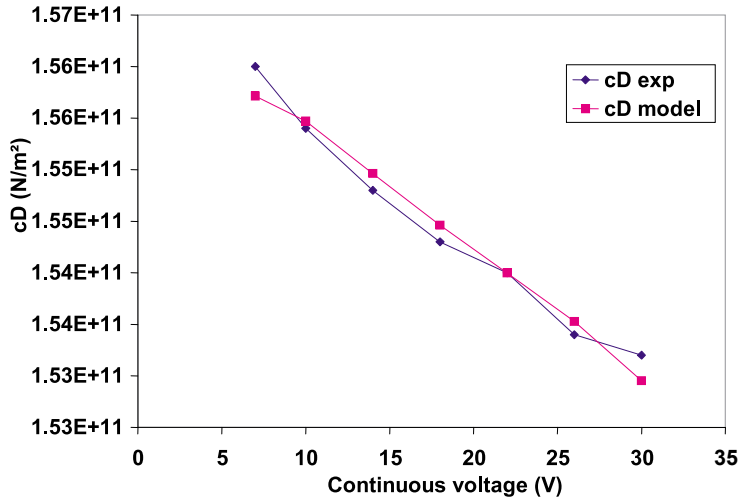

a)

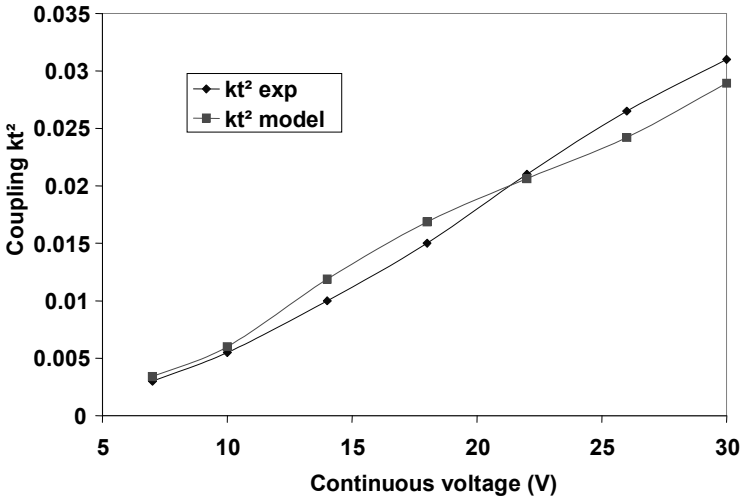

b)

Figure 12.15. *c^D and k_t^2 of the STO resonator extracted from experimental data (rhombuses) from the loaded impedance model and c^D extracted from the electrostrictive (squares) model after fitting the experimental values*

The value of the coupling coefficient obtained is low (3% at 30 V). This is related to the rather low dielectric constant of STO around 120 at 0 V, together with its weak variation with DC bias, compared to BST.

We showed that the coupling coefficient varies to the power of three with ε_r. The increase in ε_r must therefore induce an increase in coupling, as for BST. The low annealing temperature leads to a disturbed crystallization of STO, as proved by the transmission electron microscopy image in Figure 12.16. The small grains, a few nm in size, observed are cavities in STO. It is likely that these cavities have a non-negligible role on the dielectric constant of STO, as well as on the acoustic losses that induce a low quality factor.

On the other hand, X-ray diffraction diagrams showed a random orientation of STO. There are therefore grains with different orientations that are strained simultaneously during RF excitation. As STO different orientations do not have the same acoustic velocities, this induces a phase shift of the acoustic waves that could also explain a decrease in the quality factor.

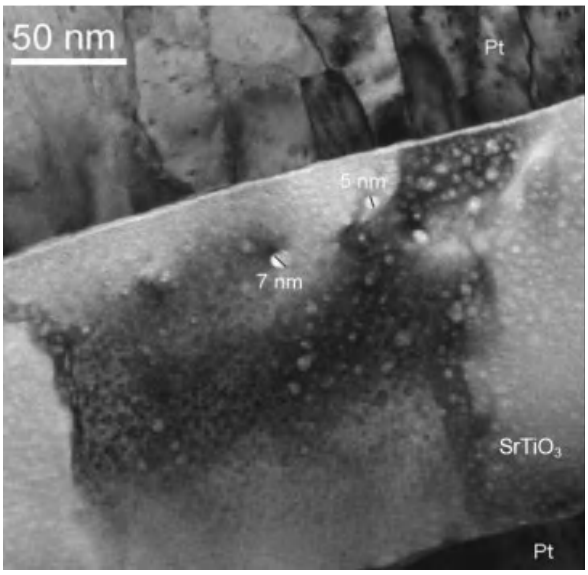

Figure 12.16. *Transmission electron microscopy image of a STO film between two Pt electrodes annealed at 450°C for 30 minutes under air*

12.3.3. *BST resonator on an acoustic Bragg mirror*

The work in this section is taken from the literature produced by the works of Professor Gevorgian's team, which is one of the precursors of these electrostrictive resonators [GEV 06]. The stack studied is very close to the example above and the test structure is identical to that of Figure 12.4. The Bragg lattice is probably made up of alternating layers of AlN and SiO_2 layers. The bottom electrode is in Pt and

the top one in Au. The electrostrictive material is BST25/75 (Ba/Sr = 25/75) obtained by pulsed laser ablation deposition (PLD).

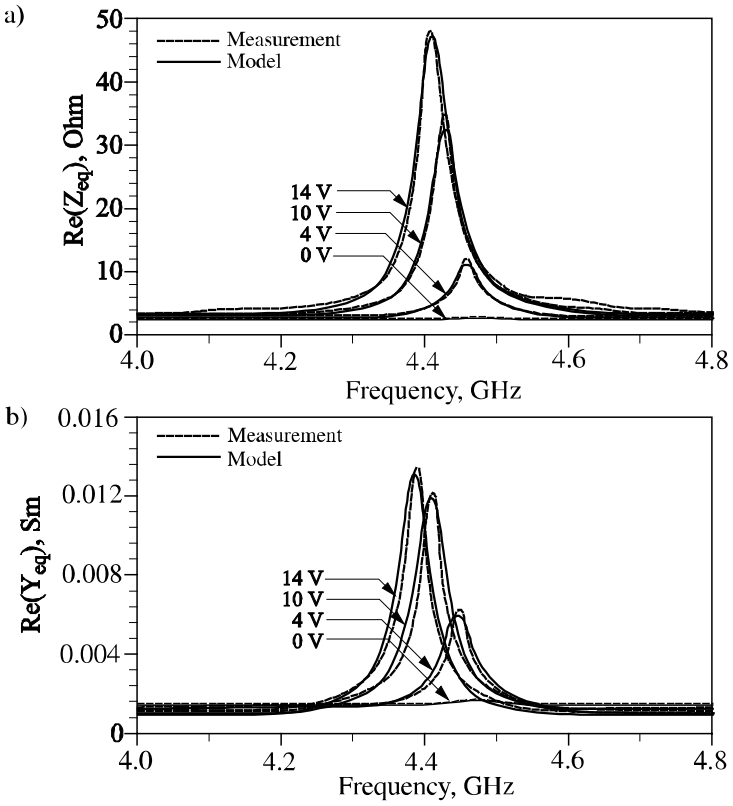

Figure 12.17. *a) Real part of impedance; and b) admittance of a BST25/75 resonator on a Bragg mirror [GEV 06]*

The experiment curves of the real parts of impedance and admittance are plotted in Figure 12.17. The authors used the same model as previously described to explain the experiment curves. The correspondence between model and experience, as seen in Figure 12.17, is good.

The maximum k_t^2 extracted reaches 1%, which is quite low. The quality factor reaches 80 for resonance and antiresonance, which is encouraging. The change in frequencies versus DC voltage is around 1%.

12.3.4. *BST resonator on a membrane*

This last example is the one published by Professor Tagantsev's team at EPFL and it is one that likely arouses the most hope with regards to future use of this technology because of the results obtained [NOT 09].

The basic structure is a BST resonator between a Pt bottom electrode and a top Al electrode. The resonator is released by back-etching of the substrate using a dry process. The paper [NÖT 09] summarizes the important points of the main approaches possible right now:

– use of paraelectric BST (coupling higher than STO);

– deposition through the PLD process enabling high quality deposited material (but not an industrial process yet);

– acoustically-insulated structure;

– electrodes that are highly conductive; and

– an acoustic model implementing the change in stiffness.

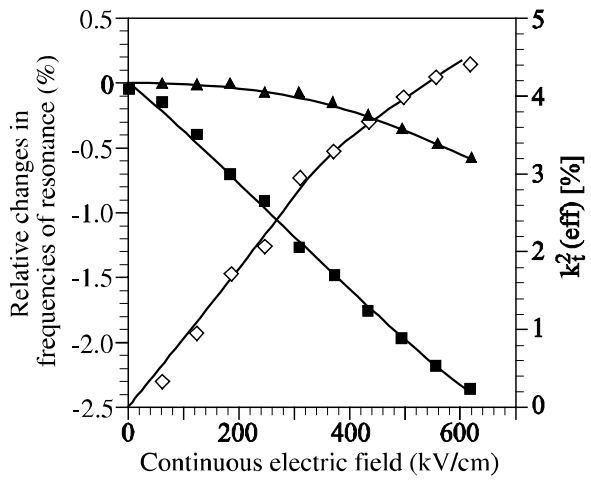

Figure 12.18. *Results obtained on BST mounted on a membrane [NOT 09]*

The typical results obtained instance a change in frequencies of resonance and antiresonance of -2.4% and -0.6%, respectively, for a field of 600 kV/cm, a maximum k_t^2 coupling of 4% for the same field and one of the best quality factors reported reaching 200 at resonance and 120 at antiresonance. Let us add here that

Professor Gevorgian recently published data on BST resonators reaching a quality factor of 350 [GEV 10]. This high value is likely the results of a special deposition mean called hot sputtering. The advantage of this technique is that no further annealing is necessary to crystallize BST, as it is already in the perovskite phase after deposition. These results are plotted in Figure 12.18 and were analyzed with the same model as the one presented above.

12.4. Simulation of a filter with electrostrictive resonators

From the model implemented, it is possible to simulate all sorts of filters in the same way as was presented for AlN-based resonators (see Chapter 10). Here we present a ladder-based structure with a single cell (a series resonator and a parallel one). The values of the model correspond to the BST developed at LETI (see Table 12.1) with a quality factor of 200. The transmission response in dB of this filter structure for different DC voltages is given in Figure 12.19.

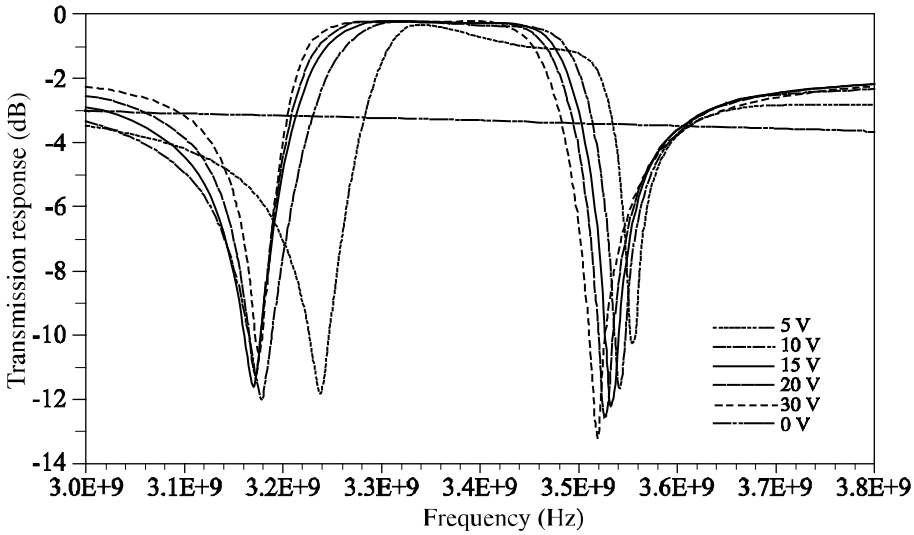

Figure 12.19. *Transmission response of a ladder filter composed of one section with two electrostrictive resonators (in dB)*

Between 10 V and 30 V, the width of the band-pass is roughly constant because of the quasi-constant value of k_t^2 (due to the equilibrium between the increase in electric field and the decrease in the dielectric constant). The band-pass shifts towards low frequencies of about 1% when the DC voltage changes from 10 V to 30 V.

We also note that at 0 V, the filter is none other than a voltage divider with capacitors since the resonators are no longer active. This simulation gives a general idea of what it is possible to design from this model but as mentioned earlier the performances of the filters in terms of loss and steepness depends mainly on the quality factor of the material.

12.5. Status of perovskite electrostrictive resonators

In Table 12.1, we resume the main results of electrostrictive resonators observed in the literature. Some values from the literature were calculated or estimated from available information.

Materials	**BST LETI**	**STO LETI**	**BST (Vendik)**	**BTO (Vendik)**	**BST (Noth)**	**STO (Saddick)**	**PZT (Muralt)**
Reference	[DEF 10]	[VOL 08]	[VEN 08]	[VEN 08]	[NOT 09]	[SAD 07]	[CON 08]
c0 (N/m²)	1.52×10^{11}	1.56×10^{11}	2.50×10^{11}	1.30×10^{11}	2.53×10^{11}	3.48×10^{11}	1.30×10^{11}
$\Delta f_p/f_p$ (%)	-1.70	-0.62	-1.12	+4.2	-0.4	?	-3.2
$\Delta f_s/f_s$ (%)	-3.20	-1.69	-1.57	+1.3	-2.0	-1.05	-5.0
M (Nm²/C²)	-8.0×10^{11}	-1.2×10^{12}	-1.5×10^{12}	4.3×10^{12}	-5.0×10^{11}	?	?
G (m/F)	2.8×10^{10}	2.5×10^{10}	1.6×10^{10}	3.0×10^{10}	1.8×10^{10}	1.6×10^{10}	6.5×10^{9}
ε_r max	320	100	140	140	300	?	1,100
ε_r min	78	76	100	100	170	80	650
Emax (MV/cm)	1.07×10^{8}	7.50×10^{7}	5.00×10^{7}	5.00×10^{7}	6.00×10^{7}	1.25×10^{8}	2.00×10^{7}
Q	>50	30	80	30	120–200	80	50
k_t^2 model (%)	8.4	2.73	0.71	4.78	6.26	1.63	9.87
k_t^2 exp (%)	8.5	3	1	6	4.5	2	9.5
Device	HBAR	SMR	SMR	SMR	FBAR	SMR	FBAR

Table 12.1. *State of the art of electrostrictive resonators (in 2009)*

It seems that BST, PZT and to a lesser extent BTO show couplings that can compete with AlN. It is worth noting that PZT and BTO, which are ferroelectrics, were considered electrostrictive by extension. However, the use of ferroelectrics prevents us from conceiving a switch operation like that for pure electrostrictive materials because of the ferroelectric hysteresis cycle.

The main physical reason that explains the strong coupling is the strong dielectric constant (and its huge variation with DC bias) associated with a high electric field. The stiffness values extracted from the literature are often quite scattered, but the order of magnitude is roughly the same. A preliminary stage of characterization by picosecond ultrasonics seems like the best solution for obtaining a correct value of acoustic velocity. We must note that this stiffness appears in the denominator in the k_t^2 formula, which induces an increase in coupling when the material is less stiff. It is likely, however, that this also produces a greater loss of energy and therefore a decrease in the quality factor. This low quality factor, regardless of the structure studied, remains a major issue with this technology.

In terms of change in characteristic frequencies, the orders of magnitude are around 1% for the antiresonance frequency for purely electrostrictive materials. Only the stiffness variation is to be invoked to explain the antiresonance frequency change. Indeed, for electrostrictive materials, electromechanical coupling is only involved in the resonance frequency change, in accordance with equation [12.20]. This change always goes in the direction of a decrease in stiffness when a DC voltage is applied. The microscopic reason for this change is not very clear but is certainly linked to the increase in the distance between atoms when voltage is applied. Experimentally, an electrostrictive material expands in the direction of thickness when a DC voltage is applied, whatever the sign of voltage. We must also note that this change in stiffness cannot be explained by the change in length induced by the electrostrictive effect, because the latter is about 20 times lower compared to the stiffness variation extracted from the model. We are therefore dealing with a real change in stiffness of the electrostrictive material. The change in resonance frequency, which includes the change in stiffness effects and those of electromechanical coupling, can reach 2–3% in the direction of the decrease in frequency. For ferroelectrics (BTO, PZT), the changes can reach 4% with a hysteresis cycle. The interpretation of the changes in frequencies is much less clear in the particular case of ferroelectric materials because coupling and change in stiffness is involved in the two frequencies due to hysteresis. Up to 5% change is observed for PZT.

These significant changes in frequencies enable us to see the potential for RF filters. The possibility to increase these changes up to 10% would permit us to reconfigure the filters in order to move from one telecommunication standard to another. These perspectives dodge very important work by design teams that it is impossible to avoid to properly gauge these electrostrictive devices in the framework of RF applications. Indeed, the combined, non-identical change of the characteristic frequencies due to the DC voltage applied complicates the traditional diagram of acoustic filters.

These perspectives are only interesting if we are able to improve the properties of the material, and especially the quality factor. There are several ways by which we can do this: high-temperature annealing; another deposition technique; or a Bragg mirror that can support a higher temperature and ensure a unique orientation. Single-crystal thin films are undoubtedly a very good path to follow, just like searching for a maximum density associated with a minimum roughness.

12.6. PZT-based tunable frequency ferroelectric acoustic resonator

12.6.1. *Introduction*

As previously discussed, it can be interesting to replace AlN, a polar piezoelectric material with a material whose resonance frequency can be adjusted by applying a DC voltage. The need to adjust the resonance frequency comes from the extreme precision that must be exhibited by the resonators. As this frequency is fixed to the first order by the thickness of the piezoelectric and the precision of current deposition machines is not sufficient, a method of frequency adjustment is mandatory. To avoid the localized ion manufacturing that is used today (trimming method), which is extremely difficult to implement, a solution enabling frequencies to be adjusted by adding a DC voltage is very attractive.

Electromechanical coupling of a piezoelectric resonator depends on the piezoelectric coefficients. In the case of ferroelectrics, these coefficients vary in terms of the state in which the dipoles inside the material are found. With the LGD formalism (see Chapter 3), we showed that for perovskite materials (like PZT), piezoelectricity in the ferroelectric phase comes from the simultaneous existence of electrostrictive properties and remanent polarization of the material. In this calculation, piezoelectric coefficients depend on this remanent polarization, the dielectric constant, the electrostrictive coefficients and the DC electric field.

Thus, the change in remanent polarization in the ferroelectric obtained by applying a DC electric field greater than the coercive field will result in a change in piezoelectric coefficients and electromechanical coupling coefficients. As the latter depend on resonance and antiresonance frequencies of a resonator, applying a DC field must let the characteristic frequencies of a ferroelectric resonator vary.

Next, we present a suspended resonator involving PZT characterized in the range of GHz. The resonance frequency is changed by applying a DC voltage.

12.6.2. *Technology*

A sketch of the final structure of this ferroelectric resonator is given in Figure 12.20a. The membrane is released by SF_6/C_4F_8 anisotropic dry etching with a stop on a thermal SiO_2 film of 1 µm. This oxide film is then etched at the end of the process by dry etching. The resonant structure released is made up of 500 nm Si_3N_4. The bottom Pt electrode (100 nm) with its supporting Ti film (50 nm), followed by 370 nm of sputtered 52/48 PZT annealed at 675°C under air for 30 minutes. The top Pt/Ti/Pt electrode (20 nm/30 nm/100 nm) is critical to improve adherence, while ensuring Pt contact with the ferroelectric. A film of SiO_2 deposited by Plasma-Enhanced Chemical Vapor Deposition (PECVD) is used to insulate the electrodes. The nitride film ensures mechanical solidity of the released membrane, although the ideal solution would be to remove this film, which has a non-negligible impact on the resonant properties of the structure. Figure 12.20b is a view from the top of the tested structure on which we see the three test probes (GSG) on the left and the capacitance with a particular non-regular shape, in order to minimize the parasitic modes originating in lateral modes of resonance. The changes in tone in Figure 12.20b are proof of a membrane deformed by relaxing residual stresses.

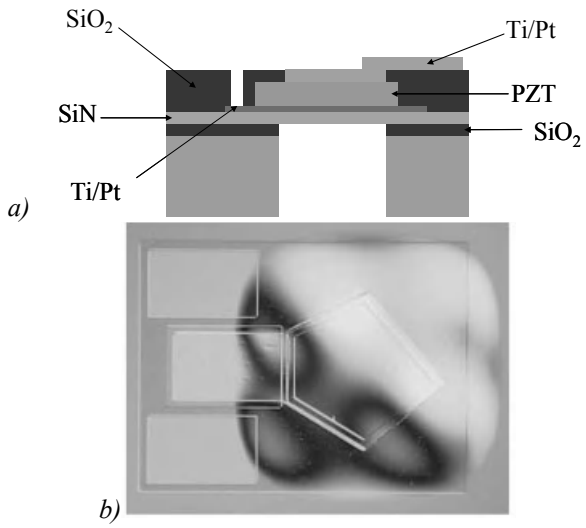

Figure 12.20. *a) Sketch of a PZT-based ferroelectric FBAR with release by the back side; and b) view from the top of the RF released tested structure*

12.6.3. *RF characterization and discussion*

RF design corresponds to a one-port structure that enables us to measure the S_{11} parameter of capacitance (network analyzer: HP8753E). Correction patterns are added to the mask in order to eliminate the parasitic capacitors of the probe pad. A DC voltage is added to the RF signal to measure the changes in resonance and antiresonance frequencies of the structure near dominant mode. This mode is located around 1.5 GHz and corresponds to a resonance of the whole stack, especially the nitride film, which is not optimal for coupling.

Figure 12.21a shows the change in frequencies f_s and f_p where the DC electric field varies between -280 kV/cm and +280 kV/cm in the two directions. A butterfly-shaped curve is observed for the two frequencies that are explained by the ferroelectric character of PZT. This hysteresis is an extra difficulty to manage in the case of an integrated device.

In Figure 12.21a, the change is more pronounced on the resonance frequency than on the antiresonance frequency. The change in resonance frequency reaches 1.9%, which could be sufficient for compensating the frequency spread of resonators due to thicknesses variation inherent of deposition techniques. We must however take into consideration the way the filter function is implemented. In the case of most common filter topologies (so-called ladder or lattice), two types of resonators (A and B) with two different resonance frequencies are needed. For the filter to work, the resonance frequency of the A resonators (series elements) must correspond to the antiresonance frequency of the B resonators (shunt elements). In these basic topologies, one can see that the side-effect of a filter frequency adjustment would be a bandwidth change due to a coupling change. Although limiting the scope of such filter, this combined change in bandwidth might be acceptable for some applications. One way to overcome this issue would be to work on filter topology that only use one of the two characteristic frequencies by adjoining passive elements in the filtering chain [CAR 05]. Theoretically a frequency adjustment could then be achieved while keeping the bandwidth identical. This technique, however induces the use of passive elements with high quality factors, which in itself constitutes a technological challenge.

In the same year as this study (2004), Schreiter *et al.* observed these changes in frequencies of resonance and antiresonance due to a DC field on a PZT FBAR resonator [SCH 04]. They reported a behavior different to the resonators following the PZT composition: in the Ti-rich tetragonal phase (PZT 25/75), the frequency of resonance barely drifts with the DC field; whereas the frequency of antiresonance drifts by a maximum of 1.9%. It is exactly the opposite for the Zr-rich rhombohedral phase (PZT 58/42). The authors explain this phenomenon by competition between two effects. On one hand, a different behavior of the material stiffness at constant

field strength (called c_{33}^E) versus the DC field following its crystalline phase. On the other hand, there is the electromechanical coupling effect.

Schreiter uses the thickness mode resonance model and obtains approximate formula for the resonance and antiresonance frequencies that only depend on c_{33}^E, the density and k_t^2. This approach is interesting because it enables us to put forward an explanation based on the field-enhanced movement of domain walls, which induces a change in stiffness in the rhombohedral case for a (111)-oriented film, which is their case. With this model, in the tetragonal phase the possible domain directions are such that no change in stiffness can occur. Therefore, for the tetragonal phase, the frequency changes are due solely to the change in k_t^2 (f_p varies and f_s is almost constant). For the rhombohedral phase, however, the influence of change in stiffness compensates that of k_t^2 for f_p, whereas it makes up the source of change of f_s. Consequently, we can consider that the rates of change in resonance and antiresonance frequencies of a PZT resonator can be adjusted in terms of the Zr/Ti ratio and so these relative quantities of the tetragonal and rhombohedral phases.

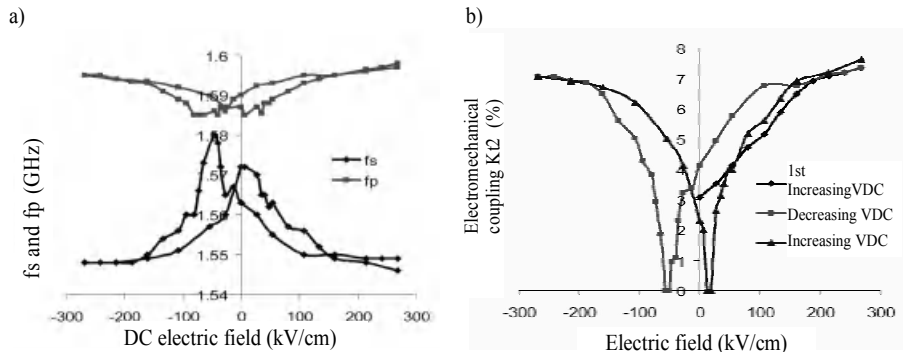

Figure 12.21. *a) Series (f_s) and parallel (f_p) change in frequencies of the PZT resonator due to the continuous electric field applied; and b) change in the equivalent coupling coefficient (k_t^2) calculated from the changes in f_s and f_p*

Figure 12.21b represents the k_t^2 coupling coefficient of the resonator calculated with the resonance and antiresonance frequencies. A butterfly-shaped curve is found with two field values that cancel any piezoelectric effect. This can be interesting for RF switch operations. The maximum value reached by k_t^2 is 7%, which is quite low for PZT. The best results in the literature reach >30% [LAR 04]. The likely reasons are first a non-optimal quality of PZT (sputtered here) and second the presence of the silicon nitride film whose volume represents about half the stack, which is not negligible in the calculation of k_t^2. Third, the quality factor of resonances is low

(<100). Here, also, the quality of PZT is to be challenged (porosity, low Pb content). We must also note that PZT intrinsically displays very high acoustic losses. Muralt discusses this problem in an article that makes reference to the subject [MUR 05].

The ferroelastic domain walls make a very important contribution to the piezoelectric effect (roughly 50%), but this movement induces considerable acoustic losses. As the morphotropic phase of PZT (Zr/Ti = 52/48) is the one that has the greatest domain wall mobility because of the presence of a monoclinic phase [NOH 00], it is also the one that must exhibit the largest losses. The movement of domain walls generates shear waves in the material that are similar to a dielectric relaxation, the characteristic frequency of which is close to that of the thickness mode, which explains these losses. Let us recall that ferroelastic domain walls appear between two domains with different directions of polarization as domains, *a* and *c* in the case of the tetragonal lattice. If the walls are between two flipped domains (called 180°-domains), they are not ferroelastic.

To suppress these unacceptable losses for a filtering application that necessitates coefficients of quality of the order of 1,000, Muralt suggests dropping domain walls by using materials that only have one possible direction of polarization, such as those belonging to a tungsten bronze structure or ilmenite ($LiNbO_3$, $LiTaO_3$). He also suggests playing on the stresses induced by the substrate to force the domains in one single direction (see Janolin's thesis on heteroepitaxy of PZT on an STO substrate [JAN 06]). The use of single-crystal films of lithium niobate or tantalate oriented in a favorable direction was already discussed in this book. Another possibility could be to use an electrostrictive effect rather than a piezoelectric one, as previously detailed.

12.7. Nonlinear effect in piezoelectric AlN

12.7.1. *Introduction*

AlN is a purely piezoelectric material, without the possibility of cancelling this effect like in ferroelectrics. It can show, however, nonlinearities when external stresses become important, like a continuous electric field for example. This effect is low but it is notable and quantifiable by a thermodynamic approach similar to that put forward for pure electrostrictives (see Chapter 8). In this section, the changes in characteristic frequencies and electromechanical coupling of AlN resonators will be explained. The main difference with pure electrostrictives like perovskites is found at the level of the dielectric constant, which is a lot lower in the case of AlN ($\varepsilon_r \approx 10$). Its change with DC voltage is also a lot more modest, which considerably limits the changes in characteristics observed on the AlN resonators. The differences

are notable, quantifiable and predictable thanks to this phenomenological model. It therefore seemed interesting to develop the model here.

12.7.2. *Piezoelectric-electrostrictive phenomenological model*

In accordance with what was observed analytically for the acoustic propagation equation, it is very practical to use D as a variable in the development of this model because the antiresonance frequency is defined directly from c^D without electromechanical coupling, which considerably simplifies extraction of parameters. It can seem more logical to use the electric field as the variable because it is this variable that is applied directly to the resonator, but this considerably complicates the development.

For the mechanical variable, as we are again considering a thin film on a substrate, it is simpler to use S because the in-plane strains are zero to the first order. We can therefore work on a one-dimensional model to explain the changes in resonance of the thickness mode. No index will be indicated in the development, but all the coefficients concerned relate to the direction of propagation, naturally the z (or 3) axis.

Just as before, the free energy considered is F, Helmholtz free energy. Temperature is considered to be constant, which eliminates the heat term in F. In the case of a piezoelectric material, there is no reason to eliminate the odd terms because there is no center of symmetry. There are therefore no more terms to determine.

The changes in frequencies of resonance of AlN due to a DC field are extremely small: it is therefore necessary to make a free energy development taking into consideration all the terms for a given order.

As we will consider the electrostrictive term, it is the third-order energy that must be considered. F takes the following form:

$$F - F_0 = \frac{1}{2} c_0^D S^2 + \frac{1}{2} \beta_0^S D^2 - h_0 DS + GD^2 S + NS^2 D + \frac{1}{3} OD^3 + \frac{1}{3} RS^3 \qquad [12.28]$$

where c_0^D, β_0^S and h_0 are, respectively, the coefficient of stiffness at constant D, impermittivity at constant S and the piezoelectric coefficient. G is the linear electrostriction coefficient.

N, *O* and *R* are defined by equation [12.28]. It does not seem useful to specifically name them.

A first-order derivation of *F* as a function of *S* and *D* gives:

$$\left.\frac{\partial F}{\partial S}\right)_D = T = c_0^D S - h_0 D + GD^2 + 2NSD + RS^2$$

$$\left.\frac{\partial F}{\partial D}\right)_S = E = \beta_0^S D - h_0 S + 2GDS + NS^2 + OD^2 \qquad [12.29]$$

By applying a DC voltage, it is possible to simplify these equations as before by only keeping the first order of the DC terms, which gives:

$$\begin{aligned} T &= \left(c_0^D + 2ND_{dc} + 2RS_{dc}\right)S + \left(-h_0 + 2GD_{dc} + 2NS_{dc}\right)D \\ E &= \left(-h_0 + 2GD_{dc} + 2NS_{dc}\right)S + \left(\beta_0^S + 2GS_{dc} + 2OD_{dc}\right)D \end{aligned} \qquad [12.30]$$

where DC stress in the propagation direction is zero in the case considered, which to the first order induces:

$$S_{dc} = \frac{h_0 D_{dc}}{c_0^D} \qquad [12.31]$$

The equation [12.30] set therefore becomes:

$$\begin{aligned} T &= \left(c_0^D + 2\left(N + \frac{Rh_0}{c_0^D}\right)D_{dc}\right)S + \left(-h_0 + 2\left(G + \frac{Nh_0}{c_0^D}\right)D_{dc}\right)D \\ E &= \left(-h_0 + 2\left(G + \frac{Nh_0}{c_0^D}\right)D_{dc}\right)S + \left(\beta_0^S + 2\left(\frac{Gh_0}{c_0^D} + O\right)D_{dc}\right)D \end{aligned} \qquad [12.32]$$

We find a formalism (*S,D*) with the following equivalent c^D, *h* and β terms:

$$h = h_0 - 2\left(G + \frac{Nh_0}{c_0^D}\right)D_{dc}$$
$$c^D = c_0^D + 2\left(N + \frac{Rh_0}{c_0^D}\right)D_{dc} \qquad [12.33]$$
$$\beta^S = \beta_0^S + 2\left(\frac{Gh_0}{c_0^D} + O\right)D_{dc}$$

Use of the above acoustic model is always valid for AlN by using the new parameters c^D, h and β. To the first order, D_{dc} can be considered the ratio E_{dc}/β_0^S. We therefore assume that the correction factors of β^S are weak. Making this approximation, the different terms of equation [12.33] become:

$$h = h_0 - 2\left(G + \frac{Nh_0}{c_0^D}\right)\frac{E_{dc}}{\beta_0^S}$$
$$c^D = c_0^D + 2\left(N + \frac{Rh_0}{c_0^D}\right)\frac{E_{dc}}{\beta_0^S} \qquad [12.34]$$
$$\beta^S = \beta_0^S + 2\left(\frac{Gh_0}{c_0^D} + O\right)\frac{E_{dc}}{\beta_0^S}$$

12.7.3. *Application: AlN resonator on a Bragg mirror*

In this example, we study an AlN resonator (1.27 µm) with Mo electrodes (250 nm each) on a Bragg lattice based on the couple of SiOC (low impedance)/SiN (high impedance) materials, as in Figure 12.22.

To observe the changes in characteristic frequencies of this resonator, a DC voltage is simultaneously applied to the RF signal. Figure 12.23 illustrates the real parts of impedance and admittance due to frequency for three DC voltages: -200 V, 0 V and 200 V.

We have to note that the maximum voltage that can be supported by AlN is very important (breakdown field >5 MV/cm). Shifts in resonance (ReY) and antiresonance (ReZ) frequencies are observed. At first sight these seem to be of the same order of magnitude, unlike those observed on BST.

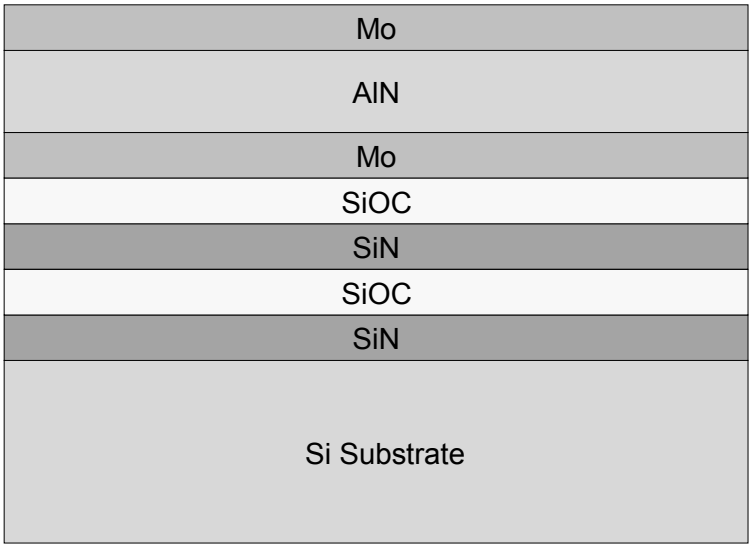

Figure 12.22. *Stack of a Mo/AlN/Mo resonator on a Bragg mirror*

We can immediately deduce from this that the change in coupling will be very low according to the continuous voltage applied. The greater part of this change is therefore due to the variation in stiffness of AlN, which is related to the change in frequency of antiresonance f_p. Indeed, in the sections above, we saw that the change in f_p can only be due to the influence of stiffness in this chosen piezoelectric formalism.

An evolution of the amplitude of ReZ and ReY in terms of continuous voltage, V_{bias}, is observed in the opposite direction. Indeed, when V_{bias} increases, the amplitude of ReY decreases when that of ReZ increases. Mason's model enables us to easily see that this opposite change is linked to the decrease (in the order of several per cent) of the AlN dielectric constant when V_{bias} increases.

Using Mason's model discussed above, it is possible to extract c^D, ε^S and k_t^2 in terms of V_{bias}. Figure 12.24 shows the results of fitting the model on the experimental data. Accuracy is not optimal because of a parasitic resonance on the experiment curves. It is however sufficient to observe the expected effects of change. The values extracted from the model are plotted in Table 12.2.

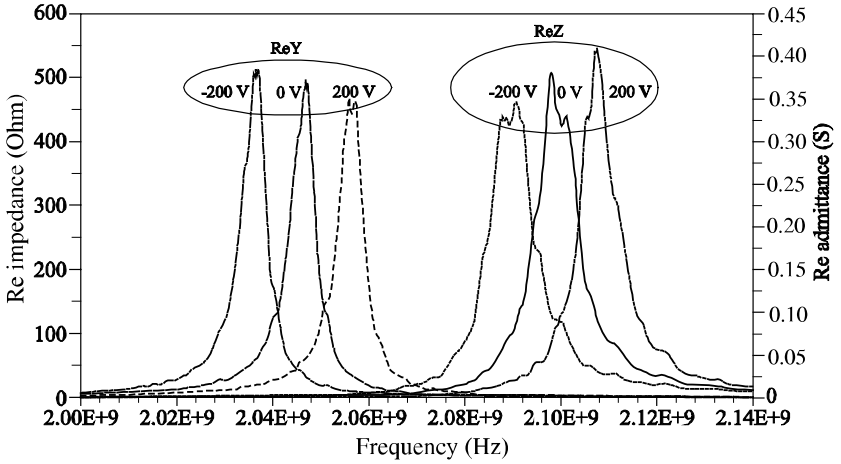

Figure 12.23. *Real parts of impedance and admittance near characteristic frequencies of the thickness mode of the AlN resonator for three DC voltages (-200 V, 0 V, 200 V)*

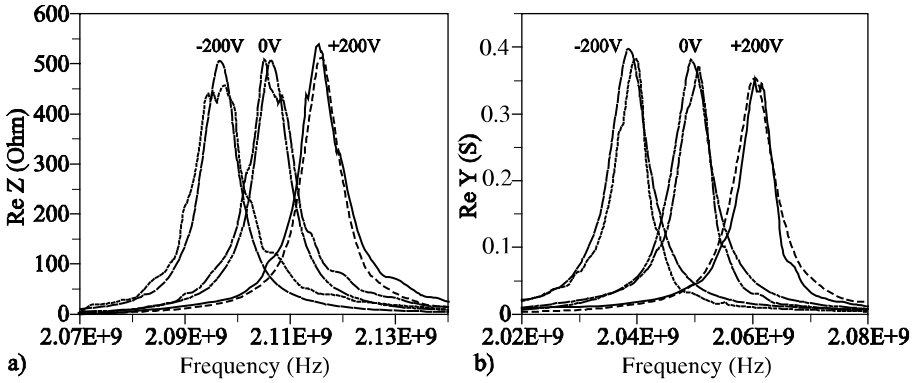

Figure 12.24. *Fitting the model on the experimental values of: a) ReZ; and b) ReY*

V bias (V)	-200	0	200
c^D (N/m²)	3.83×10^{11}	3.87×10^{11}	3.91×10^{11}
k_t^2	0.059	0.0577	0.0563
ε^S	10	9.7	9.3

Table 12.2. *Values extracted from the model after adjustment against the experimental results in Figure 12.24*

The changes are quite low (a few per cent) compared to those observed with BST. On the other hand, the changes in dielectric constant and stiffness are of the same order of magnitude. The direct consequence of this observation is that it is not possible to make the hypothesis on the cancellation of certain coefficients of free energy of AlN (equation [12.28]). We therefore end up with a system that has more unknowns than the number of equations known. In our case, fitting gives the following results:

$$\begin{aligned} G + \frac{Nh_0}{c_0^D} &= 6.2\times10^9 \\ N + \frac{Rh_0}{c_0^D} &= -1.38\times10^{11} \\ \frac{Gh_0}{c_0^D} + O &= -1.14\times10^{10} \end{aligned} \qquad [12.35]$$

It is fundamental to note that we cannot cancel parameters O and R, as they are not involved in the coupling. If these two parameters are cancelled, N and G, the coupled terms, do not succeed in explaining the changes in coupling due to V_{bias}. We therefore cannot neglect any order of degree 3 of energy. We will note that R nevertheless enters the change in stiffness in terms of V_{bias}, because of the spontaneous strain that results from V_{bias}.

12.7.4. *Conclusion with nonlinear AlN*

We have seen in this part that it is possible to explain the behavior of an AlN resonator in terms of a DC voltage with the help of a thermodynamic approach, just like BST. However, as the change in dielectric constant is a lot lower in the case of AlN, it is essential to keep all terms of the same order in the free energy development so that we can explain the changes observed. The changes in frequencies of resonance and antiresonance can reach 1.5% for 400 V DC.

12.8. Conclusion with electrostriction

We see that electrostriction is a second-order phenomenon that includes, by extension, several nonlinear effects, especially the change in stiffness in cases of pure electrostrictive materials. This phenomenon has two main characteristics: first, the electro-mechanical coupling phenomenon only appears in the presence of a DC voltage; and second, the frequencies of resonance and antiresonance present changes due to DC voltage. Most of the time, these changes are not identical, which is

characteristic of a coupling change due to this voltage. The main contribution to this phenomenon is the change in dielectric constant due to the applied DC voltage. It is for this reason that perovskite materials in the paraelectric phase at room temperature, such as BST or STO, are materials with a high electrostrictive effect. Coupling can reach values higher than that of AlN and the changes in resonance frequency can reach a few per cent.

The applications viewed are mainly located around the notion of frequency agility for RF filters (reconfigurability and compensation of process variation). The main question that remains is whether it is possible to increase the quality factor of resonances that are currently located around 300. The main ideas for improvement are around the intrinsic quality of the material: single crystals (epitaxy, Smart Cut^{TM}), hot sputtering, the decrease in roughness and the nature of electrodes.

On the other hand, we saw that the changes in frequencies of resonance of a true piezoelectric resonator can also be explained by the same phenomenological approach. To do this, we must add terms of greater orders in the free energy in relation to the second order development to explain the piezoelectric phenomenon. A third order electrostriction term is added to the free energy, but we must take into consideration all terms of the same order in the case of AlN, unlike pure electrostrictives for which the change in dielectric constant is such that it is enough to explain nearly all of the phenomena observed. The changes in frequency obtained with AlN are roughly 0.5% for 100 V, which probably makes it a difficult technique to implement.

As a final remark, let us note that the majority of research about this idea of electrostriction is currently concentrated around perovskite materials.

12.9. Bibliography

[CAR 05] CARPENTIER J.-F., TILHAC C., CARUYER G., DUMONT F., PARAT G., ANCEY P., *IEEE MTT-S Digest*, 221, 2005.

[CON 08] CONDE J., MURALT P., "Characterization of Sol-Gel Pb(Zr0.53Ti0.47)O3 in Thin Film Bulk Acoustic Resonators", *IEEE Transactions on Ultrasonics*, *Ferroelectrics*, *and Frequency Control*, vol. 55, n° 6, p. 1373, 2008.

[DEF 10] DEFAŸ E., LE RHUN G., SANCHEZ S., PARAT G., BILLARD C., MERCIER D., "Electrostrictive thin films for RF acoustic resonators", *European Frequency and Time Forum*, 2010.

[GEV 06] GEVORGIAN S., VOROBIEV A., LEWIN T., *Journal of Applied Physics*, vol. 99, 124112, 2006.

[GEV 10] GEVORGIAN S., VOROBIEV A., "Tunable thin film bulk acoustic wave resonators with improved Q-factor", *Applied Physics Letters*, vol. 96, p. 212904, 2010.

[IEE 87] IEEE Standard on Piezoelectricity, ANSI/IEEE Std 176, 1987.

[JAN 06] JANOLIN P.E., PhD Thesis, Ecole centrale Paris, 2006.

[LAR 04] LARSON J.D., GILBERT S.R., XU B., *IEEE Ultrasonics Symposium*, p. 173, 2004.

[MOR 03] MORITO K., IWAZAKI Y., SUZUKI T., FUJIMOTO M., *Journal of Applied Physics*, vol. 94, n° 8, 5199, 2003.

[MUR 05] MURALT P., ANTIFAKOS J., CANTONI M., LANZ R., MARTIN F., *IEEE Ultrasonics Symposium*, vol. 315, 2005.

[NOH 00] NOHEDA B., GONZALO J.A., CROSS L.E., GUO R., PARK S.E., COX D.E., SHIRANE G., *Physical Review B Condensed Matter*, vol. 61, n° 13, 8687, 2000.

[NÖT 09] NÖTH A., PhD Thesis, Ecole polytechnique de Lausanne, 2009.

[SAD 07] SADDIK G.N., BOESCH D.S., STEMMER S., YORK R.A., "DC electric field tunable bulk acoustic wave solidly mounted resonator using SrTiO3", *Applied Physics Letters,* vol. 91, 043501, 2007.

[SCH 04] SCHREITER M. *et al., Journal of European Ceramic Society*, vol. 24, 1589, 2004.

[TAP 04] TAPPE S., BÖTTGER U., WASSER R., *Applied Physics Letters*, vol. 85, 624, 2004.

[VEN 08] VENDIKA I.B., TURALCHUK P.A., VENDIK O.G., BERGE J., "Modeling tunable bulk acoustic resonators based on induced piezoelectric effect in $BaTiO_3$ and $Ba0.25Sr0.75TiO_3$ films", *Journal of Applied Physics,* vol. 103, 014107, 2008.

[VOL 06] VOLATIER A., PhD Thesis, IEMN, 2006.

[VOL 08] VOLATIER A., DEFAY E., AID M., NHARI A., ANCEY P., DUBUS B., "Switchable and tunable strontium titanate electrostrictive bulk acoustic wave resonator integrated with a Bragg mirror", *Applied Physics Letters*, vol. 92, n° 3: 032906, 2008.

[ZHU 07] ZHU X., PHILLIPS J.D., MORTAZAWI A., "Microwave Symposium", *IEEE/MTT-S International*, vol. 671, 2007.

[ZIN 04] ZINCK C., DEFAŸ E., CARUYER G., VOLATIER A., PELLISSIER D., FIGUIÈRE L., *2004 IEEE International Ultrasonics*, *Ferroelectrics and Frequency Control*, vol. 29, 2004.

Chapter 13

Thin Film Piezoelectric Transducers

13.1. Introduction

In this chapter, we will begin by briefly outlining state of the art of thin film piezoelectric transducers, and then we will give a few typical examples of transducers. As resonators were largely discussed in previous chapters, we will not discuss them here. In addition, in the literature there are several articles that review different applications that use piezoelectric thin films. The most complete reviews are undoubtedly those of Professor Muralt of EPFL. He has published about one state of the art review per year in this domain since 2000 [MUR 09].

In order to illustrate this chapter, we will give three examples of implementations of thin film piezoelectric transducers, from the most basic to the most elaborate. These examples use a design methodology that is representative of the domain:

– design based on analytical or FEM (finite element method) models;

– an important section dedicated to the technology of each building block that remains the heart of this domain, because many techniques are not yet normalized; and finally

– an integration of these "core bricks" in order to implement the final object.

The study ends with a series of tests adapted to each device. The objects we will describe are the following, in order of increasing complexity: an active membrane, a resonating micromirror and finally a radio frequency (RF) micro-switch.

Chapter written by Matthieu CUEFF, Patrice REY, Fabien FILHOL and Emmanuel DEFAŸ.

13.2. State of the art

Piezoelectric applications of ferroelectric thin films have greatly progressed since the beginning of the 1990s. The pioneer laboratories for these devices are located at Penn State University in the United States and at EPFL in Switzerland. Today, research has extended to other countries, especially to Asia where Korea and Japan have much activity in this domain. In Europe, apart from EPFL, several laboratories have also acquired know-how about piezoelectric materials and transducers: SINTEF in Norway, Cranfield University in England, CEA-LETI in France, and several others mainly in Northern Europe.

Details of the first thin film piezoelectric micromotor were published in 1992 by Flynn *et al*. with a PZT film on which a self-standing rotor is placed [FLY 92]. Between 1995 and 1998, the EPFL presented several more developed micromotors based on a Si/PZT membrane used as the motor stator [MUR 95, DUB 98]. The system works but efficiency is very low because electromechanical coupling in this configuration of a clamped membrane is not favorable (k^2 <1%) and because the efficiency between the stator and the rotor is 5%. A micro-pump based on manufactured microvalves and a piezoelectric accelerometer was produced in 1995 by Polla in the United States [POL 96]. Several orientable micromirrors were produced, one of which was at LETI [FIL 05, MAE 97].

Several laboratories have worked on atomic force microscopy (AFM) tips with a piezoelectric film to carry out detection thanks to the piezoelectric effect rather than by using the classic photodiode [FUJ 96]. Piezoelectric micromachined ultrasonic transducers or pMUTs were widely investigated by EPFL, especially through Ledermann's 2002 thesis and the European Parmenide project [LED 02]. The idea was to implement Si/piezoelectric bimorph membranes in order to generate acoustic waves in the air or a liquid. A potential application of this is increasing the resolution of echographic probes by multiplying the number of sensors, creating matrices from piezoelectric membranes as the size of each can be much smaller than the macroscopic sensors used today. Capacitive-MUT (c-MUT) competition is very active because the coupling factor of the latter can be much stronger. Actually, the electrostatic force is in the same direction as displacement of the membrane, whereas in pMUT we actually use a bimorph effect that limits coupling (k^2 max = 6% [LED 02]).

Finally, micro-switches are going through rapid development because there is a strong need for switches for RF devices, especially cell phones. The micro-switches with CMOS technology that are used today have a rather low insulation and therefore consume in the non-conducting state. The interest in MEMS switches is consequently great, although the technology is complex.

There are several active principles that have been developed for micro-switches: electrostatic, thermal, magnetic and piezoelectric [REB 03]. The advantage of the piezoelectric principle is that it consumes little and its dependence on electrical voltage is linear, thus enabling us to benefit from low actuating voltages, unlike electrostatic switches. For such switches, deflection for a given voltage depends on the reverse of the square of the distance between the electrodes and on the square of the voltage.

For piezoelectric devices, it is worth noting the outstanding work by LG in Korea, which put forward a solution based on a PZT and silicon nitride beam realized on a silicon wafer called the actuator wafer. A cap wafer containing the RF lines is assembled on the top of the actuator wafer. When the piezoelectric beam is directed upwards, the RF contact is switched on. In order to work properly, the height of the gap between the assembled wafers must be lower 5 µm [HEE 05, PAR 06]. LETI, in 2010, put forward a completely integrated micro-switch that has characteristics very close to LG's, but includes temperature compensation [CUE 10]. It is this last device that will be detailed at the end of this chapter.

Penn State, in 2003, put forward a switch based on a beam operated by the longitudinal piezoelectric effect (d_{33}), rather than the more standard transverse effect (d_{31}) [GRO 03]. This means that the useful strain and electric field applied are in the same direction. The latter is then applied through the use of an interdigital comb without any bottom electrode under the piezoelectric materials (PZT). The interest in this design is to use the d_{33} coefficient, which is two to three times higher than d_{31}. However, the space between the fingers of the comb is defined by the resolution of lithography, which gives widths in the micron range inducing actuating voltages higher than in the case of transverse architecture (electrodes perpendicular to strain).

The two main materials used for these applications are AlN and PZT. ZnO is used less frequently because it has piezoelectric properties close to AlN, but it is more difficult to master in terms of technology. AlN, which crystallizes in the wurzite phase, exhibits piezoelectric coefficients (e_{31} = 1 C/m² [DUB 99]) about 10 times lower than those of PZT, which remains the reference material (e_{31} = 12 C/m² [LED 03]). PZT has a relative dielectric constant 100 times bigger than that of AlN, (ε_{PZT} = 1,000, ε_{AlN} = 10).

It is worth noting that a sensor based on voltage detection will be more efficient if it exhibits a low dielectric constant. Indeed, for a given sensor and a given stimulus, if the capacitance value decreases, the output voltage increases. AlN is therefore interesting for sensor applications. PZT is the preferred choice for all actuator applications because the force that can be applied is directly proportional to the piezoelectric coefficient, regardless of the dielectric constant. The sensors based on current detection take advantage of using PZT as well.

Thus, we see that it is possible to define different factors of merit depending on applications. The analysis developed in Ledermann's thesis is very interesting [LED 02]. The sensor and actuator applications are discussed and here the figures of merit are put forward in the usual case of an electric field applied in the direction perpendicular to the plane of the films.

"Sensor" criteria	Figure of merit	Commentary
Current detection	$e_{31,effective}$	Favors PZT
Voltage detection	$\frac{e_{31,effective}}{\varepsilon_{33effective}}$	Favors AlN and ZnO because of their low dielectric constant
Signal to noise ratio	$\frac{e_{31,effective}}{\sqrt{\varepsilon_{33effective}\tan\delta}}$	AlN has very low losses compared to PZT

Table 13.1. *Figures of merit for piezoelectric sensor applications*

"Actuator" criteria	Figure of merit	Commentary
Force	$e_{31,effective}$	Favors PZT
Coupling factor (usual case of a piezo/silicon bimorph operation using the transverse effect)	$k^2_{effective} = \frac{2\left(e_{31,effective}\right)^2}{\varepsilon_{33effective}} \frac{1-\nu_{Si}}{Y_{Si}}$	PZT is the best due to its strong piezoelectric coefficient
Power efficiency	$\frac{k^2_{effective}}{\tan\delta}$	AlN has very low losses compared to PZT

Table 13.2. *Figures of merit for piezoelectric actuator applications*

The main manufacturing differences between the two materials are the following. To be piezoelectric, AlN must be properly oriented during deposition. Indeed, it is along the *c*-axis of the wurzite lattice that stands the polarization. This orientation is obtained by a wise choice of the bottom electrode, the lattice parameters of which must be close to those of AlN. Thus, Pt and Mo are commonly used with AlN [JAK 03]. With PZT being ferroelectric, it can be oriented *ex situ* by applying an electric field that will control the direction of the dipoles. It has been

theoretically and experimentally shown that the (100) orientation of PZT increases the piezoelectric properties [OUY 05]. Thus, the use of growth layers to favor this orientation has become very widespread [MUR 98].

Another big difference between the two materials is the deposition technique. AlN is deposited by direct current-pulsed reactive sputtering from an Al target at a temperature between 300°C and 450°C. PZT is mostly deposited by RF sputtering [VEL 99, ZIN 04] or by sol-gel [HDO 94] and crystallization is often ensured by a classic annealing or rapid thermal annealing (annealing by radiation), the temperature of which is generally between 600°C and 700°C.

One last difference that must be noted between AlN and PZT is the maximum working voltage. The breakdown field of AlN is around 5 MV/cm, whereas that of PZT is located around 1 MV/cm. For a given thickness, the maximum voltage applicable is therefore five times stronger in the case of AlN. On the other hand, to remain linear, PZT must not experience field strength higher than the coercive field or the field can change the domain's structure, inducing nonlinear effects. This coercive field of PZT thin films is around 50 kV/cm. Thus, we see that for a given application, the choice between AlN and PZT needs a more extensive analysis than the simple comparison of piezoelectric coefficients.

13.3. Resonant membranes

13.3.1. *Technology of PZT resonant membranes*

Following the example of Professor Muralt on piezoelectric resonant membranes published in 1995 [MUR 95b], many teams throughout the world have mastered the implementation of silicon-piezoelectric thin film heterogeneous membranes. These can, for example, serve to implement resonant membranes that can be used as pressure sensors [DEF 02]. Here we will present the major lines of standard technology as well as a few experimental results obtained with these PZT-based resonant membranes [ZIN 04].

The deposition technique of the piezoelectric material used here is sputtering, but it can be sol-gel. Two technologies are presented in Figure 13.1.

The two technologies are both based on TiO_2/Pt/PZT/Pt stack deposition on an oxidized Si substrate. The main difference relies on etching of the backside of the substrate. For KOH or TMAH wet Si etching, the etching is very delicate. Deep etching by a dry process is done by SF_6 (etching)/C_4F_8 (wall passivation) manufacturing – the Bosch process – with SiO_2 layer used as to stop the etching. The etching stop process on SiO_2, useable in dry and wet etching, is a lot easier to

manage. The size of the membrane matters because beyond a side of a few millimeters, the residual stresses can cause the membrane to break.

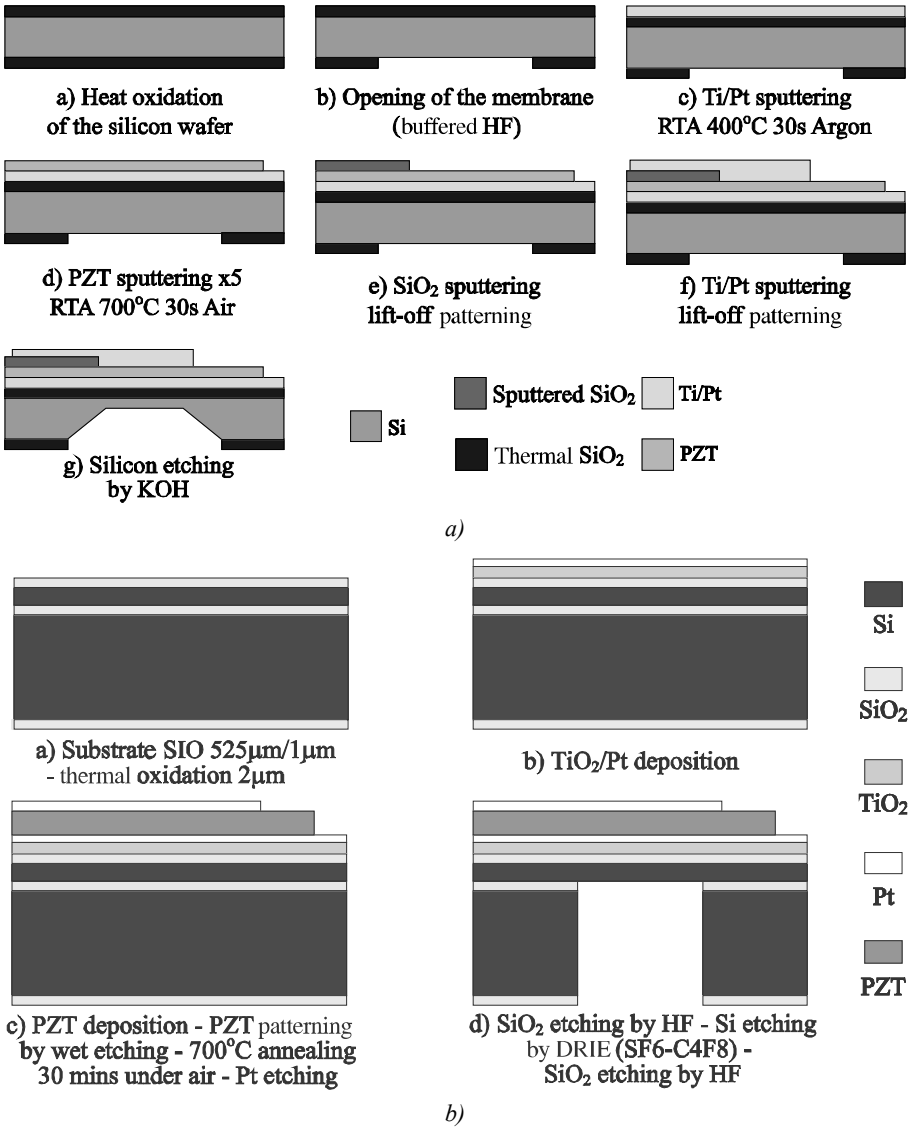

Figure 13.1. *Technology for implementing PZT resonant membranes: a) KOH backside etching; and b) dry backside etching by DRIE (Deep Reactive Ion Etching)*

13.3.2. *Frequency characterization of membranes*

Figure 13.2a shows the experimental set-up that enables us to observe the displacement of a composite Si/PZT membrane in terms of the excitation frequency of PZT. The PZT used here is 1 µm thick and pre-poled with a field of 175 kV/cm applied for 15 minutes at room temperature. The square Si membrane is 15.5 µm thick and 3 mm per side. The size and shape of the upper electrode were optimized by FEM (Ansys software) in order to maximize displacement for a given voltage. For a 3 mm-long membrane, the optimal size of the electrode is 1.7 mm per side. An alternating current signal (1.26 V amplitude) without bias voltage and with a variable frequency between 10 and 100 kHz is applied to the PZT.

Out-of-plane displacement of the membrane is observed through a laser vibrometer (Polytec OFV 2000) and is plotted in Figure 13.2b. Four modes of resonance are observed in the curve at 18.3 kHz, 40.0 kHz, 80.4 kHz and 97.3kHz. For each of these modes, a phase change of 180° is observed (not represented here). Only the first mode is clearly identified as being the fundamental mode by measurement of out-of-plane displacement from one edge to the other of the membrane, which is maximal at the center of the membrane. It exhibits a maximal sensitivity of 1.4 µm/V at resonance. Although the membrane is symmetrical, the simulation indicates that the modes observed at higher frequencies are asymmetrical. This can originate from the arrival of an electrode on one side (see Figure 13.2a), which brings the dissymmetry.

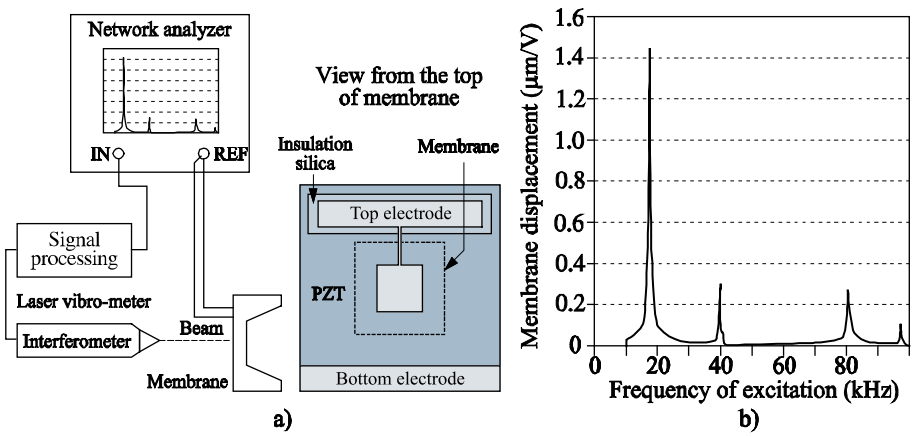

Figure 13.2. *a) Experimental connection of the frequency characterization of composite Si/PZT membranes and b) membrane displacement in terms of the frequency of excitation*

Displacement measurement using an optical method is accurate, but using a piezoelectric actuation enables us to make an electric measurement of resonance by the piezoelectric film itself. This change in impedance measurement is illustrated in Figure 13.3 for another membrane: a) out-of-plane displacement measurement with a vibro-meter; and b) change in admittance measured with a HP4194a impedance meter. We note that it is not the dominant mode that gives the strongest change in impedance. The change in admittance around 67 kHz (see Figure 13.3b) corresponds to a mode of resonance because a significant out-of-plane displacement is simultaneously observed by vibrometry (see Figure 13.3a). The change in impedance in Figure 13.3 allows us to extract dynamic k_{dyn}^2 coupling of this particular mode of resonance. Indeed, this coupling depends on the frequencies of resonance and antiresonance of the membrane, respectively, identified respectively as the maximums of the real parts of admittance and impedance. A k_{dyn}^2 of 0.7% is extracted, which is a modest value. The main reason for this is that the active part (piezoelectric film under the top electrode of 700 µm a side) is very small compared to the inert mass of the device (Si membrane 3 mm long and 10µm thick plus 2 µm of SiO_2).

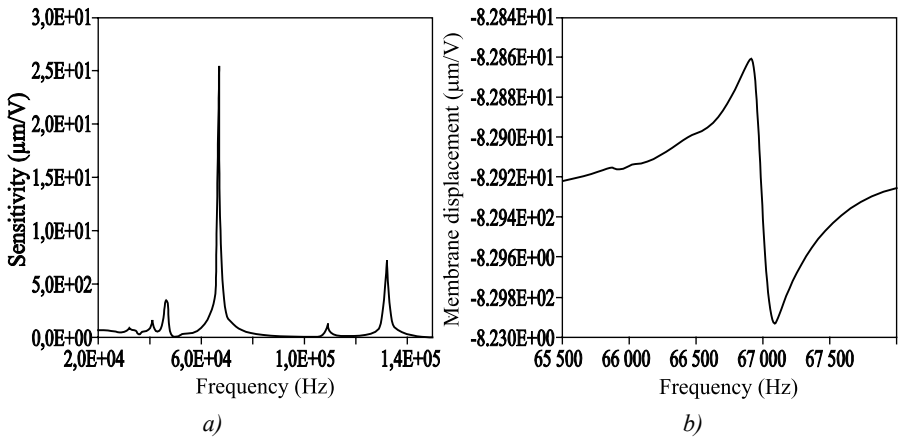

Figure 13.3. *a) Observation of the frequency sensitivity of a composite PZT/Si membrane with 3 mm long with the help of a laser vibro-meter; and b) change in admittance near the resonance of the mode at 67 kHz*

13.3.3. *A resonant pressure sensor*

One possible application of these membranes is a resonant pressure sensor. The principle is given in Figure 13.4. The idea is to measure a change in resonance frequency of a composite Si/PZT membrane according to the difference in pressure between the two sides. The experimental set-up allows us to reduce the pressure on the back by using a pump. The top side remains under atmospheric pressure.

Vacuum grease ensures a seal between the two sides. A macroscopic pressure sensor gives the value of pressure on the back. An alternate current voltage excites the PZT and its frequency is chosen in such a way as to be placed on a mode of resonance of the membrane. Out-of-plane displacement is observed thanks to a laser vibro-meter.

The characterized membrane is the same as the one shown in Figure 13.2 (Si: 15.5 µm – SiO_2: 0.5 µm – TiO_2: 20 nm – Pt: 100 nm – PZT: 1 µm – Pt: 100 nm) and it is the fundamental mode at 18.3 kHz that is observed. The change in resonance frequency measured in terms of the difference in pressure applied between the two sides of the membrane is plotted in Figure 13.4b.

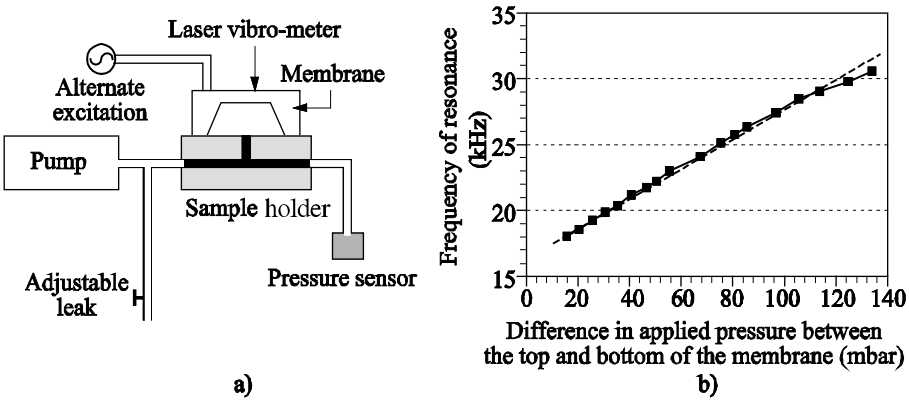

Figure 13.4. *a) Experimental set-up of the resonant pressure sensor based on a composite Si/PZT membrane; and b) frequency of resonance of the membrane in terms of the difference in applied pressure between the two sides of the membrane*

The maximum difference in pressure applicable is 140 mbar. Beyond that, it is no longer possible to observe the out-of-plane displacement of the mode of resonance with the vibro-meter. This change in frequency is linear. The sensitivity measured is 115 Hz/mbar. Normalized sensitivity ($\Delta f/(f_0 \Delta P)$) is 6,800 ppm/mbar, which is a high value. As a comparison, the resonant sensor developed by Thales exhibits a normalized sensitivity of 2,500 ppm/mbar [MAN 95].

In view of the strong sensitivity obtained, the simple principle put forward is interesting. The reason for this sensitivity originates in the increase in stresses in the membrane when the difference in pressure increases between the two sides. It is therefore strongly linked to the size and shape of the membrane as a whole.

13.3.4. *Conclusion on the study of Si/PZT resonant membranes*

The study of composite Si/PZT membranes has enabled us to measure PZT integration in a microsystem, the difficulty of which mainly focuses on the final release outside material optimization. The characterizations of resonance and the sensitivity and difference in pressure of a membrane have resulted in the operation of a resonant pressure sensor.

These works represent the beginnings of research on the implementation of piezoelectric microsystems. Other parameters must be taken into consideration in the conception stages: residual stresses in the different films; the technological compatibilities between the processes of elaboration of a complete system and the decrease in the influence of temperature on the mobile parts of microsystems.

13.4. Resonant micromirror

13.4.1. *Introduction*

Here, the objective is to design optical scanners that could be integrated with barcode readers or laser printers. New applications are conceivable with these integrated scanners: mobile phone screens with better definition, micro-projectors of images, or retinal projectors. Micromirrors can be used in a static or resonant mode. It is this last category that is focused on here. There are three integrated micromirror solutions (i.e. silicon technology microsystems) in the literature. The electrostatic solution with use of micromachined interdigitated combs requires high actuation voltages (250 V) [CON 00]. The electromagnetic solutions give good results but often require an external macroscopic inductance to generate the magnetic field [MIY 01]. Finally, there are resonant micromirrors using piezoelectric thin films [TAN 04].

The solution proposed here uses a PZT film co-integrated with a resonant mirror of optical quality. The principle is based on asymmetric position of the mirror in relation to the actuators.

13.4.2. *Technology and design of the resonant micromirror*

Figure 13.5 shows a diagram and a view from the top of a piezoelectric resonant micromirror. A circular mirror with a gold upper surface is fixed using two torsion bars on a frame equipped with thin-film piezoelectric bimorphous actuators. These actuators are found over a flexible membrane, whereas the mirror is solely linked to the actuators by the torsion arms. The operation frequency corresponds to the

resonant frequency of the system in the first torsional mode. The mirror is positioned asymmetrically in relation to the frame, in order to favor this torsional mode.

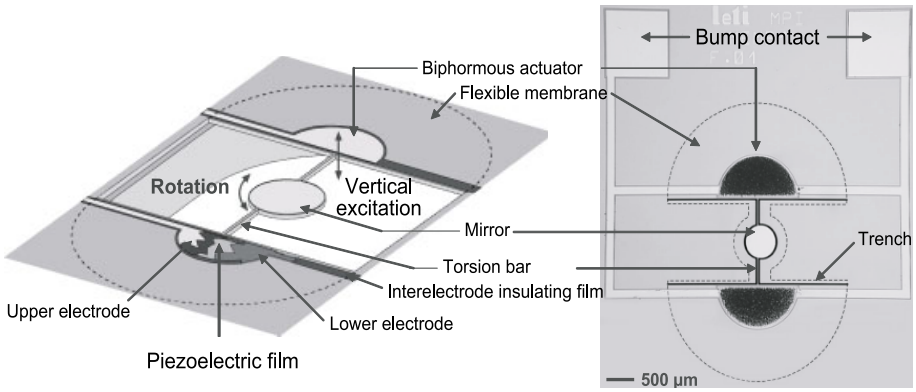

Figure 13.5. *Diagram and view from above of the piezoelectric resonant micromirror*

The design of the mirror must respect several constraints:

– a diameter large enough to limit angular spreading of the beam and thus increase the definition of the final optical device;

– a static deformation and a dynamic deformation of the mirror which must not exceed, respectively, one-quarter and one-tenth of the smallest wavelength used;

–a resonant frequency of the order of a tenth of a kHz to ensure a fast optical scan.

This design was developed with the help of analytical formulae from mechanics, as well as from modeling using the FEM with Coventor software. The optimization work results in the dimensions expressed in Figure 13.6a. The diameter of the semi-circles of the actuators is 3 mm. The maximum deformation is obtained when the diameter of the semi-circular actuators is equal to two-fifths of the diameter of the flexible membrane (see Figure 13.5). It can be noted that that the thickness necessary to achieve mirror flatness is 20 µm. The width of the torsion arms is between 4 and 20 µm, depending on the resonant frequency aimed at for the device. The diameter of the mirror is fixed at 500 µm.

There is also a rectangular version of the actuators, clamped at both ends, with a surface equivalent to those of the semi-circular actuators. The rectangular ones are more efficient. Figure 13.6b is an example of simulation of the torsional mode with

a resonance around 10 kHz, excited by rectangular actuators. This torsional mode is the one with the lowest resonance frequency for this device.

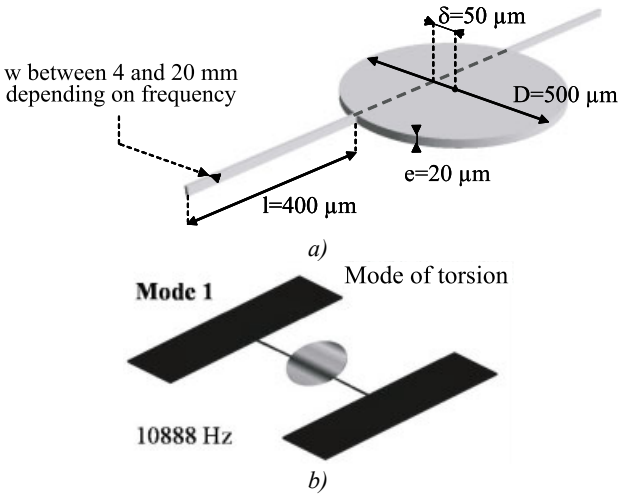

Figure 13.6. *a) Dimensions of the resonant micromirror by design;*
b) simulation of the torsional resonant mode with resonance at about 10kHz

The sequence of technological steps is given in Figure 13.7. The 20 µm thickness of the mirror is ensured by a silicon on insulator (SOI) film of Si. This choice of substrate has the advantage that it provides a very well defined etch-stop on the buried oxide layer for the silicon etch from the rear face. All films are first deposited and structured on the front face (see Figure 13.7a):

– Si oxidation (400 nm);

– lower Pt electrode deposition (150 nm) with a Ti adhesion layer (10 nm);

– PZT deposition (500 nm) by sputtering and annealing at 675°C;

– Plasma-Enhanced Chemical Vapor Desposition (PECVD) Si_3N_4 insulation between the electrodes (450 nm);

– upper Pt electrode (150 nm)/Ti (20 nm)/Au (300 nm).

This last gold film also serves as a reflective surface for the mirror. Thermal oxide and Si_3N_4 are structured by dry etching, inferior platinum by ion milling, PZT by HF/HC1 chemical etching before annealing, Ti by HF etching, upper Pt by lift-off and gold by chemical etching. Trenches are then realized in the SOI layer by deep etching (using the Bosch process, Figure 13.7b). Rear face etching is also

performed by deep etching with etch stop on the buried oxide layer (see Figure 13.7c). The latter is finally dry-etched to release the structure.

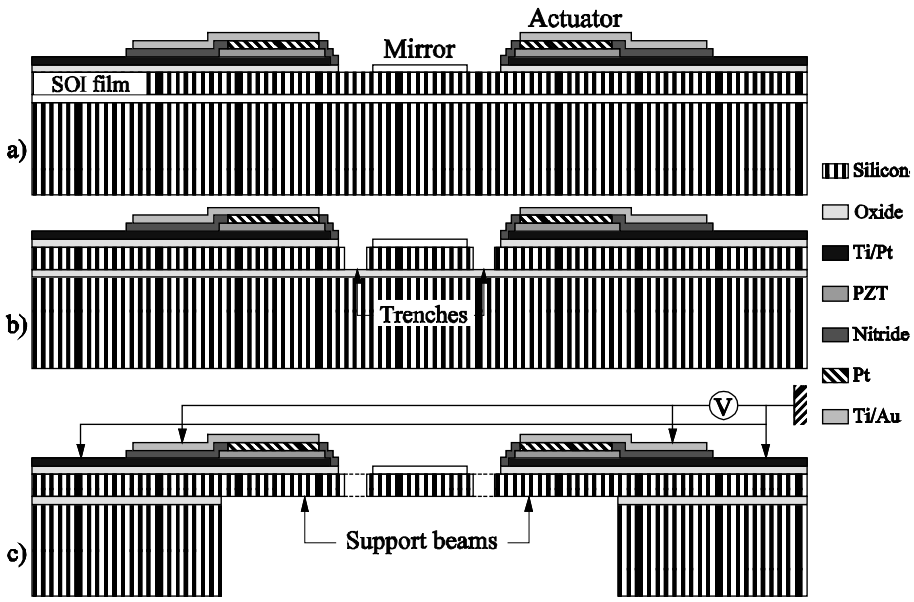

Figure 13.7. *Sequence of technological steps for the fabrication of the resonant micromirror*

13.4.3. *Characterization of the devices*

Owing to the 20 µm mirror thickness, a static deformation <100 nm (a quarter of the minimum optical wavelength used) is measured, which corresponds to the specifications. This deformation is due to residual stresses in the Ti and gold films of the mirror.

The deflection generated by the mirror is measured by projecting the steered optical beam on a screen. The deflection is too large to be measured by a laser vibrometer or an interferometer, which are limited to a few degrees. It must be borne in mind that the optical scanning angle measured is four times the oscillation amplitude of the mirror.

Figure 13.8a shows the optical scanning angle measured for a rectangular actuator structure (width of torsion arms: 8.5 µm) with respect to the amplitude of the alternative signal applied. An offset voltage of +6 V is added to the alternating signal. The shape of the signal of excitation may seem strange, but it is this choice

that gives the best results. The amplitude of the signal is greater than the coercive voltage of the PZT, located between 3 and 5 V.

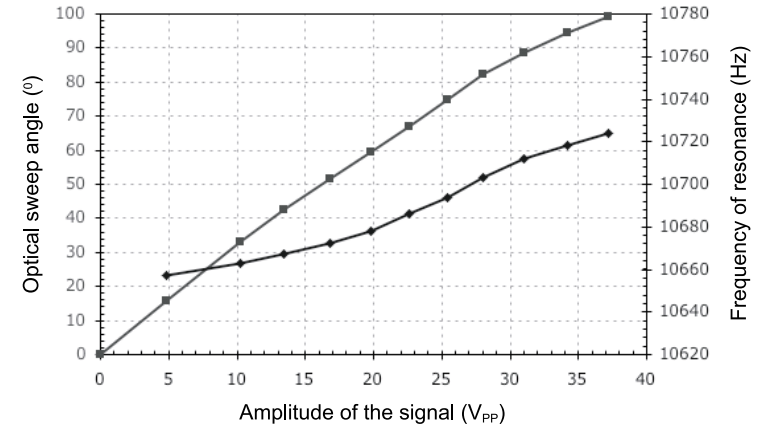

a)

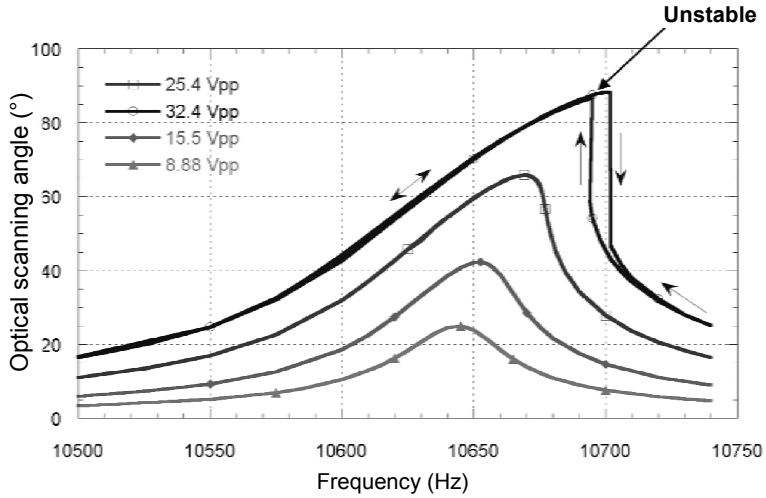

b)

Figure 13.8. *a) Optical scanning angle (light gray) and resonance frequency (dark gray) of a micromirror with rectangular actuators; and b) optical scanning angle in terms of frequency for different amplitudes of excitation, highlighting of nonlinear effects near resonance*

This means that PZT is polarized differently at each signal alternation. For a frequency of excitation, *f*, a mechanical stress due to the piezoelectric effect is

therefore applied at frequency *2f*. This in-plane tensile stress is theoretically of the same value as soon as the applied electric field exceeds the coercive field in the positive or the negative. The mirror therefore behaves as a seesaw on which an identical pulse would be given on each side at each passage. The offset voltage of +6 V limits PZT fatigue. Without this voltage, a rapid decrease in the deflection angle is observed. For a more perennial operation avoiding fatigue, unipolar excitation would be undoubtedly better adapted.

It can be noted that the optical scanning angle can reach 100°, which is very large. The increase in deflection with signal amplitude is linear up to 15 V and slows down after that. Two phenomena contribute to this effect. On one hand, PZT shows a decrease in the piezoelectric effect at high field because of the decrease in mobility of the domains. Piezoelectric strain is equal to the product of the applied electric field and the piezoelectric coefficient, which therefore decreases slightly at high field. On the other hand, the increase in the scanning angle induces an increase in the stiffness of the torsion arms, as proven by the increase in frequency of resonance of the mirror shown on the dark grey curve in Figure 13.8a. This increase in stiffness is modeled by adding a θ^3 term in the equation of movement of the mirror. For the highest amplitudes of excitation, this phenomenon can lead to instabilities near resonance belonging to nonlinear oscillators, as can be seen on Figure 13.8b. It should be noted that the scanning angle in Figure 13.8a was measured for each voltage at the resonant frequency of the system. The quality factor of the torsional mode of resonance is about 300.

13.4.4. *Conclusion about micromirrors*

This study shows that PZT can be integrated in a microsystem with complex technology. The main characteristics of the piezoelectric micromirror are an optical deflection of 100° from a mirror with diameter 500 µm for an electric excitation of 40 V with a frequency close to 10 kHz. These values meet the initial requirements and show real advantages in terms of integration compared to other solutions in the literature: no external coil, unlike the magnetic solutions, and moderate excitation voltage limited to 40 V compared to 250 V for an electrostatic solution.

13.5. Piezoelectric micro-switch

13.5.1. *Interest in piezoelectric films for micro-switches*

For a few years, micro-switches have been greatly studied for nomadic applications for which low consumption constitutes a leading issue. CMOS switches do not perform as well as microsystems because of their higher energy consumption,

bad insulation during the non-conducting state, and high insertion losses during the conducting state at high frequencies. Although potentially very interesting, MEMS micro-switches exhibit extreme integration issues, the cost of which is not the least important. Another issue for these microsystems is operation voltage. Today, a cell phone works with a battery with nominal voltage of 3.6 V, which could be further reduced in the future. It is possible to use charge pumps to increase voltage, but a solution operating at nominal voltage would be a lot closer to integration because it is less costly and more energetically efficient.

There are four major principles for micro-switch actuation: electrostatic, magnetic, thermal and piezoelectric. The electrostatic solution is the most developed. It is well adapted to micro-technologies and uses materials that are well-known in microelectronics, such as doped silicon, silica, silicon nitride and gold [RAD 10]. Consumption is quite low but actuating voltage is high (several tens of volts) because of the quadratic effect of the force applied in terms of distance between the electrodes. The decrease in this voltage needs to move the cell phone switch parts closer, which complicates the technology. Moreover, this technique is particularly sensitive to the charging effect of insulating dielectrics used to avoid contact between electrodes in the conducting state of the switch.

In addition, a distance that is too small between the electrodes harms insulation in the non-conducting state. The magnetic solution lets us reach high contact forces and deflections, but requires an external magnetic field or an integrated coil, inducing a significant consumption [MEI 01]. The thermal solution also gives good results in terms of deflections and contact forces, but the principle based on the Joule effect induces consumption that is not compatible with a nomadic system. The piezoelectric solution is attractive for this particular application because consumption is low and mechanical energy supplied by the piezoelectric film can have the order of magnitude required to actuate and maintain the switch. Technological solutions are complex and rare, but serious studies exist: LG has put forward a completely integrated and packaged piezoelectric micro-switch operating at 5 V [PAR 06].

Although problems remain, the characteristics obtained are interesting, with insertion losses of 0.63 dB in the conducting state and insulation of 26.4 dB at 5 GHz [JAE 06]. More recently, LETI, in collaboration with Freescale, put forward another solution of integrated piezoelectric switches, which will be detailed in the following section.

13.5.2. *General description of the component*

The component developed is a micro-switch whose aim is to block a RF signal in the range of several GHz or let it pass through. The actuating voltage is limited to 5 V. The temperature of use is between -40°C and +80°C. To do this, the idea is to use a piezoelectric actuation that has the advantage of being efficient from low voltages, unlike an electrostatic actuation that requires voltages of a few tens of volts [REB 03]. The device is based on assembling two silicon substrates, as described in Figure 13.9.

All commands occur from the cap substrate. Conductive paths between the two substrates are ensured by Sn-Au vias. The substrates are sealed with the help of Sn-Au alloy. To increase the contact force, and therefore to decrease contact resistance, an electrostatic hold was added to the design. The RF signal crosses the cap substrate and circulates over the mobile beam, as we will see later. The beam is actuated by a PZT piezoelectric thin film.

As the device must operate in a large temperature range, temperature compensation was also anticipated at the stacking level of the actuator.

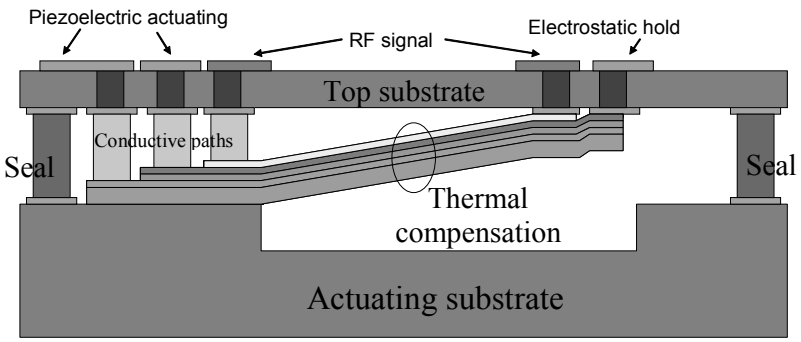

Figure 13.9. *Cross-section of the piezoelectric micro-actuator based on assembling two silicon substrates*

Figure 13.10 represents a top view of the piezoelectric actuator. On the final device, there are two actuators that surround the RF line. There are also two electrostatic holds. The emptied parts between the actuator and the hold as well as the hold and the contact allow stiffness variation of the mechanical structure.

Indeed, as represented in Figure 13.9, it is necessary to let the beam lose its shape for the electrostatic hold to be effective. Moreover, it is also necessary to manage the stiffness of the contact zone.

We will now describe the actuator more precisely.

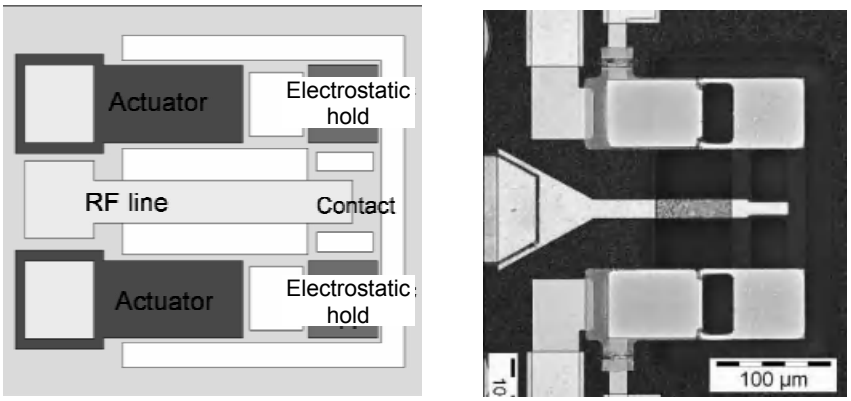

Figure 13.10. *View from the top of the piezoelectric actuator: On the left, the diagram; on the right, the photo of the final device*

13.5.3. *Analytical development of the bimorph beam as actuator of the micro-switch*

Here, we take the case where the mobile part of the micro-switch is made up of a micro beam. This beam is composed of a stack that corresponds to a bimorph in which only a purely elastic film is considered, on which a piezoelectric film is deposited, as shown in Figure 13.11. It is instructive to analyze this core structure of microsystems. This structure has the additional advantage of being able to be analytically modeled.

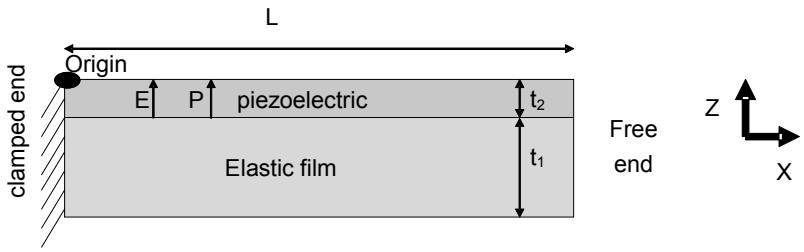

Figure 13.11. *Elastic-piezoelectric bimorphous structure considered*

In the final structure, the contact is located on the free end of the beam. For now, the mechanical role of electrodes and other possible films that are useful for the technology is neglected. The equations of this pure static bimorph bending problem

for which stresses along z and the width are neglected, have been widely developed in the literature, especially by Smits in 1991 [SMI 91]. The principle was developed for the first time by Timoshenko [TIM 68]. The explanation of the equations is based on system equilibrium and the continuity of in-plane strains at the interface between two materials. We assume that there is no sliding between the films constituting the beam. We assume that the beam is at equilibrium, even when it is deformed. In this deformed state, we imagine that this beam is cut along a section perpendicular to *x*. We are interested, for example, in the left-hand part of the section (see Figure 13.12). To maintain pre-established equilibrium, Timoshenko [TIM 68] suggested replacing the influence of the right-hand part of the beam on the left-hand part, by the forces and moments of each material making up the beam, as seen in Figure 13.12.

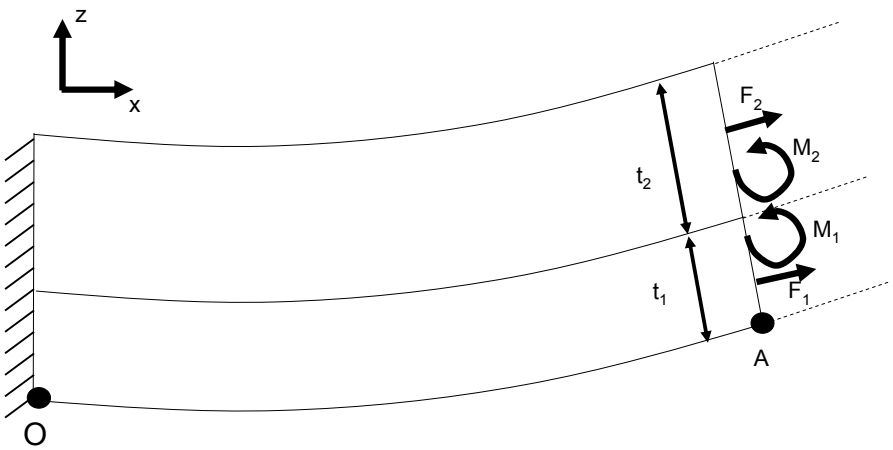

Figure 13.12. *Example of a deformed bimorph bar at equilibrium on which the dotted part was replaced by a set of forces F and moments M*

As the bar is at equilibrium, the sum of applied forces on each material is zero:

$$F_1 + F_2 = 0 \qquad [13.1]$$

In the same way, the sum of bending moments and those resulting from applied forces must be zero. The bending moments of each film are, by definition, equal to *YI/R*, with *Y* being Young's modulus, *I* the area moment of inertia and *R* the radius of curvature. They originate in the resistance of the bended beam when a radius of curvature *R* is applied to each film. We assume that the radius of curvature is the same for each film. In the case of a beam of thickness *e* and width *l* (in direction *y*),

the area moment of inertia is equal to $le^3/12$. Assuming that each force is applied to the center of each film and is perpendicular to the section, we write that the sum of moments is zero, for example at point A (see Figure 13.12):

$$\frac{l_1 Y_1 t_1^3}{12R} + \frac{l_2 Y_2 t_2^3}{12R} = F_1 \frac{t_1}{2} + F_2 \left(t_1 + \frac{t_2}{2} \right) \qquad [13.2]$$

A third equation is given by the continuity of in-plane strains at the interface between the two materials because we assume that there is no sliding between the films. The top film (2) is the piezoelectric film and the bottom film (1) is only elastic. Residual stresses (σ_r) and thermal expansion (coefficient of expansion α) of each film are taken into consideration. In-plane piezoelectric strain S_{1p} is equal to $d_{31}E_3$, with E_3 being the electric field applied:

$$d_{31}E_3 + \alpha_2 (T - T_0) - \frac{\sigma_{r2}}{Y_2} + \frac{F_2}{Y_2 l_2 t_2} + \frac{t_2}{2R} = \alpha_1 (T - T_0) - \frac{\sigma_{r1}}{Y_1} + \frac{F_1}{Y_1 l_1 t_1} - \frac{t_1}{2R} \qquad [13.3]$$

This equation is a bit more complex and deserves a few explanations. The first term is piezoelectric strain (at the very end of this chapter we will look at an important point about the sign of d_{31}). The second term is thermal expansion. The third term is strain due to residual stresses. The sign is negative because in common conventions tensile stresses are positively counted. A tensile stress however, measured for example by the Stoney method, induces a film that wants to hold less space when it can. It therefore induces a negative planar strain. The fourth term is the strain induced by the external force F_2. The fifth term is strain due to the radius of curvature of the piezoelectric film considered alone. Thus, for this contribution, the neutral fiber is in the middle of the piezoelectric film and at the interface the film is elongated, hence the strain in $+t_2/2R$.

Positive R corresponds to an upwards deflection. The argument is identical for the terms on the right-hand side, with the sign of the last term simply being reversed because of the compressive zone of the interface for film 1. Finally, we must note that the thermal expansion term is spotted in relation to the temperature T_0 at which the residual stresses were measured.

The unknowns are therefore F_1, F_2 and R. With three equations, the system must have a solution if its determinant is non-zero. We are only interested in R.

We get:

$$\frac{1}{R} = -\frac{6Y_1Y_2t_1t_2(t_1+t_2)}{Y_1^2t_1^4 + Y_2^2t_2^4 + 2Y_1Y_2t_1t_2(2t_1^2 + 3t_1t_2 + 2t_2^2)}\left(d_{31}E_3 + (\alpha_2 - \alpha_1)\Delta T + \frac{\sigma_1}{Y_1} - \frac{\sigma_2}{Y_2}\right) \quad [13.4]$$

The radius of the curvature is geometrically linked to the first and second derivatives of z in relation to x by:

$$\frac{1}{R} = \frac{\frac{d^2z}{dx^2}}{\left[1 + \left(\frac{dz}{dx}\right)^2\right]^{\frac{3}{2}}} \quad [13.5]$$

In the case of a cantilever structure like the one considered, with small strains the equation above can be simplified to:

$$\frac{1}{R} = \frac{d^2z}{dx^2} \quad [13.6]$$

We can show that this approximation is valid for clamped-freed cantilevers even for very important deflections because the overall rigidity of the structure is not very sensitive to the deformed structure, unlike a clamped-clamped structure. Thus, combining equations [13.4] and [13.6], integrating twice in relation to x, and noting that at the clamp $z(O) = 0$ and $dz/dx(O) = 0$, we have:

$$z(x) = -\frac{3Y_1Y_2t_1t_2(t_1+t_2)x^2}{Y_1^2t_1^4 + Y_2^2t_2^4 + 2Y_1Y_2t_1t_2(2t_1^2 + 3t_1t_2 + 2t_2^2)}\left(d_{31}E_3 + (\alpha_2 - \alpha_1)\Delta T + \frac{\sigma_1}{Y_1} - \frac{\sigma_2}{Y_2}\right) \quad [13.7]$$

This equation shows that the piezoelectric, thermal and residual stress effects have the same impact on the beam deflection. It is therefore essential to be able to neglect the parasitic effects of the piezoelectric motor for an integrated technological solution.

Here are a few examples using data to define the orders of magnitude. Electrical voltage is fixed at -3 V. Piezoelectric materials can be AlN or PZT. Elastic films can be SiN or SiO_2. The useful physical properties of these materials are reported in Table 13.3. The values shown are measured on materials developed at LETI, with

the exception of the coefficient of thermal expansion (CDT) of AlN originating in the literature. Young's moduli are measured by nano-indentation [DEL 06] for PZT and SiO_2 and by picosecond ultrasonics [DEV 06] for AlN and SiN. Actually, nano-indentation gives correct values provided that the probed material is not as stiff as the substrate, which is not the case of SiN and AlN. Residual stresses are measured by the wafer curvature method, called the Stoney method [STO 09]. For PZT, we confirmed measurement by X-ray diffraction with the $\sin^2\psi$ method [KUI 03]. TCE (Temperature Coefficient of Expansion) is obtained by measuring the curvature of a substrate with the probed film at different temperatures (Stoney temperature).

The piezoelectric coefficient d_{31} is deduced from measurements of e_{31} and measurements from Young's moduli.

Material	**Young's Modulus (GPa)**	**Coefficient of thermal expansion (ppm/°C)**	**Residual stresses (MPa)**	**d_{31} (pm/V)**
AlN	300	5	-450/0	-2.5
PZT	120	9.2	200	-80
SiN	220	2.1	400-1,000	-
SiO_2	70	0.4	-280	-

Table 13.3. *Typical physical properties of films susceptible to being part of the piezoelectric bimorph*

Figure 13.13a gives the deflection calculated at the free end of a 150 µm-long SiN/PZT beam, with a SiN thickness of 1.2 µm with compensation for stresses and temperature effects obtained by adjusting PZT thickness for a voltage of -3 V. Deflection increases when PZT thickness decreases and reaches 3.3 µm for a PZT thickness of 100 nm. Actually, for a given voltage, the field applied to the PZT increases in a manner that is inversely proportional to thickness. Therefore, at a given voltage, if the piezoelectric thickness decreases, the piezoelectric stress imposed in the PZT increases in the same way. The piezoelectric force, which is the product of the stress by the driving section, remains constant because the increase in stress is compensated by a decrease in the driving section. Actually, the increase in deflection comes, on one hand, from moving the driving zone away from the neutral fiber of the beam, which induces an increase in the driving moment; and on the other

hand by the decrease in stiffness of the beam, which is proportional to the cube of the total thickness.

Figure 13.13b gives the deflection calculated from the same beam in terms of PZT thickness, by adjusting the SiN thickness in order that the stiffness of the beam is always the same (Smits equations [SMI 91]). This curve confirms that for a given voltage, at constant stiffness, optimum deflection is obtained for the smallest possible thickness of piezoelectric material. At negligible piezoelectric thickness, the gain becomes zero because at constant stiffness only neutral fiber removal plays a role in the increase in deflection. As thickness is very low, distance variation is also low.

According to this calculation, optimal thickness is fixed by the breakdown field of the material. Typically, PZT has a breakdown field of 1 MV/cm, which gives a thickness of 30 nm at 3 V. A thickness of 100 nm therefore supports about one-third of the maximum field applicable on the PZT.

However, this calculation assumes that the piezoelectric properties are constant with thickness, which is far from being the case, especially for PZT. Most papers published on thin-film coefficients focus on thicknesses of about 1 µm, but the drop in d_{33} with thickness was observed by several teams, especially by Rèmiens *et al.* for PZT [RÈM 02] and Martin *et al.* for AlN [MAR 04]. Moreover, applying such a great field to PZT induces exceeding the coercive field: the voltage therefore poles the PZT each time. This can be interesting for avoiding fatigue but as field and polarization are always in the same direction, the applicable stress always has the same sign and the beam can only go upwards in the example given.

For micro-actuator application, beam stiffness plays an important role as it fixes the restoring force coming from the elastic energy stored in the beam. This force avoids sticking to the contact. For a width of 70 µm, the beam described in Figure 13.13b has a stiffness of 2.2 N/m. The maximum energy stored in the beam for a deflection of 3.3 µm is therefore around 10 pJ. If this energy is shared between the contact force and the restoring force, these are in the order of 3 µN. This value is quite low for the contact force and it is better to avoid reducing it in order to limit contact resistance. The deflection obtained (3 µm) is in the order of magnitude it is possible to master technologically. It is therefore difficult to reduce this. For this reason, we have the orders of magnitude of geometrical parameters for this problem.

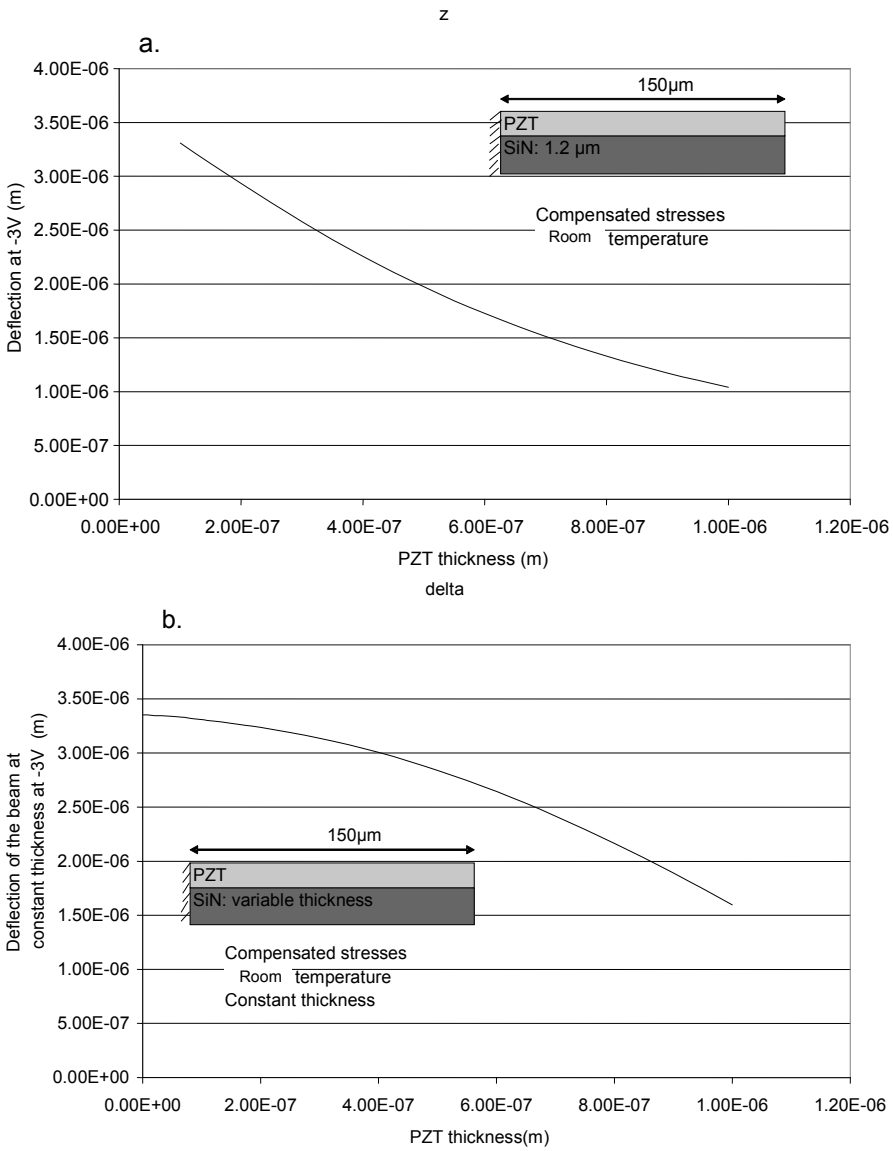

Figure 13.13. *a) Deflection calculated at -3 V of a SiN-PZT 150µm-long beam with compensated stresses and at room temperature in terms of PZT thickness; and b) same calculation as curve a) but adjusting SiN thickness in order to have a constant beam thickness*

We can now discuss the effects of residual stresses and temperature on deflection of the beam. Figure 13.14 gives deflection measured at 0 V for the same beam described before with 100 nm PZT; in terms of residual stresses in SiN at room temperature for the curve in Figure 13.14a, and in terms of a deviation in temperature compared to room temperature for compensated stresses for the curve in Figure 13.14b. The range of stress is 100 MPa and the starting point (400 MPa) corresponds to the minimum stress that can be displayed by LPCVD SiN (compatible at 700°C). Adjustment of this stress occurs during deposition (LPCVD nitride) by inserting more or less Si. We see that it is not possible with this beam to compensate for these initial stresses and that the initial deflection is 1 µm downwards. Moreover, an error of 50 MPa on the stress leads to a deflection change of 1 µm. Knowing that piezoelectric deflection is 3.3 µm, the effect of residual stresses is therefore not at all negligible.

Viewing equation [13.7], stress equilibrium is only possible between films that have the same stress sign, independently of thicknesses. Thus, using SiO_2 that is still in compression as an elastic film with PZT cannot enable us to have a straight beam.

Concerning the effect of temperature, a change of 120°C (operation between -40°C and 80°C, for example) can result in a change in the initial position of the 3 µm bimorph beam, which is of the same order of magnitude as piezoelectric deflection. For this calculation, we take room temperature as the reference because residual stresses were measured at this temperature.

The effect of temperature on the initial position must be compensated for because, unlike residual stresses for which the design can enable us to work without a straight initial beam, it is not possible to avoid the change in temperature of the integrated object.

To end this discussion on equation [13.7], we must note that if we factorize the expression by the inverse of the piezoelectric thickness $1/t_2$, we obtain a constant piezoelectric term ($d_{31}V$) added to the terms of thermoelastic and residual stresses, which are both multiplied by t_1.

Therefore, still for a given voltage, the thinner the piezoelectric is, the lower the negative effect of thermoelastic and residual stresses.

For AlN, the difficulty is greater because the piezoelectric coefficient is 20 times lower than PZT. If we suppose a bimetallic AlN/SiO_2 bimorph to balance the stresses (thin AlN and SiO_2 exhibit compressive stresses) with the same stiffness as the bimetallic SiN/PZT bimorph above, and AlN as thin as possible (30 nm, because the breakdown field is at least three times higher than PZT), deflection at 3 V is 0.5 µm.

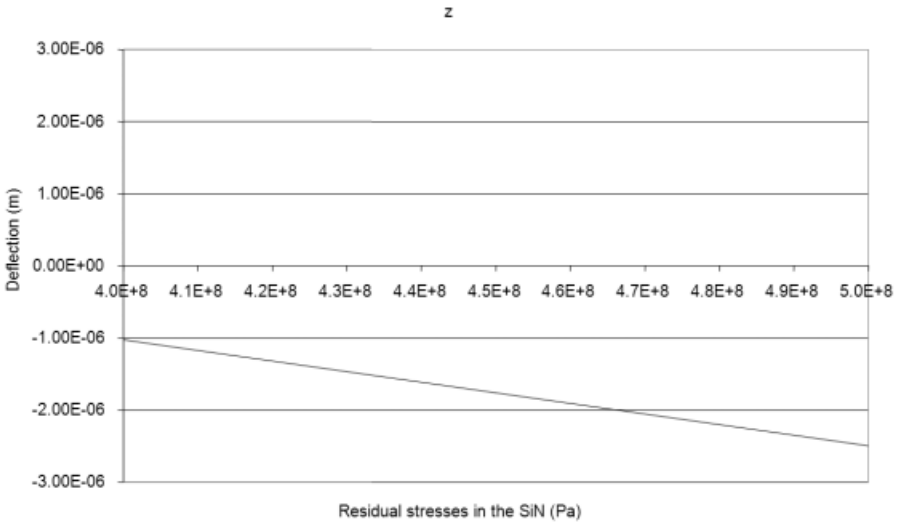

a) Room temperature and V = 0

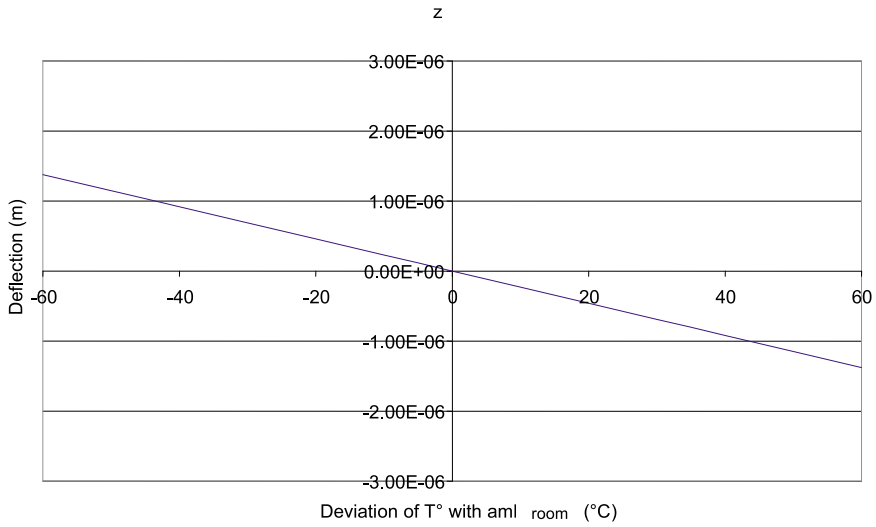

b) Compensated stresses: V = 0

Figure 13.14. *a) Deflection measured at 0 V for the same beam described above with 100 nm of PZT in function of residual stresses in SiN at room temperature; and b) in terms of a temperature variation with room temperature for compensated stresses*

The negative effects of residual stresses and temperature expansion are even more important in the case of AlN, because they are of the same order of magnitude in the two configurations.

In summary, integrating a bimorph beam for a micro-switch requires a specific control of stresses in each layer and the role of electrodes can no longer be neglected (Pt is very tensile).

Moreover, the working device needs a temperature insensitivity that is not the case described for the bimorphs. The use of thermal compensation solutions therefore turns out to be essential. There are linear analytical models that take into consideration a much larger number of films [HSU 06].

Nonlinear treatment can be ensured by simulation tools. The optimal solution put forward imposes high piezoelectric coefficients with low thickness, around 100 nm.

13.5.4. *Stack chosen for the piezoelectric actuator*

Details of the stack are given in Figure 13.15. It is quite complex because it integrates the actuator itself (Pt/PZT/Pt), an adhesion layer (TiO_2), an antidiffusion layer (SiO_2), the mechanical layer that ensures the bimorph effect with the PZT actuator (low stress SiN), a thermal compensation layer (TiN) and a SiO_2 film that protects the TiN during the actuator release (performed by XeF_2). The polysilicon layer increases the speed of release.

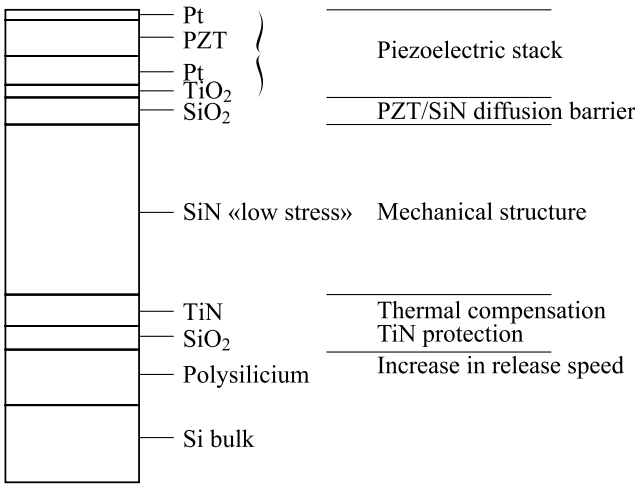

Figure 13.15. *Stack chosen for the piezoelectric actuator*

We see that this stack is quite complex and requires very good control of each one of the films as well as a reliable model. The silicon substrate has a very high resistivity. This property reduces resistive losses at RF frequencies.

13.5.5. *Multilayer analytical model*

After release, the beam is composed of eight layers. Beam deflection after release must be much smaller than the gap defined by the packaging (5 µm), just as for deflection variation over the temperature range.

Despite the complexity of the problem, beam deflection can be given thanks to a rather simple analytical model whose equations we will describe. The use of this model assumes that the mechanical and thermal characteristics (Young's modulus, stresses) of each material (coefficient of thermal expansion) are well-known.

It is possible to use the extension of the model developed above with two layers. However, this approach forces us to inverse a n x n matrix, where n is the number of layers. The formula obtained becomes extremely hard to simplify. Hsueh's model [HSU 02a] enables us to have a general formula regardless of the number of films used. The originality of this model is to explicitly calculate the beam average strain in the length c (uniform strain component) direction and the bending axis position t_b, which enables us to simplify the equations at the end.

Figure 13.16 shows notations following direction z, perpendicular to the beam length. It is a one-dimensional model for which a constant radius of curvature R is considered along the beam.

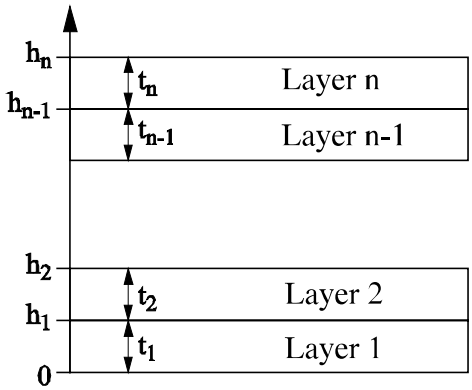

Figure 13.16. *Notations used for the multilayer model*

Deflection δ at the end of the L long beam is given by the following formula, with the same assumptions as in the case above with two layers:

$$\delta = \frac{L^2}{2R} \qquad [13.8]$$

Indeed, by assuming that the problem is linear, the radius of curvature is given as the inverse second derivative of z in relation to x. After calculation, c, t_b and R are given by the following formulae:

$$c = \frac{\sum_{i=1}^{n}\left(E_i d_{31i} V_i + E_i \alpha_i t_i \Delta T - \sigma_{ri} t_i\right)}{\sum_{i=1}^{n}\left(E_i t_i\right)}$$

$$t_b = \frac{\sum_{i=1}^{n} E_i t_i \left(2h_{i-1} + t_i\right)}{2\sum_{i=1}^{n} E_i t_i}$$

$$\frac{1}{R} = \frac{3\left(\sum_{i=1}^{n} E_i t_i \left(2h_{i-1} + t_i\right)\left(\alpha_i \Delta T + d_{31i}\frac{V_i}{t_i} - \frac{\sigma_{ri}}{E_i} - c\right)\right)}{\sum_{i=1}^{n} E_i t_i \left(6h_{i-1}^2 + 6h_{i-1}t_i + 2t_i^2 - 3t_b\left(2h_{i-1} + t_i\right)\right)} \qquad [13.9]$$

where:

– Y_i: Young's modulus of film i;

– t_i: thickness of film i;

– L: length of the bimorph;

– d_{31}: transverse piezoelectric coefficient (negative here);

– α_i: coefficients of heat expansion of film i;

– ΔT: difference in T° between working temperature and reference temperature;

– σ_i: residual stress in film i measured at reference temperature;

– V_i: applied voltage (positive here).

The results of this model are very similar to experimental results and to FEM (Finite Element Model) simulation. We must note that this comes from the fact that we are studying a simple cantilever structure. Indeed, this structure enables us to release stresses in the structure without modifying its stiffness. A full fixed beam and membrane are devices that are much trickier to model analytically. The use of FEM is therefore often recommended.

13.5.6. *Effect of temperature compensation*

Figure 13.17 represents a measurement of a compensated and released beam over a temperature range of 60°C. The stack used is the one given in Figure 13.15, with a wise choice of thicknesses.

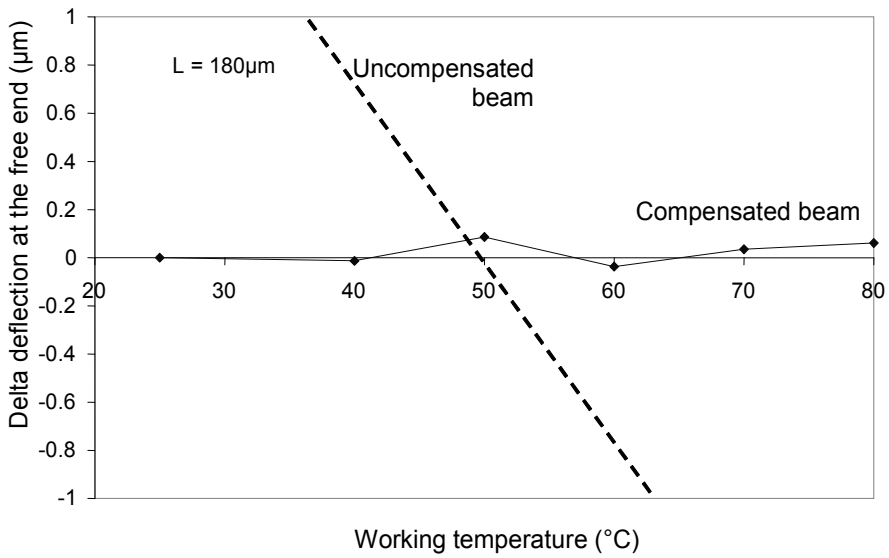

Figure 13.17. *Experimental measurement of a temperature compensated beam, represented with the calculation of an un-compensated beam*

On the same curve the deflection calculated for an uncompensated beam is given. For this one, deflection over +60°C is -5 µm, which is equal to the distance run through by the contact. We therefore notice that this compensation is mandatory for the device to be temperature functional.

13.5.7. *The piezoelectric film*

The piezoelectric film is a PZT film deposited by sol-gel method and air-annealed at 650°C. The final thickness of the film is 120 nm. Three layers deposited by spin-coating were necessary to achieve this thickness.

A cross-section of this stack is given on the left in Figure 13.18. PZT is dense and non-porous. In the top view, 100 nm wide grains are observed. The crystalline orientation of this film is (111), which is not optimal. To get a (100) orientation, it is possible to add a nucleation layer before PZT deposition. This nucleation layer can be a $PbTiO_3$ film a few tenths of a nm deposited by the sol-gel method.

Piezoelectric characterization of this PZT film by the direct method of the vibrating beam showed an e_{31} reaching -5 C/m², which is completely acceptable for such a thin PZT film. The choice of a very thin piezoelectric film is based on the fact that we want to keep a high electric field (greater than the coercive field) in the PZT film with 5 V. This enables us to have a material poled by the working voltage and to solve the PZT depolarization problem that appears during component packaging (part of the process at 260°C, which depolarizes the material).

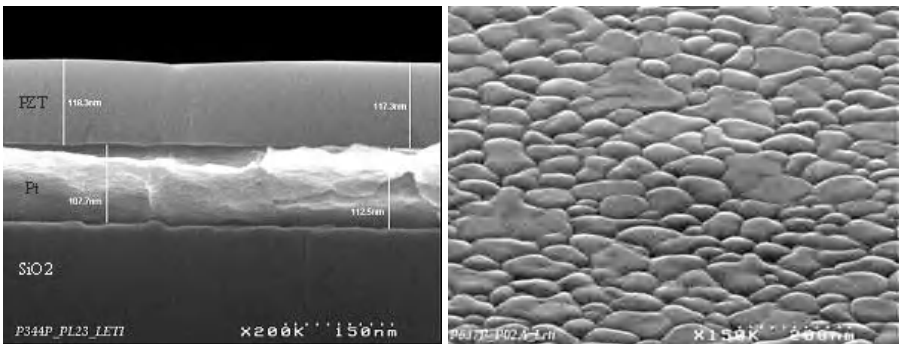

Figure 13.18. *Cross-section view (left) and top view (right) of the PZT film deposited for the piezoelectric actuator*

13.5.8. *Releasing the membrane*

The membrane is released by the XeF_2 gas process, which etches the silicon with a velocity that can reach several μm per minute.

In this device, extra subtlety involved adding SiO_2 walls to stop the etching. This enables us to precisely determine the dimensions of the structure, as shown in Figure 13.19, as well as improve the quality of anchoring.

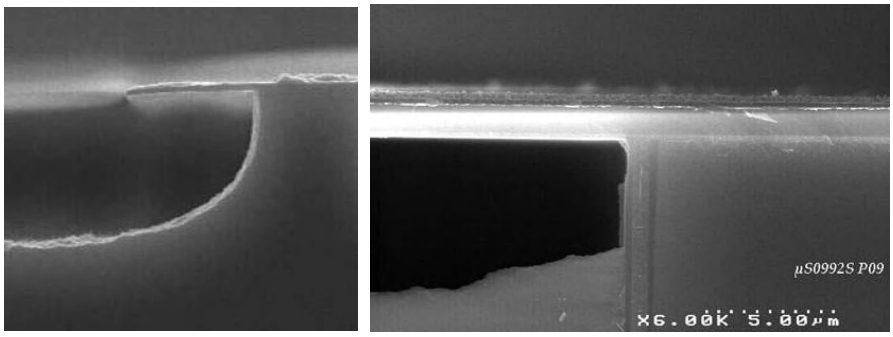

a) *b)*

Figure 13.19. *a) Isotropic etching of silicon by XeF_2; and b) etching stop thanks to SiO_2 walls on the right*

13.5.9. *Electrical characterizations*

13.5.9.1. *Measurement deflection of the actuator using the piezoelectric effect*

Measurement of the deflection obtained by the piezoelectric effect during the application of a constant voltage is realized before sealing the two substrates in order to optically measure the deflection at the beam free-end.

The measuring device is a light interferometer (Wyko) and the result is represented in Figure 13.20. A hysteresis effect due to the ferroelectric nature of PZT is observed. This induces a repolarization of the material during application of a voltage greater than the coercive voltage, which is located here around 1 V. At these voltages (-1 V and +1 V), the material is depolarized and therefore no longer displays the piezoelectric effect.

Maximal deflection is around 7 µm. To calculate e_{31} by this method we used the previous analytical method that gives -5 C/m² for a voltage of 1 V, in perfect agreement with the direct method of the vibrating beam. We must note that maximum deflection is always upwards, which is also due to the ferroelectric nature of PZT. Indeed, a high field applied on the PZT leads to polarization in the same direction as the electric field. Strain induced by the piezoelectric effect is of the same sign when the field and polarization are aligned. We therefore notice that it is

not possible in this case to use the piezoelectric effect to obtain a deflection downwards.

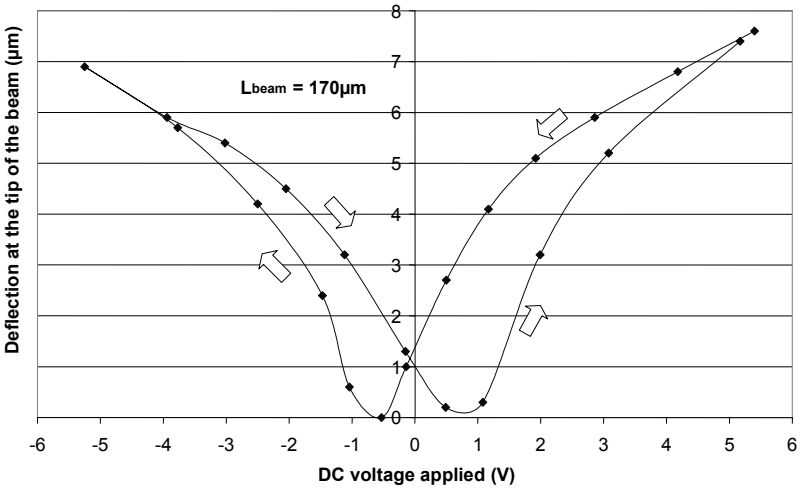

Figure 13.20. *Optical measurement of deflection of the 170 µm-long beam*

To illustrate the orders of magnitude, in Figure 13.21, we present the deflection observed (7 µm) at the tip of the 170 µm-long film by a scanning electron microscope during *in situ* application of a 5 V voltage.

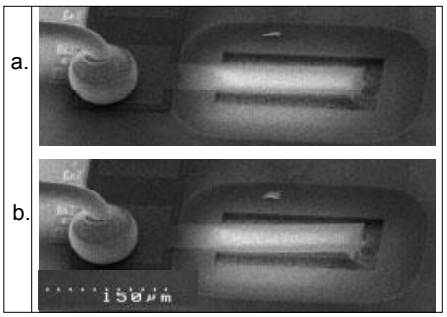

Figure 13.21. *Scanning electron microscope view of a piezoelectric film: a) at 0 V; b) at 5 V*

13.5.9.2. *Radiofrequency tests*

Figure 13.22 represents a schematic view of the implemented RF test. The S_{21} signal that crosses the switch in the conducting and non-conducting case is

measured. Contact is closed by voltage application to the PZT capacitor. Moreover, the contact force is enhanced by voltage application to the electrostatic hold. S_{21} is commonly called insertion losses.

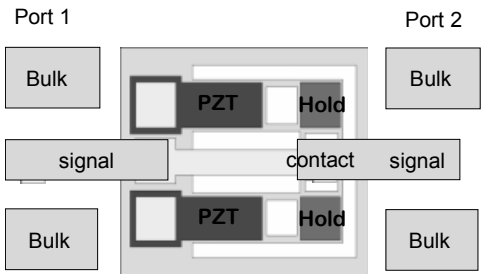

Figure 13.22. *Operational diagram of the RF test (top view)*

In Figure 13.23, the S_{21} signal (representation of the signal quantity that crosses the structure from port 1 to port 2) is observed in the conducting case. By applying a 5 V bias to the PZT, contact occurs and S_{21} reaches -0.83 dB. By applying an additional 5 V to the electrostatic support, S_{21} reaches -0.74 dB, improving the insertion losses by almost 0.1 dB. Furthermore, return losses (S_{11}) reach 27 dB at 2 GHz, which could be improved by optimizing the gold line through which the RF signal passes. When no voltage is applied to the PZT, 20 V is necessary to contact the switch with the electrostatic support only.

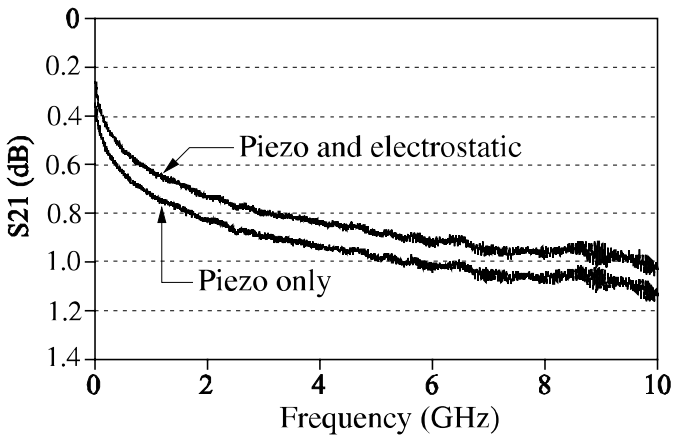

Figure 13.23. *S_{21} in the conducting case: a 5 V direct voltage is applied to the PZT (piezo only) and 5 V applied simultaneously to the PZT and the electrostatic support (piezo and electrostatic hold)*

When the switch is not conducting, insulation is measured by using S_{21}. Thanks to the wide space between the contact and the line (5 µm), this insulation reaches 43.6 dB at 2 GHz (see Figure 13.24). It is this characteristic that is particularly interesting for these devices compared to solid-state switches.

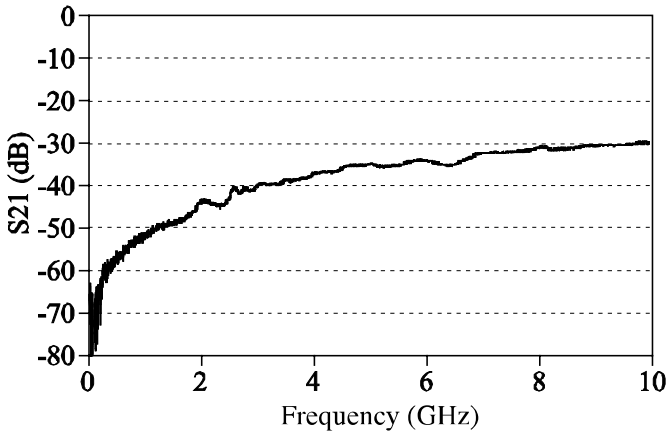

Figure 13.24. *Insulation in the case of a non-conducting switch*

Losses due to the influence of surrounding silicon only are measured by implementing RF lines, but without a switch. Insertion losses in this case reach -0.6 dB, which is considerable. This proves that the losses induced by contact with 5 V above PZT and the support are equal at $0.74 - 0.6 = 0.14$ dB. To improve this device, it is therefore essential to work on the losses due to the switch environment represented mainly by the two silicon substrates, even if we already use high resistivity substrates. Glass substrates could be an attractive solution.

Finally, this device presents remarkable characteristics for a voltage of 5 V [CUE 10].

13.6. Sign of piezoelectric coefficients

It is important to make a note about the sign of piezoelectric coefficients, especially in the case of actuators where it can be interesting to find in which direction the mobile part will go! Actually, it is common to consider positive d_{33} and negative d_{31}. In practice, it is not so simple and we should be careful. In the case of polar materials such as AlN, these signs depend on crystalline orientation. Let us take the following example (see Figure 13.25). Polarization is upwards. Axis 3 is considered to be positive upwards. Thus, when a positive voltage is applied, charges

on the electrodes are face-to-face with the polarization charges with the same sign in the dielectric. We easily imagine that the charges repel each other. The material then undergoes a decrease in its thickness by indirect piezoelectric effect. The strain S_3 that is deduced is therefore negative. As we took a positive voltage, the field E_3 is negative. Thus, as $S_3 = d_{33}E_3$, d_{33} is positive. We directly deduce that if S_3 is negative then S_1 is positive (crushing thickness inducing an in-plane lengthening). As $S_1 = d_{31}E_3$, then d_{31} is negative.

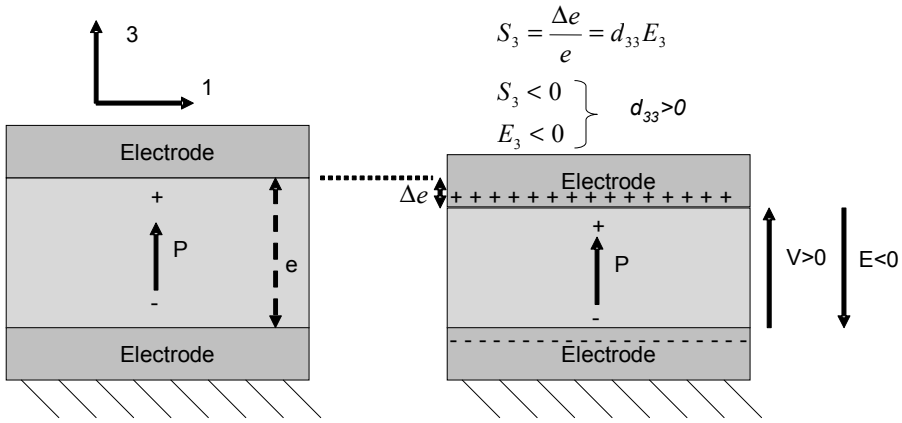

Figure 13.25. *Example of verification of the sign of the piezoelectric coefficient d_{33} in the case of a polar material with positive polarization along axis 3 (AlN type)*

If we now come to reverse polarization in the material, leaving all other parameters equal, then strain S_3 becomes positive because the opposite charges will attract each other. d_{33} then becomes negative and therefore d_{31} positive. It turns out that it is common to have downward AlN polarization when it is deposited by sputtering. d_{33} is therefore negative.

For ferroelectric materials, the fact that polarization is controllable by the electric field adds a difficulty, especially for thin films. Actually, for these films, it is very common to apply a voltage inducing an electric field greater than the coercive field. This voltage then repolarizes the ferroelectric. In this case, electric field and polarization are in the same direction, regardless of the sign of the electric field.

Let us recreate the scenario above with this argument. Let us first assume the voltage is positive (see Figure 13.26). As we assume that the electric field is greater than the coercive field, material polarization follows the electric field, therefore orienting itself downwards. In this configuration, identical to the electrostrictive

case, S_3 is positive (out-of-plane inflation of the material). As E_3 is negative, d_{33} is negative, and therefore d_{31} is positive.

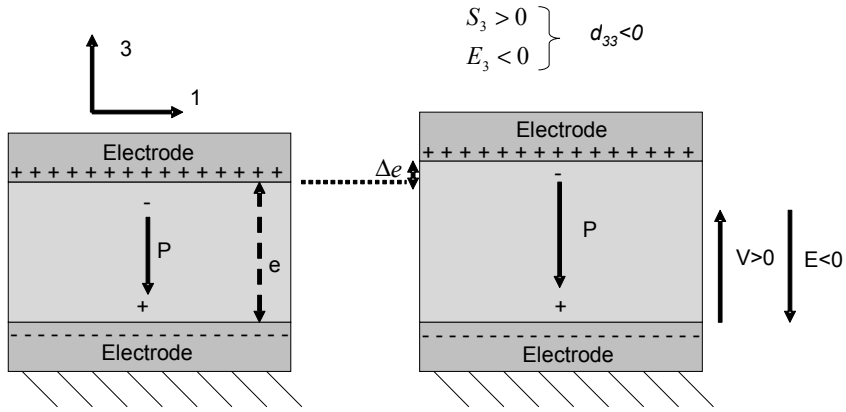

Figure 13.26. *Verification of the sign of d_{33} in the case of a ferroelectric material to which a positive voltage greater than coercive voltage is applied*

Now let us reverse the sign of the voltage applied, which then becomes negative (see Figure 13.27). Polarization follows the field and therefore becomes positive. In this case, as field and polarization are in the same direction, strain S_3 is also positive. As the field is positive, then d_{33} is positive and d_{31} negative.

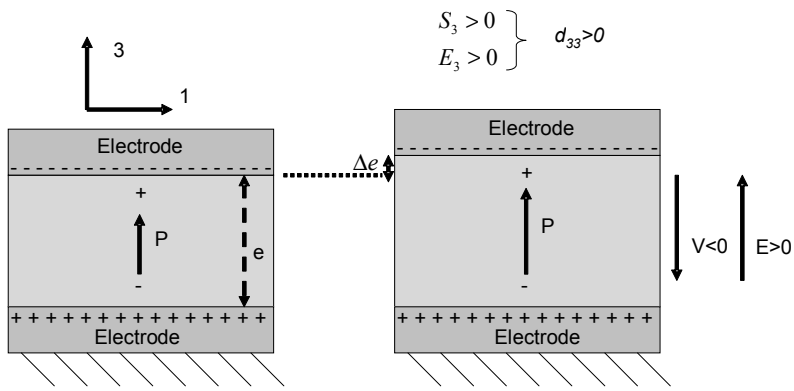

Figure 13.27. *Verification of the sign of d_{33} in the case of a ferroelectric material to which a negative voltage with absolute value greater than coercive voltage is applied*

Therefore, in the case of ferroelectric thin films to which an electric voltage greater than coercive voltage is applied, a rule of thumb is that voltage and d_{31} have the same sign.

13.7. Bibliography

[CON 00] CONANT R.A., NEE J.T., LAU K.Y., MULLER R.S., *Technical Digest*, *Solid-State Sensor & Actuator Workshop*, Hilton Head, SC, USA, 6, 4-8 June 2000.

[CUE 10] CUEFF M., DEFAŸ E., REY P., LE RHUN G., PERRUCHOT F., FERRANDON C., MERCIER D., DOMINGUE F., SUHM A., AÏD M., LIU L., PACHECO S., MILLER M., "A fully packaged piezoelectric switch with low voltage actuation and electrostatic hold", *MEMS 2010*, Hong Kong, 2010.

[DEF 02] DEFAY E., MILLON C., MALHAIRE C., BARBIER D., *Sensors and Actuators A,* vol. 99, n° 1-2, 64, 2002.

[DEL 06] DELOBELLE P., FRIBOURG BLANC E., REMIENS D., *Thin-Solid-Films*, vol. 515, n° 4, 1385, 2006.

[DEV 06] DEVOS A., EMERY P., CARUYER G., ANCEY P., *IEEE-Ultrasonics-Symposium*, 2006.

[DUB 98] DUBOIS M.A., MURALT P., "PZT thin film actuated elastic fin micromotor", *IEEE Trans. UFFC*, vol. 45, 1169, 1998.

[DUB 99] DUBOIS M.A., MURALT P., *Sensors and Actuators A*, vol. 77, 106, 1999.

[FIL 05] FILHOL F., DEFAŸ E., DIVOUX C., ZINCK C., DELAYE M.T., *Sensors and Actuators A*, vol. 123, 483, 2005.

[FLY 92] FLYNN A.M., TAVROW L.S., BART S.F., BROOKS R.A., EHRLICH D.J., UDAYAKUMAR K.R., CROSS L.E., *Journal of Electromechanical Systems*, vol. 1, 44, 1992.

[FUJ 96] FUJII T., WATANABE S., *Applied Physics Letters*, vol. 68, 467, 1996.

[GRO 03] GROSS S.J., TADIGADAPA S., JACKSON T.N., TROLIER-LC KINSTRY S., ZHANG Q.Q., *Applied Physics Letters*, vol. 83, n° 1, 174, 2003.

[HDO 94] DO H., ATSUKI T., SOYAMA H. *et al.*, *Japanese Journal of Applied Physics*, vol. 33, Part 1, n° 9B, 5159, 1994.

[HEE 05] HEE C.L., JAE H.P., HYO J.N., JONG U.B., *Journal of Micromechanical System and Microengineering*, vol. 15, 2098, 2005.

[HSU 02a] HSUEH C.H., "Thermal stresses in elastic multilayer systems", *Thin Solid Films*, vol. 418, 182-188, 2002.

[HSU 02b] HSUEH C.H., *Thin Solid Films*, vol. 418, 182, 2002.

[HSU 02c] HSUEH C.H., *Journal of Applied Physics*, vol. 91, n° 12, 9652, 2002.

[HSU 06] HSUEH C.H., LUTTRELL C.R., CUI T., *Journal of Micromechanical Systems and Microengineering*, vol. 16, 2509, 2006.

[JAE 06] JAE H.P., HEE C.L., YONG H.P., YONG D.K., CHANG H.J., JONGUK B., HYO J.N., *Journal of Micromechanical Systems and Microengineering*, vol. 16, 2281, 2006.

[JAK 03] JAKKARAJU R., HENN G., SHEARER C., HARRIS M., RIMMER N., RICH P., *Microelectronic Engineering*, 70(2-4), 566, 2003.

[KUI 03] KUI Y., SHUHUI Y., HOCK TAY F.E., *Applied Physics Letters*, vol. 82, n° 25, 4540, 2003.

[LED 02] LEDERMANN N.G., PhD Thesis, Ecole polytechnique fédérale de Lausanne, 2002.

[LED 03] LEDERMANN N., MURALT P., BABOROWSKI J., GENTIL S., MUKATI K., CANTONI M., SEIFERT A., SETTER N., *Sensors and Actuators A*, vol. 105, 162, 2003.

[MAE 97] MAEDA R., LEE C., SCHROTH A., *Materials Research Society Proceedings*, vol. 44, 233, 1997.

[MAN 95] MANDLE J., LEFORT O., MINGEON A., *Sensors and Actuators A*, vol. 46-47, p. 129-132, 1995.

[MAR 04] MARTIN F., MURALT P., DUBOIS M.-A., PEZOUS A., *Journal of Vacuum Science and Technology A*, vol. 22, n° 2, 361, 2004.

[MEI 01] MEICHUN R., JUN S., WHEELER C.B., *Journal of Microelectromechanical Systems*, vol. 10, n° 4, 511, 2001.

[MIY 01] MIYAJIMA H., ASAOKA N., ARIMA M., MINAMOTO Y., MURAKAMI K., TOKUDA K., MATSUMOTO K., *IEEE Journal of Microelectromechanical System*, vol. 10, 418, 2001.

[MUR 95a] MURALT P., KHOLKIN A., KOHLI M., BROOKS K.G., LUTHIER R., *Integrated Ferroelectrics*, vol. 11, 213, 1995.

[MUR 95b] MURALT P., KOHLI M., MAEDER T., KHOLKIN A., BROOKS K., SETTER N., LUTHIER R., *Sensors and Actuators A*, vol. 48, n° 2, 157, 1995.

[MUR 98] MURALT P., MAEDER T., SAGALOWICZ L. *et al.*, *Journal of Applied Physics*, vol. 83, n° 7, 3835, 1998.

[MUR 09] MURALT P., POLCAWICH R.G., TROLIER MCKINSTRY S., "Piezoelectric thin films for sensors, actuators and energy harvesting", *MRS Bulletin*, vol. 34, 658, 2009.

[OUY 05] OUYANG J., RAMESH R., ROYTBURD A.L., *Applied Physics Letters*, vol. 86, 152901, 2005.

[PAR 06] PARK J.H., LEE H.C., PARK Y.H., KIM Y.D., JI C.H., BU J., NAM H.J., *J. Micromech. Microeng.*, vol. 16, 2281, 2006.

[POL 96] POLLA D.L., FRANCIS L.F., *MRS Bulletin*, vol. 21, n° 7, 59, 1996.

[RAD 10] Available at the following address http://www.radantmems.com.

[REB 03] REBEIZ G.M., *RF MEMS Theory*, *Design and Technology*, Wiley Interscience, Hoboken, 2003.

[REM 02] REMIENS D., CATTAN E., SOYER C., HACCART T., *Materials Science in Semiconductor Processing*, vol. 5, n° 2-3, 123, 2002.

[SMI 90] SMITS J.G., CHOI W.S., *1990 Ultrasonics Symposium*, 1278, 1990.

[SMI 91] SMITS J.G., DALKE S.I., COONEY T.K., *Sensors and Actuators A*, vol. 28, n° 1, 41, 1991.

[STO 09] STONEY G.G., *Proceedings of the Royal Society of London*, vol. 82, 172, 1909.

[TAD 09] TADIGADAPA S., MATETI K., "Piezoelectric MEMS sensors: state of the art and perspectives", *Measurement Science and Technology*, vol. 20, 092001, 2009.

[TAN 04] TANI M., AKAMATSU M., YASUDA Y., FUJITA H., TOSHIYOSHI H., *Proceedings of the Optical MEMS 2004*, *IEEE*, vol. 188, 2004.

[TIM 68] TIMOSHENKO S.P., *Résistance des matériaux*, Dunod, Paris, 1968.

[VEL 99] VELU G., REMIENS D., *Journal of the European Ceramic Society*, vol. 19, n° 11, 2005, 1999.

[ZIN 04] ZINCK C., PINCEAU D., DEFAY E., DELEVOYE E., BARBIER D., *Sensors and Actuators A*, vol. 115, n° 2-3, 483, 2004.

List of Authors

Sylvain BALLANDRAS
FEMTO St
France

Nizar BEN HASSINE
CEA LETI Minatec
Grenoble
France

Christophe BILLARD
CEA LETI Minatec
France

Emilien BOUYSSOU
STMicroelectronics
St Tours
France

Matthieu CUEFF
CEA LETI Minatec
France

Emmanuel DEFAŸ
CEA LETI Minatec
Grenoble
France

Chrystel DEGUET
CEA LETI Minatec
Grenoble
France

Fabien FILHOL
CEA LETI Minatec
Grenoble
France

Brice IVIRA
CEA LETI Minatec
Grenoble
France

Gwenaël LE RHUN
CEA LETI Minatec
Grenoble
France

Mathieu PIJOLAT
CEA LETI Minatec
Grenoble
France

Alexandre REINHARDT
CEA LETI Minatec
Grenoble
France

Patrice REY
CEA LETI Minatec
Grenoble
France

Alexandre VOLATIER
TriQuint Semiconductor
Orlando
USA

Christophe ZINCK
TriQuint Semiconductor
Orlando
USA

Index

A

absolute temperature, 33, 34, 35, 36
acoustic, 16-17, 111, 143-147, 152-155, 158-159, 166, 171-181, 185, 192, 202, 250, 255, 259-262, 266, 299, 303-305, 316-319, 323-328, 333, 338-340, 344, 349, 351, 378
  impedance, 111
  losses, 16, 206, 265, 308, 316-317, 321, 338, 348
  resonator, 111, 192, 344
  wave, 16-17, 144, 147, 152, 155, 159, 179, 185, 299, 303
actuator, 373-374, 379, 383
admittance, 170-177, 181-184, 188-189, 257, 300, 303, 307-308, 316, 321, 328-330, 335, 339, 351-353, 364
Avogadro, 27, 30-31
axis of symmetry, 91

B

balance, 127
band curvature, 238-239
barrier, 238-244, 267
bimetallic, 374-375, 381-383
Boltzmann, 34-35
boundary conditions, 43, 67, 119, 130, 134, 164-166, 171-172, 208, 266, 319
Bragg, 250, 255, 261-265, 316-318, 322-323, 326, 333-335, 338-339, 344, 351-352
breakdown field, 332, 361, 379-381
BST, 10, 192-193, 203, 206, 315-317, 326-342, 351, 354-355
bulk wave, 252

C

cantilever, 215
capacitance, 59, 96, 99-100, 105, 111, 181, 184, 188-190, 194, 209-212, 233-235, 257-258, 304, 321, 327, 335, 345-346
capacitor, 10, 11, 97-98, 101-103, 111-112, 170, 230, 316, 326
capacity, 36, 46
ceramic, 134, 267
charge, 11, 14, 96-103, 116, 132, 133, 200, 227-228, 233-235, 240, 244-245, 320, 372
Clausius Mossoti, 106
coercive field, 361, 379
conduction, 9, 227, 233-245

conductivity, 86, 230, 233, 259
conjugated variables, 42
constant, 106
constraints, 21, 302, 367, 383
coupling, 28, 46, 67, 85, 92, 129-133, 136-137, 153-155, 161-162, 166-171, 177-180, 183-184, 189-194, 197-199, 203-206, 218, 251, 254-260, 265-267, 273, 298-312, 316-318, 321-323, 326-329, 332-340, 343-349, 352-354, 358-360, 364
critical, 26, 258, 267, 303
crystal class, 6, 7, 91, 137, 159, 161, 162, 165
  mesh, 14, 89, 149, 200-201, 306
  mesh lattice, 50
  structure, 12, 105, 200, 253
crystalline structure, 1
crystallization, 317, 327, 333, 338, 361
Curie, 5, 7, 12, 17-19, 23, 49, 52-53, 57, 60-61, 100, 109, 111, 120, 138, 192, 199, 203, 327
  temperature, 17-19, 26, 49, 52, 57, 60, 100, 138, 192, 199, 205, 327
  temperature system, 26
  -Weiss law, 53, 61, 109
cycle, 21, 55, 130-134, 222-232, 342, 343

D

Devonshire, 25-26, 41, 48, 52, 65
dielectric, 1, 10-11, 14-15, 28, 46-47, 51-58, 61-65, 86, 95-116, 134-135, 159-160, 167, 170, 191-194, 199, 203-205, 210, 222, 231-236, 266, 304, 319-321, 327-328, 332-338, 341-343, 348, 352-355, 359-360
  constant, 11, 28, 47, 51-58, 63-64, 104-112, 116, 167, 170, 191-193, 203-205, 233, 236, 321, 327-328, 332, 335-338, 341-343, 348, 352-355, 359-360
  losses, 110-115, 192, 209, 230, 233-235, 316, 318
  microscopic state, 27-31, 37, 41
  relaxation, 28, 95, 109-112, 115, 348
differential, 31, 36, 42-44, 51, 193, 229
diffraction, 8, 306, 334, 378
dipole, 9, 14-15, 22, 99-106, 127-129, 198
dispersion curve, 263
displacement, 37, 42-47, 50-64, 69-73, 76, 77, 87, 129, 133, 151, 158-160, 169, 193, 200, 202, 207, 210, 216-221, 227, 229, 233, 235, 260, 315, 318, 321, 324, 363-365
domain, 223-225, 298, 316-317, 357-358
dynamic equation, 84

E

efficiency, 358
elastic energy, 43-54, 59, 62-63, 72, 84-87, 119, 152-153, 159-160, 198-201, 379
elasticity, 68, 84, 88-89, 195-196
electric, 99, 103-104, 109, 116
  displacement, 37, 43-47, 50-64, 95, 99, 103-104, 109, 116, 129, 133, 158-159, 169, 193, 202, 210, 227-229, 233-235, 315
  energy, 43, 87, 95, 99, 111, 115-116, 128-133, 160, 183, 198
  energy density, 95, 99, 115-116

field, 9-11, 14-16, 21-23, 26-28, 37, 41-43, 47, 49-51, 55-58, 85, 92, 95-107, 112, 116, 127-129, 132, 136, 139, 144, 157-160, 166, 191-194, 197-205, 208, 210, 220-222, 225-236, 242-245, 251, 257, 315-316, 331-332, 336, 341-349, 360, 371, 376
electrical
displacement, 42
energy, 42
field, 12
electrode, 96-98, 102, 111, 116, 181, 211-213, 219, 222-225, 243, 256-258, 305-306, 309, 326-327, 338-340, 345, 360, 363-364
electromechanical, 129-136, 160-162, 168, 171, 177-179, 183-184, 189, 197-199, 254-260, 265-267, 300-307, 311-312, 316-323, 328, 334, 343-344, 347-349, 358
electronic, 236
affinity, 237
electrostriction, 15, 47, 51, 119, 191-197, 202, 222, 332-333, 336, 349, 354
energy, 26-56, 59, 62-67, 72, 84-88, 95, 99-100, 104, 111, 115-116, 119-120, 128-134, 138, 152-153, 159-162, 176, 183, 193, 198-201, 205, 233-244, 250, 262-263, 301-305, 308, 318, 343, 349-350, 354-355, 372, 379
engraving, 213, 254, 268
entropy, 27-29, 33-43, 57, 64, 98, 119
equilibrium, 26-28, 31-43, 49-54, 60-63, 71, 77-81, 128, 197-198, 219, 223, 231, 237, 341, 375, 381
etching, 252, 258, 261, 266, 326, 340, 345, 361-362

F

Fermi, 236-242
ferroelastic, 224
ferroelectric, 1, 11, 14-15, 18, 21-22, 26, 43, 47-55, 59, 62, 65, 100, 105, 108, 111, 138, 193, 200, 204, 215, 219, 222, 225-230, 236, 316-317, 342-346, 360
ferroelectricity, 1, 9, 21, 111, 225-226, 328
field, 55, 83, 109, 219
of breakdown, 351
Fowler-Nordheim, 242-243
free energy, 26, 43-45, 49, 56, 100, 119, 138, 193, 349, 354-355
frequency of
antiresonance, 170, 173, 177, 184-186, 316-317, 321, 343, 346, 349, 352
resonance, 170, 175-178, 182-185, 208, 218, 251, 254, 257-258, 265-267, 300, 316-317, 321-322, 335, 343-346, 364-367, 371
function of state, 32, 39, 42, 45

G, H

Gauss, 97-98, 103, 153
theorem, 97-98, 103
Gibbs, 43-55, 59, 62-63, 119, 128, 198
energy, 43, 52, 55
heat, 26-27, 31-32, 35-40, 44, 87, 255
Helmholtz, 43, 193, 349
Hooke, 67, 68, 73, 76, 78, 83, 92, 145, 153
Hooke's law, 104
hysteresis, 21, 55, 57, 100, 191, 192, 222, 223, 224, 225, 226, 227, 228, 230, 232, 331, 335, 342, 343, 346

I, J, K, L

ilmenite, 9-10, 16-17, 348
impedance, 146-147, 153, 158, 166, 171-181, 184-185, 189-190, 209, 228, 234, 250, 256, 259-261, 266, 273-274, 300, 318-339, 351-353, 364
impermittivity, 46, 194, 203, 349
intensive variables, 42
irreversible, 31, 68
joule, 234, 267, 372
Kramers-Kronig, 112-115
Landau, 25-26, 50
latent heat, 26, 49-52, 60, 64
lattice, 1-9, 16-17, 250, 338, 351-352
lead titanate, 105
lithium niobate, 303, 309, 348
lno, 10, 17-18, 135, 305, 309, 348
longitudinal wave, 136, 148, 151, 156, 161-162, 165-166, 170-172, 261, 304, 318
loop, 21
lto, 10, 18, 135, 348

M, N, O

Maxwell, 44-46, 86, 153, 319
  relations, 120
mechanical energy, 42, 67, 104, 130-134, 161-162, 198, 205, 372
microscopic model, 197-199
microsystems, 67, 95, 366, 371, 374
Miller, 7, 394
mirror, 17, 255, 261-265, 303, 316-318, 322-323, 326, 333-335, 338-339, 344, 351, 366-371
mode, 53, 57, 134, 137, 163, 166, 170-171, 174, 192, 209-211, 215-219, 225, 243, 252-253, 264, 292-293, 298-300, 303-305, 318, 321, 325, 328, 331, 335-336, 346-349, 353, 363-367
  soft, 53, 57, 109
molybdenum, 180, 258-259
morphotropic, 19, 51, 348
nonlinearity, 50, 197-198
oxide, 9, 242-252

P

paraelectric, 11, 15-20, 26, 43, 47-53, 59-62, 65, 89, 91, 105, 108, 138, 192-193, 197, 204, 236, 331, 340, 355
pass band, 303
permittivity, 10-11, 50, 86, 97, 111-112, 115, 136, 191-195, 203, 222, 227, 233, 236, 333
perovskite, 9-10, 14-22, 25, 49, 67, 105, 110, 192, 316, 334
phase, 8, 14, 18-26, 43, 47-53, 59-64, 91, 100, 108-111, 114, 138, 144-145, 151-153, 157, 192, 197, 220, 234, 297, 305, 309, 316-317, 324-326, 331, 334, 338, 344-348, 355, 359, 363
  diagram, 19-20, 51
  transition, 26, 43, 47
phenomenological, 25, 50, 57, 109, 205, 315, 336, 349, 355
piezoelectric coefficient, 359
  resonator, 322, 329, 344, 355
piezoelectricity, 1, 5, 9, 22, 44-46, 51, 84-85, 119-121, 126-130, 138, 153-160, 169, 191, 195-197, 207, 321, 344
plane of symmetry, 123, 137
platinum, 180, 224, 258, 305-306, 368
polarizability, 53, 57, 100, 107-109, 200
polarization, 9, 13-17, 20-23, 26, 43, 47-59, 62-63, 95-115, 127-129, 133, 138-139, 144-153, 156, 161-162, 191-194, 199-202, 208, 213,

219-232, 305, 316, 344, 348, 379, 391
remanent, 9, 22, 51, 111, 138, 213, 226-232, 344
spontaneous, 13, 14-16, 21, 100, 108-109, 127, 133, 199, 202, 226, 316
power flow, 300
pressure, 39, 40, 41, 68, 78, 88, 361, 364-366
pyroelectricity, 1, 5, 9
PZT, 10, 18-23, 51-53, 59, 91, 105, 109-110, 134-135, 142, 208, 213-224, 316, 331, 342-348, 358-373, 377-383, 387, 390, 394

Q, R

quartz, 1, 9, 12, 91, 192, 221, 249-255, 292-295, 298, 303
range, 112-113
reflection, 167, 261-263, 266, 300, 303-305
relative permittivity, 191, 233
relaxor, 191
resistance, 10, 181-183, 209-215, 234, 329, 334-336, 373-375, 379
resonance frequency, 57
resonator, 17, 130, 163, 172, 176-177, 181-193, 202, 250-268, 272, 299, 303-304, 316-318, 321-323, 326-330, 333-341, 344-355
reversible, 68, 96, 223
RF, 215, 262, 267, 292-294, 297, 303-307, 311-312, 317, 326-327, 332-334, 338, 343-347, 351, 355, 361, 373, 384, 390, 395
rhombohedral, 4, 7, 17-21, 346
rigidity, 194, 377

S

Schottky, 240, 241, 242
sensor, 359-361, 364-366
set, 164-165
shear, 18, 76, 81-82, 111, 136-137, 149, 156, 165-166, 173, 194, 253, 262-263, 304-305, 309, 316, 348
wave, 137, 149, 165-166, 304
silicium, 295
silicon, 1, 18, 90, 209, 215, 219, 252-254, 261, 268, 299, 301-302, 305, 309-311, 327-329, 360-361, 366, 372-373
sol-gel, 327, 361, 387
space charge, 240, 244-245
sputtering, 327, 361, 368
STO, 315-317, 331-342, 348, 355, 378, 396
Stoney, 376-378, 396
strain, 42-45, 67-77, 80-86, 89, 120, 125, 136, 145, 149, 152-153, 157, 160, 208, 211, 349, 375-377
stress, 25-27, 42-45, 51, 58-59, 78-88, 120, 145, 148-149, 152, 157-159, 164, 171-174, 205, 250, 324, 327, 345, 348, 362, 365-366, 369, 375-386
surface wave, 136
system, 6-7, 17-18, 25-43, 46, 50, 57, 61, 68, 90, 111, 115, 119, 150-151, 198, 230, 354, 358, 366-367, 371-372, 375-376

T

tensile, 68, 376
tension, 15, 216
tensor, 46-47, 74-91, 104-105, 120-121, 125, 144-145, 149, 152, 155, 158-159, 194-196
tetragonal, 4, 100, 221
thermodynamic, 21, 25, 26, 28, 32, 34, 36, 42, 43, 49, 50, 51, 52, 64, 65, 119, 138, 192, 199, 202, 237, 315, 333, 348, 354

thermodynamic model, 192, 315, 333
thermodynamics, 26, 32, 36, 39, 44-45
transducer, 298-301, 304, 310
transition
first order transition, 60
second-order transition, 52
phase, 49, 50, 60, 64, 108, 138
trigonal, 6-7, 17
tunnel, 240-244

V, W, Y, Z

variables
conjuguated, 50
extensive, 42, 88
of state, 32
viscoelastic losses, 303
voltage, 15, 43, 96, 111-113, 116, 167-169, 185, 192-193, 202, 209-214, 219-230, 233-235, 240-245, 315-320, 327-335, 339-354, 359-365, 369-373, 377-381
work, 25, 31-32, 35-41, 44, 86-87, 109-111, 116, 131, 191-192, 317, 338, 343, 361
function, 236-239
working, 210, 385
wurtzite, 10, 16-17
yield, 267
zinc oxide, 9